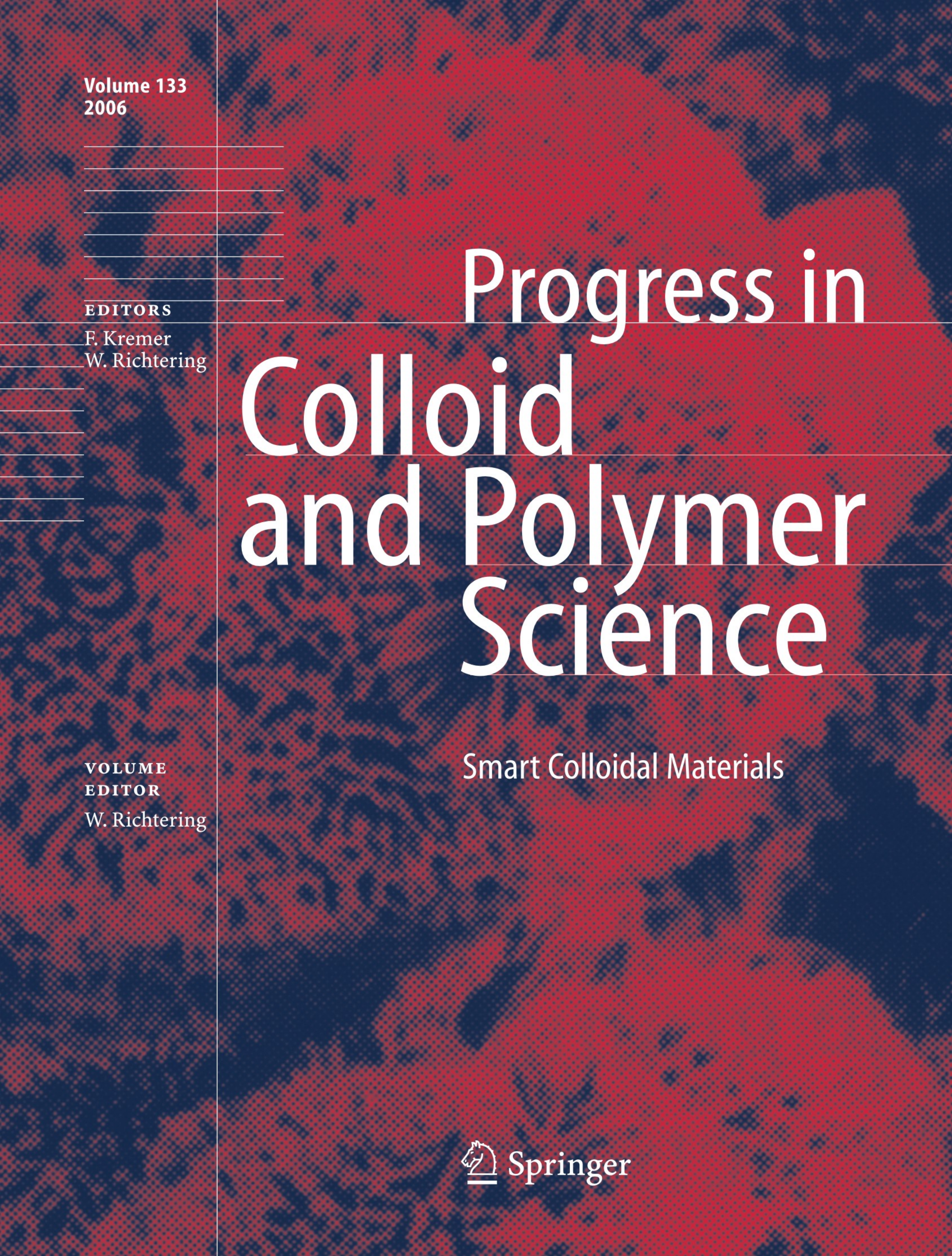

Volume 133
2006

EDITORS
F. Kremer
W. Richtering

Progress in Colloid and Polymer Science

Smart Colloidal Materials

VOLUME EDITOR
W. Richtering

Springer

Progress in Colloid and Polymer Science · Volume 133 · 2006

Progress in Colloid and Polymer Science

Recently Published and Forthcoming Volumes

Smart Colloidal Materials
Volume Editor: Richtering, W.
Vol. 133, 2006

Characterization of Polymer Surfaces and Thin Films
Volume Editors: Grundke, K., Stamm, M., Adler, H.-J.
Vol. 132, 2006

Analytical Ultracentrifugation VIII
Volume Editors: Wandrey, C., Cölfen, H.
Vol. 131, 2006

Scattering Methods and the Properties of Polymer Materials
Volume Editors: Stribeck, N., Smarsly, B.
Vol. 130, 2005

Mesophases, Polymers, and Particles
Volume Editors: Lagaly, G., Richtering, W.
Vol. 129, 2004

Surface and Colloid Science
Volume Editor: Galembeck, F.
Vol. 128, 2004

Analytical Ultracentrifugation VII
Volume Editors: Lechner, M. D., Börger, L.
Vol. 127, 2004

Trends in Colloid and Interface Science XVII
Volume Editors: Cabuil, V., Levitz, P., Treiner, C.
Vol. 126, 2004

From Colloids to Nanotechnology
Volume Editors: Zrinyi, M., Hórvölgyi, Z. D.
Vol. 125, 2004

Aqueous Polymer Dispersions
Volume Editor: Tauer, K.
Vol. 124, 2004

Trends in Colloid and Interface Science XVI
Volume Editors: Miguel, M., Burrows, H. D.
Vol. 123, 2004

Aqueous Polymer – Cosolute Systems
Volume Editor: Anghel, D. F.
Vol. 122, 2002

Molecular Organisation on Interfaces
Volume Editor: Lagaly, G.
Vol. 121, 2002

Lipid and Polymer-Lipid Systems
Volume Editor: Nylander, T.
Vol. 120, 2002

Progress in Colloid and Polymer Science

Editors: F. Kremer, Leipzig and W. Richtering, Aachen

Volume 133 · 2006

Smart Colloidal Materials

Volume Editor:
Walter Richtering

Springer

The series Progress in Colloid and Polymer Science is also available electronically (ISSN 1437-8027)

- Access to tables of contents and abstracts is *free* for everybody.
- Scientists affiliated with departments/institutes subscribing to Progress in Colloid and Polymer Science as a whole also have full access to all papers in PDF form. Point your librarian to the Springerlink access registration form at http://www.springerlink.com

ISSN 0340-255X
ISBN-10 3-540-32701-0
ISBN-13 978-3-540-32701-1
DOI 10.1007/11593256
Springer Berlin, Heidelberg, New York

Springer is a part of Springer Science + Business Media

http://www.springer.com

Printed in Germany

Cover design: eStudio Calamar S. L., F. Steinen-Broo, Pau/Girona, Spain

Typesetting and production: LE-TEX Jelonek, Schmidt & Vöckler GbR, Leipzig

Printed on acid-free paper

Progr Colloid Polym Sci (2006) 133: V

PREFACE

This volume contains selected papers presented at the 42nd Biennial Meeting (Hauptversammlung) of the Kolloid-Gesellschaft held at the RWTH Aachen University September 26–28, 2005. The meeting's emphasis was given to "Smart Materials: Foams, Gels and Microcapsules" but also provided a general overview on current aspects of colloid and polymer science in fundamental research and applications.

The contributions in this volume are representative of the diversity of research topics in colloid and polymer science. They cover a broad field including the investigation of synthesis and properties of advanced temperature sensitive particles and their biomedical applications, drug delivery systems, foams, capsules, vesicles and gels, polyelectrolytes, nanoparticles surfactants and hybrid materials.

The meeting brought together people from different fields of colloid, polymer, and materials science and provided the platform for dialogue between scientists from universities, industry, and research institutions.

Walter Richtering

Progr Colloid Polym Sci (2006) 133: VI–VII
© Springer-Verlag 2006

CONTENTS

Polymer Particles and Capsules

Polyelectrolytes, Colloidal Interactions

Surfactants

Particles and Characterization

Progr Colloid Polym Sci (2006) 133: 1–8
DOI 10.1007/2882_058

Daoji Gan
L. Andrew Lyon

Amphiphilic, Peptide-Modified Core/Shell Microgels

Daoji Gan
Present address:
E&A Company, Indianapolis, IN, USA

Daoji Gan · L. Andrew Lyon (✉)
Georgia Institute of Technology,
School of Chemistry and Biochemistry,
Atlanta, GA 30332-0400, USA
e-mail: lyon@chemistry.gatech.edu

Abstract Thermoresponsive poly(*N*-isopropylacrylamide) (pNIPAm) core/shell particles bearing primary amine groups in either core or shell were prepared via two-stage, free radical precipitation polymerization, using 2-aminoethyl methacrylate (AEMA) as a comonomer. The amine groups were then used to initiate ring-opening polymerization of γ-benzyl *L*-glutamate *N*-carboxyanhydride (BLG-NCA), producing poly(γ-benzyl L-glutamate) (PBLG) side chains covalently anchored to the particles. Photon Correlation Spectroscopy (PCS) and ^{1}H NMR were employed to characterize these particles. A shift of phase transition to a lower temperature and an increase in particle deswelling volume ratios were observed as a result of grafting hydrophobic PBLG chains to the particles. Further studies by ^{1}H NMR in different solvents indicate that the PBLG chains grafted from the particle shell phase separate on the pNIPAm networks in aqueous media but remain well solvated in DMSO. Together, these results suggest that both core- and shell-grafted architectures can be synthesized with equal ease, and that the particle structure and colloidal behavior can be manipulated by tuning the relative solubility of the network and graft portions of the particle.

Keywords Microgel · Core/shell · PBLG · pNIPAm · Phase separation

Introduction

Considerable research attention has been paid to the stimuli-responsive polymers since they can offer many great potential applications in biomedical fields and in the creation of environmentally responsive materials. Polymers that respond to pH [1], temperature [2], light [3], and protein binding [4] have been reported. Among these polymers, thermosensitive poly(*N*-alkylacrylamides), particularly poly(*N*-isopropylacrylamide) (pNIPAm), have been most widely studied [2, 5–7]. In aqueous media, pNIPAm exhibits a “coil-to-globule” phase transition around 31 °C, which is commonly referred to as a lower critical solution temperature (LCST). This is due to disruption of water-polymer hydrogen bonds and the concomitant hydrophobic association of isopropyl groups. The phase-separating nature of pNIPAm can be exploited to synthesize microgels in the sub-micron size range by precipitation polymerization. Such particles are colloidally stable and possess a sharp volume phase transition (VPT) near the polymer LCST [6]. Furthermore, strong modulation of the physical properties of these particles is observed at the phase transition, including hydrophobicity, porosity, refractive index, colloidal stability, scattering cross section, and electrophoretic mobility. Along with this progress, the particles that have a more advanced architecture have been pursued to generate multifunctional properties. One example of these could be the responsive core/shell or core/corona particles that have been synthesized either to spatially localize the chemical functionalities to the particles [1, 8–11], to render thermoresponsity to non-responsive particles [12, 13], or to modify a specific physical property of the particles [14].

Previously, we have reported preparation of multiresponsive core-shell particles via incorporation of poly (acrylic acid) into the pNIPAm particles [1]. The particles appeared to be sensitive to both solution temperature and pH. It was also found later that introduction of small amounts of hydrophobic monomer units into the particle shell could significantly change the particle deswelling kinetics without perturbation of the transition thermodynamics [15]. The results suggest that the location of functional groups is very important in the design of responsive colloidal gels. In this contribution, core/shell particles that contain primary amine groups in either the core or the shell were first constructed using the same two-stage polymerizations described previously [1, 9, 11, 15–21]. The amine-bearing particles were then used to initiate another polymerization, producing a hydrophobic polypeptide poly(γ-benzyl L-glutamate) (PBLG) covalently anchored to the desired portion of the particle (Scheme 1). PBLG is an interesting synthetic polypeptide [22] that has been studied in the design of complex colloidal [23] and polymeric structures [24, 25].

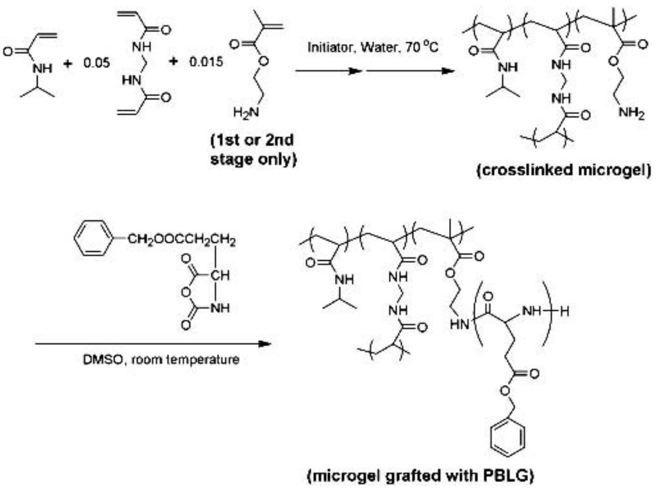

Scheme 1

Experimental Section

Materials

All the chemicals were purchased from Aldrich unless otherwise stated. The monomer *N*-isopropylacrylamide (NIPAm) was recrystallized from hexanes (J.T. Baker) before use. The cross-linker *N*,*N′*-Methylenebis(acrylamide) (BIS), and 2-aminoethyl methacrylate (AEMA), 2,2′-azobis(2-methylpropionamide) dihydrochloride (ABMPAm), and dimethyl sulfoxide (DMSO) were used as received. The amino acid γ-benzyl L-glutamate *N*-carboxyanhydride (BLG-NCA) was synthesized via the reaction of γ-benzyl L-glutamate (BLG) with excess phosgene/benzene solution (Fluka) in dry tetrahydrofuran (THF) at 65 °C; it was purified by crystallization from petroleum ether [22]. Water used in all synthesis and measurements was distilled, and particulate matter was removed via a 0.2 µm filter incorporated into a Barnstead E-Pure system that was operated at a resistance of 18 MΩ.

Synthesis

Low polydispersity pNIPAm microgels were prepared by free-radical precipitation polymerization, using ABMPAm (1 mol % based on the monomer NIPAm) as a cationic initiator and BIS (5 mol %) as a crosslinker. Core/shell microgels were constructed via two-stage polymerization, where the particle core prepared at the first stage served as nuclei in the second-stage polymerization. It should be emphasized that the polymer synthesized in the second stage preferentially precipitates onto the existing seed particles, leading to formation core/shell morphology [1, 8, 16, 26]. Both core particles and core/shell particles were purified via dialysis (Spectra/Pro 7 dialysis membrane, MWCO 10 000, VWR) against water for 14 days, with daily replacement of fresh water. Grafting of poly(γ-benzyl L-glutamate) (PBLG) to the microgels was achieved using primary amine groups incorporated into the particles to initiate ring-opening polymerization of BLG-NCA (Scheme 1). Table 1 lists the chemical compositions and particle size information of microgels used in this study.

Samples C and C–NH_2

To synthesize simple core particles (sample **C**) and amine-modified core particles (sample $C-NH_2$), NIPAm, BIS, and AEMA (1.5 mol % based on NIPAm, Sample $C-NH_2$ only) were dissolved in degassed water with a NIPAm concentration of 0.01 g/mL. The solution was bubbled with nitrogen for 2 h, followed by addition of ABMPAm to start the polymerization. The reaction was then carried out at 70 °C for 6 h.

Sample C/S–NH_2 and C–NH_2/S

To prepare sample C/S–NH_2, NIPAm, BIS, and 1.5 mol % AEMA were introduced to a suspension of sample **C**; the polymer concentration of the dispersion of sample **C** was that which resulted from the initial synthesis of sample **C**. Sample $C-NH_2/S$ was prepared via addition of NIPAm and BIS to a suspension of sample $C-NH_2$. The monomer concentrations used in both shell syntheses were 0.01 g/mL. Both reaction mixtures were nitrogen-bubbled at 70 °C for 2 h. Addition of the ABMPAm triggered the second-stage polymerization, which was then carried out at 70 °C for 6 h.

Table 1 Chemical compositions and particle size information of pNIPAm-based microgels

Sample	Core [a] AEMA, mol-% [b]	R, [c] nm	Polyd, % [c]	Shell [a] AEMA, mol-% [b]	Core-shell R, [c] nm	Core-shell Polyd, % [c]	PBLG Grafts Mass, wt % [e]	PBLG Grafts R, [c] nm	PBLG Grafts R, [d] nm
C	0	102	22						
$\mathrm{C/S-NH_2}$	0	102	22	1.5	124	23			
C/S-BLG10	0	102	22	1.5	124	23	10	128	112
C/S-BLG20	0	102	22	1.5	124	23	20	135	124
C/S-BLG60	0	102	22	1.5	124	23	60	– [f]	136
$\mathrm{C-NH_2}$	1.5	106	20						
$\mathrm{C-NH_2/S}$	1.5	106	20	0	125	17			
C-BLG10/S	1.5	106	20	0	125	17	10	120	109
C-BLG20/S	1.5	106	20	0	125	17	20	117	107

[a] Both core and shell were synthesized with BIS (5 mol % based on monomer, NIPAm) as a cross-linker

[b] feed ratio based on NIPAm

[c] Particle radii (R) and polydispersity (Polyd.) were measured by PCS at 25 °C in water suspension

[d] radius measured in DMSO at 25 °C

[e] feed ratio of BLG-NCA compared to the microgel used

[f] not measurable due to formation of flocs

Sample C/S-BLG10 and C/S-BLG20

The freeze-dried sample $\mathrm{C/S-NH_2}$ (0.07 g) was re-dispersed in 15 mL of DMSO, to which BLG-NCA (10 wt % for **C/S-BLG10**, and 20 wt % for **C/S-BLG20**, based on the $\mathrm{C/S-NH_2}$ used) was introduced. The reaction mixture was vigorously stirred at room temperature for 3 days. After this reaction was completed, 15 mL water was added to the solution, and the organic solvent was removed via dialysis against water for 10 days.

Sample C-BLG10/S and C-BLG20/S

To a $\mathrm{C-NH_2/S}$ suspension in DMSO, BLG-NCA (10 wt % for **C-BLG10/S**, and 20 wt % for **C-BLG20/S**, based on the $\mathrm{C-NH_2/S}$ used) was added, and the grafting reaction was carried out using the same procedure as described above.

Measurements

Photon Correlation Spectroscopy (PCS)

The particle sizes and the size distributions in aqueous solutions were measured by PCS (Protein Solutions, Inc.), with a programmable temperature controller. Prior to taking measurements, the particle solutions were allowed to thermally equilibrate at each temperature for 10 min. Longer equilibration times did not lead to variations in the observed hydrodynamic radii, polydispersities, or scattering intensities. All correlogram analyses were performed with manufacturer-supplied software (Dynamics v.5.25.44, Protein Solutions, Inc.). The data presented below are the averaged values of 20 measurements, with a 15 s integration time for each measurement. The deswelling volume ratios (V/V^*) of the particles were calculated via the relation: $V/V^* = (R/R^*)^3$, where R and R^* are the PCS measured particle radii at the measured temperature and at 25 °C, respectively.

^{1}H NMR

The freeze-dried particles were re-dispersed in either D_2O or DMSO-d_6, and the spectra were then recorded at ambient temperature using a Varian Unity 300 MHz NMR spectrometer. The water peak caused by residual water inside the particles was supressed, in order to more efficiently observe the proton signals of the particles.

Results and Discussion

Synthesis

In these studies, the pNIPAm-based particles were prepared via free radical, precipitation polymerization in aqueous solution at a temperature (70 °C) well above the LCST of pNIPAm. At that temperature, water is a good solvent for the monomer but a poor one for the polymer. Therefore, the growing polymer chains, once reaching a critical length, precipitate from the solution and form stable particles via coagulation of multiple unstable nuclei and by monomer and oligomer capture. A cationic initiator (ABMPAm) renders to the particles positively charged, which is largely responsible for the colloidal stability of the particles. In the synthesis, a crosslinker (BIS) is used to generate polymeric networks, and thus maintain the spherical shape and network connectivity of the particles once the solution is cooled back to room temperature. To incorporate primary amine groups into the particles, a cationic comonomer (AEMA) bearing a terminal primary amine is copolymerized with NIPAm and BIS.

The core-shell pNIPAm particles were prepared by two-stage polymerization, where the particles prepared at the first stage served as nuclei in the second stage. The oligomers that precipitate from the aqueous solution are preferentially captured by the existing particle cores, which are relatively more hydrophobic and partially deswollen at the reaction temperature [1, 8, 16, 26]. As the polymerization proceeds, the sizes of the existing particles continue to grow, leading to formation of core-shell morphology. Both theoretical prediction and experimental measurements have demonstrated that the total particle number remains constant so that the particle size is only a function of amount of polymer produced at this stage [27, 28]. As such, introducing AEMA at different stages in the polymerization can be employed to locate the amine groups in the particle core or in the shell.

The amine-bearing particles were then used to initiate the ring-opening polymerization of BLG-NCA in DMSO [25], producing PBLG side chains covalently anchored to the particles. Replacement of DMSO with water via dialysis yields a particle/water suspension. Given the much more hydrophobic character of PBLG and higher mobility of these grafted side chains compared to the crosslinked polymer main chains, the grafted PBLG chains are expected to lead to a change in the particle structure and morphology, and thus modulate the physical properties. To investigate the effects of the location of grafted side chains on the particle properties, the PBLG was grafted from either particle core or shell. The chemical compositions and particle size information for these particles are summarized in Table 1.

PBLG Chains Grafted from the Microgel Shell

To investigate the influence of PBLG grafting from a microgel shell, sample $C/S-NH_2$ that contained 1.5 mol % AEMA in the shell was prepared. Shown in Fig. 1 are the PCS measurements of the parent core particles and the core/shell particles as a function of solution temperature. For sample **C**, a simple pNIPAm microgel, the particle sizes gradually decrease with solution temperature until the VPT range (31–36 °C), where a sharply reduced particle size is observed (Fig. 1a). Once the temperature is raised above the volume phase transition temperature (VPTT), the particle sizes do not change with temperature and the curve reaches a plateau. This type of particle size variation has been widely documented as being due to expulsion of water from the particle as pNIPAm becomes insoluble in water at temperatures above the LCST[8]. This temperature induced "coil-to-globule" transition, is a result of disruption of water-polymer hydrogen bonds and concomitant formation of hydrophobic associations among isopropyl groups of pNIPAm. Addition of a pNIPAm shell that contains 1.5 mol % AEMA (sample $C/S-NH_2$) leads to a very smooth phase transition (Fig. 1a) with an increased size relative to sample **C** both below and above the pNIPAm LCST.

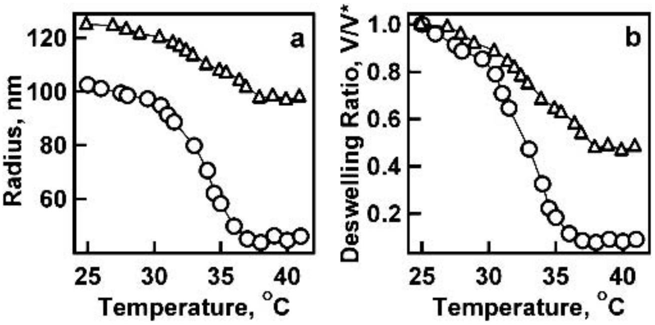

Fig. 1 Hydrodynamic radii (*panel a*) and normalized particle deswelling volume ratios (*panel b*) of samples **C** (*circles*) and $C/S-NH_2$ (*triangles*) as a function of solution temperature

To directly compare the phase transitions of the core particles and the core-shell particles, the PCS measured particle size variations were normalized to as particle deswelling volume ratios by the calculation method described in Experimental Section. After normalization, these two particles clearly show some difference in the transition behavior (Fig. 1b). Introduction of small amounts of hydrophilic and charged AEMA to the particles results in a broadened transition that apparently shifts to a slightly higher temperature. In addition, the particle deswelling volume ratio in the collapsed state is significantly reduced, i.e. the core/shell particles do not deswell to the same degree as the core particles. These changes in phase transition behavior can reasonably be ascribed to a reduced AEMA-rich phase near the particle periphery. Given the more hydrophilic character of pAEMA compared to pNIPAm, it is reasonable to assume that more pAEMA units would be located at the periphery of the particles due to phase separation during polymerization. Indeed others have combined the techniques of NMR, chemical titration and zeta potential measurements to clearly show the presence of pAEMA-rich phases at the particle periphery in these types of particles [29]. If indeed the outer portion of the shell is largely pAEMA, one would expect an overall decrease in the degree of deswelling, as pAEMA does not display LCST behavior in water and should therefore remain water-swollen even in the presence of a deswollen core.

Shown in Fig. 2 are the PCS measurements of pNIPAm particles shell-grafted with hydrophobic PBLG side chains. For comparison, the measurements of un-grafted particles are also shown in the same figure. Samples **C/S-BLG10** and **C/S-BLG20** are the particles prepared with addition of 10 wt % and 20 wt % of BLG-NCA to sam-

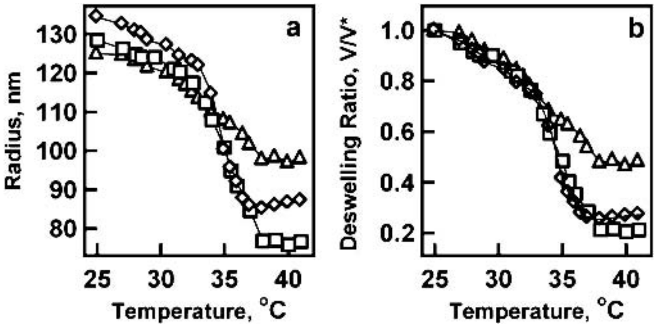

Fig. 2 Dependence of hydrodynamic radii (*panel a*) and particle deswelling volume ratios (*panel b*) on the solution temperature for samples $C/S-NH_2$ (triangles), **C/S-BLG10** (*squares*), and **C/S-BLG20** (*diamonds*)

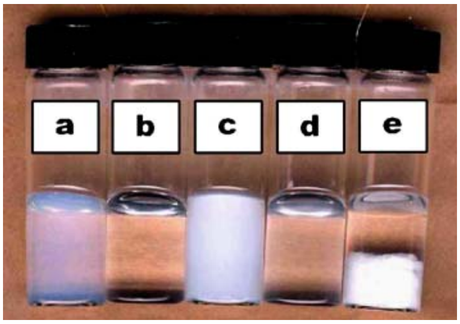

Fig. 3 pNIPAm-based microgels (0.005 g/mL) in different solvents: a, $C/S-NH_2$ in water; b, **C/S-BLG20** in DMSO; c, **C/S-BLG20** in water; d, **C/S-BLG60** in DMSO; e, **C/S-BLG60** in water

ple $C/S-NH_2$. The grafted PBLG chains cause an increase in particle size below the VPTT but a decrease in size above the VPTT relative to the parent core/shell particle (Fig. 2a). Upon normalization as deswelling volume ratios, the difference in the phase transition of those particles can be more easily observed (Fig. 2b). Grafting of PBLG chains to the particles results in a shift of the transition to a lower temperature, and concomitantly an increase in particle deswelling volume ratios in the fully collapse state. This is expected because the hydrophobic PBLG chains were anchored to the particles by amine groups of pAEMA units, which, due to loss of their hydrophilicity and charge, no longer produce a highly swollen particle periphery.

It is interesting to note that **C/S-BLG10** and **C/S-BLG20** have quite similar phase transition behaviors, with the same breadth and sharpness of the transition curves (Fig. 2b). Only a slight difference in the particle deswelling volume ratios is observed in the fully collapsed state. Since these two particles were prepared by the same amounts of initiator (shell-localized amines), it is reasonable to assume that they contain the same number of PBLG chains, and **C/S-BLG20** thus has longer PBLG chains than **C/S-BLG10**. Calculations based on the feed ratios in grafting reactions suggest that the average number of repeat units of PBLG chains are about 20 and 40 for **C/S-BLG10** and **C/S-BLG20**, respectively. In aqueous solution, the hydrophobic PBLG apparently cannot exist as extended chains, and they must fold into a "globule" to minimize contact with water. This effect will be discussed later in the paper in the context of ^{1}H NMR measurements.

Interestingly, longer PBLG chains have a detrimental effect on particle stability in water. Shown in Fig. 3 are representative particles in different solvents. Like pure pNIPAm particles, $C/S-NH_2$ containing 1.5 mol % AEMA in the shell produces a slightly turbid suspension in aqueous media (Fig. 3a) due to slight mismatch of refractive indices between water and the microgels. Sample **C/S-BLG20** is found to be colloidally stable in aqueous media, but the suspension becomes more turbid (Fig. 3c). However, large particle flocs can be seen in Fig. 3e for sample **C/S-BLG60**. In contrast to the particles in water, all particle suspensions in DMSO, including $C/S-NH_2$ (not shown) appear completely transparent, regardless of the grafted PBLG content (Fig. 3b and 3d). It should be emphasized that even though **C/S-BLG60** precipitates completely in water (Fig. 3e), it still produces very stable microgels without any precipitates in DMSO (Fig. 3d). PCS measurements indicate that **C/S-BLG60** exists as monodispersed, colloidal particles in DMSO, with an average particle size larger than that of **C/S-BLG10** and **C/S-BLG20** (Table 1). The flocculation of **C/S-BLG60** in water can be explained as formation of inter-particle hydrophobic association driven by the higher average molecular weight of the grafted PBLG chains. Obviously, this is not the case in DMSO since both pNIPAm and PBLG have good solubility in this solvent.

To further investigate the structure of the particles, ^{1}H NMR experiments were performed after re-dispersing the freeze-dried sample into deuterated solvents. Shown in Fig. 4 are representative NMR spectra of **C/S-BLG20** in two different solvents, DMSO-d_6 and D_2O. DMSO is a good solvent for both pNIPAm and PBLG segments, while we expect D_2O to be a good solvent only for the pNIPAm portion of the microgels. The characteristic proton signals of isopropyl groups from pNIPAm units are observed as Peak **a** and **b**, which can be assigned to the methyl and methylene protons, respectively. Peak **f** at 5.0 ppm is contributed by the α-methylene protons of benzyl groups from PBLG segments, whose aromatic proton signals are located at 7.1–7.5 ppm (Peak **e**). The proton signal **i** from PBLG is buried under a large peak arising from the complex formed between DMSO and residual H_2O. The proton signals **c** and **d**, contributed from polymer backbone of the particles, overlap with signal **h** and **g** of PBLG. In all, the proton assignments are consistent with the chemical structure of the polymer.

Inspection of the NMR spectrum suggests that Peak **b** and **f**, exclusively contributed from pNIPAm and PBLG, respectively, are well resolved. Therefore, taking the ratio

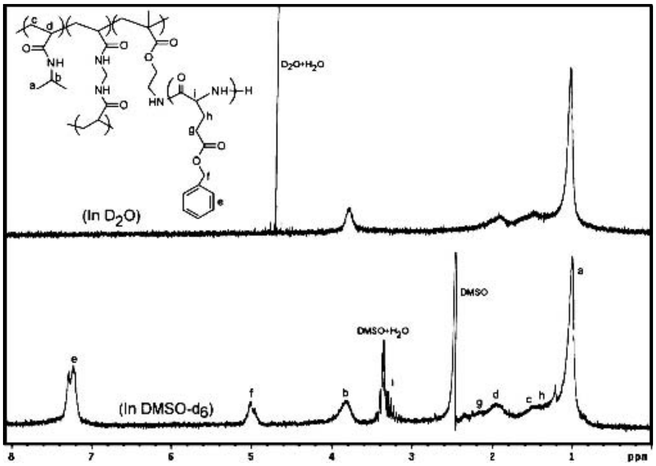

Fig. 4 ^{1}H NMR spectra of sample **C/S-BLG20** in D_2O and DMSO-d_6. The grafted PBLG side chains cannot be detected in D_2O due to phase separation

of integrated areas of these two peaks should give some information about the chemical compositions of the particles. It is surprising to find that the PBLG content observed by NMR technique is approximately two times that which is calculated from the feed ratio used in the reaction. The same phenomenon was observed for **C/S-BLG10** (about 1.5 times apparent excess). In a striking contrast, the ^{1}H NMR spectrum recorded in D_2O, which is a good solvent for pNIPAm but a poor one for PBLG, only shows the signals of pNIPAm segments with the PBLG resonances being completely absent from the spectrum.

Based on these results, a morphological description is proposed to explain the possible behavior of PBLG chains anchored to the pNIPAm particle shell. Water is a good solvent for pNIPAm (at ambient temperature) but a non-solvent for PBLG. In aqueous media, the PBLG chains may thus be forced to phase separate into a globular conformation on or inside the microgel, leading to disappearance of the proton signals of PBLG in D_2O. This phenomenon is quite similar to the widely reported micelle formation by amphiphilic block copolymers, where the hydrophobic blocks form the core and the hydrophilic ones form the shell of the micelle in aqueous media [30–32].

By comparison, DMSO is a good solvent for both PBLG and pNIPAm, thereby allowing the PBLG side chains to adopt a solvated chain conformation. The apparently higher PBLG content observed by NMR in DMSO-d_6 may arise from the inherent heterogeneity of the microgel particles. The particle core becomes compressed after shell addition and has a denser network structure [18–20]. Therefore the relaxation time of some pNIPAm units inside the particles may be too short to be detected by NMR. In contrast, the grafted PBLG chains located at the particle shell have large mobility, thus the relaxation time is long enough to be followed by the NMR techniques.

PBLG Grafted from the Microgel Core

Given the inherent porosity of microgels, we examined the feasibility of grafting PBLG chains from particle core. For this purpose, another type of core/shell particle, $C-NH_2/S$, was synthesized such that the particle core contained 1.5 mol % AEMA, while the shell was composed of pNIPAm. The temperature dependence of the particle sizes is shown in Fig. 5 for the core particles and the core/shell particles. The core particles display an elevated VPTT and a relatively small degree of deswelling, presumably due to the presence of the cationic monomer. Compared to the core particles, the core/shell particles have increased sizes in both the fully collapsed and swollen state (Fig. 5a). Furthermore, addition of pure pNIPAm shell layer diminishes the function of the hydrophilic AEMA located in the core since the particle shell plays a dominant role in the transition behavior as described in previous publications [18–20]. As a result, the core-shell particles collapse at a lower temperature than the core particles The differences in swelling behavior can be more easily observed when the particle size variations are normalized to deswelling volume ratios (Fig. 5b). Apparently, after addition of pure pNIPAm shell around the AEMA-containing core, the phase transition becomes sharper and shifts to a lower temperature. Along with those changes is a decrease in the deswelling volume ratios at fully collapsed state. All these results are consistent with those of $C/S-NH_2$ discussed above.

^{1}H NMR analysis was performed to determine the chemical compositions of the particles, and thus to evaluate the efficiency of the PBLG grafting to the particles containing amine groups in the core (Fig. 6). The ungrafted particles, $C-NH_2/S$, show proton signals mainly contributed from pNIPAm units, as well as peaks due to DMSO and DMSO/H_2O complex. It is worth mentioning that a broad peak at 7.0–7.6 ppm can be assigned to amide groups of pNIPAm. This signal cannot be detected in D_2O, because exchange of amide protons with D_2O is so fast that the signal is buried in the HDO resonance [33]. Sam-

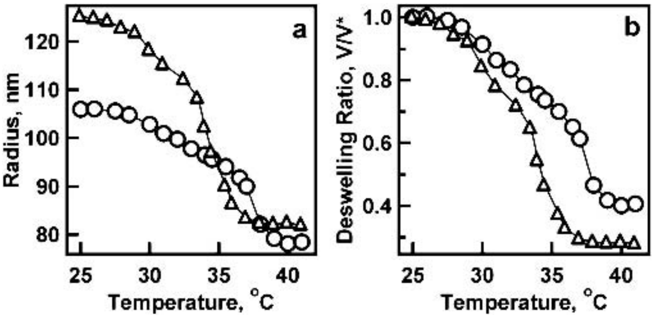

Fig. 5 Variations of hydrodynamic radii (*panel a*) and normalized particle deswelling volume ratios (*panel b*) with solution temperature for sample $C-NH_2$ (*circles*) and $C-NH_2/S$ (*triangles*)

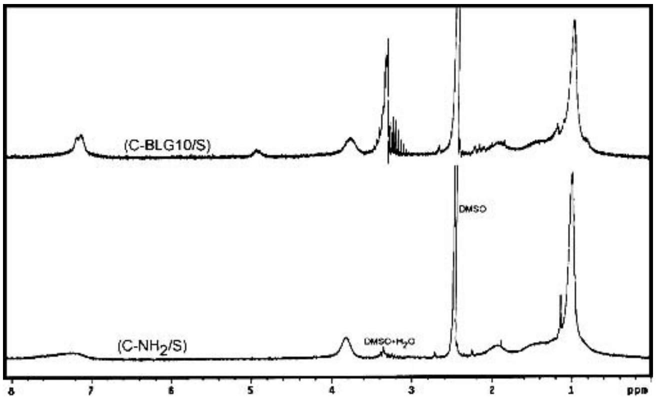

Fig. 6 ^{1}H NMR spectra of samples $C-NH_2/S$ and **C-BLG10/S** in DMSO-d_6

ple **C-BLG10/S** displayes the signature peaks of PBLG chains centered at 5.0 and 7.3 ppm, indicating a successful grafting of PBLG chains from the pNIPAm-AEMA core. The calculation of NMR integration ratios, as described above, shows that the grafted PBLG contents are very close to those used in the momomer feed. Given the previous observation of higher than expected PBLG content for the shell-grafted microgels, it is apparently the case that the core is less compressed and/or the PBLG is more restricted in the core-grafted case, thereby leading to an apparent peak integration that is closer to the predicted value.

The effects of grafting PBLG chains on the phase transition of the particles can be seen from Fig. 7, which shows the PCS measured particle size variations as a function of solution temperature. Here **C-BLG10/S** and **C-BLG20/S** denote particles with 10 and 20 wt %, respectively, of PBLG grafted to the $C-NH_2/S$ particles. Contrary to what was observed for the shell-grafted microgels, **C-BLG10/S** and **C-BLG20/S** have reduced sizes in the swollen and condensed state in comparison to the ungrafted $C-NH_2/S$ (Fig. 7a). These results may suggest that the increased hydrophobicity brought about by grafting PBLG into the particle core decrease the equilbrium swelling volume below the VPTT, as well as a decreased water content in the condensed state.

On the other hand, there are some similarities for the particles with PBLG grafted from either the core or the shell, which can be seen from the normalized particle deswelling volume ratios as shown in Fig. 7b. Again, as a result of grafting PBLG chains to the particles, a relatively sharp phase transition that also shifts to a lower temperature is observed accompanying with an increase in the particle deswelling volume ratios in the fully collapsed state. These results can be ascribed to termination of hydrophilic AEMA units by hydrophobic PBLG chains.

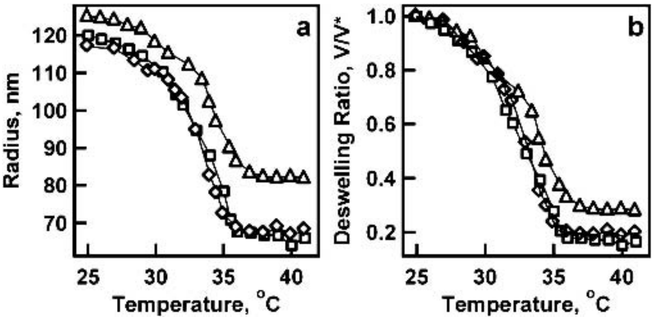

Fig. 7 Hydrodynamic radii (*panel a*) and normalized particle deswelling volume ratios (*panel b*) of sample $C-NH_2/S$ (*triangles*), **C-BLG10/S** (*squares*), and **C-BLG20/S** (*diamonds*) as a function of solution temperature

Conclusions

It has been demonstrated that hydrophobic PBLG chains can be grafted to the pNIPAm particles from either the core or the shell, using particles bearing primary amine groups to initiate ring-opening polymerization of BLG-NCA. As a result of termination of these charged hydrophilic groups in the particles, the phase transition of the particles becomes sharper and shifts to lower temperature, while the particle deswelling volume ratios increase. In aqueous media, the PBLG grafted from particle shell exists as phase separated globules on the particle surface. Surprisingly, for low degrees of polymerization (< 40 monomer units) the shell-grafted PBLG microgels are colloidally stable in water, despite the relative hydrophobicity of the shell. However, longer chains with presumably more conformational flexibility, lead to particle flocculation in water due to interparticle PBLG association.

Acknowledgement LAL acknowledges support from the National Science Foundation Division of Materials Research under Grant No. 0203707.

References

1. Jones CD, Lyon LA (2000) Macromolecules 33:8301
2. Schild HG (1992) Prog Polym Sci 17:163
3. Kungwatchakun D, Irie M (1988) Makromol Chem-Rapid 9:243
4. Kim J, Nayak S, Lyon LA (2005) J Am Chem Soc 127:9588
5. Heskins M, Guillet JE (1968) J Macromol Sci Chem A2:1441
6. Pelton R (2000) Adv Colloid Interface Sci 85:1
7. Saunders BR, Vincent B (1999) Adv Colloid Interface Sci 80:1
8. Berndt I, Pedersen JS, Richtering W (2005) J Am Chem Soc 127:9372
9. Nayak S, Lee H, Chmielewski J, Lyon LA (2004) J Am Chem Soc 126:10258

10. Nayak S, Lyon LA (2004) Angew Chem Int Ed Engl 43:6706
11. Nayak S, Gan D, Serpe MJ, Lyon LA (2005) Small 1:416
12. Makino K, Yamamoto S, Fujimoto K, Kawaguchi H, Ohshima H (1994) J Colloid Interface Sci 166:251
13. Senff H, Richtering W, Norhausen C, Weiss A, Ballauff M (1999) Langmuir 15:102
14. Shiroya T, Tamura N, Yasui M, Fujimoto K, Kawaguchi H (1995) Colloid Surf B-Biointerfaces 4:267
15. Gan D, Lyon LA (2001) J Am Chem Soc 123:7511
16. Gan D, Lyon LA (2001) J Am Chem Soc 123:8203
17. Gan D, Lyon LA (2002) Macromolecules 35:9634
18. Jones CD, Lyon LA (2003) Macromolecules 36:1988
19. Jones CD, Lyon LA (2003) Langmuir 19:4544
20. Jones CD, McGrath JG, Lyon LA (2004) J Phys Chem B 108:12652
21. Nayak S, Lyon LA (2004) Angew Chem 116:6874
22. Fuller WD, Verlander MS, Goodman M (1976) Biopolymers 15:
23. Fong B, Russo PS (1999) Langmuir 15:4421
24. Schmidtke S, Russo P, Nakamatsu J, Buyuktanir E, Turfan B, Temyanko E, Negulescu I (2000) Macromolecules 33:4427
25. Block H (1983) Poly(gama-benzyl-L-glutamate) and other glutamic acid containing polymers. New York
26. Berndt I, Richtering W (2003) Macromolecules 36:8780
27. Marion P, Beinert G, Juhue D, Lang J (1997) Macromolecules 30:123
28. Kawaguchi S, Winnik MA, Ito K (1995) Macromolecules 28:1159
29. Meunier F, Elaissari A, Pichot C (1995) Polym Adv Technol 6:489
30. Thurmond KB II, Kowalewski T, Wooley KL (1996) J Am Chem Soc 118:7239
31. Inoue T, Chen G, Nakamae K, Hoffman AS (1998) J Controlled Release 51:221
32. Zhao Y, Liang H, Wang S, Wu C (2001) J Phys Chem B 105:848
33. Larsson A, Kuckling D, Schonhoff M (2001) Colloids Surf A 190:185

Progr Colloid Polym Sci (2006) 133: 9–14
DOI 10.1007/2882_063

Abdelhamid Elaissari

Thermally Sensitive Colloidal Particles: From Preparation to Biomedical Applications

Abdelhamid Elaissari (✉)
CNRS-bioMérieux laboratory, ENS-Lyon,
46 allée d'Italie, 69364 Lyon cedex 07,
France
e-mail: Hamid.Elaissari@ens-lyon.fr

Abstract This short article is a condensed review of recent work devoted to thermally sensitive based polymer particles and their potential applications as biomolecules carriers in biomedical diagnostic. Firstly, several aspects related to synthesis of different thermally sensitive colloidal particles are presented. Secondly, the general colloidal properties of such particles are reported and illustrated. Finally, some fine applications of reactive, hydrophilic thermally sensitive particles in biomedical diagnostic are briefly presented.

Keywords Adsorption · Biomedical · Concentration · Core-shell · Desorption · Diagnostic · Microgel · Nucleic acid · Protein · Purification · Thermally sensitive

Introduction

Latex microspheres are largely studied according to their exhaustive and numerous applications in various fields: as a chromatography supports in analytical biochemistry, as a carriers in biomedical diagnostic, as a nano-capsules for drug delivery system and in academic studies as a colloidal model. Due to the versatility of the polymerization processes, various polymer latexes have been elaborated and used in numerous applications. Polystyrene-based particles for instance, have long been used as solid phase supports in diagnostic applications and principally in macroscopic agglutination assays [1]. However, in some in-vitro biomedical applications, hydrophilic particles are of great interest in order to avoid non-specific adsorption of proteins and their denaturation [2]. Then, various reactive and hydrophilic particles have been elaborated and evaluated in biomedical applications as a solid support of biomolecules. The hydrophilic character of the particles surface reduces drastically proteins adsorption [3–5] when both pH and salinity are simultaneously controlled. Stimuli-responsive biodegradable materials are reported to be of paramount importance in drug delivery. In biomedical diagnostic, such "smart materials" [6–9] are studied as new tools for biomolecules purifications: extraction, specific adsorption, and concentration enhancement. Various kinds of stimuli-responsive particles have been examined. Recently, pH, salinity- and thermally-sensitive colloidal particles have received an increasing attention as evidenced by the recent numerous papers published last decade [8–10]. In this direction, various thermally sensitive microgel particles have been elaborated and examined in biomedical diagnostic as a solid support of biomolecules [11–13].

Preparation

Various thermally sensitive materials (polymer solutions, gels and particles) have been prepared by controlling the recipe and the polymerization condition as shown in Fig. 1. To some extent, the physical aspect (gel, free polymer chains and particles) of the final polymer material depends: on the polymerization temperature (regarding the LCTS of the corresponding main homopolymer), on the crosslinker and finally, on the nature of used initiator. The gel formation is manly related to amount of used water-soluble crosslinker agent [14, 15]. Whereas, the water-soluble polymer is obtained when the polymerization is conducted in free crosslinker recipe [16]. To obtain particles, various as-

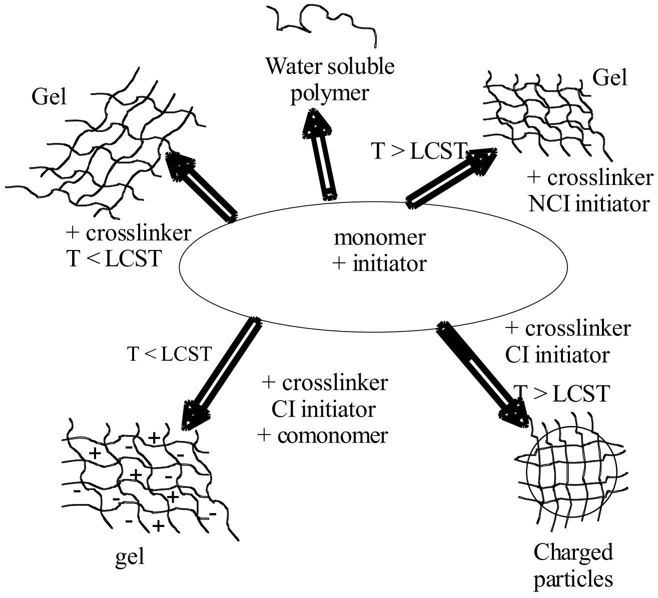

Fig. 1 Thermally sensitive materials. CI: Changed Initiator, NCI: Non Changed Initiator

pect should be controlled [11, 17, 18]: (i) the polymerization reaction temperature should be higher than the corresponding homopolymer low critical solution temperature (LCST), (ii) the colloidal stability should be induced by charge initiator (KPS, V-50 . . .) or the charged comonomer (i.e. acrylic acid) and (ii) the polymerization should be conducted in moderate solid content (preferably less than 5 w/w %) [19]. The preparation of colloidal particles is quite fastidious and delicate since various parameters affect the polymerization rate, the swelling ability of the particles, the amount of the formed water-soluble polymer and consequently, the final properties of the colloidal particles [20]. To prepare such particles, precipitation polymerization is used to obtain microgel particles and the combination of emulsion and precipitation polymerization leads to core-shell particles [12, 21].

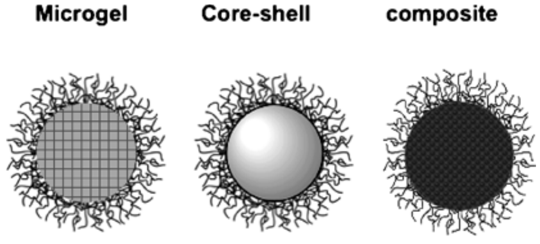

Fig. 2 Thermally sensitive microgel, core-shell and composite microspheres

Since the first works reported by Pelton et al. [11] and by Kawaguchi et al. [22], various reactive thermally sensitive microgel particles were developed such as the preparation of low charged thermally sensitive microgel using (NIPAM/MBA/cationic and anionic initiators) mixture, cyano-functionalized particles (NIPAM/MBA/Acrylonitrile/anionic initiators) [23], amino-containing poly(*N*-isopropylacrylamide) [19], polystyrene core-thermally sensitive shell latex particles [12], magnetic in nature [18, 24]. Nowadays, it is possible to obtain various thermally sensitive particles, from the relatively simple poly(*N*-isopropylacrylamide) microgel to much more complex polymers, polymer matrix and structures (i.e. core-shell, capsules) as shown in Fig. 2.

The optimization of polymerization process with a view to favour the particles formation should take into account the effect of each polymerization parameter (or reactants) on the particles conversion and water soluble-polymer formation (Fig. 3) by examining the amount of water-soluble polymer formation as a function of temperature, crosslinker agent, charged comonomer and charged initiator concentrations.

As expected, an increase of the charged initiator concentration, results in an increase of the formation of water-soluble polymers and a reduction of final particle size. The polymerization temperature must be higher than the LCST of the corresponding homopolymer, in order to promote the precipitation of oligomers formed in aqueous

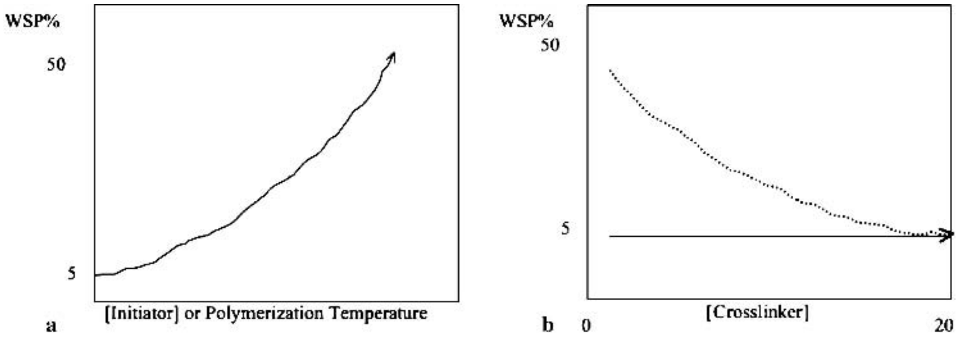

Fig. 3 **a** Influence of water-soluble initiator and temperature on the amount of water-soluble polymer formation. **b** Effect of cross-linking agent concentration on the water-soluble polymer formation

phase. As for the influence of charge initiator, increasing the temperature enhance the amount of water-soluble polymer formation. The concentration of water-soluble crosslinker used in the polymerization recipe should be appropriate in order to favour the crosslinking efficiency of the particles during the polymerization process. But, high crosslinker amount lead to low thermally sensitive particles. The charged comonomer contributes to water-soluble polymer formation and production of low particle size.

Physiochemical and Colloidal Properties

The colloidal characterization of thermally sensitive particles has been investigated by examining principally the effect of temperature on the colloidal properties of the particles. The swelling ability has been principally examined in detail.

Swelling Ability

The swelling ability of the microgels has been investigated as a function of temperature using dynamic light scattering (Fig. 4). Generally, significant reduction of hydrodynamic particle size is observed in the vicinity of the LCST of the corresponding polymer (i.e. 32 °C for *N*-isopropylacrylamide based particles) [25]. The swelling ability was found to be more significant for low crosslinked and low charged microgel particles. In the case of charged microgel particles, the influence of both salinity and pH has been investigated. It is important to notice that the volume phase transition of microgel particles occurs in a wider range of temperatures (5–10 °C) compared to the LCST of linear polymer (i.e. PNIPAM in aqueous phase). The observed swelling ability as a function of temperature is basically a consequence of the increase in the interaction parameter (χ) of the polymer. Interesting work has also been reported by Ballauff et al. [26] by investigating the volume phase transition temperature of thermally sensitive charged core-shell.

Electrokinetic Properties

The electrokinetic properties of thermally sensitive particles are examined by measuring the electrophoretic mobility as a function of temperature, pH and salinity. The general trend is the increase in the electrophoretic mobility (in absolute value) versus temperature. This phenomenon was attributed to the reduction of the particle size, which results in the increase of the interfacial charge density of the particles, and therefore the increase in electrophoretic mobility (at constant pH and salinity) as illustrated in Fig. 4. However, the investigation of electrophoretic mobility as a function of salinity, ions nature, solvent and pH as at constant temperature is questionable. In fact, only few works have been dedicated to such phenomena [27, 28].

Colloidal Stability

Nabzar et al. [28] has reported interesting research work in the colloidal stability of thermally sensitive particles by studying amino-containing *N*-isopropylacrylamide-styrene copolymer particles. The colloidal stability has been examined as a function of both temperature and salinity (at a constant pH). The emanate results from those studies revealed the high colloidal stability below the volume phase transition temperature due to electrosteric stabilization and hydration forces. Whereas, the colloidal stability was considerably reduced above the T_{VPT} as expected. In short, the increase in salt concentration reduces the T_{VPT} and consequently the colloidal stability. Then, the colloidal stability of such stimuli-responsive microgels should take into account both temperature and salinity concentration. To some extent, the colloidal stability of thermally sensitive particles is a reversible process as illustrated in Fig. 5.

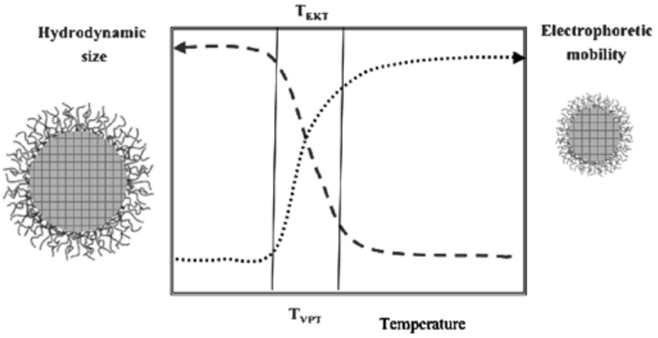

Fig. 4 The effect of temperature on the hydrodynamic size and electrophoretic mobility of PNIPAM based microgel particles. T_{VPT} is the volume phase transition temperature and T_{EKT} is the electrokinetic transition temperature

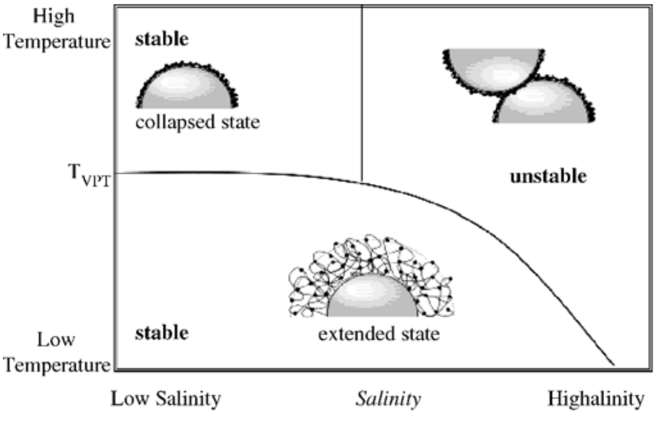

Fig. 5 Colloidal stability diagram of charged thermally sensitive particles as a function of temperature and salinity

Additional Properties

The internal and the interfacial microstructure of thermally sensitive microgel particles and core-shell latexes have been examined using the NMR technique [29] and fluorescence analysis [30] respectively. The NMR study of poly(NIPAM) microgel particles reveals that the water-soluble crossliner used is incorporated in a gradient composition (looser and looser from the core to the shell). This is in agreement with the high reactivity of such crosslinker. The Fluorescence analysis of the core-shell like particles (such as polystyrene-poly(NIPAM)) shows the complexity of the interface as a function of temperature and in some cases, the polystyrene core can be easily reached by the used hydrophobic probe. This point has been examined using fluorescent dye (pyrene).

Applications in Biomedical Diagnosis

Thermally sensitive particles exhibited outstanding capability for the immobilization of biomolecules such as proteins and nucleic acids. Various systematic studies have been reported by investigating the influence of physical chemistry parameters (i.e. pH, salinity, ions nature, temperature etc.) on the adsorption and desorption of biomolecules. Special attention has been focused on the adsorption and release of enzymes as model in drug delivery. The activity of entrapped and released enzyme molecules has been adequately examined. In this part, we will focus on some fine applications of thermally sensitive particles in biomedical diagnostic.

Proteins Purification and Concentration

The adsorption and the desorption of protein (or proteic materials) was found to be principally controlled by the incubation temperature as first reported by Fugimoto et al. [31] and then by Elaïssari et al. [32,33]. The adsorbed amount of protein material onto thermally sensitive particles was examined in view of both electrostatic and hydrophobic interactions. As a general tendency, the proteins adsorption was principally controlled by the adsorption temperature (Fig. 6), which regulates the charge density and the hydration of the particles. The desorption of adsorbed proteins is then favoured by cooling the polymer particles bearing adsorbed proteins. Using such approach, protein concentration and purification are achieved by controlling the adsorption and the desorption, temperatures, the pH and the salinity during the incubation steps in order to enhance the desorption efficiency (below the volume phase transition temperature). The protein concentration is first reported to be possible by using anionic thermally sensitive core-shell magnetic particles [34]. The protein concentration step was examined by performing the desorption in a small volume.

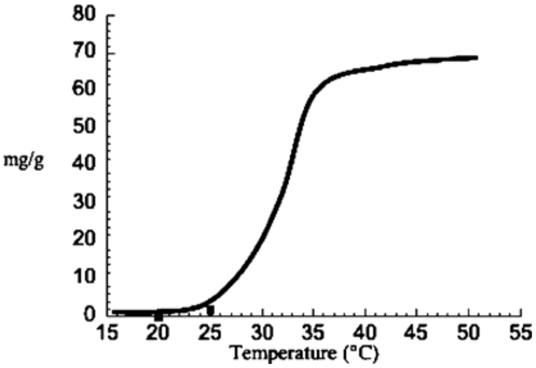

Fig. 6 Schematic illustration of proteins adsorption (in mg/g) onto thermally sensitive particles as a function of temperature [16, 18]

Nucleic Acids Extraction, Purification, Concentration and Amplification

Cationic thermally sensitive particles provide capacities that are potentially interesting for biomedical diagnosis and samples preparation (Fig. 7). The presence of cationic charges favours the attractive electrostatic interactions of nucleic acid molecules (ssDNA, DNA and RNA) negatively charged [32, 35]. It is interesting to notice that the adsorbed nucleic acids onto cationic poly(NIPAM) based particles can be desorbed by increasing both the pH and ionic strength. Whatever the incubation temperature, the quantities of nucleic acid molecules adsorbed decrease with increasing the pH, due to the reduction of cationic character of the particles. Then, to select the adsorption of nucleic acids rather than proteins, the adsorption should be performed below the T_{VPT}. To extract protein from any

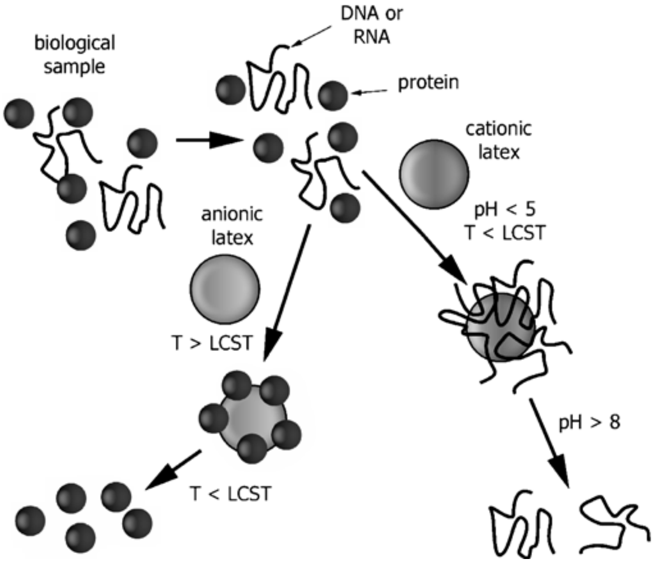

Fig. 7 Principle of separation and concentration of nucleic acids and proteins

biological sample containing nucleic acids, the use of negatively charged particles is strongly recommended.

Furthermore, amplification of captured nucleic acid molecules can be performed directly in the presence of such cationic hydrophilic particles without any release step. This is directly related the presence of hydrated shell and to total consumption of cationic charges on the particles. Consequently, for low particles amount, the PCR (Polymerase Chain Reaction) [17, 20] amplification of captured nucleic acids can be performed without removing the particles from the PCR medium, which reduces steps and then reduction in time consuming.

Conclusions

Although widespread, the use of hydrophilic monomers and functional comonomers in the precipitation polymerization often brings complex problems, some of them being far to be solved or even well understood principally in the case of combined polymerization processes. The distribution of water-soluble crosslinker in the polymer matrix is also questionable. In fact, the control of the crosslinker reactivity, will lead to well-defined microstructure particles.

The use of charged water-soluble comonomer leads to high amount of soluble oligomers and polymer chains. In such polymerization, special attention should be focussed on the reduction of water soluble-polymer formed generally after particles formation.

The colloidal characteristics of poly(*N*-alkylacrylamide) or poly(*N*-alkylmethacrylamide) based microgel particles depend on temperature, salinity and pH. The incubation temperature principally governs the swelling ability, the hydrodynamic size, the electrokinetic properties and the colloidal stability. The volume phase transition temperature is mainly related to the chemical composition of the polymer particles.

Such stimuli-responsive particles are explored in biomedical applications in order to improve the sensitivity via samples preparation (i.e. purification and concentration of targeted biomolecules). The cationic particles are explored as new tool for nucleic acids extraction, purification and concentration. Interestingly, such hydrophilic particles are compatible with various enzymatic nucleic acids amplifications. The use of negatively charged thermally sensitive particles was found to be useful for protein purification and concentration. This application has been extended to bacteria and viruses detection and found to be of great interest.

Acknowledgement I would like to express sincere gratitude to all students and permanent researches for their scientific contributions.

References

1. Kawaguchi H, Sakamoto K, Ohtsuka Y, Ohtake T, Sekiguchi H, Iri H (1989) Biomaterials 10:225
2. Kondo A, Higashitani K (1992) J of Coll Int Sc 150(2):344
3. Suzawa T, Shirahama H (1991) Advances in Colloid and Interface Science 35:139
4. Elgersema AV, Zsom RLJ, Norde W, Lyklema J (1990) J Colloid Interface Sci 138:145
5. Norde W (1986) Advances in Colloid and Interface Science 25:267
6. Chytry V, Netopilik M, Bohdanecky M, Ulbrich K (1997) J Biomater Sci Polym Edn 8:817
7. Baudys M, Serres A, Ramkissoon C, Kim SW (1997) Journal of Controlled Released 48:289
8. Park TG, Hoffman AS (1992) J Appl Pol Sci 46:659
9. Park TG (1999) Biomaterials 20:517
10. Kondo A, Kaneko T, Higashitani K (1994) Biotech Bioeng 44:1
11. Pelton RH, Chibante P (1986) Colloid and Surfaces 20:247
12. Hoshino F, Fujimoto T, Kawaguchi H, Ohtsuka Y (1987) Polym J 19(2):241
13. Pichot C, Elaïssari A, Duracher D, Meunier F, Sauzedd F (2001) Macromolecular Symposia 175:285
14. Hino T, Prausnitz JM (1998) Polymer 39:3279
15. Dong LC, Hoffman AS (1986) Journal of Controlled Released 4:223
16. Fujishige S, Kubota K, Ando I (1989) J Phys Chem 93:3311
17. Kawaguchi H, Sugi Y, Ohtsuka Y (1981) J Appl Pol Sci 26:1649
18. Kondo A, Kamura H, Higashitani K (1994) Appl Microbiol Biotechnol 41:99
19. Meunier F, Elaïssari A, Pichot C (1995) Pol Adv Tech 6:489
20. Elaïssari A (2003) In: Birdi KS (ed) Handbook of surface and colloid chemistry, second Edition, CRC Press second edition:581
21. Hoshino F, Kawaguchi H, Ohtsuka Y (1987) Polym J 19(10):1157
22. Kawaguchi H, Kawahara M, Yaguchi N, Hoshino F, Ohtsuka Y (1988) Polym J 20:903
23. Zhou G, Elaïssari A, Delair T, Pichot C (1998) Colloid & Polymer Science 276:1131
24. Sauzedde F, Elaïssari A, Pichot C (1999) Colloid & Polymer Science 277:1041
25. Wu C (1998) Polymer 39:4609
26. Kim JH, Ballauff M (1999) Colloid Polym Sci 277:1210
27. Pelton RH, Pelton HM, Morphoresis A, Rowell RL (1989) Langmuir 5:816
28. Nabzar L, Duracher D, Elaïssari A, Chauveteau G, Pichot C (1998) Langmuir 14:5062
29. Guillermo A, Cohen-Addad JP, Bazil JP, Duracher D, Elaïssari A, Pichot C (2000) Journal of Polymer Science Part B: Polymer Physics 38:889
30. Castanheira EMS, Martinho JMG, Duracher D, Charreyre MT, Elaïssari A, Pichot C (1999) Langmuir 15:6712
31. Kawaguchi H, Fujimoto K, Mizuhara Y (1992) Colloid Polym Sci 270:53

32. Elaïssari A, Holt L, Meunier F, Voisset C, Pichot C, Mandrand B, Mabilat C (1999) J Biomater Sci Polym Edn 10:403
33. Duracher D, Elaïssari A, Mallet F, Pichot C (2000) Langmuir 13:9002
34. Elaïssari A, Bourrel V (2001) Journal of Magnetism and Magnetic Materials:151
35. Elaïssari A, Rodrigue M, Meunier F, Herve C (2001) Journal of Magnetism and Magnetic Materials:127

Progr Colloid Polym Sci (2006) 133: 15–21
DOI 10.1007/2882_053

POLYMER PARTICLES AND CAPSULES

Juergen Siepmann
Florence Siepmann

Microparticles Used as Drug Delivery Systems

Juergen Siepmann (✉) ·
Florence Siepmann
College of Pharmacy, University of Lille,
3 rue du Professeur Laguesse, 59006 Lille,
France
e-mail: juergen.siepmann@univ-lille2.fr

Abstract Microparticles offer various significant advantages as drug delivery systems, including: (i) an effective protection of the encapsulated active agent against (e.g. enzymatic) degradation, (ii) the possibility to accurately control the release rate of the incorporated drug over periods of hours to months, and (iii) an easy administration (compared to alternative parenteral controlled release dosage forms, such as macro-sized implants). Desired, pre-programmed drug release profiles can be provided which match the therapeutic needs of the patient. This article gives an overview on the most important past, current and future strategies using drug-loaded microparticles to improve the efficiency of various medical treatments. Special emphasis is laid on the different types of preparation techniques that are commonly used, the physicochemical properties of the devices and practical examples illustrating the considerable benefits of this type of advanced drug delivery systems. But also the major challenges and obstacles to be overcome during the development and production of these pharmaceutical dosage forms are pointed out.

Keywords Advanced drug delivery · Controlled drug release · Microencapsulation · Release mechanism · Solvent extraction/evaporation

Controlled Drug Delivery

Controlled drug delivery systems can be extremely helpful to optimize the effects of pharmaco-therapies [1–3]. Each drug has a characteristic so-called “minimal effective concentration”, below which no therapeutic effects occur, and a characteristic “minimal toxic concentration”, above which undesired toxic side effects occur (Fig. 1). The range in-between is the so-called “therapeutic range”, or “therapeutic window”. Depending on the type of drug, this window can be rather narrow. To be able to optimize the therapeutic effects of a medical treatment it is of major importance to maintain the drug concentration within the therapeutic range over prolonged periods of time. This is particularly true for highly potent drugs, such as anticancer drugs. If the entire drug dose is administered at once using conventional pharmaceutical dosage forms, e.g. standard tablets, the whole amount is rapidly released into the stomach, absorbed into the blood stream and distributed throughout the human body. Consequently, the rate at which the drug reaches its site of action is often high. Depending on the therapeutic range and administered dose, the risk of toxic side effects can be considerable. Subsequently, as no continuous drug supply is provided and as the human body eliminates the active agent, the concentration of the latter decreases again. In some cases, the therapeutic range is attainted during only very short time periods (Fig. 1, thin curve).

To overcome these restrictions, to be able to control the resulting drug concentration-time-profiles at the site of action, controlled drug delivery systems can be used. The idea is to incorporate/surround the drug within/by a ma-

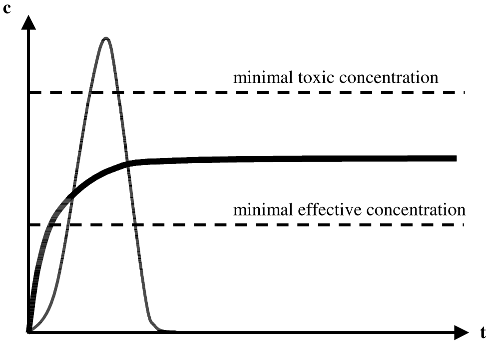

Fig. 1 Schematic presentation of the "therapeutic window" of a drug and possible drug concentration time profiles upon administration of oral immediate (*thin curve*) and parenteral controlled release dosage forms (*thick curve*) (*c* denotes the drug concentration at the site of action in the human body, *t* the time after administration)

trix former (very often polymer are used), which controls the resulting release rate. Various processes, such as diffusion, erosion and/or swelling can be involved in the control of the overall drug release rate, resulting in a broad spectrum of possible release patterns. For example, a continuous drug supply can be provided, compensating the elimination of the active agent out of the human body, thus, resulting in about constant drug concentrations at the site of action over prolonged periods of time (Fig. 1, thick curve).

Various types of controlled release dosage forms are available on the market, including tablets, capsules, pellets (spherical devices with a diameter of about 0.5–1.5 mm), patches and microparticles. The latter have significant advantages over the other types of dosage forms, such as: (i) the possibility to avoid the gastrointestinal tract (certain drugs loose their activity upon oral administration) by intramuscular or subcutaneous injection; (ii) easy administration using standard needles (in contrast to alternative controlled release parenteral dosage forms, such as macrosized implants); (iii) the possibility to directly administer the drug into the target tissue (thus, reducing the drug concentrations in the rest of the human body and the risk of related undesired side effects); (iv) the possibility to reach target tissues, which are normally not accessible for the drug (e.g., the Central Nervous System); and (v) no need of surgical removal of empty remnants, if biodegradable matrix formers are used. Poly(lactic-co-glycolic acid) (PLGA) is a frequently used biodegradable matrix former, because it is biocompatible and degraded into lactic and glycolic acid, two naturally occurring substances in the human body. However, the pH within PLGA-based microparticles can significantly decrease due to the accumulation of acidic degradation products and some drugs (especially proteins) can consequently loose their biological activity (upon denaturation).

Process Technology

Very different technologies can be used to prepare drug-loaded, controlled release microparticles, such as milling of films, spray-drying of drug-matrix former solutions, coacervation techniques and solvent extraction/evaporation methods. The latter are frequently used, especially at the lab scale. An excellent recent review on the current state of the art of this preparation technology is given by Freitas et al. [4]. At a small scale, the most frequently applied technique is the so-called "beaker method", which is illustrated in Fig. 2. The principle steps for the preparation of microparticles using a water-in-oil-in-water (W/O/W) technique are shown: (1) The drug is either dispersed or dissolved within an inner aqueous phase; (2) The latter is emulsified into an organic solution of the matrix forming polymer. Droplet formation is caused by mechanical stirring, e.g. using a propeller. (3) The obtained water-in-oil (W/O) emulsion is dispersed within an outer aqueous phase, resulting in a water-in-oil-in-water (W/O/W) emulsion. Again, droplet formation is caused by mechanical stirring, e.g. using a propeller. As soon as the organic solvent comes into contact with the outer aqueous phase, it diffuses into the latter. Due to convection and diffusion, the organic solvent reaches the surface of the W/O/W emulsion, at which it evaporates. Thus, the concentration of the polymer in the organic phase continuously increases. At a certain time point, the macromolecules start to precipitate and encapsulate the drug: The microparticles are formed. As steps (1)–(3) are all performed in beakers, this preparation technique is called "beaker method". (4) Subsequently, the microparticles are separated by filtration and

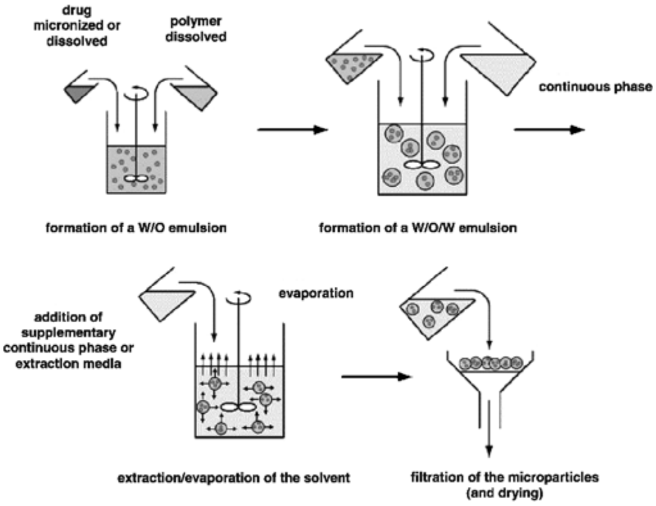

Fig. 2 Schematic illustration of the "beaker method", the most frequently used technique to prepare drug-loaded microparticles by solvent extraction/evaporation at the lab scale (adapted from [4], with permission). As an example, the preparation of microparticles using a water-in-oil-in-water (W/O/W) technique is shown

dried. A major advantage of this technique is that it does not require particularly cost-intensive equipment. However, the upscale of this process technology is not straightforward (in particular, because the "volume : surface ratio" is very important) and often the microparticle size distribution is relatively broad.

An interesting technique allowing to obtain very narrow microparticle size distributions is the so-called "jet excitation method" [5], illustrated in Fig. 3. As an example the preparation of microparticles using an oil-in-water (O/W) extraction/evaporation method is shown. The idea is to dissolve the drug together with the matrix forming polymer in an organic solution. This solution is pumped through a nozzle (nozzle #1), creating a continuous liquid stream. The latter is periodically disrupted into individual droplets due to vibration, caused for example by ultrasound. The droplets are falling into a collection/extraction fluid bath, containing an aqueous phase into which the organic solvent can diffuse. To prevent coalescence of the droplets and deformation upon impact on the surface of the fluid bath, generally an outer aqueous liquid stream of "stealth fluid" [being pumped through a second nozzle (nozzle #2)] surrounds the organic drug-polymer solution (Fig. 3). Thus, a biphasic stream is disrupted into biphasic droplets, the organic phase being in the center. As the disruption of the stream can be well controlled and is very reproducible, similar-sized droplets can be generated, resulting in microparticles with very narrow size distributions (Fig. 3).

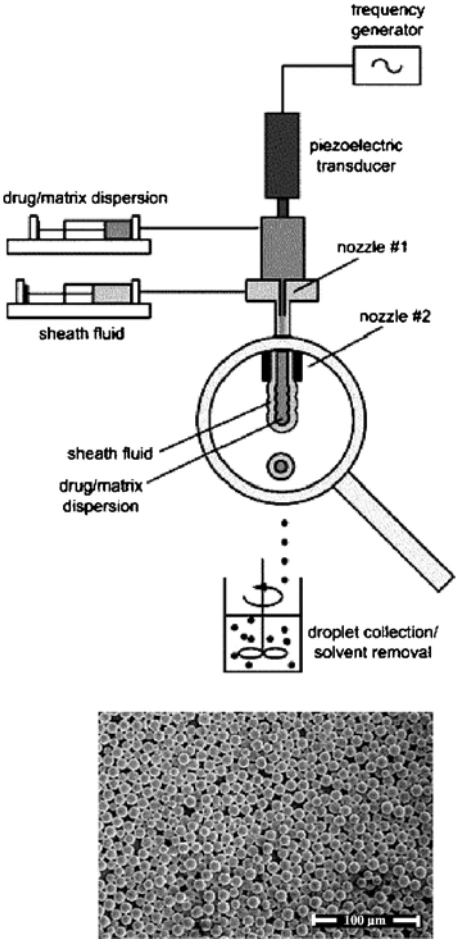

Fig. 3 Schematic illustration of the "jet excitation method" to prepare drug-loaded microparticles with a very narrow size distribution using an oil-in-water (O/W) extraction/evaporation technique (adapted from [4], with permission)

The principle of the so-called "static mixture method" to prepare microparticles by solvent extraction/evaporation is illustrated in Fig. 4 for an oil-in-water (O/W) solvent extraction/evaporation technique. The idea is to pump an organic drug-polymer solution (future inner phase) together with an aqueous phase (future outer phase) through columns containing static obstacles, e.g. baffles. Upon impact with these obstacles the liquid stream is disrupted and droplets of the organic phase are formed within the aqueous phase. If necessary, additional outer aqueous phase can be added afterwards to assure complete polymer precipitation and microparticle formation. One of the major advantages of this method is the possibility to relatively easy upscale the process by putting several static mixtures in parallel (Fig. 4). However, attention has to be paid that all mixing columns are fed with a liquid stream of identical composition. Thus, an efficient pre-blending unit is mandatory.

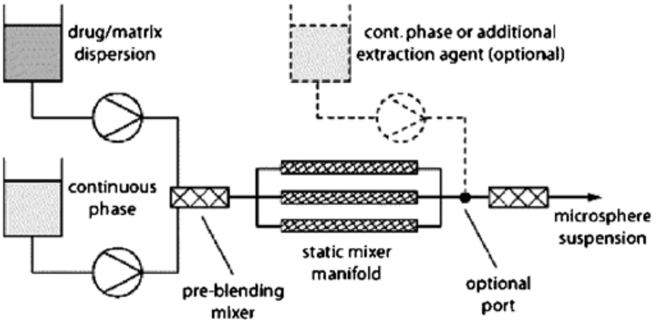

Fig. 4 Schematic illustration of the "static mixture method" to prepare drug-loaded microparticles using an oil-in-water (O/W) extraction/evaporation technique (reprinted from [4], with permission)

Practical Examples

Drug-loaded microparticles (in particular biodegradable ones) can be very useful to improve the efficiency of the treatment of various types of diseases [6–9]. Table 1 gives examples for products, which are commercially available on the market. Since 1989, Lupron® Depot containing the anticancer drug leuprorelin acetate [embedded within a poly(lactic-co-glycolic acid) (PLGA) matrix] is used for

Table 1 Examples for pharmaceutical products based on drug-loaded, biodegradable microparticles available on the market

Drug	Trade name	Company	Application
Leuprorelin acetate	Lupron Depot	Takeda	Prostate cancer
Leuprorelin acetate	Trenantone	Takeda	Prostate cancer
Recombinant human growth hormone	Nutropin depot	Genentech-Alkermes	Growth hormone deficiency
Goserelin acetate	Zoladex	I.C.I.	Prostate cancer
Octreotide acetate	Sandostatin LAR depot	Novartis	GH suppression anticancer
Triptorelin	Decapeptyl	Debiopharm	Cancer
Recombinant bovine somatropin	Posilac	Monsanto	Milk production in cattle
Risperidone	Risperdal Consta	Janssen	Schizophrenia

the treatment of prostate cancer [10]. Scanning electron micrographs of surfaces and cross-sections of these microparticles are given in Fig. 5. Clearly, the particles are spherical in shape and slightly porous. Leuprorelin acetate is a superactive luteinizing hormone-releasing hormone (LH-RH) agonist. Its biological activity is tenfold that of LH-RH. When administered chronically at a higher dose, it paradoxically produces antagonistic inhibitory effects on pituitary gonadotropin secretion and testicular or ovarian steroidogenises ("chemical castration"). These effects, attributable to a down-regulation of the receptors, are temporary and reversible. Importantly, they can be used for the treatment of hormone-sensitive tumors, such as prostate [10] and breast cancer [11] and endometriosis [12], with minimized side effects and avoiding surgical castration. The in vivo efficiency of this type of biodegradable microparticles is illustrated in Fig. 6. At the top, the serum concentration of the drug leuprorelin acetate is indicated, at the bottom the resulting testosterone levels upon monthly subcutaneous injection of the microparticles into rats. Testosterone stimulates the growth of sensitive prostate cancers. Clearly, high initial drug concentrations were observed upon each administration and about constant drug levels in-between. Importantly, the testosterone level is effectively lowered during the entire observation period (except for early time points). Thus, the growth of hormone-sensitive prostate cancers can be reduced. Trenantone® (Takeda) is a similar product, releasing the drug leuprorelin acetate over a longer period of time (during 3 month), being commercially available since 1995.

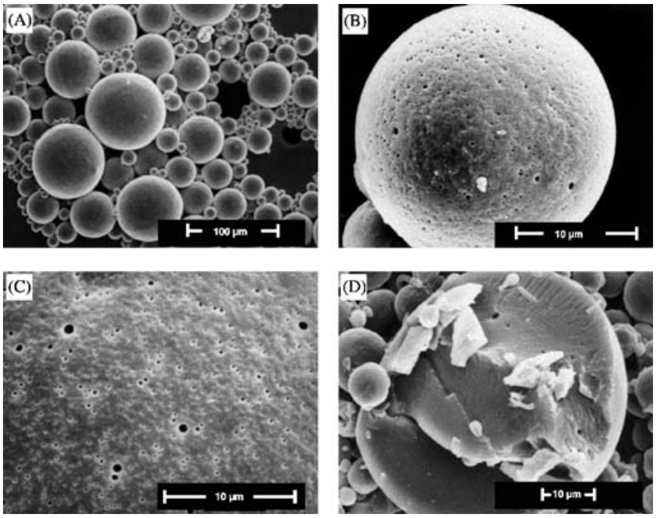

Fig. 5 Scanning electron micrographs of leuprorelin-loaded, poly(lactic-*co*-glycolic acid) (PLGA)-based microparticles (Lupron Depot®) used for the treatment of prostate cancer (adapted from [7], with permission): **A** overview on an ensemble of microparticles, **B** surface of a single (*smaller*) microparticle, **C** surface of a single (*larger*) microparticle, **D** partial cross-section of a single microparticle

In addition to the possibility to accurately time-control the release rate of an incorporated drug, microparticles offer the major advantage to be directly injectable into the target tissue. Thus, the concentration of the drug in other parts of the human body (and related undesired side effects) can be minimized. In addition, potential natural barriers, which might normally hinder the drug to reach its site of action, can be overcome. For example, the Blood-Brain-Barrier (BBB) very well protects the Central Nervous System (CNS) against potential toxins and, thus, renders the treatment of brain diseases often extremely difficult. Only low molecular weight lipid-soluble molecules and a few peptides and nutrients can cross this barrier to a significant extent, either by passive diffusion or using specific transport mechanisms. Thus, for most drugs it is difficult to achieve therapeutic levels within the brain tissue. In

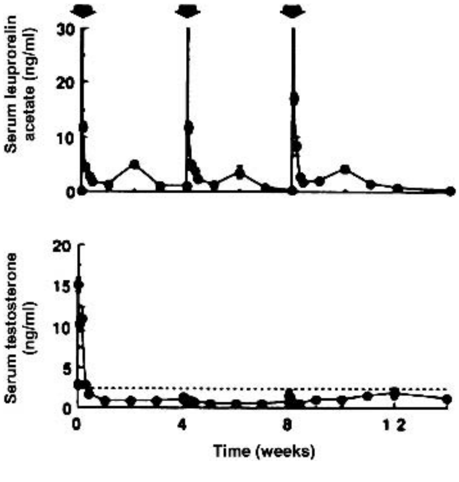

Fig. 6 In vivo efficiency (in rats) of poly(lactic-*co*-glycolic acid) (PLGA)-based, leuprorelin-loaded microparticles used for the treatment of prostate cancer (adapted from [7], with permission)

addition, highly potent drugs (e.g., anticancer drugs and neurotrophic factors) that may be necessary to be delivered to specific areas in the CNS, often cause serious toxic side effects in other parts of the human body (especially if high systematic concentrations are required to assure sufficient drug levels in the target tissue).

The stereotaxic injection of drug-loaded, biodegradable microparticles directly into the brain tissue (intracranial administration) offers a very promising possibility to overcome this restriction (Fig. 7). Optimized drug concentrations at the site of action can be provided over prolonged periods of time, improving the efficiency of the pharmacotherapy. An example for this type of treatment method is illustrated in Fig. 8. The black circle represents a brain tumor. As is can be seen, the surrounding environment has already been infiltrated by single tumor cells (Fig. 8A). If possible (if operable), the surgeon removes the tumor (Fig. 8B). However, due to the risk to affect vital functions, the surgeon cannot remove large parts of the surrounding tissue. Thus, the risk is very high that single tumor cells remain within the brain, leading to local recurrences of the cancer. In the case of malignant glioma, the average life-time expectancy is only about 11 months after diagnosis [13]. To reduce the risk of local tumor recurrences, anticancer drug-loaded, biodegradable microparticles can be injected into the walls of the resection cavity during the same operation, when the crane is still open (Fig. 8C). These microparticles release the drug in a pre-determined, time-controlled manner, assuring optimized drug concentrations over prolonged periods of time at the site of action. Recently, a phase II clinical trial with 5-fluorouracil (5-FU)-loaded, poly(lactic-co-glycolic acid) (PLGA)-based microparticles has shown promising results [14].

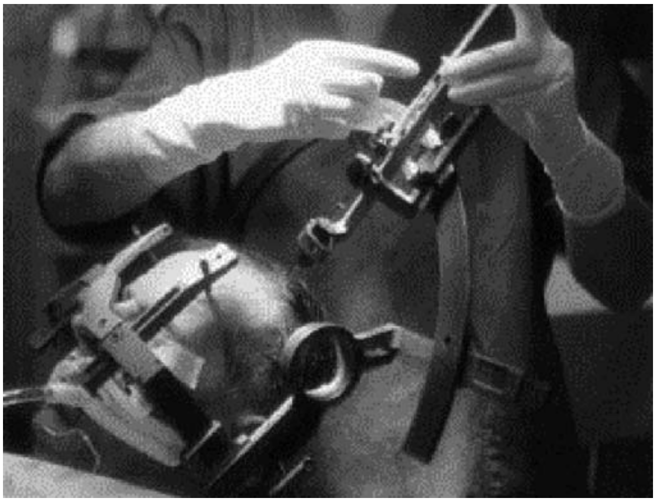

Fig. 7 Stereotaxic implantation of drug-loaded, biodegradable microparticles into human brain tissue. This procedure allows an accurate and well-controlled injection into the targeted brain regions (adapted from [15], with permission)

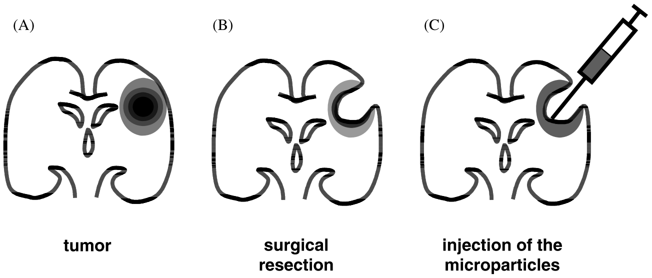

Fig. 8 Schematic cross-sections through human brains illustrating the treatment of brain cancer by surgical removal and subsequent stereotaxic injection of anticancer drug-loaded, biodegradable microparticles into the walls of the resection cavity: **A** before surgery, the *black circle* represents the tumor, **B** after surgical tumor resection, **C** during microparticle administration

Furthermore, the stereotaxic administration of anticancer drug-loaded microparticles allows the treatment of *in*operable brain tumors. In these cases, the tumors are located in brain regions that are not accessible for the surgeon without significant damage of major vital functions. Figure 9 shows a magnet resonance image and computed tomography (CT) scans of a human brain before and after microparticle injection into such tumors. Clearly, the controlled drug delivery systems could effectively be administered into the target tissue (Fig. 9C), releasing the drug in a time-controlled manner directly at the site of action. A clinical phase I trial showed first promising results with this novel treatment method [15].

Another example for the use of controlled release microparticles is the optimization of the growth and differentiation of cells used for cell therapy (living cells are implanted into human tissue). Main restrictions of this type of therapy include limited cell survival, differentiation and integration into the host tissue. The time-controlled release of drugs that can stimulate the growth and differentiation of the implanted cells can help to overcome these restrictions. For example, Tatard et al. [16] incorporated nerve

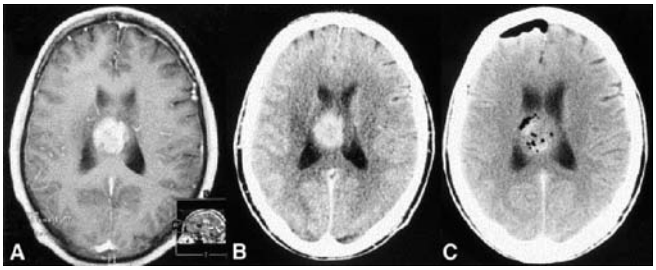

Fig. 9 Administration of anticancer drug-loaded, biodegradable microparticles into human, *in*operable brain tumors: **A** pre-operative magnetic resonance image showing a malignant glioma, **B** pre-operative computed tomography (CT) scan, **C** CT scan after implantation of the microspheres (reprinted from [15], with permission)

growth factor (NGF) in PLGA-based microparticles and obtained promising results. Figure 10A shows a schematic representation of this treatment method: Cells adhere to the microparticles, which release the growth factor in a time-controlled manner. This leads to improved cell survival and differentiation. Figure 10B,C shows optical and scanning electron microscopy pictures of PLGA-based microparticles containing NGF, with PC12 cells adhering to their surfaces. These systems are intended to be implanted into human brains: The differentiated cells can produce dopamine, which is needed to treat Parkinson's disease.

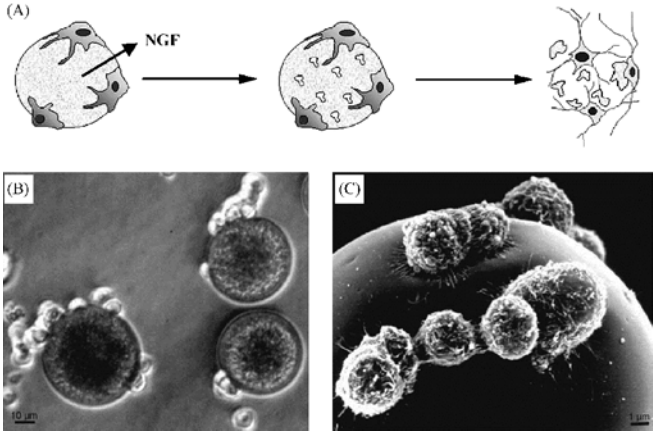

Fig. 10 Drug-loaded microparticles used to optimize cell growth and differentiation in cell therapies: **A** schematic illustration of the concept; **B** optical microscopy picture; and **C** scanning electron microscopy picture of cells adhering to the surfaces of the microparticles (adapted from [16], with permission)

Drug Release Mechanisms from PLGA-based Microparticles

Despite of the steadily increasing practical importance of poly(lactic-co-glycolic acid) (PLGA)-based microparticles as advanced drug delivery systems, yet only little knowledge is available on the underlying physical and chemical processes controlling the resulting drug release rates [17]. This can be attributed to the complexity of the occurring phenomena [18, 19]. Upon contact with aqueous body fluids water diffuses into the system (Fig. 11). Due to concentration gradients the drug subsequently diffuses out of the device. Importantly, the matrix forming polymer PLGA (being a polyester) is cleaved into shorter chain acids and alcohols upon contact with water. This significantly alters the conditions for drug diffusion with time. With decreasing macromolecular weight, the mobility of the polymer chains increases and, thus, the apparent drug diffusivity increases. As water imbibition into PLGA-based microparticles is rapid compared to the subsequent polymer chain cleavage, polymer degradation occurs throughout the entire system ("bulk erosion").

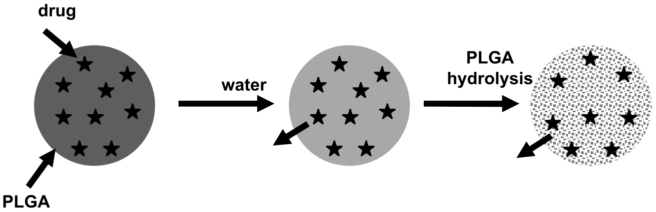

Fig. 11 Schematic illustration of a bulk-eroding, poly(lactic-*co*-glycolic acid) (PLGA)-based microparticle. Water penetration into the system is much faster than polymer hydrolysis

Often, three-phasic drug release patterns are observed with PLGA-based microparticles. An example is illustrated in Fig. 12, showing the release of 5-FU-loaded systems in phosphate buffer pH 7.4. The three phases can essentially be attributed to: (i) pure diffusion at early time points (the very short diffusion pathway lengths lead to high initial drug release rates, so-called "burst effects"); (ii) a combination of drug diffusion, polymer chain cleavage and the limited solubility of 5-FU, leading to approximately constant drug release rates (the increase in the diffusion pathway lengths is compensated by an increase in drug diffusivity); and (iii) to the breakdown of the polymeric network as soon as a critical threshold value is reached, resulting in the disintegration of the microparticles. Consequently, the surface area available for diffusion significantly increases and the diffusion pathway lengths decrease. Both effects result in a pronounced increase in

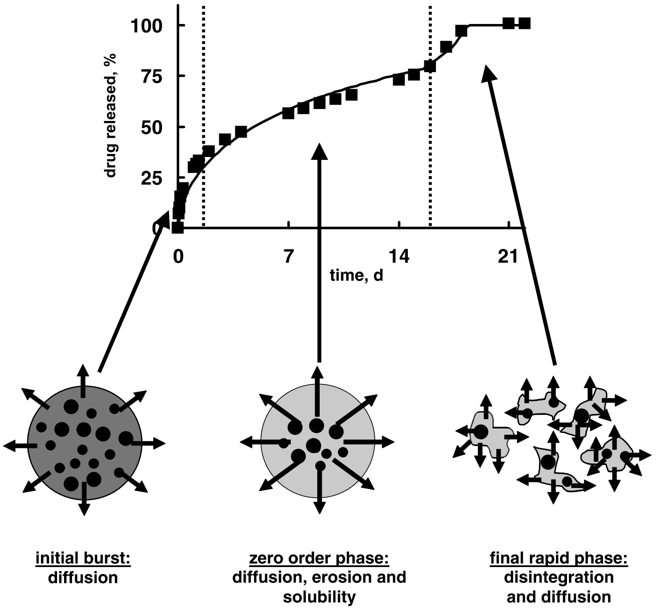

Fig. 12 Drug release from and drug release mechanisms in 5-fluorouracil (5-FU)-loaded, poly(lactic-*co*-glycolic acid) (PLGA)-based microparticles

the resulting drug release rate (final rapid drug release phase), leading to complete drug exhaust.

It has to be pointed out that the composition, inner and outer structure (e.g., porosity), size and preparation technique of the microparticles can significantly affect the underlying drug release mechanisms. Depending on various parameters, including the type of drug and matrix former, drug loading, presence of additional excipients and dimension of the systems, different physical and chemical phenomena can be dominating and control the resulting drug release kinetics. To be able to assure a secure pharmacotherapy, it is obviously highly desirable to know which processes are of importance in the particular product. Furthermore, based on this knowledge the optimization of this type of controlled drug delivery system can be significantly facilitated.

Conclusions

Microparticles can effectively be used as controlled drug delivery systems, allowing to optimize the resulting drug concentration-time-profiles at the sites of action in the human body and, thus, the therapeutic effects of the medical treatments. Furthermore, they can be directly injected into the target tissues. This reduces the drug concentrations in the other parts of the human body (and consequently the risk of undesired side effects) and permits to reach target tissues, which are normally not accessible for the drug (e.g., the Central Nervous System). Various process technologies can be used for the preparation of these advanced drug delivery systems and broad ranges of drug release patterns can be provided, matching the therapeutic needs of the patient. However, the development and production of drug-loaded microparticles is not straightforward, because many physical and chemical processes can be involved in the control of drug release. Thus, great care has to be taken when identifying the optimal system design (composition and dimension) and preparation procedure.

Acknowledgement The authors are grateful for the support of this work by the French Association for Cancer Research “ARC” (“Association pour la Recherche sur le Cancer”: postdoctoral fellowship for Florence Siepmann).

References

1. Tanquary AC, Lacey RE (1974) Controlled Release of Biologically Active Agents. Plenum Press, New York
2. Baker R (1987) Controlled Release of Biologically Active Agents. Wiley, New York
3. Fan LT, Singh SK (1989) Controlled release. A Quantitative Treatment. Springer, Berlin
4. Freitas S, Merkle HP, Gander B (2005) J Controlled Release 102:313
5. Berkland C, King M, Cox A, Kim K, Pack DW (2002) J Controlled Release 82:137
6. Sinha VR, Trehan A (2003) J Controlled Release 90:261
7. Okada H (1997) Adv Drug Del Rev 28:43
8. Okada H, Heya T, Ogawa Y, Toguchi H, Shimamoto T (1991) Pharm Res 8:584
9. Okada H, Inoue Y, Heya T, Ueno H, Ogawa Y, Toguchi H (1991) Pharm Res 8:787
10. Okada H, Toguchi H (1995) Crit Rev Ther Drug Carrier Syst 12:1
11. Spicer DV, Ursin G, Parisky YR, Pearce JG, Shoupe D, Pike A, Pike MC (1994) J Natl Cancer Inst 86:431
12. Takeuchi H, Kobori H, Kikuchi I, Sato Y, Mitsuhashi N (2000) J Obstet Gynaecol Res 26:325
13. Benoit JP, Faisant N, Venier-Julienne MC, Menei P (2000) J Controlled Release 65:285
14. Menei P, Benoit JP (2003) Acta Neurochir Suppl 88:51
15. Menei P, Jadaud E, Faisant N, Boisdron-Celle M, Michalak S, Fournier D, Delhaye M, Benoit JP (2004) Cancer 100:405
16. Tatard VM, Venier-Julienne MC, Saulnier P, Prechter A, Benoit JP, Menei P, Montero-Menei CN (2005) Biomaterials 26:3727
17. Siepmann J, Göpferich A (2001) Adv Drug Del Rev 48:229
18. Faisant N, Siepmann J, Benoit JP (2002) Eur J Pharm Sci 15:355
19. Siepmann J, Faisant N, Benoit JP (2002) Pharm Res 19:1885

Progr Colloid Polym Sci (2006) 133: 22–29
DOI 10.1007/2882_066

Christian Mayer
Alina Bauer

Molecular Exchange Through Capsule Membranes Observed by Pulsed Field Gradient NMR

Christian Mayer (✉) · Alina Bauer
Universität Duisburg-Essen,
Fachbereich Chemie, 47057 Duisburg,
Germany
e-mail: hi408ma@uni-duisburg.de

Abstract Molecular exchange through membranes of dispersed vesicles is studied using nuclear magnetic resonance spectroscopy combined with pulsed field gradients. Encapsulated molecules are differentiated from those in the continuous phase by their mean square displacement depending on a variable time interval Δ. Generally, two field gradient pulses are combined with a stimulated pulse echo sequence. In case of small capsules and vesicles with diameters below 1 μm, the Brownian motion of the capsules dominates the lateral motion for the encapsulated fraction and the echo decay curve can be analyzed with a simple analytical approach. In case of larger vesicles and capsules with diameters above 1 μm, the diffusion inside the encapsulated domain becomes the dominating phenomenon and the echo decay has to be fitted with a numerical approach based on a finite element approximation. For very slow exchange processes with average residence times above 10 s, permeation is directly observed in a time resolved measurement on the non-equilibrium state. In all cases, a careful analysis yields data on the release of a given encapsulated ingredient as well as, under variation of the tracer molecule, on the specific permeability of the capsule walls for molecules of various size, polarity or flexibility.

Keywords Exchange · Nanocapsules · Permeability · PFG-NMR · Vesicles

Introduction

Hollow spherical capsules in liquid dispersion may occur naturally as well as artificially as synthetic vesicles [1] or nanocapsules [2, 3]. In most cases, their principal purpose is to separate small spherical compartments from the continuous phase. Therefore, one of their key properties is the permeability of their membranes for molecules which are dissolved in the continuous and discontinuous liquid phases. From the analytical side, the characterization of molecular exchange through the capsule membranes is not straightforward as the location of the molecules is difficult to be detected directly. In many cases, the inner and the outer continuum represent almost identical environments in terms of their physical and chemical properties. This makes it very hard to separate encapsulated molecules from their counterparts in the continuous phase by means of, e.g., simple absorption or emission spectroscopy. Under these circumstances, the only physical property distinctly connected to the encapsulated state of the molecule is its reduced mean square displacement for an extended period of time Δ. While the “free” fraction of molecules undergoes practically unhindered self diffusion, the encapsulated fraction is experiencing a certain degree of hindrance in its lateral mobility. For completely impermeable capsule membranes, the situation can be treated as hindered diffusion in a spherical compartment. In most cases however, the thin capsule or vesicle membranes allow for a considerable amount of molecular exchange between the internal and the external continuum, connected to a corresponding change in the mean square displacement for individual molecules.

A very powerful experimental technique for the direct observation of the mean square displacement of molecules even in complex mixtures is nuclear magnetic resonance spectroscopy (NMR) in presence of pulsed field gradients (PFG) [4–6]. In an NMR echo experiment which is combined with two pulsed magnetic field gradients with a separation Δ, the relative echo intensity I_{rel} strongly depends on the average lateral shift of the molecules with respect to the gradient direction. The corresponding echo attenuation is easily calculated for free diffusion [5] and, using somewhat more sophisticated approaches, also for molecules encapsulated in hollow spheres [7–9]. The resulting analytical expressions allow for a complete analysis on the structure of o/w and w/o emulsions [10–14]. In addition, approaches have been developed to describe molecular exchange phenomena in these systems. This includes adsorption–desorption processes of amphiphilic molecules on the surface of nanoparticles or vesicle membranes [15–17] as well as the molecular permeation and exchange through the phase boundaries [18–23]. A two-dimensional variety of the PFG-NMR experiment, diffusion–diffusion exchange spectroscopy (DEXSY) has recently been proposed and applied to systems undergoing exchange [23, 24]. A detailed mathematical description of the effect of limited diffusion together with molecular exchange on the result of a PFG-NMR experiment can be developed numerically [21, 25, 26]. Based on numerical simulations of the PFG-NMR experiment for given diffusion constants and various exchange rates, the experimental data can be analyzed to yield the relevant parameters for the molecular exchange in a capsule system. If the permeation process is slow enough, it can also be observed under non-equilibrium conditions in a time resolved experiment.

The resulting exchange constant is an important parameter whenever a chemical component is meant to be confined by nanocapsules or vesicles for an extended period of time, such as an active ingredient in a pharmaceutically relevant carrier system. On the other hand, a study under systematic variation of the observed tracer molecule in terms of its molecular weight, its polarity or its flexibility yields valuable data on the permeability properties of the separating membrane [21]. Altogether, PFG-NMR turns out to be a versatile approach for a detailed study on nanocapsules and vesicles. Its only severe drawback, a general lack of sensitivity, may be compensated by the choice of tracer molecules or extended measuring time. In the following, we want to summarize an analytical as well as a numerical description of PFG-NMR echo decay curves. These are applied to colloidal dispersions which may be used as pharmaceutical carrier systems. Exchange phenomena with time constants over more than three orders of magnitude are discussed, characterized by average residence times in the encapsulated state varying between 54 ms and 93 s.

Theory and Simulation Procedure

Echo Decay for Free Diffusion

In the given case, all PFG-NMR experiments consist of the application of two field gradient pulses with a stimulated echo pulse sequence ($90° - \tau_1 - 90° - \tau_2 - 90° - \tau_1$-echo) [5]. The pulse gradients with a gradient strength G and duration δ are applied during both waiting periods τ_1 with an overall separation Δ. In presence of free diffusion with a diffusion coefficient D, this leads to a decay of the echo intensity I with respect to the original value I_0 (for $G = 0$) according to:

$$I/I_0 = I_{\mathrm{rel}} = \exp\left[-\gamma^2\delta^2G^2D\,(\Delta - \delta/3)\right] \qquad (1)$$

With encapsulated domains of the observed spin system (e.g. inside of vesicles), the situation becomes more complicated. In this case, the molecules reside in different compartments, the capsules and the continuous phase, and only the continuous phase allows for random motion that comes close to free diffusion. The capsule walls form something like a diffusion barrier that partially restricts the passage between the two compartments.

Echo Decay for Chemical Exchange: Analytical Approximation

In case of very small capsules or vesicles with diameters significantly below 1 μm the hindered diffusion inside the encapsulated volume has little or no effect on the echo decay. In addition, the Brownian motion of the capsules becomes very efficient and dominates the echo decay for the enclosed molecules. In this case, it is a good approximation to consider the situation as an exchange between two molecular reservoirs with two different exponential relaxation times. These circumstances have been treated in detail by Woessner [27] for a general type of relaxation and can be adapted to the PFG-NMR measurement (see [16] or [28] for examples). In the following, we will assume that spin-spin and spin-lattice relaxation does not differ for the internal and the external domain. For vesicles and nanocapsules, this condition is justified as long as the solvent and the concentrations of all constituents are identical for both domains. Further, we neglect the influence of spin diffusion, a process which could principally contribute to the magnetization exchange for stimulated echo experiments with consequences similar to molecular exchange. However, this phenomenon would not depend on molecular mass of the observed tracer, so this issue can later be discussed based on the experimental results (see Results and Discussion). With the approximation $\Delta \cong (\Delta - \delta/3)$ which is valid for short gradient pulses and long separations, the echo decay is described by:

$$I_{\mathrm{rel}} = P'_{\mathrm{a}} \exp\left(-k'_{\mathrm{a}}\Delta\right) + P'_{\mathrm{b}} \exp\left(-k'_{\mathrm{b}}\Delta\right) \qquad (2)$$

with:

$$k'_{\mathrm{a}} = C_1 - C_2 \tag{3}$$

$$k'_{\mathrm{b}} = C_1 + C_2 \tag{4}$$

$$P'_{\mathrm{a}} = \frac{1}{2} + \frac{\frac{1}{4}\left[(P_{\mathrm{b}} - P_{\mathrm{a}})\,(k_{\mathrm{a}} - k_{\mathrm{b}}) + \frac{1}{\tau_{\mathrm{a}}} + \frac{1}{\tau_{\mathrm{b}}}\right]}{C_2} \tag{5}$$

$$P'_{\mathrm{b}} = \frac{1}{2} - \frac{\frac{1}{4}\left[(P_{\mathrm{b}} - P_{\mathrm{a}})\,(k_{\mathrm{a}} - k_{\mathrm{b}}) + \frac{1}{\tau_{\mathrm{a}}} + \frac{1}{\tau_{\mathrm{b}}}\right]}{C_2} \tag{6}$$

$$C_1 = \frac{1}{2}\left(k_{\mathrm{a}} + k_{\mathrm{b}} + \frac{1}{\tau_{\mathrm{a}}} + \frac{1}{\tau_{\mathrm{b}}}\right) \tag{7}$$

$$C_2 = \frac{1}{2}\left[\left(k_{\mathrm{a}} - k_{\mathrm{b}} + \frac{1}{\tau_{\mathrm{a}}} - \frac{1}{\tau_{\mathrm{b}}}\right)^2 + \frac{4}{\tau_{\mathrm{a}}\tau_{\mathrm{b}}}\right]^{1/2} \tag{8}$$

$$k_{\mathrm{a}} = \gamma^2 G^2 D'_{\mathrm{a}} \delta^2 \quad \text{and} \tag{9}$$

$$k_{\mathrm{b}} = \gamma^2 G^2 D'_{\mathrm{b}} \delta^2 \tag{10}$$

with P_{b} and P_{a} being the relative populations of the encapsulated and the free phase, respectively (with $P_{\mathrm{a}} + P_{\mathrm{b}} = 1$). The apparent diffusion constants D'_{a} and D'_{b} determine the initial and the final slope of an individual plot I_{rel} vs. G^2, while the average residence times τ_{a} and τ_{b} take influence on the dependence of the final plateau level on the diffusion time Δ (with $\tau_{\mathrm{a}}/\tau_{\mathrm{b}} = P_{\mathrm{a}}/P_{\mathrm{b}}$). This analytical approach can be further improved by introducing an apparent diffusion coefficient that accounts for the internal diffusion [29], however, it still relies on considerations that are valid for restricted diffusion.

Echo Decay for Exchange and Restricted Diffusion: Numerical Simulation

For larger capsules or vesicles with diameters above 1 μm, the approximations made above do not hold any longer, as the internal diffusion becomes dominating while at the same time the Brownian motion is slowed down. In addition, the simultaneous permeation process through the membranes acts together with the internal and external self diffusion, leading to a complicated superposition of lateral motions. Therefore, an alternative numerical procedure has been developed which is based on a finite element approximation: the z-axis of a cubic (or, more general, a rectangular-prismatic) subspace of the sample (the z-direction being coaxial with the direction of the magnetic field gradient) is segmented into sites of equal length Δz corresponding to sample "slices" of equal thickness, identified by their time dependent magnetization contributions $M_{\mathrm{n}}(t)$ [21, 25]. Each such magnetization element is further split into contributions from the continuous phase ($m = 1$) as well as from the various capsules being located at z_n ($m = 2, 3, 4, \ldots$) such that

$$M_{\mathrm{n}}(t) = \sum_m M_{nm}(t) \tag{11}$$

The continuous diffusive motion is now modeled by a first order exchange of contributions $M_{\mathrm{n}}(t)$ according to Fick's law, while at the same time the magnetization of each slice develops according to its individual time dependent Larmor frequency $\omega(n, t)$. This, in first approximation, leads to a new magnetization element $M_{nm}(t + \Delta t)$ after a short time interval Δt [21, 25, 26]:

$$\begin{aligned} M_{nm}(t + \Delta t) = {} & M_{nm}(t) \exp\left[\mathrm{i}\omega(n, t)\Delta t\right] \\ & + \sum_{n',m'} \big\{ -k_{nn'mm'} \Delta t M_{nm}(t) \\ & \times \exp\left[\mathrm{i}\omega(n, t)\Delta t\right] + k_{n'nm'm} \Delta t M_{n'm'}(t) \\ & \times \exp\left[\mathrm{i}\omega(n', t)\Delta t\right]\big\} \end{aligned} \tag{12}$$

with $k_{nn'mm'}$ being the first order rate constant for the flow of magnetization from site (n, m) to (n', m'). The Larmor frequency depends on time as well as on the lateral position z_n according to

$$\omega(n, t) = -\gamma G(t) z_n \tag{13}$$

with γ being the gyromagnetic ratio of the observed nucleus. The gradient function $G(t)$ depends on the particular experiment to be simulated, in the given case it reflects the action of two rectangular gradient pulses (with gradient strength G) during the time intervals τ_1.

The equilibrium populations P_{nm} of the sites (n, m) reflect the geometry of the diffusion compartments, which is infinite for the continuous phase and spherical for the encapsulated volumes [21, 25]. They are given by

$$P_{n1} = (1 - x_{\mathrm{in}})/n_{\mathrm{max}} \tag{14}$$

for the continuous phase with x_{in} being the encapsulated fraction of observed molecules and n_{max} being the total number of sites in z, and

$$P_{nm} = \frac{x_{\mathrm{in}}}{n_{\mathrm{cap}}} \frac{P'_{nm}}{\sum_n P'_{nm}} \quad \text{for} \quad m > 1 \tag{15}$$

with

$$P'_{nm} = \left[a_m^2 - (z_n - z_{0m})^2\right] \quad \text{for} \quad a_m^2 \geq (z_n - z_{0m})^2$$

$$P'_{nm} = 0 \quad \text{for} \quad a_m^2 < (z_n - z_{0m})^2$$

for the molecules in an individual spherical capsule m, where n_{cap} is the overall number of capsules in the regarded subspace while a_m and z_{0m} stand for the radius of the capsule and the position of the capsule center, respectively.

The set of rate constants $k_{nn'mm'}$ fully describes the diffusive motions in the different environments as well as the molecular exchange through the capsule wall. Consequently, each rate constant depends on the diffusion constants D_b and D_a for the encapsulated and the continuous phase, on the average exchange rate k_ex, and on the populations of the sites nm and $n'm'$. Details on the calculation of the full set of rate constants are given elsewhere [21, 25, 26].

For the simulation of a PFG-NMR measurement based on a stimulated echo, every step of the experiment is represented by a corresponding element of the calculation:

a) The magnetization in the x,y-plane after the initial 90°-pulse is reflected by the following starting condition:

$$\mathrm{Re}[M_{nm}(0)] = P_{nm} \quad \mathrm{Im}[M_{nm}(0)] = 0$$

b) During the following time-dependent evolution of all complex magnetization elements $M_{nm}(t)$ according to Eq. 3, the gradient function $G(t)$ is set to G for the duration δ.

c) The second 90°-pulse which transfers part of the magnetization in the longitudinal direction is represented by setting the real part of $M_{nm}(t)$ to zero at $t = \tau_1$, while the imaginary part is maintained.

d) This step is followed by a further evolution in τ_2, where the values $M_{nm}(t)$ describe the development of the magnetization in the z-direction.

e) The third 90°-pulse is represented by formation of the conjugated complex of $M_{nm}(t)$ at $t = \tau_1 + \tau_2$. Hereafter, $M(t)$ again describes the magnetization elements in the x,y-plane.

f) Finally, the action of another field gradient G with a duration δ represented by a corresponding function $G(t)$ leads to partial refocusing of the magnetization elements $M_{nm}(t)$ and the formation of an echo signal. The time that evolves between the onsets of the two gradient pulses is given by Δ. The echo signal is directly obtained as I/I_0 by a summation over all magnetization elements $M_{nm}(t)$ over the sites n and m.

Experiments

Vesicles from two different block-copolymers, poly[(isoprene)$_{53}$-*b*-(ethylenegylcol)$_{28}$] (PI-PEO9) and poly[(2-vinylpyridine)$_{54}$-*b*-(ethylenegylcol)$_{34}$] (P2VP-PEO10), have been obtained from the research group of S. Förster, University of Hamburg, Germany. The general preparation procedure for the vesicles has been described elsewhere [21]. Samples of polyethylene oxide (PEO) of various molecular mass (from PEO-200 with 200 g/mol to PEO-1500 with 1500 g/mol) have been purchased from Merck-Schuchardt OHG, Hohenbrunn, Germany and Sigma–Aldrich Chemie, Munich, Germany. For sample preparation, the polyethylene oxide (PEO) samples have been added to the vesicle dispersion to yield a concentration of 1%. Earlier studies had shown that the complete equilibration was assumed after a few minutes [21].

All measurements are performed on a Bruker Avance 400 spectrometer (Bruker AG, Karlsruhe, Germany) equipped with a BAFPA 40 gradient amplifier and a Bruker DIFF30 probe. The instrument is tuned to 400 MHz proton frequency, gradient pulses are adjusted to gradient strengths between 0 and 4 T/m with individual durations of 1.2 ms. For all measurements, the stimulated echo ($90° - \tau_1 - 90° - \tau_2 - 90° - \tau_1$-echo) is used in combination with the gradient pulses during each τ_1 waiting period. The spacing Δ between the two gradient pulses is varied between 50 and 300 ms. All measurements are performed at 293 K. The samples are filled into regular 5 mm NMR sample tubes and are used without further sample preparation.

In case of time resolved measurements, the tracer signal from the continuous phase is simply filtered out by an adequate setting of δ, Δ and G which leads to a complete relaxation of the mobile fraction. At a given point of time $t = 0$, the tracer is added and mixed homogeneously with the dispersion. Subsequently, a set of successive PFG-NMR measurements is started and the echo amplitude is determined as a function of t.

Results and Discussion

Rapid Exchange of Water

The most natural candidate for a study on molecular exchange in an aqueous vesicle dispersion is obviously water. Figure 1 shows two sets of echo decay curves observed on the water signal of vesicle dispersions under variation of the field gradient strength G for different spacings Δ between the two gradient pulses. Logarithmic relative echo amplitudes I_rel are plotted vs. the parameter $\gamma^2 G^2 \delta^2 (\Delta - \delta/3)$ such that a linear dependence with the slope equal to the negative self diffusion constant ($-D$) is obtained for free diffusion according to (Eq. 1). In many cases such as for P2VP-PEO10, the exchange of water molecules through a vesicle membrane is very rapid and only free diffusion can be observed (Fig. 1, top). This is only partially a consequence of the limitations of the experiment, but rather due to the fact that some vesicle membranes do not represent a significant barrier for the self diffusion. In vesicles from P2VP-PEO10, the inner part of the vesicle membrane is formed by poly(2-vinylpyridine), a polymer which still exhibits some residual polarity which facilitates the water permeation. In contrast, the inner part of membranes of PI-PEO9 vesicles consists of poly(isoprene), a polymer which is distinctly unpolar and therefore represents a much stronger barrier for water molecules. Consequently, the permeability is sufficiently reduced to lead to significant confinement of water molecules (Fig. 1, bottom). Here, the complete set of curves has been fitted based on Eqs. 2–10 with a single data set (see caption to Fig. 1). The initial very steep slope down to $\ln(I/I_0) = -5$, which is very similar to the one for P2VP-PEO10, corresponds to the

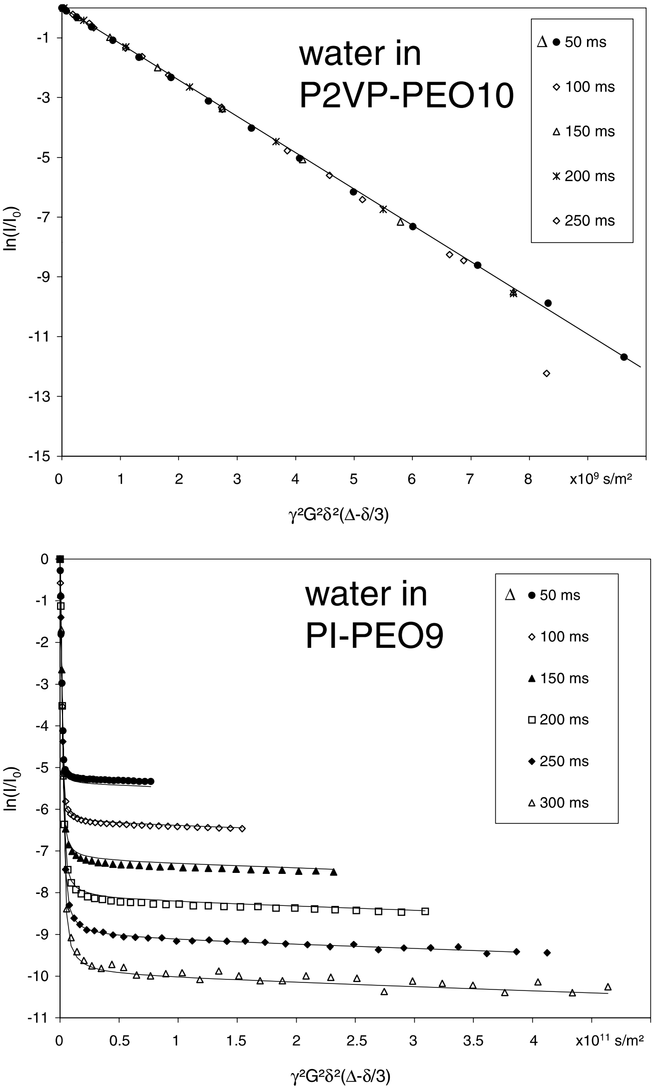

Fig. 1 Echo decay curves observed on the water signal of dispersed vesicles from P2VP-PEO10 (*top*) and PI-PEO9 (*bottom*) under variation of the field gradient strength G for different spacings Δ between the two gradient pulses. Experimental data are given as symbols, the *solid lines* show the best fit obtained by Eqs. 2–10 using a single data set. For PI-PEO9 (*bottom*), the common simulation parameters are as follows: $D_\mathrm{a} = (1.99 \times 10^{-9} \pm 0.013 \times 10^{-9})\,\mathrm{m^2/s}$, $D_\mathrm{b} = (9.5 \times 10^{-13} \pm 0.66 \times 10^{-13})\,\mathrm{m^2/s}$, $P_\mathrm{a} = (0.9887 \pm 0.00016)$, $\tau_\mathrm{b} = (54 \pm 0.25)$ ms

nearly free diffusion of the water in the continuous phase, which here contributes to $(98.87 \pm 0.016)\%$ of the overall water content. The common slope of all six curves reflects a self diffusion constant of $D_\mathrm{a} = (1.99 \times 10^{-9} \pm 0.013 \times 10^{-9})\,\mathrm{m^2/s}$ which comes close to the value for free self diffusion of pure water with $2.26 \times 10^{-9}\,\mathrm{m^2/s}$ for 298 K (source: AIP). The final slope, again shared by all six echo decay curves, is related to the Brownian motion of the vesicle which, according to the overall best fit, amounts to a diffusion coefficient of $D_\mathrm{b} = (9.5 \times 10^{-13} \pm 0.66 \times 10^{-13})\,\mathrm{m^2/s}$. For Brownian motion in water at 298 K, this is in accordance with spherical particles with a diameter of 520 nm, a value which corresponds well to the expected size of the vesicles.

Finally, the dependence of the echo intensities on Δ for larger gradients reveals the exchange rate between the states (a) and (b). According to the overall best fit, the average residence time for an individual water molecule in the encapsulated state amounts to $\tau_\mathrm{b} = (54 \pm 0.25)$ ms. This result is based on the assumption of a first order kinetics of the exchange process. However, one has to be careful to assign this transfer between the states (a) and (b) completely to actual molecular exchange. In fact, the migration of protons as well as spin diffusion during the stimulated echo experiment could contribute to the transfer of magnetization between the two domains. In order to estimate this contribution, a systematic study under variation of the molecular weight of the tracer molecule is required.

Exchange of Tracer Molecules with Variable Molecular Weight

A study on molecular exchange for variable molecular weight is performed on P2VP-PEO10 vesicles using polyethylene oxide (PEO) tracer molecules [21]. The echo decay curves for PEO at five different molecular weights between 200 and 1500 g/mol are observed using the single proton signal at 3.2 ppm, three examples are shown in Fig. 2. Due to the relatively large size of the vesicles ($d = 1.4\,\mu\mathrm{m}$), the internal diffusion inside of the vesicles can no longer be neglected. Consequently, the numerical simulation procedure according to Eqs. 11–15 has to be applied for a suitable description of the PFG-NMR experiment. The simulated echo decays, resulting from a single data set for each PEO tracer, are shown as solid lines in Fig. 2 (simulation parameters are given in the figure caption). All initial slopes are much smaller as compared to water which is expected for the slower self diffusion of the larger PEO molecules. The diffusion coefficients clearly decrease with increasing molecular weight which is in accordance with the growing hydrodynamic radii of the PEO chains in water. On the other hand, the final slopes for high field gradients are shallower which indicates the slower Brownian motion due to the larger vesicles. From the hydrodynamic radius of the vesicles, a Brownian motion with $D_\mathrm{b} = 3.5 \times 10^{-13}\,\mathrm{m^2/s}$ can be expected. Compared to the contributions of the internal and the external self diffusion of the PEO, this phenomenon can be neglected in good approximation.

More interestingly, the dependence of the exchange rate between the states (a) and (b) on the pulse spacing Δ strongly varies with the molecular mass of the PEO tracer. This is directly represented by the dependence of the echo intensities on Δ for larger gradients. While the data on PEO-300 exhibit a large variation within the given

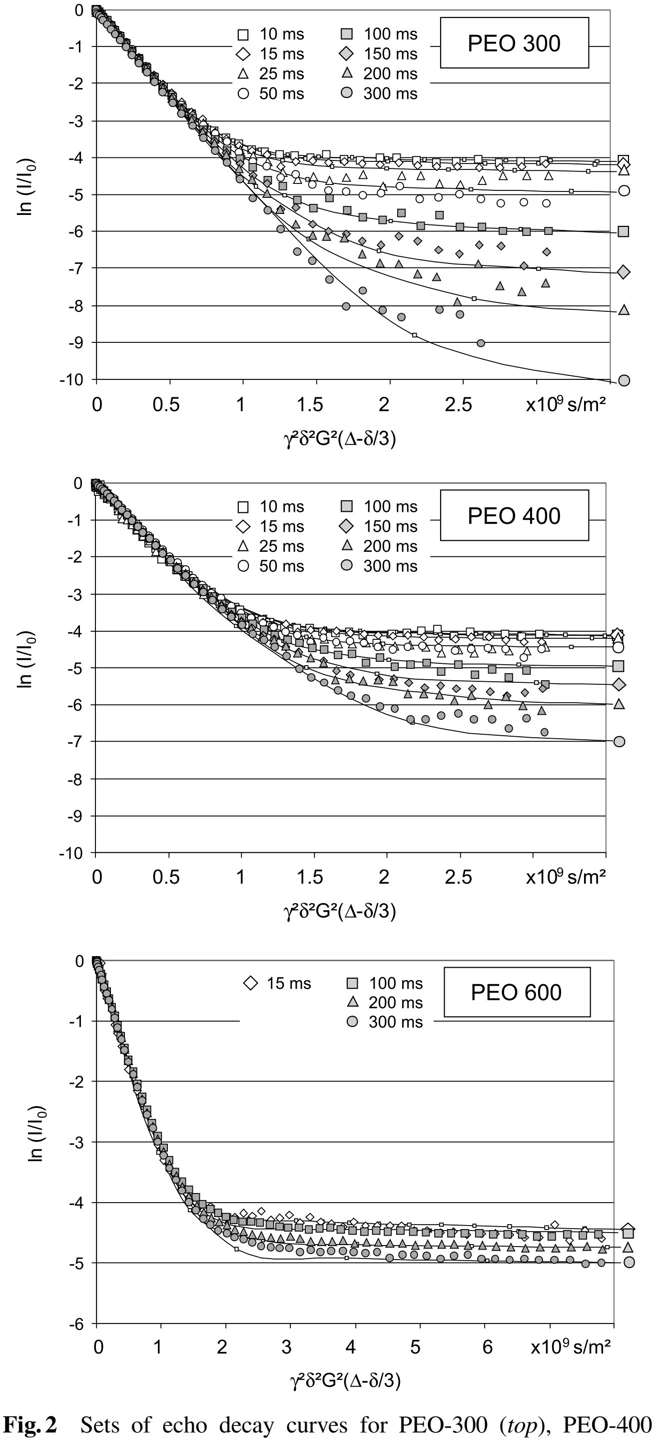

Fig. 2 Sets of echo decay curves for PEO-300 (*top*), PEO-400 (*centre*) and PEO-600 (*bottom*) in a P2VP-PEO10 vesicle dispersion. Each individual plot refers to a given pulse spacing Δ as shown in the *inserts*. *Symbols* mark the experimental data, *solid lines* the results for the best fit simulations according to Eqs. 11–15. The latter are labelled with corresponding symbols on the *right margin*. Simulation data sets are as follows: PEO-300 ($D_a = 4.91 \times 10^{-10}\,\mathrm{m^2/s}$, $P_b = 0.022$, $\tau_b = 157\,\mathrm{ms}$), PEO-400 ($D_a = 4.28 \times 10^{-10}\,\mathrm{m^2/s}$, $P_b = 0.0205$, $\tau_b = 329\,\mathrm{ms}$), PEO-600 ($D_a = 3.58 \times 10^{-10}\,\mathrm{m^2/s}$, $P_b = 0.015$, $\tau_b = 1420\,\mathrm{ms}$)

range of pulse spacings (with the value for $\Delta = 15$ ms being approximately 150 times larger than for $\Delta = 300$ ms, see Fig. 2 top), the dependence of the data for PEO-600 is quite small (with the value for $\Delta = 15$ ms being only 1.8 times larger than for $\Delta = 300$ ms, see Fig. 2 bottom) and almost completely vanishes for PEO 1500 (data not shown). The parameters for the complete set of simulated echo decay curves (as shown for PEO-300, PEO-400 and PEO-600 in Fig. 2) yield data for the average exchange rates k_{ex} which are related to the overall exchange rates and the average residence times in the encapsulated state [21]. In Fig. 3, the average residence times τ_b are plotted against the hydrodynamic radii of the PEO tracers as obtained from their self diffusion coefficients. As expected, increasing residence times are found for increasing hydrodynamic radii of the PEO tracers. For PEO-200 up to PEO-600, the logarithm of the residence time depends linearly on the hydrodynamic radius. This fact indicates that the activation energy for the permeation process is proportional to the radius of the tracer molecule. In addition, this clear dependency rules out a strong contribution of those exchange phenomena which are not occurring on a molecular basis, in this case mainly represented by spin diffusion. With the given dependency, it can be stated that the spin diffusion is definitely slower than the molecular diffusion and the exchange of PEO-600.

However, the situation looks somewhat different for PEO-1500. Its value for τ_b clearly deviates from the linear behaviour of its smaller counterparts. This could be related to a different mechanism of permeation, possibly connected to an uncoiling of the PEO chain. Alternatively, this could also indicate the growing contribution of proton spin diffusion which could dominate the exchange of the magnetization between the domains while the parameter for the molecular exchange still would follow the original linear dependence. On the basis of the given experimental

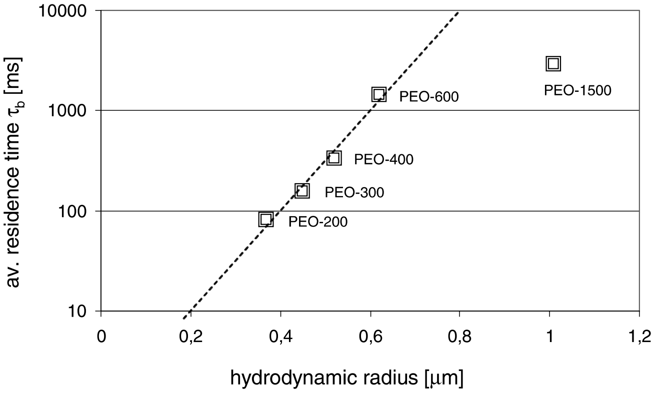

Fig. 3 Logarithmic plot of average residence times for PEO tracers of different molecular weights and hydrodynamic radii in dispersed P2VP-PEO10 vesicles. Except for PEO-1500, the values for log τ_b approximately follow a linear dependence on the hydrodynamic radius (*broken line*)

data, this fact remains unclear. On the other hand, the clear relation between exchange rate and hydrodynamic radius for the other tracers already gives valuable information on the permeability of the vesicle membrane.

Slow Exchange: A Time Resolved Experiment

The actual limits for the detection of the exchange rates using the methods described so far are defined by the range of the pulse separation Δ. For technical reasons, it becomes very difficult to use pulse separations shorter than 10 ms, given that the duration of each pulse is already in the range of one ms. On the other hand, experiments with pulse spacings significantly above 300 ms are generally suffering from the consequences of spin-lattice relaxation and bad signal to noise ratio. However, with average residence times above 10 s, slow exchange processes allow for an observation in a time resolved PFG-NMR measurement. In this case, the tracer signal from the continuous phase is simply filtered out by an adequate setting of δ, Δ and G which leads to a complete relaxation of the mobile fraction. At a given point of time $t = 0$, the tracer is added and mixed homogeneously with the dispersion. Subsequently, a set of successive PFG-NMR measurements is started and the echo amplitude is determined as a function of t. In this non-equilibrium situation, the PEO molecules are now migrating through the separating membranes into the encapsulated domain where they can be directly detected. With good signal to noise ratio, a single echo experiment with four scans can be performed within a few seconds, such that the determination of average residence times above 10 s are possible. In Fig. 4, examples are shown which refer to PEO-12 000 and PEO-35 000 in P2VP-PEO10 vesicles. In good approximation, both plots follow first order kinetics up to the point where the equilibrium concentration is reached (solid lines in Fig. 4). The average residence times can be obtained from the best fit exponential and amount to $\tau_b = 66.7$ s for PEO-12 000 and $\tau_b = 83.7$ s for PEO-35 000.

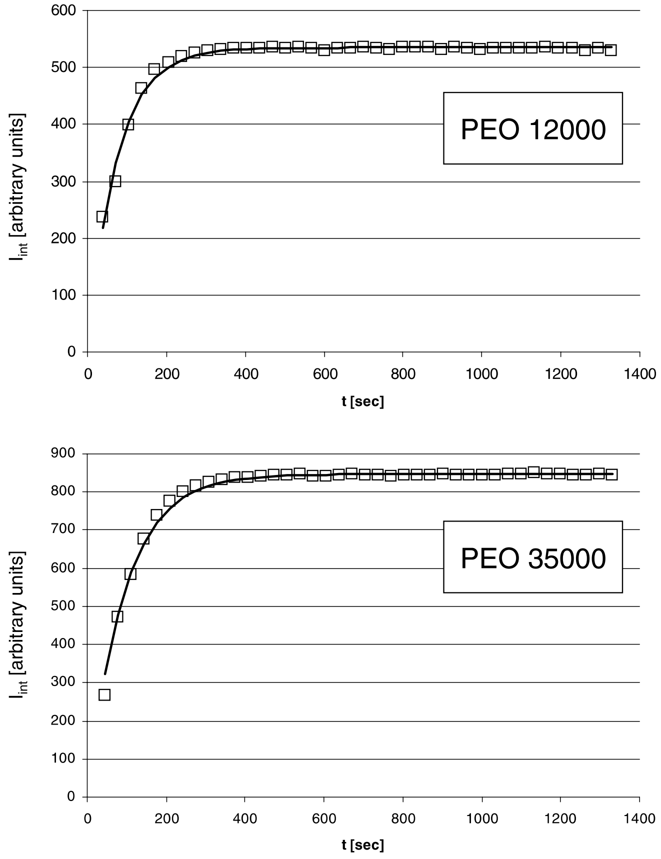

Fig. 4 Result of a time resolved PFG-NMR experiment on PEO-12 000 (*top*) and PEO-35 000 (*bottom*) in presence of dispersed P2VP-PEO10 vesicles. In each case, the PEO tracer is added to the dispersion at $t = 0$. A constant setting for δ, Δ and G is used to erase all signal contributions from the continuous phase. Under these conditions, the signal contribution I_{int} of the encapsulated fraction which derives from the permeation under non-equilibrium conditions is directly detected over time

Conclusion

PFG-NMR represents an elegant and powerful tool for the analysis of exchange phenomena in dispersed systems. In case of dispersed vesicles or nanocapsules, an experiment using a stimulated echo sequence in combination with two gradient pulses is suitable for the observation of trans-membrane exchange of active ingredients or tracer molecules. For small capsules and vesicles with diameters below 1 μm, the Brownian motion dominates the echo attenuation for the encapsulated fraction and the echo decay curve can be analyzed with a simple analytical approach. In case of larger vesicles and capsules with diameters above 1 μm, the internal diffusion becomes the dominating phenomenon and the echo decay has to be fitted with a numerical approach based on a finite element approximation. For very slow exchange processes with average residence times above 10 s, the permeation process is directly observed in a time resolved measurement. Following this principle, similar studies on tracers under variation of polarity or flexibility of the molecule could be carried out to further elucidate the mechanism of trans-membrane permeation. In addition, this kind of information turns out to be extremely valuable in cases where capsules or vesicles are being used as pharmaceutical carrier systems.

Acknowledgement The authors gratefully acknowledge the gift of block-copolymers from the research groups of S. Förster, University of Hamburg and R. Schubert, University of Freiburg, Germany. We also thank for the generous funding by the Volkswagen-Stiftung, Germany, in connection with the project "Block copolymer vesicles with controlled uptake/release functions for drugs and genes".

References

1. Discher DE, Eisenberg A (2002) Science 297:967
2. Couvreur P, Barrat G, Fattal E, Legrand P, Vauthier C (2002) Crit Rev Therap Drug Carrier Syst 19:99
3. Meier W (2000) Chem Soc Rev 29:295
4. Stilbs P (1987) Prog Nucl Magn Reson Spectrosc 19:1
5. Kimmich R (1997) NMR Tomography Diffusometry Relaxometry. Springer, Berlin, Heidelberg, New York
6. Johnson CS (1999) Prog Nucl Magn Reson Spectrosc 34:203
7. Balinov B, Jönsson B, Linse P, Södermann O (1993) J Magn Reson A 104:17
8. Callaghan PT (1995) J Magn Reson A 113:53
9. Codd SL, Callaghan PT (1999) J Magn Reson 137:358
10. Lönnqvist I, Khan A, Södermann O (1990) J Colloid Interface Sci 144:401
11. Södermann O (1997) Progr Colloid Polym Sci 106:34
12. Hakansson B, Pons R, Södermann O (1998) Magn Reson Imag 16:643
13. Topgaard D, Malmborg C, Södermann O (2002) J Magn Reson 156:195
14. Ambrosone L, Murgia S, Cinelli G, Monduzzi M, Ceglie A (2004) J Phys Chem 108:18472
15. Valentini M, Vaccaro A, Rehor A, Napoli A, Hubbel JA, Tirelli N (2004) J Am Chem Soc 126:2142
16. Schönhoff M, Södermann O (1997) J Phys Chem 101:8237
17. Schönhoff M, Södermann O (1998) Magn Reson Imag 16:683
18. Kuchel PW, Durrant CJ (1999) J Magn Reson 139:258
19. Momot KI, Kuchel PW, Chapman BE, Whittaker D (2003) Langmuir 19:2088
20. Mayer C, Hoffmann D, Wohlgemuth M (2002) Int J Pharm 242:37
21. Rumplecker A, Förster S, Zähres M, Mayer C (2004) J Chem Phys 120:8740
22. Adalsteinsson T, Dong WF, Schönhoff M (2004) J Phys Chem B 108:20056
23. Callaghan PT, Furó I (2004) J Chem Phys 120:4032
24. Qiao Y, Galvosas P, Adalsteinsson T, Schönhoff M, Callaghan PT (2005) J Chem Phys 122:214912
25. Mayer C (2002) Prog Nucl Magn Reson Spectrosc 40:307
26. Mayer C (2005) Ann Rep NMR Spectrosc 55:205
27. Woessner DE (1995) Relaxation effects of chemical exchange. In: Grant DM, Harris RK (eds) Encyclopedia of NMR. Wiley, Chichester, p 4018–4027
28. Wohlgemuth M, Mayer C (2003) J Colloid Interface Sci 260:324
29. Pfeuffer J, Flögel U, Dreher W, Leibfritz D (1998) NMR Biomed 11:19

Progr Colloid Polym Sci (2006) 133: 30–34
DOI 10.1007/2882_049

Marc Herold
Maria Håkanson
Herwig Brunner
Günter E.M Tovar

Modular Surfmers with Activated Ester Function – A Colloidal Tool for the Preparation of Bioconjugative Nanoparticles

Marc Herold · Maria Håkanson
Institute for Interfacial
Engineering (IGVT), University Stuttgart,
Nobelstr. 12, 70569 Stuttgart, Germany

Herwig Brunner ·
Günter E.M Tovar (✉)
Fraunhofer Institute for Interfacial
Engineering and Biotechnology (IGB),
University Stuttgart, Nobelstr. 12,
70569 Stuttgart, Germany
e-mail: guenter.tovar@igb.fraunhofer.de

Abstract Copolymerization of methylmethacrylate (MMA) and the polymerisable surfactant (surfmer) *p*-(11(acrylamido)undecanoyloxy)-phenyldimethylsulfonium methylsulfate (AUPDS) by emulsion polymerization resulted *p*(MMA-co-AUPDS) particles with a yield $> 95\%$. The particle diameter depended on the surfmer feed concentration and was to be chosen in the range of 116 nm to 145 nm. The particle surface area per activated ester surfmer residue depended on the surfmer concentration and amounted to $0.7\,\text{nm}^2$ to $1.24\,\text{nm}^2$. All area-per-charge values were found to be smaller then the analogous value from *cmc* measurements of an AUPDS solution in ultrapure water which was found to be $1.42\,\text{nm}^2$. The protein conjugate streptavidin peroxidase (SAv-POD) was immobilized covalently on the particle surface by incubating particles in PBS buffer containing this enzyme. By addition of the enzyme substrate 3,3′,5,5′ tetramethylbenzidine (TMB) the activity of the particle-bound enzymes was determined at pH 7.2 to $(5.3 \pm 0.2)\ \text{mU mg}^{-1}$. The enzyme activity was raised to $(15.5 \pm 0.2)\ \text{mU mg}^{-1}$ when the particles were incubated in a pH 8.0 buffer. The non-specific binding was determined to 37% when compared to the total binding by incubating particle blank samples with the same amount of SAv-POD.

Keywords Bioconjugation · Emulsion polymerization · Nanoparticles · Surface charge titration · Surfmers

Introduction

Nanosized polymer particles have become important tools in modern biotechnology research. They are mainly used as solid phase carriers for the handling of proteins and peptides. The advantage of using nanoparticles for these purposes is primarily their high surface area that allows the creation of a high number of binding sites for biomolecules. Another important feature of the particles is that they can be used in fluid handling systems which enable for a relatively easy use.

In order to conjugate with a biomolecule, the particles must have a specific chemical function on their surface that can react chemically and form a covalent bond with an available functional group of the biomolecule. This reaction must proceed under mild conditions so that the three-dimensional structure and biological activity of the biomolecule is maintained. The activated ester is a functional group that fulfills these conditions excellently. An activated ester reacts with an adequate nucleophilic group such as a primary amine on proteins under mild conditions [1, 2]. One way to achieve a surface with activated esters is to use specific polymerizable surfactants, so-called surfmers, to introduce the activated ester group [3–5] (see Fig. 1). Such surfmers can be employed in emulsion copolymerization and enable to obtain in a controlled way

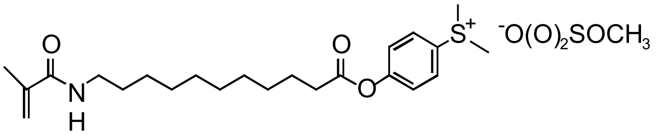

Fig. 1 Chemical structure of the surfmer *p*-(11(acrylamido)undecanoyloxy)phenyldimethylsulfonium methylsulfate (AUPDS) with an activated ester functionality

nanosized particles with an activated ester surface in a one-stage reaction [6].

We found earlier in a comparative study employing a variety of surfmer molecules and different comonomers that a well suited activated ester system for protein immobilization was *p*-(11(acrylamido)undecanoyloxy)phenyldimethylsulfonium methylsulfate (AUPDS) copolymerized with methylmethacrylate (MMA) [7].

In the present study we prepared and characterized also *p*(MMA-*co*-AUPDS) nanoparticles. The particle diameter was determined by dynamic light scattering and the ζ-potential by microelectrophoresis. The charge density on the particle surface was calculated by using results from polyelectrolyte titration combined with the calculated surface area from light scattering. A protein conjugate consisting of streptavidin and the enzyme peroxidase (SAv-POD) was immobilised on the functional particles. Peroxidases belong to the group of oxido-reductases, enzymes that catalyze oxidation-reduction reactions [8]. Peroxidases catalyze different oxidative reactions using hydrogen peroxide (H_2O_2) as electron acceptor.

Experimental

Materials. AUPDS was synthesized according to literature [3]. 3,3′,5,5′ tetramethylbenzidine (TMB substrate kit 34021, Pierce, Rockford, USA), Streptavidin (SAv, Boehringer-Ingelheim, Germany), streptavidine peroxidase conjugate (SAv-POD, Roche AG, Germany), biotin-4-fluorescein (Pierce, Rockford, USA), PBS (phosphate buffered saline) buffer (0.01 mol L^{-1} Applichem, Germany) and 2,2′-Azobis (Methyl-propiomamidine)-dihydrochlorid (AIBA, Fluka, Switzerland) were used without further purification. Methylmethacrylate (MMA), stabilized with hydrochinon (99% Fluka, Switzerland), was purified by washing with a 10% sodiumhydroxide solution, drying over $CaCl_2$ followed by distillation. Polydiallyldimethylammonium chloride (PDADMAC) and sodium polyethensulfonate (NaPES) (both Mütek, Herrsching, Germany) were also used without purification.

Instrumentation. The particle size measurements were carried out with purified particles by photon correlation spectroscopy at a scattering angle of 90° using a Zetasizer HS 3000® (Malvern, Germany).

The light absorption measurements where performed at 450 nm using a SPECTRA max PLUS 384 instrument (Molecular Devices, München, Germany).

The polyelectrolyte titrations were carried out with a PCD 3 PH (Mütek, Herrsching, Germany) particle charge detector equipped with a Titrino 702 SM titrator (Metrohm, Herisau, Switzerland). For titration 1 mmol L^{-1} PDADMAC- und NaPES-solutions were used.

The sulfur amount in the dried latex-particles was determinated by an Vario EL elemental analyzer (ELEMENTAR, Hanau, Germany). 4–20 mg of solid were folded in tin foil and ashed at 1200 °C in an oxygen atmosphere.

The fluorescence intensity was measured with the fluorescence reader "Spectraflour plus" (Tecan, Crailsheim, Germany) at an excitation wavelength of 485 nm and an emission wavelength of 535 nm.

Preparation of the latexes. Preparation of the latex is carried out in a 100 mL three-necked-flask equipped with a reflux condenser, rugby-ball-shaped magnetic stirrer bar and an argon supply-line. 30 mL of water were degassed by altering vacuum and argon atmosphere for three times and 30 min argon bubbling through the liquid.

Surfmer dissolved in 2 mL degassed water and monomer was added with a syringe through a rubber-septum. The emulsion was stirred (400 U min^{-1}) and heated to the reaction temperature of 60 °C at which the water dissolved initiator (AIBA) is added. After two hours, the latex solution is heated to 65 °C for ten minutes, then the heating is removed and the product is allowed to reach room temperature. The yield was determinated by weighing the solid content from a dried aliquot of the latex. The remaining part of the latex was purified by centrifugation and redispersion at 4 °C three times with water before further application. After the last redispersion step the solid content of the latex was adjusted with water to 5 wt % and subsequently stored at 4 °C.

Experimental conditions for the latexes were described as following: An initiator (AIBA) concentration of 1.1 mmol L^{-1} (36 µmol per 34 mL), a MMA concentration of 0.47 mol L^{-1} (1.8 mL per 34 mL) and a surfmer

Table 1 AUPDS-concentrations c_{AUPDS}, particle diameter and calculated particle numbers N_{c} for samples PA 0 to PA 4

Sample	c_{AUPDS}	100* $c_{\mathrm{AUPDS}}/c_{\mathrm{MMA}}$	$\bar{d}_{\mathrm{DLS}}$	N_{c}
	mmol L^{-1}	%	nm	L^{-1}
PA 0	0	–	601 ± 30	$(3.6 \pm 0.7) \times 10^{14}$
PA 1	5.0	1	132 ± 5	$(3.6 \pm 0.3) \times 10^{16}$
PA 2	5.9	1.2	146 ± 5	$(2.6 \pm 0.4) \times 10^{16}$
PA 3	10.0	2	120 ± 3	$(5.0 \pm 0.5) \times 10^{16}$
PA 4	15.0	3	116 ± 4	$(5.8 \pm 0.7) \times 10^{16}$

concentration from 0 mmol L^{-1} to 15 mmol L^{-1} (see Table 1), 2 h of polymerization at 60 °C.

Preparation of control samples. For the immobilization experiments we used the PA2 copolymer particles and PA2 particles with a hydrolyzed surface as blank samples. Through the hydrolysis the activated ester groups are removed. To hydrolyze the PA2 particle surface the particles where allowed to stand overnight in a borate buffer (pH 9). Then the particles where washed by repeated centrifugation and dispersion cycles.

Determination of the SAv-POD concentration. The concentration of the used SAv-POD solution was determined by the fluorescence titration method developed by Kada [9, 10]. A 1 : 1000 dilution of the original SAv-POD solution was used as sample. The reference solution was prepared from lyophilized SAv. First 0.750 mg SAv were dissolved in 1 ml phosphate puffer (pH 7.0). Then the solution was further diluted to give a 134 nM SAv solution. The biotin-4-fluorescein solution was prepared in MES buffer (pH 5.0) to yield a final concentration of 670 nM. From the titration a concentration value for the relation between enzyme activity and amount of SAv-POD can be calculated for (96 ± 26) pmol U^{-1}.

Immobilization of SAv-POD on the Latex

The immobilization experiment was performed at 22 °C in two different PBS buffers, one with pH 7.2 and one with pH 8.0. *p*(MMA-co-AUPDS) particles (sample PA 2) were incubated with the SAv-POD solution in plastic test tubes. For each pH value three different types of samples where prepared; one with normal particles, one with hydrolyzed particles and one control sample without particles. To the first two types of samples 0.4 mg of the particles where added. SAv-POD was added to all samples so that the enzyme activity in each sample was 8.3 mU. The final volume of the samples was adjusted to 1 ml with buffer. Three multiples of each different sample with particles and one control sample for each buffer where made. The samples where placed in a test tube shaker and incubated for 5 hours. After the incubation a washing procedure followed. Three times the samples where centrifuged for 10 min at 13 000 rpm. After each centrifugation step the pellet was dispersed in PBS buffer (pH 8.0) using ultrasonification combined with vigorous shaking. The enzyme activity was measured from each solution by taking a 50 μL aliquot on a microplate. Then 100 μL of the TMB substrate was added to each well by which a colour change from clear to brilliant blue appears where enzyme is present. After a few minutes the desired colour is developed. The reaction was stopped by addition of 100 μL 0.5 M sulphuric acid. After this addition the absorption was immediately measured at 450 nm.

Results and Discussion

Particle Preparation and Characterization

The copolymerization of AUPDS with MMA yielded nanoparticles in a diameter range from 116 nm to 146 nm (see Table 1). As stated in our earlier work the particles showed a narrow size distribution in scanning electron microscopy and in dynamic light scattering [4].

The numbers of particles were in the range from $(2.6 \pm 0.4) \times 10^{16}\,L^{-1}$ to $(2.6 \pm 0.4) \times 10^{16}\,L^{-1}$. The diameter as well as the particle numbers were in a typical range for latexes made by emulsion polymerization [11, 12]. The polyelectrolyte titration of the purified *p*(MMA-*co*-AUPDS) particles yielded a charge-to-mass ratio from 48 μeq g^{-1} to 95 μeq g^{-1}. Taking into account that the particles have a spherical shape we were able to calculate the surface area of the nanoparticles from their diameter determined by dynamic light scattering (Table 2). By combination of surface area, density and charges-per-mass ratio the charge-to-area, and closely related the area-to-charge ratio, were calculated. The results shown in Table 2 depict that the area which was occupied by one charge decayed from 1.24 nm^2 to 0.72 nm^2 when the surfmer concentration was raised. The blank sample PA 0 showed an area-to-charge ratio of 3.3 nm^2. We supposed that in contrast to the PA 1, PA 3 and PA 4 samples, positive charges in the blank originated from polymer end groups generated by the amidinium initiator.

To rate the calculated area per charge values, we used a geometric model of the single surfmer molecule shape and coverage. Assuming by van der Waals length calculations we approximated that every molecule covered an area of 0.6 nm × 0.6 nm which equals a 0.36 nm^2. Based on this minimum area approximation the coverage with the surfmer molecules rised from 29% to 51% (Table 2)

Table 2 Results from polyelectrolyte titration of *p*(MMA-*co*-AUPDS) particles with NaPES, radius of the particles and calculated surface area for samles PA 0, PA 1, PA 3 and PA 4

Sample	Radius nm	Charges per Mass (μeq g^{-1})	Surface Area ($m^2\,g^{-1}$)	Charges per Area (m^{-2})	Area per Charge (nm^2)	Coverage (%)
PA 0	350	3	6.7	3.3×10^{17}	3.3	5 [1]
PA 1	66	48	35.5	8.1×10^{17}	1.24	29 [2]
PA 3	60	71	39.1	1.2×10^{18}	0.92	39 [2]
PA 4	58	95	40.4	2.4×10^{18}	0.70	51 [2]

[1] The coverage of the blank sample PA 0 was calculated with an area of 0.43 nm, 0.43 nm = 0.18 nm^2 per amidinium residue

[2] The coverage of the *p*(MMA-*co*-AUPDS) samples were calculated based on an area of 0.43 nm × 0.43 nm = 0.18 nm^2 per amidinium residue

with increasing surfmer content in the nanoparticles. The increasing surfmer concentration therefore caused a decreasing particle diameter and a closer surfmer package on the colloidal surface. Further on the adsorption parameter a_{AUPDS} resulting from cmc determination of AUPDS by surface tension measurements took a value of 1.42 nm^2 [7]. Hence the surfmer molecules at the particle surface were more closely packed than at the air-water interface.

Immobilization of an Enzyme on the Particle Surface

Immobilization of SAv-POD on *p*(MMA-*co*-AUPDS) nanoparticles in pH 8.0 resulted in almost three times as much enzyme activity on the particles (Fig. 2) as incubation in pH 7.2 with (5.3 ± 0.2) mU mg^{-1}). The enzyme activity on one mg of *p*(MMA-*co*-AUPDS) was calculated to (15.5 ± 0.2) mU when the incubation was proceeded at pH 8.0.

Also the non-specific binding which was determined through incubation of hydrolyzed particles with SAv-POD, was higher at an increased pH. Expressed as a percentage value of the total enzyme immobilization the non-specific binding was 53% for incubation in pH 7.2 and only 31% when the incubation was made in pH 8.0. The control samples without particles lost their activity completely.

With the relation between the enzyme activity and the amount of SAv-POD from the titration results in experimental section and by using the hydrodynamic particle diameter of (146 ± 5) nm we were able to calculate also the enzyme immobilization density to a value of (1.49 ± 0.45) nmol SAv per 1 g particles or (4.3 ± 1.3) μm^2 per Sav-POD molecule. For comparison the maximum immobilization of pure SAv on *p*(styrene-*co*-AUPDS) with a radius of 53 nm is (500 ± 90) nmol per 1 g particles or 160 nm^2 per SAv tetramer [7]. Even though 1 g of these smaller particles possessed a larger surface this is a large difference. The relation between enzyme activity and the amount of SAv in the SAV-POD solution determined by biotin titration was considered to be a minimum value. Therefore we assumed that the values of enzyme activities per mass of particles attained in this experiment were still below the possible maximum value. So the optimization of the immobilization process has to be expanded on other parameters as surfmer structure or copolymer composition such as using surfmers with oligoethyleneglycol spacers or more hydrophilic comonomers.

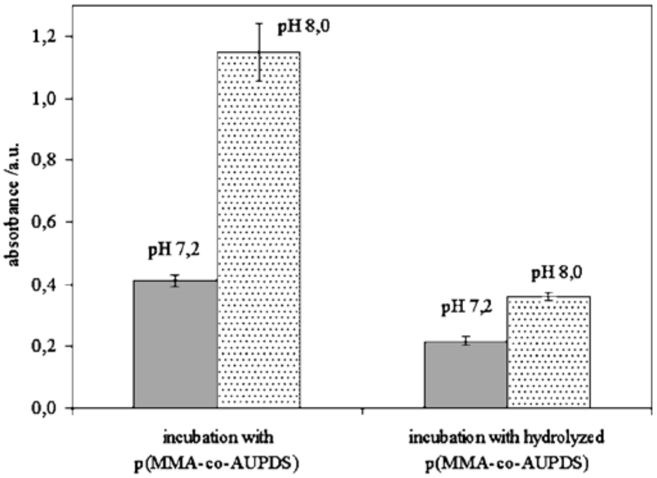

Fig. 2 Results from the incubation of 0.4 mg *p*(MMA-*co*-AUPDS) nanoparticles and hydrolyzed control particles with 8.3 mU SAv-POD in PBS-buffers with different pH values. TMB substrate was added to the different samples after incubation and absorption was measured at 450 nm. A high absorption value indicates a larger consumption of substrate and thereby a higher enzyme activity

Conclusions

The copolymerization of MMA and AUPDS yielded particles with a surfmer concentration dependent diameter between 116 nm and 145 nm. The activated ester surfmer residues covered an area of 0.7 nm^2 to 1.24 nm^2 depending on surfmer feed concentration. This area-per-charge was smaller than the analogous value of 1.42 nm^2 taken from cmc measurements.

The protein conjugate streptavidin peroxidase (SAv-POD) was immobilized on the particle surface by incubating particles in PBS buffer containing this enzyme. By addition of the enzyme substrate TMB the enzyme activity on the particles was determined. A higher enzyme activity was achieved if the particles were incubated in a buffer with pH 8.0 than with pH 7.2. The non-specific binding could be determined to 37% of the total binding by incubating particle blank samples with the same amount of protein. The experiments showed that SAv-POD can be immobilized on surfmer copolymer particles with preserved activity. This result shows that the surface of the surfmer copolymer is able to act as a stabilization agent similar to the proteins like BSA used for enzyme preservation. This ability of the surfmer copolymers may proof to be advantageous for the particulate formulation of enzymes in biotechnological applications. Additionally the covalently linked streptavidin conjugates still contain their free biotin binding sites. These could be used e.g. for immobilization of another type of enzyme thus enabling enzyme cascade reactions in the confined space around the nanoparticles.

Acknowledgement The authors of this paper would like to thank the “BMBF”, the “Fraunhofer-Gesellschaft” and the “Land Baden-Württemberg” for their financial support of a junior research group on “Biomimetic Interfaces” (FKZ 0312180).

References

1. Korri-Youssoufi H, Richard C, Yassar A (2001) A new method for the immobilisation of antibodies in conducting polymers. Materials Science and Engineering: C 15:307
2. Luo Y, Prestwich GD (2001) Hyaluronic Acid-*N*-hydroxysuccinimide: A Useful Intermediate for Bioconjugation. Bioconjugate Chem 12:1085
3. Herold M, Brunner H, Tovar GEM (2002) Synthesis of novel activated ester surfmers for use in preparation of latexes for bioconjugation. Polymer Preprints 43:1003
4. Herold M, Brunner H, Tovar GEM (2003) Polymer nanoparticles with activated-ester surface by using functional surfmers. Macromol Chem Phys 204:770
5. Herold M, Brunner H, Tovar GEM (2004) Polymerkolloide mit Aktivester-Surfmer-Oberfläche für die Biokonjugation in einstufiger Synthese. Macromolecular Rapid Communications 25:F16
6. Weber A, Herold M, Brunner H, Tovar GEM (2004) Bioconjugative Polymer Nanospheres Studied by Isothermal Titration Calorimetry. Thermochimica Acta 415:69
7. Herold M (2004) Herstellung und Charakterisierung von Polymernanopartikeln mit Aktivesteroberfläche, Universität Stuttgart, http://elib.uni-stuttgart.de/opus/volltexte/2004/2077/
8. Berks BC, Ferguson SJ, Moir JW, Richardson DJ (1995) Enzymes and associated electron transport systems that catalyse the respiratory reduction of nitrogen oxides and oxyanions. Biochim Biophys Acta 1232:97
9. Gruber HJ, Kada G, Marek M, Kaiser K (1998) Accurate titration of avidin and streptavidin with biotin-fluorophoreconjugates in complex, colored biofluids. Biochim Biophys Acta 1381:203
10. Kada G, Kaiser K, Falk H, Gruber HJ (1999) Rapid estimation of avidin and streptavidin by fluorescence quenching or fluorescence polarization. Biochimica et Biophysica Acta 1427:44
11. Gilbert RG (1995) Emulsion Polymerisation: A Mechanistic Approach. Academic Press, San Diego
12. Asua JM, Schoonbrood HAS (1998) Reactive surfactants in heterophase polymerisation. Acta Polym 49:671

Progr Colloid Polym Sci (2006) 133: 35–40
DOI 10.1007/2882_048

Ingo Berndt
Jan Skov Pedersen
Peter Lindner
Walter Richtering

Structure of Doubly Temperature Sensitive Core-Shell Microgels Based on Poly-*N*-Isopropylacrylamide and Poly-*N*-Isopropylmethacrylamide

Abstract Swelling properties of doubly temperature sensitive core-shell microgels consisting of two thermosensitive polymers namely poly-*N*-isopropylacrylamide (PNIPAM) with a lower critical solution temperature (LCST) at ca. 34 °C and poly-*N*-isopropylmethacrylamide (PNIPMAM) with a LCST of ca. 44 °C have been investigated by small-angle neutron scattering (SANS). Two types of microgels with different core-shell composition were studied: PNIPAM-core – PNIPMAM-shell microgels as well as a microgel with inverse structure, i.e. PNIPMAM-core – PNIPAM-shell. A core-shell form factor has been employed to evaluate the structure and the real space particle structure is expressed by radial density profiles. By this means the influences of composition and temperature on the internal structure have been revealed. At temperatures between the LCSTs the swelling of the PNIPMAM-shell leads to an expansion of the PNIPAM-core. At temperatures below the core LCST, the core cannot swell to its native size (i.e. in the absence of a shell) because the maximum expanded shell network prohibits further swelling. Thus depending on temperature the shell either expands or compresses the core. The inverse PNIPMAM-core – PNIPAM-shell microgel displays qualitatively different behavior. At intermediate temperatures, the segment density of the shell is higher as compared to the core. Since the density ratio of shell and core depends on temperature, such core-shell microgels provide interesting opportunities for encapsulation and controlled release.

Keywords Core-shell · Data modelling · Microgel · Poly-*N*-isopropylacrylamide (PNIPAM) · Poly-*N*-isopropylmethacrylamide (PNIPMAM) · Small angle neutron scattering (SANS)

Ingo Berndt · Walter Richtering (✉)
Institute of Physical Chemistry,
RWTH Aachen University, Landoltweg 2,
52056 Aachen, Germany
e-mail: richtering@rwth-aachen.de

Jan Skov Pedersen
Department of Chemistry,
University of Aarhus, Langelandsgade 140,
8000 Aarhus C, Denmark

Peter Lindner
Institut Laue-Langevin,
6, rue Jules Horowitz,
BP 156-38042 Grenoble Cedex 9, France

Introduction

Materials composed of chemically cross-linked polymers that are sensitive to external stimuli have been used in a wide variety of applications as, e.g. in catalysis [1], drug delivery [2], sensors [3], biomolecule immobilization [4], colloidal crystals [5], and micro-optics [6]. Poly-*N*-isopropylacrylamide (PNIPAM) is the most widely investigated temperature sensitive microgel system [7] and shows structural changes upon heating above the lower critical solution temperature (LCST) in aqueous solution [8]. The temperature sensitive properties of PNIPAM can be extended to react on further stimuli as, e.g. ionic strength [9], solvent composition [10], pH [11], and selective reaction [12] by copolymerization with monomers that show sensitivity to one of those stimuli.

Lyon and co-workers introduced multi-responsive microgels with a core-shell morphology preparing PNIPAM core-PNIPAM-*co*-acrylic acid shell microgels which are sensitive to temperature and pH [13]. Our group recently presented core-shell microgels composed of two temperature sensitive polymers, PNIPAM and poly-*N*-isopropylmethacrylamide (PNIPMAM) with LCST of 34 and 44 °C, respectively, in either core or shell [14].

Detailed knowledge of the internal microgel structure is important for their application in fields where particular properties are required. Scattering methods as small-angle neutron scattering (SANS), small-angle X-ray scattering (SAXS) as well as dynamic (DLS) and static light scattering (SLS) are powerful tools to explore the structure of macromolecules and have been successfully applied to microgels [15, 16].

Stieger et al. have been the first to apply a direct modelling approach to describe SANS data of PNIPAM microgels over a wide q-range (where $q = \frac{4\pi}{\lambda}\sin\frac{\Theta}{2}$ is scattering vector at wavelength λ and scattering angle Θ) [17]. They convoluted a homogeneous sphere form factor with a Gaussian obtaining density profiles that gradually decreased at the surface to describe the surface fuzziness at temperatures below the LCST. This particle structure agrees with studies revealing that the cross linker is consumed faster than the monomer [18]. The same model was applied to SLS data of PNIPAM microgels and it was demonstrated that a stepwise addition of cross linker during the synthesis leads to a more homogenous structure [19]. Boyko et al. combined a hard sphere form factor with the form factor of a randomly branched polymer to describe SANS data of temperature sensitive poly-*N*-vinylcaprolactam-*co*-*N*-vinylpyrrolidone microgels [**?**]

The mutual influence of core and shell swelling was observed with core-shell systems where both core and shell consist of swellable polymer networks [14, 21, 22]. Experiments by Lyon and co-workers employing fluorescence resonance energy transfer techniques (FRET) revealed that swelling properties of the core are affected by the shell and the phase transition temperature of the core shifted towards higher temperatures as the shell thickness increased. This technique also allows for a calculation of core-shell interface thickness [23, 24].

Our group recently established a form factor model to describe scattering data and analyze the structure of microgel particles with core-shell morphology [25–28]. The model accounts for an interpenetrating layer of core and shell network and a graded particle surface. Here we demonstrate what structural information on core-shell microgels can be obtained from SANS combined with direct data modelling. Data from PNIPAM-core – PNIPMAM-shell microgels as well as from a microgel with inverse structure, i.e. PNIPMAM-core – PNIPAM-shell will be discussed.

Experimental Section

The synthesis of the core-shell microgel particles has been described in detail previously [14, 26]. Specifications of the shell composition of PNIPAM-core – PNIPMAM-shell microgels are given in the sample name scheme, for example *CS-5/0.69*, where the first number denotes the molar percentage of cross linker monomer in the shell (omitting the units) and the second number gives the relative mass ratio $m_{\text{shell}}/m_{\text{core}}$ after purification (see below), where m_{shell} is the mass of the shell and m_{core} is the mass of the core. The samples were purified by repeated ultra-centrifugation, decantation of the supernatant and redispersion in deionized water. Dynamic light scattering experiments have been performed with a modified ALV goniometer setup. SANS experiments were carried out at the D11 beam line at the Institut Laue-Langevin (ILL) in Grenoble, France. ILL provided software GRAS$_{\text{ANS}}$P was used for absolute calibration, background correction, and azimuthal averaging following standard procedures at the ILL. The microgels were investigated at mass concentrations of 0.2 wt % in D_2O.

Theory and Data Analysis

Small-angle neutron scattering experiments provide an intensity distribution $I(q)$ in reciprocal space as a function of momentum transfer q and real space information can be revealed from data analysis [29]. A convenient way to express the scattering intensity distribution of a sample is the introduction of the differential scattering cross section $\frac{d\sigma(q)}{d\Omega}$ as it is independent of the transmission and form of the sample. In general the differential scattering cross section may be expressed for a dispersion of spherically symmetric particles by

$$\frac{d\sigma}{d\Omega} = n\,P(q)S(q)\,, \qquad (1)$$

where n is the number density of particles. $P(q)$ is the particle form factor that describes the structure of the particle and $S(q)$ is the structure factor. $P(q)$ is normalized so that $P(0) = \Delta\rho^2 V_{\text{polymer}}^2$, where $\Delta\rho$ is the scattering contrast of the polymer and V_{polymer} the volume of the polymer within the particle. The structure factor accounts for the interference of scattering from different particles. In the present paper we present only data obtained at high dilution (0.2 wt %); hence, inter-particle correlations can be neglected and $S(q) = 1$.

Microgel particles are expected to have an inhomogeneous structure with a fuzzy surface due to faster consumption of cross linker molecules during at the earlier stages of the synthesis [18]. As a consequence our model of the structure of core-shell microgels employs a profile like the one shown in Fig. 1, with a graded outer surface characterized by σ_{out}, and an interface between core and

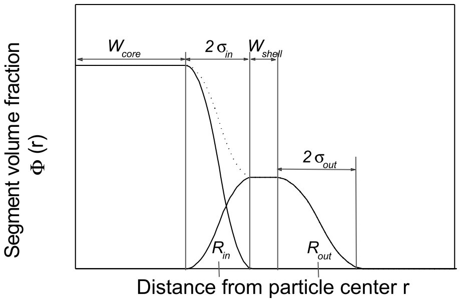

Fig. 1 Schematic illustration of the internal structure of core-shell microgels. W_{core} and W_{shell} describe the widths of central core and shell boxes. The interpenetration layer of core and shell is characterized by $2\sigma_{\text{in}}$ and σ_{out} denotes the half width of the outer surface. The *dotted line* represents the total of core and shell

shell characterized by σ_{in}. The inner part of the core is described by a box of width W_{core} and the central part of the shell by a box of width W_{shell}. The central portions may have different densities depending on the swelling state of the particles. We used a parabolic shape for the fuzzy interfaces.

The radial density profile $\rho(r)$ of a particle with a graded surface can also be expressed by the half width radius R and the interface half width σ. The Fourier transformation of this profile can be calculated analytically and the normalized Fourier transformation is

$$\begin{aligned}\Phi(q, R, \sigma) = \frac{4\pi}{V}\Bigg[&\left(\frac{R}{\sigma^2}+\frac{1}{\sigma}\right)\frac{\cos(q(R+\sigma))}{q^4}\\ &+\left(\frac{R}{\sigma^2}-\frac{1}{\sigma}\right)\frac{\cos(q(R-\sigma))}{q^4}\\ &-\frac{3\sin(q(R+\sigma))}{q^5\sigma^2}-\frac{3\sin(q(R-\sigma))}{q^5\sigma^2}\\ &+\frac{2\cos(qR)}{q^5\sigma^2}+\frac{6\sin(qR)}{q^5\sigma^2}\Bigg]\,. \qquad (2)\end{aligned}$$

Thus the scattering amplitude of a core-shell particle can be expressed by

$$\begin{aligned}A(q) = {} & \Delta\rho_{\text{shell}} V_{\text{shell}} \Phi_{\text{shell}}(q, R_{\text{out}}, \sigma_{\text{out}})\\ & + (\Delta\rho_{\text{core}} - \Delta\rho_{\text{shell}}) V_{\text{core}} \Phi_{\text{core}}(q, R_{\text{in}}, \sigma_{\text{in}})\,. \qquad (3)\end{aligned}$$

Particle size polydispersity was described by a normalized Gaussian number distribution. The finite collimation of the neutron beam, wave length spread, and the finite resolution of the detector contribute to the experimental smearing and can each be approximated by a Gaussian function [30] so that the experimental smearing can be expressed by a combined resolution function.

Results and Discussion

Core-shell microgels composed of PNIPAM, that exibits a LCST of 34 °C in the core, and PNIPMAM with a LCST of 44 °C in the shell show distinct changes in particle size at temperatures corresponding to the transitions of core and shell polymers. (All experiments were performed with D_2O as solvent; in H_2O the transition temperatures are slightly lower.) In Fig. 2 the temperature dependent hydrodynamic radius is plotted for a PNIPAM–PNIPMAM as well as for a PNIPMAM–PNIPAM core-shell microgel, the data of the corresponding core particles is shown for comparison.

The collapsed state at high temperatures can be regarded as a reference state since the synthesis proceeded at 70 °C, which is well above the core LCST and thus the shell is polymerized onto the collapsed core microgel. At temperatures above 45 °C all the core-shell particles have a larger radius as compared to the parent core.

PNIPAM-core – PNIPMAM-shell microgels reveal two transitions when the temperature is reduced. First the solvent quality changes from poor to good for the shell polymer and at 44 °C a distinct transition is found. With further decreased temperature below 34 °C the PNIPAM core starts swelling and a second transition is observed. For the inverse system PNIPMAM-core – PNIPAM-shell only a slight increase of the hydrodynamic radius is observed when lowering the temperature below the LCST of PNIPMAM. The core-shell microgel is smaller as compared to the naked core at temperatures between 35 and 41 °C.

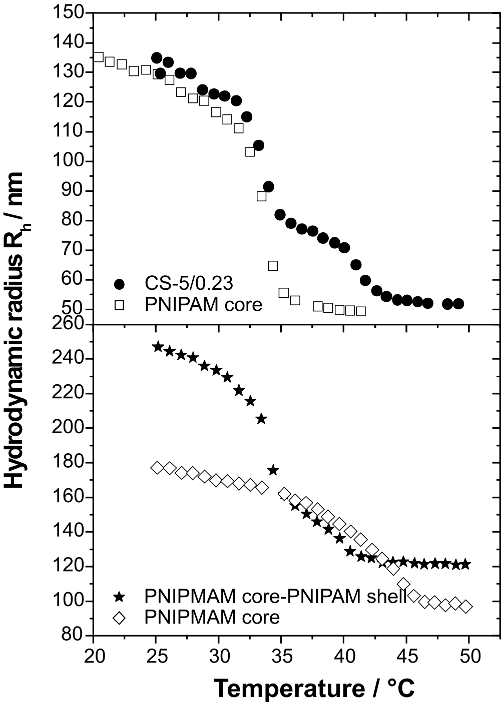

Fig. 2 Particle sizes as obtained from DLS in heavy water for core-shell microgels and the parent core. *Top*: PNIPAM-core – PNIPMAM-shell microgel sample CS-5/0.23, *bottom*: inverse PNIPMAM-core – PNIPAM-shell microgel

SANS is a powerful technique to investigate internal structural changes of core-shell microgels whereas DLS only provides information on the total hydrodynamic particle size. SANS experiments were carried out at three temperatures: 50, 39, 25 °C. These temperatures correspond to the states where (a) both core and shell are collapsed, (b) one part is swollen and the other is collapsed, and (c) both core and shell are swollen. A broad q-range (0.001–0.2 Å^{-1}) was studied which allows to obtain information on the internal as well as on the overall structure of the core-shell microgel particles.

PNIPAM-core – PNIPMAM-shell Microgels

The modeling of SANS data in the fully collapsed state is straightforward and the structure of the core-shell particles can be well described by two-box profiles with a narrow core-shell interface and a sharp outer surface. The width of the core-shell interfaces for the different samples is $2\sigma_{\text{in}} = 3.4$–$4.2$ nm and slightly smaller than the surface thickness of the collapsed pure core which is 5.4 nm. The width of the outer surface $2\sigma_{\text{out}} = 3.4$–$5.2$ nm is similar to that of the pure core. Increased shell/core mass ratios lead to thicker shells. The core profiles show only minimal deviations from the pure core profile. The total particle sizes quantitatively agree with the hydrodynamic radii as measured by DLS.

Behavior at intermediate temperature: In Fig. 3 scattering data and fits at 39 °C are presented. A slight shift of the form factor minima towards lower q-values is found with increased shell mass with samples CS-5/0.23, CS-5/0.69 and CS-5/1.42 indicating slightly increased dimensions of the dense PNIPAM core. Obviously, the scattering profile of sample CS-5/2.50 is more affected by contributions from the shell in the range $q = 0.015$–$0.04\ \text{Å}^{-1}$ and an even stronger shift to lower q is observed.

The scattering profiles reveal a steeper slope in the low q range ($q = 0.002$–$0.008\ \text{Å}^{-1}$) with increased core-shell mass ratio indicating a bigger radius of gyration. This intuitively agrees with the DLS results as a thicker shell is more swellable than a thinner one. Furthermore, one observes that the slope of the scattering profiles in the intermediate q-range from 0.01–0.04 Å^{-1} becomes less steep with higher shell mass. Thus there are only small contributions from swollen shell $\left(I(q) \propto q^{-2}\right)$ to the scattering profile in this regime.

A swelling of the shell polymer network proceeds in tangential and radial direction. The radial swelling directly leads to an increase of the shell thickness. Swelling in the tangential directions influences the core as it leads to a mechanical stress at the core-shell interface [23, 25, 26]. This stress is released by expanding the flexible core and core-shell interface; in other words, the core-shell interface is pulled outwards. The force which is developed from the swollen shell to stretch the core increases with the shell mass [31, 32]. The core dimensions will be increased until equilibrium between the force exerted by the shell and the resisting elastic force developed in core is reached. Radial density profiles obtained from SANS curves at 39 °C are displayed in Fig. 3b.

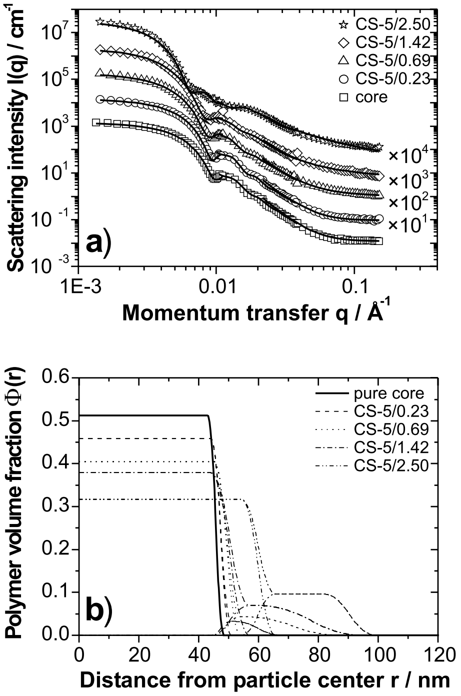

Fig. 3 **a** Scattering profiles of core-shell microgels with varied shell/core mass ratios taken at 39 °C. Samples CS-05/0.23, CS-5/0.69 and CS-5/1.42 exhibit a slight shift of the form factor minima towards lower q compared to the pure core indicating increased dimensions of the core. The scattering profile of CS-5/2.50 is more affected from contributions of the shell in the intermediate q range. **b** Density profiles at 39 °C. The PNIPAM core has a compact structure, but its dimension is increased due to the influence of the swollen shell. The effect increases with higher shell mass. *Dotted lines* represent the total polymer density distribution

Generally, the density profiles reveal that the structure can be described by a dense box profile for the core and a highly swollen shell. The dimensions of the core (described by R_{in}) grow from 47 nm to 60 nm as the shell mass increases and the width of the interface increases from $2\sigma_{\text{in}} = 7$ nm at the sample with the thinnest shell to 12 nm at the sample with the thickest shell. The polymer volume fraction of the core decreases from 46% to 32% in the same order. One observes that the volume fraction of the shell increase from 3.3 to 9.7% as the shell mass increases. The thickness of the shell as given by $\sigma_{\text{in}} + W_{\text{shell}} + 2\sigma_{\text{out}}$ increases from 20 to 39 nm.

The sample with the highest shell mass (CS-5/2.50) reveals a much broader box in the shell profile. This may explain why this sample shows a much larger stretching of the core. From a chemical point of view, one may assume a much higher cross linker gradient in the shell than in the core, so that in case of thin shells (low shell mass) only a narrow layer of highly cross-linked polymer close to the core-shell interface is present and the fuzzy surfaces of the these samples mainly consist of only loosely cross-linked polymer chains. Only the cross-linked layers in the shell close to the core-shell interface will develop the force, which expands the core. Thus samples CS-5/0.23, CS-5/0.69 and CS-5/1.42 show small expansions of the core as the shell mass increases, but compared to sample CS-5/2.50 the deformations a rather small. Due to a much higher shell/core mass ratio CS-5/2.50 provides a much thicker layer of highly cross-linked polymer in the shell and will consequently develop a stronger expanding force than the other samples. Calorimetric measurements revealed that the core transition is shifted to higher temperatures when the swollen swell restrains the core to collapse. The temperature shift increases with the mass of the shell [31, 32].

Behavior at low temperature: The scattering data at 25 °C show fewer details as compared to higher temperatures. The total density profiles of all samples smoothly decay similar to the profiles of pure core microgels in the fully swollen state.

More remarkably for the PNIPAM-core – PNIPMAM-shell microgels is the fact that the dimensions of the core are significantly reduced to about 80–90 nm as compared to the naked core where $R_{\text{in}} + 2\sigma_{\text{in}}$ was found to be 122 nm. The situation at 25 °C is opposite to what happens at temperatures just below the shell's LCST. At 34 °C the core begins to swell and pushes the shell in radial direction and an opposing force is developed in the shell due to the elasticity of the network. The cross-links in the shell close to the core-shell interface limit the core swelling. Even stronger forces from the core cannot lead to further size increase when the shell network is expanded to a maximum extent. The cross-linker content is similar in all shells, so that one may understand why the reduced core swelling is almost independent of the shell mass.

PNIPMAM-core – PNIPAM-shell (Inverse) Microgel

Figure 4 displays the calculated radial density profiles obtained from SANS data on the inverse PNIPMAM-core – PNIPAM-shell microgel. At high temperatures, i.e. above both LCSTs, both core and shell are collapsed and the structure is well described by a density profile consisting of two boxes with a narrow interface and a sharp surface with a total width of 3–4 nm. The polymer volume fractions in core and shell are similar at ca. 50%. The particle size obtained from SANS agrees nicely with the hydrodynamic radius determined by dynamic light scattering. At 25 °C, both core and shell networks are swollen. The density profile still shows a change in the segment density between core and shell, and the profile decays constantly from the center to the periphery.

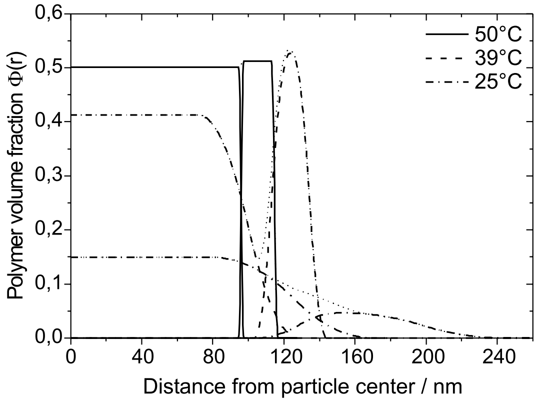

Fig. 4 Radial density profiles calculated from the modeling procedure at 25, 39, and 50 °C. At the intermediate temperature the shell reveals a higher density than the swollen core

Most interesting is the density profile obtained at 39 °C. The dimensions of the core are increased due to the swelling of the PNIPMAM at this temperature and the water content in the core increased. Nevertheless, the dimensions of the core at 39 °C (128 nm) are still reduced as compared to the pure, naked core at 39 °C which were determined independently from SANS measurements to 148 nm (not shown in the plot). More important, however, the density of the shell is *higher* than the density inside the core. At this temperature D_2O is already a good solvent for the PNIPMAM core but still a bad solvent for the PNIPAM shell. Apparently, the thermodynamic hydration forces that lead to the swelling of the core are not sufficient to expand the PNIPAM network in the shell. Consequently, a structure is obtained with a shell that is *denser* as compared to the core. Thus the inverse PNIPMAM-core – PNIPAM-shell microgel shows a qualitatively different density profile as the PNIPAM-core – PNIPMAM-shell microgels discussed above.

Conclusions

The data presented here demonstrate how polymers with different temperature sensitivity can be combined in microgels with a core-shell morphology in order to tailor and control the polymer density in different regions of the particle. Most important is the sequence of polymer, i.e. whether the component with the higher transition temperature forms the core or the shell. In the former case, core-shell microgels with a higher density in the shell can be obtained. Since the density ratio of shell and core depends on temperature, such core-shell microgels provide interesting opportunities for encapsulation and controlled release.

Furthermore the temperature dependent swelling can be controlled by the shell-core mass ratio and the cross link density in core and shell. Depending on temperature and microgel composition, the shell can develop a mechanical force which expands the core or restricts its swelling.

This mutual influence can be studied in detail by scattering experiments that cover a broad q-range so that the entire particle structure is probed.

Acknowledgement Financial support by the Deutsche Forschungsgemeinschaft (DFG) and the Danish Natural Science Research Council is gratefully acknowledged.

References

1. Bergbreiter DE, Case BL, Liu Y-S, Caraway JW (1998) Macromolecules 31:6053–6062
2. Castro Lopez V, Raghavan SL, Snowden MJ (2004) React Funct Polym 58:175–185
3. Gerlach G, Guenther M, Suchaneck G, Sorber J, Arndt K-F, Richter A (2004) Macromol Symp 21:403–410
4. Cornelius VJ, Snowden MJ, Silver J, Fern GR (2004) React Funct Polym 58:165–173
5. Senff H, Richtering W (1999) J Chem Phys 111:1705–1711
6. Kim J, Serpe MJ, Lyon LA (2005) Angew Chem 117:1357–1360
7. Pelton R (2000) Adv Colloid Interf Sci 85:1–33
8. Heskins M, Guilett J (1968) Macromol Sci Chem A2(8):1441–1455
9. Rasmusson M, Vincent B (2004) React Funct Polym 58:203–211
10. Mielke M, Zimehl R (1998) Ber Bunsenges Phys Chem 102:1698–1704
11. Hoare T, Pelton R (2004) Macromolecules 37:2544–2550
12. Nayak S, Lyon LA (2004) Angew Chem 116:6874–6877
13. Jones CD, Lyon LA (2000) Macromolecules 33:8301–8306
14. Berndt I, Richtering W (2003) Macromolecules 36:8780–8785
15. Kratz K, Hellweg T, Eimer W (2001) Polymer 42:6631–6639
16. Saunders BR (2004) Langmuir 20:3925–3932
17. Stieger M, Richtering W, Pedersen JS, Lindner P (2004) J Chem Phys 120:6197–6206
18. Wu X, Pelton RH, Hamielec AE, Woods DR, McPhee W (1994) Colloid Polym Sci 272:467–477
19. Meyer S, Richtering W (2005) Macromolecules 38:1517–1519
20. Boyko V, Richter S, Grillo I, Geissler E (2005) Macromolecules 38:5266–5270
21. Jones CD, Lyon LA (2003) Langmuir 19:4544–4547
22. Jones CD, Lyon LA (2003) Macromolecules 36:1988–1993
23. Gan D, Lyon LA (2001) J Am Chem Soc 123:8203–8209
24. Jones CD, Mc Grath JG, Lyon LA (2004) J Phys Chem B 108:12652–12657
25. Berndt I, Pedersen JS, Richtering W (2005) J Am Chem Soc 127:9372–9373
26. Berndt I, Pedersen JS, Lindner P, Richtering W (2006) Langmuir 22:459–468
27. Berndt I, Pedersen JS, Richtering W (2006) Angew Chem 118:1769–1773
28. Berndt I, Pedersen JS, Richtering W (2006) Angew Chem Int Ed 45:1737–1741
29. Pedersen JS (1997) Adv Colloid Interf Sci 70:171–210
30. Pedersen JS, Posselt D, Mortensen K (1990) J Appl Crystallogr 23:321–333
31. Berndt I, Popescu C, Wortmann F-J, Richtering W (2006) Angew Chem 118:1099–1102
32. Berndt I, Popescu C, Wortmann F-J, Richtering W (2006) Angew Chem Int Ed 45:1081–1085

Progr Colloid Polym Sci (2006) 133: 41–44
DOI 10.1007/2882_050

Magalie Faivre
Clement Campillo
Brigitte Pepin-Donat
Annie Viallat

Responsive Giant Vesicles Filled with Poly(*N*-isopropylacrylamide) Sols or Gels

Magalie Faivre · Clement Campillo ·
Annie Viallat (✉)
Laboratoire de Spectrométrie Physique,
UMR C5588 (CNRS)—Université Joseph
Fourier, 38402 Saint Martin d'Hères,
France
e-mail: viallat@marseille.inserm.fr

Annie Viallat (✉)
Present address:
U600 INSERM, UMR 6212 (CNRS),
163 av. de Luminy, Case postale 937,
13288 Marseille Cedex09, France
e-mail: viallat@marseille.inserm.fr

Brigitte Pepin-Donat (✉)
Laboratoire de Microélectronique
Organique et Hybride, UMR 5819,
DRFMC, CEA-Grenoble, France
e-mail: brigitte.pepin-donat@cea.fr

Abstract We prepared giant unilamellar vesicles (GUVs) enclosing solutions or covalent gels of Poly(N-isopropylacrylamide) (PolyNipam). Concentrated suspensions of GUVs were prepared by applying an alternative field on a lipid film hydrated by a monomer solution containing N-isopropylacrylamide, crosslinker (*N*,*N′*-methylene-bis-acrylamide), initiator and sucrose. Vesicle inner medium was polymerised and crosslinked by UV irradiation of the suspension, yielding viscous vesicles enclosing a solution of linear PolyNipam chains (when no bisacrylamide was used) or elastic vesicles filled with a covalent PolyNipam gel. We show that gel-filled vesicles are responsive systems triggered by the temperature: they shrink, reducing by a factor eight their volume below the critical temperature (32 °C in water, lower in glucose solution) and re-swell in a reversible and reproducible way upon decreasing temperature. In both cases, we show that the vesicle lipid membrane interacts with the internal polymer, resulting in an strong resistance of the vesicles to external mechanical stresses (enhanced tension of lysis).

Keywords Gels · Poly(N-isopropylacrylamide) · Vesicles polymer · Volume transition

Introduction

Giant unilamellar vesicles (GUVs) are fluid and semi-permeable soft lipid shells. They have been extensively studied because their sizes and curvatures are similar to that of living cells and their lipid bilayer membrane exhibits basic properties of biological membranes [1, 2]. However, their poor mechanical properties due to the absence of cytoplasm and cytoskeleton, limit their relevance as minimal models for living cells. The goal of this study is to prepare viscoelastic GUVs with controlled mechanical properties, which confer to them an enhanced resistance to external stresses, thus allowing to address open physical questions relative to the behaviour of deformable soft shells submitted to external stresses (flow, pressure). A second objective is to obtain responsive systems, triggered by an external parameter, and able for instance to release material or to move by themselves in successive contraction/extension stages. Hydrophilic polymers are well-suited candidates to confer such properties to vesicles although only a few works have been devoted to combinations of polymer networks and liposomes. Apart studies concerning gel beads coated with lipids [3–9], lipid vesicles were mainly combined with physical gels, used as external coating (rigid actin filaments [10]) or internalized in the vesicle volume (rigid actin networks [11, 12], agarose gels [13], solutions of aggregated Poly(N-isopropylacrylamide) (PolyNipam) [14]). A recent work dealt with controlled covalent PolyNipam gels but concerned submicronic liposomes [15, 16].

Here, we report the preparation, first characterisation and the responsive behaviour of GUVs enclosing PolyNipam solutions or gels. PolyNipam is known to present a volume transition at 32 °C, see for example [17].

Experimental Section

The lipid is 1,2-dioleolyl-sn-glycero-3-phosphocholine (DOPC) (Sigma; St Quentin-Fallavier, France). One experiment was performed using 5% biotynilated 1,2-dioleoyl-sn-glycero-3-phosphoethanolamine-*n*(biotinyl) (Sigma; St Quentin-Fallavier, France) lipid, incubated with FITC-streptavidin in order to make the membrane fluorescent. The monomer intended to constitute the polymer gel is N-isopropylacrylamide (NIPAM) (Acros Organics; Janssens Pharmaceuticalaan 3A, Belgium). The crosslinker is N,N'-methylene-bis-acrylamide (MBA) (Sigma) and the initiator is 2,2-diethoxyacetophenone (DEAP) (Acros Organics).

Vesicles were electroformed [18] in a pregel aqueous solution containing sucrose (100 mM), NIPAM (300 mM), MBA (0 mM, 3 mM, 9 mM or 15 mM) and DEAP (1 µl/ml). A small volume of the obtained vesicle suspension was injected in small chambers filled with a solution of glucose (100 mM), NIPAM (300 mM), DEAP (1 µl/ml), but which did not contain the crosslinker. This former solution i) allows vesicle sedimentation since the density of sucrose is smaller than that of glucose, and makes easier the observation of vesicles from phase contrast microscopy (sucrose and glucose have different refractive indexes); ii) ensures osmotic sucrose/glucose equilibrium; iii) equilibrates Nipam concentration (Nipam can diffuse through the lipid membrane); iv) prevents gelation of the external solution (since no crosslinker is present), which would trap gel-filled vesicles in the external medium.

All solutions were deoxygenated by bubbling with dry argon for 30 mn and kept in a glove bag under argon atmosphere. Finally, the chambers were covered by a quartz coverslip and placed over an ice pack (Medicool coolpack MC-15) to keep temperature below 30 °C. UV irradiation was performed for five minutes to one hour using a UV lamp (UV-B Mid-range 300 nm Sunlight-Erythemal AH 68-1091 F6T5E, Harvard Apparatus). Photo-illuminated vesicles were then diluted in a 100 mM glucose solution and observed by phase contrast or fluorescence (inverted microscope Olympus IX71, CCD camera). Image analysis was performed using the image software (NIH, 1.62c). A detergent (Decon90, Prolabo, France) is used to dissolve the gel-filled vesicles membrane and Rhodamine 6G (Sigma) is used as fluorophore for membrane labelling.

Results

The vesicles observed after photo-illumination are well contrasted and generally present very regular spherical shapes of radii in the range 10–60 µm (Fig. 1a).

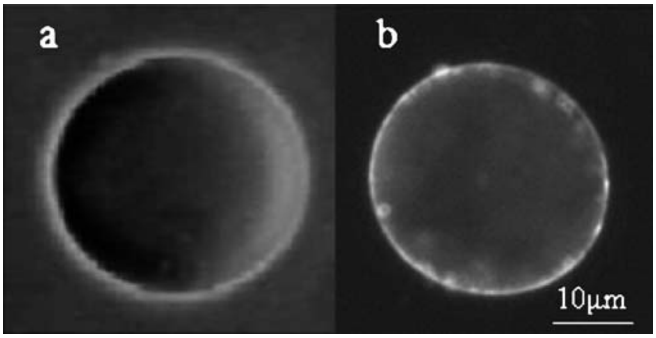

Fig. 1 Gel-filled vesicle observed from phase contrast microscopy (**a**) and fluorescence microscopy: FITC-streptavidin fixed on biotynilated lipids on the membrane (**b**)

Characterisation of Vesicles Enclosing a Gel or a Polymer Sol

The presence of the lipid membrane is clearly demonstrated from fluorescence observations of vesicles prepared with biotynilated lipids bearing FITC-streptavidin, as illustrated in Fig. 1b.

The sol or gel nature of the inner vesicle volume was characterised after breakage of the membrane upon injection of a detergent close to the vesicle. The behaviour of a polymer sol filled-vesicle is illustrated in Fig. 2a–c. Upon Decon injection, the membrane of the vesicle (initial state, Fig. 2a) breaks and the inner polymer solution progressively vanishes, since it is fully soluble (Fig. 2b,c).

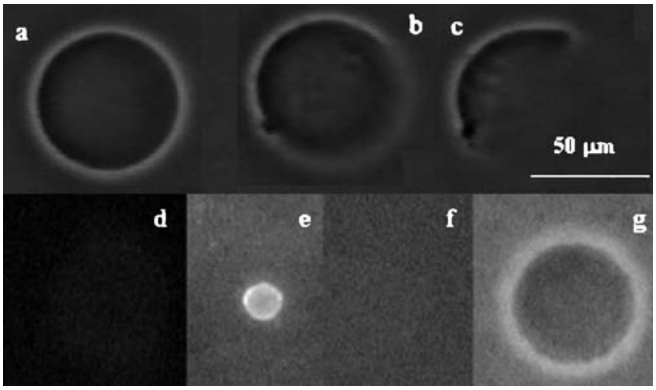

Fig. 2 Attack of a vesicle by a detergent (Decon). Vesicle filled with a PolyNipam solution observed by phase contrast microscopy: **a**: initial state, **b**,**c**: the membrane is broken and the vesicle progressively vanishes; gel-filled vesicle (MBA concentration 9 mM) and observed by fluorescence microscopy (**d**–**f**): **d**: initial state; **e**: gel collapse after membrane rupture; **f**: re-swelling of the gel after Decon dilution. Gel after membrane destruction observed by phase contrast microscopy: **g**: diameter of the gel is greater than the initial vesicle diameter

The behaviour of a gel-filled vesicle is shown in Fig. 2d–f. First, rhodamine is added to the solution. It concentrates in the hydrophobic lipid bilayer and permits to see the membrane by fluorescence microscopy (initial state: Fig. 2d). After Decon injection, the inner volume of the vesicle shrinks and keeps its shape (Fig. 2e), thus disclosing the presence of a 3D gel network. Shrinkage is attributed to the gel collapse at the contact of PolyNipam with Decon, (non-solvent of PolyNipam) after the breakage of the membrane. Concomitantly, rhodamine accumulates in the collapsed hydrophobic gel. Finally, glucose solution is injected close to the gel, which reswells (Fig. 2f) and releases rhodamine. No more fluorescence is detected on the object: the lipid membrane has been destroyed. The final size of the gel bead is larger than the initial vesicle size (Fig. 2g), which indicates that when the gel was enclosed in a vesicle, it was not swollen at its maximal degree.

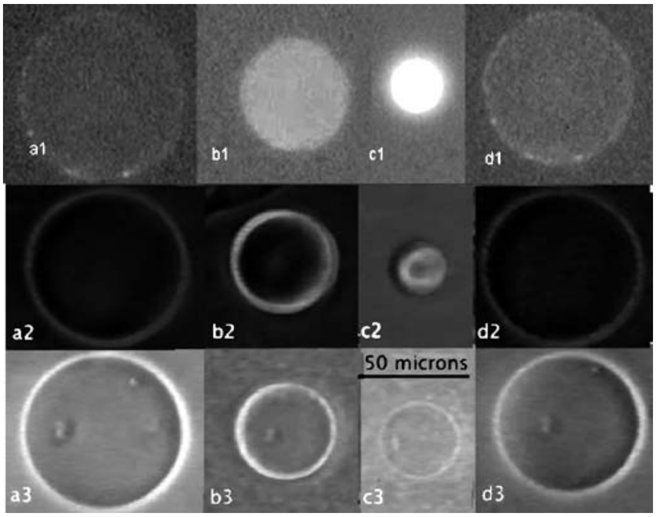

Fig. 4 Heating above the PolyNipam demixion temperature and cooling stages of gel-filled vesicles: fluorescence observation of a gel-filled vesicle (MBA: 9 mM) incubated with rhodamine: **a1** initial state $T = 20\,°\mathrm{C}$, **b1**,**c1** heating $T = 40\,°\mathrm{C}$, **d1** final state after cooling $T = 20\,°\mathrm{C}$; phase contrast observations: vesicle (MBA: 3 mM): **a2** initial state $T = 20\,°\mathrm{C}$, **b2**,**c2** heating $T = 40\,°\mathrm{C}$, **d2** cooling and final state $T = 20\,°\mathrm{C}$; vesicle (MBA: 9 mM): **a3** initial state $T = 20\,°\mathrm{C}$: $t = 0$ sec, **b3**: heating: $t = 10.7 = 40\,°\mathrm{C}$ sec, **c3** heating: $t = 30$ sec $T = 40\,°\mathrm{C}$, and **d3** cooling $T = 20\,°\mathrm{C}$

Responsive Vesicles: Temperature-induced Phase Transition

PolyNipam solutions and gels are known to exhibit a reversible microphase separation and a sharp volume change respectively, which are triggered by the temperature upon crossing the lower critical solution temperature ($T = 32\,°\mathrm{C}$ in water, 29 °C, 25 °C and 21 °C in 0.1 M, 0.25 M and 0.5 M glucose solutions respectively). Indeed, microphase separation upon heating with formation of large aggregates in the inner volume of linear PolyNipam-filled vesicles is observed, as shown in Fig. 3 and recently reported by Jesorka et al. [14]. More interesting is the behaviour of gel-filled vesicles. Figure 4 depicts selected time frames from movies that show the typical size changes induced by a cycle of temperature (25 °C – 40 °C – 25 °C) of three gel-filled vesicles. Above the transition temperature, vesicles contract rapidly (Fig. 4a,b) while keeping their shape. They reach a stationary size when the temperature is maintained at 40 °C (Fig. 4c). Finally, when the temperature is lowered back to 25 °C, vesicles re-swell and retrieve their initial size, (Fig. 4d). The first vesicle (a1–d1) is observed by fluorescence after addition of rhodamine. It is clearly seen that the membrane is not destroyed during both gel contraction and expansion stages. It also indicates that the membrane is coupled to the gel during the volume transition and is believed to crumple onto the surface. The mechanisms of crumpling and the origin of PolyNipam-lipid interactions have still to be studied. The cycle of temperature was successively repeated six times without apparent vesicle damage.

Gel Membrane Interaction

In order to test the vesicle membrane strength, we performed micropipette suction experiments to produce a uniform membrane tension and stretch bilayers of sol and gel-filled vesicles. The applied pipette suction (up to 10^4 Pa) is small compared to osmotic driving forces (10^5 Pa) required to displace water on the time scale of the experiment and small compared to the osmotic activity of the

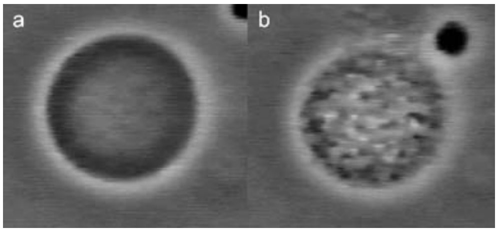

Fig. 3 Vesicle filled with a PolyNipam solution: **a** intial state **b** micro-phase separation after heating (40 °C)

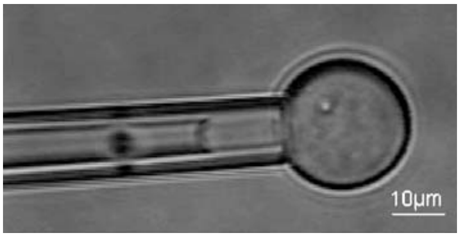

Fig. 5 Micropipette aspiration of a sol-filled vesicle held by micropipette suction (10^4 Pa)

trapped sucrose (2×10^5 Pa). Thus, the vesicle volume remains fixed during the test. A typical experiment is shown in Fig. 5 on a sol-filled vesicle. The pipette suction is increased up to more than 10^4 Pa without membrane lysis occurring. The corresponding tension, measured from a geometric relation based on the pipette caliber and the diameter of the vesicle spherical segment exterior to the pipette [19] reached ~ 0.1 Nm. Gel-filled vesicles present a similar behavior under pipette suctions of 10^4 Pa and higher, though the aspirated projection length inside the pipette is comparatively smaller. In particular, no separation of the membrane from the gel is detected.

The value reached for the membrane tension and pipette suction are about one order of magnitude higher than that obtained for the lysis tension and maximal applied pressure for simple DOPC vesicles [20]. This result clearly suggests that the membrane of PolyNipam filled vesicles is strongly strengthened, likely due to lipid/PolyNipam interactions.

Conclusion

We prepared GUVs containing solutions and elastic gels of PolyNipam. The concentration and the nature of components in the inner volume of the vesicles can be varied to modulate both their mechanical properties and the phase transition temperature. We showed that gel-filled vesicles are responsive systems, which exhibit a reversible volume transition triggered by temperature. The membrane of both sol and gel-filled vesicles is strongly strengthened compared to that of simple vesicles and is coupled with the inner gel. These systems appear as excellent candidates to isolate and mimick certain cell mechanical features.

References

1. Menger FM, Angelova MI (1998) Acc Chem Res 31:789
2. Lipowsky R, Sackmann E (1995) Structure and dynamics of Membrane. Elsevier, North-Holland
3. Gao K, Huang L (1987) Biochim Biophys Acta 897:377
4. Jin T, Pennefather P, Lee PI (1996) FEBS Let 397:70
5. Kiser PF, Wilson G, Needham D (1998) Nature (London) 394:459
6. Yang Q, Liu X, Ajiki S, Hara M, Lundahl P, Miyake V (1998) J Chromatog B 707:131
7. Hara M, Yuan H, Miyake M, Iijima S, Yang Q, Miyake (2000) J Mater Sci Eng C 1:3:117
8. Collier JH, Messersmith PB (2001) Annu Rev Mater Res 31:237
9. Kazalov S, Kaholek M, Teraoka I, Levon K (2002) Macromol 35:1911
10. Helfer E, Harlepp S, Bourdieu L, Robert J, MacKintosh FC, Chatenay D (2001) Phys Rev E 63:021904
11. Haeckl W, Baermann M, Sackmann E (1998) Phys Rev Lett 80:1786
12. Limozin L, Sackmann E (2002) Phys Rev Lett 89:1681031
13. Viallat A, Dalous J, Abkarian M (2004) Biophys J 86:2179
14. Jesorka A, Amarkström M, Orwar O (2005) Langmuir 21(4):1230
15. Stauch O, Uhlmann T, Fröhlich M, Thomann R, El-Badry M, Kim YK, Schubert R (2002) Biomacromolecules 3:324
16. Stauch O, Schubert R, Savin G, Burchard W (2002) Biomacromolecules 3:565
17. Matsuo ES, Tanaka T(1988) J Chem Phys 89:1695–1703
18. Angelova MI, Soléau S, Méléard P, Faucon J, Bothorel P (1992) Progr Coll Pol Sci 89:127
19. Kwok R, Evans EA (1981) Biophys J 35:637
20. Olbrich K, Rawicz W, Needham D, Evans E (2000) Biophys J 79:321

Progr Colloid Polym Sci (2006) 133: 45–51
DOI 10.1007/2882_056

John E. Wong
Walter Richtering

Surface Modification of Thermoresponsive Microgels via Layer-by-Layer Assembly of Polyelectrolyte Multilayers

John E. Wong (✉) · Walter Richtering
Institute of Physical Chemistry,
University of Aachen, Landoltweg 2,
52056 Aachen, Germany
e-mail: wong@pc.rwth-aachen.de

Abstract This study describes the layer-by-layer (LbL) assembly of polyelectrolyte multilayers of poly(diallyldimethylammonium chloride) (PDADMAC) and poly(styrenesulfonate) (PSS) on soft and porous supports as provided by the entangled mesh network of poly(*N*-isopropylacrylamide) (PNiPAM) microgels with varying thermoresponsive core and core-shell structures. Dynamic light scattering was used to follow the build-up of the PDADMAC/PSS multilayer assembly on thermoresponsive microgel particles and electrophoresis measurements were used to confirm charge reversal after each layer deposition. We demonstrate an "odd-even" effect of the size of the coated microgel depending on the type of polyelectrolytes in the outermost layer. We also show that a priming layer of polyethyleneimine (PEI) causes drastic surface modification of the microgel, but that on subsequent adsorption of the next layer (PSS) the thermoresponsive behavior of the native microgel can be recovered. Similarities and differences to LbL assembly of polyelectrolyte multilayers on hard and rigid supports will be discussed.

Keywords Core-shell microgel · Layer-by-layer · PNiPAM · Polyelectrolytes · Thermoresponsive

Introduction

In the early 1990s, Decher developed the layer-by-layer (LBL) assembly [1–3] of polyelectrolyte multilayers on charged substrates. LbL has become a versatile way of fabricating thin films with tailored architecture on substrates of virtually any size and shape [1–13]. A tremendous amount of research has been done on LBL assembly on rigid and planar substrates to study the physicochemical [14, 15] aspects of film formation and growth as influenced by the degree of charge of polyelectrolytes, pH, salt and ionic strength [16–24] from which the film is deposited from. It was once thought that electrostatic interactions are the main driving force for multilayer formation between two oppositely charged polyelectrolytes. However it has been recently demonstrated that secondary (non electrostatic) or cooperative interactions such as hydrogen-bonding and hydrophobic interactions [25–29], could also play a substantial role as well. The polyelectrolyte conformation, its adsorbed layer structure, and the degree of charge reversal upon adsorption determine ultimately, not only the film formation behavior but also, the structure of the resulting multilayer films (thickness, porosity, permeability, etc.). Polyelectrolyte multilayers deposited on hard and rigid planar substrates have been shown to be extremely interdigitated [30, 31] but with nevertheless distinct regions within the film assembly [32, 33] depending on whether the layers are situated closest to the substrate (inner layers), or in the middle core, or furthest from the substrate (outermost layers).

The LbL technique was subsequently extended to solid and hard particles, substituting planar substrates with colloids as precursors to hollow capsules. In the late 1990s, Sukhorukov [4–6] and Caruso [7–9] systematically studied the LbL of polyelectrolytes on sacrificial core particles, which were then dissolved to leave well-defined hollow capsules made up of only polyelectrolyte multilayers. The size of the hollow capsules was determined by the template diameter while the capsule wall thickness was controlled with nanoscale precision by the number of layers deposited on the particles. In this case as well the permeability of these capsule walls was additionally determined by the interdigitation of the multilayers, which confers the elastic properties of the capsules wall. Since then it has opened up a new era for the potential use of these hollow capsules for drug (or any other active agents) encapsulation (storage), transport, and delivery [10].

Recently, Caruso demonstrated the feasibility of LbL assembly of polyelectrolyte multilayers onto rigid but porous templates [11, 12]. Caruso exploited the electrostatic interactions between charged polymers (poly(acrylic acid), PAA and poly(allylamine hydrochloride), PAH) and mesoporous silicas to sequentially infiltrate and coat the inside of the pores. The mesoporous silica spheres used by Caruso possessed a bimodal pore structure; that is they possess small (2–3 nm) and large pores (10–40 nm), while the particles themselves have a diameter of 2–4 µm. Evidence of the successive deposition of polyelectrolytes within the pores was obtained by Fourier transform infrared experiments [11].

This paper demonstrates the LbL assembly of polyelectrolyte multilayers onto soft and porous templates as provided by the entangled mesh network of a commonly studied microgel, Poly(*N*-isopropylacrylamide) (PNiPAM) [34–36]. PNiPAM is thermoresponsive with a lower critical solution temperature (LCST) of around 32 °C, which means that below the LCST PNiPAM is water-soluble with a hydrophilic coil and becomes water-insoluble with a hydrophobic globule above the LCST. Microgel particles have a very high surface area to volume ratio and usually contain between 80 and 99% water in the swollen state [35] making them suitable for dye or drug encapsulation and delivery as well as providing support for immobilization of functionalized monomer units (e.g. enzymes, proteins, DNA, etc.) within the particles or on the surface. Unlike hard and rigid templates, we are now dealing with soft and porous templates [13] whereby adsorbed polyelectrolyte layers can not only interdigitate among themselves, but also penetrate the templates, conferring novel surface modification and properties to soft and porous substrates. In an attempt to vary the LCST or the swelling and deswelling behavior of microgels, hydrophobic or hydrophilic components (with polyelectrolyte structures) have been widely employed to be chemically incorporated into the microgel as a copolymer. In contrast, this paper actually explores the LbL assembly of polyelectrolyte multilayers to coat microgels [13], and investigates the characterizations of both the substrate (microgel) and the multilayer coated microgel. The physicochemical behavior of the swelling and deswelling of the coated microgels as influenced by the presence of the polyelectrolytes "shell" is also assessed.

Experimental Section

Materials: Poly(diallyl dimethylammoniumchloride) (PDADMAC, $M_\mathrm{W} = 100\,000$), Poly(styrene sulfonate) (PSS, $M_\mathrm{W} = 70\,000$), and Polyethyleneimine (PEI, $M_\mathrm{W} = 750\,000$) were purchased from Sigma–Aldrich. All chemicals from commercial origin were used without purification. The water used in all experiments (unless otherwise stated) was double-distilled Ultrapure water (Milli-Q-plus system, Millipore). The polyelectrolytes were dissolved in 0.5 M NaCl at a concentration of 1 $\mathrm{mgmL^{-1}}$ and used as such with no further adjustment of the pH.

Preparation of microgels: Three different types of building block were investigated: (a) a "neutral" core, constituted of poly(*N*-isopropylacrylamide) (PNiPAM), N; (b) a core-shell, wherein the shell is negatively charged (made up of a PNiPAM core and a poly(*N*-isopropylacrylamide-*co*-acrylic acid) (P(NiPAM-*co*-AA) shell), NC; and (c) a core-shell, wherein the core is negatively charged (made up of a P(NiPAM-*co*-AA) core and a PNiPAM shell), CN (inverse configuration of NC). The PNiPAM core microgel, N, was prepared via free radical polymerization [37, 38] while NC and CN were prepared by seed-and-feed polymerization of NiPAM/AAc onto a PNiPAM core [37–40] and NiPAM onto a PNiPAM/AAc core [41] respectively. The size of our building block varies between 140 nm for N, 200 nm for NC, and 250 nm for CN in the swollen state (at low temperatures) and 50 nm for N and 80 nm for NC and CN in the collapsed state (at high temperatures).

Layer-by-Layer assembly: The LbL assembly of polyelectrolyte was done by slowly adding an aqueous solution of the microgel to a 0.5 M NaCl solution of the polycat-

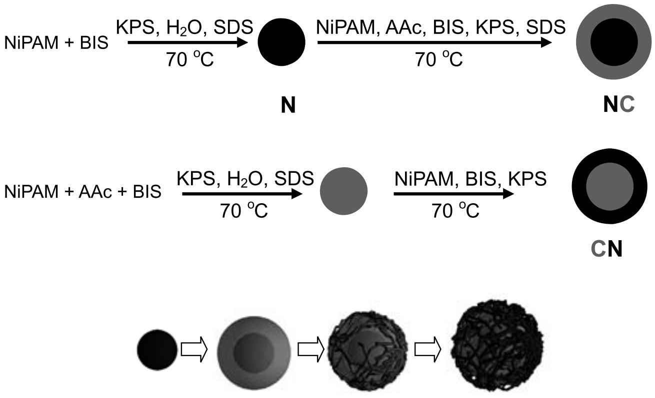

Scheme 1 Reaction pathways to obtain various core, core-shell structure microgels as template for LBL assembly of polyelectrolyte multilayers

ion (step 1), PDADMAC (or PEI) in a volume ratio of 1 : 5 under constant stirring for 30 minutes. The excess polycation was removed by centrifugation at 40 000 rpm for 20 minutes at 20 °C (step 2). The coated microgel was redispersed in water by vigorous shaking (step 3). Step 3 was repeated three times before adsorption of the next layer, which is the polyanion, PSS (step 4). Again the excess polyanion is removed (step 2) and redispersed in water three times (step 3). The whole sequence was repeated until the desired number of layers was obtained, after which time the coated microgel was redispersed in water overnight. Prior to characterizations, the coated microgel was filtered at least three times through a non-pyrogenic single-use 0.45 μm filter (Minisart from Sartorius) in a laminar-flow box.

Particle size determination: The particle size was measured by dynamic light scattering (DLS) as a function of temperature (ranging from 20 to 60 °C). Light scattering experiments were carried out on highly diluted samples (double-distilled Milli-Q water) with an ALV goniometer equipped with an avalanche photodiode. The samples were allowed to equilibrate for 20 minutes before a reading is done, and three sets of recordings were measured at each temperature. Temperature was varied from 20 to 60 °C, in steps of 2 °C, in both directions, so that one complete cycle consists of a heating curve followed by a cooling curve. Scattered light was detected at 60° with an integration of 120 s and computed with a digital ALV 5000E autocorrelator using an ALV Software version 5.3.2. Particles size was calculated by cumulant fits.

Electrophoretic measurements: The zeta potential and the electrophoretic mobility of the particles were measured with a Zetasizer 3000HSA (from Malvern Instruments, England) as a function of the number of layers and temperature (from 20 to 60 °C). Each point is the average of at least ten measurements. For temperature dependent measurements, the sample was allowed to equilibrate for 15–20 minutes to the set temperature before any recording was done.

Results and Discussion

DLS was used to monitor the stepwise deposition of each layer onto microgels by measuring the hydrodynamic radius, R_H, of the microgel. Figure 1 shows the thermoresponsive behaviors of various microgels coated with different number of layers as a function of temperature. The uncoated microgels differ not only in their architecture and size but also in their responsive behaviors: N undergoes a sharp LCST around 32 °C, Fig. 1a; CN presents a rather broad LCST around 35 °C, Fig. 1b while NC presents a timid two transitions at 33 (sharp) and 42 °C (broad), Fig. 1c; and swelling and deswelling are completely reversible for all the uncoated microgels. On adsorption of polyelectrolyte layers, the thermoresponsive behavior of

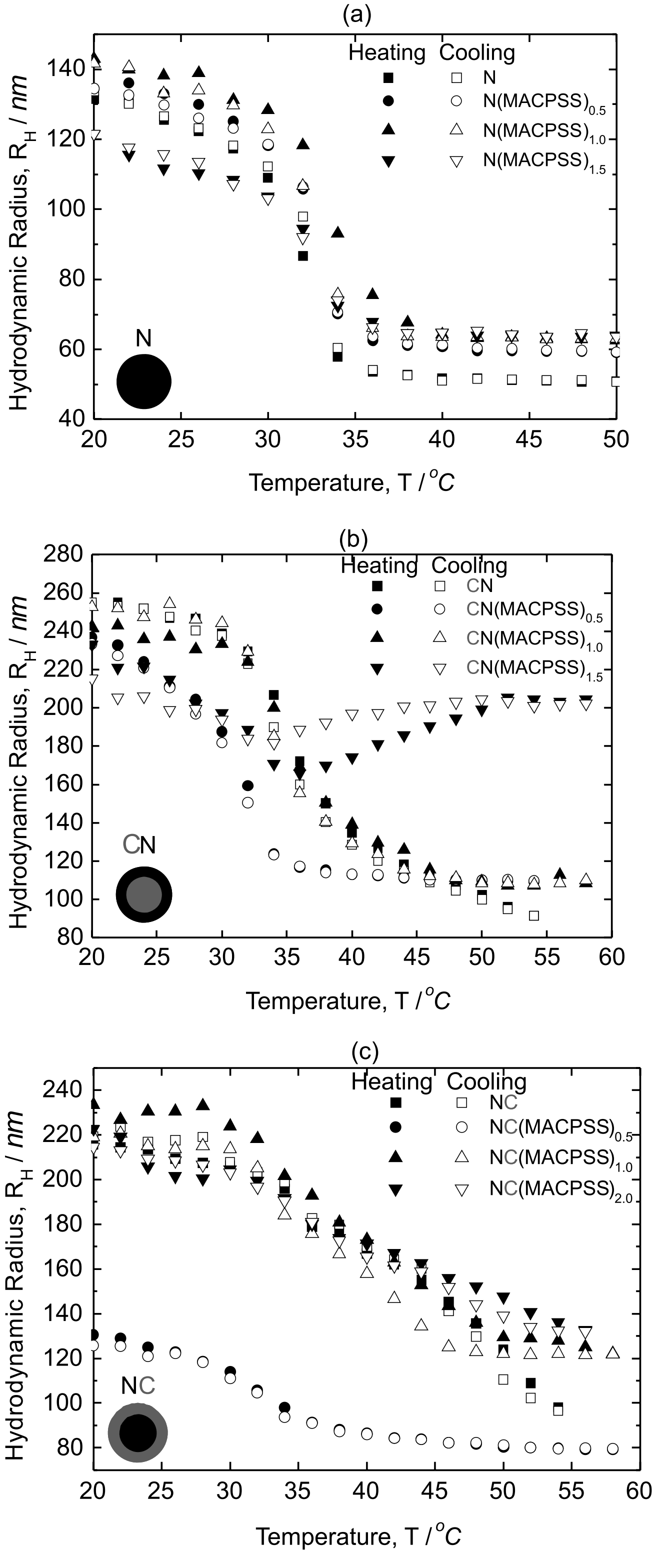

Fig. 1 Thermoresponsive behaviors of PDADMAC/PSS-coated **a** *N*, **b** CN and **c** NC

the coated microgels differs dramatically and can be seen to be template-dependent, or in other words, dependent on the location of charges in the uncoated microgel. LbL polyelectrolyte multilayer on a "neutral" microgel core does not affect the LCST of the microgel, Fig. 1a. In fact, N is not quite neutral since it still has some charges from the synthesis. However, there cannot be too many of them as confirmed by the zeta potential of N (data not shown) and the sharp LCST at around 32 °C. In the swollen state, the coated N shows an expected, but very minimal, increment in size when two layers (PDADMAC/PSS) are deposited but an additional layer of PDADMAC causes a collapse of the size (from 140 to 120 nm). In the collapsed state however all the coated N have about the same size (60 nm), which is, as expected, bigger than the uncoated N (50 nm). In the case of the CN system, Fig. 1b, the first layer (PDADMAC) has for effect to (i) decrease the size of the coated microgel in the swollen state, (ii) shift the LCST to lower temperature (32 °C), and (iii) make the transition from swollen to collapsed state a sharper one, as compared to the uncoated microgel. On addition of a second layer (PSS), the behavior of the uncoated microgel is recovered. A third layer (PDADMAC) again causes a collapse of the size of the coated microgel at low temperatures with an additional feature beyond the LCST, Fig. 1b. Above 34 °C, the three-layer coated CN microgel appears to exhibit a "reverse-effect" – starting to swell again before leveling off around 50 °C. The cooling curve shows some hysteresis, but taking into account conformational rearrangements, this additional feature is well present and can be fully reproduced.

In the case of NC system, Fig. 1c, we notice an "odd-even" effect on the size of the particle depending on the type of polyelectrolytes in the outermost layer. Deposition of the first layer (PDADMAC) anneals the native two-transition behavior of NC. NCMAC is drastically smaller (125 nm) in the swollen state than the uncoated NC (220 nm) – a situation analogous to [11]. Caruso found that the first layer deposited (PAA) on mesoporous silicas dramatically decreased the surface area by nearly 50%, and the author explained this decrease by the high PAA loading and blocking of some of the mesopores. Here it is unlikely that the pores are blocked since we are dealing with deformable substrates with "transient" pores. It could be due to a combination of two main effects. It could be that in the swollen state of NCMAC, PDADMAC chains are able to penetrate the microgel particle interior. The increase in "contact points" due to electrostatic interactions between the microgel and the polyelectrolyte restricts the extent of swelling of the ensemble. The deposition of this first layer forms like a network structure around the microgel [39]. The deposition of the second layer (PSS) now causes the coated microgel to expand (225 nm) in the swollen state. It was not possible to run any heating/cooling cycle during the DLS measurement on NC coated with 3 layers as the particles start to bridge and aggregate as the temperature is increased. However, at 20 °C, NC(MACPSS)$_{1.5}$ has a R_H of about 145 nm (data not shown), which means that every time PDADMAC is deposited there is a decrease in the particle size in the swollen state and on addition of each PSS layer the particle size increases again. To the best of our knowledge it is the first time that an "odd-even" effect is shown on LbL assembly of polyelectrolytes on soft and porous building blocks.

Particle swelling is entropy driven and is dependent on the hydrogen-bonding between the microgel segments and water. An increase in temperature causes rupture of these H-bonds causing the microgel to deswell and collapse as water is excluded from the microgel. Above the LCST, inter- and intra-chain hydrogen bonding and hydrophobic interactions are dominant. However, due to the polyelectrolyte coating, attractive electrostatic interactions between the polyelectrolyte layer and the microgel offer some opposition to this deswelling, which results in somewhat larger particles size for the coated microgel in the collapsed state as compared to the uncoated one. On cooling, previously buried, trapped, entangled segments become accessible to the continuous phase and become mobile and have the possibility to reorient, restructure, and reorganize as more water flows in the microgel, thence explaining the different hydrodynamic radii observed, and the hysteresis imparted to the microgel. This hysteresis can be exploited to tune novel surface properties conferred to coated microgel particles.

By substituting the first PDADMAC layer by a priming layer of PEI, a highly branched high molecular weight polyelectrolyte known for its high surface charge density and excellent anchoring properties, we cause a drastic change in the thermoresponsive behavior of the coated microgel. Figure 2 shows the hydrodynamic radius, R_H, of the coated microgel particles (NPEI) as a function of temperature. Due to the high branching and high molecular weight, PEI is assumed impenetrable in N, and this is translated as an increase in the particle size (from 140 to 150 nm) in the swollen state. As the temperature is in-

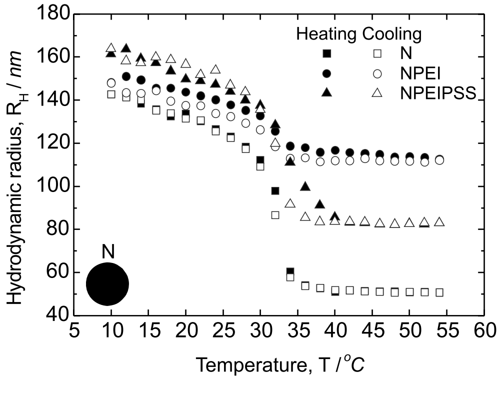

Fig. 2 Thermoresponsive behavior of *N* coated with a priming layer of PEI

creased the N core tendency to collapse is restricted by the electrostatic interaction of the PEI layer with N, resulting in a higher particle size, even around the LCST of *N* – which is also slightly shifted towards higher temperature by about 2 °C. Beyond the LCST, the coated microgel (NPEI) undergoes an abrupt and rapid transition to reach the collapsed state with a size particle of about 120 nm, which is about twice the size of the uncoated N in the collapsed state. The flow of water out of PEI-coated *N* is drastically impeded by the branched network around N and also the elastic properties conferred by the interactions between N and PEI chains allow the entire particle to expand further than the uncoated N. Deposition of a PSS layer on the PEI-coated N amazingly recovers partially the native thermoresponsive sensitivity of N. The LCST of NPEIPSS is shifted by about 5 °C to higher temperatures, and the particle size in the collapsed state is now surprisingly lower than NPEI but, as expected, higher than N. The positive charges inherent to PEI is now "shared" between interactions with N and this new layer of PSS layer; in other words, we have simultaneously a reinforcement of interactions between polyelectrolyte multilayers (PEI and PSS) and a diminishment of interactions between polyelectrolyte (PEI) and the microgel (N), resulting in the microgel to collapse more – bearing in mind, that it is, after all, the microgel which is thermosensitive.

In Fig. 2, we can see new features in the behavior of NPEIPSS: some form of hysteresis between the heating and cooling curves. Figure 3 shows the thermoresponsive response of NPEIPSS after different periods of time. In between experiments the samples were stored at room temperature. We previously reported [13] hysteresis on a two-layer coated NC where we found that the first heating cycle results in major alteration of the particle, and that extended time periods under harsher conditions leads only to small changes. In the case of NPEIPSS the highly branched positively charged PEI causes fast and permanent alteration, Fig. 3. The only difference after 1 month was that, in the swollen state (below the LCST), the particles size was bigger than that originally prepared. However on the cooling curve, the original behavior of NPEIPSS was restored. Above the LCST, swelling and deswelling were completely reversible.

Because of the expansion and contraction of the soft template during adsorption of polycations and polyanions on microgels (NC and CN), it is difficult to obtain a direct measurement of the increment in film thickness upon deposition of the polyelectrolyte at each adsorption step. Therefore, evidence of the successive deposition of polyelectrolytes on the microgels was obtained qualitatively by electrophoretic measurements as a function of temperature. Figure 4 shows the zeta potentials and electrophoretic mobility of the coated microgel as a function of the number of layers, here only shown for NC measured at 20 °C. Figure 4 clearly indicates that the surface charge of the microgel is reversed with each additional adsorption step, suggesting that polyelectrolytes are adsorbed in discreet layers. The result is consistent with electrophoretic measurements of polyelectrolyte multilayers adsorbed on rigid particles. Of particular interest is the value of the zeta potential after deposition of each PDADMAC layer. It is well-documented that the zeta potential of PDADMAC/PSS system on rigid particles alternates between +40 and −40 mV upon addition of every PDADMAC and PSS layer respectively. However for assembly on soft and porous supports, we find that we reach −40 mV whenever we deposit PSS, but hardly reach +40 mV when PDADMAC is deposited. Similarly, for N (data not shown), after deposition of the first (PDADMAC) and second (PSS) layer, the zeta potential alternates between +40 and −40 mV but on addition of the third (PDADMAC) layer, only −5 mV is reached, indicating that no charge reversal occurs. In the case of NC, this low positive surface potential is a possible cause for particles bridging observed during the heating cycle of the DLS measurements. In this respect, polyelectrolyte multilayer assembly on soft and porous supports differs from that on

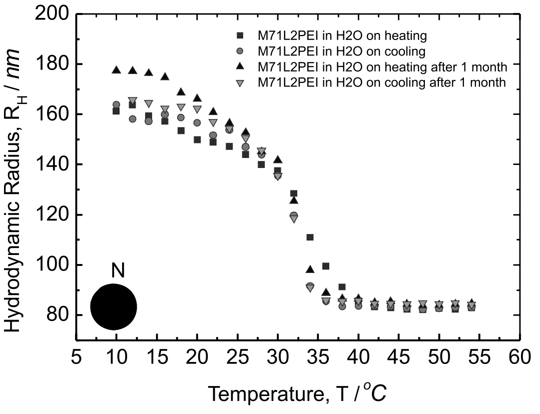

Fig. 3 Hysteresis behavior of NPEIPSS over different periods of time

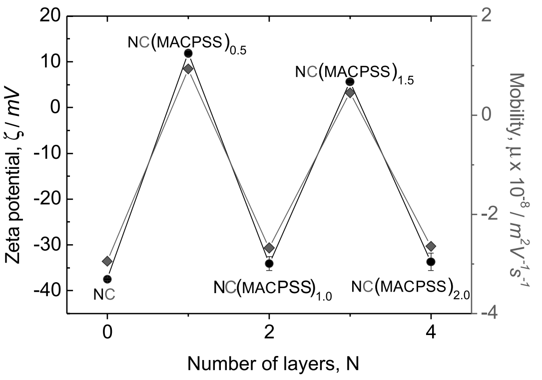

Fig. 4 Electrophoretic measurements as a function of number of layers coated on NC

rigid and solid substrates – it is support-dependent. The nature of the soft and porous template (core or core-shell system) dictates whether we have (i) complete or partial coverage of the surface, (ii) penetration of the polyelectrolyte in the interior of the support or not, and/or (iii) secondary cooperative interactions coming into play during the LbL assembly.

Figure 5 shows the electrophoretic measurements as a function of temperature for NC coated with different number of layers. One striking feature is that every time the outermost layer is PSS, the absolute zeta potential either slightly decreases (NC(MACPSS)$_{1.0}$) with temperature or remains roughly constant (NC(MACPSS)$_{2.0}$), while the absolute value of the electrophoretic mobility increases smoothly with temperature. However, when NC is PDADMAC-terminated (NC(MACPSS)$_{0.5}$ and NC(MACPSS)$_{1.5}$) the absolute value of both zeta potential and electrophoretic mobility are roughly constant below the LCST and increase abruptly above it. At this point it is not clear why we observe such differences in behavior, but it is nevertheless obvious from these results that polyelectrolyte adsorption strongly influence the thermoreponsive behavior of microgels. Hysteresis between the heating and cooling cycle, Fig. 5, is particularly noticeable after the very first layer adsorption (NC(MACPSS)$_{0.5}$). On cooling, there are drastic reorganization of the interdigitation and interpenetration of polyelectrolyte and microgel.

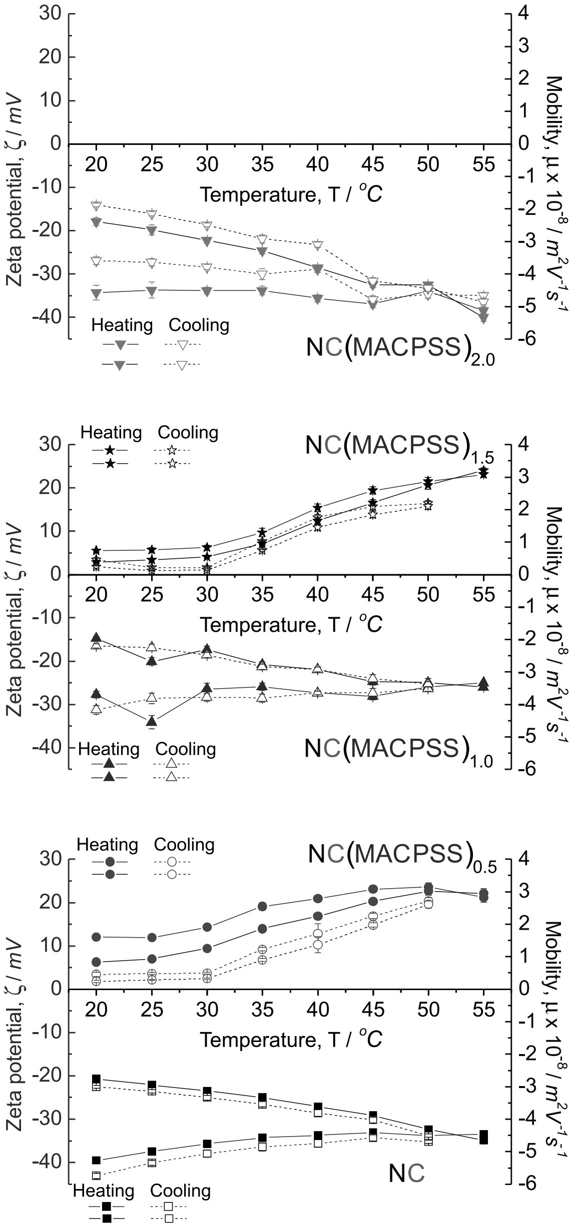

Fig. 5 Temperature dependence of the electrophoretic measurements for coated NC

Conclusions

The results presented in this work demonstrate the feasibility of layer-by-layer polyelectrolyte multilayer assembly on soft and porous building block as provided by the entangled mesh network of various core/core-shell microgels. Charge reversal was achieved and indicated successful deposition of polyanions and polycations, although there are indications that build-up could be incomplete or assisted by cooperative interactions. Polyelectrolyte coated microgels possess new thermoresponsive behaviors through new surface properties. We demonstrated for the first time an "odd-even" effect in the size of the coated microgel depending on the type of polyelectrolyte in the outermost layer. We also showed that a priming layer of PEI drastically modifies the surface properties of the microgel, but that the native thermoresponsive sensitivity of the microgel could be recovered on subsequent layer deposition on the PEI layer.

References

1. Decher G, Hong JD (1992) Thin Solid Films 210:831
2. Decher G, Schmitt JJ (1992) Prog Colloid Polym Sci 89:160
3. Decher G (1997) Science 277:1232
4. Donath E, Sukhorukov GB, Caruso F, Davis SA, Möhwald H (1998) Angew Chem Int Ed 37:2202
5. Sukhorukov GB, Donath E, Lichtenfeld H, Knippel E, Knippel M, Budde A, Möhwald H (1998) Coll Surf A 137:253
6. Sukhorukov GB, Donath E, Davis S, Lichtenfeld H, Caruso F, Popov VI, Möhwald H (1998) Polymers Adv Technol 9:759
7. Caruso F, Caruso RA, Möhwald H (1998) Science 282:1111

8. Caruso F, Lichtenfeld H, Giersig M, Möhwald H (1998) J Am Chem Soc 120:8528
9. Caruso F (2003) T Curr Chem 227:145
10. Ibarz G, Dähne L, Donath E, Möhwald H (2001) Adv Mater 13:1324
11. Wang Y, Yu A, Caruso F (2005) Angew Chem Int Ed 44:2888
12. Wang Y, Caruso F (2005) Chem Mater 17:953
13. Greinert N, Richtering W (2004) Colloid Polym Sci 282:1146
14. Hammond PT (1999) Curr Opin Colloid Interface Sci 4:430
15. Schönhoff M (2003) Curr Opin Colloid Interface Sci 8:86
16. Schlenoff JB, Ly H, Li M (1998) J Am Chem Soc 120:7626
17. Dubas ST, Schlenoff JB (1999) Macromolecules 32:8153
18. Schlenoff JB, Dubas ST (2001) Macromolecules 34:592
19. Steitz R, Jaeger W, Klitzing Rv (1999) Langmuir 15:8265
20. Voigt U, Jaeger W, Findenegg GH, Klitzing Rv (2000) J Phys Chem B 107:5273
21. Shiratori SS, Rubner MF (2000) Macromolecules 33:4213
22. Glinel K, Moussa A, Jonas AM, Laschewsky A (2002) Langmuir 18:1408
23. Schoeler B, Kumaraswamy G, Caruso F (2002) Macromolecules 35:889
24. Klitzing Rv, Wong JE, Jaeger W, Steitz R (2004) Curr Opin Colloid Interface Sci 9:158
25. Stockton WB, Rubner MF (1997) Macromolecules 30:2717
26. Kotov NA (1999) Nanostruct Mater 12:789
27. Sukhishvili SA, Granick S (2002) Macromolecules 35:301
28. Yang SY, Rubner MF (2002) J Am Chem Soc 124:2100
29. Schoeler B, Sharpe S, Hatton TA, Caruso F (2004) Langmuir 20:2730
30. Lösche M, Schmitt J, Decher G, Bouwman WG, Kjaer K (1998) Macromolecules 31:8893
31. Arys X, Laschewsky A, Jonas AM (2001) Macromolecules 34:3318
32. Ladam G, Schaad P, Voegel JC, Schaaf P, Decher G, Cuisinier F (2000) Langmuir 16:1249
33. Wong JE, Rehfeldt F, Hänni P, Tanaka M, Klitzing Rv (2004) Macromolecules 37:7285
34. Schild HG (1992) Prog Polym Sci 17:163
35. Saunders BR, Vincent B (1999) Adv Colloid Interface Sci 80:1
36. Pelton R (2000) Adv Colloid Interface Sci 85:1
37. Senff H, Richtering W (1999) J Chem Phys 111:1705
38. Senff H, Richtering W (2000) Colloid Polymer Sci 278:830
39. Jones CD, Lyon LA (2000) Macromolecules 33:8301
40. Berndt I, Richtering W (2003) Macromolecules 36:8780
41. Meyer S (2004) Diploma Thesis Universität Kiel

Progr Colloid Polym Sci (2006) 133: 52–57
DOI 10.1007/2882_062

Dzina Kleshchanok
John E. Wong
Regine v. Klitzing
Peter R. Lang

Potential Profiles Between Polyelectrolyte Multilayers and Spherical Colloids Measured with TIRM

Dzina Kleshchanok · Peter R. Lang (✉)
Forschungszentrum Jülich, IFF, Weiche Materie, 52425 Jülich, Germany
e-mail: p.lang@fz-juelich.de

John E. Wong
RWTH Aachen, Institut für Physikalische Chemie, Landoltweg 2, 52056 Aachen, Germany

Regine v. Klitzing
Christian-Albrechts-Universität, Institut für Physikalische Chemie, Ludewig-Meyn-Str. 8, 24118 Kiel, Germany

Abstract We investigated the potential profile between colloidal probes floating above a polyelectrolyte multilayer (PEM), built up by the layer by layer technique with Total Internal Reflection Microscopy (TIRM). The interaction between a single poly(ethyleneimine) layer and an amino-terminated polystyrene latex sphere can be accurately described by the superposition of electrostatic repulsion and gravity. PEM with more than one layer exhibit laterally inhomogeneous potentials with extremely long ranging repulsive contributions.

Keywords
Polyelectrolyte multilayers · Total internal reflection microsocopy · Interaction potential

Introduction

Polyelectrolyte Multilayers

The ongoing miniaturization of devices causes a further increasing interest in ultrathin coatings of interfaces, because such films serve to modify surface properties in an easy and controlled way. In the early 1990s Decher and coworkers proposed a new technique to prepare ultra-thin polymer films. Polyelectrolyte multilayers (PEM) can be prepared with the layer-by-layer (LbL) method [1, 2] by alternating adsorption of polyanions and polycations from aqueous solutions. The main feature of PEM is, that the film thickness can be easily tuned to Ångstrom precision by the number of deposited layers or the ionic strength of the ployelectrolyte solution. Further, the macroscopic properties (optical or conductive) are controlled by the type of polyelectrolyte used for the preparation. Besides planar surfaces also colloidal particles can be coated [3] or even objects with a highly irregular shape.

During the adsorption process of a new layer, polyanion/polycation complexes are formed with the formerly adsorbed polyelectrolyte layer [4] due to the exchange of the counterion by the oppositely charged polyelectrolyte. This means that most of the charges within the polyelectrolyte multilayer are compensated by the opposite polymer charges and not by small counterions. A consequence of this "intrinsic" charge compensation might be the strong interdigitation between adjacent layers found by neutron reflectometry [5–7]. The rms-roughness of the internal interfaces can be of the order of the thickness of a single layer.

One of the questions still under discussion concerns the driving force for the multilayer formation. For a long time, electrostatic attraction between polylelectrolytes in solution and the oppositely charged surface was discussed as the only driving force for the formation of multilayers [2]. Indeed, it has been shown that a minimum polymer charge density is required for the formation of multilayers [8–11]. Electrokinetic measurements at multilayer coated colloidal particles in an electrical field show that the potential changes sign after each adsorption step, i.e. the zeta-potential as a function of the number of adsorbed layers shows a kind of zig-zag curve with alternating charge sign (e.g. [3]). It is assumed that a charge reversal is required for the built-up of PEM.

On the other hand, this assumption is contradicted by the observation that PEM can be formed at an ionic strength of the polyelectrolyte solution as high as 1 mol/L. Since at these salt concentrations the electrostatic interactions are mostly screened (the Debye length is about 3 Å [11]), the PEM formation has to be driven by other effects. Another contradiction to the simple model of electrostatic attraction of polyelectrolytes by the surface is the fact that it is possible under certain conditions to build up consecutive layers of the same charge sign [12].

With regard to these observations the question arises what kind of surface potential is presented by the top layer to its surroundings. Since polyelectrolyte tails are directed towards the solution, it is assumed that electrokinetic experiments measure the potential at a kind of shear plane near the end of the tails. Of course the conformation of the tails can be changed due to the directional flux along the particles. The potential includes also all free and entrapped ions between the shear plane and the particle surface. All these factors could affect the surface potential and make it different from the local potential which the polyelectrolyte chains really experience. The same problems occur in streaming potential measurements, where a liquid flows along the surface [13]. The surface potential was also studied by static measurements like in a surface force apparatus (SFA) [12] or by an atomic force microscope (AFM) [14]. The SFA measures forces between two half cylinders normalized to their curvature raduis (typically 1–2 cm). This results in a very low lateral resolution. This problem is overcome in Colloidal Probe AFM studies where the AFM cantilever tip is replaced by a micron sized sphere, which determines the lateral resolution. In the present paper we propose a different technique, i.e. Total Internal Reflection Microscopy (TIRM) [15] to measure the surface potential. While TIRM and AFM provide roughly the same spatial resolution, the "force resolution" of TIRM is in the order of 0.01 pN, which is about two orders of magnitude higher than that of AFM.

Total Internal Reflection Microscopy

A charged colloidal sphere in solution, which sediments due to gravity will eventually come close enough to the bottom wall of the container, and experience electrostatic repulsion from that, if the wall carries like charges. The superposition of gravity and electrostatic leads to an interaction potential between the particle and the wall with a shallow minimum at a distance $h_{\min}$. However, the particle will not stay statically at this equillibrium distance. Due to Brownian motion it will rather sample a distribution of heights, $p(h)$, which is related to the interaction potential profile by Boltzman's equation

$$p(h) = A \exp\left\{-\frac{\phi(h)}{k_{\mathrm{B}}T}\right\} . \tag{1}$$

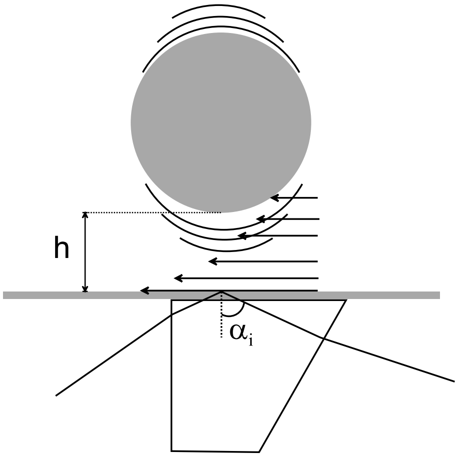

Fig. 1 Sketch of the evanescent wave optics

Here $p(h)\mathrm{d}h$ is the probability to find the particle in the height interval $h + \mathrm{d}h$ and A is a constant normalizing the integrated distribution to unity.

The height fluctuations resulting from the thermal motion can be directly observed by TIRM. For this purpose a Laser beam is directed via a prism to the container/solution interface as sketched in Fig. 1, with an incident angle α_i such that it is totally reflected. The electric field of the Laser beam penetrates the interface causing an evanescent wave, the amplitude of which decays exponentially with the distance from the interface. A single colloidal sphere, interacting with this evanescent wave will scatter light depending on its position as [16]

$$I_S(h) = I(h = 0) \exp\{-\xi h\} , \tag{2}$$

where h is the minimum distance of the sphere from the wall in the normal direction and ξ is the inverse penetration depth of the evanescent wave. By virtue of this relation the particle's height fluctuations will cause fluctuations of the scattered intensity and

$$p(I_S(h))\mathrm{d}I_S(h) = p(h)\mathrm{d}h , \tag{3}$$

where $p(I_S(h))\mathrm{d}I_S(h)$ is the probability to observe scattered intensity in the interval $I_S(h) + \mathrm{d}I_S(h)$. Introducing Eqs. 1 and 2 into Eq. 3 relates the the probability density of the scattered intensity to the interaction potential by

$$-p(I_S(h))\frac{I_S(h=0)}{\xi}\exp\{-\xi h\} = A \exp\left\{-\frac{\phi(h)}{k_{\mathrm{B}}T}\right\} . \tag{4}$$

In a typical TIRM experiment static scattering intensities are measured with a time resolution in the range of 10 ms, which translates as 3×10^4 data points recorded for a five minutes measurement. This is sufficient to make the normalized intensity histogram $N(I_S(h))$ converge to $p(I_S(h))$. Therefore, dividing Eq. 4 by the corresponding expression for the intensity which occurs with the highest frequency, $I_S(h_m)$ yields

$$\frac{N(I_S(h))}{N(I_S(h_m))}\frac{I_S(h)}{I_S(h_m)} = \exp\left\{-\frac{\phi(h)-\phi(h_m)}{k_\mathrm{B}T}\right\} . \tag{5}$$

When solving Eq. 5 for the potential difference $\Delta\phi = \phi(h) - \phi(h_m)$, it can be expressed as a function of four measurable quantities

$$\frac{\Delta\phi}{k_\mathrm{B}T} = \ln\left(\frac{N(I_S(h_m))}{N(I_S(h))}\right) + \ln\left(\frac{I_S(h_m)}{I_S(h)}\right) . \tag{6}$$

Finally, the second logarithmic term on the right hand side of Eq. 6 can be related to the particle's distance to the wall using Eq. 2

$$\frac{\Delta\phi}{k_\mathrm{B}T} = \ln\left(\frac{N(I_S(h_m))}{N(I_S(h))}\right) + \Delta h\xi , \tag{7}$$

where $\Delta h = h - h_m$ and $\xi = 2\pi/\lambda_0\sqrt{(n_1 \sin\alpha_i)^2 - n_2^2}$ with λ_0 the laser vacuum wavelength, n_1 and n_2 the index of refraction of the glass and the solvent, respectively. According to Eq. 7 it is possible to detect the potential *profile* in front of the surface by TIRM.

Experimental

Multilayer Preparation

Branched polyethylene imine (PEI) and poly(styrene sulfonate) sodium salt (PSS) were obtained from Aldrich (Steinheim, Germany). The molecular weight of PEI is 750 000 g/mol and 70 000 in the case of PSS. Poly(diallylamine dimethylammonium bromide) (PDADMAC) was a donation from Werner Jaeger (Fraunhofer Institute for Applied Polymer Research, Potsdam, Germany) and has a molecular weight of 100 000. The polymer solutions contained 10^{-2} monomol/l (concentration of monomer units) of the respective polyelectrolyte in Milli-Q-water. The dipping solutions were prepared in 0.1 molar NaCl without adjustment of pH. The substrates were conventional microscope slides and cleaned for 30 min in 1 : 1 H_20_2/H_2SO_4 mixture. After that they were coated with a PEI layer. On some substrates then, PSS and PDADMAC were deposited consecutively via the layer-by-layer technique by immersion for 20 min into the respective aqueous polymer solutions and by rinsing with Milli-Q-water three times after each deposition step. The films were dried in an air stream only after completion of the desired multilayer assembly.

TIRM

Our TIRM instrumentation is a home-built set-up, which was in parts assembled with standard microscope components from Olympus. We use a 15 mW HeNe-Laser with $\lambda_0 = 632.8$ nm to generate the evanescent wave. The Laser is mounted on a vertically oriented goniometer, to allow for the variation of incident angles, i.e. the variation of penetration depth. For all experiments of this contribution we applied an angle of incidence of 67.5 degree, which corresponds to a penetration depth of ca. 120 nm. Scattered light was collected through an infinity corrected objective (Olympus SLCPLFL 40X) and split into two paths both of which contained a tube lens to image the field of view either to the chip of a CCD-camera (JAI M1) or the photo-cathode of a photomultiplier tube (PMT) (Hamamatsu H7421-40). In the path of the PMT we introduced a diaphragm with a diameter of 400 µm in the image plane of the tube lens to cut off most of the observed background. This ensured a signal to noise ratio better than 25. The CCD-camera was used to make sure a single particle was located in the center of the area observed through the diaphragm. Since we did not apply optical tweezers and the particles are in thermal motion they have a limited residence time in the area observed through the diaphragm of the order of 10 minutes for a freely floating sphere of radius $R \approx 5$ µm. This limited the observation time to the range of about 300 seconds. The PMT was operated in the single photon counting mode with a time resolution of 500 ns. It was read out by a National Instruments counter card at a frequency of typically 100 to 1000 Hz. An example of the resulting intensity trace is shown in Fig. 2. For further evaluation the raw data were converted to intensity histograms and potential profiles using Origin (by OriginLab Corporation) work sheet scripts.

Two kinds of probe spheres were applied to measure the potential of differently charged top layers of the PEM-assembly. If the top layer was positively charged (PEI or PDADMAC) we used an amino-terminated polystyrene latex (Fisher Scientific) with a radius of $R = 2.92$ µm according to the manufacturer's specifications. To probe the negatively charged surface of PSS layers we used a polystyrene latex with sulfonate end-groups and a radius of $R = 4.54$ µm. In the following we will refer to these probes as PSA and PSS respectively. The latex spheres were diluted from their stock suspension down to a volume fraction of 10^{-8} and the solutions were contained in a carbonized PTFE-frame sandwiched between the PEM-coated microscope slide and a bare glass slide on top. The ionic strength of the solutions was adjusted by addition of NaCl if PSS top layers were to be probed and in the other cases HCl was added to adjust pH and ionic strength.

Results and Discussion

Raw data from a PSA-sphere floating above a glass slide coated with a single PEI-layer are shown in Fig. 2. The pH of the solution containing the PSA-particle was adjusted to 4 which corresponds to a Debye screening length of $\kappa^{-1} = 30$ nm. To check reproducibility we collected data from three different spheres. The resulting intensity

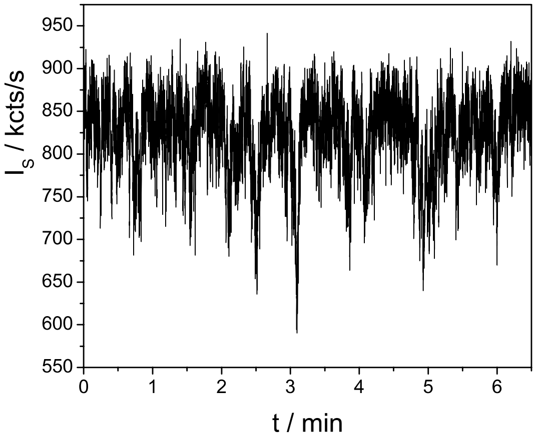

Fig. 2 Raw data of intensity vs time from a TIRM experiment on a 2.92 µm PSA sphere floating above a glass surface coated with a single PEI-layer

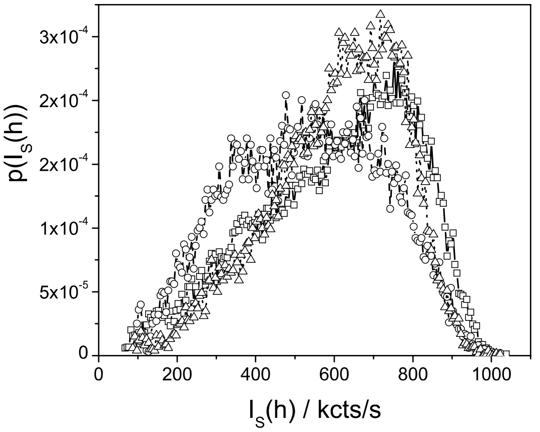

Fig. 3 Intensity histograms from TIRM experiments on PSA spheres floating above a glass surface coated with a single PEI-layer. Different line types and symbols represent different spheres at different locations

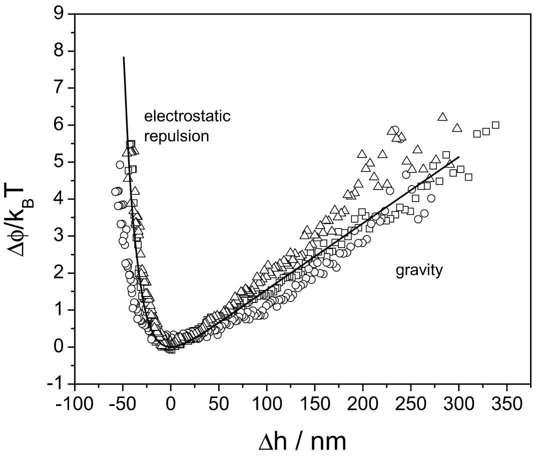

Fig. 4 Interaction potential between PSA spheres and a glass surface coated with a single PEI-layer. The potentials were calculated from the histograms shown in Fig. 3

histograms and potential profiles are displayed in Figs. 3 and 4. The experimental potential profiles were linear least squares fitted with the superposition of a gravitational contribution and an electrostatic term. According to Prieve [15] this can be expressed as

$$\frac{\Delta\phi}{k_{\mathrm{B}}T} = \frac{G}{k_{\mathrm{B}}T}\left[\frac{1}{\kappa}(\exp\{-\kappa\Delta h\} - 1) + \Delta h\right], \tag{8}$$

where $G = 4\pi R3\Delta\rho g/3$ is the buoyancy corrected net weight of the sphere with $\Delta\rho$ the particles excess mass density and g the acceleration of gravity. According to Eq. 8 G can be directly extracted from the linear branch of the potential profiles at large Δh. The average value we get from the three potential profiles is $G \approx 0.08$ pN. The complete list of fitting parameters is given in Table 1. The full line in Fig. 4 was calculated using the mean values for G and κ^{-1} from Table 1, which shows that the experimental data for this case can be described by this simple model within an experimental error of about 10% for the gravitational part and of ca. 15% for the electrostatic repulsion.

However the situation changes dramatically when the probed coating consists of more than one polyelectrolyte layer. An example for the raw scattering data from a PSS sphere above a PEI/PSS double layer is shown in Fig. 5. The raw data are not anymore statistically distributed as in Fig. 2 but they rather appear to have two privileged mean values around which they fluctuate. Accordingly the histograms show two maxima. The experiments could not be reproduced, even if the same sphere is observed at different times. Furthermore we observe that contrary to the behavior of a PSA sphere above a single PEI-layer, the spheres do not move laterally, i.e. they stay in the area observed through the diaphragm for hours.When we applied a gentle flow with the peristaltic pump we usually use to exchange solvent in the sample cell, the probe particles were not displaced. They moved out of position for some particle diameters, but snapped back as soon as the pump was switched off. After 24 to 48 hours usually all particles are found to stick to the surface, which we did not observe for the single PEI-layer.

This behavior does not quantitatively change neither with the number of layers nor with the chemical nature of

Table 1 Net particle weight G and Debey screening length κ^{-1} obtained by fitting Eq. 8 to the potential profiles shown in Fig. 4. The values for the particle radii, R, were calculated from G assuming a constant excess mass density of $\Delta\rho = 0.05$ mg/mL

Sphere no.	G/pN	κ^{-1}/nm	R/µm
1	0.07	15	3.4
2	0.07	19	3.2
3	0.09	15	3.6

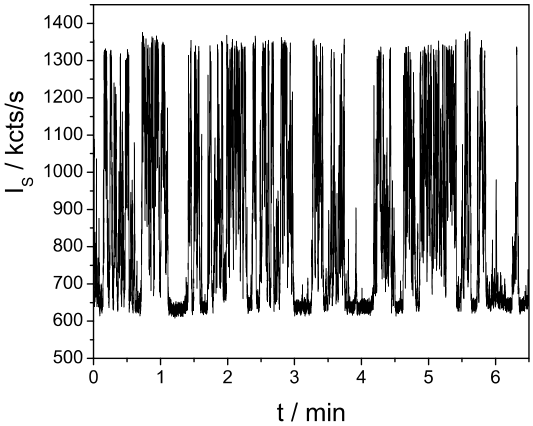

Fig. 5 Raw data of intensity vs time from a TIRM experiment on a 4.54 μm PSS sphere floating above a glass surface coated with a PEI/PSS double layer

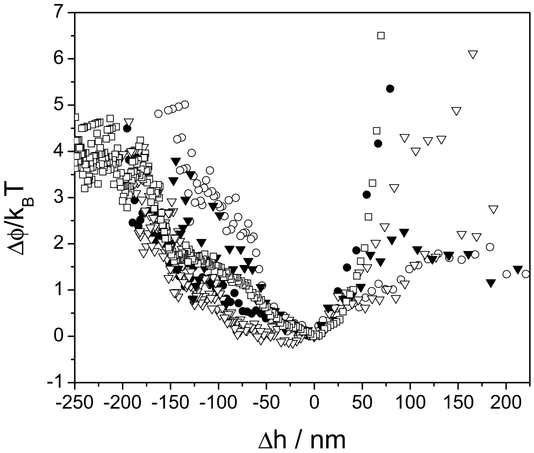

Fig. 6 Various interaction profiles of polystyrene latex spheres with PEM. *Circles*: 4.54 μm PSS spheres above eight PDADMAC/PSS double layers; *Down Triangles*: 4.54 μm PSS spheres above one PDADMAC/PSS double layer; *Square*: 2.92 μm PSA spheres above a PEI/PSS/PDADMAC assembly. *Open symbols* refer to a nominal Debye length of $\kappa^{-1} \approx 30$ nm, *full symbols* to $\kappa^{-1} \approx 14$ nm

the topmost layer nor with the strength of the electrostatic repulsion. This is demonstrated in Fig. 6 where we have collected randomly chosen potential profiles from various experiments under different conditions.

It is however noteworthy, that the width of the potential profiles extracted from these systems are much larger than observed for the PEI single layer. The repulsive part of the profiles generally extends over more than 200 nm. This is in agreement with the results of osmotic pressure measurements on PEM-coated silica particles reported recently [17]. These authors argue that the chains of the topmost polyelectrolyte layer at very low ionic strength may reach out into the surrounding solvent up to a distance of about half its contour length. Due to this chain stretching the electrostatic repulsion is caused to range much further than one would expect for a collapsed top layer based on DLVO calculations. Although we were working at moderate ionic strengths a similar effect might cause the long ranging repulsion also observed in our experiments.

While in the case of a PSA sphere above a single PEI layer the repulsive part of the potential can be attributed to gravity alone, this is not possible in all other cases. For this deviation we can offer only a speculative interpretation at the moment. It is in some cases possible to fit the experimental data to a harmonic potential profile, as if the probe sphere were stuck to a Hookian spring, which hints to the possibility that the particle might be adsorbed to a oppositely charged chain stretching out into the solvent. This requires that also the second layer from top is to a certain degree extended into the surrounding solution. Such a strong interdigitation between adjacent polyelectrolyte layers was detected in neutron reflectometry measurements [5, 7]. It was observed that polyanion layers may penetrate up to three consecutive polycation layers. If this holds also for the second layer from top, then chains from this layer can stretch out into the solution far enough to get in contact with the probe sphere. That might explain why the particles do not move laterally when floating above a multilayer and why the PSA sphere floating above single PEI layer behaves as expected. In this case there are no oppositely charged chains to which the probe sphere could stick.

In summary our experiments show that the interaction potential, which PEM deliver to their surroundings is not a simple laterally homogeneous DLVO-potential. Rather, the PEM is laterally inhomogeneous containing patches where electrostatic repulsion is over compensated by an attractive contribution to the interaction potential. The area fraction of these patches was roughly quantified with chemical probe experiments reported recently by Bosio et al. [14]. There the authors find that related PEM-systems cause adhesive forces to like charged spheres at about 30–50% of the locations probed. This behavior does, like in our experiments, not change with the number of layers. The reason for the existence of these adhesive areas is probably the strong interdigitation of adjacent polyelectrolyte layers.

Conclusions

We investigated the potential profiles between polyelectrolyte multilayers and spherical colloidal probes by total internal reflection microscopy. The interaction potential between a single PEI layer and a PSA sphere can be accurately described by the superposition of a pseudo-attractive part caused by gravity and a repulsive electrostatic contribution. If the polyelectrolyte assembly consists of more than one layer we observe that the experimental interaction profiles become irreproducible and that the probe spheres cease to move laterally. This is independent of the number of layers and the charge sign of the top layer. As a common feature all profiles exhibit a repulsive part which is very long ranged. These findings are further support to earlier observations of PEM-layers being laterally inhomogeneous [14] and chains of the top layer stretching out into the surrounding solution [17].

References

1. Decher G (1997) Science 277:1232
2. Bertrand P, Jonas A, Laschewsky A, Legras R (2000) Macromol Rapid Commun 21:319 (and references therein)
3. Sukhorukov GB, Dontah E, Lichtenfeld H, Knippel E, Knippel M, Budde A, Möhwald H (1998) Colloids Surfaces A: Physicochem Eng Aspects 137:253
4. Farhat T, Yassin G, Dubas ST, Schlenoff JB (1999) Langmuir 15:6621
5. Schmitt J, Grünewald T, Decher G, Pershan PS, Kjaer K, Lösche M (1993) Macromolecules 26:7058
6. Tarabia M, Hong H, Davidov D, Kirstein S, Steitz R, Neumann R, Avny Y (1998) J Appl Phys 83:725
7. Lösche M, Schmitt J, Decher G, Bouwman WG, Kjaer K (1998) Macromolecules 31:8893
8. Steitz R, Jaeger W, v. Klitzing R (2001) Langmuir 17:4471
9. Glinel K, Moussa A, Jonas AM, Laschewsky A (2002) Langmuir 18:1408
10. Schoeler B, Kumaraswamy G, Caruso F (2002) Macromolecules 35:889
11. Voigt U, Jaeger W, Findenegg GH, v. Klitzing R (2003) J Phys Chem B 107:5273
12. Lowack K, Hem CA (1998) Macromolecules 31:823
13. Adamczyk Z, Zembala M, Warszynski P, Jachimska B (2004) Langmuir 20:10517
14. Bosio V, Dubreuil F, Bogdanovic G, Fery A (2004) Colloid And Surfaces A: Physicochem Eng Aspects 243:147
15. Prieve DC (1999) Adv Colloid Interface Sci 82:93
16. Prieve DC, Walz JY (1993) Appl Opt 32:1629
17. Schönhoff M (2005) Oral presentation L30A at the 42nd Meeting of the German Colloid Society, Aachen, Germany

Progr Colloid Polym Sci (2006) 133: 58–64
DOI 10.1007/2882_064

POLYELECTROLYTES, COLLOIDAL INTERACTIONS

A. Wittemann
B. Haupt
M. Ballauff

Polyelectrolyte-mediated Protein Adsorption

A. Wittemann · B. Haupt · M. Ballauff (✉)
Physikalische Chemie I,
University of Bayreuth, 95440 Bayreuth,
Germany
e-mail: matthias.ballauff@uni-bayreuth.de

Abstract We review recent experiments on the interaction of proteins with anionic polyelectrolytes in aqueous solution. Data from literature demonstrate that proteins can form soluble complexes even on the "wrong side" of the isoelectric point, that is, for pH values above the isoelectric point of the proteins under which the polyelectrolytes and the proteins are like-charged. All data published so far demonstrate that this type of adsorption becomes weaker with increasing ionic strength. A much stronger interaction is found if the polyelectrolyte chains are grafted onto solid surfaces to form polyelectrolyte brushes. Here it has been shown that spherical polyelectrolyte brushes consisting of a core of ca. 100 nm diameter and long attached polyelectrolyte chains strongly adsorb proteins at low ionic strength ("polyelectrolyte-mediated protein adsorption"; PMPA). Virtually no adsorption takes place onto the spherical polyelectrolyte brushes at high ionic strength. A critical comparison of data obtained on free polyelectrolytes and on polyelectrolyte brushes shows that both phenomena can be traced back to patches of positive charge on the surface of the proteins. Moreover, the PMPA may directly be related to the Donnan-pressure within the brush layer.

Keywords Protein · Adsorption · Polyelectrolyte · Donnan-equilibrium · Polyelectrolyte brush

Introduction: Interaction of Polyelectrolytes with Proteins

We review recent work on the interaction of polyelectrolytes with proteins in solution. This problem is twofold: One must first consider the interaction of proteins with linear polyelectrolyte chains in solution. In a second step the interaction of proteins with polyelectrolyte chains grafted to a surface is to be discussed. In the following we shall demonstrate that these problems are closely related to each other:

Free Polyelectrolytes

Proteins carry positive and negative charges on their surface and may be regarded as polyampholytes. This fact has been recognized quite early and the behaviour in solutions of electrolyte as the function of the pH can be understood on this base [1, 2]. Depending on the pH proteins may have either a net positive or negative charge which is balanced at the isoelectric point. Given this fact it is obvious that proteins must interact strongly with linear polyelectrolytes of opposite charge in solution. More than 80 years ago, Bungenberg de Jong and Kruyt were the first to explore this complex formation in closer detail [3]. Much of the older work has been summarized in the second volume of the treatise of Kruyt [4]. Very recently, a comprehensive review was given by de Kruif and coworkers [5].

It has been recognized that proteins may interact with polyelectrolytes even on the "wrong side" of the isoelectric point pI, that is under a pH where the polyelectrolytes and the proteins are like-charged. Dubin and coworkers (see [6–8] and further citations given therein) demonstrated that in this case soluble complexes may be formed at a critical value $\mathrm{pH_c}$ above the isoelectric point. The value of $\mathrm{pH_c}$ goes through a distinct maximum as the function of the concentration of added salt. Dubin and coworkers could explain this unexpected finding by the presence of positive "patches" on the surface of the proteins that persist beyond the isoelectric point. The interaction of linear polyelectrolytes may hence be rationalized in terms of a balance of attraction of the positive patches and the repulsion by the overall negative charge of the protein. In particular, the theory of Rubinstein and coworkers [9] treating the protein as a dipole may be applied to this problem. Dubin et al. were able to show that the theory of Rubinstein et al. can give a semi-quantitative description of the strength of interaction between the polyelectrolyte and a number of proteins as, e.g. bovine serum albumin (BSA) [7]. For an overview on this work the reader is deferred to exhaustive review by Dubin and coworkers given in [8].

A different theoretical approach for the interaction of proteins with polyelectrolytes was given by de Vries and coworkers [10]. Here the problem of complex formation is addressed in terms of polyelectrolyte adsorption on randomly charged surfaces. The strength of interaction is predicted to vary as the function of the pH and the concentration of added salt. Moreover, soluble complexes are expected to form at the "wrong side" if the ionic strength is low enough. De Vries et al. could correlate their experimental data with this model in a semi-quantitative fashion. More details on this approach may be found in the recent review by de Vries and coworkers [5].

Polyelectrolyte Brushes

If linear polyelectrolytes are densely grafted to a solid surface, a polyelectrolyte brush results [11]. Recently, we have shown that polyelectrolytes as poly(acrylic acid) (PAA) and poly(styrene sulfonic acid) (PSS) can be grafted to the surface of colloidal latex particles leading to spherical polyelectrolyte brushes (SPB) [12–14]. Figure 1 displays the structure of these particles in a schematic fashion. The linear dimensions of the grafted chains are of the order of 50 to 250 nm whereas the distance between two chains directly at the surface is of the order of 3–6 nm only. Hence, the dense layer of linear chains is in the so-called brush limit. Since the chains attached to the solid surface are carrying the same charge as the dissolved proteins, a strong repulsion is expected to result from both steric interaction and electrostatic repulsion. However, we have demonstrated that bovine serum albumin (BSA) and several other proteins adsorb strongly on spherical polyelectrolyte brushes if the ionic strength is low. No adsorption takes place at high ionic strength [15–20]. This "polyelectrolyte-mediated protein adsorption" (PMPA) is also observed on planar polyelectrolyte brushes [21, 22].

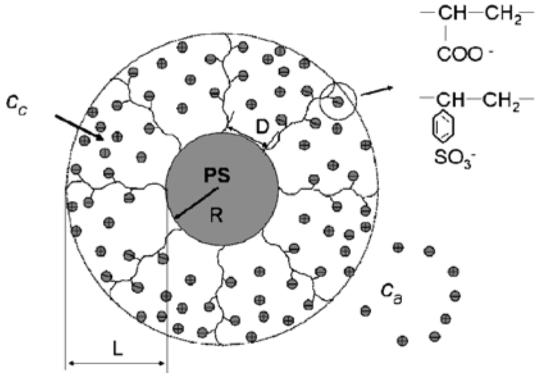

Fig. 1 Scheme of the radial structure of the spherical polyelectrolyte brushes used in previous studies of the polyelectrolyte-mediated protein adsorption. Attachment of chains of the weak polyelectrolyte poly(acrylic acid) leads to an *annealed brush* [11–14]. The pH in the system was chosen to be high enough in order to ensure full ionization of the charged groups within the brush layer [14]. If the strong polyelectrolyte poly(styrene sulfonic acid) is attached, a *quenched brush* results [14]. The average distance D between the chains on the surface is of the order of a few nanometers only. Hence, the polyelectrolyte chains strongly interact and form a polyelectrolyte brush. The thickness L of the brush layer can be tuned by the salt concentration c_a in the system that determines the salt concentration c_c within the brush layer through a Donnan-equilibrium [13, 14, 39]

All experimental findings obtained so far thus indicated that the PMPA is a general phenomenon that can be traced back to the interaction of the positive patches on the surface of the protein and the polyelectrolyte chains in the brush layer [15, 23].

Concluding this brief comparison one can state that the PMPA and the interaction of proteins with free polyelectrolyte chains seem to be closely related phenomena: Both can take place on the "wrong side" of the isoelectric point and the ionic strength within the system is one of the decisive factors. In the subsequent section we shall delineate the main experimental findings on the PMPA process available so far. This includes a brief comparison with data obtained on free polyelectrolytes. Section III then will discuss the main driving forces for the PMPA. A brief Sect. IV will conclude this paper.

Polyelectrolyte-mediated Protein Adsorption: Experimental Results

The experimental findings related to the PMPA obtained so far can be summarized as follows:

i) All investigations done so far demonstrate that the polyelectrolyte-mediated protein adsorption is a spontaneous process [15–23]. Figure 2 shows the experiment in a schematic fashion: The protein and the spherical polyelectrolyte brush (SPB) particles are mixed in

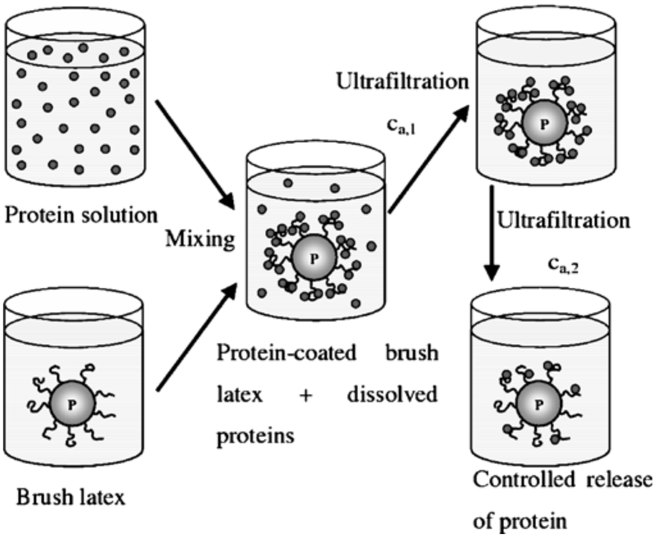

Fig. 2 Schematic representation of the experiment: Solutions of BSA were prepared in buffer solutions with defined concentrations of added salt. These solutions were added to the SPB dissolved in the same buffer. After equilibration for 24 hours the non-adsorbed protein was removed by careful serum replacement [15]. For the desorption experiment BSA is first adsorbed onto the spherical polyelectrolyte brushes at low ionic strength $c_{a,1}$. Unbound protein is flushed away by ultrafiltration against buffer solution of the same ionic strength. The controlled release of the BSA is induced by ultrafiltration with buffer solution of higher ionic strength $c_{a,2}$ [23]

an aqueous buffer solution of defined ionic strength. The PMPA process takes place and the unbound protein is removed by ultrafiltration against a buffer solution of the same ionic strength. It needs to be noted that the ultrafiltration in this step is done with a large excess of solution. Yet, no protein is liberated. This experimental finding points to a non-equilibrium state within the brush layer. If there would be an equilibrium distribution of the protein between the SPB and the solution, the process of ultrafiltration would flush away all the bound protein as well. This, however, is not observed and the strong binding of the proteins to the SPB is to be explained by the theoretical models to be discussed in turn.

ii) The decisive parameter of the PMPA is the ionic strength in the system [15, 23]. This is shown schematically in Fig. 3. Here the amount of adsorbed protein per gram of the SPB τ_{ads} is plotted against the concentration c_{sol} of the protein remaining in solution. In this way the resulting curves resemble much the usual adsorption isotherms. Investigations by small-angle X-ray scattering (SAXS) [24] and cryogenic transmission electron microscopy [25] have demonstrated that proteins as BSA enter deeply into the brush. SAXS furthermore shows that the protein is closely correlated to the polyelectrolyte chains. The same finding was reported for planar polyelectrolyte brushes [22].

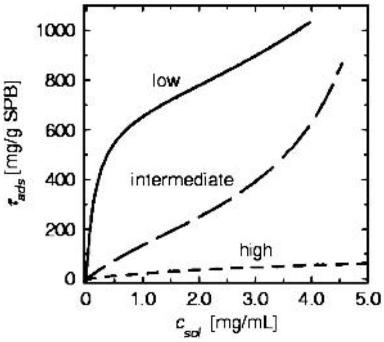

Fig. 3 Schematic presentation of the adsorption of proteins onto spherical polyelectrolyte brushes. The amount of adsorbed protein per gram of the carrier particles τ_{ads} is plotted against the concentration of the protein c_{sol} remaining in solution. Parameter of the curves is the concentration c_{a} of added salt defining the ionic strength in the system. Strong adsorption takes place at low ionic strength whereas little protein is adsorbed if the ionic strength is high

In some cases the adsorption is so strong that virtually no protein is left in the solution. In this case the "isotherm" shoots up at the origin and bends over only at high adsorption degrees [15]. At intermediate ionic strength the amount of protein varies linearly with c_{sol} in first approximation. Only at high ionic strength (see Fig. 3) the brush layer becomes more and more protein-resistant. In this regime the steric repulsion between the dissolved proteins and the brush layer of the SPB finally becomes operative and only marginal adsorption results.

iii) Previous studies have shown that the secondary structure of the adsorbed BSA, β-lactoglobulin and of ribonuclease A is nearly undisturbed [17, 19]. Moreover, the activity of adsorbed enzymes as e.g. glucoamylase is largely preserved [18, 20]. The same conclusion was drawn from a study of the fluorescence activity of the fluorescent protein mEosFP [26]. It becomes hence evident that the PMPA presents a very mild way of immobilizing proteins which circumvents the denaturation that may easily occur on solid surfaces [27].

iv) The protein molecules are evenly distributed within the brush layer [24]. This could be shown directly by analyzing the SPB before and after the adsorption of proteins by small-angle X-ray scattering (SAXS). These findings have been qualitatively corroborated by cryogenic transmission electron microscopy [25] and indicate clearly that the driving force for the PMPA must be related to the direct interaction of the proteins with the polyelectrolytes within the brush layer.

v) Most of the adsorbed proteins as e.g. BSA can be liberated again by raising the ionic strength in the system [15, 23]. This release can be done in a controlled fashion and the amount of protein released for each raise of the ionic strength is well-defined [23]. This finding again underscores the decisive role of the ionic strength for the PMPA.

vi) The amount τ_{ads} of adsorbed protein per unit weight of the SPB is uniquely related to the concentration c_{sol} of the protein remaining in the serum. It can be described by an expression which is akin the conventional BET-isotherm describing the equilibrium adsorption of multilayers [15, 23]. The resulting expression reads [20]

$$\frac{\tau_{\text{ads}}}{\tau_{\text{ads, M}}} = \frac{z \cdot w_{\text{ads}} c_{\text{sol}}^{1/n}}{\left(1 - w_{\text{ads}} c_{\text{sol}}^{1/n}\right)\left[1 + (z-1) w_{\text{ads}} c_{\text{sol}}^{1/n}\right]}, \qquad (1)$$

where $\tau_{\text{ads, M}}$ denotes the maximum mass of protein needed for the strongest adsorbed layer and $z w_{\text{ads}} c_{\text{sol}}$ with $z > 1$ is the probability of the adsorption of a protein molecule onto this layer. The probability for the adsorption of subsequent layers is only $w_{\text{ads}} c_{\text{sol}}$. Hence, τ_{ads} as function of c_{sol} may be described in terms of four adjustable parameters $\tau_{\text{ads, M}}$, w_{ads}, z and n. Hence, the strength of the PMPA can be given quantitatively in terms of $\tau_{\text{ads, M}}$. This parameter is found to depend strongly on the ionic strength of the solution. However, we reiterate that the PMPA does not lead to an equilibrium distribution of the protein between the surface layer of the SPB and the serum in which the SPB and the protein is dissolved (see above).

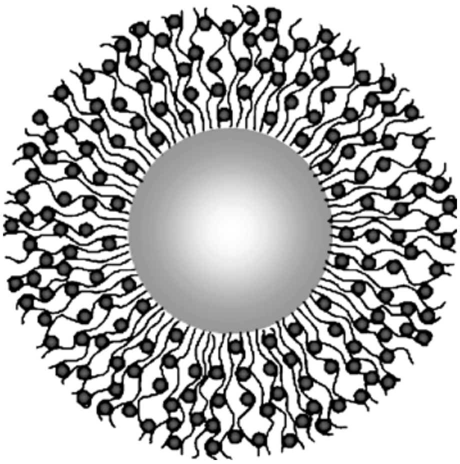

Fig. 4 Schematic representation of the protein molecules embedded into the spherical polyelectrolyte brush. The diagram shows right in scale the dimension of a typical annealed brush system. The distribution of the adsorbed proteins within the brush layer could be stated by SAXS measurements for BSA and RNase A. Taken from [24]

Polyelectrolyte-mediated Protein Adsorption: Driving Forces

In the following we shall discuss the driving forces of the PMPA discussed so far: 1) A charge reversal of the protein by a pH lower within the brush layer than outside [28], and 2) the counterion release forces [22, 29–32]. Both effects have already been discussed previously in a qualitative manner [15].

Charge Reversal

The localization of counterions within a weak polyelectrolyte may be followed by a smaller pH within the brush layer if the ionic strength is low. This effect and its implication for the PMPA was recently discussed in detail by Biesheuvel and Wittemann [28]. By suitable combination of the pH adjusted in the system and a low ionic strength, the local pH within the brush layer may be lower than the pI of the protein. Hence, the net charge of the protein is reversed and a strong electrostatic attraction between unlike charged objects becomes operative. The theory of Biesheuvel and Wittemann [28] predicts therefore a strong dependence on the pH and the adsorption is predicted to vanish for a sharply defined pH.

Previous experiments, however, have revealed that the pH is a parameter of secondary importance [15]. This can be seen from the discussion of Fig. 8 of [15]. Here the amount τ_{ads} of adsorbed protein per unit weight of the SPB is plotted against c_{sol} as shown schematically in Fig. 3. Parameter is the pH which ranges from a value just above the isoelectric point pI up to a value more than two units above the isoelectric point. There is a very pronounced adsorption of BSA in the immediate vicinity of the isoelectric point. The curves of τ_{ads} as the function of c_{sol} will therefore shoot up and only bend over at very high values of τ_{ads} (see Fig. 3). In this region charge reversal is certainly operative and leads to a marked adsorption of proteins. Here charge reversal is certainly the main driving force for the PMPA. However, strong adsorption still takes place at considerably higher pH. This points to the fact that the pH is an important but not a decisive parameter.

Counterion Release

The main difference between free polyelectrolyte chains as compared to a polyelectrolyte brush is the strong localization of the counterions in the latter case. Pincus [33] and Borisov, Birshtein and Zhulina [34] were the first to predict that most of the counterions cannot evade the brush layer but are confined within. This leads to an enormous osmotic pressure for salt-free systems ("osmotic brush") which in turn will stretch the polyelectrolyte chains of the brush layer to nearly full length. For spherical polyelectrolyte brushes it can be shown by dynamic light scattering [13, 14] and by direct osmotic measurements that 95 to 97% of the counterions are osmotically inactive [35]. Nearly all counterions are confined within the brush layer. The high osmotic pressure thus created determines the structure and interaction of these particles [36]. This is quite in opposite to what is found for linear polyelectrolytes in solution. Here only the Manning fraction of the counterions is immobilized by the electric field of the linear macroion [37, 38]. For typical polyelectrolytes as e.g. the poly(acrylic acid) used for the synthesis of the SPB, this fraction is of the order of 75%, that is, the osmotic coefficient giving the fraction of free counterions is around 0.25.

The driving force for the PMPA can now be discussed in terms of the number of released counterions. We consider the uptake of a protein from solution as shown in Fig. 5. Here we enumerate the net release of counterions in this process. Because of pH > pI, the number N_- of negatively charged groups on its surface is slightly greater than N_+, the number of positively charged groups on the surface. Evidently, these charges must be balanced by an equally high number of counterions of the opposite sign. Therefore each protein carries along N_+ negative and N_- positive counterions. We now consider the immersion of the protein in the brush layer (see Fig. 5). The N_+ positive charges on the surface of the protein now become counterions of the negatively charged polyelectrolyte chains. As a consequence, N_+ positive counterions previously immobilized within the brush layer as well as the N_+ negative counterions formerly carried along by the protein in solution are released. On the other hand, the N_- negative charges on the surface of the protein carry along their N_- positive counterions which will increase the number of small ions within the brush layer again. The balance between the release and the uptake, however, is positive since a total of $\Delta N = 2N_+ - N_- > 0$ counterions have been released in this process. The concomitant lowering of the free energy is of the order of $kT\Delta N$.

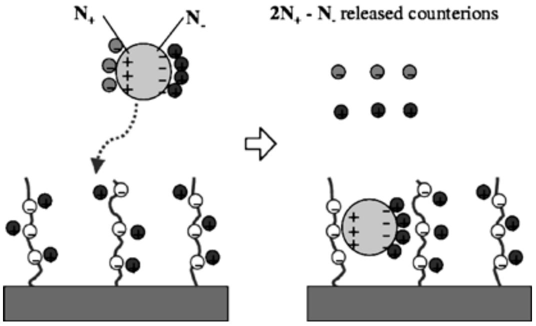

Fig. 5 Enumeration of the released counter- and coions during the process of protein adsorption. N_- is the number of negatively charged groups on the surface of the protein which is slightly greater than N_+, the number of positively charged groups on the surface (pH > pI). For each protein molecule a total of $\Delta N = 2N_+ - N_- > 0$ counterions of the protein and the brush layer is released. The decrease of Donnan-pressure $\Delta\Pi_\mathrm{D}$ (cf. Eq. 2) within the brush layer thus obtained leads to the strong adsorption of proteins at low ionic strength. At high salt concentration c_a the effect must vanish because $\Delta\Pi_\mathrm{D} = 0$ in this case. See text for further explanation

A point to be made in conjunction with Fig. 5 is the size of the patches on the surface. These patches must necessarily be of a minimum size to ensure the strong correlation of the respective counterions. A single charge on the surface would not localize the counterion and there would be no difference upon putting the protein into the brush layer. However, patches of a few charges will bind their counterions more strongly and become multivalent counterions in turn when the protein is located within the brush layer. Therefore the counterion release mechanism is bound to the presence of charged patches on the surface of the proteins. Hence, the above balancing leading to ΔN must be restricted to the number of localized counterions.

This relief of the osmotic pressure within the brush layer can now be treated quantitatively in terms of the classical Donnan-equilibrium ([39]; see also [13, 14]). The brush layer is characterized by its thickness L (cf. Fig. 1). The concentration of the counterions c_c is given by the number of charges within the brush layer because we assume full dissociation. Counterion condensation [37, 38] is taken into account [14, 39] by assuming that counterions will condense onto the polyelectrolyte chains until the distance between two charges is given by the Bjerrum-length l_B (= 0.714 nm in water at 25 °C). Therefore c_c follows as [14, 39]

$$c_\mathrm{c} = \frac{3R^2\sigma L_\mathrm{c}}{l_\mathrm{B}\left[(R+L)^3 - R^3\right]}\,, \tag{2}$$

where R is the radius of the core particles, σ is the number of grafted chains per unit area, and L_c is the contourlength of the grafted chains (cf. Fig. 1). The thickness L is determined for each concentration of added salt c_a by dynamic light scattering [13, 14]. From this the Donnan-pressure $\Delta\Pi_\mathrm{D}$ can be calculated to [23]

$$\Delta\Pi_\mathrm{D} = RT2c_\mathrm{a}\left[\left(\left(\frac{c_\mathrm{c}}{2c_\mathrm{a}}\right)^2 + 1\right)^{1/2} - 1\right]. \tag{3}$$

The Donnan-pressure $\Delta\Pi_\mathrm{D}$ is the difference of the osmotic pressure inside and outside the brush. For small c_a it assumes a maximum value determined by c_c. Raising c_a leads to a gradual decrease of $\Delta\Pi_\mathrm{D}$, of course. In the limit of the salted brush where $c_\mathrm{a} \gg c_\mathrm{c}$, $\Delta\Pi_\mathrm{D} = 0$ and the SPB is expected to behave as an uncharged system.

If the counterion release is to be the main driving force it should be possible to correlate $\Delta\Pi_\mathrm{D}$ with parameters characterizing the strength of adsorption. The discussion given in [15] suggests to take the quantity $\tau_\mathrm{ads,\,M}$ which denotes the maximum mass of protein needed for the first adsorbed layer (see above). Figure 6 displays the plot of both quantities for the adsorption of BSA. The experimental data have been taken from [15]. Evidently, both $\Delta\Pi_\mathrm{D}$ and $\tau_\mathrm{ads,\,M}$ are strongly related to each other: A high $\Delta\Pi_\mathrm{D}$

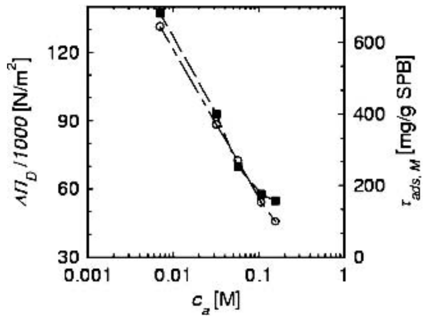

Fig. 6 Correlation of the Donnan-pressure $\Delta\Pi_D$ (*hollow circles*; cf. Eq. 3) and the quantity $\tau_{ads,\,M}$ (Eq. 1) [15]; *filled quadrangles*). The excellent correlation between the two quantities demonstrates that the release of counterions, that is, the lowering of $\Delta\Pi_D$ is the main driving force for the polyelectrolyte-mediated protein adsorption. See text for further explanation

is followed by a marked adsorption as expressed through $\tau_{ads,\,M}$ a small Donnan-pressure $\Delta\Pi_D$ leads to nearly negligible adsorption.

In principle, the release of strongly bound counterions thus effected by the interaction of the protein with the brush layer also occurs when the protein interacts with single linear polyelectrolyte chains in solution. However, the gain of free energy gained for the brush layer must be considerably higher because of the high Donnan-pressure which does not exist for single chains, of course. This leads to the marked stretching of the polyelectrolyte chains in the brush mentioned earlier. Counterion release from a brush layer is thus related to the partial relief of the high Donnan-pressure. The PMPA must therefore be a more pronounced effect than the interaction of proteins with single polyelectrolyte chains.

Conclusion

The interaction of proteins with polyelectrolytes in solution above the isoelectric point has been considered. Two cases are to be discussed: The formation of soluble complexes with free polyelectrolytes and the polyelectrolyte-mediated protein adsorption on spherical polyelectrolyte brushes. Both types of protein/polyelectrolyte interaction can be traced back to the presence of positive patches on the surface of the proteins. These patches must be of sufficient size to induce the binding to free polyelectrolytes as well as the PMPA in case of spherical polyelectrolyte brushes. However, the Donnan-pressure $\Delta\Pi_D$ is a feature which is unique for the SPB. The data displayed in Fig. 6 suggest clearly that the strength of the PMPA as expressed through the parameter $\tau_{ads,\,M}$ is related to the Donnan-pressure $\Delta\Pi_D$. This underscores the importance of the counterion release for the PMPA.

Acknowledgement The authors gratefully acknowledge financial support by the Deutsche Forschungsgemeinschaft, SFB 481, Bayreuth, and by the Fonds der Chemischen Industrie.

References

1. Cohn EJ, Edsall JT (1943) Proteins, Amino Acids and Peptides. Reinhold Publishing Corporation, New York
2. Tanford Ch (1961) Physical Chemistry of Macromolecules. Wiley, New York
3. Bungenberg de Jong HG, Kruyt HR (1929) Proc K Ned Wet 32:849
4. Bungenberg de Jong HG (1949) Crystallization – coacervation – flocculation. In: Kruyt HR (ed) Colloid Science, vol II. Elsevier Publishing, Amsterdam, p 232, chap. VIII
5. de Kruif CG, Weinbreck F, de Vries R (2004) Curr Opinion Colloid Interf Sci 9:340
6. Grymonpre KR, Staggemeier BA, Dubin PL, Mattison KW (2001) Biomacromolecules 2:422
7. Seyrek E, Dubin PL, Tribet Ch, Gamble EA (2003) Biomacromolecules 4:273
8. Cooper CL, Dubin PL, Kayitmazer AB, Turksen S (2005) Curr Opinion Colloid Interf Sci 10:52
9. Bowman WA, Rubinstein M, Tan JS (1997) Macromolecules 30:3262
10. de Vries R, Weinbreck F, de Kruif CG (2003) J Chem Phys 118:4649
11. Advincula R, Brittain WJ, Caster KC, Rühe J (2004) Polymer Brushes. Wiley, Weinheim
12. Guo X, Weiss A, Ballauff M (1999) Macromolecules 32:6043
13. Guo X, Ballauff M (2000) Langmuir 16:8719
14. Guo X, Ballauff M (2001) Phys Rev E 64:051406
15. Wittemann A, Haupt B, Ballauff M (2003) Phys Chem Chem Phys 5:1671
16. Jackler G, Wittemann A, Ballauff M, Czeslik C (2004) Spectroscopy 18:1671
17. Wittemann A, Ballauff M (2004) Anal Chem 76:2813
18. Neumann Th, Haupt B, Ballauff M (2004) Macromol Biosci 4:13
19. Wittemann A, Ballauff M (2005) Macromol Biosci 5:13
20. Haupt B, Neumann Th, Wittemann A, Ballauff M (2005) Biomacromolecules 6:948
21. Czeslik C, Jackler G, Hazlett T, Gratton E, Steitz R, Wittemann A, Ballauff M (2004) Phys Chem Chem Phys 6:5557
22. Czeslik C, Jackler G, Steitz R, von Grünberg HH (2004) J Phys Chem B 108:13395
23. Wittemann A, Haupt B, Ballauff M, in preparation
24. Rosenfeldt S, Wittemann A, Ballauff M, Breininger E, Bolze J, Dingenouts N (2004) Phys Rev E 70:061403
25. Wittemann A, Drechsler M, Talmon Y, Ballauff M (2005) J Am Chem Soc 127:9688
26. Anikin C, Röcker C, Wittemann A, Wiedenmann J, Ballauff M, Nienhaus GU (2005) J Phys Chem B 109:5418
27. Czeslik C (2004) Z Phys Chem 19:1861

28. Biesheuvel PM, Wittemann A (2005) J Phys Chem B 109:4209
29. Record MT, Anderson CF, Lohman TM (1978) Quart Rev Biophys 11:103
30. Sens P, Joanny J-F (2000) Phys Rev Lett 84:4862
31. Fleck C, von Grünberg HH (2002) Phys Rev E 63:061804
32. Meier-Koll AA, Fleck CC, von Grünberg HH (2004) J Phys Condens Matter 16:6041
33. Pincus P (1991) Macromolecules 24:2912
34. Borisov OV, Birshtein TM, Zhulina EB (1991) J Phys II (France) 1:521
35. Das B, Guo X, Ballauff M (2002) Progr Colloid Polym Sci 121:34
36. Jusufi A, Likos CN, Ballauff M (2004) Colloid Polym Sci 282:919
37. Manning G (1972) Ann Rev Phys Chem 23:117; and further references cited therein
38. see the discussion of this point in Deserno M, Holm Ch, Blaul J, Ballauff M, Rehahn M (2001) Eur Phys J E 5:97
39. Hariharan R, Biver C, Russel WB (1998) Macromolecules 31:7514

Progr Colloid Polym Sci (2006) 133: 65–73
DOI 10.1007/2882_051

Barry W. Ninham

The Present State of Molecular Forces

Barry W. Ninham (✉)
Department of Applied Mathematics,
Research School of Physical Sciences,
Australian National University,
2601 Canberra A.C.T, Australia
e-mail: barry.ninham@anu.edu.au

Abstract The DLVO theory of colloidal particle interactions has been at the core of colloid science for a long time. Quantitatively, agreement between experiment and theory was illusory except at salt concentrations less than about 10-2 molar. The same problem with theory exists for pH measurements, buffers, electrochemistry, zeta potentials, electrolyte activities, interfacial tension of salt solutions and a host of phenomena that depend on so called specific ion effects, This is so, most dramatically in biology, but also in colloid, polymer and surface science generally. The problems date back to Hofmeister whose work stands in the scheme of things as Mendel's did to genetics. Where problems occurred we have tended to argue them away, capturing specificity in unquantifiable terms embodied in words like cosmotropes, chaotropes, hydrophilicity, hydrophobicity, soft and hard ions, pi–cation interactions, hydration and hydrophobic forces, water structure. To complicate the puzzle further the role of dissolved atmospheric gas or other sparingly soluble (hydrophobic) solutes is sometimes major, and has been completely ignored in theories or simulations.

Some progress in unravelling these difficulties has been made. It turns out that theories have been seriously flawed. They depend on an ansatz that separates electrostatic forces from the totality of non electrostatic (NES) quantum mechanical electrodynamic fluctuation (Lifshitz or dispersion) forces. These NES forces are ignored, as for the Born self energy of an ion, or its decorations. Or else the electrostatic forces are treated in a non linear theory (e.g. Poisson Boltzman), and the quantum forces via Lifshitz theory as for DLVO. Even for the continuum solvent approximation this violates both the Gibbs adsorption equation, and the gauge condition on the electromagnetic field.

These problems are highly non trivial and occur equally in quantum field theories and biophysical problems that couple electron and photon transfer.

When the faults are repaired, the revised theory does seem to account for ion specificity and a veritable zoo of postulated new forces begin to fall into place quantitatively. An account will be given of the emerging situation, the role of dissolved gas and "hydrophobic" forces. This leads to new insights into the necessary cooperativity that occurs with water in biological and other systems.

Keywords Molecular Forces · Hofmeister · Specific Ion Effects · Interactions in Colloids · in Biology

Introduction

F. Wilhelm Ostwald (1853–1932) received the Nobel Prize for Chemistry in 1909, the citation being for his work in catalysis, chemical equilibria and reaction velocities. His interests included enzymes that he recognised were catalysts. He did a vast amount too in electrochemistry. His students included Arrhenius, Van't Hoff and Nernst, all Nobel laureates.

And the students presumably included his son Wolfgang Ostwald (1883–1943), generally regarded as the founder of colloid chemistry, after whom this award is named. Wolfgang began life as a zoologist.

Whether designated by the fashionable new word, nanotechnology, or its original name, mathematical physics (coined by the Reverend Challis of Trinity College Cambridge in two lectures to the British Association in 1836), colloid and surface chemistry is still colloid and surface chemistry. The 19th century biologists and the physiologists believed that advances in their subjects had to depend on advances in colloid science. In this they were certainly correct. But the fact is that physical chemistry and colloid and surface science today sit in splendid disjunction from modern cell and molecular biology. The reasons are now becoming a little clearer.

They have to deal with several things. One is our awareness now that structural models for self assembly are much too crude, and have to allow bicontinuous, cubic, cubosomes and mesh phases that are ubiquitous. A second has to do with our inability to explain Hofmeister, or specific ion effects that are equally ubiquitous. These date to Hofmeister's pioneering work starting in 1880. A third is due to the neglect of the role of dissolved gas.

Foundations

Before doing so recall that – according to all the books – colloid interactions (DLVO theory), in first approximation, are based on the competition between two separate forces. (Fig. 1). These are the electrical double layer, with decorations to include surface dissociation equilibrium, and van der Waals–Lifshitz forces. Both assume a continuum model for an intervening solvent. The attractive van der Waals forces are treated in a theory equivalent to quantum field theory. The theory of Lifshitz and its extensions includes all non electrostatic forces. They are many body dipole–dipole, dipole–induced dipole, and induced dipole–induced dipole forces, ion fluctuation forces. They are temperature dependent, include retardation and are accessible from measured bulk dielectric susceptibilities as a function of electromagnetic frequency. The forces can NOT be derived from two body molecular potentials.

For a single charged or uncharged surface in an electrolyte we have the limiting double layer theory of Onsager. It does not work.

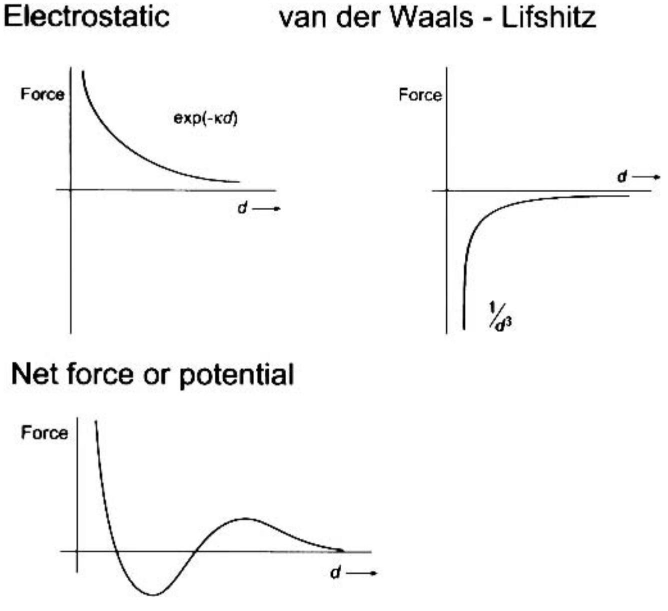

Fig. 1 Standard Representation of Forces acting in Colloid Science. Specific In effects are not included

At a higher level, for bulk electrolytes, we have correlation energies (Debye Huckel theory or its extensions) and further still the Born electrostatic free energy of a single ion.

Whether they are extended to include a molecular model of the solvent or not, the Born, Debye-Huckel and Onsager type theories ignore NES forces acting on ions.

Where these text book theories fail, we have been used to invoking a slew of extra parameters and forces, and words-hydration, hydrophilic, hydrophobic, cosmotropic, chaotropic, hard and soft ions, pi–cation interactions and so on. It is important to remark that the intuition on forces in biology, whether it be membrane potentials, ion binding, zeta potentials, proton or ion pumps, pH, buffers, or in physical chemistry generally all derives from DLVO, the double layer, Debye Huckel and Born electrostatic theories.

A Problem with Enzymes

With this in mind let us begin with a problem that combines the interests of the Ostwald's, father and son.

Restriction enzymes are one of the several basic tools of molecular biology. They are catalysts that cut DNA at a particular symmetric small sequence of nucleotides. Some things are known about these (Fig. 2). The enzyme has a hydrophobic pocket of nucleotides, the "active site", which has dimensions of about 10–20 Å. To fold up right it needs to bind specifically some Mg^{++}. Other divalent ions like Mn^{++} can substitute. The enzyme attaches to DNA, driven by molecular forces that we are familiar with. It

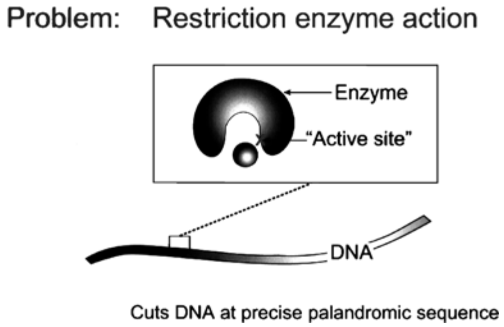

Fig. 2 Cartoon of the Problem of Restriction Enzymes

then dimerises and diffuses along the DNA until the active site of the enzyme finds the required (lock ad key) sequence. Then it cuts the DNA at a phosphate bond – with exquisite, repeated regularity. But a question remains as for all catalysis and surface chemistry. What is the source of the energy that drives this? The weak molecular forces of association are somehow harnessed, presumably cooperatively, to produce a much higher chemical energy. A buffer is usually used, and is apparently necessary.

This is ought to be a problem of colloid science. (polymer–protein interactions) [1]. Figure 3 shows the efficiency of cutting as a function of salt concentration for different salts, and in 2 different buffers at pH 7.5, phos-

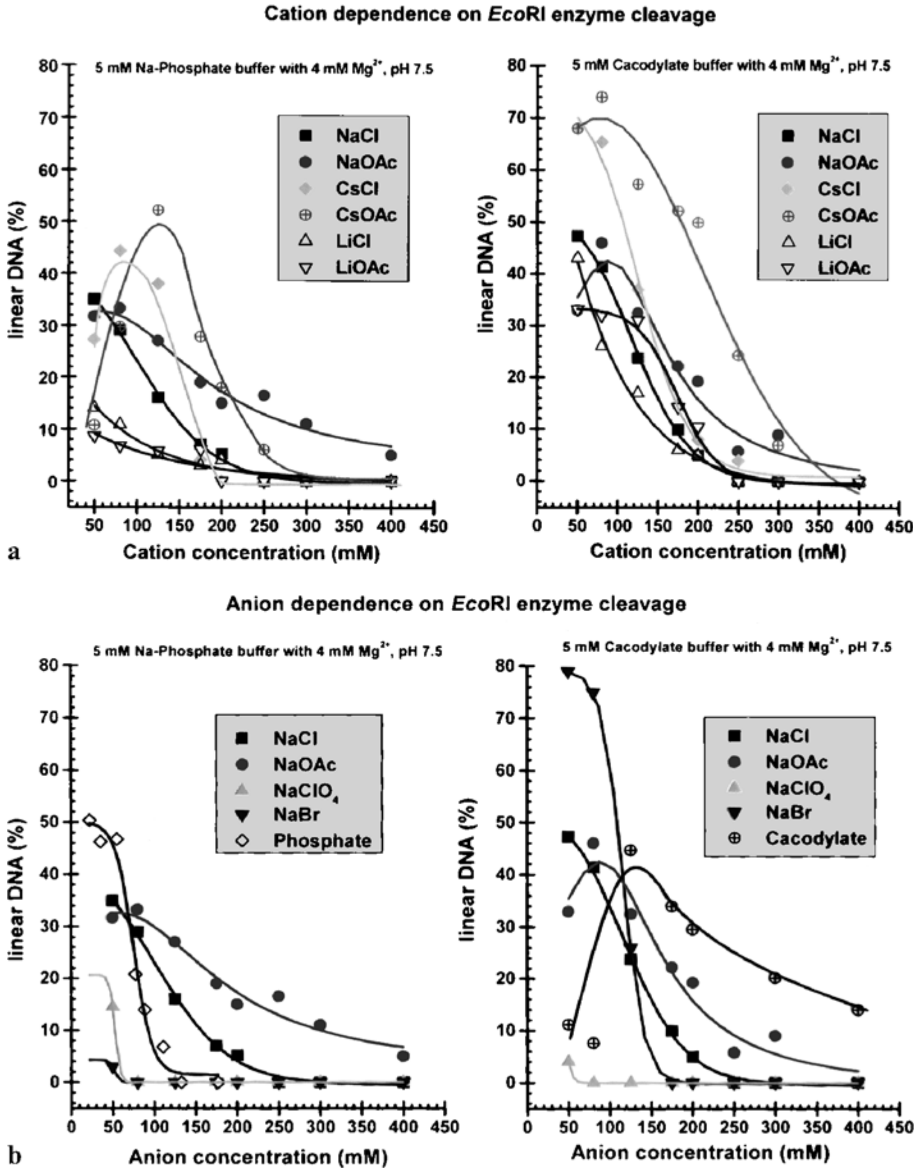

Fig. 3 Efficiency of a Standard Restriction Enzyme in Cutting DNA as a function of salt and salt type. The buffers (4 mM) are phosphate and cacodylate at pH 7.5. The Hofmeister series reverses with change in buffer. **a** Cation variation **b** Anion variation

phate and cacodylate. Anions rather than cations show the greatest variation. In both buffers the increase in efficiency up to about 0.1–0.2 M agrees with what we expect: Both protein and polymer are negatively charged. Then with added salt the electrostatic forces are reduced, exponentially screened with range given by the Debye length, and so enhancing association. Thereafter all is confusion. The efficiency follows a Hofmeister sequence, more or less, for phosphate buffer. But with cacodylate buffer at the same pH the sequence is reversed. Such specific ion effects are ubiquitous in biological problems, and indeed in physical chemistry proper.

The Debye Length is not the Debye Length

Usually the Hofmeister effects appear at high salt concentrations. So one might argue that the electrostatic – double layer – theory should provide a more or less reasonable description of matters at physiological salt concentrations, which is about 0.15 M. But this is illusory. In biology there is a good amount of highly charged proteins or polymers like 7+ RNA in the soup. So too in chemical engineering. The Debye length is completely different from that for standard 1 : 1 electrolytes here. Even an extremely small amount of added multivalent electrolyte reduces the Debye screening length dramatically and the specific ion effects dominate even at low concentrations [2–5].

Hofmeister with pH

Consider a simple problem that we think we know about.

Figure 4 shows pH measured by a standard glass electrode. The standard pH measurement depends on the interpretation of the potential set up by the electrical double layer.

Again, with pH, we have Hofmeister series with very significant systematic variations [6, 7]. The sequence is reversed for phosphate and cacodylate buffers. CO2 is not a problem here. (The standard sequence is H2PO4 > SO4 >F> Cl> Br> NO3, >I>CLO4> SCN. The left side are considered strongly "structure making" cosmotropic merging into "structure breaking" chaotropic. But the order depends on substrate.) The dashed curve shows pH calculated from the standard theory of electrolytes (extended Debye Huckel theory). The trends are roughly correct, but to fit a particular electrolyte one would have to choose fitting parameters for buffer anion radii that vary for each salt and are absurdly large. (There is no correlation between apparent pH and cutting efficiency of our enzyme.)

If we change Na$^+$ for K$^+$ the pH dependence for phosphate reverses to that of cacodylate!

The problem is getting awkward. Bearing in mind our caveat on the Debye length in real biological systems, we simply have no idea what pH means.

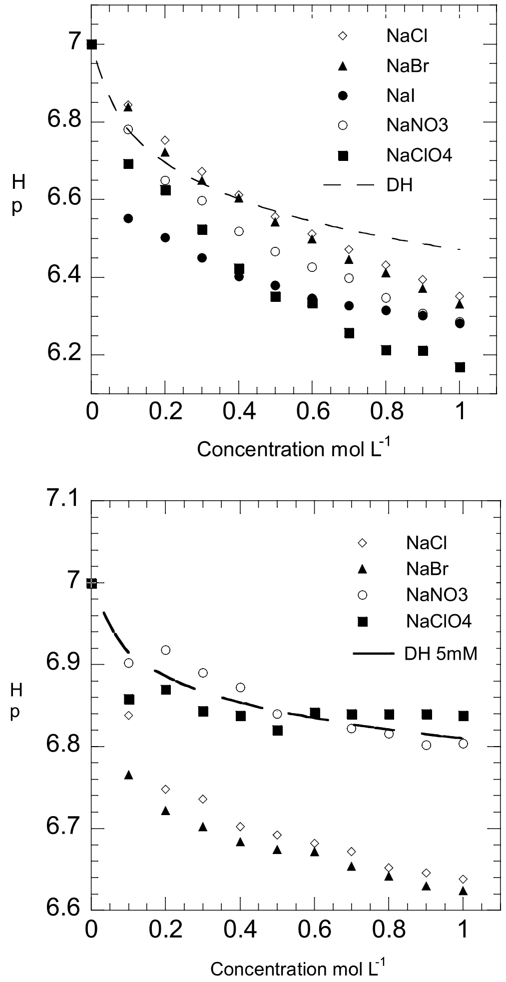

Fig. 4 Hofmeister series for pH measurements with glass electrode. *Upper curves* are for phosphate buffer at 5 mM, *lower* for cacodylate. pH is fixed initially at 7.5 and salt added. The apparent pH sequence is reversed for the two buffers. With cacodylate and K$^+$ instead of Na$^+$, the sequence reverses again!

Dissolved Gas

Except for an awareness of CO_2 effects that can be overcome by using buffers or high salt, nowhere in our theories have we considered the effects of dissolved atmospheric gas (oxygen or nitrogen) on forces. The concentration is typically around 5×10^{-2} M at one atmosphere pressure. This is about the same as the electrolyte concentration above which DLVO breaks down and starts to show up Hofmeister effects. At an air water interface the gas concentration changes from 1 atmosphere (1 Mole per liter) to 5×10^{-2} M over a distance of two or three water molecules. So the interface is difficult to define.

Consider then what ought to be a less difficult colloid flocculation problem. We look at the rate of flocculation of a hydrophobic colloid, here paraffin particles functionalised by stearic acid [8]. The zeta potential is around 40 millivolts, nothing special, and typical.

We explore rates of flocculation, again for different salts. The rates more or less follow trends predicted by the DLVO theory. Some are peculiar – citrates and salicylates follow the 1 : 1 electrolyte curves. But the theoretical predictions are wrong quantitatively by an order of magnitude at least. This is a bit alarming. More so is what happens if we do the same experiment with the atmospheric gas removed. The rates drop by one or two orders of magnitude [8]! If we attribute the failure of theory to "hydrophobic" forces, then these "extra-DLVO" forces are switched off when gas is removed. The same happens with emulsions, and emulsion polymerisation [9]. Something peculiar is missing. This shows up dramatically with experiments on nanosecond pulse neon laser experiments [10–13]. In gas-containing water, a plasma flash, indicating dielectric breakdown appears every 25 or so pulses. At hydrophobic surfaces the rate increases by a factor of 100 compared with that for hydrophilic surfaces.

When we remove the gas the flashes disappear. With salt something qualitatively different occurs for say Cl – vs acetate above 0.15 M.

Bubble–Bubble Interactions

We can try an apparently simpler experiment [14], illustrated in Fig. 5. Nitrogen gas is bubbled through a glass frit and ascends a column. The bubbles fuse and the column stays clear. At and above 0.15 M salt (physiological concentration) the bubbles do not fuse. (The same experiment can be done with single bubbles.) The fact that the bubbles do not fuse as salt increases seems quite counter-intuitive. According to DLVO theory, the (charged bubble–bubble interactions) ought to be more strongly screened with added salt, and bubble fusion enhanced, not inhibited with salt. Even more peculiar is the fact that for some salts there is no effect at all on bubble fusion even up to 5 M. There is an apparently universal rule. One can assign a characteristic A or B to each ion. Then AA and BB pairs give rise to the phenomenon, AB and BA pairs have no effect at all!

With different isomers of sugars the same effects occur but at much higher concentrations around 1 M rather than 0.15 M.

Direct Force Measurements

Admitting that the simple problem of bubbles is too hard, we can try direct force measurements between molecularly smooth mica to test the theory. Figure 6 shows force measurements between mica in electrolytes KBr and KAc.

They do decay according to double layer theory [15]. But the forces are 100 times larger with acetate than with bromide. Attempts to explain this by postulating 80% of Br is "bound" is contrary to the theories and experiments on ion binding that depend on double layer theory. But such forces are real enough, as can be seen by the differences in self assembly of double chained quaternary

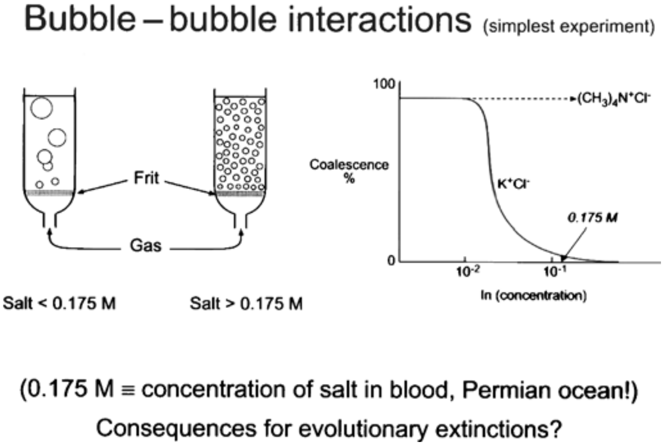
Bubble – bubble interactions (simplest experiment)

(0.175 M ≡ concentration of salt in blood, Permian ocean!)
Consequences for evolutionary extinctions?

Fig. 5 Schematic of bubble–bubble interaction experiment with addition of salts

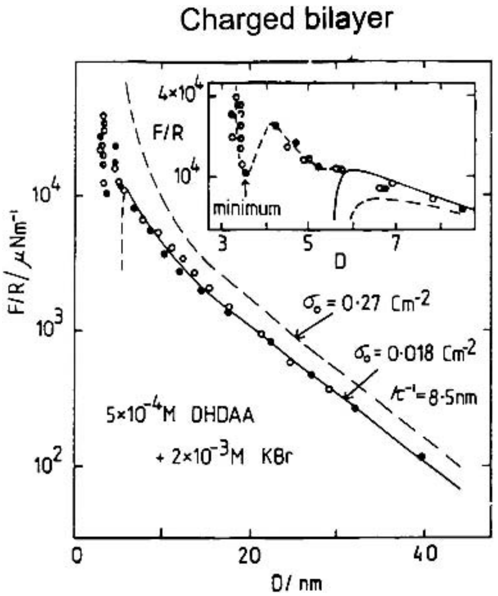
Charged bilayer

Fig. 6 Direct Force measurements between molecularly smooth mica sheets coated with an adsorbed bilayer of double chained cationic surfactant, in electrolyte. With added salt KBr or KAc, the forces are about 50 times larger with acetate as counterion as compared with bromide. The forces decay with the correct Debye length, the form predicted by double layer theory. The fit is perfect with KAc, with no free parameters. For Bromide one has to postulate that 90% Br is bound to the surfaces ammonium surfactants. Spontaneous vesicles form with one counterion, collapse into lamellar phases with others [16, 17]. The same is true for microemulsions, and for anionic lipids with Li^+ and Na^+ salts giving totally different phase behaviour in accordance with the different ion specific forces operating [16, 17].

Addition of mM phosphate to electrically neutral phospholipids results in immediate adsorption, charging and a huge zeta potential of 140 millivolts! No way in conventional theory can this make sense.

What Went Wrong? Towards a Reconciliation

The list is endless [18, 19], from Hofmeister's original work on protein precipitation, to interfacial tensions at air water or oil water interfaces, electrochemistry to micelles and microemulsions, ion exchange columns, flow of salts through porous rocks in oil recovery, flotation of minerals, water uptake by wool [20, 21], and even to bacterial growth rates [20, 21]. None of these effects are remotely explained by standard theories.

It appears that nothing is sacred.

The answer is embarrassing. It turns out that we made a mistake at the very beginning. The ansatz of DLVO is that double layer electrostatic (ES) and quantum mechanical many body van der Waals non electrostatic (NES) forces can be treated separately. It is just plain wrong [22–24]. The one is treated in a non linear theory, the other in a linear theory. It can be shown that this violates both the Gibbs adsorption equation and the gauge condition on the electromagnetic field, (charge–current conservation equation).

What to do about it [22–24]? We can take a first step to fixing the theory as follows. First, one can extract ion–substrate interactions from Lifshitz theory. Then use those potentials at the same level and in concert with the double layer potentials acting on ions. Linearisation of the new (combined) distribution function gives back the old theory. When the theory is so redone, specific ion effects do emerge. The same is true for the double layer itself, air and oil–electrolyte interfaces, for pH, buffers, additional contributions to the Born energy, ion binding, microemulsions, lipids and so on.

The meaning of a quantities as fundamental as measured potential or pH has to be revisited, as has ion transport.

The Born energy, extended to include NES forces gives specificity and does seem to encompass the notions of soft and hard ions, cosmotropes and chaotropes [25–40].

So there is a reconciliation. It would take me too far afield to outline the progress that has been made with taking account of these new effects properly. (There are a large number of recent papers by the author with M. Bostrom and colleagues that discuss some progress that has been made. Some of these are listed within [25–40].) Bulk and surface effects are both involved, and both contribute. The first is obvious to anyone who swallows epsom salts (Mg SO4), what Hofmeister termed the "water withdrawing power" of salts.

But surface adsorption driven by NES forces missing from standard theories seem to play an equally important role.

Ion specificity does emerge naturally from the repaired theory.

Bubbles and Hydrophobic Interactions

If, as I claim, we now begin to better understand how to turn forces on or off and to control curvature and association in self-assembled systems, we can approach the more difficult problem of hydration within a better, unified consistent framework. But what about very long ranged hydrophobic forces between colloids or surfaces? Model water simulation, and work of James Clerk Maxwell dating back more than 100 years tells us that surface induced water structure can extend to at most about a separation distance of at most about 6 water layers, three for each surface. The same conclusion can be reached from dimensional analysis.

We can envisage subcritical fluctuations in the gap between hydrophobic surfaces (contact angle greater than zero) [41–46]. Think of these like the crazing of a polymeric material, flaws in the material or cylinder like cracks that extend from one surface to another. The dimensions are only a cylinder of about 1/10 angstrom diameter corresponding to a surface induced cooperative realignment of water dipoles. The resulting water density depletion in the gap gives rise to a "hydrophobic" force. At contact angles above 90 degrees the fluctuations are critical and expel water in the gap.

Then how can these forces be so long ranged? The answer seems to be because of dissolved gas (or other hydrophobic solutes). It seems to be because such hydrophobic solutes, at 5×10^{-2} M, are about 30 angstroms apart in bulk water, much closer near a hydrophobic surface. These act as far as these tiny subcritical fluctuations are concerned as hydrophobic surface themselves. They can propagate fluctuations from one solute molecule to another over large distances. Chaotropic or cosmotropic salts either assist the propagation of these density fluctuations or oppose it.

The bubble–bubble problem is bit more complicated. It probably involves expansion of such cracks via necks between two bubbles as for emulsion droplets, but with the above in mind it makes some sense.

It is a misnomer to speak of THE hydrophobic force. The long ranged "hydrophobic" forces that occur with adsorbed submonolayers of surfactant [41–46] have a very different driving mechanism.

Restriction Enzymes

On one matter we are certainly on solid ground. The failure of the DLVO ansatz is proven to be wrong. It is not an hypothesis. If we can accept that there may be some truth in these things, we can come back now to our initial problem. Where did the energy come from to cut a phosphate bond? A reasonable hypothesis is this.

1. The enzyme is associates with the DNA polymer, under the influence of familiar forces, dimerises and diffuses along.
2. It finds the active (hydrophobic) site by stereochemistry.
3. Spontaneous cavitation occurs expelling water.
4. It is known from sonochemistry that due to the instantaneous high pressures and temperatures in such a cavity free radicals are formed.
5. The free radical so formed then cuts the bond (addition of a free radical scavenger like vitamin C stops the enzyme activity).
6. In different salts, and at different concentration, specific ion adsorption changes the active site, both its conformation, and hydrophobicity to inhibit and switch off the cavitation process.

It is not clear if dissolved gas (O2 or N2) would be necessary to produce the proper radical. Probably it is.

1–6 provide at least a plausible hint at the answer to our question. What is involved is a way of harnessing the weak NES specific ion forces cooperatively to do the job. No one has tested this.

If this is correct the mechanism need not be universal. For possibly the most studied enzyme, horseradish peroxidase, no one has identified an active site. There may not be one.

In that case a different mechanism must be involved. That would involve adsorption of reactants and their diffusion along the catalytic surface. Changes in dispersion (NES) self energies on adsorption are cooperative again, and involve interactions with the collective modes of the enzyme, specially in the infrared. These can either weaken or enhance the strength of chemical bonds depending on substrate. The mechanism in such cases would be exactly like that involved in catalysis by zeolites of hydrocarbons [47]. Specific ion adsorption of cations and anions driven by the missing NES forces changes not just "surface" hydration but also the collective modes. Hence we can guess one possible source of superactivity. It makes some sense in that it would explain why enzymes like ATPase generally are so big.

Conclusion

Whatever the validity of such speculations, some things are not in dispute. Even given its simplifying assumptions (continuum model for water), perfectly smooth surfaces, hydrated ions, the DLVO theory, however decorated, violates two fundamental physical laws. Ion specificity determined by NES forces is not included. This is acceptable even allowing the assumptions, only for very dilute systems. The same defects hold true for the Born self energy, correlation energies (Debye Huckel and its extensions) and interfacial tensions. When the flaws are removed, the difficulties disappear and ion specificity emerges. When the born and ionic interaction energies are modified to include the NES contributions, notions of "hard" and "soft" ions, "cosmotropy" and "chaotropy", the "civilised" model of electrolytes of Stokes, emerge naturally. Further they are quantitatively accessible from dielectric data. There is no conflict between old and new ideas except that the new ones allow quantification. We know how to exploit specific ion effects to switch forces on or off and control curvature in self assembling systems. Changes of hydration on adsorption are included in principle. The fact that the Debye length is NOT the simple Debye length in systems containing only very low concentrations of multivalent ions means that even at low salt concentrations $< 5 \times 10^{-2}$ M) where the electrostatic forces should win out, the older theories are inapplicable, as in real biology.

Further the whole question of what we mean by pH and buffers has to be revisited. And that of concepts like membrane potentials and transport across pores. Most of the intuition in biology is based on the older theories, So for example the transport of ions through pores, however sophisticated the water models used, depends on and ignores anion transport that is excluded by electrostatic forces.

Another example that illustrates our point is this. It is known that red blood cells have very different concentrations of K^+, higher inside than outside, and of Na^+ higher outside than inside. The differences are attributed to ion pumps. But the evidence for such pumps is somewhat dubious and energetically impossible. The concentration of haemoglobin inside the cell is almost close packed. It is then comprehensible that specific ion adsorption driven by NES forces alone might explain the differences and in the (finite volume) blood cell system give rise naturally to a membrane potential. Such ionic segregation does indeed occur in two phase phospholipid water electrolyte systems (see the challenging article of Ludwig Edelmann "Doubts about the Sodium-Potassium Pump are not Permissible in Modern Science" in Special Issue of Cell and Molecular Biology, 2005, Issue 8: Those Scholars who Talk to the Wind).

Even if these problems are sorted out, we have another. The role of dissolved gas and other sparingly soluble hydrophobic solutes, in mediating especially hydrophobic interactions, and the complex interplay between this role and electrolytes looms large. At least the problem is identified, and once recognised, can be used to guide and interpret experiment.

Finally let us finish on another note. Exactly the same (linear) Lifschitz theory for condensed media is equivalent to a semiclassical theory. It is equivalent to quantum electrodynamics, and despite its apparent complexity depends on just Maxwell's equations for the electromagnetic field and the Planck hypothesis on quantisation of light. The Casimir interaction between perfect metal plates and Casimir Polder interaction are trivial specialisations of Lifschitz theory. It turns out that these are strictly valid only at zero temperature. The same semi classical theory can be used to derive the resonance or Forster interaction (photon transfer) between an excited state and ground state atom. Which is relevant to photosynthesis. Remarkably, this classical result is not even correct at zero temperature!

From the Casimir interaction it is possible to derive a theory of mesons and nuclear forces. It is as for our cases still a linear theory and is used to evaluate the binding energies of nucleons in nuclei – a competition between electrostatic and NES forces. So the same ansatz underlies nuclear physics which is just as flawed as our classical colloid science theories [48–53]!

With thanks to Morris Kline's wonderful book Mathematics the Loss of Certainty, the present situation might be summarised in the words of Greek philosopher Xenophanes:

The gods have not revealed all things
from the beginning.
But men seek and so find out better in time.
Let us suppose these things are like the truth.
But surely no man knows or ever will know
The truth about the gods and all I speak of,
For even if he happens to tell the perfect truth,
He does not know it,
but appearance is fashioned over everything.

At least we have some things to do. And I am sure the Ostwald's would have liked that.

References

1. Kim H-K, Tuite E, Nordén B, Ninham BW (2001) Co-ion dependence of DNA nuclease activity suggests hydrophobic cavitation as a potential source of activation energy. Eur Phys J E4:411–417
2. Kékicheff P, Ninham BW (1990) The Double-layer interaction of asymmetric electrolytes. Europhys Lett 12(5):471–477
3. Nylander T, Kékicheff P, Ninham BW (1994) The effect of solution behaviour of insulin on interactions between adsorbed layers of insulin. J Coll Interface Sci 164:136–150
4. Waninge R, Paulsson M, Nylander T, Ninham BW, Sellers P (1998) Binding of sodium dodecyl sulphate and dodecyl trimethyl ammonium chloride to beta-lactoglobulin. A Calorimetric Study. Int Dairy J 18:141–148
5. Pashley RM, Ninham BW (1987) Double-layer forces in ionic micellar solutions. J Phys Chem 91:2902–2904
6. Bostrom M, Craig VJS, Albion R, Williams DRM, Ninham BW (2003) Hofmeister Effects and the Role of Coions in pH Measurements. J Phys Chem B 107:2875–2877
7. Salis A, Pinna MC, Bilaniĉova D, Monduzzi M, Lo Nostro P, Ninham BW (2006) Specific anion effects on pH Measurements of Buffer Solutions: Bulk and Surface Phenomena. J Phys Chem B 110:2949–2956
8. Alfridsson M, Ninham BW, Wall S (2000) Role of cooions and atmospheric gas in colloid interaction. Langmuir 16:10087–10091
9. Karman ME, Ninham BW, Pashley RM (1996) Effects of dissolved gas on emulsions, emulsion polymerisation and surfactant aggregation. J Phys Chem 100:15503–15507
10. Vinogradova OI, Bunkin NF, Churaev NV, Kiseleva OA, Lobeyev VA, Ninham BW (1995) Submicrocavity structure of water between hydrophobic and hydrophilic walls as revealed by optical cavitation. J Coll Interface Sci 173:443–447
11. Bunkin NF, Kochergin AV, Lobeyev AV, Ninham BW, Vinogradova OI (1996) Existence of charged submicrobubble clusters in polar liquids as revealed by correlation between optical cavitation and electrical conductivity. Colloid Surf A: Physicochem Eng Aspect 10:207–212
12. Bunkin NF, Kiseleva OA, Lobeyev AV, Movchan TG, Ninham BW, Vinogradova OI (1997) Effect of salts and dissolved gas on optical cavitation near hydrophobic and hydrophilic surfaces. Langmuir 13:3024–3028
13. Bunkin NF, Lobeyev AV, Lyakhov GA, Ninham BW (1999) Mechanism of low-threshhold hypersonic cavitation stimulated by broad band laser pump. Phys Rev E60:1681–1690
14. Craig VSJ, Ninham BW, Pashley RM (1993) The Effect of Electrolytes on Bubble Coalescence in Water. J Phys Chem 97:10192–10197
15. Pashley RM, McGuiggan PM, Ninham BW, Evans DF, Brady J (1986) Direct measurements of surface forces between bilayers of double-chained quaternary ammonium acetate and bromide surfactants. J Phys Chem 90:1637–1642
16. Ninham BW, Evans DF (1986) The Rideal Lecture: Vesicles and molecular forces. Faraday Disc Chem Soc 81:1–17
17. Karaman ME, Ninham BW, Pashley RM (1994) Some aqueous solution and surface properties of dialkylsulfosuccinate surfactants. J Phys Chem 98:11512–11518
18. Kunz W, Henle J, Ninham BW (2004) Zur Lehre von der Wirkung der Salze (About the science of the effect of salts): Franz Hofmeister's historical papers. Curr Opin Coll: Surf Sci 9:19–37
19. Kunz W, Lo Nostro P, Ninham BW (2004) The Present State of Affairs with Hofmeister effects. Curr Opin Coll: Surf Sci 9:1–18
20. Lo Nostro P, Fratoni L, Ninham BW, Baglioni P (2002) Water Absorbency by Wool Fibers: Hofmeister Effect. Biomacromolecules 3:1217–1224
21. Lonostro P, Ninham BW, Lo Nostro A, Pesavento G, Fratoni L, Baglioni P (2005) Specific Ion Effects on the Growth Rates of Staphyloccus aureus and Pseudomonas aeuginosa. Phys Biol 2:1–7

22. Ninham BW, Yaminsky VV (1997) Ion binding and ion specificity – The Hofmeister effect, Onsager and Lifschitz theories. Langmuir 13:2097–2108
23. Ninham BW (2002) Physical Chemistry: The Loss of Certainty Progress in Colloid. Polym Sci 120:1–12
24. Ninham BW, Boström M (2005) Building Bridges between the Physical and Biological Sciences. Cell Mol Biol 51:803–815
25. Bostrom M, Tavares FW, Finet S, Skouri-Panet F, Tardieu A, Ninham BW (2005) Why Forces between Proteins follow different Hofmeister series for pH above and below pI. Biophys Chem 117:115–122
26. Boström M, Ninham BW (2004) Dispersion self-free energies and interaction free energies of finite sized ions in salt solutions. Langmuir 20:7569–7547
27. Boström M, Ninham BW (2005) Energy of an ion crossing a low dielectric membrane: the role of dispersion self-free energy. Biophys Chem 114:95–101
28. Bostrom M, Ninham BW (2004) Contribution from Dispersion, Born Self Energies to the Solvation Energies of Salt Solutions. J Phys Chem B 108:12593–12595
29. Bostrom M, Williams DR, Ninham BW (2002) Ion Specificity of Micelles and Microemulsions Explained by Ionic Dispersion Forces. Langmuir 18:6010–6014
30. Bostrom M, Williams DR, Ninham BW (2002) Influence of Hofmeister effects on surface pH and binding of peptides to membranes. Langmuir 18:8609–8615
31. Bostrom M, Williams DR, Ninham BW (2002) Influence of ionic dispersion potentials on counterion condensation on polyelectrolytes. J Phys Chem B 106:7908–7912
32. Bostrom M, Williams DRM, Ninham BW (2003) Specific Ion Effects: why the properties of Lysozyme in Salt Solutions follow a Hofmeister Series. Biophys J 85:686
33. Bostrom M, Williams DR, Ninham BW (2003) Specific Ion Effects: the role of coions in biology; the influence of salts on conformational equilibria in Rhodopsin. Europhys Lett 63(4):610–615
34. Bostrom M, Williams DR, Ninham BW (2004) Specific Ion Effects: Role of Salt & Buffer on Protonation of Cytochrome c. Eur Phys J E 13:239–245
35. Kunz W, Belloni L, Bernard O, Ninham BW (2004) Osmotic Coefficients, Surface tension of Aqueous Electrolyte Solutions: Role of Dispersion Forces. J Phys Chem B 108:2398–2404
36. Bostrom M, Williams DR, Stewart PR, Ninham BW (2003) Hofmeister Effects in Membrane Biology – The Role of Ionic Dispersion Potentials. Phys Rev E 68:041902
37. Lonetti B, Lo Nostro P, Ninham BW, Baglioni P (2005) Anion Effects on Calixarene Monolayers: a Hofmeister Series Study. Langmuir 21:2242–2249
38. Lo Nostro P, Lopes JR, Ninham BW, Baglioni P, Effect of Cations and Anions on the Formation of Polypseudorotaxanes. J Phys Chem B 106:2166–2174
39. Bostrom V, Kunz W, Ninham BW (2005) Hofmeister effects in surface tension of aqueous electrolyte solution. Langmuir 21:2619–2623
40. Boström M, Kunz W, Ninham BW (2005) Hofmeister Effects in Surface Tension of Electrolytes: Role of Interfacial Solvation Energies and Ionic Dispersion Potentials. Langmuir 21:2242–2249
41. Pashley RM, McGuiggan PM, Ninham BW, Evans DF (1985) Attractive forces between uncharged hydrophobic surfaces: Direct measurements in aqueous solution. Science 229:1088–1089
42. Yaminski VV, Ninham BW (1993) The hydrophobic force: The lateral enhancement of subcritical fluctuations. Langmuir 9:3618–3624
43. Yaminsky V, Ohnishi S, Ninham BW, Long-Range Hydrophobic Forces are due to Capillary Bridging. Encyclopaedia of Surfaces and Materials, vol 4, Chap 3. Academic Press
44. Yaminsky VV, Ninham BW, Christenson HK, Pashley RM (1996) Adsorption forces between hydrophobic monolayers at long distances. Langmuir 12:1936–1943
45. Yaminsky VV, Jones C, Yaminsky F, Ninham BW (1996) Onset of hydrophobic attraction at low surfactant concentrations. Langmuir 12:3531–3535
46. Yaminski VV, Ninham BW, Pashley RM (1998) Interaction between surfaces of fused silica in water Evidence of cold wetting and effects of cold plasma treatment. Langmuir 14:3223–3235
47. Blum Z, Hyde ST, Ninham BW (1993) Adsorption in zeolites, dispersion self energy and Gaussian curvature. J Phys Chem 97:661–665
48. Ninham BW, Daicic J (1998) Lifschitz theory of Casimir forces at finite temperature. Phys Rev A 57:1870–1880
49. Wennerstrom H, Daicic J, Ninham BW (1999) Temperature dependence of atom–atom interactions. Phys Rev A 60:2581–2584
50. Boström M, Longdell J, Ninham BW (2001) Atom–atom interactions at and between metal surfaces at non-zero temperature. Phys Rev A 64:D622702
51. Bostrom M, Longdell JJ, Mitchell DJ, Ninham BW (2003) Resonance Interaction between one excited and one ground state atom. Eur Phys J D 22:47–52
52. Bostrom M, Longdell J, Ninham BW (2002) Resonance Interaction in Channels. Europhys Lett 59:21
53. Ninham BW, Bostrom M (2003) Screened Casimir Force at Finite Temperatures. A Possible role for Nuclear Interactions. Phys Rev A 67:030701–1030701–4

Progr Colloid Polym Sci (2006) 133: 74–77
DOI 10.1007/2882_060

M. Boström
F. W. Tavares
D. Bratko
B. W. Ninham

Ion Specific Interactions Between Pairs of Nanometer Sized Particles in Aqueous Solutions

M. Boström (✉)
Department of Physics and Measurement Technology, Linköping University,
58183 Linköping, Sweden
e-mail: mabos@ifm.liu.se

F. W. Tavares
Escola de Química, Universidade Federal do Rio de Janeiro, CEP 21.949.900, Brazil

D. Bratko
Department of Chemistry,
Virginia Commonwealth University,
Richmond, 23284, USA

B. W. Ninham
Research School of Physical Sciences and Engineering, Australian National University, 0200 Canberra, Australia

Abstract For the classical DLVO theory, which deals only with electrostatic forces acting between ions and colloids, all ions in solution with the same charge should result in the same force between colloids. Ion specificity does occur in the opposing attractive Lifshitz forces but only very weakly. Ion size parameters, inner and outer Helmholtz planes are used to fit the specificity but that do not work. At, and above, biological salt concentrations other, non electrostatic (NES) ion specific forces act that are ignored in such modeling. To exemplify the general ideas we use a system that corresponds to pairs of nanoparticles. We show that ion specific double layer forces can be understood once NES forces acting between ions and colloids are included consistently in non-linear theory and in Monte Carlo simulations.

Keywords Nanoparticle · Hofmeister Effect

Introduction

Precipitation is often used as an initial step in purification of proteins from complex solutions because of its low cost and selectivity [1]. Precipitation and many important bioengineering and biochemical processes [1, 2], as well as processes in ceramic suspensions [3], depend on interparticle forces. Lewith and Hofmeister showed in a series of papers during the 1880s that these forces, in blood serum plasma and in hen-egg-white protein solutions, could be manipulated, in a highly ion specific way, by the addition of different salt solutions. Recent English translations of a few of Hofmeister's publications can be found in [4]. Depending on the anion, different concentrations were required to precipitate a prescribed concentration of egg white. The salts could be ordered in what is now referred to as a Hofmeister sequence of effectiveness. Solubility experiments [5] and low angle X-ray scattering [6] have revealed that for pH < pI, where salt anions are counterions, the repulsive double layer force between two proteins increase in the order NaSCN < NaI < NaCl. In contrast, at higher pH > pI, where anions are co-ions, the forces increase in the order NaCl < NaI < NaSCN.

Ninham and Yaminsky [7] demonstrated that one important reason for the failure of double layer theory to explain the observed ion specificity was the neglect of ionic dispersion potentials acting between ions and macroions. These potentials that originate from quantum electrodynamic fluctuations must for consistency be included at the same non-linear level in the theory as the electrostatic potentials. At physiological salt concentrations (around 0.1 M and above) electrostatic potentials become strongly screened and these ionic dispersion potentials often dominate the interaction. We have in a series of papers demonstrated that it is possible to understand the observed ion specificity in a large number of systems when these ionic dispersion potentials are included in theory and simulations. A few examples include surface tension of electrolytes [8], double layer forces [9, 10], protein charges [11], and electrochemical potentials near surfaces (what we refer to as "surface pH") [12]. We will here demonstrate how the experimentally observed ion specificity in hen-egg-white lysozyme crystallization can be understood when ionic dispersion potentials acting between ions and between each ion and the proteins are included in Monte Carlo simulations. Our predictions are also valid for other types of colloids (e.g. silica nanoparticles).

We rehearse briefly in Sect. "Theory" the theory of Monte Carlo simulations (they have been described in detail in Refs. [10, 14, 15]). Numerical results for protein-protein interactions are give in Sect. "Mean Force of Hen-Egg-White Lysozyme". We will also demonstrate that it is possible to obtain qualitative agreement between second virial coefficients obtained from theory with published experimental results. We end with a few concluding remarks in Sect. "Conclusions".

Theory

Near a charged protein ions experience an electrostatic potential that leads to accumulation (depletion) of counterions (co-ions). According to classical DLVO theory all monovalent salts should give the same results and there should be no co-ion adsorption or co-ion effects since these ions should be pushed away from the interface. However electrostatic potentials are not the only potentials that influence the ionic distributions near a protein. We let $U_\pm(r)$ be the non-electrostatic effective interaction potential beyond pure electrostatics experienced by the ions. We include here ionic dispersion potentials acting between ions and between ions and the interface. There will in general also be contributions from image potentials and solvation energy changes near interfaces and charge groups.

The non-retarded dispersion interaction between a point particle and a sphere of radius r_p can within the pair summation approximation be written as

$$U_\pm = \frac{B_\pm}{(r-r_\mathrm{p})^3\left[1+(r-r_\mathrm{p})^3\Big/\left(2r_\mathrm{p}^3\right)\right]}\,. \quad (1)$$

Here the dispersion coefficient ($B_\pm$) will be different for different combinations of ion and spherical protein membrane. When retardation is neglected we can calculate the dispersion coefficients from the corresponding planar interface result as a sum over imaginary frequencies ($\mathrm{i}\omega_n = \mathrm{i}2\pi k_\mathrm{B} Tn/\hbar$, where $\hbar$ is Planck's constant).

$$B_\pm = \sum_{n=0}^{\infty} \frac{\left(2-\delta_{n,0}\right)\alpha^\pm\left(\mathrm{i}\omega_n\right)\left[\varepsilon_\mathrm{w}\left(\mathrm{i}\omega_n\right)-\varepsilon_\mathrm{oil}\left(\mathrm{i}\omega_n\right)\right]}{4\beta\varepsilon_\mathrm{w}\left(\mathrm{i}\omega_n\right)\left[\varepsilon_\mathrm{w}\left(\mathrm{i}\omega_n\right)+\varepsilon_\mathrm{oil}\left(\mathrm{i}\omega_n\right)\right]}\,. \quad (2)$$

For Na^+, F^-, Cl^-, Br^-, and I^- the following B values have been used [10]: $-0.45\times10^{-50}\,\mathrm{JM}^3$; $-1.43\times10^{-50}\,\mathrm{Jm}^3$; $-3.57\times10^{-50}\,\mathrm{Jm}^3$; $-4.44\times10^{-50}\,\mathrm{Jm}^3$; $-5.71\times10^{-50}\,\mathrm{Jm}^3$. It would be desirable to have a better characterization of the ionic excess polarizabilities and the dielectric properties of proteins. But although the values presented may deviate slightly from the correct values for a specific ion and a specific surface area of a protein they are of the right order of magnitude. Our results are quite general since many proteins (such as lysozyme and cytochrome c) are built up from similar groups and hence have similar dielectric properties in the visible and UV frequency range.

Canonical Monte Carlo simulations were used to calculate the mean-force between two macroions in an electrolyte solution. Details of the NVT Monte Carlo simulations are given elsewhere [10, 14, 15].

Mean Force of Hen-Egg-White Lysozyme

Using Monte Carlo simulations Tavares et al. [10] demonstrated that it is possible to obtain the correct trends for second virial coefficients of colloids in salt solutions. We will here show that we can obtain qualitative agreement between theoretical and experimental second virial coefficients for hen-egg-white lysozyme in 0.1 M NaCl, 0.2 M NaCl, and 0.2 M NaI. The lysozyme protein was modeled as a hard homogeneously charged (+10 e0) sphere with an effective diameter of 33 Å. The charge of the protein depends on the particular pH and salt solution used [11]. It is important to note that the large size of the protein requires that we perform a much larger simulation compared to the one by Tavares et al. [10]. This is because there will be a large amount of counterions physisorbed on the protein surface for highly polarizable anions. In order to have a sufficiently large amount of ions in solution to obtain good statistics we performed a simulation with 600 monovalent ions. For each macroion-macroion distance the mean force were obtained by performing 60×10^6 trial moves for equilibration and 120×10^6 for production. The Monte-Carlo simulation is carried in a cubic simulation box contains two identical macroions (proteins) and 600 small ions that satisfy overall charge neutrality. The volume of the box is adjusted to give a specified ionic strength (i.e., 0.1 or 0.2 M). In all cases, the box length is about one order of magnitude larger than the Debye screening length; therefore, the electrostatic interaction between macroions (proteins) due to the introduction of periodic boundary conditions is negligible. Standard canonical Monte Carlo simulation is applied to calculate the average forces and internal energies. During each run, the two proteins are fixed at a given separation distance, along the box diagonal, while the small ions are free to move throughout the box. The Ewald-sum method is applied to account for long-range electrostatic interactions. Trial moves of proteins are used to determine collision probabilities and the mean force [10].

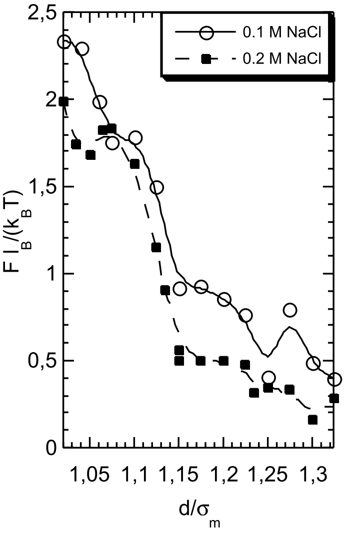

Fig. 1 Total mean force between two macroions with size and charge corresponding to hen-egg-white lysozyme proteins at pH 4.5 in "NaCl" electrolytes of ionic strength 0.1 M and 0.2 M. (The *lines* are smooth fitted curves obtained using KaleidaGraph.) The colloid-colloid centre to centre distance is normalized with the colloid particle diameter

We show in Fig. 1 the total mean force between two macroions with size and charge corresponding to hen-egg-white lysozyme proteins at pH 4.5 in "NaCl" electrolytes of ionic strength 0.1 M and 0.2 M. The overall interaction becomes less repulsive as the solution salt concentration increases. Notably, in agreement with experiments, the attraction also increases with increasing polarizability (Fig. 2). The total mean force is more attractive with 0.2 M "NaI" than with 0.2 M "NaCl". We show in Fig. 3 the different contributions to the total mean force between two "lysozyme" colloids in 0.2 M "NaCl" salt solution. We note that there is a large degree of cancellation between the collision and the ionic dispersion potential contributions. This is so since the main influence on these two terms are from the ions that are very close to the colloidal surface. We show in Fig. 4 the potential of mean force obtained from smoothened mean force curves (shown in Fig. 2). There can be an attractive minimum when the distance between the colloidal surfaces is equal to one ion diameter, i.e. when exactly one counterion layer can be pressed between the two colloidal particles.

The osmotic second virial coefficient is commonly used to estimate the strength of protein-protein interactions and provide important information about colloid-solution stability. The second virial coefficient A_2 can be written as a function of the total interaction potential of mean force

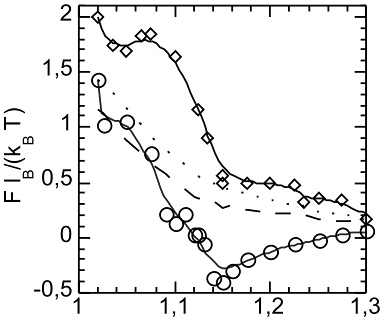

Fig. 2 Total mean force between two "lysozyme" macroions in a monovalent electrolyte of ionic strength 0.2 M for "NaCl" (*diamonds*) and "NaI" (*circles*). The electrostatic contributions are shown as *dotted line* for "NaCl" and *dashed line* for "NaI". (The *solid lines* are smooth curve fit to the total mean forces obtained using KaleidaGraph.) The colloid-colloid centre to centre distance is normalized with the colloid particle diameter

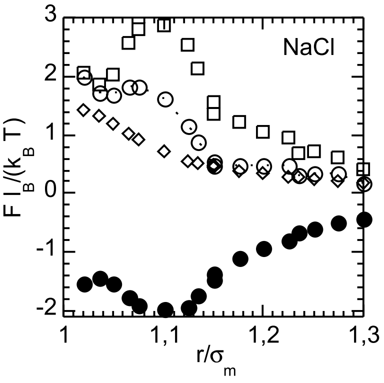

Fig. 3 Contributions to the mean force between two "lysozyme" macroions in a monovalent electrolyte of ionic strength 0.2 M for "NaCl". The *open circles*, *squares*, *diamonds*, and *solid circles* are the total mean force, and the contributions from collision, electrostatic, and ionic dispersion potentials, respectively. The colloid-colloid centre to centre distance is normalized with the colloid particle diameter

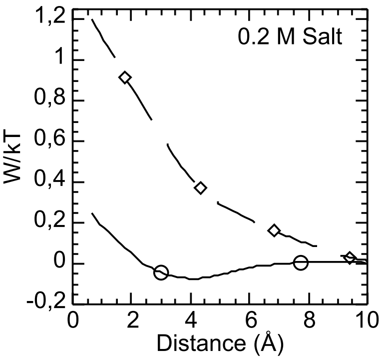

Fig. 4 Potential of mean force between two "lysozyme" macroions in a monovalent electrolyte of ionic strength 0.2 M for "NaCl" (*diamonds*) and "NaI" (*circles*). Distance show the centre to centre distance minus the colloidal diameter

between two lysozyme particles in solution:

$$MA_2/v = 2\pi N_\mathrm{A}/(Mv) \int_0^\infty \{1 - \exp[U_\mathrm{tot}(r)/k_\mathrm{B}T]\} r^2 \mathrm{d}r\,, \tag{3}$$

$$U_\mathrm{tot}(r) = \begin{cases} +\infty & \text{for } r < 2r_\mathrm{p} \\ W(r) - \dfrac{\varepsilon}{r^6} & \text{for } r > 2r_\mathrm{p} \end{cases}\,. \tag{4}$$

Here M is the molecular weight, v the partial specific excluded volume (for lysozyme equal to 0.74 [6]). With this normalization MA_2/v is equal to 4 for hard spheres. $W(r)$ is the potential of mean force obtained from simulations (described above) which does not include the direct van der Waals interaction between the two globular proteins. We use for this second term the same effective attractive van der Waals/hydrophobic interaction ($\varepsilon = 8.4 \times 10^9$ kJ/(mol Å^6)) that Linse and co-workers found could reasonably well accommodate second virial coefficients in NaCl solutions. A positive second virial coefficient indicates overall repulsive forces in the colloidal (protein) solution. The solution is more likely to crystallize the more attractive the overall forces are, i.e. the more negative the second virial coefficient become. We find that the normalized second virial coefficient of lysozyme is around −0.8 in 0.2 M NaCl and more negative than −5 in 0.2 M NaI. The compressibility obtained from the structure factor is related to the osmotic pressure and hence with the second virial coefficient. This means that one can compare our theoretical results with experimental results deduced from small angle X-ray scattering. Bonneté et al. [17] deduced $MA_2/v = -0.78$ for 0.20 M NaCl at 20 °C (prepared with a 50 mM NaOAc buffer at pH 4.5 which should give a net protein charge close to our model protein). The normalized second virial coefficient became more attractive with increasing salt concentration (increased screening) and with increasing polarizability of the ions. With 0.15 M $NaNO_3$, and keeping other things as above, gives for example $MA_2/v = -9.06$.

Conclusions

We have exploited the Monte Carlo simulation program developed originally by Wu et al. [14, 15] and extended to incorporate ion-ion and ion-protein dispersion interactions [10] to investigate the mean force between a pair of lysozyme globular proteins. It is evident that inclusion of non-electrostatic (dispersion) potentials can account, at least, qualitatively for the observed ion specific trends. Future work will explore how other non-electrostatic contributions may contribute to the effective potential of mean force between pairs of nanometer sized colloidal particles.

Acknowledgement M.B. thanks the Swedish Research Council for financial support and computer time.

References

1. Curtis RA, Ulrich J, Montaser A, Prausnitz JM, Blanch HW (2002) Biotechnol Bioeng 79:367
2. Kunz W, Lo Nostro P, Ninham BW (2004) Curr Op Colloid Int Sci 9:1
3. Franks G (2002) J Colloid Int Sci 249:44
4. Kunz W, Henle J, Ninham BW (2004) Curr Op Colloid Int Sci 9:19
5. Ries MM, Ducruix AF (1989) J Biol Chem 264:745
6. Finet S, Skouri-Panet F, Casselyn M, Bonnete F, Tardieu A (2004) Curr Op Colloid Int Sci 9:112
7. Ninham BW, Yaminsky V (1997) Langmuir 13:2097
8. Boström M, Williams D, Ninham BW (2001) Langmuir 17:4475, Boström M, Ninham BW (2004) Langmuir 20:7569; Boström M, Kunz W, Ninham BW (2005) Langmuir 21:2619
9. Boström M, Williams DRM, Ninham BW (2001) Phys Rev Lett 87:168103
10. Tavares FW, Bratko D, Blanch H, Prausnitz JM (2004) J Phys Chem B 108:9228; Tavares FW, Bratko D, Prausnitz JM (2004) Curr Op Colloid Int Sci 9:81
11. Boström M, Williams DRM, Ninham BW (2003) Biophys J 85:686
12. Boström M, Craig V, Albion R, Williams D, Ninham BW (2003) J Phys Chem B 207:2875
13. Jönsson B, Wennerström H, Halle B (1980) J Phys Chem 84:2179
14. Wu J, Bratko D, Prausnitz JM (1998) Proc Natl Acad Sci USA 95:15169
15. Wu J, Bratko D, Blanch HW, Prausnitz JM (1999) J Chem Phys 111:7084
16. Carlsson F, Malmsten M, Linse P (2001) J Phys Chem B 105:12189
17. Bonneté F, Finet S, Tardieu A (1999) J Cryst Growth 196:403

Progr Colloid Polym Sci (2006) 133: 78–87
DOI 10.1007/2882_067

Federica Lo Verso
Christos N. Likos
Luciano Reatto

Star Polymers with Tunable Attractions: Cluster Formation, Phase Separation, Reentrant Crystallization

Federica Lo Verso (✉) · Christos N. Likos
Institut für Theoretische Physik II,
Heinrich-Heine-Universität Düsseldorf,
Universitätsstraße 1, 40255 Düsseldorf,
Germany
e-mail: federica@thphy.uni-duesseldorf.de

Luciano Reatto
Dipartimento di Fisica,
Università degli Studi di Milano,
Via Celoria 16, 20133 Milano, Italy

Abstract We consider a model to describe starlike polymers featuring a steric repulsion accompanied by a dispersion- or depletion-induced tunable attraction. The range and depth of the latter can be controlled by suitable choices of the solvent, salt concentration and/or depletant size and type, whereas the strength of the steric repulsions is set by the arm number f of the stars. We focused on star polymers with arm number $f = 32$. Depending on the choice of the attraction characteristics and on the temperature, the system exhibits, in addition to the usual ultra-soft repulsion, a relatively short range attraction and a secondary repulsive barrier at longer distances. Our results show a variety of structurally distinct states. In the fluid phase we find evidence for cluster formation which is accompanied by fluid-phase separation. Moreover the system presents unexpected fluid-solid transitions which are *completely absent* for the purely repulsive case. The dependence of the cluster and solid regions, and the location of the critical point on the potential parameters is quantitatively analyzed.

Keywords Polymers · Soft colloids · Clusters

Introduction

Soft matter systems are characterized by a high degree of structural complexity. This complexity expresses itself both in terms of the architecture of the constituent particles and in terms of the vast separation of length- and time-scales between the dissolved, mesoscopic aggregates and the microscopic solvent. A statistical mechanical approach towards analyzing such systems would be therefore unfeasible if one attempted to keep track of all degrees of freedom involved. It turns out that an efficient strategy to overcome these difficulties is to integrate out the fast, microscopic degrees of freedom, so that only the mesoscopic ones remain in the picture. The result of this process is the introduction of an *effective interaction potential* between the heavy particles, which is to a large extent induced by the degrees of freedom that have been integrated out [1]. Consequently, the effective interaction potential can be tuned in a number of ways, giving rise to an unprecedented flexibility in controlling the interparticle interactions, a feature absent in atomic systems.

A prominent example of a tunable and, from an atomistic point of view, unusual effective interaction is the one acting between the centers of two star-polymers in good solvents. These macromolecules consist of f chains anchored on a common center [2]. The effective interaction between star polymers shows a logarithmic dependence on their center-to-center separation r for small distances and it crosses over to a Yukawa form for larger ones [3, 4]. Moreover, the overall strength of the interaction scales with temperature and is also proportional to $f^{3/2}$. Thus, f controls the softness of the stars which, formally, reduce to hard spheres in the limit $f \to \infty$.

Due to recent advances in the synthesis of regular, monodisperse stars [5], and to their several medical and industrial applications [2], star-polymer solutions received a great deal of attention in the recent past. In addition, star polymers are excellent model systems as colloids with tunable softness. Accordingly, there has been a large amount of theoretical [3,4,6–15] and experimental [4, 16–26] work pertaining to their equilibrium and rheological properties. Moreover, the non-equilibrium phase behavior of mixtures between stars and linear chains has also attracted considerable attention [27–29]. Here we summarize those findings that are most relevant to the present work. First simulation and theory have shown that a critical functionality $f_c = 34$ exists, below which star polymer solutions never crystallize, at any concentration [10]. Secondly, the density-functionality phase diagram of the stars features several regions of reentrant melting upon density increases [10]. Thirdly, the ideal glass transition lines from Mode Coupling Theory roughly follow the equilibrium crystallization transition [12]. And, finally, experiments and theory have shown that ergodicity can be restored in a dynamically arrested star solution by addition of smaller linear homopolymer [27].

One-component solutions of regular star polymers with a pointlike center, dispersed in an athermal solvent feature the above-mentioned, purely repulsive and entropic effective interaction. However, attractions that must be superimposed to the steric chain repulsion can be present due to a number of additional factors. First, suppose that the polymer chains are grafted on a colloidal particle of finite size b (still $b \ll \sigma$, with σ denoting the chains' spatial extent). In that case, the attraction is caused by the ubiquitous dispersion force between the compact spherical colloids [30,31]. In fact, grafting of the chains has been originally put forward as precisely a means of providing a steric barrier to counteract this attraction [3]. Further, effective, depletion-like attractions between stars emerge in multicomponent star-chain [28,29] or star-star mixtures [32], which have been looked upon recently, both in theory and in experiment. Other interesting systems, in this context, are star polymers with attractive polar end groups, telechelic associating polymers with hydrophobic terminal groups and associating polyelectrolytes in homogeneous solutions [33–35]. Theoretical approaches have been developed to describe flower-like micelles with hydrophobic terminal groups that self-assemble in water. Such aggregates show a characteristic "bridging attraction" [36,37]. Hence, the study of a system interacting by a combination of a starlike repulsion and an additional attraction is physically motivated.

Along these lines, a model potential to describe star-polymer solutions in which, in addition to the excluded volume effects, attractions emerge, has been recently studied [38]. For this model the fluid-fluid phase diagram has been determined using mean field theory and two fluid-state-theories, the modified hypernetted chain closure (MHNC) [39] and the hierarchical reference theory (HRT) [40,41] for different f-values. If the strength of the interaction is strong enough a fluid-fluid phase transition appears but the density-temperature coexistence curve bifurcates at a triple point into two lines of coexistence terminating at two critical points. This peculiar phase behavior is related to the unusual form of the repulsive contribution. For the same pair interaction, dynamical properties as well as the appearance of glass transition have been studied [13]. The interplay between attractive interactions of different range and ultra-soft core repulsion has been investigated analyzing the effect on the dynamics and on the occurrence of the ideal glass transition line, together with the interplay between equilibrium and non equilibrium phase behavior.

In [13,38], the parameters were chosen in such a way that the total potential featured just the ultrasoft repulsion at short distances and a pure attraction for longer ones. However, this is not the case, e.g., for depletion-induced attractions: the total potential features both an attractive part and a secondary, repulsive barrier at longer distances. It is the purpose of this paper to analyze quantitatively the behavior of such systems. Our results show a remarkable variety of structural and thermodynamic phenomena, including the formation of clusters, fluid-fluid phase coexistence as well as the emergence of stable solids, which are unstable in the absence of attractions. This paper is organized as follows: in Sect. 2 we introduce the system and the effective interaction we employed. In Sect. 3 we describe the theoretical and numerical tools to study structural properties and phase behavior, whereas in Sect. 4 we present and critically discuss our results. Finally, in Sect. 5 we summarize and draw our conclusions.

The Model System: Effective Pair Interaction

The steric part of effective pair interaction between star polymers with f arms in a good solvent, $v_{\mathrm{st}}(r)$, is given by the functional form [4]:

$$\beta v_{\mathrm{st}}(r) = \frac{5}{18} f^{3/2} \begin{cases} \left[-\ln\left(\frac{r}{\sigma}\right) + \frac{1}{1+\sqrt{f}/2} \right] & \text{if} \quad r \leq \sigma; \\ \frac{1}{1+\sqrt{f}/2} \left(\frac{\sigma}{r}\right) \exp\left[-\frac{\sqrt{f}(r-\sigma)}{2\sigma} \right] & \text{if} \quad r \geq \sigma, \end{cases} \tag{1}$$

where $\beta = (k_{\mathrm{B}} T)^{-1}$, with Boltzmann's constant k_{B} and the absolute temperature T, and σ is the corona diameter of the stars, related to the experimentally measurable radius of gyration R_{g} via $\sigma \simeq 1.26 R_{\mathrm{g}}$ [8]. On top of this repulsion, now superimpose an attraction $w(r)$, introducing thereby the total interaction potential $V_{\mathrm{tot}}(r) = v_{\mathrm{st}}(r) + w(r)$. The form of $w(r)$ follows from the physical motivation put forward in [38]. In order to maintain the $\sim 1/r$-scaling of the effective force $F(r) = -\nabla V_{\mathrm{tot}}(r)$ at short distances, the attractive contribution $w(r)$ is chosen to have the form of a Fermi potential, which is essentially constant for small r-values, and whose point of inflection and sharpness are free parameters. In particular, $w(r)$ reads as:

$$w(r) = -C\left\{\exp\left[\frac{r-A}{B}\right]+1\right\}^{-1} . \tag{2}$$

Let us briefly discuss the meaning of the various parameters and the physical mechanisms that allow them to be externally controlled. C is an energy scale, whereas A and B are length scales. The relevant physical quantity is the reduced temperature

$$T^* \equiv \frac{k_B T}{C} . \tag{3}$$

If the attraction results from dispersion forces, then C can be tuned by modifying the solvent that affects the value of the Hamaker constant [30, 31]. In this case, C is temperature-independent and the system is thermal. If the attraction is caused due to the addition of athermal depletants (such as polymer coils [28, 29] or smaller stars [32]), then C scales with $k_B T$, hence temperature is irrelevant, but it acquires a dependence on the depletant concentration. In this case, the above-defined quantity T^* can be interpreted, roughly, as an inverse depletant reservoir concentration. The length scales A and B can also be tuned externally. In the case of dispersion-induced attraction, they can be influenced by screening the dipole–dipole interaction through addition of salt, which remains mainly in the intermolecular space, not affecting therefore the conformation of the stars. In the case of depletant-induced attraction they can be influenced by modifying the softness and size of the smaller component.

For this model, the case in which the full potential, $V_{\mathrm{tot}}(r)$, is deprived of secondary maxima at large $r \gtrsim \sigma$ has been previously discussed in detail, focusing on the equilibrium phase diagram [38] and the presence of glass transitions [13]. Some peculiar and interesting characteristics have been found, such as, e.g., the existence of *two* critical points and, for $46 \lesssim f \lesssim 70$ and shrinking the well potential, a progressively shift of the glass region to higher density. Moreover, it has been shown that for a two-component asymmetric star-star mixture, the introduction of small depletant stars determine, for certain ranges of f and density of the depletant, an attractive contribution to the interaction plus a repulsive bump for long distances [32]. In that case, the big-macromolecules in solution have a high arm number, $f \simeq 270$ value. The phase diagram of asymmetric mixture has been considered, finding in particular that the addition of small stars melts the crystal formed by the big ones.

In this paper we modify the parameters A and B in order to analyze the effect of the repulsive barrier on the interaction that we obtain by "shrinking" the well potential, moving at the same time the minimum to lower interparticle separations. In order to avoid excessive freedom associated with many parameters, we fix the value of A to $A = 1.35\sigma$ throughout and the functionality to $f = 32$, varying solely the parameter B that controls the sharpness of the Fermi potential, (Eq. 2). In Fig. 1a we show the total interaction potential $V_{\mathrm{tot}}(r)$ for the three values of B employed in this work, $B = 0.15\sigma$, 0.1σ, and 0.05σ. It can be seen that decreasing B has the effect of lowering the depth of the attractive well, reducing its range and enhancing the height of the secondary, repulsive barrier. In the same Figure, we also show the potential shape for the choice of parameters employed in previous work [38], namely $A = 2.1\sigma$ and $B = 0.35\sigma$. Here, it can be seen that $V_{\mathrm{tot}}(r)$ is free of repulsive barriers and that the attraction is much deeper and longer in range. In Fig. 1b we see that for high enough temperatures, $T^* \gtrsim 2.0$, $V_{\mathrm{tot}}(r)$ essentially reduces to the purely repulsive interaction $v_{\mathrm{st}}(r)$, as the thermal energy is sufficiently strong to wash out the attraction. Finally, in Fig. 1c we show the Fermi-like attraction $w(r)$ for the same combination of A- and B-values as in Fig. 1a.

The reasons to focus on star polymers with functionality $f = 32$ are many fold. First, we wish to analyze here a typical intermediate-functionality case right between the polymer-like ($f \gtrsim 1$) and the colloid-like ($f \gg 1$)-limits. Secondly, $f = 32$ is a truly interesting case: below this value the purely repulsive star solution as well as the model attraction considered till now (i.e., without repulsive bump and with a long range attraction [38]) is always fluid changing the relevant thermodynamic parameters. Thus, for this *borderline* case the peculiar features with respect to the previously analyzed cases are more evident. And, finally, $f = 32$-arms star polymers are quite common experimentally, since they can be synthesized by growing

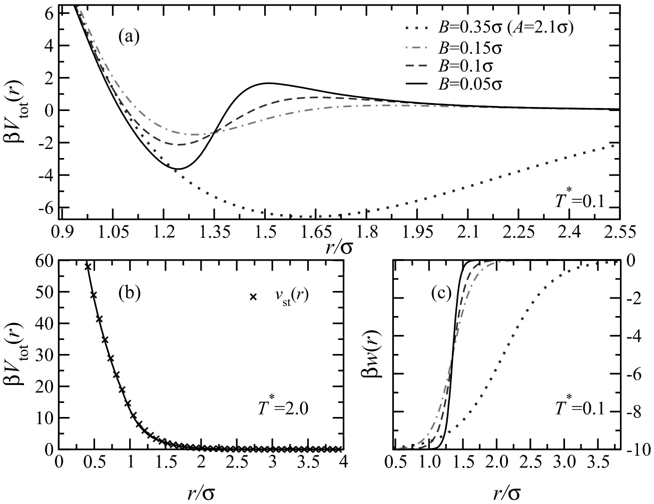

Fig. 1 **a** The total interaction potential $\beta V_{\mathrm{tot}}(r)$, versus the interparticle separation $r^* = r/\sigma$ for temperature $T^* = 0.1$, $f = 32$ and several value of the parameter B in Eq. 2. The *dotted line* shows a case considered in [38]. **b** Comparison between $T^* = 2.0$ for $B = 0.05\sigma$ and the purely repulsive interaction. **c** The attractive contribution $w(r)$ for the B-values of panel (**a**)

living polymers on the reaction sites located at the ends of dendritic cores.

Modified Hypernetted Chain (MHNC) Integral Equation

Our analysis is based on the examination of the pair correlation functions of the system, in particular the radial distribution function $g(r)$ and the structure factor $S(q)$ [42]. The latter depends on the momentum transfer $\hbar q$ in a scattering experiment, q being the magnitude of the scattering wavevector. The relation between $S(q)$ and $g(r)$ reads as:

$$S(q) = 1 + \rho \int \mathrm{d}^3 r e^{-\mathrm{i}\boldsymbol{q}\cdot\boldsymbol{r}} [g(r) - 1] \,, \tag{4}$$

where ρ is the density of the system. We define the dimensionless density ρ^* as

$$\rho^* = \rho\sigma^3 \,. \tag{5}$$

The pair correlation functions can be calculated for any given interaction potential and thermodynamic parameters (ρ^*, T^*) by employing approximate closures to the Ornstein–Zernike relation [42], resulting thereby in a variety of integral equation theories for uniform fluids. In this work, we employ the modified hypernetted chain (MHNC) integral equation [39], which is very accurate, both for purely repulsive potential as well as in presence of attractive contribution. In the particular case of star polymers, the high accuracy of this theory to describe fluid and metastable states in good solvent [12] as well as in presence of attractive contributions [13, 38] has been verified for a large range of f, density values and temperatures.

From a cluster expansion origin, one obtains the exact relation connecting the radial distribution function $g(r)$ to any given interparticle potential $\phi(r)$:

$$g(r) = \exp[-\beta\phi(r) + g(r) - 1 - c(r) + E(r)] \,, \tag{6}$$

where $E(r)$ is the bridge function and $c(r)$ the direct correlation function [42], related to $g(r)$ with the aforementioned Ornstein-Zernike relation:

$$g(r) - 1 = c(r) + \rho \int \mathrm{d}^3 r' [g(|\boldsymbol{r}' - \boldsymbol{r}|) - 1] c(r') \,. \tag{7}$$

In the MHNC scheme, the exact bridge function $E(r)$ is replaced by that of a fluid of hard spheres, $E_{\mathrm{HS}}(r)$, of a suitably chosen diameter d. To optimize this choice, which depends on the parameter d, the free energy is minimized [39] via the relation:

$$\int \mathrm{d}\boldsymbol{r} \, [g(r) - g_{\mathrm{HS}}(r;\, \eta_{\mathrm{HS}})] \, \frac{\partial E_{\mathrm{HS}}(r;\, \eta_{\mathrm{HS}})}{\partial \eta_{\mathrm{HS}}} = 0 \,, \tag{8}$$

where $\eta_{\mathrm{HS}} = \pi\rho d^3/6$ is the packing fraction of the effective hard sphere system and $g_{\mathrm{HS}}(r,\, \eta_{\mathrm{HS}})$ the radial distribution function of the same. Verlet and Weis [43] provided an accurate parametrization of $g_{\mathrm{HS}}(r,\, \eta_{\mathrm{HS}})$ based on the Percus–Yevick solution, with a correction which incorporates thermodynamical consistency through the Carnahan-Starling state equation [42]. This, together with Eqs. 6–8 gives a closed set of equations which are solved by a standard iterative method. The dependence of η_{HS} on the density as determined by Eq. 8 reflects the peculiar features of the interparticle interaction [38].

Results and Discussion

We analyzed three different solutions of star polymers in presence of attractive interactions, modeled by Eq. 2, all with functionality $f = 32$ and at fixed $A = 1.35\sigma$. As mentioned before, three different values of the parameter B were examined, namely $B = 0.15\sigma$ (system code SP-B.15), $B = 0.1\sigma$ (system code SP-B.1), and $B = 0.05\sigma$ (system code SP-B.05). At fixed temperature, a decrease in B has the effect of increasing the depth of the attractive well, shrinking its range and at the same time increasing the height of the accompanying repulsive bump. Our goal is to gain insight into the influence that these changes of the interparticle potential have on the phase diagram of the system and to quantify the effects of the competition between a relatively short-range attraction and a longer-range repulsion in a system with a peculiar ultra-soft repulsive core. Though systems with a combination of attraction and a repulsive hump have been studied in the past [44–50] the short-range steric repulsion has always been steep; the presence of the ultrasoft repulsion in our system, which is not able to support stable crystals in and of its own [10, 38] provides an additional novel aspect of the system at hand.

Unlike purely repulsive star polymers, in the present system the temperature is a relevant thermodynamic variable. We begin with a relatively high temperature, $T^* = 2.0$. In Fig. 2 we show the structure factor of the SP-

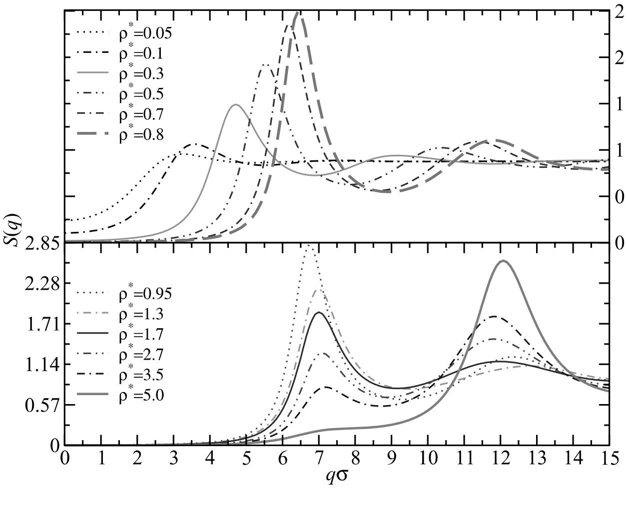

Fig. 2 Structure factor of the SP-B.15-model for at $T^* = 2.0$

B.0.15 system at this temperature and for a wide range of densities. We found essentially the same structure factors obtained for purely repulsive one component stars [6]. Indeed, at sufficiently high temperatures, the Fermi contribution to our model-interaction becomes unimportant because it is washed out by the thermal energy. Thus, the anomalous dependence of $S(q)$ on density, known from usual star polymers, is recovered. Starting at low densities, the first peak of $S(q)$ grows in height and moves to higher q-values, which scale as $\sim \rho^{1/3}$, up to the overlap density $\rho^* \simeq 0.8$. For higher values of the density, the main peak height starts decreasing, the second peak height starts increasing (eventually replacing the first peak as the highest) and the peak positions become density-independent. All these features arise from the interplay between the long-distance Yukawa decay of the interaction of Eq. 1 and its short-distance ultrasoft, logarithmic dependence. Below the overlap density, the former is felt, giving rise to normal structure factors, whereas above the overlap density the logarithmic repulsion causes the peak anomalies. These features have been analyzed in detail in [6]. For the whole density range, the peaks in the structure factor never exceed the value of 2.85: in agreement with the Hansen–Verlet criterion [51], this means that the system is always a fluid, an assertion explicitly confirmed by extensive Monte-Carlo simulations [10] and in full agreement with experimental results [21]. The indistinguishability of the structure factors at $T^* \gtrsim 2.0$ from those of the purely repulsive system has been found for all three systems studied, SP-B.0.15, SP-B.0.1, and SP-B.0.05.

Let us now look at the effects of decreasing the temperature. We examined temperatures in the range $0.1 \le T^* \le 2.0$, whereas the density was varied in a wide range, typically $0 \le \rho^* \le 10.0$. In Fig. 3 we present the structure factor for the system SP-B.15 at $T^* = 0.1$, which shows marked differences as compared with the same quantity at $T^* = 2.0$, Fig. 2. For small densities $\rho^* = 0.04$, (Fig. 3, upper panel), we can already observe a value of $S(q = 0) > 1$, which is a signature of a neighboring spinodal, on which $S(q = 0)$ diverges. At the same time, more unusual features of $S(q)$ show up. Unlike its high-temperature counterpart, $S(q)$ has two distinct peaks, a pre-peak at $q\sigma \simeq 1$, whose position moves to higher q-values with increasing density and a main peak at $q\sigma \simeq 6$, whose position is strictly *density-independent*, up to a density $\rho^* \lesssim 0.6$. These characteristics carry the signature of *cluster formation* within the uniform fluid [47]. The interparticle potential features a minimum at $r_{\min} \simeq 1.3\sigma$, which leads to particle aggregation with an interparticle separation $r_{\min}$. The accompanying repulsive barrier limits the growth of the aggregates, leading thereby to the formation of finite clusters of a typical size R_{cl} and intercluster separation L. As the length scale $r_{\min}$ is set by the interaction and not by the concentration, the particle–particle distance within a cluster manifests itself, in momentum space, in the form of a density-independent peak at $q \simeq 2\pi/r_{\min}$. The low-q pre-peak, on the other hand, is the cluster-peak that is related to the intercluster separation as $q \simeq 2\pi/L$. Indeed, as the density grows, the clusters approach each other, resulting into the observed displacement of the cluster peak to higher q-values. At a density $\rho^* \simeq 0.6$ the cluster peak disappears altogether. We interpret this as a merging of different clusters, which leads to the loss of cluster identity and thus leaves individual particles as the only distinguishable scattering units in the system. This assertion is corroborated by the fact that for $\rho^* \gtrsim 0.6$ the particle–particle peak, which was previously density-independent in its location, now does shift to higher q-values with increasing ρ.

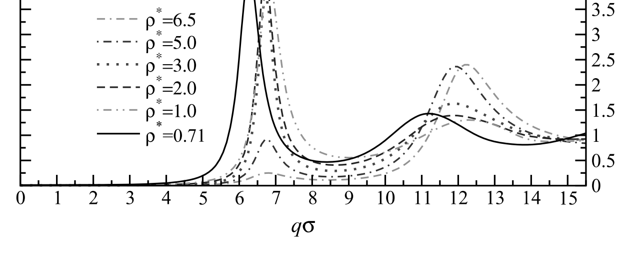

Fig. 3 Structure factor for the system SP-B.15 at $T^* = 0.1$. *Top*: notice the appearance of a low-density small peak. *Bottom*: for high density the main peak of the structure factor is considerably higher than 2.85 at $\rho^* = 1.0$

In Fig. 3, lower panel, we see how $S(q)$ then further develops upon density increase. Whereas the main peak position shifts to higher q's up to a density $\rho^* \simeq 1.0$, the usual star-polymer scenario [6] takes over thereafter: the position of the main peak does not evolve with ρ^*, its height decreases and that of the second peak increases, as in the purely repulsive case. These effects are due to the ultrasoft logarithmic divergence of the potential. Yet, a very important *quantitative* difference with respect to the case $T^* = 2.0$ shows up: the *height* of the main $S(q)$-peak now markedly exceeds the Hansen–Verlet value 2.85, clearly pointing to the possibility that the added attractions now *stabilize* a crystal that is thermodynamically unstable in their absence.

The same behavior has been found for the systems SP-B.1 and SP-B.05; selected, representative results are shown in Figs. 4 and 5, respectively. Referring to Fig. 4 and in comparison with Fig. 3, we see that the effect of reducing the value of B is to enhance the growth of the height of the principal peak of $S(q)$ at a given temperature.

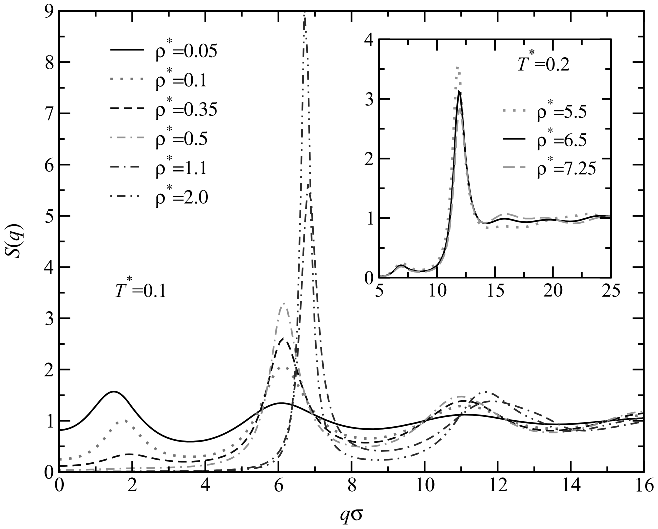

Fig. 4 Structure factor of the SP-.1-system at $T^* = 0.1$. In the *inset*, we show the trend of $S(q)$ for high densities and $T^* = 0.2$ at increasing densities

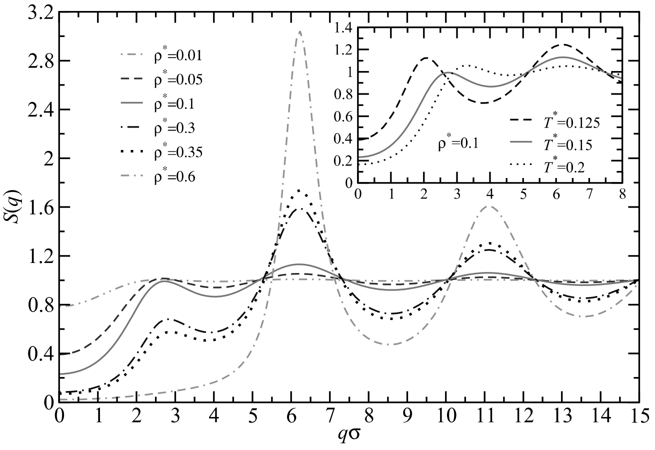

Fig. 5 Structure factor for for the system SP-.05 at $T^* = 0.15$ for several densities. *Inset*: structure factor for fixed density $\rho^* = 0.1$ changing the temperature

Otherwise, clustering is still clearly visible at, roughly, the same range of densities as in the case $B = 0.15$. Once again, we discover that the position of the highest peak does not change with concentration and it is accompanied by a cluster pre-peak, whose position moves to slightly higher q-values. In the inset of Fig. 4, we see the evolution of $S(q)$ for much higher densities: it can be seen that the particle peak at $q\sigma \simeq 7$, which used to be quite high at lower densities, has all but disappeared and the peak at $q\sigma \simeq 12$ has taken its role as the main one [6]. Yet, even this second peak diminishes now in height upon increasing ρ. In conjunction with the Hansen–Verlet freezing rule, this points to a reentrant melting scenario, similar to the one occurring in usual star polymers [10] or in other systems interacting by means of ultrasoft potentials [52, 53].

In Fig. 5, the evolution of the structure factor for the system SP-B.05 is shown. Note that here we had to move to a higher temperature than in the preceding cases, $T^* = 0.15$, because large parts of the $T^* = 0.10$-isotherm are, for this system, subcritical (see below). In the main plot of Fig. 5, the evolution of $S(q)$ with density is shown, featuring once again the typical characteristics of cluster formation. More insight into the nature of the clusters and the incipient macroscopic phase separation can be gained by looking at $S(q)$ at *fixed* density and *lower* temperatures, shown the inset of Fig. 5. Here, it can be seen that the position of the particle–particle peak of $S(q)$ hardly moves upon temperature changes. However, the cluster peak moves to lower q-values, signaling a growth of the cluster size R_{cl} and, concomitantly, the cluster separation L. At fixed density, this corresponds to a growth of the population of the individual clusters, i.e., the number of particles participating in a particular cluster. Consequently, the intercluster separation grows, and the compressibility of the system, which is proportional to $S(q = 0)$ [42], increases as well. Further lowering of the temperature leads then to a formation of a cluster of macroscopic dimensions. The local minimum of $S(q)$ at $q = 0$ turns into a maximum at the Lifshitz line [54, 55] and at the spinodal line this maximum diverges. In other words, a macroscopic phase separation into two fluids at different concentration takes place.

Before proceeding into a quantitative description of all phenomena associated with such systems (clustering, condensation, and crystallization), it is informative to take a look at the emergence of clustered phases in real, as opposed to reciprocal, space. In Fig. 6 we show the radial distribution function $g(r)$ for all three systems considered here at fixed density $\rho^* = 0.05$ and temperature

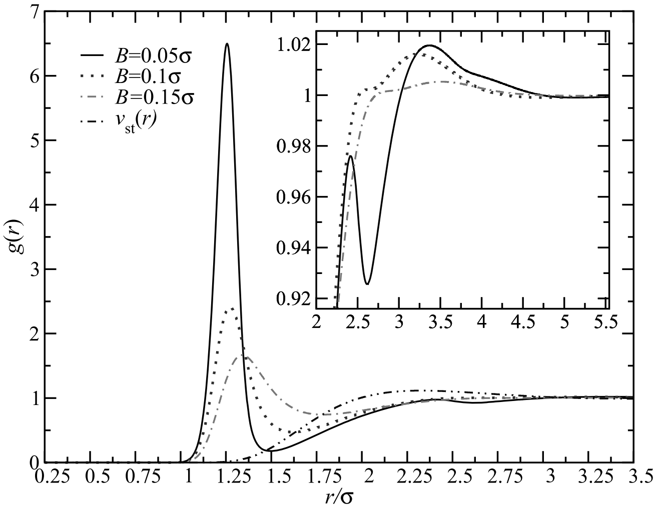

Fig. 6 The radial distribution function $g(r)$ of the systems considered in this work at density $\rho^* = 0.04$ and temperature $T^* = 0.125$. *Inset*: detail of the second peak region

$T^* = 0.125$, together with the same quantity for the purely repulsive star polymer solution interacting by means of the potential of Eq. 1. Whereas the radial distribution function of the latter is rather flat and has a very weak maximum at $a \simeq \rho^{1/3}$, the corresponding quantities for the models SP-B.15, SP-B.1, and SP-B.05 are very different. A pronounced maximum at $r = r_{\min}$ can be seen, clearly signaling the tendency of the particles to stick together at this distance. Note, however, at the same time, the depression at distances $1.5 \lesssim r/\sigma \lesssim 2.0$, arising from the repulsive barrier, which limits the growth of the clusters. Moreover, it can be clearly seen that the stiffness of the clusters is most pronounced for the SP-B.05-system, which features the deepest and shortest-range attraction, together with the strongest repulsive bump. In the inset of Fig. 6, we show the region around the second peak of $g(r)$. For SP-B.15 a broad second peak appears around $r/\sigma = 3.5$, this distance roughly corresponding to the cluster–cluster separation. Decreasing B we can observe a more structured second peak. In particular, for SP-B.05 there is a small additional first peak around $r/\sigma = 2.5$ which can be interpreted as a weak second-shell of neighbors within a given cluster. The height and the number of the peak around $r/\sigma = 3.5$ increases with the density until, as sufficiently high ρ^*, the clusters come close to each other, merge, and thereafter the radial distribution function recovers a shape that describes a usual, unclustered fluid.

The competition between attraction, which favors cluster formation for low T^*, and long range repulsion that favors small aggregates [47,48], is evident under consideration of all three cases investigated. Whereas the occurrence of macrophase separation is sharply defined through the *divergence* of $S(q)$ at $q = 0$, marking the spinodal line of the system, cluster formation in a thermodynamically stable fluid is not associated with any accompanying phase transition. In this respect, the emergence of clusters on a supramolecular scale is akin to the formation of mesoscopic spatial structures in other soft matter systems, such as the random, "sponge" phase in ternary mixtures of oil, water and amphiphilic surfactants [56]. Indeed, also in this case, there is no clear phase boundary between the sponge- and random-mixture states, and one has to resort to somewhat arbitrary structural criteria in order to delineate the regions of stability of the two [54–56]. In our case, we decided to use the existence of the cluster pre-peak in $S(q)$ at low but finite q-values in order to characterize a clustered fluid. In particular, we introduce the criterion than whenever the pre-peak local maximum exceeds the neighboring local minima by more than 0.05, the fluid consists of clustered superstructures.

In Fig. 7 we show the cluster regions as well as the spinodal curves for the systems we investigated. For fixed B, an increase in temperature reduces the range of stability of the cluster region, due to the reduction of the attractive forces in our system. Decreasing B leads to a broadening of the region of the clustered fluid. This behavior is connected to the intensity of the attraction which for such low density has to be strong enough to determine cluster aggregation. In the same figure, the spinodal curves are shown as well: the critical temperature increases with decreasing B and the critical density moves to slightly lower densities. This trend is in agreement with the evolution of the second virial coefficient $B_2(T)$ of the interaction potential, which becomes more and more negative, at fixed temperature, passing from SP-B.15 to SP-B.1 and finally to SP-B.05. More precisely, at $T^* = 0.1$, we have $B_2 = -0.13\sigma^3$ for SP-B.15, $B_2 = -0.20\sigma^3$ for SP-B.1, and $B_2 = -2.66\sigma^3$ for SP-B.05. To provide a comparison, we calculated this coefficient also for the case investigated in [38], which is free of repulsive barriers, finding a value $B_2 = -4.59\sigma^3$ at the same temperature. This is consistent with the result that the critical temperature there has a high value, $T^*_{\text{crit}} = 0.623$ (MHNC calculation).

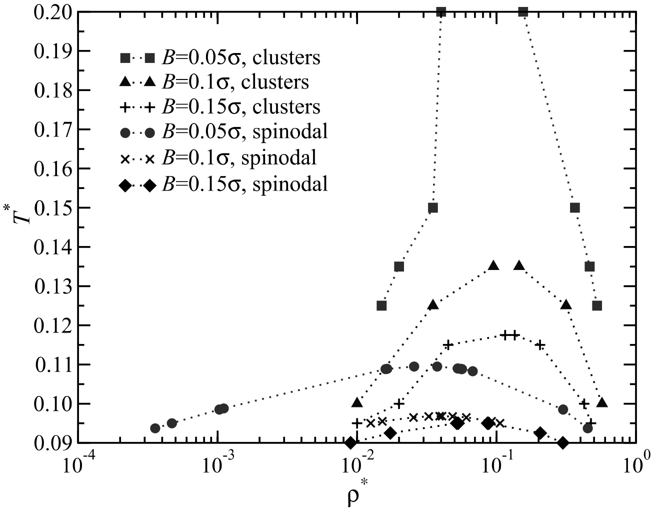

Fig. 7 Cluster region and fluid–fluid coexistence region as delimited by the spinodal line

The occurrence of finite-size clusters in the system is a direct consequence of the existence of a repulsive potential barrier that accompanies the short-range attraction. In this respect, our results are in line with a wealth of theoretical [45–49] and experimental [29,50] results in three-dimensional systems as well as with a recent theoretical analysis of a two-dimensional model that shows the formation of stable circular and stripe patterns [44]. The phenomena observed here can be understood in terms of the competition between the (generally complex) poles of the structure factor $S(q)$ [46,57,58]. Let $q_{\text{R}} + \mathrm{i}q_{\text{I}}$ be such a pole, with q_{R} and q_{I} denoting its real and imaginary parts, respectively. If $q_{\text{i}} = 0$ and $q_{\text{R}} \neq 0$, then the fluid is thermodynamically unstable with respect to *microphase separation*, i.e., ordered microstructures of wavelength $\lambda = 2\pi/q_{\text{R}}$, such as lamellae or periodic crystals, spontaneously form. On the other hand, the case $q_{\text{i}} = 0$ *and* $q_{\text{R}} = 0$ leads to a spinodal curve and *macrophase separa-*

tion. In the case of the systems we examined, the former pole does not occur, but the imaginary part q_{i} is sufficiently small, so that the cluster pre-peak shows up. At appropriate thermodynamic conditions, the second type of pole occurs and the system phase-separates. The system at hand shows a tendency to form microregions of clustered particles, however true microphase separation is inhibited. The structure factor pre-peak remains finite and the cluster phase possesses full translational symmetry (uniform fluid). Under competition between the attractive plus repulsive parts of the potential, we expect the cluster peak to become the dominant feature of $S(q)$, leading to true microphase separation which at least in $2D$ gives rise to a thermodynamic signature in terms of a peak in the specific heat [44].

Depending on the potential parameters, only one, both, or none of the two scenarios regarding the existence of real poles of $S(q)$ will materialize. In some cases, the existence of the repulsive barrier may lead to a complete disappearance of the spinodal line, which would be otherwise present under the influence of the attraction alone. Here, we rather have a situation in which the repulsive barrier suppresses the critical point without altogether eliminating it, in agreement with the recently studied case of mixtures between multiarm star polymers and depleting, homopolymer chains [29].

Finally, we briefly discuss the occurrence of stable crystals in the system, which are unstable both in the complete absence of attractions [10] and in the presence of long-range, smooth attractions [38]. The very high values of the structure factor peak, see Figs. 3–5, are a clear structural signature of the stability of crystal phases. Moreover, there exist regions in the density-temperature plane, deep in the solid, where the MHNC fails to converge or yields physically unacceptable results, e.g., negative parts of $S(q)$. Thus, the interactions at hand give rise to freezing transitions. Tracing out the precise phase boundaries would require the calculation of the free energies of the competing, fluid and solid phases. This is a cumbersome task, which is additionally complicated by the fact that the precise crystal structure is unknown. Therefore, we resort here to a structural criterion to delineate roughly the freezing lines, namely we trace out the locus of points for which the maximum of $S(q)$ attains the Hansen–Verlet value 2.85. This approach has been shown to reproduce phase boundaries quite well, even for ultrasoft potentials, such as the Gaussian interaction [52]

In Fig. 8 we describe the full "phase diagram", drawn under the procedure described above. The system shows a spinodal line, a cluster line and a line of crystallization. The solid region increases with decreasing B. Irrespective of quantitative details, we can distinguish within the solid region two structures: one region centered around $\rho^* = 0.85$ plus a tail for higher densities. The first region is connected to the evolution of the main peak of $S(q)$, which corresponds to the first peak for $\rho^* \gtrsim 0.6$.

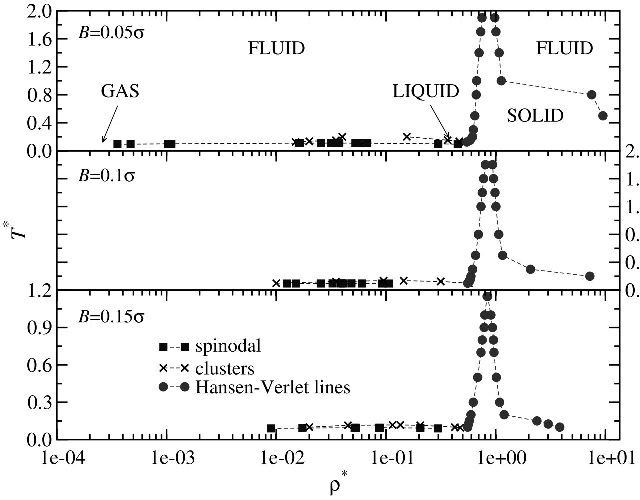

Fig. 8 Full "phase diagrams" for SP-B.15, SP-B.1, and SP-B.05

The second density region is connected to the evolution of the second peak in the structure factor. We observe that for SP-B.15 and $\rho^* \gtrsim 5.0$, the first/main peak disappears and the second peak becomes the main one, but for all the temperatures investigated this peak did not exceed the value 2.85. On the contrary, for SP-B.1 and SP-B.05 there exist some regions where the second peak in the structure factor becomes higher then 2.85 and the first peak becomes lower than this value, at temperatures around $T^* \lesssim 0.4$ and $T^* \lesssim 0.8$, respectively. In this high density tail, we can have small intervals of reentrant melting.

The stabilization of the crystal phase is an effect of the attractive part of the potential and of its range. Indeed solid phases are not present neither for the purely repulsive interaction or for the case studied e.g., in [38] where the attractive interaction is really longer ranged. Changing density and temperature, for the three different model attractions, we could have also a change in the symmetry of the lattice in relation to the position of the repulsive bump with respect to characteristic nearest neighbor and second neighbor distances. The observed trend of broadening of the region of stability of the solid upon shrinking of the attractive well is fully consistent with previous results on the double Yukawa system [59]. Contrary to the case of [59], however, our freezing transition is *forced* to disappear at sufficiently high temperatures, since then we recover the purely repulsive case, which does not support stable solids. Consequently, the freezing line is of *reentrant* type, similarly to the case of the Gaussian model [52] or indeed a whole class of ultrasoft potentials [53].

Finally, we remark that for high densities and low temperatures, $T^* \ll 0.1$ we found evidence of the increasing of $S(q = 0)$, signaling the appearance of a fluid–fluid phase separation, in agreement with the occurrence of a second critical point ($\rho^* = 1.96$, $T^* = 0.247$) in [38]. However, for such a low temperature and high density, this region is metastable with respect to the freezing.

Conclusions

We have examined the structural and thermodynamic behavior of a system of intermediate-functionality star polymers with additional attractions. The resulting total potential features the original, logarithmic repulsion for close interparticle approaches, dressed with a short-range attraction, which is followed by a repulsive hump at large separations. This is a flexible and tunable system, since the characteristics of the interaction can be tuned by, e.g., suitable choices of smaller polymeric entities to be added to the star polymer solution. We found a wealth of new phenomena, such as a fluid–fluid phase separation, accompanied by a formation of clusters in the stable fluid at supercritical temperatures. The internal structure of the clusters can not be resolved with the tools at hand and it will be the subject of future work. Moreover, the attraction brings about a stabilization of crystal phases, which cannot be supported by the ultrasoft repulsions alone, for the functionality value $f = 32$ studied here. This freezing transition features a maximum crystallization temperature and is reentrant along the density axis.

A number of questions open up, which are related to both the equilibrium and the dynamical behavior of the system at hand. The crystal structures should be identified and the question should be answered as to whether we have polymorphic transitions between lattices of different symmetry. To this end, the powerful tool of genetic algorithms [60] can be employed, to allow for a bias-free search of the crystal structures. Associated with freezing is the possibility of formation of repulsive glasses, in analogy with the case of usual star polymers, for which indeed the region of ideal glass formation is strongly correlated with the domain of stability of the solid [12]. In this respect, the depletants here could have an effect *opposite* to that seen for multiarm star polymers [27]: whereas for $f \gg 1$ added chains *melt* the glass formed by the stars, in our case the exciting possibility opens up that they might *induce* a glass transition in a system that shows no vitrification, at arbitrary densities [12]. At the same time, the property of this system to form clusters makes it possible that a *gelation* transition could find place at *low* densities, in analogy with the recently-studied case of Sciortino et al. [47]. Application of computer simulations and Mode-Coupling Theory should help clarify the questions of the types of arrested states that can occur in our system. The investigation of these questions is the subject of ongoing work.

Acknowledgement This work was funded in part by a grant of the Marie Curie Programme of the European Union, contract number MRTN-CT2003-504712, and in part by the Deutsche Forschungsgemeinschaft (DFG) within the SFB-TR6, Project Section C3.

References

1. Likos CN (2001) Phys Rep 348:267
2. Grest GS, Fetters LJ, Huang JS, Richter D (1996) Adv Chem Phys XCIV:67
3. Witten TA, Pincus PA (1986) Macromolecules 19:2509
4. Likos CN, Löwen H, Watzlawek M, Abbas B, Jucknischke O, Allgaier J, Richter D (1998) Phys Rev Lett 80:4450
5. Zhou L-L, Roovers J (1993) Macromolecules 26:963
6. Watzlawek M, Löwen H, Likos CN (1998) Phys J: Condens Matter 10:8189
7. Likos CN, Löwen H, Poppe A, Willner L, Roovers J, Cubitt B, Richter D (1998) Phys Rev E 58:6299
8. Jusufi A, Watzlawek M, Löwen H (1999) Macromolecules 32:4470
9. Witten TA, Pincus PA, Cates ME (1986) Europhys Lett 2:137
10. Watzlawek M, Likos CN, Löwen H (1999) Phys Rev Lett 82:5289
11. Dzubiella J, Likos CN, Löwen H (2002) Chem J Phys 116:9518
12. Foffi G, Sciortino F, Tartaglia P, Zaccarelli E, Lo Verso F, Reatto L, Dawson KA, Likos CN (2003) Phys Rev Lett 90:238301
13. Lo Verso F, Reatto L, Foffi G, Tartaglia P, Dawson KA (2004) Phys Rev E 70:061409
14. Benzouine F, Benhamou M, Himmi M (2004) Eur Phys J E 13:345
15. Benhamou M, Himmi M, Benzouine F, Bettachy A, Derouiche A (2004) Eur Phys J E 13:353
16. Dozier WD, Huang JS, Fetters LJ (1991) Macromolecules 24:2810
17. Richter D, Jucknischke O, Willner L, Fetters LJ, Lin M, Huang JS, Allgaier J, Roovers J, Toporowski C, Zhou L-L (1993) Physique J IV 3:3
18. Willner L, Jucknischke O, Richter D, Roovers J, Zhou L-L, Toporowski PM, Fetters LJ, Huang JS, Lin M, Hadjichristidis N (1994) Macromolecules 27:3821
19. Kapnistos M, Vlassopoulos D, Fytas G, Mortensen K, Fleischer G, Roovers J (2000) Phys Rev Lett 85:4072
20. Loppinet B, Stiakakis E, Vlassopoulos D, Fytas G, Roovers J (2001) Macromolecules 34:8216
21. Vlassopoulos D, Fytas G, Pakula T, Roovers J (2001) Phys J: Condens Matter 13:R855
22. Bang J, Lodge TP, Wang X, Brinker KL, Burghardt WR (2002) Phys Rev Lett 89:215505
23. Lodge TP, Bang J, Park MJ, Char K (2004) Phys Rev Lett 92:145501
24. Bang J, Lodge TP (2004) Phys Rev Lett 93:245701
25. Stellbrink J, Rother G, Laurati M, Lund R, Willner L, Richter D (2004) Phys J: Condens Matter 16:S3821
26. Laurati M, Stellbrink J, Lund R, Willner L, Richter D, Zaccarelli E (2005) Phys Rev Lett 94:195504
27. Stiakakis E, Vlassopoulos D, Likos CN, Roovers J, Meier G (2002) Phys Rev Lett 89:208302

28. Stiakakis E, Petekidis G, Vlassopoulos D, Likos CN, Iatrou H, Hadjichristidis N, Roovers J (2005) Europhys Lett 72:664
29. Likos CN, Mayer C, Stiakakis E, Petekidis G (2005) Phys J: Condens Matter 17:S3363
30. Russel WB, Saville DA, Schowalter WR (1989) Colloidal Dispersions. Cambridge University Press, Cambridge
31. Pusey PN (1991) In: Hansen J-P, Levesque D, Zinn-Justin J (eds) Les Houches, Session LI, Liquids, Freezing and Glass Transition. North-Holland, Amsterdam
32. Mayer C, Likos CN, Löwen H (2004) Phys Rev E 70:041402
33. Pitsikalis M, Mays JW, Hadjichristidis N (1996) Macromolecules 29:179
34. Vlassopulos D, Pakula T, Fytas G, Pitsikalis M, Hadjichristidis N (1999) Chem J Phys 111:1760
35. Clément F, Johner A, Joanny J-F, Semenov AN (2000) Macromolecules 33:6148
36. Semenov AN, Joanny J-F, Khokhlov AR (1995) Macromolecules 28:1066
37. Bhatia SR, Russel WB (2000) Macromolecules 33:5713
38. Lo Verso F, Tau M, Reatto L (2003) Phys J: Condens Matter 15:1505
39. Lado F, Foiles SM, Ashcroft NW (1983) Phys Rev A 28:2374
40. Parola A, Reatto L (1984) Phys Rev Lett 53:2417; Phys Rev A 31:3309 (1985)
41. For an ample review of the HRT, see: Parola A, Reatto L (1995) Adv Phys 44:211
42. Hansen JP, McDonald IR (1986) Theory of Simple Liquids, 2nd edition. Academic, London
43. Verlet L, Weis J-J (1972) Phys Rev A 5:939
44. Imperio A, Reatto L (2004) Phys J: Condens Matter 16:S3769
45. Peyre V, Spalla O, Belloni L, Nabavi M (1997) Colloid J Interface Sci 187:184
46. Sear RP, Gelbart WM (1999) Chem J Phys 110:4582
47. Sciortino F, Mossa S, Zaccarelli E, Tartaglia P (2004) Phys Rev Lett 93:055701
48. Mossa S, Sciortino F, Tartaglia P, Zaccarelli E (2004) Langmuir 20:10756
49. Liu Y, Chen W-R, Chen S-H (2005) Chem Phys J 122:044507
50. Stradner A, Sedgwick H, Cardinaux F, Poon WCK, Egelhaaf SU, Schurtenberger P (2004) Nature 432:492
51. Hansen JP, Verlet L (1969) Phys Rev 184:151
52. Lang A, Likos CN, Watzlawek M, Löwen H (2000) Phys J: Condens Matter 12:087
53. Likos CN, Lang A, Watzlawek M, Löwen H (2001) Phys Rev E 63:31206
54. Hornreich RM, Liebmann R, Schuster HG, Selke W (1979) Phys Z B 35:91
55. Gompper G, Schick M (1990) Phys Rev B 41:9148
56. Likos CN, Mecke KR, Wagner H (1995) Chem J Phys 102:9350
57. Archer AJ, Likos CN, Evans R (2002) Phys J: Condens Matter 14:12031
58. Archer AJ, Likos CN, Evans R (2004) Phys J: Condens Matter 16:L297
59. Tejero CF, Daanoun A, Lekkerkerker HNW, Baus M (1995) Phys Rev E 51:558
60. Gottwald D, Kahl G, Likos CN (2005) Chem J Phys 122:204503

Progr Colloid Polym Sci (2006) 133: 88–94
DOI 10.1007/2882_052

Patrick Wette
Hans Joachim Schöpe

Consistence of the Mean Field Description of Charged Colloidal Crystal Properties

Patrick Wette · Hans Joachim Schöpe (✉)
Institut für Physik, Universität Mainz,
Staudinger Weg 7, 55128 Mainz, Germany
e-mail: jschoepe@mail.uni-mainz.de

Abstract The Debye-Hückel-Potential in combination with an effective or renormalized charge is a widely and often successfully used concept to describe the interaction in charged colloidal model systems and the resulting suspension properties. In particular the phase behaviour can be described in dependence of the parameters particle number density, salt concentration and effective charge. We performed simultaneous measurements of the phase behaviour, the shear modulus and the low frequency conductivity of deionised aqueous suspensions of highly charged colloidal spheres. From the shear modulus the interaction potential at the nearest neighbour distance in terms of a Debye-Hückel potential can be determined with an effective charge Z^*_G as free parameter. Conductivity measures the number of freely moving small ions Z^*_σ and thus relates to the ion condensation process in the electric double layer under conditions of finite macro-ion concentrations. We present the first experimental access of the pair energy of interaction in charged colloidal suspensions which describes both the elastic properties and the fluid crystalline phase behaviour. This means that a consistent description of the suspension properties is obtained, when Z^*_G is taken from the elasticity measurement.

Keywords Charge spheres · Colloids · Effective charge · Phase behaviour

Introduction

Due to the long ranged nature of the screened Coulomb interaction, colloidal crystals may form in suspensions of highly charged spherical particles at volume fractions as low as $\Phi \approx 10^{-3}$, if the concentration c of screening electrolyte is kept on or below the µM-level. Melting of the colloidal solid is achieved by reducing the electrostatic interaction between the particles either by reducing the particle number density $n_\mathrm{p} = 3\Phi/(4\pi a^3)$ (a is the particle radius) or increasing c. As early as 1988 this melting line was theoretically predicted from computer simulations on monodisperse particles using a Debye Hückel (DH) potential with an effective charge Z^* [1]. Later work resulted in quantitative corrections but the general form of the melting line was retained and further also confirmed by perturbation theoretical calculations [2–4]. On the other hand the phase behaviour of charged colloidal suspensions was also intensively studied experimentally under well defined conditions for n_p and c and Z^* determined in independent experiments [5–7]. Here no consistency with the theoretical predictions was obtained. The correct determination and description of the phase behaviour in charged stabilised colloidal suspensions is a long standing problem that is mostly related to the lack of precise knowledge of the correct interaction potential between highly charged particles and the influence of polydispersity.

Recently there has been an enormous theoretical effort to improve the theoretical foundation of this key quantity in the description of system properties. It comprises both charged and uncharged colloidal systems as well as mixtures of different particles [8]. For charged spheres in particular theoretical approaches on different levels of approximation were investigated [9–11]. In all cases the long distance behaviour of the interaction potential is well described analytically using the solution of the DH-equation with an effective charge Z^*, which is much smaller than the structural charge Z. This concept of charge renormalization is very general and is interpreted as condensation of counter ions. The functional form was also confirmed by experiments on pairs of isolated particles [12]. On the mean field level a solution of the non-linearized Poisson Boltzmann equation in a cell model (PBC-model) with successive fit of a DH potential to the parts far off the surface is general practice [13–15]. Different implementations, however, may yield slightly different Z^* and also a quantitatively different behaviour of Z^* in dependence on n_P [10, 11, 16]. While most authors agree about the functional form of the far field effective potential, the question of the value for Z^* and the screening parameter is not settled yet. Another important point is the influence of many body interaction. Usually a superposition of pair potentials is applied. Newer investigations give hints that many body interaction must be considered describing the interaction in charged colloidal suspensions comprehensively [17]. This situation clearly demands further tests of the potential form under conditions of strong interaction and a comparison of experimental methods to access Z^*.

The experimental determination of the strength and curvature of the interaction potential is still a great challenge. Different methods are used to get a right idea of the potential or of Z^*. All these different methods show quite different results, so that there is clarification needed. Measurements of the fluid structure factor in combination with theoretical description is one possibility [18–20]. Also the determined values for Z^* show a big deviation in dependence of the measurement technique and in dependence of the used theoretical model (MSA, RMSA, Rogers Young). Another entrance offers the electrokinetic properties of charged colloidal suspensions [21, 22]. The ζ-potential can be determined using electrophoretic measurements. But up to now the relationship between the ζ-potential and the effective interaction is not understood and so the physical properties of colloidal suspension can not be described using the ζ-Potential. Measuring the low frequency conductivity σ in colloidal suspensions allows to appoint a transported conductivity charge [23, 24]. This method can be achieved over a wide range of n_P and c. It is found empirically, that this conductivity charge is in quite good conformity to the effective charge assuming the PBC-model [25, 26]. A new application used in the last few years is optical tweezing. Here Crocker and Grier showed measurement of the two particle interaction potential [12, 27]. However this method can not be used to determine the interaction potential in higher concentrated samples, for example in the bulk. Rarely used is the torsional resonance spectroscopy (TRS) to determine the interaction in the bulk [28, 29]. The shear modulus G shows a direct dependence on the crystalline structure and solid state morphology and the strength and shape of the interaction potential. So if the morphology and the crystalline structure are known, the interaction can be determined with high accuracy in the solid state. So it is obvious that only conductivity measurements (CM) and TRS can be used to conceive the interaction potential in higher concentrated suspensions over a wide range of n_P, c, and Z.

We here investigated extensively the fluid-crystalline phase behaviour for different very well characterised charge stabilised colloidal model systems using static light scattering (SLS), TRS, CM and Bragg microscopy (BMC). The interaction potential is determined by CM and TRS, so that the experimental melting line can be compared to the theoretical prediction.

Experiment

We used commercially available charged stabilised Polystyrene (PS), *n*-Butylacrylate-Styrene (PnBAPS) and PTFE spheres for our measurements. The characteristic properties of the used particles like diameter, charge from conductivity, charge from elasticity and phase boundaries are listed in Table 1. For sample preparation we used a continuous conditioning technique, which allows fast and reproducible adjustment of the interaction parameters and the simultaneous measurement of different suspension properties. Our technique has already been described in detail elsewhere [21, 29]. This technique allows in situ control of both particle number density n (in the deionised state) and electrolyte concentration c (for known n_P). Residual uncertainties are on the order of 1–2% at $n_\mathrm{P} = 3\,\mu\mathrm{m}^{-3}$ and $c = 1\,\mu\mathrm{mol\,l}^{-1}$. The particles and the small ions contribute to the suspension conductivity σ which can described via [22]

$$\sigma = n_\mathrm{P} e \left(Z^*_\sigma \left(\mu_\mathrm{P} + \bar{\mu}^+ \right) + M \left(\bar{\mu}^+ + \bar{\mu}^- \right) \right) + \sigma_\mathrm{B} \,, \qquad (1)$$

where e is the elementary charge, Z^*_σ denotes the effective transported charge, σ_B is the background conductivity of unidentified small ions and μ_P is the particle mobility, which is on the order of $(2\text{–}10) \times 10^{-8}\,\mathrm{m^2 V^{-1} s^{-1}}$ as determined by laser Doppler electrophoresis. $M = c\,1000 N_\mathrm{A}/n_\mathrm{P}$ is the number concentration of small ions per particle and $\bar{\mu}^+$ and $\bar{\mu}^-$ are arithmetic mean small ion mobilities. The arithmetic mean small ion mobilities are given by the mobility of the electrolyte ions of the species i assessed with the number concentration M_i:

$$\bar{\mu}^+ = \frac{\sum \mu_i M_i^+}{\sum M_i^+} \,; \quad \bar{\mu}^- = \frac{\sum \mu_i M_i^-}{\sum M_i^-} \,. \qquad (2)$$

For full deionised conditions M_i becomes zero and $\bar{\mu}^+ = \mu_{\mathrm{H}^+}$ where μ_{H^+} is the proton mobility of $36.5 \times$

Table 1 Investigated colloidal model systems

Sample	Batch No.	2a$_{\text{TEM}}$/ nm	n_P Freeze/ μm^{-3}	n_P Melt/ μm^{-3}	Z^*_σ	Z^*_G
PNBAPS68	BASF ZK2168/7387	68	8.0 ± 0.5	8.0 ± 0.5	450 ± 16	331 ± 3
PS85	IDC 767.1	85	3.8 ± 0.5	4.4 ± 0.5	530 ± 32	350 ± 20
PS90	Bangs Lab 3012	90	4.0 ± 0.5	7.0 ± 0.5	504 ± 35	315 ± 8
PS100/1	Bangs Lab 3512	100	3.9 ± 0.5	4.5 ± 0.2	527 ± 30	349 ± 10
PS100/2	Bangs Lab 3067	100	4.2 ± 0.5	5.5 ± 0.2	530 ± 38	327 ± 10
PS120	IDC 10-202-66	120	0.30 ± 0.02	0.44 ± 0.05	685 ± 10	474 ± 10
PS156	IDC 2-179-4	156	0.28 ± 0.05	0.4 ± 0.05	945 ± 70	615 ± 50
PTFE180	Hoechst TF9201	180	2.7 ± 0.2	3.1 ± 0.2	520 ± 50	350 ± 20

$10^{-8}\,\text{m}^2\,\text{V}^{-1}\,\text{s}^{-1}$. Equation 1 can then be written as [22]

$$\sigma = n_\text{P} e Z^*_\sigma \left(\mu_\text{P} + \mu_{\text{H}^+}\right) + \sigma_\text{B}\,. \tag{3}$$

Under these conditions we can determine the effective transported charge Z^*_σ by measuring σ in dependence of the particle number density n_P.

BMC is used to identify the morphology for coexistence and the freezing and melting point of the samples [30, 31]. Here a cell of rectangular cross section ($2\times 10\,\text{mm}^2$) is illuminated with white light under an angle combination ψ and Θ to obtain a Bragg reflection in the direction of the observing microscope objective. With this simple experimental set up systematic measurements of the position of the freezing and melting in colloidal systems with high accuracy can easily done.

For SLS and TRS measurements a multi-purpose light scattering experiment is used which was recently described in detail elsewhere [29]. Quasi simultaneous static and dynamic light scattering (SLS and DLS) which probe the structure and morphology of colloidal solids, respectively their dynamics, are combined with torsional resonance spectroscopy (TRS) to determine the shear modulus [29].

To determine the structure and the morphology of the colloidal solids SLS is used. Here the scattered light intensity $I(q)$ is detected for different scattering vectors of magnitude

$$q = (4\pi\nu_\text{S}/\lambda)\sin(\Theta/2)\,, \tag{4}$$

where ν_S is the refractive index of the suspending medium, λ the vacuum wavelength of the used laser light and Θ the scattering angle. The scattered intensity can be written as

$$I(q) = I_0 \frac{1}{\sin\Theta} P(q) S(q) + B(q)\,. \tag{5}$$

The first term I_0 contains several experimental boundary conditions. For more details see Reference [29]. The observed scattering volume is inversely proportional to the sine of the observation angle. $P(q)$ is the particle form factor and $S(q)$ the static structure factor. Further there possibly is an additive background $B(q)$ stemming e.g., from dust in the match bath, as well as a static background stemming from ill alignment or unavoidable parasitic reflections. For powder averaged experiments on polycrystalline samples sharp diffraction peaks are observed at the scattering vector

$$q_{h,k,l} = \frac{2\pi}{g}\sqrt{h^2+k^2+l^2}\,, \tag{6}$$

where g is the lattice constant of the crystal and h, k, l are the Miller indices of the considered diffraction plane. For an ideal crystal $S(q)$ takes the form of a delta function. In the case of finite crystal size considerable broadening may be observed. In the fluid state, the shear melt or in vitreous samples only the first maximum is pronounced and for large q $S(q)$ goes to 1.

For TRS the sample cell is put into weak oscillation about its vertical axis, which excites the solid in the cell to resonant vibrations. Then the shear modulus can be determined by identifying the resonance frequencies of the sample [29]

$$\omega^2_{jm} = \frac{G\left(\mu_j^2 + (m+1)^2\pi^2\alpha^2\right)}{\rho R^2} \tag{7}$$

where R is the inner radius of the cylindrical vial, $\alpha = 0.5$ the ratio between R and the filling height H, ρ is the mass density of the suspension, and μ_j are the zeros of the 1st order Besselfunction J_1. Then G can be derived as [32]:

$$G_\text{bcc} = f_\text{A}\frac{3\sqrt{3}}{4d^3}\left(\frac{4}{9}\frac{\partial^2 V(r)}{\partial r^2}\bigg|_{r=d} d^2 + \frac{8}{9}\frac{\partial V(r)}{\partial r}\bigg|_{r=d} d\right)\,, \tag{8a}$$

$$G_\text{fcc} = f_\text{A}\frac{1}{\sqrt{2}d^3}\left(\frac{1}{2}\frac{\partial^2 V(r)}{\partial r^2}\bigg|_{r=d} d^2 + \frac{3}{2}\frac{\partial V(r)}{\partial r}\bigg|_{r=d} d\right)\,. \tag{8b}$$

$f_\text{A} = 0.5$ is a numerical factor which accounts for the sample morphology [33]. $V(r=d)$ is the interaction pair energy at the nearest neighbour distance d. In highly charged colloidal monodisperse systems it can be written as:

$$V(r) = \frac{(Z^* \mathrm{e})^2}{4\pi\varepsilon_0\varepsilon_\mathrm{r}} \left(\frac{\exp(\kappa a)}{1+\kappa a}\right)^2 \frac{\exp(-\kappa r)}{r} \tag{9a}$$

$$\kappa^2 = \frac{\mathrm{e}^2}{\varepsilon_0\varepsilon_r k_\mathrm{B} T} \left(n_\mathrm{p} Z^* + 2000 N_\mathrm{A} c\right) \tag{9b}$$

with the screening parameter κ. $\varepsilon_0\varepsilon_\mathrm{r}$ is the dielectric permittivity of the suspension and $k_\mathrm{B}T$ is the thermal energy. Using Eq. 9 in Eq 8 we obtain the following expression for the shear modulus:

$$G_\mathrm{bcc} = f_\mathrm{A} \frac{4}{9} n_\mathrm{p} V(d) \kappa^2 d^2 \tag{10a}$$

$$G_\mathrm{fcc} = f_\mathrm{A} \frac{1}{2} n_\mathrm{P} V(d) \left(\kappa^2 d^2 - \kappa d - 1\right) . \tag{10b}$$

The particle number density and the nearest neighbour distance in the crystals are connected via

$$d_\mathrm{bcc} = \frac{\sqrt{3}}{\sqrt[3]{4 n_\mathrm{p}}} \tag{11a}$$

$$d_\mathrm{fcc} = \frac{\sqrt[6]{2}}{\sqrt[3]{n_\mathrm{p}}} . \tag{11b}$$

So that Eq. 10 can be written in terms of n_p as

$$\begin{aligned} G_\mathrm{bcc} =& f_\mathrm{A} \frac{\sqrt[3]{16}}{\sqrt{27}} \frac{Z^{*2} e^4}{4\pi\varepsilon_0^2\varepsilon_\mathrm{r}^2 k_\mathrm{B} T} \\ &\times \frac{\exp\left[-\sqrt{\frac{e^2}{\varepsilon_0\varepsilon_\mathrm{r} k_\mathrm{B} T}\left(n_\mathrm{p} Z^* + n_\mathrm{Salt}\right)}\left(\frac{\sqrt{3}}{\sqrt[3]{4 n_\mathrm{p}}} - 2a\right)\right]}{\left[1 + \sqrt{\frac{e^2}{\varepsilon_0\varepsilon_\mathrm{r} k_\mathrm{B} T}\left(n_\mathrm{p} Z^* + n_\mathrm{Salt}\right)} a\right]^2} \\ &\times \left(n_\mathrm{p} Z^* + n_\mathrm{Salt}\right) \sqrt[3]{n_\mathrm{p}^2} \end{aligned} \tag{12a}$$

$$\begin{aligned} G_\mathrm{fcc} =& f_\mathrm{A} \frac{1}{2} \frac{Z^{*2} e^2}{4\pi\varepsilon_0\varepsilon_\mathrm{r}} n_\mathrm{p} \\ &\times \frac{\exp\left[-\sqrt{\frac{e^2}{\varepsilon_0\varepsilon_\mathrm{r} k_\mathrm{B} T}\left(n_\mathrm{p} Z^* + n_\mathrm{Salt}\right)}\left(\frac{\sqrt[6]{2}}{\sqrt[3]{n_\mathrm{p}}} - 2a\right)\right]}{\left[1 + \sqrt{\frac{e^2}{\varepsilon_0\varepsilon_\mathrm{r} k_\mathrm{B} T}\left(n_\mathrm{p} Z^* + n_\mathrm{Salt}\right)} a\right]^2} \\ &\times \left(\frac{e^2}{\varepsilon_0\varepsilon_\mathrm{r} k_\mathrm{B} T}\left(n_p Z^* + n_\mathrm{Salt}\right) \frac{\sqrt[3]{2}}{\sqrt[3]{n_p^2}} \right. \\ &\left. - \sqrt{\frac{e^2}{\varepsilon_0\varepsilon_\mathrm{r} k_\mathrm{B} T}\left(n_\mathrm{p} Z^* + n_\mathrm{Salt}\right)} \frac{\sqrt[6]{2}}{\sqrt[3]{n_\mathrm{p}}} - 1 \right) . \end{aligned} \tag{12b}$$

By varying the particle number density (or the nearest neighbour distance) the interaction potential is modified via the inter particle distance and via the screening length. The shear modulus which depends on the first and the second deviation of the interaction potential is very sensitive of the species of the interaction potential by varying the particle number density.

The colloidal systems are prepared under fully deionised conditions to obtain fast and reproducible measurements. First the systems are prepared in the crystalline state. Then n_p is lowered step by step by diluting the suspension. At each step SLS and TRS measurements are performed to determine shear modulus, particle number density and crystalline structure. By reducing n_p the interaction potential becomes lower and the crystal begins to melt. The phase boundaries of all samples are always determined in a combination of SLS, TRS and BMC measurements. At the melting point no shear modulus can be determined while with BMC we can specify this point by identifying small fluid regions in the sample. By lowering n_p the freezing point can be appointed with SLS. Here in the structure factor just no crystalline contribution can be found. With BMC the freezing point can be easily appointed when no crystalline areas are visible.

Following we will show how to determine $V(r)$ using CM and TRS. For demonstration we show measurements at PNBAPS68 samples. Under full deionised conditions Z_σ^* can be determined by measuring σ in dependence of n_p calibrated by Bragg scattering and fitting Eq. 3 to the data points. In Fig. 1a the linear dependence of σ on n_p can clearly be seen. The quality of this linear fit to the data also demonstrates the performance of our preparation technique. Using Z_σ^* $V(r)$ can be calculated using Eq. 9.

In Fig. 1b we now plot G as inferred from the resonance spectra versus n_p as inferred from crystalline $S(q)$. Each point represents an average over 3 measurements, then the residual errors are about 5%. The line is the best two parameter fit (Eq. 12) using $f_\mathrm{A} = 0.5$ and to obtain

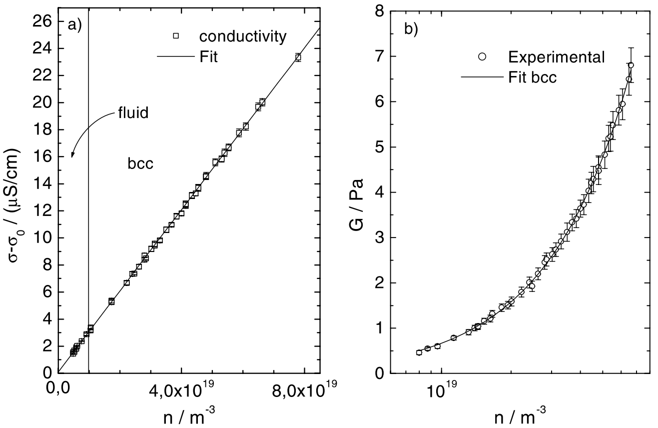

Fig. 1 **a** Conductivity of PNBAPS68 as a function of particle number density. σ increases linearly with n_p. **b** Shear modulus as a function of n_p for PNBAPS68. (—) Best two parameter fit ($f_\mathrm{A} = 0.5$, $Z^* = 331 \pm 3$, $c = (2.2 \pm 2.1) \times 10^{-7}$ mol)

an effective charge $Z^*_G = 331 \pm 3$ and a salt concentration of $c = (2.2 \pm 2.1) \times 10^{-7}$ mol. The data fit very well to the form of the theoretical curve (reduced $\chi^2 = 0.0022$) which also demonstrates the outstanding performance of our preparation technique and our multi-purpose light scattering experiment.

In all CM and in all TRS measurements the data can be well described using a constant Z^* over a wide range of n_p e.g. PnBAPS68 Z^*_σ: $3 \times 10^{18}\,\mathrm{m}^{-3} < n_p < 8 \times 10^{19}\,\mathrm{m}^{-3}$. There is no dependence of Z^* on n_p observable in contrast to theoretical predictions [11, 14, 15]. Figure 2 shows the effective charge Z^*_{num} in dependence of the volume fraction for the PNBAPS68 numerical calculated using a program of Luc Belloni [16]. The effective charge is first decreasing to reach a minimum value and shows a strong increase after that. The increase at high volume fractions is caused by the self screening based on counterions. The increase starting from the minimum to low volume fractions is based on an entropic effect: here more counterions can evaporate from the particle's surface. The vertical lines represent the investigated concentrations using TRS. The relative deviation of the effective charge inside the investigated concentration range is about 4% for Z^*_{num}, 3% for Z^*_σ and 1% for Z^*_G. So we can conclude that our observation of a constant effective charge observed in the experiment is not absolutely inconsistent with the theoretical models. Table I gives an overview of the determined phase boundaries and Z^* for the different systems. It is flashily, that Z^* from CM is always larger than from TRS and the relation ship between these two charges is constant for all used particles ($Z^*_\sigma / Z^*_G = 1.44 \pm 0.03$).

To compare the phase behaviour of the different samples following we use the phase diagram calculated by Robbins, Kremer and Grest (RKG) [1, 2]. Here the inverse normalised interaction energy $k_B T / V(\bar{d})$ at the averaged inter particle distance $\bar{d} = n_p^{-1/3}$ is plotted versus a coupling parameter $\lambda = \kappa \bar{d}$. The straight line from the lower left to the upper right is the melting line calculated in [1], the dotted line a bit lower the melting line calculated in [2]. The dashed line corresponds to the bcc-fcc phase transition. In dependence of the experimental parameters n_p, c, a and Z^* different states in this diagram can be reached. The pathway of a suspensions in the $k_B T / V(\bar{d}) - \kappa \bar{d}$-plane upon changes of the experimental parameters is represented by state lines. To demonstrate this fact Fig. 3 shows the phase diagram including four different theoretical lines of state (two lines each with different a, Z^*, c) in dependence of n_p.

Starting with the black circles ($2a = 100$ nm, $Z^* = 200$, $c = 0\,\mu$M) we can discuss the behaviour by varying the particle concentration. Beginning with high diluted sample increasing of n_p leads to an increasing of $V(\bar{d})$. The number of small ions is dominated by the self-dissociation of water so that κ stays nearly constant, while $\bar{d}$ is decreasing. At higher n_p this behaviour changes because κ is dominated by the particle counter ions, λ increases with $n_p^{1/6}$ and the state line turns right. The state line crosses the melting line at $n_p = 1.25 \times 10^{20}\,\mathrm{m}^{-3}$. At very high n_p self-screening becomes important and $V(\bar{d})$ shows a smaller increase up to a higher limit or is decreasing. For different system parameters c, a and Z^* different behaviour

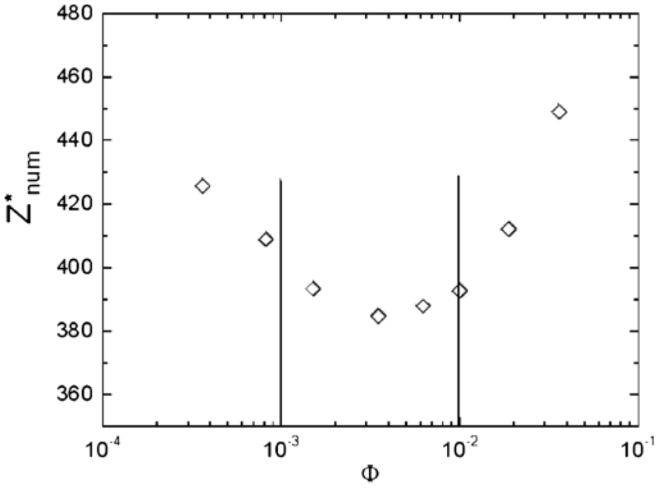

Fig. 2 Z^* of PNBAPS68 from numerical calculations in dependence of volume fraction. The *vertical lines* represent the investigated concentrations using TRS

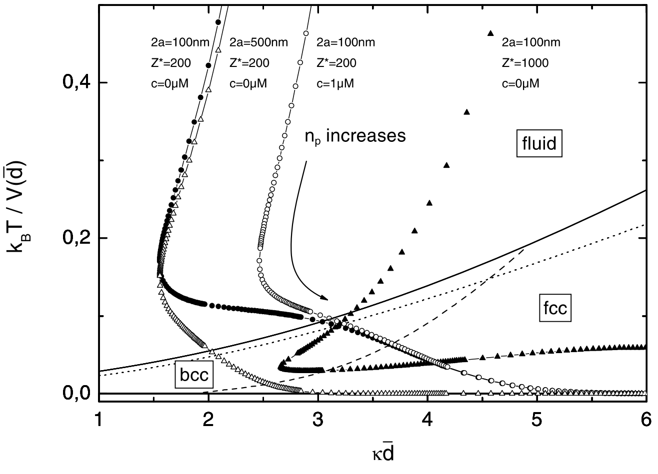

Fig. 3 Universal phase diagram [1, 2]; — *melting line* [1], ☐ *melting line* [2], - - bcc-fcc transition [1]. In dependence of c, a and Z^* different *lines of state* are shown by varying n_p: ● $2a = 100$ nm, $Z^* = 200$, $c = 0\,\mu$M, $n_p = 2.25 \times 10^{17} - 8.75 \times 10^{21}\,\mathrm{m}^{-3}$, △ $2a = 500$ nm, $Z^* = 200$, $c = 0\,\mu$M, $n_p = 2.25 \times 10^{17} - 8.75 \times 10^{21}\,\mathrm{m}^{-3}$, ○ $2a = 100$ nm, $Z^* = 200$, $c = 1\,\mu$M, $n_p = 2.5 \times 10^{18} - 8.75 \times 10^{21}\,\mathrm{m}^{-3}$, ▲ $2a = 100$ nm, $Z^* = 1000$, $c = 0\,\mu$M, $n_p = 2.75 \times 10^{16} - 7.0 \times 10^{19}\,\mathrm{m}^{-3}$; in all curves n_p is increased in steps of 0.25 in every decade

is observed. By changing the particle radius to a larger value ($2a = 500\,\text{nm}$, $Z^* = 200$, $c = 0\,\mu\text{M}$) the interaction is increasing more rapid and the melting line is reached at lower concentrations ($n_\text{P} = 1 \times 10^{19}\,\text{m}^{-3}$). There is no change in the curvature of the curve which means that self screening is less important. Changing the salt concentration to a slightly higher value ($2a = 100\,\text{nm}$, $Z^* = 200$, $c = 1\,\mu\text{M}$) leads to a small shift of the melting point to higher concentrations ($n_\text{P} = 1.5 \times 10^{20}\,\text{m}^{-3}$). The upper part of the state line shifts to the right which means that the potential becomes steeper compared to the salt free case. The change in the curvature is less pronounced which means that self screening in that area is less pronounced. A high n_P kappa is dominated by counterions and so the two curves coincide. Changing the charge of the particles to a higher value ($2a = 100\,\text{nm}$, $Z^* = 1000$, $c = 0\,\mu\text{M}$) the melting line is crossed at much lower concentration ($n_\text{P} = 5.75 \times 10^{16}\,\text{m}^{-3}$) while the curve is still bent to the left which means that the potential becomes flatter. The changing in the screening is obtained when the suspension is still in the crystalline region. In a system where the stateline crosses the melting line under an angle close to 90° the system is very sensitive in terms of the fluid crystalline phase transition by varying n_P while under a flat angle higher variation of n_P can be tolerated.

In Fig. 4 we see the behaviour of all used systems using $V(\bar{d})$ determined by CM. Here for all systems the lines of state are drawn under full deionised conditions. The error bars indicate the position of the determined melting point. Like in earlier investigations no agreement with the theoretical prediction can be found [6, 7]. By observing the different lines of state it is obvious that the theoretical melting line can only be reached by reducing n_P about one to two decades! These facts show a big discrepancy to the experiment. In the previous investigations Okubo and Monovoukas had to reduce Z^* determined by conductivity by a factor 1.36 to get their experimental results in good agreement with the theoretical predictions [6, 7]. Similarly we can describe the phase behaviour by lowering our effective Z^*_σ by a factor of 1.4. Whereas using $V(\bar{d})$ determined by TRS (Fig. 5) we find quite good conformity of our data with the theoretical melting line. Here the theoretical melting line is reached by varying n_P about zero to one decades.

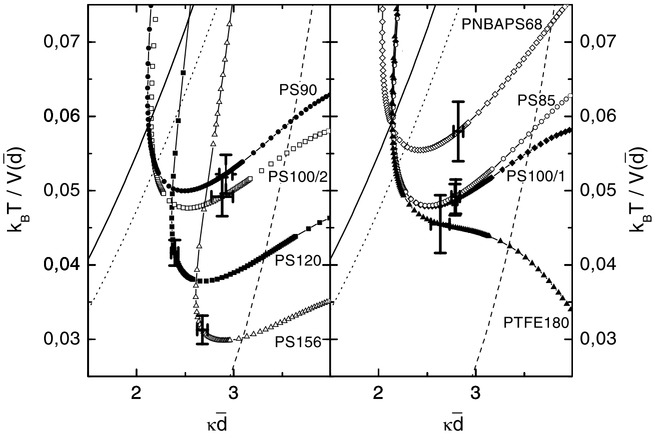

Fig. 4 Comparison of our data using Z^*_σ to the results of RKG. *State lines* shown: ◇ PNBAPS68, ○ PS85, ● PS90, ◆ PS100/1, □ PS100/2, ■ PS120, △ PS156, ▲ PTFE180, — predicted *melting line* [1], □ predicted *melting line* [2], - - predicted bcc-fcc transition [1]. *Error bars* indicate the melting points. n_P is increased in steps of 0.25 in every decade

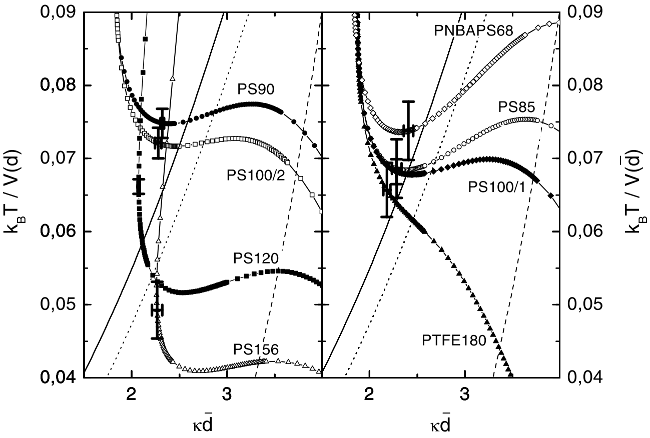

Fig. 5 Comparison of our data using Z^*_G to the results of RKG. *State lines* shown: ◇ PNBAPS68, ○ PS85, ● PS90, ◆ PS100/1, □ PS100/2, ■ PS120, △ PS156, ▲ PTFE180, — predicted *melting line* [1], □ predicted *melting line* [2], - - predicted bcc-fcc transition [1]. Error bars indicate the melting points. n_P is increased in steps of 0.25 in every decade

Conclusions

We determined the phase boundaries for different charged colloidal systems systematically by a combination of SLS, TRS and BMC with high accuracy under full deionised, well characterised conditions. Effective charges were determined using conductivity and shear modulus measurements. The conductivity is increasing linearly with particle concentration not being influenced by phase boundaries and can well described using a constant effective charge Z^*_σ. The shear modulus in dependence of the particle number density can described brilliant using a Debye-Hückel potential proposed in the PBC-model with an constant effective charge Z^*_G. The independence of Z^* of n_P is not inconsistent with theoretical predictions. We observe systematic differences and correlations of the two effective charges. With Z^*_σ and Z^*_G there exist two different kind of effective charges. The first one is determined measuring the conductivity which is related to the number of freely moving small ions Z^*_σ and thus relates to the ion condensation process in the electric double layer under conditions of finite macro-ion concentrations. The second one is determined by measuring the shear modulus which is directly connected to the interaction potential at the nearest neighbour distance in the bulk. The two charges have a constant relationship $Z^*_\sigma / Z^*_\mathrm{G} = 1.44 \pm 0.03$ independent of particle size and surface charge density.

Using the interaction potential determined by TRS we are able to describe the experimental fluid crystalline phase boundaries in a universal theoretical phase diagram proposed by RKG for the first time. We present the first experimental access of the pair energy of interaction in charged colloidal suspensions which describes both the elastic properties and the fluid crystalline phase behaviour. This means that a consistent description of the suspension properties is obtained, when Z^*_G is taken from the elasticity measurement.

At first sight this result is surprising because it suggests that the approximation of superposition of pair potentials still holds in the case of long ranged interaction. By calculating the theoretical phase diagram the authors used the superposition approximation: The interaction in charged colloidal systems is reduced to the pair wise additivity of single particle potentials. This superposition approximation is also applied by describing the elastic properties of a crystal in dependence of the interaction potential. So the physical picture describing phase behaviour and elastic properties is consistent and so it is understandable that experiment and theory met together.

An interesting open question is still the experimentally quantitative validation of packing fraction dependence and the salt dependence of Z^* predicted in the PBC-model. New investigations are still in progress.

Acknowledgement We gratefully acknowledge financial support by the DFG (Pa459/10-1 and 11-1) and the MWFZ Mainz.

References

1. Robbins MO, Kremer K, Grest GS (1988) J Chem Phys 88:3286
2. Meijer EJ, Frenkel D (1991) J Chem Phys 94:2269
3. Voegtli LP, Zukoski CF (1991) J Colloid Interface Sci 141:79
4. Schram PPJM, Trigger SA (1996) Physica B 228:170
5. Sirota EB et al. (1989) Phys Rev Lett 62:1524
6. Okubo T (1994) ACS Symposium Series 548:364
7. Monovoukas Y, Gast AP (1989) J Colloid Interf Sci 128:535
8. Löwen H, Denton AR, Dhont JKG (1999) J Phys Condens Matter 11:10047
9. Belloni L (2000) J Phys Cond Matter 12:R549
10. Groot RD (1991) J Chem Phys 94:5083
11. Stevens MJ, Falk ML, Robbins MO (1996) J Chem Phys 104:5209
12. Crocker JC, Grier DG (1994) Phys Rev Lett 73:352
13. Alexander S et al. (1984) J Chem Phys 80:577
14. v Grünberg HH (2000) J Phys Cond Matter 12:6039
15. Gisler T et al.(1994) J Chem Phys 101:9924
16. Belloni L (1998) Colloid Surf A 140:227
17. Brunner M, Bechinger C, Strepp W, Lobaskin V, von Grünberg HH (2002) Europhys Lett 58:926
18. Hansen JP, Hayter JB (1982) Molecular Physics 46:651
19. Taylor TW, Ackerson BJ (1985) J Chem Phys 83:2441
20. Härtl W, Versmold H (1988) J Chem Phys 88:7157
21. Evers M, Garbow N, Hessinger D, Palberg T (1998) Phys Rev E 57:6774
22. Hessinger D, Evers M, Palberg T (2000) Phys Rev E 61:5493
23. Schaefer DW (1977) J Chem Phys 66:3980
24. Yamanaka J, Yoshida H, Koga T, Ise N, Hashimoto T (1998) Phys Rev Lett 80:5806
25. Dozier WD, Lindsay HM, Chaikin PM (1985) J Phys (Paris) Colloq
26. Palberg T, Mönch W, Bitzer F, Piazza R, Bellini T (1995) Phys Rev Lett 74:4555
27. Grier DG, Crocker JC (2000) Phys Rev E 61:980
28. Schöpe HJ, Decker T, Palberg T(1998) J Chem Phys 109:10068
29. Schöpe HJ, Palberg TJ (2001) Colloid Interface Sci 233:149
30. Liu J, Schöpe HJ, Palberg T (2002) J Chem Phys 116:5901
31. Maaroufi MR, Stipp A, Palberg T (1998) Progr Coll & Polym Sci 108:83
32. Leibfried G (1955) In: Encyclopedia of Physics. Vol VII, Part I, Crystal Physics I. Springer, Berlin
33. Zeller R, Dederichs PH (1973) Phys Stat Sol (b) 55:831

Progr Colloid Polym Sci (2006) 133: 95–99
DOI 10.1007/2882_061

Alexander Uvarov
Stephan Fritzsche

Restricted Rotational Diffusion of Non-rigid Dumbbell-Type Macromolecules on Surfaces: Effects of the Bead-Bead and Bead-Surface Interaction

Alexander Uvarov (✉) · Stephan Fritzsche
Institut für Physik, Universität Kassel,
Heinrich-Plett-Str. 40, 34132 Kassel,
Germany
e-mail: uvarov@physik.uni-kassel.de

Abstract A recently derived Difusion equation [Uvarov A, Fritzsche S (2004) J Chem Phys 121(13):6561] is utilized to analyze the restricted rotational motion of macromolecules in solution if they are immobilized on a surface. Both, the bead–bead and bead–surface interactions are taken into account in order to describe the orientational dynamics of non-rigid macromolecules and its relaxation in time after a perturbation has occured. Using several realistic bead–bead and bead–surface potentials, detailed numerical investigations have been carried out for the rotational diffusion coefficient as well as for the conformational phase–space distribution function of the macromolecules. From this phase-space distribution, the orientational correlation function are derived and compared with phenomenological computations from the literature. Such correlation function can be observed in dielectric relaxation and fluorescence depolarization experiments.

Keywords Correlation functions · Diffusion equation · Immobilized molecule · Rotational diffusion · Orientational relaxation

Introduction

Accurate dynamical studies on macromolecules in solution are still a challenge for modern DNA and protein research. During the past decade, therefore, a large number of experiments have been carried out in order to understand the translational and rotational motion as well as the shape formation and deformation processes of such molecules. Apart from free macromolecules in solution [1, 2], these experiments concerned in particular the restricted mobility of macromolecules which are immobilized on a surface [3–6]. On the theoretical side, moreover, several (often quite large) Molecular and Brownian dynamical simulations [7–11] as well as analytical case studies have been performed [12–15]. In all these investigations, the macromolecules are usually described by means of their molecular subsystems to which we refer below as the beads of the macromolecule. When immersed into a solvent and immobilized onto a surface, of course, the shape and the orientation relaxation dynamics of the macromolecules will be determined not only by the interaction of the beads with the surrounding solvent but also by the interaction among their (neighboring) beads as well as with the surface.

In the present contribution, emphasis is placed on the internal rotational dynamics of macromolecules which are immersed into a solution. In contrast to most previous investigations, in which more often than not a rigid molecule was assumed [16–20], here we consider the rotational dynamics of a non-rigid macromolecule as described recently by us in [21]. In particular, we explore the question of how the bead–bead as well as bead–surface interactions affect the (restricted) rotational diffusion of such molecules at a surface. In the next section, we start with a brief outline and the basic assumptions which are made for the "non-rigid macromolecule on a surface" in order to derive the diffusion equation for the time evolution of its configuration–space distribution function. These expressions are later utilized in section III to obtain the rotational diffusion coefficient as well as the orientation correlation function for an "extended" dumbbell molecule. Here, the results from our "semi-phenomenological" theory are compared with computations from Doi and Edwards [12, 13] which are based on a rigid-rod model of the macromolecule; finally, a few conclusion are given in section IV.

Basic Model Equations and Computations

Since we are interested mainly on the internal rotational dynamics of macromolecules and on how the bead–bead and bead–solvent interactions affects their dynamics, let us start from the Diffusion equation (DE)

$$\begin{aligned}\frac{\partial\psi}{\partial t} =& D_{\perp}^{(Q)}\left[\Delta\psi+\beta\psi\Delta U+\nabla\psi\cdot\nabla U\right]\\ &+\left(D_{\|}^{(Q)}-D_{\perp}^{(Q)}\right)\left[\frac{\partial^2\psi}{\partial Q^2}+\beta\psi\frac{\partial^2 U}{\partial Q^2}+\beta\frac{\partial\psi}{\partial Q}\frac{\partial U}{\partial Q}\right]\\ &+\left(\frac{\partial D_{\perp}^{(Q)}}{\partial Q}+\frac{2\left(D_{\|}^{(Q)}-D_{\perp}^{(Q)}\right)}{Q}\right)\left[\frac{\partial\psi}{\partial Q}+\beta\psi\frac{\partial U}{\partial Q}\right]\end{aligned} \qquad (1)$$

as derived recently for the time evolution of the configuration–space distribution function $\psi=\psi(\vec{Q};t)$ of a dumbbell molecule. In this equation, Q denotes the length of the end-to-end vector $\vec{Q}$ of the two beads (with radius σ) of a dumbbell molecule while Δ is the Laplacian in a coordinate-free notation and $\beta=1/k_{\mathrm{B}}T$ the (inverse) temperature of the overall system. In [21], this diffusion equation was obtained by starting from a Fokker-Planck equation for the phase–space distribution function of the N-bead macromolecule. However, to remove the explicit dependence of this equation from the momenta of the molecular beads, a number of assumptions had to be made about the dynamical behaviour of macromolecules on a surface. Apart from (i) a fast relaxation of the velocities of the molecular beads (when taken relative to the relaxation of their position), here we assumed (ii) that all the effects of the solvent onto the dynamics of the macromolecule can be well described by means of the parallel $D_{\|}^{(Q)}$ and perpendicular $D_{\perp}^{(Q)}$ components of the "diffusion tensor" of the internal motion of the macromolecule. As seen from Eq. 1, these two components describe the mobility of the dumbbell along and perpendicular to the direction of the end-to-end vector $\vec{Q}$.

A further assumption concerned (iii) the interaction potential $U=U_{\mathrm{BB}}(Q)+U_{\mathrm{BS}}$ including the bead–bead and bead–solvent interaction of the macromolecule immobilized on a surface (cf. Fig. 1).

Here, U_{BS} refers to the interaction of the "upper bead" of the dumbbell molecule with the surface while the bead–bead potential U_{BB} only depends on the distance of the beads. In the following, moreover, we shall restrict ourselves to an "extended" dumbbell molecule with two spherical beads, for which the bead–bead separation is much larger than the radii of the beads. With the assumption (i–iii) in mind, of course, we can use the configuration–space distribution function from Eq. 1 in order to investigate various dynamical properties $A=A(\vec{Q})$ of macromolecules in solution by taking the time average

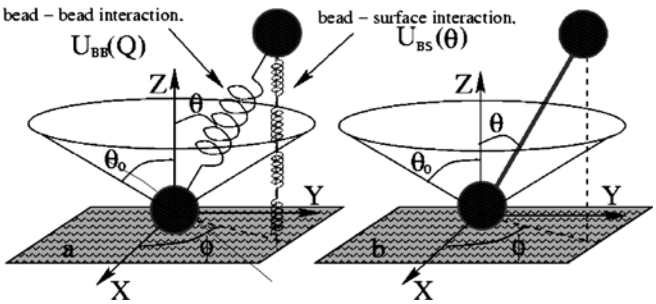

Fig. 1 Two models of the dumbbell macromolecule immobilized on a surface: (*left*) the non-rigid dumbbell and (*right*) the rigid-rod model

$$\langle A\rangle=\int \mathrm{d}\vec{Q}A(\vec{Q})\psi\left(\vec{Q};t\right)\,. \qquad (2)$$

Taking the time average over the configuration-space distribution function $\psi(\vec{Q};t)$ may in general result in quite lengthy computations as the – parallel and perpendicular – components of the diffusion tensor depend not only on the shape of the beads but also on hydrodynamic interactions [12, 13, 15, 23]. For the case of an extended dumbbell molecule, we may neglect the hydrodynamic interactions and assume an "isotropic" diffusion tensor $D_{\|}^{(Q)}=D_{\perp}^{(Q)}=D$ with the parameter D being as the self-diffusion constant coefficient of the bead if macromolecule is immersed in the unbounded solvent [21]. However, for the beads in the present of the surface, the parallel $D_{\|}^{(Q)}$ and perpendicular $D_{\perp}^{(Q)}$ components of the diffusion tensor are no longer of constant values but – due to the bead – surface hydrodynamic interaction – have to be described via the scalar mobility functions $\lambda_{\|}(h)$ and $\lambda_{\perp}(h)$ which depend on the bead–surface distance $h=Q\cos\theta$ and described [24, 25] the mobility of the beads along and perpendicular to the bead–surface direction, respectively, i.e. $D_{\|,\perp}^{(Q)}=D\lambda_{\|,\perp}(h)$. While, moreover, the bead–surface hydrodynamic interaction is really inhibit the diffusion of the beads near the surface (especially when the bead–surface distance $h\le 2\sigma$) [24, 25], in this work we will not take into account the bead–surface hydrodynamic effects by assuming that $\lambda_{\|,\perp}(h)=1$. Since, we consider only restricted rotational motion of the dumbbell, the simplification about behaviour of the mobility functions $\lambda_{\|,\perp}(h)$, of course, can critically distort our results only when the maximal value of polar angle θ_0 is more than 70°. This can be seen, for instance, from the fact that averaged bead–bead distance Q of the extended dumbbell is always approximately assumed [21] to be more than 7σ. Therefore, the minimal bead–surface distance is $h_{\mathrm{min}} = Q \cos\theta_0 \geq 2.1\,\sigma$ and therefore the mobility functions $\lambda_{||,\perp}(h)$ always close to 1. Nevertheless, an extension of this approach in order to fully include the effects of the bead–surface interaction on the configuration-space distribution function is currently under work and will be published elsewhere.

In the following, we shall not go into the details for deriving the configuration–space distribution function $\psi(\vec{Q} \equiv (Q, \theta, \varphi); t)$ of a non-rigid dumbbell; using the ansatz $\psi(Q, \theta, \varphi; t) = T(t) R(Q) \Theta(\theta) \Phi(\varphi)$, Eq. 1 can be separated into four ordinary differential equations for the variables Q, θ, φ and the time t which fully describe the dynamical behaviour of the molecule. In order to use these equations, however, we need to specify the proper boundary conditions for $\psi(\vec{Q}; t)$, since the configuration–space distribution function is supposed to be continuous, it must satisfy the reflection (von Neumann) condition for the polar angle and the bead–bead distance as well as the periodic boundary condition for the azimuthal angle:

$$\left.\frac{\partial\psi\,(Q, \theta, \varphi; t)}{\partial\theta}\right|_{\theta=\theta_0'} = 0\,,\ \left.\frac{\partial\psi\,(Q, \theta, \varphi; t)}{\partial Q}\right|_{Q=Q_0'} = 0\,, \tag{3}$$

$$\psi\,(Q, \theta, \varphi = 0; t) = \psi\,(Q, \theta, \varphi = 2\pi; t)\ . \tag{4}$$

Making use these boundary conditions, the configuration–space distribution function $\psi(Q, \theta, \varphi; t)$ can be written in the form [21]

$$\begin{aligned}\psi(Q, \theta, \varphi; t) = \sum_{n=1}^{\infty} \sum_{m=-\infty}^{\infty} &\mathrm{e}^{-\nu_n^m (\nu_n^m + 1) D_{\mathrm{R}} t} \\ &\times \left(A_n^m \cos m\varphi + B_n^m \sin m\varphi\right) \\ &\times P^{\mathrm{m}}_{\nu_n^m}(\cos\theta) \Psi_{\nu_n^m}(Q)\,,\end{aligned} \tag{5}$$

where

$$D_{\mathrm{R}} = D \left\langle \frac{1}{Q^2} \right\rangle \tag{6}$$

is the diffusion coefficient for the rotational motion or, shortly, the rotational diffusion coefficient of the dumbbell at the surface. This coefficient still contains all the information about the influence of the solvent as well as the bead–bead and bead–surface interactions owing to the self diffusion coefficient D and the time average of the end-to-end distance (cf. Eq. 2). In expression (5), $\Psi_{\nu_n^m}(Q)$ is called the radial distribution function of the end-to-end distance, while $P^{\mathrm{m}}_{\nu_n^m}(\cos\theta)$ denotes an associated Legendre function of degree ν_n^m and order m. For both indices, ν_n^m and m, the allowed values are obtained from the boundary conditions (3, 4). Since the azimuth φ is not restricted and, hence, the configuration–space distribution should have a period 2π, m must be an integer. For the degree ν_n^m (of the Legendre polynomial and radial distribution function), in contrast, the restriction in the polar angle $\theta \leq \theta_0 \leq \pi/2$ leads to non-integer values in general which, for fixed values of m and n, have to be calculated numerically from the boundary conditions (3). A more detailed discussion about these computations and the properties of the associated Legendre function with a non-integer degree can be found in [16, 21]. To calculate and understand the behaviour of the configuration space distribution function (5), it is essential to use properties the associated Legendre functions. As known from the literature, the associated Legendre functions obey the symmetry $P^m_{\nu_n^m}(\cos\theta) = P^m_{-\nu_n^m - 1}(\cos\theta)$ even in the case if ν_n^m has a non-integer value. In addition, the associated Legendre functions have the well-known orthogonality properties

$$\int\limits_0^{\theta_0} \sin\theta\ \mathrm{d}\theta P^m_{\nu^m_{n_1}}(\cos\theta) P^m_{\nu^m_{\mathrm{n}_2}}(\cos\theta) = H^m_{n_1} \delta_{n_1 n_2}$$

with

$$\delta_{n_1 n_2} = \begin{cases} 1 & \text{if } n_1 = n_2 \\ 0 & \text{if } n_1 \neq n_2 \end{cases}$$

being the usual Kronecker symbol. In the general form (5) of the configuration–space distribution $\psi(Q, \theta, \varphi; t)$, therefore, the coefficients A_n^m and B_n^m are given by [21]

$$\begin{aligned} A_n^m &= \frac{\cos\varphi(0) P^m_{\nu_n^m}(\cos\theta\,(0))\ Q(0) \Psi_{\nu_n^n}(Q(0))}{\pi H_n^m (1 + \delta_{m0})}, \\ B_n^m &= \frac{\sin\varphi(0) P^m_{\nu_n^m}(\cos\theta\,(0))\ Q(0) \Psi_{\nu_n^n}(Q(0))}{\pi H_n^m}, \end{aligned} \tag{7}$$

where $Q(0)$ denote the initial values of the bead–bead distance as well as $\varphi(0)$ and $\theta(0)$ are the initial values of the azimuthal and polar angles, respectively.

As seen from expressions (7), the coefficients A_n^m and B_n^m now depend – via the non-integer degree ν_n^m – on the (maximal allowed) polar angle θ_0 in the restricted motion of the dumbbell molecule. Below, we make use of these coefficients and the orthogonally property of the associated Legendre functions from above in order to calculate the radial distribution function as well as rotational diffusion coefficient of the dumbbell macromolecule.

Results and Discussions

From the Diffusion equation (1), we see that the dynamics of the macromolecule depend on the overall potential U, i.e. the interaction $U_{\mathrm{BB}}(Q)$ between the beads as well as the interaction U_{BS} of the (upper) bead with the surface. To obtain further insight into the rotational behaviour of a dumbbell molecule at a surface, therefore, let us consider four particular combinations of the bead–bead and bead–surface interactions. Most of these potential have their origin in the field of physical chemistry where they were constructed in order to simulate the chemical bonds in different (chemical) environments. In the following, we will consider (i) a Frenkel potential [22]

$$U^{\mathrm{Fr}}_{\mathrm{BB}}(Q) = k_{\mathrm{Fr}}\,(Q - Q_0)^2 \tag{8}$$

or (ii) a DNA-type bead–bead potential [23]

$$U^{\mathrm{DNA}}_{\mathrm{BB}}(Q) = k_{\mathrm{DNA}}\left(\frac{1}{4\left(1-\frac{Q}{Q_0}\right)} - \frac{1}{4}Q + \frac{Q^2}{2Q_0} - \frac{1}{4}\right) \tag{9}$$

while, for the bead–surface interaction, we take (iii) the Cone potential [21]

$$U^{\mathrm{Cone}}_{\mathrm{BS}}(\theta) = \begin{cases} 0 & \text{if } \theta \le \theta_0 \\ \infty & \text{if } \theta > \theta_0 \end{cases} \tag{10}$$

and (iv) the effective double well (Sin) potential

$$U^{\mathrm{Sin}}_{\mathrm{BB}} = k_{\sin}\sin^2\theta. \tag{11}$$

In these potentials (8, 9) and (11), the corresponding (interaction) constant $k_{\dots}$ determines the strength of the interaction. Note, moreover, the different meaning of Q_0 in the bead–bead potentials (8) and (9); while Q_0 is the equilibrium distance in the case of the Frenkel potential, this quantity denotes the maximal length beyond which the beads of the dumbbell cannot be stretched further in the case DNA-type potential.

Having selected a bead–bead and bead–surface potential, we can calculate the (set of) radial distribution functions $\Psi_{\nu_n^m}(Q)$. Figure 2 displays the behaviour of the first several normalized functions $\Psi_{\nu_n^m}(Q)$ for a Cone bead–surface potential (10) and by comparing a DNA-type and Frenkel bead–bead potential. Since $\Psi_{\nu_1^0}(Q)$ is just the equilibrium distribution function, it is independent of the maximum polar angle θ_0 in the restricted motion of the dumbbell molecule. As seen from Fig. 2, however, all other distribution functions with order $m \neq 0$ are rather sensitive to the opening angle of the cone. Moreover, the structure of the radial distribution functions becomes less pronounced for, say, $40° \le \theta_0 \le 90°$. Nevertheless, Fig. 2 clearly demonstrates that maximal value of the radial distribution functions decreases with increasing of the n and m quite quickly. It was found, in particular, that in order to calculate the time behaviour of the end-to-end correlation function $Q(0)Q(t)$ it is enough to use first 12 radial distribution functions $\Psi_{\nu_n^m}(Q)$ for $n \le 3$ and $m \le 3$.

Figure 3 shows the rotational diffusion coefficient D_{R} and the orientational correlation function $P_1 = \langle\cos\theta\rangle$ for the different bead–bead and bead–surface potentials (14–17). Apparently, the rotational diffusion coefficient behaves quite different for different combinations to the two potentials.

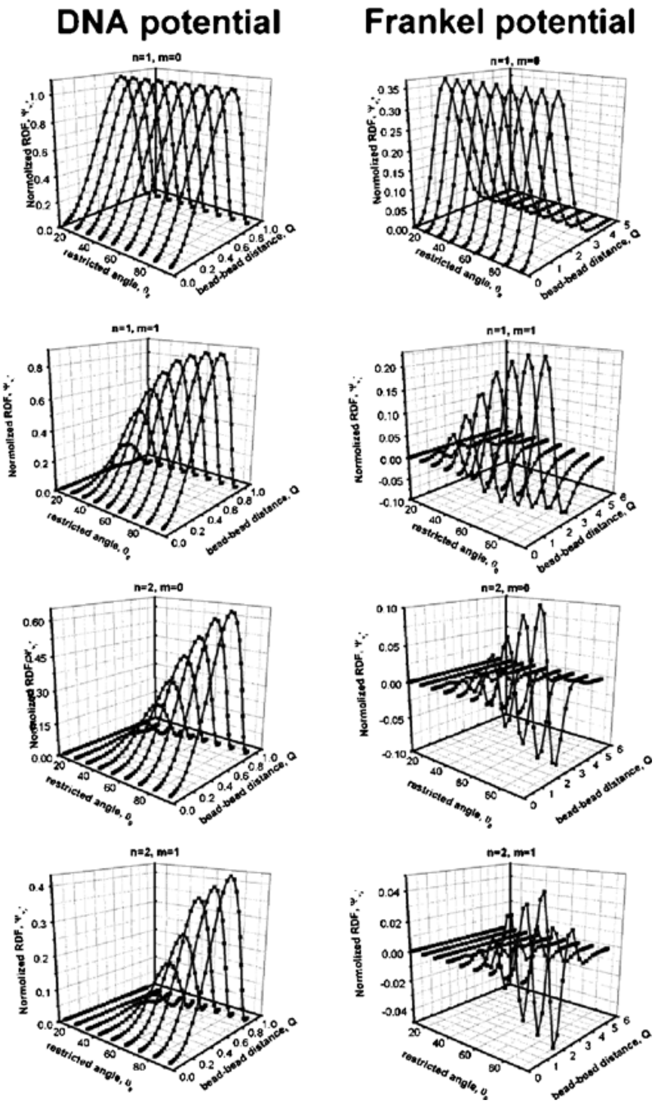

Fig. 2 Behaviour of the first three radial distribution functions $Q^2\Psi_{\nu_n^m}(Q)$ of the macromolecule with (*left*) DNA-type (8) and (*right*) Frenkel (9) bead–bead potential as function of the bead–bead distance Q and restricted angle θ_0

While, for example, the rotational diffusion coefficient D_{R} goes smoothly to zero at a maximal bead–bead separation of $Q_0 \approx 3$ in the case of a Frenkel potential, we find $D_{\mathrm{R}} \ge 0.5$ at this and even of larger values of Q_0 for a DNA-type potential. For a large maximal separation Q_0, moreover, the diffusion coefficient of the dumbbell with the (strong) DNA-type of the bead–bead potential is approximately the same like for the rigid-rod macromolecule, while it always stays large if compared with the rotational diffusion coefficient of the dumbbell with the (soft) Frenkel potential. In addition to the rotational diffusion coefficient, the Fig. 3 also demonstrates the behaviour of the orientational correlation function $P_1 = \langle\cos\theta\rangle$ as function of the (maximal) restricted polar angle θ_0 which is

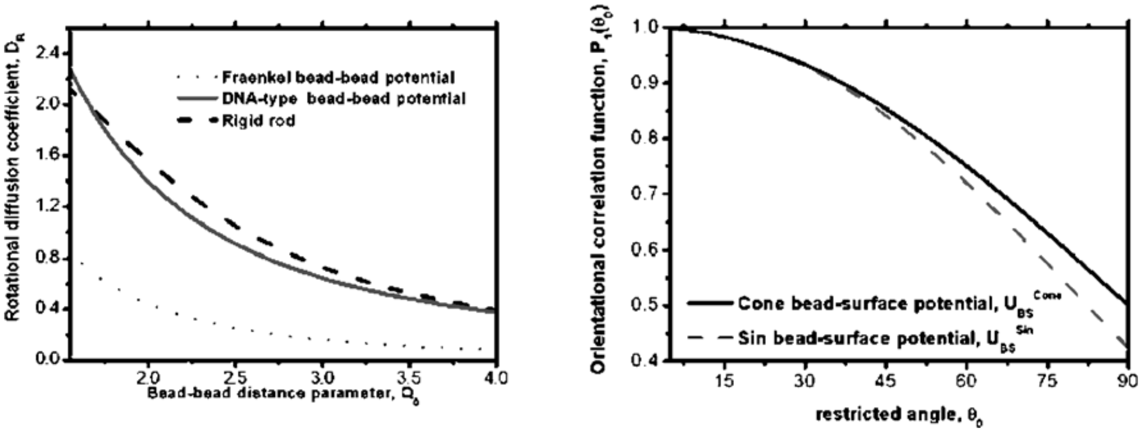

Fig. 3 *Left*: Rotational diffusion coefficient D_R as function of the distance bead–bead separation parameter Q_0 of the dumbbell molecule for the Frenkel, DNA-type bead–bead potential U_{BB} respectively. *Right*: Orientational correlation function $P_1 = \langle\cos\theta\rangle$ as function of the maximal restricted angle θ_0 for different bead–surface potentials when the bead–bead potential is assumed as DNA-type (9)

very sensitive to the particular choice of the bead–surface interaction potential. Since the rotational diffusion coefficient as well as the orientational correlation function can be observed directly by means of dielectric relaxation and scattering as well as fluorescence experiments [1–6], the Fig. 3 can be – at least in principle – used in order to find the value of the restricted angle θ_0 as well as in order to analyze the properties of both the bead–bead and bead–surface interaction potential.

Conclusion

In this work we have analyzed the influence of the bead–bead and bead–surface interactions on the restricted rotational dynamics of nonrigid macromolecules in solution if they immobilized with one end at a surface. For such (N-bead) macromolecules, we derived earlier a Diffusion equation from first principles [21]. Here, this equation is applied to investigate numerically the behaviour of the conformational phase space distribution function as well as of the rotational diffusion coefficient and the orientational correlation functions. This correlation functions, in particular, can be observed directly by means of dielectric relaxation and fluorescence experiments and can be used to analyze and better understand the internal structure of the macromolecule. As seen from our analysis, both the rotational diffusion coefficient and the radial distribution function clearly depend not only on the bead–bead but also the bead–surface interaction as well as on the maximum polar angle θ_0 for the case of a rotational diffusion in a cone. In the future, we hope that the radial distribution functions from above will help interpret (NMR) experiments from dielectric relaxation and correlation spectroscopy as carried out, for instance, for biological molecules.

References

1. Wu C et al. (1996) Macromolecules 29:228
2. Chirico G, Beretta S, Baldini G (1999) J Chem Phys 110:2297
3. Krishna M, Das R, Periasamy N (2000) J Chem Phys 112:8502
4. Dale R et al. (1999) Biophys Journal 76:1606
5. Helbing J et al. (2005) J Chem Phys 122:124505
6. Ha T et al. (1998) Phys Rew Letters.80:2093
7. Tao Y-G et al. (2005) J Chem Phys 122:244903
8. Ohmoria T, Kimura Y (2000) J Chem Phys 119:7328
9. Carrasco B, de la Torre G (1999) Biophys Journal 75:3044
10. Kaznessis Y, Hill D, Maginn E (1998) J Chem Phys 109:5078
11. Kaznessis Y, Hill D, Maginn E (1998) Macromolecules 31:3116
12. Doi M, Edwards SF (1986) The Theory of Polymer Dynamics. Oxford University, Oxford
13. Grossberg M, Khokhlov A (1989) Statistical Physics of Macromolecules. Nauka, Moscow
14. Blokhin A, Gelin M, Uvarov A (1999) Nonlinera Phenom in Complex Systems 2(3):72
15. Uvarov A, Fritzsche S (2004) Macrom Theory and Simul 13:241
16. Wang C, Pecora R (1980) J Chem Phys 72:5333
17. Kumar A (1989) J Chem Phys 91:1232
18. Fujiwara T, Nagayama K (1985) J Chem Phys 83:3110
19. Kumar G, Levy C (1986) J Chem Phys 85:458
20. Koenderink G, Lettinga M, Philipse A (2002) J Chem Phys 117:7751
21. Uvarov A, Fritzsche S (2004) J Chem Phys 121(13):6561
22. Curtis C, Bird R (1997) J Chem Phys 107:5254
23. Noguchi H, Takasu M (2001) J Chem Phys 114:7260
24. Feitosa M, Mesquita N (1991) Phys Rev A 44:6677
25. Cichoki B, Jones R (1998) Physica A 258:273

Progr Colloid Polym Sci (2006) 133: 100–105
DOI 10.1007/2882_070

SURFACTANTS

D. Weaire
S. Hutzler
W. Drenckhan
A. Saugey
S. J. Cox

The Rheology of Foams

D. Weaire · S. Hutzler (✉) ·
W. Drenckhan · A. Saugey
School of Physics, Trinity College Dublin,
Dublin 2, Ireland
e-mail: stefan.hutzler@tcd.ie

S. J. Cox
Institute of Mathematical
and Physical Sciences,
University of Wales, Aberystwyth, UK

Abstract We review recent progress concerning an understanding of the rheological properties of foams, both in bulk form and confined in narrow channels, and including the problem of foam sliding along a solid wall. Our calculations contribute not only to the interpretation of rheological data, but also to the coupling of foam drainage and rheology.

Keywords Rheology · Foams · Complex fluids · Dilatancy

Introduction

Much of the usefulness and appeal of liquid foams lies in their rheological properties. They combine the properties of an elastic solid at low stress with those of a liquid when the yield stress is exceeded [1]. It is this that makes shaving easy.

There is no mystery in their dual nature. Above the yield stress, rearrangements of bubbles become possible – or *topological changes*, in the language preferred for relatively dry foams.

Many other substances behave in much the same way, yet this side of the general theory of rheology seems curiously neglected in favour of viscoelastic materials. In getting to grips with foam rheology we have been hampered by this lack of an adequate theoretical background.

In the present paper we review some of the faltering attempts to overcome this difficulty[1]. In addition to surveying bulk rheology we shall report recent progress on confined foam structures, and the problem of slip at a wall – the so-called Bretherton problem.

Structure and Properties

The equilibrium structure that undergoes rearrangement under high stress is surely one of the most beautiful in nature (Fig. 1), a thicket of thin films conspiring to meet everywhere in the manner prescribed by the rules of Plateau, with surface tension in balance with pressure differences across each film. Most basic theories of foam proper-

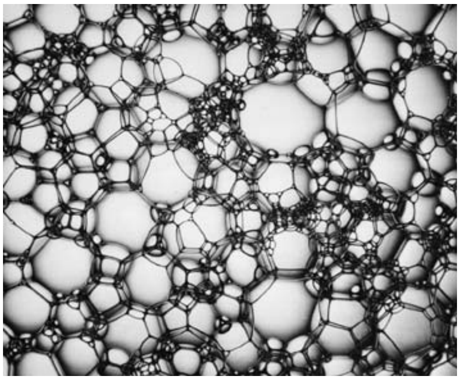

Fig. 1 An aqueous foam as seen by the photographer Michael Boran

---

[1] An excellent collection of recent papers on foam rheology can be found in *Colloids and Surfaces A: Physicochem. Eng. Aspects*, **263**, August 2005.

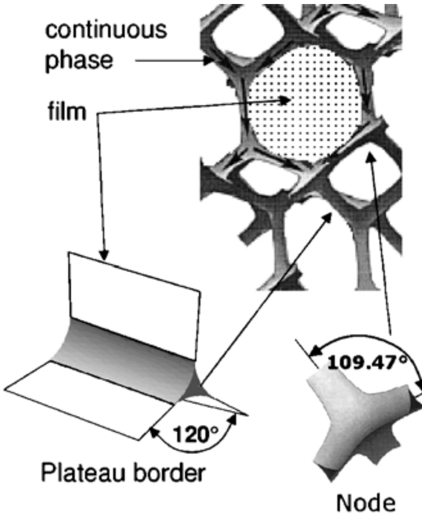

Fig. 2 The structure and geometry of dry foam was first described by the 19th century scientist Joseph Plateau [1]

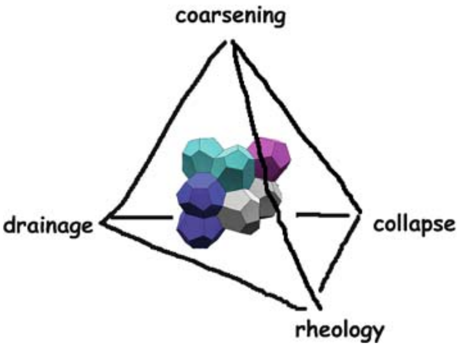

Fig. 3 The properties of a foam are interdependent and linked to its structure

ties find their way back to some aspect of that structure (Fig. 2).

Four main dynamic properties may be identified. *Drainage* is the transport of liquid through the foam, *rheology* is the description of the response to stress, *coarsening* is the gradual growth of average bubble size (and progressive elimination of bubbles) by gas diffusion through the films, and *collapse* is the eventual fate of most foams, as films rupture. In practice they are often interdependent. For example, drainage may be the precursor of collapse, and slow creep below the yield stress may be attributable to the gradual change of structure associated with coarsening (Fig. 3).

Foam Flows

This heading is the title of an excellent review by A. Kraynik [2] in which he stressed from the outset the importance of the ratio of average bubble diameter d to the characteristic length scale L of the vessel that contains the foam. A *microflow* regime ($d \approx L$), may be found in foam flow in a porous medium, but also in the recent area that has been called “Discrete Microfluidics” [3]. In the latter, individual bubbles are pushed through a network of specifically designed channels with the aim of controlled transport and manipulation of small amounts of gases (or liquids, in the analogous case of emulsions). An example is shown in Fig. 4. Relevant experiments pose a variety of questions concerning the detailed local mechanism of bubble transport, and relate to the Bretherton problem, as described below.

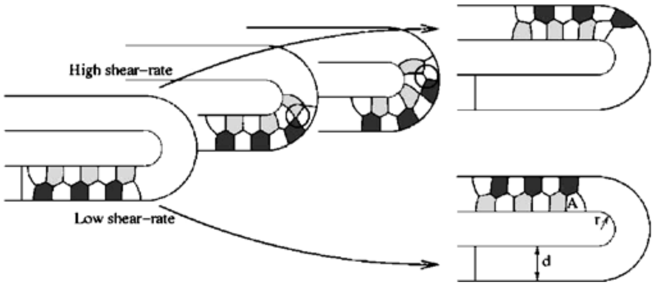

Fig. 4 Viscous froth simulation of a 2D ordered foam flowing aound a U-bend. As seen in experiments, at a sufficiently high velocity the bubbles successively change neighbours [4]

A continuum description of bulk foam is valid for $d/L \ll 1$. Such *macroflow* is challenging to theory, partly due to the non-linearity of the constitutive flow equations. Above the yield stress, S_y (which depends non-linearly on the liquid fraction of the foam), the shear stress S may be described by the *Herschel–Bulkley relation* as

$$S = S_y + \eta_{\mathrm{p}} \dot{\varepsilon}^m \, ,$$

where $\dot{\varepsilon}$ is the strain rate, and η_{p} is some asymptotic plastic viscosity (at high strain rate), also called foam consistency. In the *Bingham model* the exponent $m = 1$, but in the absence of convincing experimental data this is only one possible choice. The corresponding decrease of effective viscosity ($S/\dot{\varepsilon}$) with strain rate is often called shear thinning [1].

However, the above equation is of limited applicability, if any. It may be appropriate for such cases as the continuous application of a positive shear rate, but there is hysteresis upon its reversal. Various attempts are underway to encapsulate such *history dependence* in a workable formulation. If the goal of our research is to find a continuum description, it faces this obstacle, which may well be the root cause of the deficiency in adequate treatments of rheology for yield stress materials, lamented above. So long as it is not overcome, a simulation (whether realistic or simplified) capturing all the local dynamics of the thin films is the more practical approach in many cases.

Dilatancy

Dilatancy traditionally describes the expansion of a dense packing of granular material when sheared [5] and was first described by Osborne Reynolds in 1885 [6]. In 2003 quasi-static computer simulations were reported which feature the same effect in liquid foams [7]. Its possible importance was suggested by the late pioneer of foam rheology, Henry Princen, in 1989 [8]. In foams, dilatancy constitutes the local increase of liquid fraction due to shear. Experimental evidence is still sparse. Marze et al. [9] designed an experiment where a foam is continuously locally sheared. Observations and measurements of local electrical conductivity (which increases with liquid fraction) show that the sheared region is wetter. This is attributed to *dynamic* dilatancy, i.e. a shear-*rate* dependent effect which differs from the static dilatancy described by current theory [7, 10], and is less easily calculated (see however our discussion of the Bretherton problem below).

Real Foams

Foams are usually polydisperse and disordered. Around the time of Kraynik's review, it began to be possible to simulate reasonably large (static) samples of disordered foam, if only in two dimensions [11], and to compute stress/strain curves [12] (Fig. 5), and hence shear modulus and yield stress.

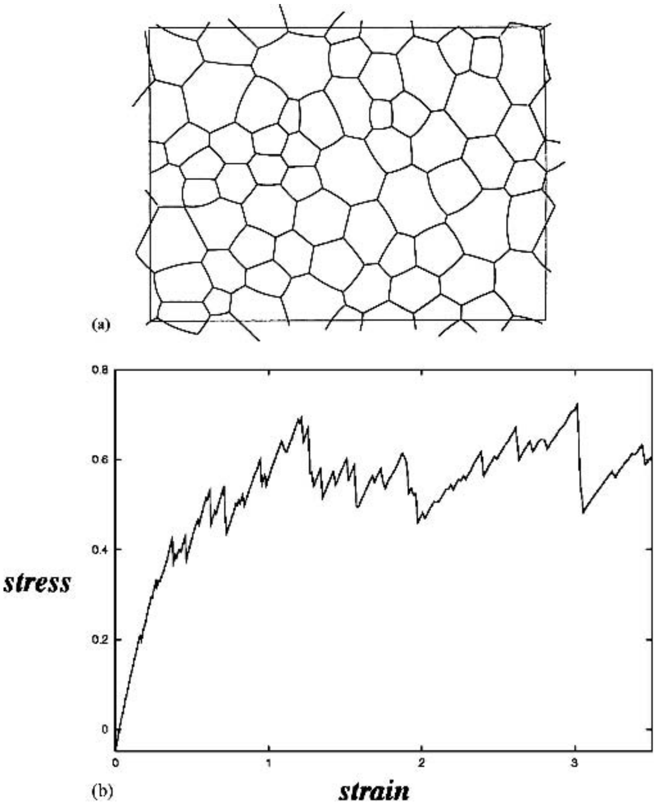

Fig. 5 (**a**) Early computer simulation of a two dimensional liquid foam [11] which can be used for the computation of a stress–strain curve as shown in (**b**) [12]. The slope of the initially linear variation of stress with strain is proportional to the shear modulus of the foam. In large bulk sample the jagged curve is smoothed out

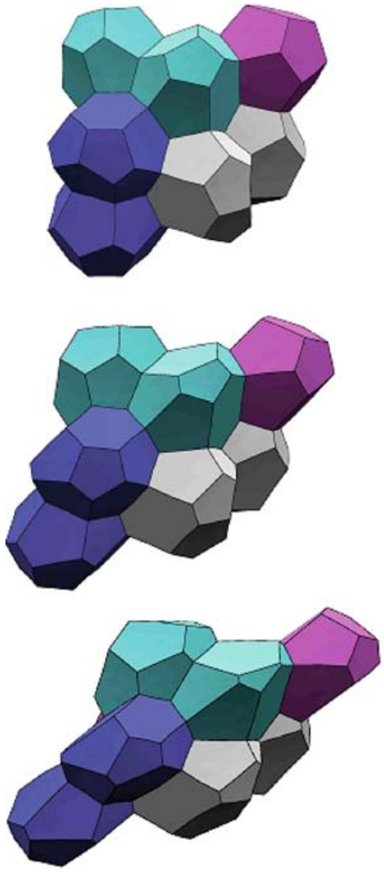

Fig. 6 The structure of three dimensional foams is conveniently computed using the Surface Evolver software of Ken Brakke [14] (free download at http://www.susqu.edu/brakke/). Here we show a simulation of the shearing of a Weaire–Phelan foam [13]. (Reproduced with kind permission of A.M. Kraynik)

In some ways, such a disordered system is much simpler than the ideal ordered one: for example the yield stress is not dependent on orientation. The shear elastic modulus is close to that of the honeycomb structure with the same mean cell area.

Nowadays similar calculations are pursued for 3d foams [13] as illustrated in Fig. 6, so we have a good appreciation of many quasi-static properties in both cases. There is good general agreement with experiment.

Experiments

We have not paid enough attention to experiment up to this point. There exists a plethora of rheological measurements in foams, with a variety of rheometers, pipes with and without constrictions etc. Mostly this has drawn on

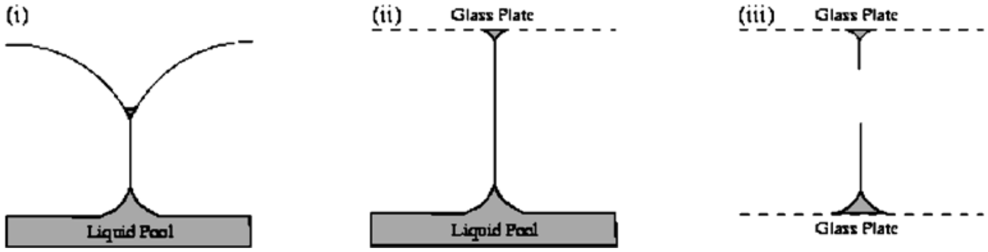

Fig. 7 Three different set-ups used for experiments with so-called two-dimensional foam. (i) Bragg raft, (ii) bubbles between a liquid pool and a glass-plate, (iii) bubbles trapped between two glass plates [19]

strong practical motivations in the field of chemical engineering: the consequent spirit of empiricism has not been very fruitful. Hence, as a greater interest in basic understanding developed in recent years, several groups have resorted to a familiar tactic of the foam physicist: a retreat into two dimensions. The shearing of a 2d foam sample can be viewed and imaged directly, recorded by video, and analysed in complete detail, in addition to relating the applied stress to the shear rate [15].

Such experiments have included the 2d equivalent of a Couette viscometer [16], as well as flow around obstacles [17] and through constrictions [18]. The recorded results have revealed some surprises and are still being digested.

There are qualitative disagreements between some of the experiments, which may be due to the use of different kinds of 2d foam. There are at least three kinds, depending on whether the bubbles are trapped between two plates, one plate and underlying liquid, or just floating on the liquid (Fig. 7) [19].

Simulations

If such experiments are to be simulated beyond the quasi-static approximation, we require the inclusion of dissipative forces. In an attempt to do this, we have developed the ideal *2d viscous froth model* [20]. In this the normal motion of each line (representing a film) is opposed by a drag force proportional to velocity. As will be explained below, this simple linear relation is usually not correct, but it has served to simplify the computational algorithm used in an initial search for qualitative understanding. It also has the merit of forming a bridge between foams and the curvature-driven boundary problems which are standard in the description of grain boundary motion [21].

Such understanding can only be transferred to 3d in the most general, qualitative way. The origin of viscous drag in that case must be completely different. It was considered long ago by Kraynik and others [2, 22, 23] but is still a region of uncharted waters.

One of the first specific applications of the 2d model concerned the flow of an ordered foam structure around a narrow bend as part of a feasibility study of discrete microfluidics [20]. The computer simulations successfully reproduced the experimentally observed swapping of neighbours of bubbles once a certain flow velocity is exceeded; see Fig. 4. Whereas it was initially thought that quasi-static simulations would be a sufficient guide for the design of components for the use in discrete microfluidics, we have found that there are large velocity-dependent effects, as illustrated by this case.

To date, a variety of standard rheological experiments, such as Couette shear (Fig. 8), creep (due to coarsening) or constant stress experiments have become accessible to similar modelling [24].

Our intention in introducing the viscous froth model has been to explore it exhaustively in a search for qualitative understanding of the role of dissipative effects. Its dir-

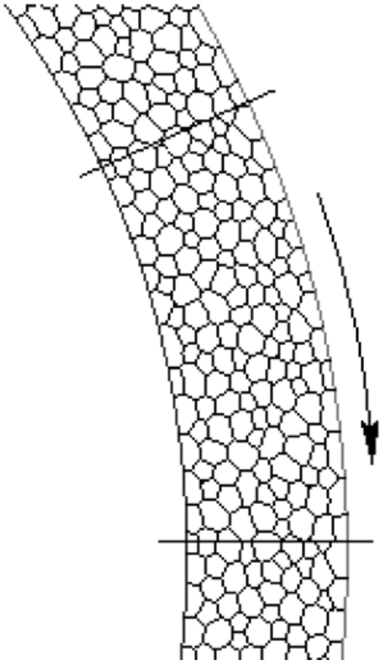

Fig. 8 Viscous froth simulation of a Couette shear experiment in which the outer boundary (with its contacting vertices) is moved clockwise, while the inner boundary (and its associated vertices) remains fixed. The *solid lines* demarcate the region used in the actual computation [24]

ect relevance to any particular system is questionable since other kinds of dissipative forces may well enter. Indeed Durand and Stone [25] have performed experiments with simple 2d configurations, accurately measuring their relaxation to equilibrium, and found rather different behaviour in some cases. Whenever a T1 change was produced the initial displacement of the vertices scaled linearly with time rather than with the square root which is the implication of the viscous froth model.

Moreover, the present viscous froth model is confined to the simulation of dynamic effects in dry foams. A recently developed lattice-gas based model allows for the simulation of foams over the entire range of liquid fraction [26]. It was applied to the flow of foam past an obstacle with the aim of determining the scale of the resulting bubble rearrangements [27]. Although this is a dynamic model, its representation of viscosity is inherently undetermined in lattice-gas models.

Weaire et al. [30] have recently formulated an elementary continuum model which can account for the localisation in the experiment of Debregeas et al. [16]. It combines the elements of the Bingham model with a viscous drag term associated with the two plates; the localisation length is given by the square root of ratio of the coefficients of Bingham viscosity and viscous drag.

The Bretherton Problem

One important source of drag in the 2d case is a wall effect. Whenever a foam slides along a wall, as in two of the 2d foams shown in Fig. 5, it is opposed by a dissipative force that depends on its velocity, which we had in mind in framing the viscous froth model.

It arises in 3d foam rheology as well, wherever there are walls. It is also a key factor in the motion of bubbles in channels (Fig. 4), in the context of the kind of microfluidics mentioned above.

In a classic paper [22], Bretherton concluded that the wall stress due to the frictional force of a single bubble rising in a tube scales as $\tau_w \propto (Ca)^{2/3}$, where the capillary number Ca is given by $Ca = \eta V/\gamma$ (for many purposes it represents velocity). Here η is the liquid viscosity, γ is the surface tension and V is the relative velocity of the bubble with respect to the wall. Naively, the power-law index for this viscous effect might be expected to be unity: it is the presence of free surfaces in the system and their variation with velocity that lies behind this non-trivial result.

This result has been found to apply to other situations that involve wall slip. Further afield, but still highly relevant here, is the relationship found for tension and rate of extension for the pulling of a film out of a Plateau border.

Bretherton's result was derived for a model in which the surfaces are mobile (that is, have zero surface viscosity). Denkov pursued the same approximations for immobile surfaces and found the exponent $1/2$ in this case [28].

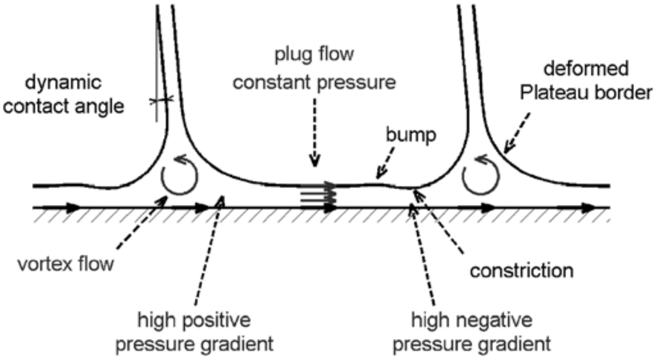

Fig. 9 Schematic of the key features of foam flow along a wall

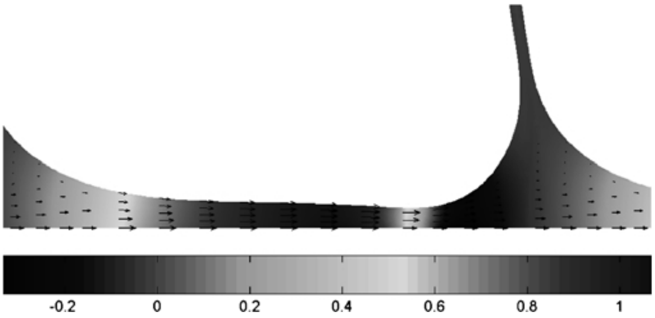

Fig. 10 Computed velocity profile and pressure fields for the flow of a foam along a wall

All of this has been based on analytic approximations for the flow in the thin film which adjoins the wall. It is the variation of the thickness of this film with velocity that is the root cause of the surprising nonlinear relationships that have been found in the above theories (and confirmed to a large degree by experiment).

We have recently succeeded in setting up a complete 2d simulation of the Bretherton problem, including the free surfaces which lie at its heart [29]. This exposes the full details of flow and the associated dissipation. At low velocities, Bretherton's semi-analytic result was confirmed. The simulation will be helpful in understanding the previous work and extending it to other situations.

Figure 9 illustrates the essential features of these calculations, and Fig. 10 is a detailed example. These calculations corroborate all of Bretherton's findings. In the case of wholly or partially immobile surfaces, there are difficulties in developing a 2d model. Pursuing the same line as Denkov, the same result was found. However, the role of surface stresses has yet to be incorporated.

Conclusions

Foams can provide a prototype for all those complex fluids that exhibit a yield stress. For that reason, as well as their intrinsic interest and applications, the rheological properties of foams are likely to be assiduously pursued in the years to come. It will take some time to reach the same competence that we enjoy in relation to static properties, but that end is almost in sight. Systematic and disciplined simulations offer a way forward.

Acknowledgement Research was funded by the European Space Agency (MAP AO-99-108:C14914/02/NL/SH, MAP AO-99-075: C14308/00/NL/SH) and Enterprise Ireland (BRG SC/2002/011). WD is an IRCSET Postdoctoral Fellow, funded by the Embark Initiative Ireland. AS was supported by the Conseil Régional de Rhône Alpes (France).

References

1. Weaire D, Hutzler S (1999) The physics of foams. Clarendon Press, Oxford
2. Kraynik AM (1998) Foam Flows. Ann Rev Fluid Mech 20:325–357
3. Drenckhan W, Cox SJ, Delaney G, Holste H, Weaire D, Kern N (2005) Rheology of ordered foams – on the way to Discrete Microfluidics. Colloids and Surfaces A: Physicochem Eng Aspects 263:52–64
4. Kern N, Weaire D, Martin A, Hutzler S, Cox SJ (2004) The two-dimensional viscous froth model for foam dynamics. Physical Review E 70:041411 (13 pages)
5. Durand J (2000) Sands, Powders and grains: an introduction to the physics of granular materials. Springer, New York
6. Reynolds O (1885) Proc Brt Assoc p 896, Proc R Instn GB, presented February 12
7. Weaire D, Hutzler S (2003) Dilatancy in liquid foams. Philosophical Magazine 83:2747–2760
8. Marze SPL, Saint-Jalmes A, Langevin D (2005) Protein and surfactant foams: linear rheology and dilatancy effect. Colloids and Surfaces A: Physicochem Eng Aspects 263:121–128
9. Princen HM, Kiss D (1989) Rheology of foams and highly concentrated emulsions. VI. An experimental study of the shear viscosity and yield stress of concentrated emulsions. J Coll Int Sci 121:176–187
10. Rioual F, Hutzler S, Weaire D (2005) Elastic dilatancy in wet foams: a simple model. Colloids and Surfaces A: Physicochem Eng Aspects 263:117–120
11. Kermode JP, Weaire D (1983) Computer simulation of a two-dimensional soap froth. 1. Method and motivation. Phil Mag B 48:245–259
12. Hutzler S, Weaire D, Bolton F (1995) The effects of Plateau borders in the two-dimensional soap froth, III. Further results. Phil Mag B 71:277–289
13. Kraynik AM, Neilsen MK, Reinelt DA, Warren WE (1999) Foam Micromechanics. In: Sadoc JF, Rivier N (eds) Foams and Emulsions. Kluwer Academic Publishers, Dordrecht/Boston/London
14. Brakke K (1992) The Surface Evolver. Experimental Mathematics 1:141–165
15. Lauridsen J, Twardos M, Dennin M (2002) Shear-induced stress relaxation in a two-dimensional wet foam. Phys Rev Lett 89:098303
16. Debregeas G, Tabuteau H, di Meglio JM (2001) Deformation and flow of a two-dimensional foam under continuous shear. Phys Rev Lett 87:178305
17. Dollet B, Elias F, Quilliet C, Huillier A, Aubouy M, Graner F (2005) Two-dimensional flows of foam: drag exerted on circular obstacles and dissipation. Colloids and Surfaces A: Physicochem Eng Aspects 263:101–110
18. Jiang Y, Asipauskas M, Glazier JA, Aubuoy M, Graner F, Jiang Y (2000) Ab initio derivations of stress and strain in fluid foams. In: Zitha P, Banhart J, Verbist G (eds) Foams, emulsions and their applications. MIT-Verlag, Bremen, p 297–304
19. Cox SJ, Vaz MF, Weaire D (2003) Topological changes in a two-dimensional foam cluster. Eur Phys J E 11:29–35
20. Kern N, Weaire D, Martin A, Hutzler S, Cox SJ (2004) The two-dimensional viscous froth model for foam dynamics. Physical Review E 70:041411 (13 pages)
21. Weaire D, McMurry S (1997) Some fundamentals of grain growth. Solid State Physics – Advances in Research and Applications 50:1–36
22. Bretherton FP (1961) The motion of long bubbles in tubes. J Fluid Mech 10:166–188
23. Princen HM (1985) Rheology of foams and highly concentrated emulsions. II. Experimental study of the yield stress and wall effects for concentrated oil-in-water emulsions. J Coll Int Sci 105:150–171
24. Cox SJ (2005) A viscous froth model for dry foams in the Surface Evolver. Colloids and Surfaces A: Physicochem Eng Aspects 263:81–89
25. Durand M, Stone HA. Relaxation time associated with the elementary topological T1 process in a two-dimensional foam. (to be submitted)
26. Sun Q, Hutzler S (2004) Lattice gas simulations of two-dimensional liquid foams. Rheologica Acta 43:567–574
27. Sun Q, Hutzler S (2005) Studying localised bubble rearrangements in 2D liquid foams using a hybrid lattice gas model. Colloids and Surfaces A: Physicochem Eng Aspects 263:27–32
28. Denkov ND, Subramanian V, Gurovich D, Lips A (2005) Wall slip and viscous dissipation in sheared foams: Effect of surface mobility. Colloids and Surfaces A: Physicochem Eng Aspects 263:129–145
29. Saugey A, Drenckhan W, Weaire D (2006) Wall slip of bubbles in sheared foams. Physics of Fluids (in press)
30. Weaire D, Janiaud E, Hutzler S (2006) Two dimensional foam rheology with viscous drag. arXiv:cond-mat/0602021 v1 1 Feb 2006

Progr Colloid Polym Sci (2006) 133: 106–110
DOI 10.1007/2882_047

Julian Eastoe

Photo-destructible Surfactants in Microemulsions

Abstract A photo-destructible surfactant sodium 4-hexylphenylazosulfonate (C6–PAS, Scheme 1) has been employed in normal AOT-stabilized water-in-heptane microemulsions. Phase studies are consistent with initially homogeneous microemulsions, for which significant changes in stability as a function of UV irradiation time are observed. Photolysis of C6–PAS in these systems results in eventual separation of water to yield a Winsor II system. Proton NMR spectra show that C6–PAS undergoes UV-induced decomposition, to yield a mixture of 4-hexylphenol and the non-surface active hexylbenzene as main product. This photo-triggered breakdown gives rise to changes in adsorption and aggregation properties of C6–PAS, representing a unique route to induce microemulsion destabilization. Small-angle neutron scattering (SANS) was used to follow the resulting UV-induced shrinkage of the water nanodroplets: a maximum volume decrease was found to be in the order of 60–70%. Multi-contrast SANS experiments gave further insight, for example it was demonstrated that the surfactant shell thickness remained constant (~ 9 Å). This study represents a novel example of light-induced microemulsion destabilization.

Keywords Photo-aggregation · Photo-surfactants · Surfactants · Small-angle neutron scattering · w/o microemulsion

Julian Eastoe (✉)
School of Chemistry, University of Bristol,
Bristol, BS8 1TS, UK
e-mail: julian.eastoe@bris.ac.uk

Introduction

Surfactant molecules adsorb at interfaces, thereby modifying surface properties: this is the physical chemistry underlying biological cell membranes, lung action, emulsion and foam formation and detergents. For chemically inert surfactants used in common commercial products, control over molecular aggregation and adsorption states is normally only achieved after significant changes, like addition of electrolyte, jumping pH or temperature. Now imagine a photosensitive surfactant, which could be "switched off" via a photolysis pathway that generates non-surface-active products. The concept is that UV light could be used to control surface activity and drive destabilization of interfaces. In principle, other properties could be affected though changes in aggregate morphology, leading ultimately to breakdown in structures such as micelles, vesicles and emulsion drops. A recent review of the latest advances in photosurfactants, covering a wide range of different chemistries and physico-chemical effects can be found elsewhere [1]. The photo-surfactant used here, sodium 4-hexylphenylazosulfonate (C6–PAS, shown in Scheme 1), was introduced by Sherrington et al. [2], and has been employed previously in emulsion polymerization [3], for which a successful UV-induced separation of polymethylmetacrylate (PMMA) latex particles was demonstrated.

As shown in Scheme 1, this C6–PAS (**1**) provides opportunities for photo-control of properties, since in the photoscission reaction oil-loving organic chains can be

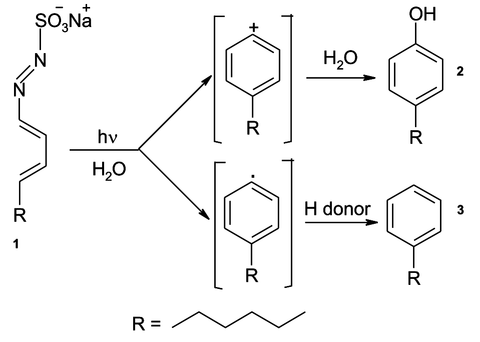

Scheme 1 Photolysis of sodium 4-hexylphenylazosulfonate (C6–PAS), a surfactant that is broken up into its water and oil-loving segments by light

split away from the water-soluble portion. Hence with photodegradable surfactants like 1 it is possible to controllably "switch off" the surface activity, by generation of inactive compounds like 2 and 3. In fact 3 is actually an oily substance with no interfacial activity whatsoever, and should partition strongly into organic solvents. The example described here concerns a water-in-oil nanodroplet dispersion (microemulsion), stabilized by a mixture of **1** and common Aerosol-OT (AOT). This latter surfactant is inert under the UV irradiation employed in the experiments. The concept is shown schematically in Scheme 2. Initially nanometer-sized spherical water droplets are present, encapsulated by the interfacial surfactant film, and dispersed in an organic solvent. Application of UV light ($h\nu$) is expected to selectively destroy the photo-surfactant **1**, leaving the inert co-surfactant AOT intact. As a result the composition of the stabilizing layer will change in favor of AOT surfactant. This should then feed through to changes in the microemulsion phase stability, and also the preferred size of the nanodroplets (Scheme 2). Here, the photochemical reactions have been followed, and characterized by Nuclear Magnetic Resonance (NMR) spectroscopy, and changes in the nanodroplet structures in water-in-oil (w/o) microemulsions containing C6-PAS have been examined by contrast variation small-angle neutron scattering (SANS) experiments.

The destabilization or resolution of microemulsions and emulsions is an important process in areas such as pharmaceuticals, organic synthesis, oil recovery, drug delivery, cosmetics and nanotechnology. As such these separations represent product recovery/release mechanisms. Several methods have been used to affect phase separation of thermodynamically stable microemulsions, such as pervaporation, addition of electrolytes, low or high temperature, pH change and saturation with water and finally addition of anti-solvents (for references see citations in [1]). Here, the utility of a photo-surfactants in microemulsions is demonstrated, therefore, extending the applications to oil–water interfaces and nanoreactor droplets, which are systems of interest to the nanotechnologist.

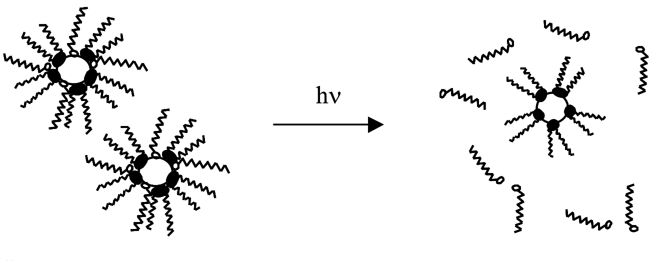

Scheme 2 The concept behind photo-tunable films in microemulsions comprising a photo-destructible surfactant

Experimental

Materials

Photo-surfactant **1** (sodium 4-hexylphenylazosulfonate C6–PAS) was synthesized, purified and characterized as detailed elsewhere [2, 4, 5]. The Krafft temperature ($T_k =$ 25 °C) and the critical micelle concentration (CMC at 30 °C $= 2.25 \times 10^{-2}$ mol dm^{-3}) compare favorably with literature values [2, 4, 5]. The water-in-oil microemulsions were prepared containing AOT sodium salt (Sigma, 99% min, recrystallized from $CHCl_3$ and purified over activated charcoal), *n*-heptane (Aldrich, HPLC grade, 99% min), *d*-heptane (Aldrich, 99%), D_2O (Fluorochem, 99.9%) and **1**. The surfactant is hence a mixture of C6–PAS and AOT with a composition defined by $X_1(\%) = 100\{[\mathbf{1}]/([\mathrm{AOT}] + [\mathbf{1}])\}$; the total concentration of surfactant $\{[\mathbf{1}] + [\mathrm{AOT}]\}$ was either 0.05 or 0.10 mol dm^{-3}. The initial dispersion ratio prior to UV-irradiation w ([water]/[surfactant]) was held constant at $w = 40$, but total surfactant concentration and mole ratios were varied (Table 1). Samples were irradiated with a 100 W high pressure Hg lamp (LPS-220/250 power supply from PTI;

Table 1 Fitted droplet core radius as a function of $X_1(\%)$ and $\{[\mathrm{AOT}] + [\mathbf{1}]\}$, before and after irradiation (core contrast)

$\{[\mathrm{AOT}] + [1]\}$/ mol dm^{-3}	$X_1(\%)$	Core radius, before irradiation/Å	Core radius, after irradiation/Å	% Volume Shrinkage
0.05	0.0	55.2	55.1	0.3
0.05	2.5	56.9	45.1	50.2
0.05	5.0	58.4	43.2	59.7
0.05	7.5	58.1	43.1	59.1
0.05	10.0	58.8	42.9	61.0
0.10	0.0	52.5	51.6	5.1
0.10	2.5	53.0	44.1	42.4
0.10	5.0	55.0	42.6	53.7
0.10	7.5	55.7	37.4	69.7
0.10	10.0	57.5	35.8	75.9

lamp housing from HI-TECH Scientific and Mercury short arc photo optic lamp HBO® 103 W/2), polychromatic to maximize photon flux.

NMR

^{1}H NMR spectra were measured as a function of UV irradiation time with a JEOL Delta GX/270, for microemulsion samples initially at $w = 40$ $X_1(\%) = 7.5\%$ and total surfactant concentration $\{[\mathbf{1}] + [\mathrm{AOT}]\} = 0.05\,\mathrm{mol\,dm^{-3}}$. These systems were prepared in *d*-cyclohexane (Goss Scientific, 99.5% D) instead of the more expensive *d*-heptane (note *h*-heptane and *d*-heptane was used for droplet sizing by neutron scattering). This switch in solvent is known to affect phase diagram and maximum water uptake; hence, the compositions of the cyclohexane samples were arranged to provide single stable phases at 25 °C. The use of cyclohexane in place of heptane for these NMR experiments will have no significant effect on the conclusions concerning photoproduct formation. Reference microemulsions containing standards (Aldrich, 99%) 4-octylphenol (structurally similar to **2**) and 4-octylbenzene (similar to **3**) were also characterized in order to determine the spectra of the expected photoproducts. The octyl instead of the hexyl-substituted markers had to be used since the latter are not commercially available; the ^{1}H NMR spectra and chemical shifts are expected to be very similar (when comparing octyl vs. hexyl).

Small-Angle Neutron Scattering (SANS)

SANS experiments were carried out in the time-of-flight LOQ instrument at ISIS, UK, or at the D22 diffractometer at ILL (Grenoble, France). The experimental conditions and data normalization procedures were as described elsewhere [4, 5]. D_2O water droplets were contrasted against *h*-surfactant and *h*-heptane (core contrast) whereas *h*-surfactant shell was contrasted against D_2O and *d*-heptane (shell contrast). Measurements were conducted at 25 °C except for $X_1 = 0$ and 2.5% which were done at 40 °C. For post-irradiated bi-phasic systems the neutron beam was scattered from the upper transparent microemulsion phase, missing the denser separated part. Firstly, equilibrium experiments (core contrast) were performed in order to study the effect of concentration of **1**, measuring the scattering before and after UV-irradiation for a fixed time (1 hour for $\{[\mathbf{1}] + [\mathrm{AOT}]\} = 0.05\,\mathrm{mol\,dm^3}$, 2 hours for $\{[\mathbf{1}] + [\mathrm{AOT}]\} = 0.10\,\mathrm{mol\,dm^3}$); the completion of the reaction was confirmed by UV-Vis absorption. Equilibrium experiments at a chosen concentration ($X_1(\%) = 7.5\%$ and $\{[\mathbf{1}] + [\mathrm{AOT}]\} = 0.05\,\mathrm{mol\,dm^3}$) and two different contrasts (core and shell) were also performed.

SANS data were fitted using FISH [6], which is a flexible multi-model package comprising a variety of different form factors P(Q), structure factors S(Q), and polydispersity functions. After extensive trials, including Porod and Guinier approximations, and based on previous literature [7] the most appropriate model was found to be for Schultz polydisperse two shell hard spheres. In the case of multi-contrast experiments a simultaneous model was used to analyze the core and shell contrast experiments together [8]. The Schultz polydispersity factor was a fitting parameter, and in all cases was between 0.20–0.23, which is consistent with previous studies of AOT microemulsion systems [e.g. 7].

Results and Discussion

Photochemical studies of the microemulsion containing C6–PAS show obvious effects of UV irradiation (Fig. 1). Prior to irradiation a clear monophasic system was present (Fig. 1a): after a 10 min burst of UV partial separation of the water and loss of some of the photosurfactant gave rise to an opaque emulsion, shown in Fig. 1b. After 1 hour irradiation, and 1 hour equilibration a biphasic system resolved comprising a Winsor II microemulsion, which is an upper oily w/o phase in equilibrium with an aqueous phase (Fig. 1c).

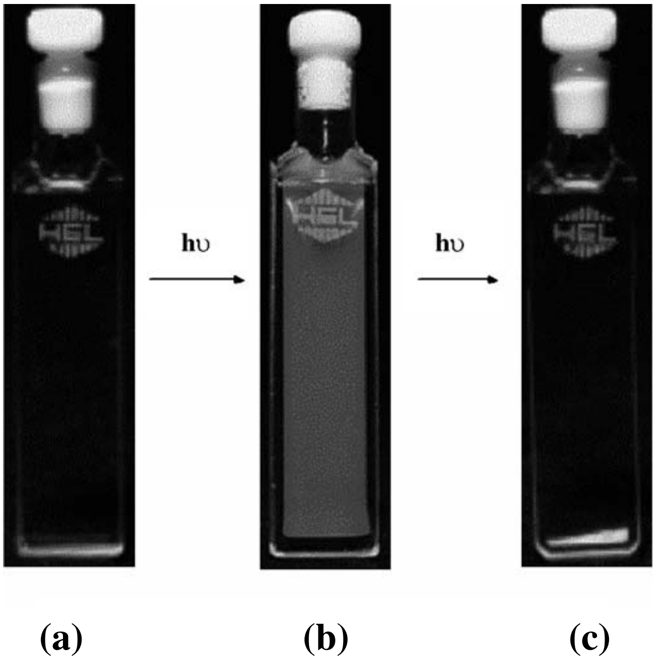

Fig. 1 Photo-induced destabilization of AOT/water/heptane microemulsions containing C6–PAS. $X_1(\%) = 7.5$ and $\{[\mathrm{AOT}] + [\mathbf{1}]\} = 0.05\,\mathrm{mol\,dm^3}$. **a** Initial transparent single-phase sample, **b** intermediate irradiated milky emulsion, **c** Winsor II microemulsion with excess aqueous separated phase

NMR

^{1}H NMR spectra show that C6–PAS undergoes UV-induced decomposition (Fig. 2), to yield a mixture of 4-hexylphenol and hexylbenzene (Scheme 1). It might be expected that the photolysis pathway is strongly dependent on solvent type or microenvironment: in a bulk aqueous phase below the CMC the ionic mechanism would yield photoproduct hexylphenol. In more hydrophobic environments such as micelles, or in the present case w/o droplets, hexylbenzene would be favored.

Figures 2a,b show ^{1}H NMR spectra in the high δ aromatic region for microemulsions containing only AOT as the surfactant and related amounts ($X_1(\%) = 7.5\%$) of standards 4-octylphenol (equivalent to expected spectrum for **2**) and octylbenzene (equivalent to **3**) respectively. Figures 2c–f show corresponding spectra for microemulsions stabilized by the C6–PAS + AOT mixture ($X_1(\%) = 7.5\%$, $\{[\text{AOT}] + [1]\} = 0.10\,\text{mol}\,\text{dm}^{-3}$) as a function of irradiation time. The peaks initially from surfactant **1** ($\delta = 7.86$ and 7.26) decay as photolysis proceeds, whereas new peaks also appear. The lines at $\delta = 6.71$ and $\delta = 6.88$ indicate the presence of an alkylphenol **2**, while the multiplet at $\delta = 7.1$ is characteristic of alkylbenzene **3**. The temporary doublets that appear at intermediate irradiation times (Figs. 2d,e) around $\delta = 8.60$ and 7.55 could be attributed to an intermediate diazonium salt; further analysis is needed to confirm the presence of such intermediates. The reaction is essentially complete, and a photostationary state is reached after about 110 minutes irradiation, corresponding to a composition of 10.6% of **1**, 37.0% of **2** and 52.4% of **3**, based on the initial amount of **1**. In terms of remaining **1** it is difficult to discriminate between this and other potential (hard to identify) photoproducts, since the doublet at $\delta = 7.26$ indicating the presence of **1** overlaps partially with the multiplet from **3**. It is possible that as the reaction proceeds, and the sample goes from monophasic to Winsor II, the position of the peaks could shift slightly (peak at $\delta \sim 7.8$). Nevertheless, the main photoproduct appears to be non-surface active alkylbenzene **3**, indicating that the reaction is preferentially following a radical mechanism (Scheme 1). Considering the final composition (total surfactant concentration decreases to $\sim 0.045\,\text{mol}\,\text{dm}^{-3}$), the effective w value increases from $w = 40$ to about $w = 44$; furthermore, the major photoproduct (hexylbenzene) is expected to partition strongly into the continuous oil phase, rather than contribute towards any surface-activity.

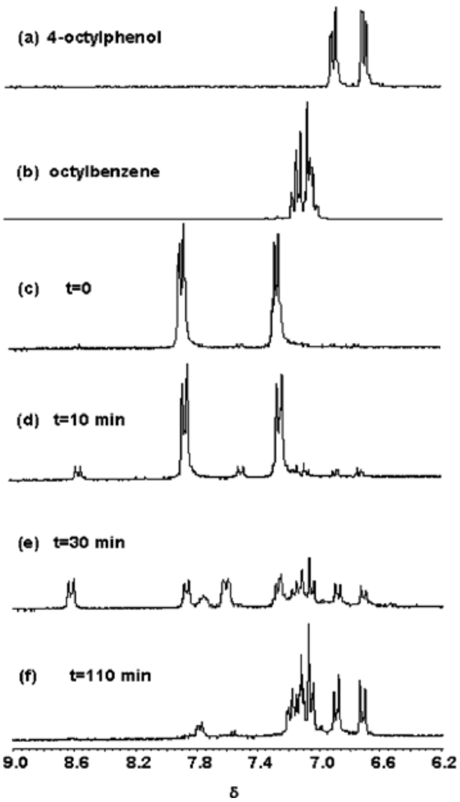

Fig. 2 Partial ^{1}H NMR spectra of AOT/water/d-cyclohexane microemulsions containing: **a** 4-octylphenol; **b** octylbenzene; **c** non-irradiated C6–PAS; **d**–**f** are samples from **c** recorded after different irradiation times

Small-Angle Neutron Scattering

The phase separation seen after exposure to UV might be expected to result in shrinkage of the D_2O droplet cores: small-angle neutron scattering (SANS) was used to follow possible changes in the microemulsion structure. To this end contrast variation SANS experiments were performed, with water core (D_2O + h-surfactants + h-oil) and surfactant shell contrast (D_2O + h-surfactants + d-oil). Owing to space limitations the core contrast SANS curves are not shown. Results from fitting analyses are summarized in Table 1 for samples as a function of X_1, which were irradiated for sufficiently long to achieve the photostationary state.

In general the mean droplet core radius becomes smaller after irradiation, consistent with the accompanying loss of water from the dispersion. In all cases the % of volume shrinkage (related to the volume of lost water) is around 50–60% for samples when $\{[\text{AOT}] + [\mathbf{1}]\} = 0.05\,\text{mol}\,\text{dm}^{-3}$, and ~ 40–76% with $\{[\text{AOT}] + [\mathbf{1}]\} = 0.10\,\text{mol}\,\text{dm}^{-3}$. This shrinkage is evidently due to the destruction of nearly all present C6–PAS as indicated by ^{1}H NMR. Hence, the change in chemical nature of the surfactant moves the system to a different position in the phase diagram and therefore it becomes unstable and phase separates. With increasing X_1 the droplet radius slightly increases. Increasing X_1 represents replacement of the double chain AOT, which favors $-$ve curvature, with the single-chain **1** favoring $+$ve curvature. These second

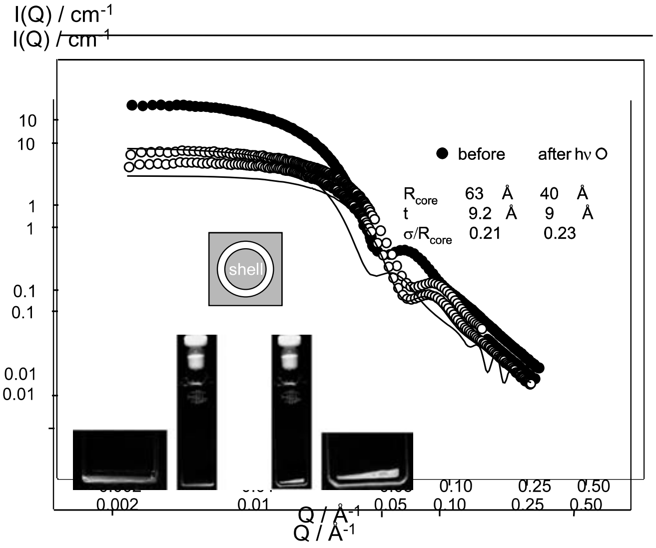

Fig. 3 SANS data in shell contrast from D_2O/*h*-AOT/*d*-heptane microemulsions containing C6–PAS at $X_1(\%) = 7.5$ and $\{[\text{AOT}] + [\mathbf{1}]\} = 0.05\ \text{mol dm}^3$ before and after irradiation. Lines are simultaneous fits to the shell scattering, but constrained by both core and shell contrast data sets

order effects are consistent with previous studies of mixtures of inert double chain and single chain surfactants in microemulsions [9].

Shell contrast (*d*-water/*h*-surfactant/*d*-oil) is used to see a "hollow shell" of surfactant, with characteristic interference pattern. As shown elsewhere, a robust analysis can be performed by a simultaneous fit to data from the two different contrasts (core, shell [8]). As shown in Fig. 3, the shifts in maxima/minima to high Q are consistent with UV-induced shrinkage of the water core. Model analyses show that before UV the mean water droplet radius is ~ 63 Å, decreasing to ~ 40 Å in the irradiated sample. These dimensions are in acceptable agreement with the analyses of core contrast data (Table 1). Fitted shell thickness t are given on Fig. 3 and this dimension remains almost unaltered: the value of ~ 9 Å is in good agreement with previous studies of AOT-stabilized water-in-heptane microemulsions [8]. The molecular length of both surfactants is very similar, and therefore destruction of **1** is in this context is essentially equivalent to reducing the effective surfactant concentration, rather than affecting the interfacial thickness significantly.

Conclusions

Formulation of water-in-oil microemulsions containing a photolyzable surfactant C6–PAS generates novel light-sensitive dispersions. Photolysis of the C6–PAS component changes the surfactant composition, driving changes in phase stability and internal structure of the microemulsions. This UV-driven destruction of C6–PAS is equivalent to reducing the effective surfactant concentration, which has consequences for the stability and size of the dispersed water droplets.

Chemicals like C6–PAS **1** represent a new generation of surfactants with added functionality and tunability, offering exciting new possibilities for controlling surface tensions, molecular aggregation and bulk fluid properties such rheology. Recent research [1] shows this to be a general concept, and photo-surfactants can be employed to affect different properties such as adsorption, micellization and formation of vesicles, emulsion stability and gelation of both aqueous and organic phases.

References

1. Eastoe J, Vesperinas A (2005) Soft Matter 1: in press
2. Dunkin IR, Gittinger A, Sherrington DC, Wittaker P (1996) J Chem Soc, Perkin Trans 2:1837
3. Mezger T, Nuyken O, Meindl K, Wokaun A (1996) Progress in Org Coatings 29:147
4. Eastoe J, Sanchez-Dominguez M, Wyatt P, Cumber H, Burnett G, Heenan RK (2003) Langmuir 19:6579
5. Eastoe J, Sanchez-Dominguez M, Wyatt P, Cumber H, Cumber H, Heenan RK (2003) Langmuir 20:1120
6. Heenan RK (1989) FISH Data Analysis Program; Rutherford Appleton Laboratory; Report RAL-89–129; CCLRC: Didcot, UK
7. Kotlarchyk M, Chen S-H, Huang JS, Kim MW (1984) Phys Rev A 29:2054
8. Eastoe J, Hetherington KJ, Dalton JS, Sharpe D, Lu JR, Heenan RK (1997) J Coll Int Sci 190:449
9. Bumajdad A, Eastoe J, Griffiths P, Steytler DC, Heenan RK, Lu JR, Timmins P (1999) Langmuir 15:5271

Progr Colloid Polym Sci (2006) 133: 111–115
DOI 10.1007/2882_046

Hui Ning
Rio Kita
Simone Wiegand

Soret Effect in a Nonionic Surfactant System

Hui Ning · Simone Wiegand (✉)
Forschungszentrum Jülich GmbH,
IFF – Weiche Materie, 52428 Jülich,
Germany
e-mail: s.wiegand@fz-juelich.de

Rio Kita
Department of Physics, Tokai University,
259-1292 Hiratsuka, Japan

Abstract We studied the thermal diffusion behavior of $C_{10}E_8$ (decyl octaethylene glycol ether) in water by means of thermal diffusion forced Rayleigh scattering (TDFRS). We determined the two diffusion coefficients D_T, D and the Soret coefficient S_T in a concentration range from $w = 5$ wt % to 25 wt % in a temperature range from $T = 20\,°C$ to $40\,°C$. The obtained Soret coefficients S_T were positive for all temperatures and concentrations. Additionally, we also performed dynamic light scattering experiments in the same temperature range in order to compare the measured diffusion constants and characterize the system. Special attention was paid to the tiny amount of inert dye which needs to be added for absorption and thermalization of the light energy. The influence of an organic dye and an organic coloured salt on the experimentally determined transport properties has been studied. The results show that all coefficients are independent of the choice of the dye for this particular surfactant system.

Keywords Ludwig–Soret effect · Thermal diffusion · Diffusion · Nonionic surfactant

Introduction

Surfactants are widely used as emulsifying agents and detergents and have been investigated thoroughly [1, 2]. Those systems often exhibit interesting physicochemical properties. Especially nonionic surfactants of the general type C_mE_n, where m indicates the number C-atoms in the hydrocarbon chain, and n represents the number of ethylene oxide units $(-OCH_2CH_2)_n$-OH, have been studied intensively [3–5]. Due to alteration of m and n, headgroup interactions and micelles size can be changed systematically. The delicate balance of alkyl-chain/water repulsion and repulsion between adjacent headgroups within the micelle, together with surface curvature and limitations due to alkyl chain packing lead to specific characteristics of C_mE_n as structural changes of the micelles, phase separation, critical phenomenon, and so on [3, 4]. Furthermore, the addition of electrolytes and nonelectrolytes have a large effect on the phase behavior of nonionic surfactants because of their effect on the water structure and their hydrophilicity.

So far many properties of the nonionic surfactant systems have been investigated but there is limited knowledge on the thermal diffusion behavior for nonionic micellar solutions. Thermal diffusion describes the thermal diffusion current in the presence of a temperature gradient. In a binary fluid mixture with non-uniform concentration and temperature, the mass flow J_m of one component contains both contributions stemming from the concentration and from the temperature gradient [6]:

$$J_m = -\rho D \nabla w - \rho w \,(1 - w)\, D_T \nabla T \,. \qquad (1)$$

D denotes the collective diffusion coefficient, D_T the thermal diffusion coefficient, ρ the mass density, and w the concentration in weight fractions. In a stationary state where the diffusion flow J_m vanishes the Soret coefficient

S_T is given by

$$S_T \equiv \frac{D_T}{D} = -\frac{1}{w\,(1-w)}\frac{\nabla w}{\nabla T}\,. \tag{2}$$

In recent years, considerable experimental effort has been devoted to the thermal diffusion of complex molecular systems, such as micellar phases of soluted surfactants, colloidal suspensions, and polymer solutions [7–11]. The Soret coefficient has been measured as a function of various parameters, such as charge, temperature and concentration of the diffusing particles, and the salt content [7]. For aqueous systems it turned out that hydrogen bonds can change the thermal diffusion behavior significantly by reversing the sign [10]. All experiments show that specific interactions and surface effects have a strong impact on thermodiffusive behavior. Also, the formation of micelles is dominated by interfacial effects. Therefore, it is expected that the shape of the micelles has an influence on the thermal diffusion behavior.

In the past, mainly ionic surfactant systems have been investigated [12, 13]. Recently, strong interaction effects for the Soret coefficient of an ionic micellar system have been observed, where the salt concentration dependence of the Soret coefficient for the micellar system is reversed going from very dilute to higher surfactant concentrations [7]. There is, however, very little knowledge about the thermal diffusion behavior of nonionic surfactants except for some preliminary studies on C_8E_4 in a thermal diffusion cell in the group of Piazza [14]. Due to the fact that the surfactant has a lower density than water and moves to the cold side, the measurements were complicated by convection.

Convection problems can be effectively avoided by the so called thermal diffusion forced Rayleigh scattering (TDFRS) method. In the experiment rather small temperature differences of several μK are sufficient to obtain a reliable measurement signal. A drawback of the method might be the fact that a tiny amount of dye is needed to convert the electric field energy by absorption into thermal energy. The chosen dye should show a strong optical absorption at the writing wavelength, but only a weak absorption at the readout wavelength of the otherwise transparent liquids. Ideally, the dye is inert, which means that the dye should not show any photobleaching and does not contribute to the diffraction signal. For organic mixtures it has been shown that the addition of an organic dye leads only to a very weak contribution, which does not influence the mean values but leads to slightly asymmetric error bars [15]. In the case of aqueous systems it is much harder to find an inert dye. Typically, the water soluble dyes change their properties and are dependent of pH, ionic strength and other parameters. For the investigation of the surfactant system we used two different dyes: basantol yellow [16], a tri-valent metal organic salt which is directly soluble in water, and alizarin, an organic dye which becomes soluble only in the presence of the surfactant. Both organic compounds probably change the balance of the hydrogen bond formation and it is expected that the phase behavior of the micelles is influenced. Especially for electrolytes there are numerous studies for surfactant systems [17–23]. Depending on the nature of the anion the two-phase boundary either shifts to lower or higher temperatures [23]. Due to the fact that the added dye is a tri-valent salt we expect a change of the phase behavior by addition of the dye. In order to study the influence of the dye we performed all measurements with both dyes.

In this paper we describe thermal diffusion measurements of the surfactant $C_{10}E_8$ in water in a concentration range from $w = 5$–25%wt at 20, 30 and 40 °C. Additionally, we also performed dynamic light scattering measurements to characterize the system.

Experiment and Data Analysis

Sample Preparation and Contrast Factors

$C_{10}E_8$ ($[CH_3(CH_2)_9-(OCH_2CH_2)_8OH]$, decyl octaethylene glycol ether; purity ≥ 98%; M.W. = 510.72) was purchased from Fluka BioChemika, Japan. The surfactant was used without further purification. The alizarin was purchased from Riedel-deHaën and basantol yellow we obtained from BASF.

In order to prepare the samples for the TDFRS experiment a small amount of dye needs to be added to the samples. The dye has an absorption band at the wavelength of the writing beam, $\lambda_w = 488$ nm and is transparent at the read-out wavelength, $\lambda_r = 633$ nm. The absorption coefficient at λ_w was adjusted to a value $\alpha = 1.5$–$3\,\mathrm{cm}^{-1}$. This low absorption leads to a weight fraction of less than 10^{-5} basantol yellow. The weight fraction of the alizarin is of the same order of magnitude.

If we used basantol yellow as the dye, we first prepared an aqueous solution with the desired absorption using deionized water (Milli-Q). Then the surfactant was added and stirred at least for 4 hours at room temperature. In the case of the organic dye alizarin, we added the dye and the surfactant at the same time. The mixture was then also stirred at least for 4 hours at room temperature to mix all components thoroughly. After preparation the solutions were filtrated by a 0.45 μm filter (Spartan) directly in the sample cells. The sample cells for the TDFRS experiment were Quartz cells (Hellma) with a layer thickness of 0.2 mm. For the light scattering experiment we used cylindrical glass cells with an inner diameter of 8.5 mm. The optical path length of the cells for the $(\partial n/\partial T)_{w,p}$ experiment was 10 mm.

The temperature derivative of the refractive index $(\partial n/\partial T)_{w,p}$ was determined at $\lambda_r = 632.8$ nm, using a scanning Michelson interferometer [24]. Figure 1 shows $(\partial n/\partial T)_{w,p}$ of $C_{10}E_8$ in water as a function of the weight fraction. The refractive index increments $(\partial n/\partial w)_{p,T}$ were

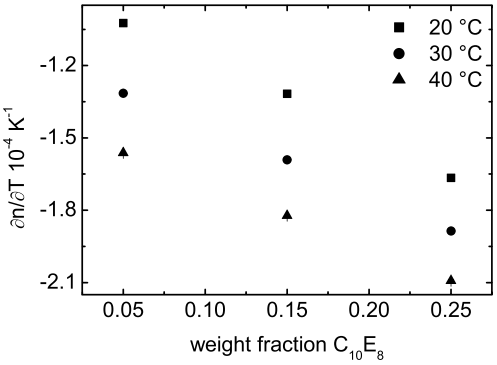

Fig. 1 $(\partial n/\partial T)_{w,p}$ of $C_{10}E_8$ in water as a function of the surfactant weight fraction at 20 °C (■), 30 °C (●) and 40 °C (▲). The samples contained the same small amount of basantol yellow [16] as used in the TDFRS experiment

determined with an Abbe refractometer at three different temperatures $T = 20, 30$ and 40 °C to $(\partial n/\partial w)_{p,T} = 0.134$, 0.132 and 0.130, respectively.

TDFRS and DLS

The TDFRS experiment operates as follows: A grating, created by the interference of two laser beams ($\lambda_w = 488\,\text{nm}$), is written into a sample. A small amount of dye, dissolved in the sample, converts the intensity grating into a temperature grating (thermal grating), which in turn causes a concentration grating by the effect of thermal diffusion. Both gratings contribute to a combined refractive index grating, that is read out under Bragg condition by another laser of different wavelength ($\lambda_r = 632.8\,\text{nm}$). Analyzing the time dependent diffraction efficiency the transport coefficients (mutual diffusion coefficient D, thermal diffusion coefficient D_T and Soret coefficient S_T) can be obtained, requiring neither external calibration nor absolute intensity measurement. Other characteristic features of TDFRS experiments are the elimination of convection due to the low temperature modulation of several μK, and the short equilibration times of the order of milliseconds, as well as the simultaneous yielding of the transport coefficients in one single measurement. A more detailed description of the set-up can be found elsewhere [25, 26].

The dynamic light scattering (DLS) measurements were carried out in the angular range $20\,°\text{C} < \theta < 120\,°\text{C}$. A Kr-ions laser was used as the light source (wave length $\lambda = 647.1\,\text{nm}$). An ALV-5000E correlator was used to measure the correlation function of scattered light. The cylindrical sample cell was placed in a temperature controlled bath with a temperature stability of $\delta T = \pm 0.1\,°\text{C}$, the temperature of which was controlled with an uncertainty of 0.1 °C. The sample solutions were kept at measured temperature for at least 30 minutes to ensure equilibrium before starting data acquisition.

Data analysis

The normalized heterodyne diffraction intensity of the TDFRS experiment for a binary mixture is given by:

$$\zeta_{\text{het}}(t) = 1 + \left(\frac{\partial n}{\partial T}\right)^{-1}_{w,p} \left(\frac{\partial n}{\partial w}\right)_{p,T} \times S_T w(1-w)\left(1 - e^{-q^2 Dt}\right) . \quad (3)$$

The quantities $(\partial n/\partial T)_{w,p}$ and $(\partial n/\partial w)_{p,T}$ do not follow from the TDFRS experiment and have to be determined separately.

Results and Discussion

Figure 2 shows the phase diagram for decyl octaethylene glycol ether ($C_{10}E_8$) in water [27], which shows in the displayed temperature range no two-phase region. In the literature it is reported that there is a critical temperature around 85 °C but no critical concentration is given [5, 28]. TDFRS experiments were carried out in the micellar solution phase which are indicated by solid circles in the phase diagram. In the investigated temperature and concentration range $C_{10}E_8$ in water forms probably only spherical micelles, but it might be expected that at higher concentrations close to the hexagonal phase also cylindrical micelles are formed [4]. The experimental temperature and concentration range is far from the critical temperature so that the diffusion of the micelles is still not dominated by the critical slowing down.

One crucial aspect is the addition of the dye. It needs to be scrutinized that the dye does not change the phase behavior of the surfactant system. As already mentioned

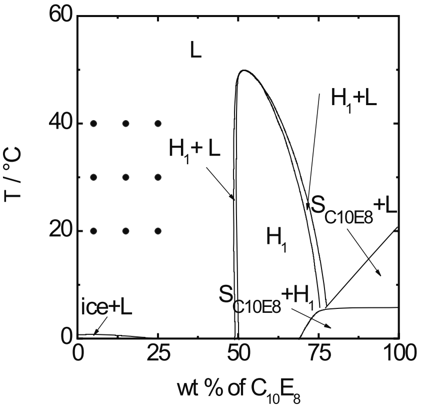

Fig. 2 Schematic phase diagram of $C_{10}E_8$ [27] in water. The different regions are abbreviated in the following way: micellar solution (L), hexagonal (H_1) and the solid of pure $C_{10}E_8$ (S_{C10E8}). The *solid circles* represent the concentrations and temperatures where TDFRS measurements have been performed

in Introduction, especially due to the addition of an electrolyte as in the case of basantol yellow, the phase behavior of the surfactant system can be changed significantly [23]. Another complication might come from the hydrophobic/hydrophilic hybrid nature of basantol yellow which might act as a cosurfactant. Therefore, we made also measurements with alizarin as organic dye and compared the results obtained for the diffusion coefficient by the TDFRS experiment with DLS measurements, which were also performed without dye. The results for a surfactant concentration of $w = 0.15$ are displayed in Fig. 3. The Soret coefficients show a very weak temperature dependence, while the thermal diffusion and diffusion coefficient increase with temperature. The obtained results are independent of the chosen dye. The diffusion coefficients agree with the diffusion coefficients which were obtained from DLS experiment with and without dye. These results indicate that the added dyes do not have any significant influence on the diffusion of micelles, which implies the size and the structure of micelles are not modified by the addition of dyes in the experimental condition. This is also confirmed in Fig. 4, which shows the diffusion coefficients for $C_{10}E_8$ for different concentrations ($w = 0.05$, 0.15, 0.25) in dependence of temperature measured by DLS and TDFRS. The solutions for the DLS measurements contained the same amount basantol yellow as the TDFRS sample. The diffusion constants increase with temperature and the values obtained with the different methods agree within the error bars. The error bars refer to one standard deviation. Nevertheless, the diffusion coefficients determined by DLS seem to be systematically lower than the values obtained by TDFRS. This is probably caused by the different weighting of the two methods. The TDFRS signal is weighted by the mass, M, of the micelle, while the DLS correlation function is weighted by the square of the mass, M^2, of the micelle.

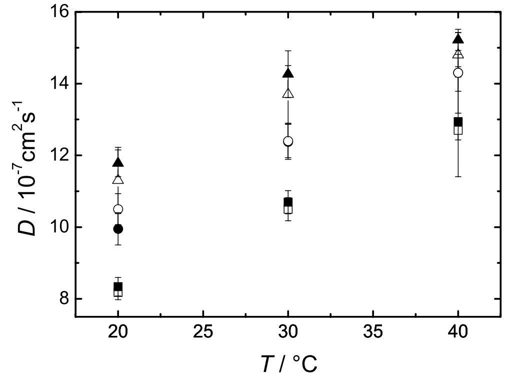

Fig. 4 Diffusion coefficient of $C_{10}E_8$ in water for different surfactant concentrations ($w = 0.05$ (■), $w = 0.15$ (●), $w = 0.25$ (▲) in dependence of temperature. The *open symbols* refer to DLS experiment while the *solid symbols* refer to the TDFRS measurements. In both experiments the solutions contained basantol yellow

The Soret coefficient of $C_{10}E_8$ is $S_T = 0.032 \pm 0.005$ which is obtained from averaging over all data points shown in Fig. 3. The positive sign of S_T corresponds to that the concentration gradient is established with the migration of micelles towards the cold side of the fluid. Here we use the sign notation for S_T as follows: In a binary mix-

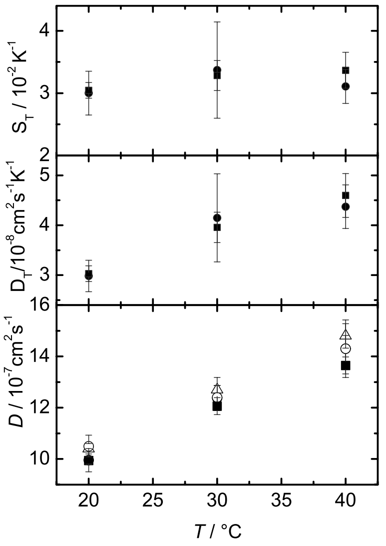

Fig. 3 Soret coefficient, thermal diffusion coefficient and diffusion coefficient of $C_{10}E_8$ ($w = 0.15$) in water at different temperatures containing basantol yellow (●) and alizarin (■). For comparison the diffusion coefficients were also determined by DLS measurement without dye (△) and with basantol yellow (○)

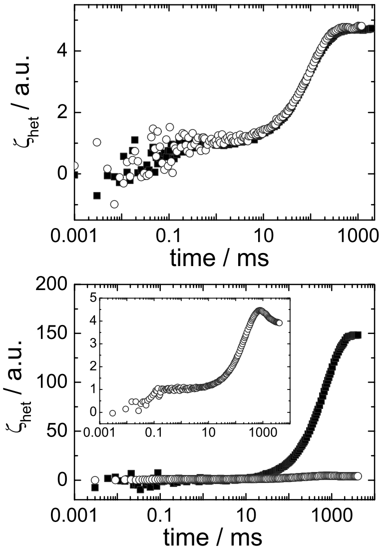

Fig. 5 Normalized heterodyne signal ζ_{het} measured for $C_{10}E_8$ ($w = 0.15$, T=20 °C; *top figure*) and $C_{12}E_6$ ($w = 0.05$, T=30 °C; *bottom figure*) in water. The solutions contained either basantol yellow (○) or alizarin (■) as dye. In the *lower figure* the *inset* shows the enlarged diffraction signal ζ_{het} for the aqueous $C_{12}E_6$ with basantol yellow

ture of A and B, S_T of A is positive if A moves to the cold side. Therefore, the sign does not depend on the density of two components. In the case of the SDS (sodium dodecyl sulfate) micelles, the sign of S_T is also positive [7]. The value of S_T of $C_{10}E_8$ has the same order of magnitude with SDS micelles, although we can not directly compare the magnitudes because of a huge contribution of electrostatic forces on thermal diffusion behavior for SDS systems. So far, there are no data for the Soret coefficient of nonionic micelle systems for comparison. It is desired, for example, to study other nonionic surfactants in the same family as C_mE_n. Indeed, ongoing research shows interesting features in regard to the choice of dye and to the dependencies of temperature and surfactant concentration. For instance, $C_{12}E_6$ in the micellar phase show a dramatic changes in their thermal diffusion behavior. The use of dye, alizarin, induces ca. 30-folds intensity of TDFRS signal in comparison with the dye basantol yellow (Fig. 5). Furthermore, $C_{12}E_6$ solution with basantol yellow showed a two-mode behavior. At the present stage, we do not discuss this point. But it needs to be pointed out that $C_{10}E_8$ is a well characterized system which forms only spherical micelles while other surfactants often show a transition to more elongated micelles. It suggests that a modification of interactions at the interface leads to a structural change of micelles which may have a relation with the thermal diffusion behavior to a great extent. To clarify these system dependence behaviors we will report the experimental results for several nonionic surfactant systems in the future.

Conclusions

The presently investigated surfactant $C_{10}E_8$ in water which shows the same behavior on thermal diffusion independently of the nature of the added dye by means of TDFRS and DLS experiments. On going research shows that this is not a general feature. Another nonionic surfactant $C_{12}E_6$ shows a drastic change in thermal diffusion behavior with the choice of the dye. To clarify under which circumstances the behavior remains stable or is changed will be object of future research.

Acknowledgement We are grateful for many fruitful discussions with Dina Kleshchanok, Peter Lang, Jutta Luettmer-Strathmann, Roberto Piazza and Remco Tuinier. This work was partially supported by the Deutsche Forschungsgemeinschaft grant Wi 1684. We gratefully acknowledge the Fonds der chemischen Industrie for financial support.

References

1. Chevalier Y, Zemb T (1990) Rep Prog Phys 53:279
2. Banat IM, Makkar RS, Cameotra SS (2000) Appl Microbiol Biotechnol 53:495
3. Mitchell DJ, Tiddy GJT, Waring L, Bostock T, McDonald MP (1983) J Chem Soc-Faraday Trans I 79:975
4. Schick M (1987) Nonionic surfactants – Physical Chemistry, vol 23. Marcel Dekker Inc., New York Basel
5. van Os N, Haak J, Rupert L (1993) Physico-chemical properties of selected anionic, cationic and nonionic surfactants. Elsevier, Amsterdam
6. de Groot S, Mazur P (1984) Non-equilibrium Thermodynamics Dover, New York
7. Piazza R, Guarino A (2002) Phys Rev Lett 88:208302
8. Lenglet J, Bourdon A, Bacri JC, Demouchy G (2002) Phys Rev E 65:031408
9. Blums E, Odenbach S, Mezulis A, Maiorov M (1998) Phys Fluids 10:2155
10. de Gans BJ, Kita R, Wiegand S, Luettmer-Strathmann J (2003) Phys Rev Lett 91:245501
11. Rauch J, Köhler W (2002) Phys Rev Lett 88:185901
12. Leaist DG, Hui L (1989) J Phys Chem 93:7547
13. Takeyama N, Nakashima K (1993) J Phys Soc Jpn 62:2180
14. private communication
15. Wittko G, Köhler W (2003) Philos Mag 83:1973
16. Basantol Gelb 215® is a registered tradename of BASF. It is a tri-valent salt soluble in water with a strong absorption around 480 nm
17. Kahlweit M, Lessner E, Strey R (1984) J Phys Chem 88:1937
18. Firman P, Haase D, Jen J, Kahlweit M, Strey R (1985) Langmuir 1:718
19. Kahlweit M, Strey R, Haase D (1985) J Phys Chem 89:163
20. Kahlweit M, Strey R, Firman P, Haase D, Jen J, Schomacker R (1988) Langmuir 4:499
21. Kahlweit M, Strey R, Schomacker R, Haase D (1989) Langmuir 5:305
22. Wilcoxon JP (1990) J Phys Chem 94:7588
23. Sharma KS, Patil SR, Rakshit AK (2003) Colloids and Surfaces A 219:67
24. Becker A, Köhler W, Müller B (1995) Ber Bunsen-Ges Phys Chem Chem Phys 99:600
25. Köhler W, Schäfer R (2000) Adv Polym Sci 151:1
26. Wiegand S (2004) J Phys: Condens Matter 16:R357
27. Nibu Y, Inoue T (1998) J Colloid Interface Sci 205:305
28. Cox KR, Benson HL (1986) Fluid Phase Equilib 30:173

Progr Colloid Polym Sci (2006) 133: 116–122
DOI 10.1007/2882_069

Taegyu Shin
Gerhard H. Findenegg
Astrid Brandt

Surfactant Adsorption in Ordered Mesoporous Silica Studied by SANS

Taegyu Shin · Gerhard H. Findenegg (✉)
Stranski Laboratorium für Physikalische
und Theoretische Chemie, Technische
Universität Berlin, 10623 Berlin, Germany
e-mail: Findenegg@chem.TU-Berlin.DE

Astrid Brandt
Hahn-Meitner-Institut Berlin,
14109 Berlin, Germany

Abstract The organisation of cationic surfactants (DPCl and CPCl) adsorbed in the cylindrical pores of a periodic mesoporous silica (SBA-15, pore diameter ca. 8 nm) has been studied by small-angle neutron scattering at different solvent contrast conditions. In the experimental q range the scattering curve of SBA-15 is dominated by Bragg peaks resulting from the ordered array of mesopores. It is found that the peak intensities are strongly affected by the surfactant adsorption and the solvent contrast. The scattering curves can be modelled by combining the structure factor of a 2D hexagonal lattice with the form factor of a core-shell cylinder, in which the adsorbed surfactant film is represented by the shell of the cylinder. This simple model accounts for the main experimental findings and provides a direct method for estimating the thickness of the adsorbed film in the pores.

Keywords Surfactant adsoption · Cylindrical nanopores · Ordered mesoporous silica · Small-angle neutron scattering · Structure of surfactant films in pores

Introduction

Adsorption of surfactants from aqueous solutions onto flat silica surfaces and colloidal silica beads has been studied by a variety of techniques including ellipsometry [1], neutron reflectometry [2], atomic force microscopy (AFM) [3] and SANS [4, 5]. These studies have produced a wealth of information about the thickness and lateral organization of the adsorbed layer as a function of surfactant chain length and head-group size, and on the influence pH and ionic strength in the case of ionic surfactants. Relatively little attention has been paid so far to the effects of confinement on the adsorption and surface aggregation of surfactants. Confinement in one dimension of space (slit-pore geometry) can be probed by AFM. For the adsorption of cationic surfactants between two glass/solution interfaces a strong dependence of the surface concentration on separation was found in the so-called proximal adsorption regime [6]. Confinement in two dimensions is expected in cylindrical pores. Until recently, studies of this situation had been impeded by the lack of suitable porous materials with cylindrical mesopores of uniform size. This situation changed with the advent of periodic mesoporous silica materials like MCM-41 or SBA-15 which constitute a regular (2D hexagonal) packing of cylindrical mesopores of uniform size [7]. These materials are synthesized by using micellar aggregates of surfactants (MCM-41) [8] or amphiphilic block copolymers (SBA-15) [9] as structure-directing template and their pore size can be tailored by the choice of the amphiphile.

In this work, we study the aggregative adsorption of alkyl pyridinium chloride (C_nPCl) surfactants in the pores of a SBA-15 silica of ca. 8 nm pore diameter using small-angle neutron scattering. The SANS curve of SBA-15 silica exhibits Bragg peaks in the small-angle regime which result from the regular packing of the cylindrical pores, and the intensity of the individual peaks is modulated by a surfactant layer at the pore walls. Information about this layer can be extracted by analysing the scattering data in terms of a model which combines the structure factor of the 2D hexagonal lattice with the form factor of a uniform core-shell cylinder [10].

Experimental Section

Chemicals

Dodecylpyridinium chloride (DPCl, 98%) and cetylpyridinium chloride (CPCl, 99%) were obtained from Sigma-Aldrich and used without further purification. Pro-analysis quality KCl was received from Merck. D_2O (99.9% isotope purity) was received from Sigma-Aldrich. High purity water (H_2O) was obtained from a Milli-Q pure-water system.

Sample Preparation

A high-quality sample of SBA-15 silica was synthesized by the method reported by Zhao et al. [9] using a technical-grade poly(ethylene oxide)-poly(propylene oxide)-poly(ethylene oxide) triblock copolymer (Pluronic P103) as the structure-directing agent and tetraethyl orthosilicate (TEOS) as the silicate precursor. Details of the synthesis and thermal post-treatment of the sample are given elsewhere [11]. The pore structure of the calcined SBA-15 sample was characterized by nitrogen adsorption at 77 K and X-ray small angle diffraction. The adsorption isotherm exhibits a hysteresis loop with steep adsorption and desorption branches characteristic of good-quality samples, and the X-ray diffractogram shows 5 well-separated peaks which can be indexed according to a 2D hexagonal lattice. Values of the specific surface area a_s, specific pore volume v_p, pore diameter D and lattice constant a_0 are given in Table 1.

Samples of SBA-15 with adsorbed surfactant layers corresponding to the plateau value of the adsorption isotherm at different ionic strengths of the solution were prepared by combining appropriate amounts of surfactant and silica in aqueous KCl solutions ("mixing-type" samples). Initially, KCl solutions of required concentration (0.1 or 0.001 M) were prepared with water samples of different D_2O volume fractions, denoted as solvent A, B and C (Table 2). A suspension of 0.25 g SBA-15 in 10 g of this solution was prepared at pH 9, and the estimated amount of surfactant was added. After sonication and equilibration the supernatant was decanted, and the silica slurry was transfered into the sample cell. Samples of SBA-15 containing lower amounts of adsorbed surfactant were prepared from mixing-type samples by equilibration with known amounts of the H_2O/D_2O appropriate solvent and removal of the supernatant solution ("washing-type" samples).

Table 1 Characterization of the calcined SBA-15 silica by nitrogen adsorption and X-ray diffraction: Specific surface area a_s (BET), specific pore volume v_p, pore diameter D, and pore center-to-center distance a_0. The pore diameter was determined from the ascending branch of the pore condensation loop and the FHH prescription for the adsorbed film

$a_s/\mathrm{m^2 g^{-1}}$	$v_p/\mathrm{cm^3 g^{-1}}$	D/nm	a_0/nm
801	0.873	8.1	10.70

Table 2 Composition ϕ_H (volume fraction of H_2O) and scattering length density ρ_l of the three H_2O/D_2O mixtures; I_{inc} represents the incoherent scattering of SBA-15/water samples in the absence of surfactant, I_0 is the respective value in SBA-15/D_2O

Solvent	ϕ_H	$\rho_l/10^{10}\ \mathrm{cm^{-2}}$	$I_{inc}/\mathrm{cm^{-1}}$	$(I_{inc} - I_0)/\mathrm{cm^{-1}}$
A	0	6.34	0.05	0
B	0.197	5.0	0.17	0.12
C	0.385	3.7	0.29	0.24

Sample Cell

Specially designed aluminium cells as shown in Fig. 1 were used for the SANS measurements. The width of the sample space between two quartz glass windows (thickness ca. 1 mm) is determined by an aluminium ring of 1 mm thickness. The cell is sealed by O-rings. This construction of the sample cell allows to expose reproducible amounts of the silica sample to the neutron beam.

Small-angle Neutron Scattering

Measurements were made at instrument V4 of the Berlin Neutron Scattering Center at the Hahn-Meitner Institut (Berlin). Neutrons of wavelength $\lambda = 0.605$ nm with a wavelength distribution $\Delta\lambda/\lambda = 0.12$ (fwhm) and

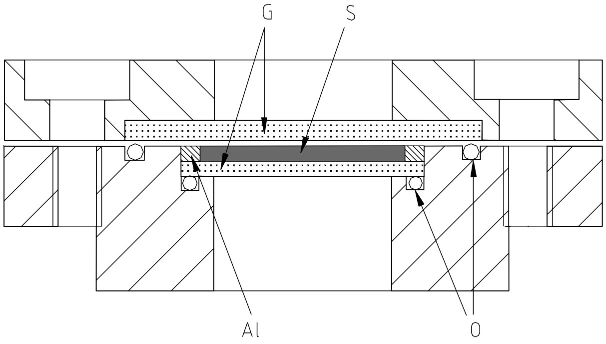

Fig. 1 Sample cell (aluminium) used for the SANS measurements: S: sample; Al: aluminium ring; G: quartz glass windows; O: O-rings

sample-to-detector distances of 1 (with hub), 4, and 12 m were used to cover a range of scattering vectors q from 0.05 to 5 nm^{-1}.

Theoretical Background

For the analysis of the SANS curves a model [10] was adopted which combines the structure factor of a 2D hexagonal lattice of cylindrical pores with the form factor of a three-density-level core-shell cylinder (Fig. 2). It is assumed that the pores are monodisperse and of circular cross-section and perfectly ordered on the lattice. The system is fully isotropic due to the powder form of the SBA-15 matrix. The spherically averaged total scattered intensity is modelled as [10, 12, 13]

$$I(q) = KS(q)\,|F(q)|^2 + I_{\mathrm{diff}}(q) + I_{\mathrm{inc}}\,, \tag{1}$$

where the first term describes the Bragg reflections from the ordered structure, with $S(q)$ the structure factor and $F(q)$ the scattering amplitude of the cylindrical pores with or without an adsorbed film, and K is a constant. $I_{\mathrm{diff}}(q)$ represents the diffuse scattering due to micropores or other inhomogeneities of the matrix, and I_{inc} is the incoherent scattering mostly due to protons of the solvent and surfactant. Using the Miller indices (hk) for the lattice planes of a 2D lattice, the structure factor $S(q)$ of an ideal undistorted lattice can be written as

$$S(q) \propto \frac{1}{q^2} \sum_{(\mathrm{hk})} m_{\mathrm{hk}} L_{\mathrm{hk}}(q) \tag{2}$$

with m_{hk} the peak multiplicity ($m_{\mathrm{h0}} = m_{\mathrm{hh}} = 6$, otherwise $m_{\mathrm{hk}} = 12$) and $L_{\mathrm{hk}}(q)$ the peak shape function, which for a Gaussian peak shape becomes $L_{\mathrm{hk}}(x) = (2/\pi\delta)\exp(-4x^2/\pi\delta^2)$, where δ is a parameter related to the standard deviation [13], $x = (q - q_{\mathrm{hk}})$, and

$$q_{\mathrm{hk}} = \frac{4\pi}{a_0\sqrt{3}} \sqrt{h^2 + k^2 + hk}\,. \tag{3}$$

The scattering amplitude of a uniform core-shell cylinder with scattering length densities of the core (ρ_1), adsorbed film (ρ_2) and matrix (ρ_3) (cf. Fig. 2) is [14, 15]

$$F(q) = 2\pi \left[(\rho_3 - \rho_2) R^2 \frac{J_1(qR)}{qR} + (\rho_2 - \rho_1) r^2 \frac{J_1(qr)}{qr} \right]\,, \tag{4}$$

where R is the pore radius, r the inner radius of the adsorbed film, and J_1 is the Bessel function of the first order. Calculations for the form factor $|F(q)|^2$ with fixed values of the pore radius ($R = 4.0$ nm) and scattering length density of the silica matrix ($\rho_3 = 3.7 \times 10^{10}\ \mathrm{cm}^{-2}$) and appropriate choices of the parameters r, ρ_1 and ρ_2 are shown in Figs. 4b and 5b. Results for the whole model function of Eq. 1 are shown in Fig. 6.

Result and Discussion

SBA-15 in Water

Scattering curves of SBA-15 embedded in water of three different scattering length densities (Table 2) are shown in Fig. 3. The positions of the four leading Bragg reflexes (10, 11, 20, 21) of this sample are indicated by vertical lines. In D_2O (solvent A), which gives a high scattering contrast against the silica matrix, the (10) reflex appears as an intense, broad peak centred at $q_{10} = 0.678\ \mathrm{nm}^{-1}$. The (11) and (20) reflexes are not resolved but form a joint peak due to the wavelength broadening of the neutron beam, and the (21) reflex appears only as a shoulder on top of the scattering background. The diffuse scattering intensity I_{diff} of the sample in D_2O falls off by about one order of magnitude in the q range from 0.4 to 4 nm^{-1}. When the scattering contrast of the liquid against the matrix is lowered, all Bragg peaks become less intense (curve for solvent B in Fig. 3). In the contrast-matching H_2O/D_2O mixture (solvent C) the Bragg peaks and diffuse scattering

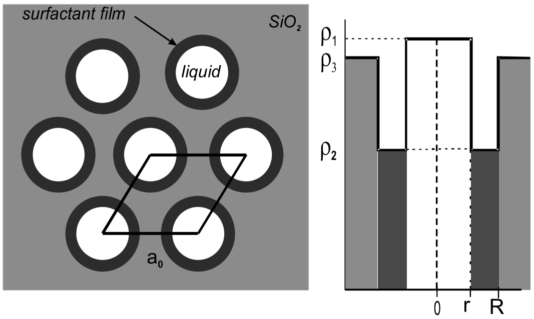

Fig. 2 Sketch of the 2D hexagonal packing of cylindrical pores coated with an adsorbed surfactant film (*left*) and density profile $\rho(r)$ of a three density level core-shell cylinder (ρ_1, liquid core; ρ_2, surfactant film; ρ_3, matrix) (*right*)

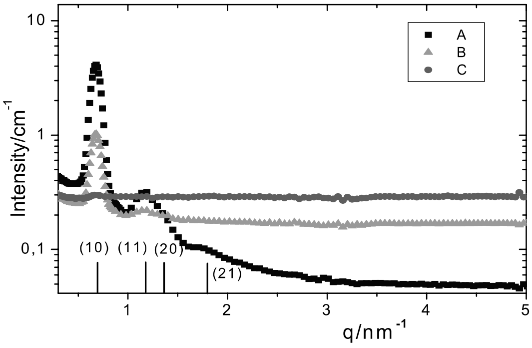

Fig. 3 SANS curve of SBA-15 in pure D_2O and two H_2O/D_2O mixtures of different scattering length densities. The positions of the leading Bragg reflections (hk) of SBA-15 are indicated by *vertical lines*

are entirely suppressed, except for an incoherent background I_{inc}, which is due mostly to the incoherent scattering of the protons of H_2O. In the present work we assume that this incoherent background is given by the scattering intensity at $q > 4\,\mathrm{nm}^{-1}$ where the scattering is independent of q. Figure 3 shows that for SBA-15 in water, I_{inc} increases strongly from solvent A to C, and Table 2 indicates that the experimental values of I_{inc} are proportional to the H_2O content of the solvent, except for a small contribution I_0 which is also present in D_2O. This finding is to be expected as the amount of liquid in our slurry samples is similar in all measurements.

SBA-15 with Adsorbed Surfactant

Solvent Contrast Variation. Figure 4a shows scattering curves from SBA-15 carrying an adsorbed layer of the surfactant DPCl, embedded in aqueous solutions of different scattering length densities (solvents A, B and C). The incoherent scattering background I_{inc} has been subtracted from the measured intensities in these graphs. The three samples were prepared in the same way (1 mM KCl solution, "mixing type" protocol) and thus the state of the adsorbed surfactant film will be similar in these samples. Hence the curves in Fig. 4a show the influence of the solvent contrasts on the scattering at a given thickness of the adsorbed surfactant film. It is seen that the intensity of the (10) Bragg reflection decreases sharply with decreasing solvent contrast, but the broad peak centred near the (11) reflection and extending into the q range of the higher Bragg reflections is not strongly affected by the solvent contrast: There is some decrease in the scattered intensity from solvent A to solvent B, but no further decrease from B to C, where this broad peak is much stronger than the (10) peak. The main features of the scattering curves of Fig. 4a can be rationalized on the basis of the form factor model introduced above. Figure 4b shows graphs of the form factor $|F(q)|^2$ as given by Eq. 4 for an adsorbed surfactant layer of thickness $d = R - r = 1$ nm and scattering length density $\rho_2 = 1.65 \times 10^{10}\,\mathrm{cm}^{-2}$, and scattering length densities of the liquid (ρ_1) as given for the three solvents in Table 2, based on the assumption that the liquid in the core of pores represents pure solvent. The graphs in Fig. 4b show that $|F(q)|^2$ is strongly dependent on ρ_1 in the q range near the (10) Bragg peak but only weakly dependent on ρ_1 in the q range near the (11) and (20) Bragg peaks. As the Bragg intensity $I(q_{\mathrm{hk}})$ is proportional to $|F(q)|^2$ at $q = q_{\mathrm{hk}}$ (Eq. 1), this result implies that the intensity of the (10) Bragg peak will decrease with decreasing scattering length density of the solvent while the intensity of the combined (11) + (20) peak will be nearly independent of ρ_1, in agreement with the experimental results of Fig. 4a. Hence the form factor model accounts for the observed influence of the solvent contrast on the intensities of the first and second Bragg peak. In particular, it shows that the pronounced decrease of the (10) peak intensity with decreasing scattering length density of the aqueous solvent is due to a decrease of the form factor at q values near the (10) peak.

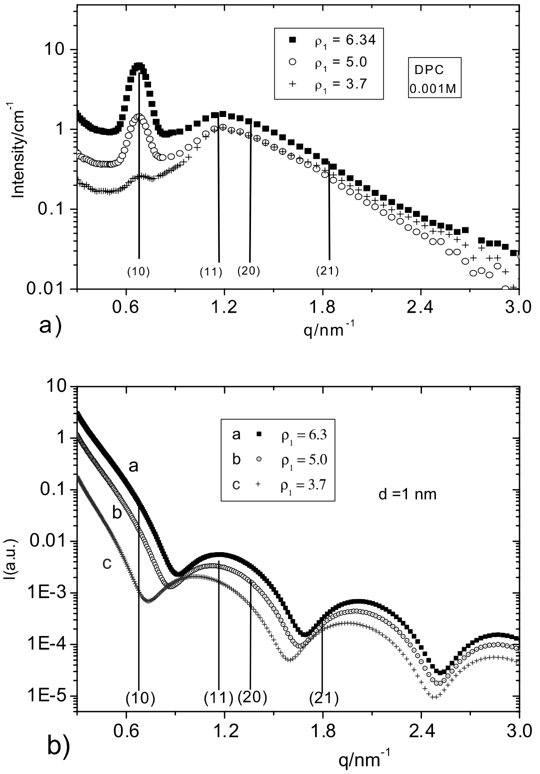

Fig. 4 **a** SANS curves from SBA-15 with an adsorbed film of DPCl for three solvent contrasts (water solvents A, B, C) at low salt concentration (1 mM KCl). The incoherent scattering has been subtracted for all samples; **b** Form factor of a core-shell cylinder with parameters appropriate for the SANS curves in Fig. 3a. The positions of the Bragg reflections q_{hk} are indicated by *vertical lines*

Variation of Layer Thickness. The influence of the layer thickness of adsorbed surfactant films on the scattering curve of SBA-15 was studied with adsorbed films of DPCl and CPCl. It is well-established that the plateau value of the adsorption isotherm of cationic surfactants on silica increases with increasing ionic strength of the solution. Specifically, for the adsorption on a nonporous silica (Aerosil OX50) under the experimental conditions of the present work (pH 9) it is reported that an increase of the ionic strength from 10^{-3} M to 10^{-1} M KCl causes an increase of the plateau value of the adsorption isotherm from 2.7 to 4.0 $\mu\mathrm{mol\,m}^{-2}$ for DPC, and from 4.3 to above 5 $\mu\mathrm{mol\,m}^{-2}$ for CPC [16]. Preliminary adsorption measurements of the two surfactants in the pores of SBA-15 support these trends, although the plateau values of the adsorption in the mesoporous SBA-15 matrix are significantly lower than at the surface of nonporous silica. Figure 5a shows the influence of the surfactant layer thickness on the scattering curves of SBA-15 samples in film contrast (solvent C). In this figure, curves (a) and (b) represent films of CPCl corresponding to the plateau value of the adsorption isotherm in 10^{-1} M and 10^{-3} M KCl, respectively (mixing type samples), and curve (c) represents a film of DPCl prepared by the washing protocol in 10^{-3} M KCl. Hence the thickness of the adsorbed surfactant film decreases from (a) to (c). Figure 5a shows that this decrease of the film thickness causes a systematic decrease of the (10) peak intensity. In the q range of the (11) and (20) reflexes the scattering intensity of samples (a) and (b) is similar and significantly higher than for sample (c), but in the q range of the (21) reflex sample (c) has the highest scattering intensity of the three samples. Again these experimental observations can be accounted for in a qualitative manner by our form factor model. This is shown in Fig. 5b, where the form factor $|F(q)|^2$ is plotted for three values of the film thickness d (1, 2, and 3 nm) in a pore of radius $R = 4$ nm for fixed values of the scattering length densities of the core liquid ($\rho_1 = 3.7 \times 10^{10}\,\mathrm{cm}^{-2}$), surfactant film ($\rho_2 = 1.65 \times 10^{10}\,\mathrm{cm}^{-2}$), and matrix ($\rho_3 = 3.7 \times 10^{10}\,\mathrm{cm}^{-2}$). It is seen that at $q = q_{10}$ the value of $|F(q)|^2$ decreases in a systematic way with decreasing film thickness. In the q range of the (11) and (20) reflexions $|F(q)|^2$ is of similar magnitude for films of thickness 3 and 2 nm, but significantly smaller for a film of 1 nm thickness, while in the q range of the (21) reflexion the smallest film thickness leads to the highest value of $|F(q)|^2$. All these findings are in qualitative agreement with the observed effects of the film thickness on the scattering intensities in the q regions of the Bragg reflexions.

Values of the film thickness d ranging from 1 to 3 nm, as adopted in the above model calculation, imply rather pronounced differences in the amount of adsorbed surfactant. For CPCl, a limiting adsorption $\Gamma_{\max} \approx 5\,\mu\mathrm{mol\,m}^{-2}$ (corresponding to 3 molecules/nm^2) is reported on a flat silica surface at pH 9 and high ionic strength (0.1 M KCl) [16], but considerably lower values of $\Gamma_{\max}$ were found for the adsorption between two glass/solution interfaces at separations below 10 nm [6]. Whereas on flat surfaces the surfactant can form a symmetric bilayer film, geometrical restraints in cylindrical nanopores will cause asymmetric bilayers in which the number of molecules in the inner layer is less than that in the outer layer. A relation between the adsorption $\Gamma_{\max}$ and the film thickness d in cylindrical pores can be obtained on the basis of the volume and mean cross-sectional area of the surfactant molecules, and an ad-hoc relation for the fraction of molecules accommodated in the inner layer as a function of pore radius R and film thickness d. With such a model one finds that film thicknesses of 1, 2 and 3 nm correspond to Γ values of ca. 1, 2 or $3\,\mu\mathrm{mol\,m}^{-2}$, with the volume fraction of water in the adsorbed layer decreasing from ca. 55% for the lowest film thickness to ca. 35% at the highest film thickness. Preliminary measurements of the adsorption isotherm of CPCl in our SBA-15 sample at pH 9 give $\Gamma_{\max} = 2.5 \pm 0.5\,\mu\mathrm{mol\,m}^{-2}$ at high ionic strength (0.1 M KCl). Accordingly, the film thickness is expected to be between 2 and 3 nm for sample (a) and significantly less for samples (b) and (c), as shown in the model calculation in Fig. 5. Further work to corroborate these results is in progress.

Modelling the Overall Scattering Curves. To represent the entire scattering curves $I(q)$ of the surfactant-loaded SBA-15 samples, the diffuse scattering $I_{\mathrm{diff}}(q)$ caused by the silica matrix has also to be modelled. As SBA-15 consists of particles of submicrometer diameter, Porod scattering $I_{\mathrm{P}}(q)$ from the outer surface of the particles will be dominant in the q range well below q_{10}, and diffuse scattering $I_{\mathrm{D}}(q)$ due to micropores and other inhomogeneities of the matrix will contribute in a q range extending to well above q_{10}. Such contributions from frozen fluctuations induced by a random field can be represented by a Lorentzian square term [17, 18]. Hence the overall diffuse scattering is modelled as

$$I_{\mathrm{diff}}(q) = I_{\mathrm{P}}(q) + I_{\mathrm{D}}(q) = \frac{A_{\mathrm{P}}}{q^4} + \frac{A_{\mathrm{D}}}{\left(1 + \xi^2 q^2\right)^2}\,, \qquad (5)$$

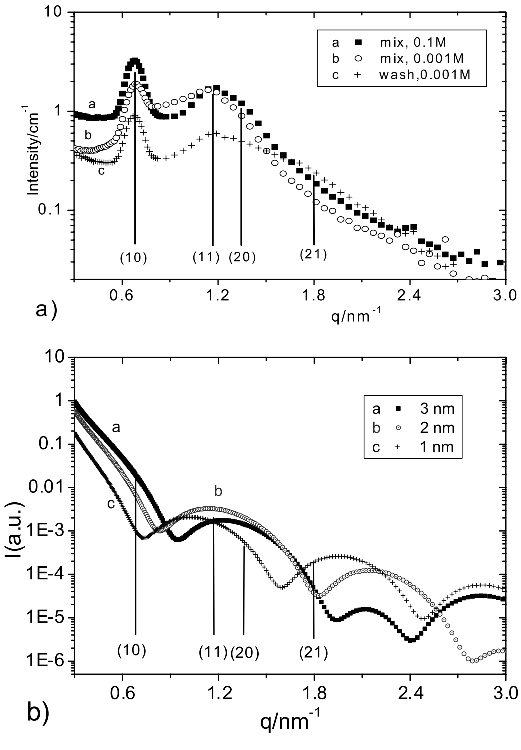

Fig. 5 **a** SANS curves from SBA-15 with adsorbed surfactant films in contrast-matching H_2O/D_2O (solvent C): CPCl at 0.1 M KCl (*curve a*), CPCl at 10^{-3} M KCl (*curve b*), and DPCl at 10^{-3} M KCl (washing type; *curve c*); **b** Form factor calculation with film thickness 3, 2 and 1 nm film thickness

where ξ is the correlation length of the fluctuations. Figure 6a shows how the overall scattering curve of a sample can be modelled by a superposition of the Bragg scattering with the diffuse scattering according to Eq. 5, with an appropriate choice of the model parameters ($\xi = 0.9\,\mathrm{nm}$, $A_\mathrm{D} = 0.9\,\mathrm{cm}^{-1}$, $A_\mathrm{P} = 0.1 \times 10^{26}\,\mathrm{cm}^{-5}$, and $\delta = 0.12\,\mathrm{nm}^{-1}$). Comparison of the resulting function $I(q)$ with the experimental scattering curve for SBA-15 with an adsorbed surfactant film (Fig. 6b) indicates that the main features of the experimental data can be represented reasonably well by this formalism. However, several important details have not been taken into account in the present analysis, e.g., the effect of the wavelength distribution of the neutron beam, effects resulting from the lattice disorder (displacement of the pore centres from their ideal positions) and possible further contributions to the diffuse scattering which are not represented by the Lorentzian square term. Further systematic work is needed to assess the importance of such contributions for a physically meaningful representation of the scattering curves.

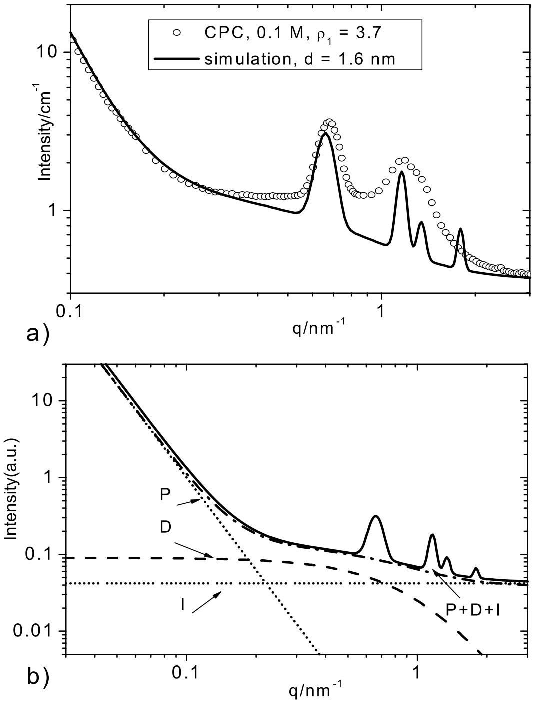

Fig. 6 Analysis of SANS data for CPCl in SBA-15 (0.1 M KCl): **a** Experimental data (*open circles*) and simulation (*full line*); **b** Individual contributions to the model function (Eqs. 1 and 2): (P) particle surfaces (Porod); (D) diffuse scattering of the matrix; (I) incoherent scattering; the *full line* shows the sum of all contributions plus Bragg scattering

Conclusion

The present work shows that neutron small-angle scattering offers a useful tool for studying the organisation of surfactant layers adsorbed in the cylindrical pores of periodic mesoporous silica such as SBA-15. In the experimental q range the scattering curve is dominated by Bragg peaks resulting from the ordered arrangement of the mesopores in the silica matrix. The intensities of the individual Bragg reflexes are strongly affected by the surfactant adsorption and by the solvent contrast. The observed behavior can be understood by modelling the pore by the form factor of a core-shell cylinder. As the form factor exhibits pronounced minima in the q range of the Bragg reflexions, the intensity of the Bragg peaks can vary in a systematic way with the thickness of the adsorbed film. The overall scattering curve of the SBA-15 samples can be modelled by adding appropriate terms for the Porod and diffuse scattering of the matrix and the incoherent scattering resulting from the aqueous solvent. A major drawback of small-angle neutron scattering is the broad wavelength distribution, which implies that only the first Bragg reflex of SBA-15 is resolved while the higher Bragg reflexes appear as a combined peak. On the other hand, the possibility to study the surfactant films in different contrast conditions by using H_2O/D_2O mixtures of different scattering length density, greatly helps to verify the chosen model.

Acknowledgement The authors wish to thank Tobias Fütterer, Roland Steitz and Steffen Uredat for helpful discussions. This work was supported by the Deutsche Forschungsgemeinschaft in the framework of SFB 448.

References

1. Tiberg F, Landgren M (1993) Langmuir 9:927, DOI: 10.1021/la00028a009
2. Penfold J, Staples E, Tucker I (2002) Langmuir 18:2967 DOI: 10.1021/la011575s
3. Subramantian V, Ducker WA (2000) Langmuir 16:4447 DOI: 10.1021/la991245w
4. Cummins PG, Staples E, Penfold J (1990) J Phys Chem 94:3740 DOI: 10.1021/j100372a071
5. Despert G, Oberdisse J (2003) Langmuir 19:7604, DOI: 10.1021/la0300939
6. Lokar WJ, Ducker WA (2004) Langmuir 20:378, DOI: 10.1021/la035288v
7. Selvam P, Bhatia SK, Sonwane CG (2001) Ind Eng Chem Res 40:3237 DOI: 10.1021/ie0010666
8. Kresge CT, Leonowicz ME, Roth WJ, Vartuli JC, Beck JS (1992) Nature 359:710, DOI: 10.1038/359710a0
9. Zhao D, Feng J, Huo Q, Melosh N, Fredrickson GH, Chmelka BF, Stucky GD (1998) Science 279:548, DOI:10.1126/science.279.5350.548

10. Imperor-Clerc M, Davidson P, Davidson A (2000) J Amer Chem Soc 122:11925, DOI: 10.1021/ja002245h
11. Schreiber A, Ketelsen I, Findenegg GH (2001) Phys Chem Chem Phys 3:1185, DOI: 10.1039/b010086m
12. Zickler GA, Jähnert S, Wagermaier W, Funari SS, Findenegg GH, Paris O (2006) Phys Rev B, in print
13. Förster S, Timmann A, Konrad M, Schellbach C, Meyer A, Funari SS, Mulvaney P, Knott R (2005) J Phys Chem B 109:1347 DOI: 10.1021/jp0467494
14. Mittelbach P, Porod G (1961) Acta Phys Austriaca 14:405
15. Glatter O, Kratky O (1982) Small Angle X-ray Scattering. Academic Press, London
16. Goloub TP, Koopal LK (1997) Langmuir 13:673, DOI: 10.1021/la960690d
17. Lin MY, Sinha SK, Drake JM, Wu Xl, Thiyagarajan, Stanley HB (1994) Phys Rev Lett 72:2207, DOI: 10.1103/PhysRevLett.72.2207
18. Schemmel S, Rother G, Eckerlebe H, Findenegg GH (2005) J Chem Phys 122:244718, DOI: 10.1063/1.1931528

Progr Colloid Polym Sci (2006) 133: 123–130
DOI 10.1007/2882_071

Christian Eckert
Helmut Durchschlag
Klaus-Jürgen Tiefenbach

Thermodynamic Analysis of Lysozyme Denaturation by Surfactants

Christian Eckert ·
Helmut Durchschlag (✉) ·
Klaus-Jürgen Tiefenbach
Institute of Biophysics and Physical Biochemistry, University of Regensburg, Universitätsstrasse 31, 93040 Regensburg, Germany
e-mail: helmut.durchschlag@biologie.uni-regensburg.de

Abstract Spectroscopic techniques (UV absorption, fluorescence and circular dichroism) are applied for probing the conformational stability of lysozyme as a model protein after the impact of surfactants. The investigations allow the equilibrium constant, K, and the free energy change, ΔG, of the transition from the folded (native) to the unfolded (denatured) state to be estimated. ΔG at 25 °C in the absence of additives allows quantifying the conformational stability of the protein. Though the results are based on the validity of several assumptions regarding folding/unfolding mechanism, evaluation procedure, and environmental conditions, the thermodynamics of surfactant-induced unfolding may be estimated. Compared to the unfolding induced by the chaotropic denaturant guanidinium chloride, cationic and zwitterionic surfactants are found to yield lower ΔG values. In the case of lysozyme, anionic and nonionic surfactants did not result in transition curves. The interpretation of the transition curves indicated the existence of a two-state behavior. Quantities which do not significantly depend on the unfolding mechanism, such as the midpoints of denaturant concentrations and thermal unfolding curves, $c_{1/2}$ and T_m, may also be applied for comparing conformational stabilities of proteins, even in the case of irreversible transitions. The evaluation of the thermal denaturation allows the derivation of enthalpy and entropy changes, ΔH and ΔS.

Keywords
Impact of surfactants · Protein denaturation · Protein stability · Spectroscopy · Thermodynamic analysis of unfolding curves

Introduction

The solubilities of proteins in aqueous solutions vary over a wide range [1]. Under physiological conditions some proteins (e.g. simple globular proteins) are highly soluble, while others (e.g. structural proteins) are totally insoluble. The solubility of a protein in water is governed by its free energy; differences in the free energy occur as a consequence of interactions with other molecules present in solution (protein or solvent molecules or any other additives). The interactions of a protein molecule are determined essentially by its surface. The most favorable interactions with aqueous solvent occur via charged and polar groups of the hydrophilic polypeptide side chains. Since the envelopes of water-soluble globular proteins are covered primarily by charged and polar groups, their solubilities are determined by the interactions of these groups with water [2]. Of course, the extent of interactions is influenced by the pH of the medium used. Since protein unfolding usually leads to the exposure of nonpolar groups to the solvent, protein solubility may be affected drastically by any kind of unfolding process. Many proteins can be solubilized by additives such as certain surfactants or denaturants. Thermodynamic considerations [3] are especially important when interactions are to be discussed, both with respect to the proteins and the additives under analysis. The comparison of the effects of surfactants and chaotropic interactions allows information on the weak interactions responsible for the stability and stabilization of native proteins to be gained.

In general, surfactants and denaturants bind to proteins, however to a different extent depending on the additives and proteins applied [1]. Commonly, natural ionic surfactants and nonionic surfactants do not cause significant structural alterations of proteins, whereas most synthetic ionic surfactants cause protein denaturation, owing to competing intermolecular ionic and hydrophobic interactions. The behavior of proteins at moderate concentrations of ionic surfactants differs considerably from that at elevated concentrations. The size and structure of protein-surfactant complexes vary not only for each individual protein but for the solubilization conditions and the chemical nature of the surfactant.

Among the physicochemical techniques available for the structural characterization of protein-surfactant complexes and their constituents, the spectroscopic techniques turned out to be highly effective for providing local and global structural information very fast. Spectral measurements of surfactant-induced equilibrium unfolding transitions may be used for estimating the free energy of protein stabilization [3–7].

The present study is focused on unreduced lysozyme as a model protein, and on various representatives of anionic, cationic, zwitterionic and nonionic surfactants. The thermodynamic parameters of complex formation were compared with those obtained for other ionic and nonionic denaturants (GdmCl, urea) or for heat denaturation. In the case of potent surfactants, the maximal level of protein denaturation (partial unfolding) requires only millimolar concentrations, while high molar denaturant concentrations (e.g. 6 M guanidinium chloride (GdmCl), 8 M urea) are needed for a complete breakdown of the native protein structure.

Materials and Methods

Samples and Solutions

Hen egg-white lysozyme was obtained from Serva, Heidelberg; surfactants, denaturants and cosolvents were of the highest available purity, preferably of analytical grade. The protein (final concentration: 0.1 g/l, except calorimetry (1 g/l)) and the additives were dissolved in 0.1 M sodium phosphate buffer pH 5.5 (ionic strength approx. 0.2 mol/l). For surfactants/denaturants a wide range of concentrations was used: generally 0–1 g/l surfactant (trimethylammonium bromides (C_{12}TMABr, C_{14}TMABr, C_{16}TMABr), sodium dodecyl sulfate (SDS), dimethyl-alkylammoniopropane sulfonate (Zwittergent 3–16), C_{12}-maltoside, etc.), 0–7 M GdmCl, 0–8 M urea. Stock solutions of proteins plus additives were incubated for at least 12 h at 25 °C, to allow reaching the final state of denaturation. All experiments were performed at 25 °C.

Techniques

Monitoring of absorption, fluorescence and circular dichroism (CD) spectra was performed using a Perkin-Elmer Lambda 5 spectrophotometer, a Jobin Yvon-Spex Fluoromax-2 spectrofluorometer and an Aviv 62A-DS spectropolarimeter, respectively. Spectroscopic data were evaluated and interpreted as described [8–15]. In the context of surfactants, the investigations have to consider several caveats [5, 16]: e.g., (i) separation of manifold effects contributing to the spectroscopic signals (effects of proteins and surfactants as well, unfolding events, quenching phenomena), (ii) establishment of initial states (baselines of native and denatured states) and potential intermediates, application of more than one technique, to discriminate between two- and multi-state behavior, (iii) usage of certain wavelengths for monitoring, close (but not identical) to the maxima of absorption/dichroism or fluorescence emission/excitation, to gain optimal signal-to-noise ratios (frequently wavelengths in the slopes of the spectroscopic peaks are used to enlarge the observables). Spectroscopic studies were complemented by differential scanning calorimetry (DSC) in a CSC 6100 Nano DSC II device, to obtain information on the heat dependence of the protein; evaluations were carried out as described by the manufacturer (program CpCalc v. 2.1) or in [13, 14, 17].

Thermodynamic Analysis of Protein Denaturation

Comparing the native, folded (F) and denatured, unfolded (U) states of a protein allows its conformational stability to be estimated. Provided the $F \leftrightarrow U$ transition is reversible, the equilibrium constant, K, and the free energy change, ΔG, can be determined. The difference in free energy between the native and the denatured state, $\Delta G(H_2O)$ at 25 °C and zero denaturant concentration, is usually defined as the conformational stability of a protein [3, 5, 18–23]. Spectroscopic techniques such as UV absorption, fluorescence and far-UV CD turned out to be extremely useful for monitoring protein unfolding transitions, apart from application of the more time-consuming hydrodynamic techniques [5–7]. UV absorption and fluorescence are used for monitoring changes in the environment of the aromatic chromophores Trp and Tyr, this way signaling, very fast and effective, changes of the tertiary structure of the protein under analysis, while alterations of the secondary structure (α-helix, β-structure, random coil content) can be followed by recording far-UV CD spectra. For the calculation of the free energy of stabilization, ΔG, equilibrium conditions and complete reversibility of the unfolding/folding transition are mandatory, and the existence of significant pre-transition and post-transition regions is required.

Unfolding of small, monomeric, globular proteins commonly obeys the two-state model, $F \leftrightarrow U$; multidomain and oligomeric proteins may exhibit more complex unfolding curves, owing to the accumulation of intermediates [5, 18–21]. In two-state folding transitions only the folded and unfolded conformations exist:

$$f_F + f_U = 1\,, \tag{1}$$

$$y = y_F f_F + y_U f_U\,. \tag{2}$$

Here, f_F and f_U are protein fractions in the folded and unfolded states, y represents an experimental parameter at any point along the denaturation curve, and y_F and y_U are the measured characteristics of the folded and unfolded conformations. Values for y in the transition range are obtained by extrapolation of the pre- and post-transition ranges of the denaturation curve (y vs. c plot, where c symbolizes the denaturant concentration). The values for the equilibrium constant K are estimated in a $\ln K$ vs. c plot by extrapolating several data points near the equilibrium state (i.e. near the midpoint of the denaturation curve). Using the definition of K and the relation between K and ΔG leads to:

$$K = f_U/f_F = (y_F - y)/(y - y_U) \quad \text{and} \tag{3}$$

$$\Delta G = -RT \ln K = -RT \ln[(y_F - y)/(y - y_U)]\,, \tag{4}$$

where R denotes the gas constant, and T the absolute temperature. Investigations of many proteins are evidence for the fact that ΔG varies essentially linearly with the denaturant concentration, at least in the concentration range near the midpoint. Therefore, it is generally assumed that the free energy change in the absence of denaturant, $\Delta G(H_2O)$, can be calculated by extrapolating the experimental data points to zero denaturant concentration:

$$\Delta G = \Delta G(H_2O) - mc\,, \tag{5}$$

where the m value characterizes the dependence of ΔG on the denaturant concentration, c.

Differences in the conformational stabilities of proteins under varying denaturation conditions can also be found by exploiting parameters which do not depend markedly on the unfolding mechanism. For simplicity, the midpoints of the denaturant concentration, $c_{1/2}$, or, in the case of heat experiments, of the thermal unfolding curves, T_m, can be applied, whereas the parameter m turns out to be helpful for unraveling the occurrence of multi-state behavior.

Calorimetric experiments made use of thermodynamic standard equations [13, 14, 19], to derive heat capacities of the U and F states of the protein, $C_p(U)$ and $C_p(F)$. This allows the temperature dependence of the enthalpy change, ΔH, to be calculated:

$$d\Delta H/dT = \Delta C_p = C_p(U) - C_p(F)\,. \tag{6}$$

At the inflection point of the thermal unfolding curve, T_m, the free energy vanishes:

$$\Delta G(T_m) = 0 = \Delta H_m - T_m \Delta S_m\,, \tag{7}$$

where ΔS characterizes the corresponding entropy change.

Results and Discussion

The investigation of the additive-induced effects on the model protein under consideration, monomeric lysozyme, primarily made use of the following surfactants and denaturants: C_{16}TMABr, C_{14}TMABr, C_{12}TMABr, SDS, Zwittergent 3–16, and C_{12}-maltoside as representatives of cationic, anionic, zwitterionic and nonionic surfactants, respectively, and GdmCl and urea as well-known chaotropic denaturants.

For the thermodynamic analysis of the denaturation behavior, spectroscopic investigations at selected wavelengths (monitoring at 292, 360, 280 or 295, and 220 or 230 nm for UV absorption, fluorescence emission, fluorescence excitation, and far-UV CD, respectively) were performed, in order to derive transition curves and equilibrium constants K. As follows from Eq. 4, the ordinate intercepts in the $\ln K$ vs. c plots are proportional to the transition energies ΔG.

The UV absorption of native lysozyme shows only slight changes upon binding of surfactants/denaturants: no significant change of the position of the absorption maximum and only marginal alterations of the absorbance (increases/decreases). In the case of C_{16}TMABr, C_{14}TMABr, C_{12}TMABr, Zwittergent 3–16, and GdmCl, moderate changes of the absorbancies were monitored, the data obtained with GdmCl still being the most reliable ones. Because of unfavorable low signal-to-noise ratios, both the transition curves, absorbance A vs. c, and the $\ln K$ vs. c plots are afflicted with considerable errors, and the same holds true for the changes in free energy, ΔG, derived from K (not shown).

Contrary to the insignificant changes in absorbance, fluorescence emission or excitation data exhibit pronounced changes upon lysozyme-additive complex formation. As proved by the emission at both excitation wavelengths applied, 280 and 295 nm, Trp and Tyr residues must be involved in the interactions between protein and additives. For both fluorophores considerable increases in fluorescence intensity are observed; in the case of GdmCl slight redshifts of their emission maxima are monitored. Pronounced effects can be found for the cationic surfactants C_{16}TMABr (Fig. 1), C_{14}TMABr, and C_{12}TMABr, the zwitterionic surfactant Zwittergent 3–16, and the strong denaturant GdmCl (Fig. 2). The transition curves of these additives (Figs. 3 and 4), fluorescence intensity F vs. c, together with the $\ln K$ vs. c plots, allow ΔG to be estimated, although the curves for C_{12}TMABr and Zwittergent 3–16 reveal experimental deficiencies. SDS, the

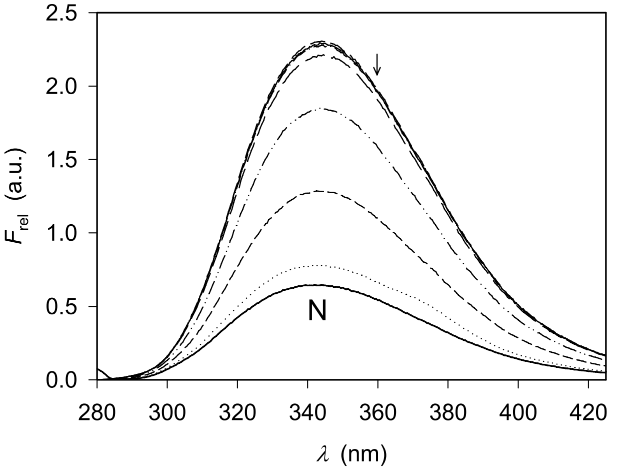

Fig. 1 Selected fluorescence emission spectra ($\lambda_{exc} = 280$ nm) of native lysozyme (0.1 g/l; *N*, *bold solid line*) and lysozyme-C_{16}TMABr complexes (0.05, 0.10, 0.15, 0.20, 0.30, 0.40, 0.50, 0.80 g/l surfactant; the surfactant concentration increases from *bottom* to *top*); the *arrow* indicates the wavelength used for further evaluation

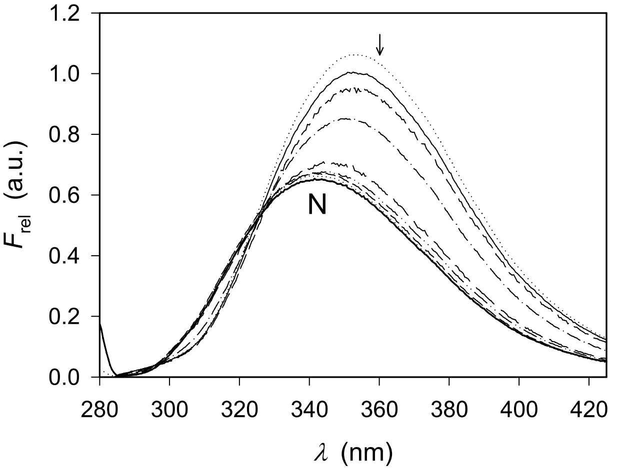

Fig. 2 Selected fluorescence emission spectra ($\lambda_{exc} = 280$ nm) of native lysozyme (0.1 g/l; *N*, *bold solid line*) and lysozyme-GdmCl complexes (1.0, 2.0, 3.0, 3.5, 4.0, 4.5, 5.0, 6.0 M denaturant; the denaturant concentration increases from *bottom* to *top*); the *arrow* indicates the wavelength used for further evaluation

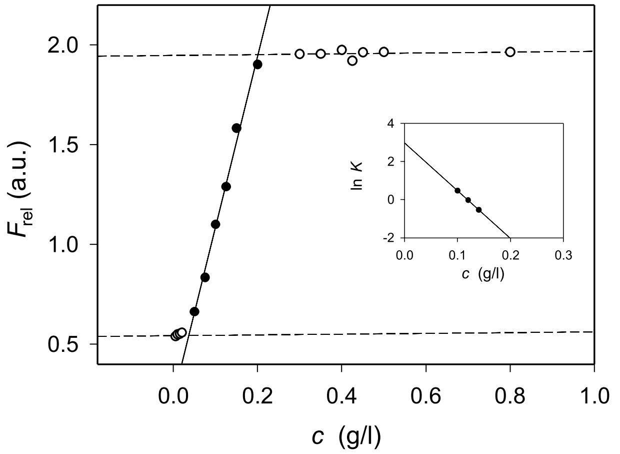

Fig. 3 Conformational stability of lysozyme in the presence of C_{16}TMABr, as monitored by fluorescence emission spectroscopy ($\lambda_{exc} = 280$ nm). The transition curve was constructed from the fluorescence intensities at 360 nm of all spectra monitored. The *lines* illustrate the transition range (*solid line*) and the pre- and post-transition regions (*dashed lines*). *Inset*: Calculation of transition energies, ΔG, from the logarithm of the equilibrium constant, K, for a two-state transition. The *filled circles* illustrate selected points of the regression line in the transition range (at about $c_{1/2}$ and at positions close-by)

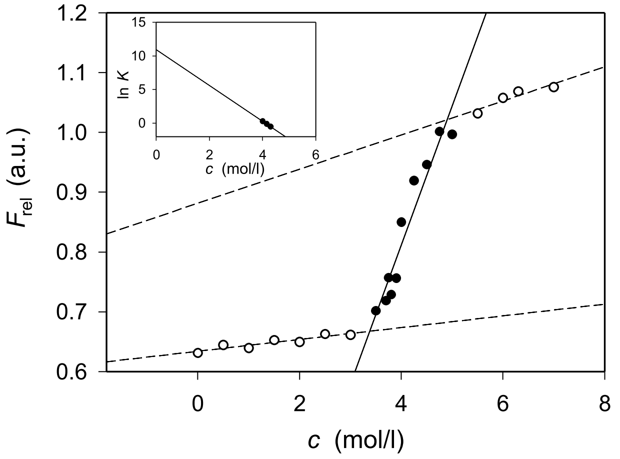

Fig. 4 Conformational stability of lysozyme in the presence of GdmCl, as monitored by fluorescence emission spectroscopy ($\lambda_{exc} = 280$ nm). The transition curve was constructed from the fluorescence intensities at 360 nm of all spectra monitored. The *lines* illustrate the transition range (*solid line*) and the pre- and post-transition regions (*dashed lines*). *Inset*: Calculation of transition energies, ΔG, from the logarithm of the equilibrium constant, K, for a two-state transition. The *filled circles* illustrate selected points of the regression line in the transition range (at about $c_{1/2}$ and at positions close-by)

nonionic surfactants and urea did not allow reliable transition curves to be monitored. Concerning the obtained transition curves and ΔG values, similar results were obtained for all types of fluorescence spectra applied (emission and excitation). The fluorescence results for different types of denaturation are compared in Table 1.

Binding of C_{16}TMABr, C_{14}TMABr, C_{12}TMABr, Zwittergent 3–16, and GdmCl induce slight changes in the far-UV CD spectra, while SDS and urea exhibit only marginal changes in ellipticity, and the nonionic surfactants did not induce any alterations. In the case of surfactant binding, the observed spectral changes, e.g. given as mean-residue weight ellipticities $[\Theta]_{MRW}$, can be interpreted in terms of a slightly reduced helicity of the protein (Fig. 5). The changes obtained upon GdmCl denaturation

Table 1 Midpoint concentration, $c_{1/2}$, dependence of ΔG on denaturant concentration, m, and free energy change, $\Delta G(\mathrm{H_2O})$, for probing the conformational stability of unreduced lysozyme upon addition of various additives at 25 °C, as revealed by evaluating different types of fluorescence data (emission spectra: excitation at 280 or 295 nm; excitation spectra: emission at 339 nm) and the assumption of two-state transitions

Additive	$c_{1/2}$ ($\mathrm{g\,l^{-1}}$)	m ($\mathrm{kJ\,mol^{-1}\,g^{-1}\,l}$)	$\Delta G(\mathrm{H_2O})$ ($\mathrm{kJ\,mol^{-1}}$)
$\mathrm{C_{12}TMABr}$	1.18 ± 0.19	13.7 ± 2.7	-15.4 ± 2.9
$\mathrm{C_{14}TMABr}$	0.50 ± 0.00	44.4 ± 0.4	-22.5 ± 0.2
$\mathrm{C_{16}TMABr}$	0.12 ± 0.00	60.7 ± 0.1	-7.3 ± 0.1
Zwittergent 3–16	0.10 ± 0.01	69.7 ± 0.4	-7.7 ± 0.3
GdmCl	395 ± 4 [a]	0.077 ± 0.013 [b]	-30.0 ± 4.9

[a] corresponding to 4.14 ± 0.04 M

[b] corresponding to $7.34 \pm 1.24\ \mathrm{kJ\,mol^{-1}\,M^{-1}}$

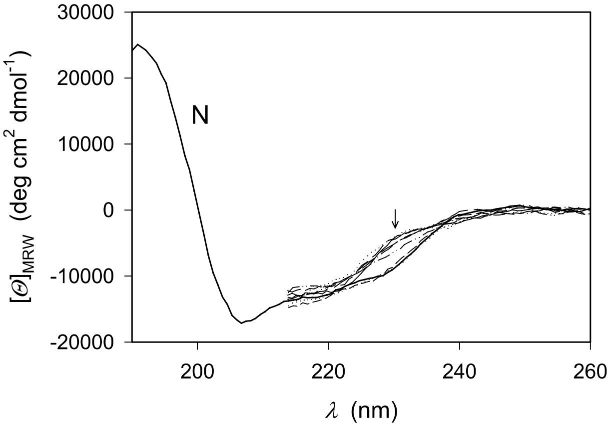

Fig. 5 Selected far-UV CD spectra of native lysozyme (0.1 g/l; *N*, *bold solid line*) and lysozyme-$\mathrm{C_{16}TMABr}$ complexes (0.05, 0.10, 0.15, 0.20, 0.30, 0.40, 0.50, 0.80 g/l surfactant; the surfactant concentration increases from *bottom* to *top*). The CD curves of the complexes were terminated at low wavelengths because of unfavorable signal-to-noise ratios; the *arrow* indicates the wavelength used for further evaluation

represent the most extensive reductions of the helix content (Fig. 6). An analysis of the CD signals in terms of transition curves (Figs. 7 and 8), ellipticity $[\Theta]$ vs. c, and $\ln K$ vs. c plots again reveal a two-state mechanism, as already observed with the fluorescence behavior.

For comparison, DSC was used for monitoring the thermal unfolding of the surfactant-free protein. The partial molar heat capacity, C_p, obtained as a function of temperature, can be used for determination of T_m and establishment of a two-state model (after preceding deconvolution). The following values were obtained: $T_\mathrm{m} = 77.6\,°\mathrm{C}$, $\Delta C_\mathrm{p} = 5.9\ \mathrm{kJ\,mol^{-1}\,K^{-1}}$, $\Delta H_{\mathrm{m(cal)}} = 590\ \mathrm{kJ\,mol^{-1}}$, and $\Delta S_\mathrm{m} = 1.7\ \mathrm{kJ\,mol^{-1}\,K^{-1}}$.

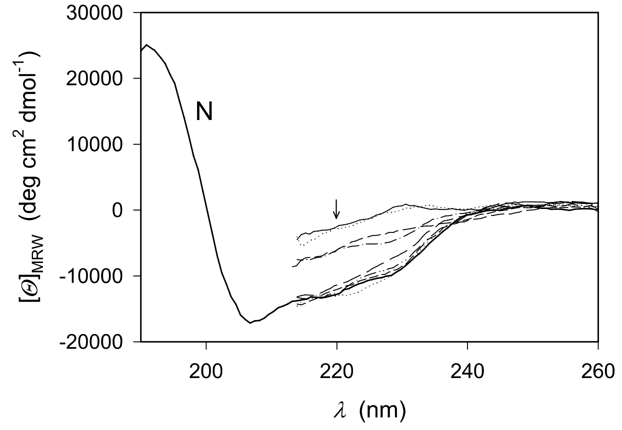

Fig. 6 Selected far-UV CD spectra of native lysozyme (0.1 g/l; *N*, *bold solid line*) and lysozyme-GdmCl complexes (1.0, 2.0, 3.0, 3.5, 4.0, 4.5, 5.0, 6.0 M denaturant; the denaturant concentration increases from *bottom* to *top*). The CD curves of the complexes were terminated at low wavelengths because of unfavorable signal-to-noise ratios; the *arrow* indicates the wavelength used for further evaluation

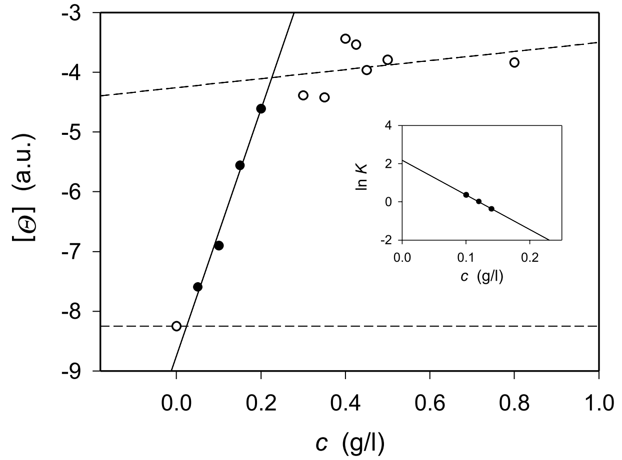

Fig. 7 Conformational stability of lysozyme in the presence of $\mathrm{C_{16}TMABr}$, as monitored by far-UV CD spectroscopy. The transition curve at 230 nm (average of values between 228 and 232 nm) was obtained from the whole set of spectra. The *lines* illustrate the transition range (*solid line*) and the pre- and post-transition regions (*dashed lines*). *Inset*: Calculation of transition energies, ΔG, from the logarithm of the equilibrium constant, K, for a two-state transition. The *filled circles* illustrate selected points of the regression line in the transition range (at about $c_{1/2}$ and at positions close-by)

Conclusions

UV absorption, fluorescence and CD spectra were applied to quantify the denaturing effect of different ionic and nonionic surfactants as well as chaotropic denaturants on lysozyme. In several cases, equilibrium transitions could be registered and allowed the Gibbs free energy induced by the additives to be determined. Because of the simplic-

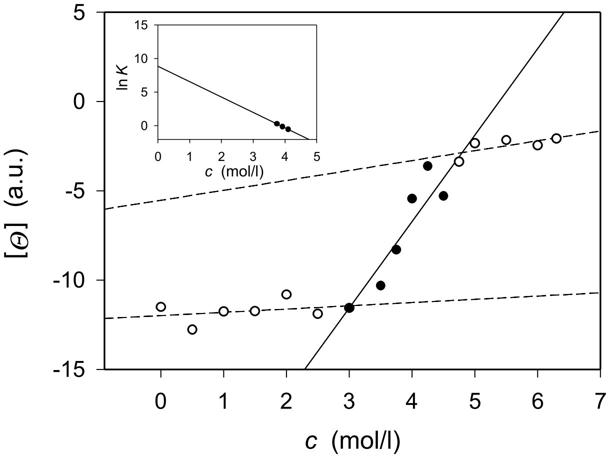

Fig. 8 Conformational stability of lysozyme in the presence of GdmCl, as monitored by far-UV CD spectroscopy. The transition curve at 220 nm (average of values between 218 and 222 nm) was obtained from the whole set of spectra. The *lines* illustrate the transition range (*solid line*) and the pre- and post-transition regions (*dashed lines*). *Inset*: Calculation of transition energies, ΔG, from the logarithm of the equilibrium constant, K, for a two-state transition. The *filled circles* illustrate selected points of the regression line in the transition range (at about $c_{1/2}$ and at positions close-by)

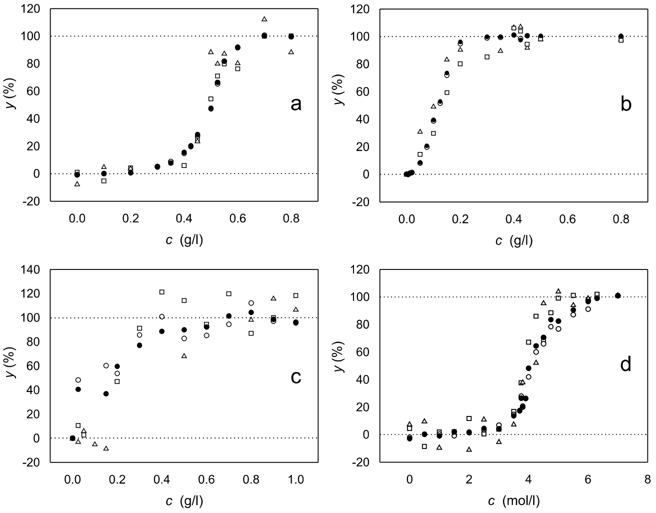

Fig. 9 Spectral properties of lysozyme (0.1 g/l) treated with varying amounts of surfactants (0–1 g/l) or GdmCl (0–7 M). The spectral signals were derived at the wavelengths applied for monitoring the transition curves: (Δ) absorbance (evaluation at 292 nm); (●) fluorescence emission (excitation at 280 nm, evaluation at 360 nm); (○) fluorescence emission (excitation at 295 nm, evaluation at 360 nm); (□): ellipticity (evaluation at 230 or 220 nm). The normalized spectral properties were plotted vs. the respective additive concentrations: **a** C_{14}TMABr, **b** C_{16}TMABr, **c** Zwittergent 3–16, **d** GdmCl

ity of the experimental transition curves, simple two-state models could be applied to interpret the transitions, although the existence of slight amounts of intermediates cannot be excluded completely. In principle all applied spectroscopic techniques can be applied for deriving transition curves and stabilization energies (Fig. 9, Table 1). However, fluorescence spectroscopy (emission or excitation) should be the method of choice, since this technique yields by far the most pronounced conformational changes and, therefore, the most reliable results concerning the establishment of stabilization energies. Owing to the varying size of the observed effects for different techniques and additives, the quality of the monitored transition curves is quite different. It is not surprising that nonionic surfactants do not unfold the protein.

Contrary to many other proteins, e.g. bovine serum albumin (BSA) [5–7], the anionic surfactants, including the strong denaturant SDS, however, seem to have no severe effect on the native protein structure. In the case of lysozyme, this is presumably caused by the surface features of this protein [2, 24, 25]. In this context it is also of interest that, at moderate SDS concentrations (< 0.2 g/l), the surface-charge peculiarities of lysozyme also cause some protein precipitation, a phenomenon which has already been addressed earlier [24]. On the other hand, the far-reaching resistance of the enzyme to urea might be due to the higher purity of the samples (protein and additives) available nowadays, if compared to the missing resistance of the protein in previous denaturation attempts [26].

The ΔG values found for the surfactants which are effective in the case of lysozyme, namely the cationic and zwitterionic surfactants, turn out to be substantially lower than the value observed after the impact of excess of the strong chaotropic denaturant GdmCl (Table 1: -7.3 to $-22.5\,\mathrm{kJ\,mol^{-1}}$ compared to $-30.0\,\mathrm{kJ\,mol^{-1}}$). This is in accord with previous observations on BSA [5–7]. With the cationic trimethylammonium bromides, the influence of the hydrophobic chain length was tested. As may be taken from the values in Table 1, however, currently no clear-cut answer can be given. The $c_{1/2}$ values obviously follow the influence of the chain length ($1.18 \rightarrow 0.50 \rightarrow 0.12$ g/l for C_{12}TMABr → C_{14}TMABr → C_{16}TMABr), while the ΔG data ($-15.4 \rightarrow -22.5 \rightarrow -7.3\,\mathrm{kJ\,mol^{-1}}$) seem to be influenced by additional factors. These factors might include different reversibility of the reactions, existence of intermediates, different influence of the additives on the aromatics (Trp and Tyr) and the elements of the secondary structure of the protein, and, thus, on the ΔG values obtained for different processes and monitored by different experimental techniques.

Calorimetric determinations as well as GdmCl- and heat-induced denaturation studies of many proteins have been reported to yield ΔG values varying between about -20 and $-60\,\mathrm{kJ\,mol^{-1}}$ [22, 23, 27, 28]. As follows from an inspection of manifold data for lysozyme (e.g., [19, 26, 29–33]) and other proteins (summarized in [22, 23]), the broad range of the values mentioned is caused by varying experimental conditions, evaluation models, assumptions, and investigation techniques. The experimental conditions refer to variations of pH, temperature, nature and concentration of denaturants and other additives including reductants etc. Thus, the choice of the conditions may lead to different extents of unfolding/denaturation, even under strong chaotropic conditions. For example, the (frequently unavoidable) absence of reduction steps preserves the existence of disulfide bonds that stabilize the tertiary structure of many proteins. Therefore, even for GdmCl-unfolded disulfide-containing proteins, pronounced deviations from random coil properties may exist. Denatured unreduced proteins behave as cross-linked random coils, i.e. as essentially structureless coils constrained by disulfide bonds.

According to the results presented in Table 1, even the impact of high concentrations of surfactants yields incomplete randomization of the protein conformation; appreciable amounts of secondary structure remain unaffected, even under saturation conditions of the protein with these ligands. The insufficient unfolding/denaturation behavior provided by surfactants is similar to the weak effect caused by acid denaturation [16]. By contrast, strong denaturants such as GdmCl or heat may lead to a maximum chaotropic effect, producing a more or less complete loss of the helix content or other ordered structure and maximum random-coil formation.

As a consequence of the different efficacy of heat or strong chaotropes on protein unfolding/denaturation, on the one hand, and of surfactants or acid denaturation, on the other, the values obtained for ΔG seem to bear a quite different meaning. While the former agents yield specific values for the stabilization energy of the proteins under investigation, the latter ones rather characterize the unfolding/denaturation power of a chosen surfactant/denaturant. In this context, different techniques of investigations may detect different unfolding events, thereby leading to different values concerning the parameters analyzed. This also holds for the use of the various spectroscopic techniques addressing quite different molecular aspects such as certain chromophores and their environment or the elements of the secondary structure of the proteins, respectively.

Future experiments should cover a variety of experimental conditions such as the use of various proteins with different characteristics (e.g. varying Trp/Tyr and helix contents), numerous surfactants of different nature (including variable chain length), and usage of different experimental techniques. This should allow reliable statements on the influence of structural details of surfactants, such as nature of head groups or chain length, on the thermodynamic processes involved (surfactant binding, unfolding behavior of the proteins) to be established.

References

1. Creighton TE (1993) Proteins. Structures and Molecular Properties, 2nd edn. Freeman, New York
2. Durchschlag H, Zipper P (2004) Prog Colloid Polym Sci 127:98–112
3. Jones MN (1988) In: Jones MN (ed) Biochemical Thermodynamics, 2nd edn. Elsevier, Amsterdam, p 182–240
4. Jones MN, Chapman D (1995) Micelles, Monolayers, and Biomembranes. Wiley-Liss, New York
5. Tiefenbach K-J, Durchschlag H, Schneider G, Jaenicke R (2003) Prog Colloid Polym Sci 122:130–140
6. Durchschlag H, Tiefenbach K-J, Bayersdorfer F, Pachmann G, Jaenicke R (2003) Jorn Com Esp Deterg 33:281–293
7. Tiefenbach K-J, Durchschlag H, Jaenicke R (2004) Prog Colloid Polym Sci 127:136–147
8. Schmid FX (1997) In: Creighton TE (ed) Protein Structure: A Practical Approach, 2nd edn. IRL, Oxford, p 261–297
9. Shirley BA (1995) Methods in Molecular Biology, vol 40: Protein Stability and Folding: Theory and Practice. Humana Press, Totowa NJ
10. Demchenko AP (1986) Ultraviolet Spectroscopy of Proteins. Springer, Berlin
11. Lakowicz JR (1999) Principles of Fluorescence Spectroscopy, 2nd edn. Kluwer/Plenum, New York
12. Fasman GD (1996) Circular Dichroism and the Conformational Analysis of Biomolecules. Plenum, New York
13. Holtzhauer M (1996) Methoden in der Proteinanalytik. Springer, Berlin
14. Winter R, Noll F (1998) Methoden der Biophysikalischen Chemie. Teubner, Stuttgart
15. Durchschlag H, Tiefenbach K-J, Gebauer S, Jaenicke R (2001) J Mol Struct 563–564:449–455
16. Durchschlag H, Tiefenbach K-J, Weber R, Kuchenmüller B, Jaenicke R (2000) Colloid Polym Sci 278:312–320
17. Freire E (1995) Methods Mol Biol 40:191–218
18. Pace CN (1986) Methods Enzymol 131:266–280
19. Pace CN, Shirley BA, Thomson JA (1989) In: Creighton TE (ed) Protein Structure: A Practical Approach. IRL, Oxford, p 311–330
20. Shirley BA (1992) In: Ahern TJ, Manning MC (eds) Stability of Protein Pharmaceuticals, Part A: Chemical and Physical Pathways of Protein Degradation. Plenum, New York, p 167–194
21. Shirley BA (1995) Methods Mol Biol 40:177–190
22. Pfeil W (1986) In: Hinz H-J (ed) Thermodynamic Data for Biochemistry and Biotechnology. Springer, Berlin, p 349–376
23. Pfeil W (1998) Protein Stability and Folding: A Collection of Thermodynamic Data. Springer, Berlin, and (2001) Supplement 1

24. Fukushima K, Murata Y, Nishikido N, Sugihara G, Tanaka M (1981) Bull Chem Soc Jpn 54:3122–3127
25. Subramanian M, Sheshadri BS, Venkatappa MP (1984) J Biochem 95:413–421
26. Ahmad F, Bigelow CC (1982) J Biol Chem 257:12935–12938
27. Pfeil W (1988) In: Jones MN (ed) Biochemical Thermodynamics, 2nd edn. Elsevier, Amsterdam, p 53–99
28. Pfeil W (1996) In: Holtzhauer M (ed) Methoden in der Proteinanalytik. Springer, Berlin, p 276–310
29. Aune KC, Tanford C (1969) Biochemistry 8:4586–4590
30. Greene RF Jr, Pace CN (1974) J Biol Chem 249:5388–5393
31. Ahmad F, Contaxis CC, Bigelow CC (1983) J Biol Chem 258:7960–7963
32. Makhatadze GI, Privalov PL (1992) J Mol Biol 226:491–505
33. Gupta R, Ahmad F (1999) Biochemistry 38:2471–2479

Progr Colloid Polym Sci (2006) 133: 131–141
DOI 10.1007/2882_072

SURFACTANTS

Paulo A. R. Pires
Omar A. El Seoud

Benzyl (3-Acylaminopropyl) Dimethylammonium Chloride Surfactants: Structure and Some Properties of the Micellar Aggregates

Paulo A. R. Pires · Omar A. El Seoud (✉)
Instituto de Química, Universidade de São Paulo, C.P. 26077, 05513-970 São Paulo, Brazil
e-mail: elseoud@iq.usp.br

Abstract The title cationic surfactants were synthesized by the scheme in Fig. 1, where RCO_2H refers to decanoic, dodecanoic, tetradecanoic and hexadecanoic acid, respectively. In aqueous solution, the micelle/water interface may be located at the quaternary ammonium ion or at the amide group. The following pieces of evidence indicate that the interface lies at the latter site: theoretically calculated aggregation numbers and those determined by static light scattering; dependence on surfactant concentration, below and above the critical micelle concentration, cmc, of both the IR frequency of amide I band and ^{1}H NMR chemical shifts of the discrete surfactant protons. Solution conductance and calorimetric titration have been employed to study the aggregation of these surfactants in water at 25 °C. Increasing the length of R resulted in a decrease of the cmc and the degree of counter–ion dissociation, α_{mic}. Gibbs free energies of micelle formation were calculated and divided into contributions from the methylene groups of the hydrophobic tail, and the terminal methyl plus head-group. The former are similar to those of other surfactants, whereas the latter are more negative, i.e., the transfer of the head-group from bulk water to the micelle is more favorable. This is attributed to direct or water-mediated H-bonding of the micellized surfactant molecules, via the amide group, in agreement with the IR data presented.

Keywords Aggregation numbers · Benzyl (3-acylaminopropyl) dimethylammonium chloride surfactants · Cationic surfactants · Counter–ion dissociation · Critical micelle concentration

Introduction

The structural variables of surfactants include the length of the hydrophobic tail, the nature of the counter–ion, and the structure/charge of the head-group. Although many important applications of surfactant solutions, e.g., solubilization, emulsion formation and catalysis reflect substrate–head-group interactions, the latter structural variable has been much less studied than the former ones [1–7]. Cationic surfactants are amenable to this line of study because the structure of their head-group can be changed while maintaining constant the nature of the head-ion, e.g. quaternary ammonium. Work has been carried out on surfactants whose general structure is given by: $RN^+R'R''R''' X^-$, where $X^- =$ halide ion; R = octyl to octadecyl; R′, R″, and R‴ generally represent iden-

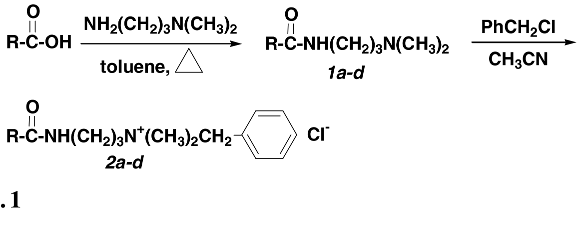

Fig. 1

tical alkyl groups, e.g., trimethyl. A number of studies have employed R′ and R″ = methyl and R‴ = alkyl, benzyl or alkylphenyl group [1–3, 8–11]. One of the alkyl groups of the head-ion may carry functionality, e.g., the 2-hydoxyethyl group. Interestingly, the effects of this group on the micellar parameters are not significantly different from those of an ethyl group [12–16]. Surfactants that carry the amide group may, in principle, form direct or water-mediated inter-molecular hydrogen-bonds, akin to those formed by *N*-alkylamides, and polypeptides [17–19]. Additionally, surfactants that carry the amide group and a (negative) charge, separated by a "spacer" have some interesting interfacial properties, due to the simultaneous presence of both moieties [20]. We were interested, therefore, in investigating how a similar structural feature (amide group and a positive charge) bears on solution properties of surfactants.

Recently, we studied the micellar properties of $RCONH(CH_2)_2N^+(CH_3)_3Cl^-$, and $RCONH(CH_2)_2N^+(CH_3)_2CH_2C_6H_5Cl^-$, where RCO = C_{10}, C_{12}, C_{14} and C_{16}, respectively. Gibbs free energies of micelle formation were found to be more favorable than those of structurally similar cationic surfactants that do not carry the amide group. This was attributed to direct or water-mediated hydrogen-bonding between the surfactant molecules in the aggregate [21–26]. We report here on the synthesis of the following series: $RCONH(CH_2)_3N^+(CH_3)_2CH_2C_6H_5Cl^-$, where RCO = C_{10}, $C_{10}APrBzMe_2Cl$; C_{12}, $C_{12}APrBzMe_2Cl$; C_{14}, $C_{14}APrBzMe_2Cl$; and C_{16}, $C_{16}APrBzMe_2Cl$; (A), (Pr) and (Bz) stand for ($-NH(CH_2)_3N^+$), *n*-C_3H_6 and the benzyl group, respectively. IR data of the amide I band of $C_{10}APrBzMe_2Cl$ and that of a short-chain, i.e., non-aggregated analogue indicated that the amide group in the micelle is hydrated, i.e., present in the interfacial region. ^1H NMR data of the discrete surfactant protons, below and above the cmc, indicated that the benzyl group "folds back" toward the aggregate interior. Gibbs free energies of micellization of the surfactants studied are more favorable than those of $RN^+(CH_3)_2CH_2C_6H_5Cl^-$, $RBzMe_2Cl$, due to the above-mentioned hydrogen-bonding.

Experimental

Materials

The chemicals were purchased from Acros or Merck, and were purified by standard procedures [27]. The series $RBzMe_2Cl$ was available from a previous study [25].

Apparatus

Melting points were determined with Electrothermal IA 6304 apparatus. We used Shimadzu model GC 17A-2 gas chromatograph equipped with FID detector and Supelcowax 10 capillary column (from Supelco). FTIR spectra were recorded with a Bruker Vector 22 spectrometer. ^1H and ^{13}C NMR spectra were recorded with Varian Innova-300 or Bruker DRX-500 spectrometers. Elemental analyses were carried out on Perkin-Elmer model 2400 CHN apparatus in the Elemental Analyses laboratory of this Institute.

Synthesis

Chromatographically pure carboxylic acids were obtained as follows: Ethyl esters of the decanoic to hexadecanoic acids were prepared by their reaction with anhydrous ethanol (Mensalão Química, DF), in the presence of H_2SO_4 as catalyst. The esters were purified by fractional distillation under reduced pressure in a 50 cm Vigreux column. This process was repeated until the ester was chromatographically pure. The following conditions were employed in the CG analysis: Injector temperature 250 °C; FID temperature 280 °C; carrier gas N_2, 1.5 cm^3/min, split ratio 1 : 50. The column was kept at 100 °C for 8 minutes, heated at 10 °C/minute for 5 minutes, kept at 150 °C for 15 minutes, heated at 10 °C/minute for 5 minutes, then kept at 200 °C for the rest of the analysis. The retention times were 15.7, 24.7, 34.0, 41.2 minutes, for the ethyl esters of decanoic, dodecanoic, tetradecanoic, and hexadecanoic acid, respectively. The corresponding acids were obtained by alkaline hydrolysis in 50% aqueous methanol, followed by removal of the solvent and acidification with HCl. The carboxylic acid was separated, washed with hot water until the aqueous phase was free of Cl^-, and dried. The physical properties of the acids obtained agree with literature values [28].

Amidoamines, $RCONH(CH_2)_3N(CH_3)_2$, Compounds 1a to 1d

The following reaction was carried out under dry, oxygen-free nitrogen: to a stirred solution of the carboxylic acid (0.70 mol) in 250 mL of toluene were added, drop-wise, 88 mL (0.70 mol) of 3-*N*,*N*-dimethylamino-1-propylamine. The bath temperature was raised to 120–130 °C, and the formation of the product was followed by measuring the volume of the water produced (Dean-Stark trap), and by monitoring the disappearance of the $\nu_{C=O}$ peak of the free acid at ca. 1720 cm^{-1}; usually 16 hours were required for reaction completion. After solvent evaporation, product (**1**) was purified either by fractional distillation, **1a** and **1b**, or by recrystallization from anhydrous acetone, **1c** and **1d**. TLC analysis of each product showed a single spot.

Compound **1a**, $C_9H_{19}CONH(CH_2)_3N(CH_3)_2$.

Colorless, viscous liquid, b.p. 179.5–181.0 °C (1.5 mm Hg); yield, 74%. IR (film, NaCl plates, frequencies are reported in cm^{-1}) 3290 (n_{N-H}, secondary amide), 1645 (amide I band), 1554 (amide II band). The structures depicted below show the numbering employed for reporting the ^{1}H, and ^{13}C NMR data, respectively, where n = total number of equivalent hydrogens (due to virtual coupling) or equivalents carbons of the chain:

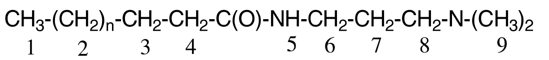

$CH_3\text{-}(CH_2)_n\text{-}CH_2\text{-}CH_2\text{-}C(O)\text{-}NH\text{-}CH_2\text{-}CH_2\text{-}CH_2\text{-}N\text{-}(CH_3)_2$

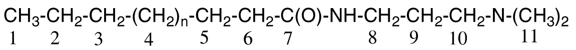

$CH_3\text{-}CH_2\text{-}CH_2\text{-}(CH_2)_n\text{-}CH_2\text{-}CH_2\text{-}C(O)\text{-}NH\text{-}CH_2\text{-}CH_2\text{-}CH_2\text{-}N\text{-}(CH_3)_2$

^{1}H NMR (CDCl$_3$, chemical shifts, δ and coupling constants, J, are reported in ppm and Hz, respectively): 0.88 (t, 3H, **H1**, $J_{1-2} = 7.1$), 1.27 (broad peak, 12H, **H2**), 1.61 (quintet, 2H, **H3**, $J_{2-3} = 7.3$ and $J_{3-4} = 7.5$), 2.17 (t, 2H, **H4**), 7.60 (broad singlet, 1H, **H5**), 3.28 (multiplet, 2H, **H6**, $J_{6-5} = 6.1$; $J_{6-7} = 6.4$); 1.67 (doublet of triplets, 2H, **H7**, $J_{7-8} = 6.7$); 2.38 (triplet, 3H, **H8**), 2.24 (s, 6H, **H9**).

^{13}C NMR (CDCl$_3$): 14.12 (C**1**), 22.69 (C**2**), 31.91 (C**3**), 29.34 to 29.55, (*four lines*, C**4**), 25.93 (C**5**), 36.73 (C**6**), 173.37 (C**7**), 38.59 (C**8**), 26.63 (C**9**), 58.03 (C**10**), 45.23 (C**11**).

Compound **1b**, $C_{11}H_{23}CONH(CH_2)_3N(CH_3)_2$.

White waxy solid; mp 31–33 °C, bp 208–211 °C (3.5 mm Hg); yield, 90%. IR (KBr) 3306 (n_{N-H}, secondary amide), 1641 (amide I band), 1555 (amide II band).

The ^{1}H NMR and ^{13}C NMR spectra of compounds **1b**–**1d** (CDCl$_3$) were found to be similar to those of **1a**, within the following limits: ^{1}H NMR (0 to ±0.005 ppm) and ^{13}C NMR (±0.03 ppm). For all compounds, the ^{13}C NMR region for C**4** showed 6 lines.

Compound **1c**, $C_{13}H_{27}CONH(CH_2)_3N(CH_3)_2$.

White waxy solid; mp 48–49 °C; bp 193–195 °C (0.5 mm Hg); yield, 60%. The IR spectra (KBr) of compounds **1c,d** are similar to that of **1b**, within the following limits: $\pm 3\ cm^{-1}$ for n_{N-H} and $\pm 1\ cm^{-1}$ for amide I and II bands.

Compound **1d**, $C_{15}H_{31}CONH(CH_2)_3N(CH_3)_2$.

White solid; mp 57–58 °C; yield, 83%.

Surfactants

The following reaction was carried out under dry, oxygen-free nitrogen: a mixture of 0.1 mol of compound **1** and 12.6 mL (0.11 mol) of benzyl chloride in 100 mL of anhydrous acetonitrile was refluxed for 8 hours. The solvent and un-reacted benzyl chloride were removed, the product was recrystallized from anhydrous acetone and dried under reduced pressure. All surfactants were hygroscopic solids, and were analyzed as (non-hygroscopic) perchlorate salts. The structures depicted below show the numbering employed for reporting the ^{1}H, and ^{13}C NMR data of the surfactant cation, respectively. Note that the (ortho) and (meta) ring protons form the AA′ and BB′ part of the aromatic ring:

For ^{1}H NMR

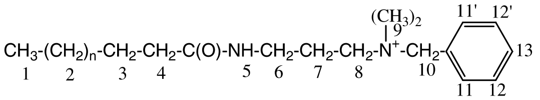

For ^{13}C NMR

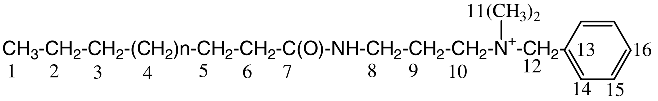

Surfactant 2a, C_{10}APrBzMe$_2$Cl**:** yield, 80%; Anal. Calcd for $C_{22}H_{39}N_2O_5Cl$: C, 59.16; H, 8.81; N, 6.28. Found: C, 58.94; H, 8.64; N, 6.35. IR (KBr), 3277 (n_{N-H}, secondary amide), 1649 (amide I band), 1555 (amide II band). ^{1}H NMR: (CDCl$_3$): 0.87 (t, 3H, **H1**, $J_{1-2} = 7.1$), 1.22 (broad peak, 12H, **H2**), 1.53 (quintet, 2H, **H3**, $J_{2-3} = 6.5$ and $J_{3-4} = 7.2$), 2.22 (t, 2H, **H4**), 3.32 (quadruplet, 2H, **H6**, $J_{6-5} = 10.4$ and $J_{6-7} = 6.0$), 2.17 (doublet of triplets, 2H, **H7**, $J_{7-8} = 9.7$), 3.63 (t, 3H, **H8**), 3.17 (s, 6H, **H9**), 4.81 (s, 2H, **H10**); 7.61 (d, 2H, **H11**(**11**′), $J_{11-12} = 6.9$); 7,39 (multiplet, 2H, **H12**(**12**′), $J_{12-13} = 7.2$); 7.44 (multiplet, 1H, **H13**).

^{13}C NMR (CDCl$_3$): 14.11 (C**1**), 22.63 (C**2**), 31.84 (C**3**), 29.30 to 29.52 (four lines, C**4**), 25.83 (C**5**), 36.29 (C**6**), 174.52 (C**7**), 36.16 (C**8**), 23.06 (C**9**), 62.27 (C**10**), 49.74 (C**11**); 67.33 (C**12**); 127.36 (C**13**); 133.15 (C**14**); 129.17 (C**15**); 130.66 (C**16**).

Surfactant 2b, C_{12}APrBzMe$_2$Cl**:** yield, 72%. Anal. Calcd for $C_{24}H_{43}N_2O_5Cl$: C, 60.72; H, 9.14; N, 5.90. Found: C, 60.86; H, 8.95; N, 5.83.

The spectroscopic data for this surfactant and for the others below, are similar to those of **2a**, within the following limits: IR ($\pm 2\ cm^{-1}$, and $4\ cm^{-1}$ for the N – H proton, amide I and amide II band, respectively), ^{1}H NMR (0 to ±0.01 ppm for the aliphatic and aromatic protons and 0.02 ppm for the NH proton), ^{13}C NMR (±0.02 ppm).

Surfactant 2c, C_{14}APrBzMe$_2$Cl**:** yield, 69%. Anal. Calcd for $C_{26}H_{47}N_2O_5Cl$: C, 62.11; H, 9.43; N, 5.58. Found: C, 62.14; H, 9.30; N, 5.82.

Surfactant 2d, C_{16}APrBzMe$_2$Cl**:** yield, 75%. Anal. Calcd for $C_{28}H_{51}N_2O_5Cl$: C, 63.35; H, 9.69; N, 5.28. Found: C, 63.27; H, 9.40; N, 5.15.

Short-chain Analogue of Surfactants, C_4APrBzMe$_2$Cl

This compound (white solid) was synthesized according to the procedure described above, by employing butyric acid. The structure depicted below shows the numbering employed for reporting the ^{1}H NMR data of the cation:

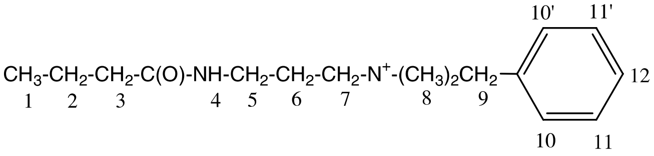

IR (KBr): 3446 ($n_{\mathrm{N-H}}$, secondary amide), 1653 (amide I band), 1548 (amide II band). ^{1}H NMR ($CDCl_3$): 0.88 (t, 3H, **H1**, $J_{1-2} = 7.4$), 1.60 (sextet, 2H, **H2**, $J_{2-3} = 7.5$), 2.26 (t, 2H, **H3**), 3.36 (doublet of triplets, 2H, **H5**, $J_{4-5} = 6.0$ $J_{5-6} = 6.0$), 2.19 (quintet, 2H, **H6**, $J_{6-7} = 7.4$); 3.77 (triplet, 2H, **H7**); 3.23 (s, 9H, **H8**), 4.89 (s, 2H, **H9**); 7.64 (doublet of triplets, 2H, **H10(10′)**, $J_{10-11} = 7.0$ and $J_{10-12} = 1.3$); 7,43 (multiplet, 2H, **H11(11′)**, $J_{11-12} = 7.6$); 7.48 (multiplet, 1H, **H12**).

Measurements of Properties of Micellar Solutions

Glass double-distilled, de-ionized water was used throughout. Before use, all glassware was soaked in 0.001M EDTA solution and thoroughly washed with water. Each surfactant was weighted, dried under reduced pressure, over P_4O_{10} until constant weight before making up the solution.

Solution Conductivity

Conductivity measurements were recorded for RAPrBz Me_2Cl or $RBzMe_2Cl$ at 25 °C with a PC-interfaced Fisher model Accumet 50 ion-meter, provided with a DM-C1 micro-conductivity cell (Digimed, São Paulo) and a Schott model Titronic T200 programmed burette. Home-developed software was employed for addition of the surfactant solution and data acquisition. Plots of conductivity versus the total surfactant concentration, $[\mathrm{Surf}]_t$, gave two straight lines intersecting at the cmc. The following equation was employed in order to obtain a more accurate cmc [29]:

$$\kappa([\mathrm{Surf}]_t) = \kappa(0) + S_1[\mathrm{Surf}]_t + \mathrm{d}x(S_2 - S_1)\ln\left(\frac{1+\mathrm{e}^{([\mathrm{Surf}]_t-\mathrm{cmc})/\mathrm{d}x}}{1+\mathrm{e}^{-\mathrm{cmc}/\mathrm{d}x}}\right), \qquad (1)$$

where $\kappa([\mathrm{Surf}]_t)$, $\kappa(0)$, S_1, S_2, and $\mathrm{d}x$ are the conductivity of the solution (i.e., at $[\mathrm{Surf}]_t$) and at infinite dilution, the slopes of the pre- and post-micellar regions of conductivity versus [surfactant] plot, and the width of the cmc transition ($\mathrm{d}x \approx 10\%$ of the cmc), respectively.

The degree of dissociation of the surfactant counter–ion, α_{mic}, was calculated from conductance data by use of two equations, that of Frahm [30]:

$$\alpha_{\mathrm{mic}} = (S_2/S_1), \qquad (2)$$

where S_1 and S_2 are the slopes of the pre- and post-cmc regions of conductivity versus [surfactant] plot. The second equation is that of Evans [31]:

$$1000S_2 = \frac{\alpha_{\mathrm{mic}}^2}{(N_{\mathrm{agg}})^{-2/3}}\left(1000S_1 - \Lambda_{\mathrm{Cl}^-}\right) + \alpha_{\mathrm{mic}}\Lambda_{\mathrm{Cl}^-}, \qquad (3)$$

where Λ_{Cl^-} refers to the equivalent conductance of the surfactant counter–ion at infinite dilution and N_{agg} is the micellar aggregation number; the other symbols have their usual meaning.

FTIR Measurements

The cmc of $C_{10}APrBzMe_2Cl$ in D_2O was determined by FTIR, by employing the above-mentioned spectrometer, and a 0.025 mm path-length CaF_2 cell (Wilmad Glass). The spectrometer sample compartment was flushed with dry nitrogen. The frequency of amide I band was measured as function of [surfactant], at 0.5 cm^{-1} digital resolution. The background spectrum of pure D_2O was subtracted from the spectrum of the sample.

Static Light Scattering (SLS)

Static light scattering was recorded at 25 ± 0.1 °C with Malvern 4700 system. The surfactant solutions contained 0.1 $\mathrm{mol\,L^{-1}}$ NaCl, and were filtered through 0.22 µm cellulose acetate membranes. All measurements were recorded at 90° scattering angle, by employing a home-developed software for scattering data acquisition. Solution refractive index increment was measured with Wyatt Optilab 903 interferometric differential refractometer, operating at 633 nm.

The micellar weight-averaged molar mass, M_{w}, was calculated by [3]:

$$K([\mathrm{Surf}]_t - \mathrm{cmc})/\Delta R_{90} = 1/M_{\mathrm{w}} + 2B([\mathrm{Surf}]_t - \mathrm{cmc}), \qquad (4)$$

where ΔR_{90} is the Rayleigh ratio of micellized surfactant, $\Delta R_{90} = R_{90}$ (surfactant solution) – R_{90} (surfactant solution at cmc), $[\mathrm{Surf}]_t$ and cmc are expressed in g/L, B is the second virial coefficient, and K is the optical constant, expressed by:

$$K = \frac{2\pi^2 n_0^2 (\mathrm{d}n/\mathrm{d}[\mathrm{Surf}]_t)^2}{N_{\mathrm{AV}}\lambda^4}, \qquad (5)$$

where n_{o} is the refractive index of the solution at the cmc, $\mathrm{d}n/\mathrm{d}[\mathrm{Surf}]_t$ is the solution refractive index increment, N_{AV} is the Avogrado's number and λ is the wave length of the laser light in vacuum. N_{agg} is obtained by dividing M_{w} by the molecular weight of the monomer.

Titration Calorimetry

The experiments were carried out at 25 °C. Enthalpies of micellization, $\Delta H^{\circ}_{\mathrm{mic}}$, were measured with Thermometric AB 2277 TAM Thermal Activity Monitor system. Under constant stirring, 10 to 40 µL aliquots of the concentrated surfactant solution ([surfactant] $\approx 20 \times$ cmc), were added to 2 mL of water in the sample cell. Each injection of the titrant solution resulted in a peak, whose corresponding area was calculated, then employed in plotting the calorimetric titration curve of the heat of dilution, H_{dil}, versus [surfactant]. The cmc may be calculated from the resulting sigmoidal plot. One problem with this calculation is the small number of points registered in the cmc region, a consequence of the abrupt rise of the enthalpy as a function of [surfactant]. To improve the precision of the cmc calculated, we have fitted Eq. 6 to the heats of dilution versus [surfactant] curves [32]:

$$H_{\mathrm{dil}} = \frac{a_1 \cdot [\mathrm{Surf}]_t + a_2}{1 + \mathrm{e}^{\frac{([\mathrm{Surf}]_t - a3)}{\mathrm{d}x}}} + a_4 \cdot [\mathrm{Surf}]_t + a_5 \,, \tag{6}$$

where a_1 to a_5 are fitting parameters and the other symbols have their usual meaning. For all surfactants studied the best fit was obtained by taking, as initial guesses, a_1, a_4, and a_5 = unity, $a_2 = \Delta H^{\circ}_{\mathrm{mic}}$, obtained graphically from the calorimetric titration curve, a_3 = conductivity-based cmc, and $\mathrm{d}x = 10\%$ of the cmc. In all computations, convergence was achieved, and iteration-based a_2 and a_3 were in agreement with the values determined experimentally. The cmc values reported were taken as the maximum, or minimum of the first derivative of Eq. 6.

Calculation of the Thermodynamic Parameters of Micellization

Gibbs free energy of micellization, $\Delta G^{\circ}_{\mathrm{mic}}$, was calculated by the use of Eq. 7 (based on the Mass-Action Law):

$$\Delta G^{\circ}_{\mathrm{mic}} = (2 - \alpha_{\mathrm{mic}})\mathrm{R}\,T\,\mathrm{Ln}(\chi_{\mathrm{cmc}}) \,, \tag{7}$$

where χ_{cmc} is the cmc expressed on mole fraction scale, R is the universal gas constant and T is the temperature, in K. From calorimetry-based $\Delta H^{\circ}_{\mathrm{mic}}$ and Gibbs free energy equation, the entropy of micellization, $\Delta S^{\circ}_{\mathrm{mic}}$ may be readily calculated by Eq. 8:

$$\Delta G^{\circ}_{\mathrm{mic}} = \Delta H^{\circ}_{\mathrm{mic}} - T\Delta S^{\circ}_{\mathrm{mic}} \,. \tag{8}$$

Results and Discussion

Site of the Micelle-water Interface

Values of cmc and α_{mic} may be readily calculated from conductance measurements. Data treatment according to Evans equation requires knowledge of the micelle aggregation number, N_{agg}. A problem arises, however, with surfactants that carry the amide group, because of the uncertainty regarding the (average) site of the micellar interface. This may be at the amide group, or at the quaternary ammonium ion, $\mathrm{R\underline{CO-N}H(CH_2)_3\underline{N^+}(CH_3)_2BzCl^-}$, respectively. Additionally, the conformation of the benzyl group with respect to the interface is unknown. We start our discussion, therefore, by addressing these questions. Figure 2 shows some limiting possibilities for the micelle: Structures 1 and 2 show that the interface lies at the quaternary ammonium ion, i.e., the amide group is present in a relatively hydrophobic medium, some 3 methylene groups away from the interface. The same structures show two possible conformations for the benzyl group, perpendicular and parallel to the interface, respectively. Alternatively, the interface may lie at the amide group, as depicted in structures 2 to 5. Because of the flexibility of the $\mathrm{NH(CH_2)_3N^+(CH_3)_2-CH_2C_6H_5}$ "tether", the benzyl group may assume different conformations with respect to the interface, perpendicular, parallel, or may "fold back" toward the micellar interior.

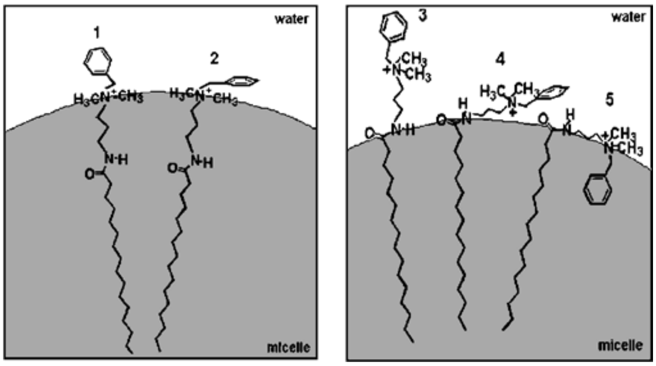

Fig. 2 Possible sites for the micelle/water interface and conformations of surfactant polar group with respect to the aggregate surface

These questions have been solved by employing theoretical calculations, SLS, FTIR and ^{1}H NMR, respectively. Values of N_{agg} may be calculated by dividing the volume of the micelle by that of the monomer. The former was calculated by taking R1 or R2 as the micellar radius (see Fig. 3), by assuming that the aggregate is spherical and that monomers inside the micelle are present in stretched, all-trans conformation. The geometry of the monomer was optimized by employing the PM3 semi-empirical method.

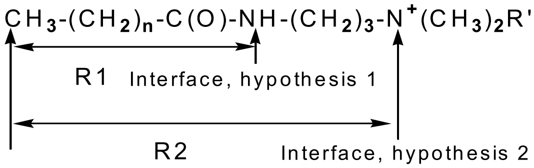

Fig. 3 Possible Sites for the micelle/water interface

Table 1 Use of different technique to study the dependence on surfactant structure of the critical micelle concentrations, cmc, degree of counter–ion dissociation, α_{mic}, micellar aggregation number, N_{agg}, Gibbs free energy of micelle formation, ΔG°_{mic}, enthalpy, ΔH°_{mic}, and the entropic term, $T\Delta S^{\circ}_{mic}$[a]

Surfactant	N_{agg} [b]	$10^3 \times$ Cmc, mol/L, conductance	$10^3 \times$ Cmc, mol/L, calorimetry	α_{mic} [c]	ΔG°_{mic} [d] (kJ mol^{-1})	ΔH°_{mic} (kJ mol^{-1})	$T\Delta S^{\circ}_{mic}$ [d] (kJ mol^{-1})
$C_{10}APrBzMe_2Cl$	43; 48	21.0	21.6	0.27 (0.34)	−33.8, −33.7	0.6	34.4, 34.3
$C_{12}APrBzMe_2Cl$	61; 89	5.00	6.1	0.23 (0.30)	−40.9, −40.7	−2.1	38.8, 38.6
$C_{14}APrBzMe_2Cl$	82; 114	1.35	1.31	0.21 (0.42)	−47.1, −47.3	−5.2	41.9, 42.1
$C_{16}APrBzMe_2Cl$	107; 167; (101)	0.30	0.39	0.19 (0.48)	−54.4, −53.2	−7.2	47.2, 46.0
$C_{10}AEtBzMe_2Cl$ [e]	43	24.0	24.6	0.28 (0.35)	−32.7, −32.9	0.6	33.3, 33.5
$C_{12}AEtBzMe_2Cl$ [e]	61	5.9	6.0	0.23 (0.35)	−40.1, −40.0	−2.3	37.8, 37.7
$C_{14}AEtBzMe_2Cl$ [e]	82	1.41	1.33	0.22 (0.38)	−46.3, −46.9	−6.0	40.3, 40.9
$C_{16}AEtBzMe_2Cl$ [e]	107	0.35	0.37	0.19 (0.38)	−53.0, −53.4	−8.8	44.2, 44.6
$C_{10}BzMe_2Cl$	43	37.3	37.0 [f]	0.32 (0.43)	−30.5, −30.4	4.0 [f]	34.5, 34.4
$C_{12}BzMe_2Cl$	61	8.09	7.93 [f]	0.24 (0.38)	−38.3, −38.6	2.1 [f]	40.4, 40.7
$C_{14}BzMe_2Cl$	82	1.94	2.41 [f]	0.23 (0.46)	−45.0, −44.1	−1.7 [f]	43.3, 42.4
$C_{16}BzMe_2Cl$	107, 90 [g]	0.39	0.33 [f]	0.22 (0.40)	−52.3, −53.1	−4.6 [f]	47.7, 48.5

[a] All measurements were carried out at 25 °C. The uncertainty limits of cmc, determined by *each technique* were found to be $\leq 0.5\%$. The reasons for the observed (small but persistent) dependence of cmc on the technique employed have been discussed elsewhere. For example, Mukerjee and Mysels [66] have compiled 54 cmcs for sodium dodecyl sulfate and cetyltrimethylammonium bromide (measurements at 25 °C) , differing, for the same technique, by 100% and 22%, respectively.

[b] For $RAPrBzMe_2Cl$ the values of N_{agg} are those calculated by using molecular geometry, and those derived from SLS measurements (in the presence of 0.1 M NaCl). The third N_{agg} reported for $C_{16}APrBzMe_2Cl$ (101) is that in the absence of additional electrolyte, NaCl. For $RAEtBzMe_2Cl$ and $RBzMe_2Cl$ the values of N_{agg} were calculated by using molecular geometry

[c] Values of α_{mic} are listed in following order: calculated by Evan's method, and by Frahm's method (value within parentheses).

[d] Values of ΔG°_{mic} and $T\Delta S^{\circ}_{mic}$ are based on α_{mic} calculated by Evan's method, and conductance-based and calorimetry-based cmc, respectively

[e] Cmc values were taken from [26], α_{mic} and ΔG°_{mic} were taken from [22], and ΔH°_{mic} were taken from [25]

[f] Cmc by calorimetry and ΔH°_{mic} taken from [25]

[g] N_{agg}, determined by fluorescence, taken from [11]

The following N_{agg} were calculated: 43, 61, 82, 107 (interface at R1) and 83, 108, 136, 167 (interface at R2), for RCO = C_{10}, C_{12}, C_{14}, and C_{16}, respectively. The latter values were considered too high and may, therefore, be rejected. SLS-based N_{agg} are listed in the second column of Table 1. They are higher than those based on molecular volume calculations because the "solvent" employed was 0.1 mol/L NaCl, in order to screen inter-micellar interactions. The presence of an additional electrolyte (with the same counter–ion) leads to micellar growth, i.e., higher N_{agg} [1–3]. The cmc of $C_{16}APrBzMe_2Cl$ is, however, small so that electrostatic interactions may be safely ignored. As seen in column 2 of Table 1, the aggregation number obtained in the absence of NaCl, 101, is in good agreement with volume-based N_{agg}.

IR data of amide I bands of $C_4APrBzMe_2Cl$ and $C_{10}APrBzMe_2Cl$ (in D_2O) support the previous conclusion about the site of the micelle/water interface. As previously shown for amides and polypeptides, this band is a sensitive probe for the state of hydration of the $C=O$ group [17–19, 33, 34]. Consider *N*-methylacetamide, because it has been extensively employed as a model compound. In dilute aqueous solutions, the carbonyl group is hydrated, resulting in $\nu_{C=O}$ at ca. 1626 cm^{-1} [35–39]. Solubilization of this amide in binary solvent mixtures whose polarities mimic that of interfacial water, e.g., aqueous alcohols results in a blue shift of $\nu_{C=O}$, directly proportional to the concentration of the organic component of the binary mixture [40, 41]. This has been attributed to dehydration of the CO group, due to partial substitution of CO-water hydrogen-bonds with amide-amide ones [9a, 18c]. Further loss of hydrogen-bonding leads to much higher $\nu_{C=O}$, e.g., 1697 cm^{-1}, 1683 cm^{-1} and 1667 cm^{-1} in hexane, THF and DMSO, respectively [35–39].

A similar behavior has been observed for amide I band of $C_4APrBzMe_2Cl$, a short-chain, i.e., non-aggregated model for the surfactants. Thus the following results were observed for 0.05 mol/L solutions ($\nu_{C=O}$ in cm^{-1}, solvent employed): 1663, DMSO; 1620, D_2O; 1622, 45 mol/L D_2O in CH_3OD; 1625, 30 mol/L D_2O in CH_3OD. Comparison of the results in pure D_2O and in D_2O/CH_3OD clearly shows the blue shift caused by partial loss of

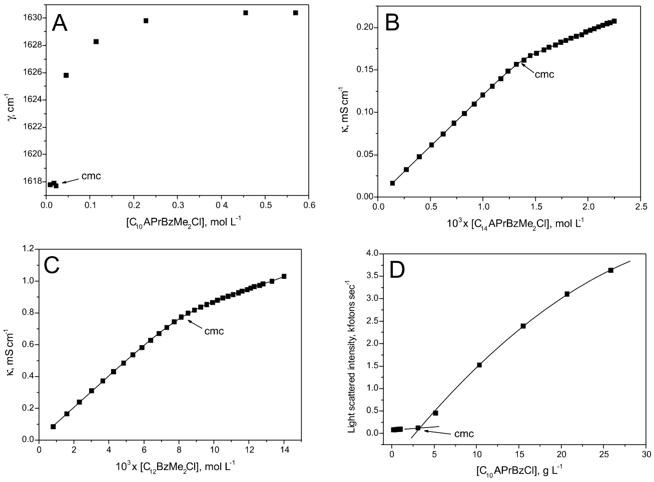

Fig. 4 Dependence of solution properties on surfactant concentration, at 25 °C: **A** $\nu_{C=O}$ of amide I band; **B** and **C** solution conductance; **D** intensity of light scattering. In **B** and **C** the *points* are experimental and the *lines* were calculated by using Eq. 3. The light scattering experiment was carried out in the presence of 0.1 mol/L NaCl, see Experimental

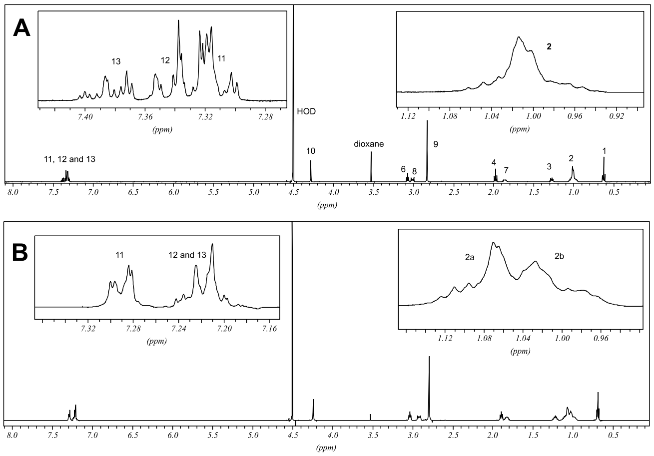

Fig. 5 Dependence of the ^{1}H NMR spectrum of $C_{12}APrBzMe_2Cl$, at 500.13 MHz, on surfactant concentration, at 6.0×10^{-3} mol L^{-1} (**A** below cmc), and 2.0×10^{-2} mol L^{-1} (**B** above cmc). See Experimental for proton designation. The spectra of the aromatic protons, below and above the cmc, may be reproduced by simulation (MestRe-C program package, version 4.5.9.1, Mestrelab Research, Santiago de Compostela, Spain). The parameters employed were: $J_{ortho} = 7.5$ Hz; $J_{meta} = 0.8$ Hz and $J_{para} = 0.5$ Hz, and the following δ (in ppm, below and above the cmc, respectively): H11 = 7.307, 7.286; H12 = 7.330, 7.172; H13 = 7.382 and 7.123

hydrogen-bonding to water, due to addition of CH_3OD. That is, the response of $\nu_{C=O}$ of $C_4APrBzMe_2Cl$ to changes in hydrogen-bonding is similar to that of *N*-methylacetamide.

At [surfactant] < cmc, the frequency of amide I band of $C_{10}APrBzMe_2Cl$ in D_2O is constant at ca. 1618 cm^{-1}, increasing rapidly to 1625 cm^{-1} just after the cmc, then levels off at 1630 cm^{-1}, at [surfactant] ≥ 0.4 mol L^{-1}, see Fig. 4A. The first frequency indicates that the monomer amide group is hydrated, akin to *N*-methylacetamide or $C_4APrBzMe_2Cl$. Above the cmc, $\nu_{C=O}$ observed, 1630 cm^{-1}, is close to that of self-associated *N*-methylacetamide. This indicates dehydration and hydrogen-bonding between molecules of $RAPrBzMe_2Cl$ in the aggregate. The relative strength of this bonding may be judged by comparing $\Delta\nu$ (= $\nu_{C=O}$ after cmc − $\nu_{C=O}$ before cmc) for $C_{10}APrBzMe_2Cl$ (12 cm^{-1}) with that of the (strongly hydrated) carboxylate head-group of sodium nonanoate or decanoate, ≤ 3 cm^{-1} [42]. Comparison of the limiting $\nu_{C=O}$ of micellized $C_{10}APrBzMe_2Cl$ with that of *N*-methylacetamide in DMSO and of $C_4APrBzMe_2Cl$ in aqueous alcohols, vide supra, shows that this group is appreciably hydrated in the aggregate, i.e., is not present in the micellar interior, as depicted by structures 1 and 2 of Fig. 2; these, therefore, may be safely rejected.

A decision regarding the conformation of the head-group may be reached by examining the dependence of δ (^{1}H NMR), and line shape on [surfactant], below and above the cmc, as shown in Fig. 5 for $C_{12}APrBzMe_2Cl$ (see Experimental for proton designation). Thus aggregation resulted in a splitting of the broad peak of H2, and an inversion of the order of δ of the aromatic ring protons, being $\delta_{H13} > \delta_{H12(12')} > \delta_{H11(11')}$ and $\delta_{H11(11')} > \delta_{H12(12')} > \delta_{H13}$, at [surfactant] below and above the cmc, respectively. This behavior has been observed for all surfactants studied (^{1}H NMR spectra not shown). Consider first the aliphatic H2 protons. Although this peak is usually broad due to virtual coupling, no splitting has been observed as a result of micellization of other ionic surfactants, e.g., sodium dodecyl sulfate or dodecyl-trimethylammonium chloride [43]. The results of $C_{12}APrBzMe_2Cl$ raise the following question: Does peak splitting of the aliphatic hydrogens occur with other surfactants that carry an aromatic head-group? Figure 6 shows that this is not necessarily the case, since there are no noticeable differences between the spectra of dodecylpyridinium chloride below, and above the cmc, except for small changes in line width and δ of the discrete groups. The preceding results point out to the following picture: the heterocyclic ring of dodecylpyridinium chloride lies perpendicular to the micellar interface, so that there is no diamagnetic deshielding/shielding of segments of the hydrophobic tail by (ring current effect of) the pyridinium ring [9]. A different behavior may be observed, however, when the surfactant carries anisotropic head-group, *whose movement is not restricted in the micelle*, e.g., the benzyl group. The flexibility of the tether allows the benzyl group of $RAPrBzMe_2Cl$ to fold back toward the micellar interior, causing the observed splitting

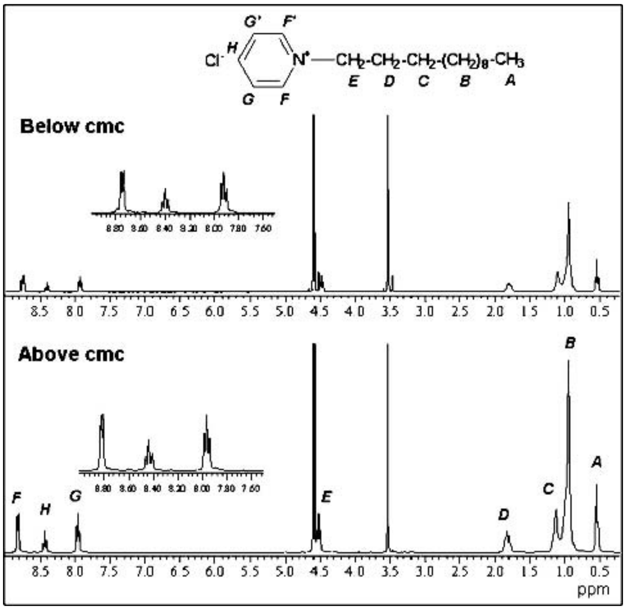

Fig. 6 Dependence of the ^{1}H NMR spectrum (300 MHz) of dodecylpyridinium chloride in D_2O on [surfactant] below (0.005 mol/L) and above (0.08 mol/L) the cmc. The singlet at 3.53 ppm is that of dioxane, employed as an internal reference

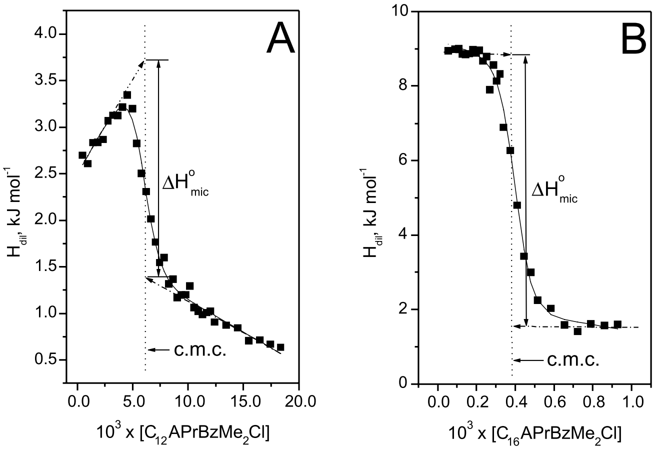

Fig. 7 Calorimetric titration curves at 25 °C, for C_{12}APrBzMe$_2$Cl (**A**) and C_{16}APrBzMe$_2$Cl, (**B**). The *points* are experimental and the *solid line* was calculated by using Eq. 6

of the main CH_2 peak [24, 44]. The dependence of δ of the aromatic protons on [surfactant] is another evidence for folding back of the benzyl moiety. Below cmc the order is $\delta_{H13} > \delta_{H12(12')} > \delta_{H11(11')}$. Above the cmc, the peaks of H_{13} and $H_{12(12')}$ move up-field relative to $H_{11(11')}$ because they are transferred, on micellization, from an aqueous pseudo-phase to a less polar environment, the micelle [44].

In summary, N_{agg} calculated and those determined by SLS (in particular that of C_{16}APrBzMe$_2$Cl in the absence of NaCl) and the dependence of $\nu_{C=O}$ on [surfactant] show that the amide head-groups in the micelles are hydrated and hydrogen-bonded, either directly or via water molecules. ^{1}H NMR chemical shifts of both aromatic and aliphatic protons show that there is interaction between the former moiety and a few of the (CH_2) groups in the surfactant alkyl group; this interaction is absent when the head-group is perpendicular to the interface, as in dodecylpyridinium chloride. Therefore, FTIR and ^{1}H NMR data indicate that structure 5 of Fig. 2 is the most plausible conformation of the head-group in the micelle. As discussed below, this conclusion is also corroborated by Gibbs free energy of micellization.

Aggregation: Critical Micelle Concentration, Degree of Micelle Dissociation and Thermodynamic Parameters of Micellization

Examples of the dependence on [surfactant] of solution conductance and intensity of scattered light are shown in parts B to D of Fig. 4. Examples of calorimetric titration curves are shown in Fig. 7. In both figures, each graph shows a distinct break at the cmc, these are listed Table 1, along with available data for the corresponding RAEtBzMe$_2$Cl and RBzMe$_2$Cl.

Regarding this Table, the following is relevant:

(i) There is an excellent agreement between the cmc values obtained by calorimetry and conductance, even for the C_{10} and C_{12} homologues, whose titration calorimetry plots clearly show non-ideal behavior. The dependence of the shape of these plots on the length of the surfactant hydrophobic tail has been discussed in terms of cmc, N_{agg} and α_{mic}. Small cmc and α_{mic}, and a large N_{agg} result in an intense heat pulse, exothermic or endothermic, detected by the calorimeter. A small cmc also means that the solutions in both sample cell and the injection syringe are essentially ideal (i.e., concentrations are equal to activities), so that the linear parts of the calorimetry titration plot, before and after the cmc, are independent of surfactant concentration, as shown for C_{16}APrBzMe$_2$Cl, Fig. 7B. A decrease in the length of the surfactant tail is accompanied with an increase of cmc and α_{mic}, and a decrease of N_{agg} [2, 3]. Consequently, the surfactant solution in the syringe and, with increasing injection number, in the sample cell, cannot be assumed to be ideal. This results in a concentration-dependent heat evolution and a smaller enthalpy variation at the cmc, as can be seen in Fig. 7A [45–47].

(ii) The IR-based cmc of C_{10}APrBzMe$_2$Cl is 24.6×10^{-3} mol/L, i.e., ca. 10% higher than the cmc obtained by other techniques, in agreement with the fact that the tendency of surfactant aggregation in D_2O is larger than that in H_2O, because the former is a more structured solvent [48–51]. This is one of the few studies in which IR spectroscopy has been used to determine cmc of surfactants [52–54], although IR and Raman spectroscopy have been fruitfully employed to study interactions (including hydrogen-bonding) within organized assemblies [55–58];

(iii) Value of α_{mic} is required in order to calculate Gibbs free energy of micelle formation, ΔG°_{mic}. Although Frahm's method is simple [30], it does not take into account the conductivity of the micelle (a "macroion") and leads, therefore, to α_{mic} higher than that calculated by Evans method, where this contribution is explicitly considered [31, 59]. Therefore, we use Evans equation-derived α_{mic} for calculation of ΔG°_{mic}, although both α_{mic} are listed in Table 1. We stress that α_{mic} calculated by Evans equation depends only slightly on N_{agg}. E.g., for $C_{14}APrBzMe_2Cl$ α_{mic} were found to be 0.22, 0.21 and 0.20 for $N_{agg} = 60$, 80 and 100, respectively;

(iv) For the same surfactant, $|\Delta H^{\circ}_{mic}|$ contributes less than $|T\Delta S^{\circ}_{mic}|$ to ΔG°_{mic}, i.e., micelle formation at 25 °C is entropy-driven. This can be understood in terms of the hydrophobic effect, namely micellization leads to a large gain in entropy because of the accompanied decrease in the hydrophobic surface area exposed to water. Additionally, the hydration of the head-group in the micelle is also readjusted due to monomer association and counter–ion condensation [1–3];

(v) Table 1 shows that increasing the length of the hydrophobic chain increases $T\Delta S^{\circ}_{mic}$ and decreases ΔH°_{mic} and ΔG°_{mic}. This is due to the accompanying increase in contribution of the hydrophobic hydration, due to an increase in N_{agg}, with a concomitant closer packing of the surfactant molecules in the micelle, and less water penetration between the head-groups. The accompanied increase in head-group repulsion is compensated by an increase in counter–ion binding [60];

(vi) The data listed in Table 1 show the following order: $|\Delta G^{\circ}_{mic}|_{RAPrBzMe_2Cl} > |\Delta G^{\circ}_{mic}|_{RAEtBzMe_2Cl} > |\Delta G_{mic}|_{RBzMe_2Cl}$. This order may be analyzed in terms of the contributions of the surfactant discrete segments, namely, the terminal CH_3 group of the hydrophobic chain, $\Delta G^{\circ}_{CH_3}$; the methylene groups of the alkyl chain, $(N_{CH_2}\Delta G^{\circ}_{CH_2})$ and the head-group, $\Delta G^{\circ}_{\text{head-group}}$, (Eq. 9) [1–3]:

$$\Delta G^{\circ}_{mic} = N_{CH_2} \cdot \Delta G^{\circ}_{CH_2} + \Delta G^{\circ}_{\text{head-group}} + \Delta G^{\circ}_{CH_3} \tag{9}$$

This equation predicts a linear correlation between ΔG°_{mic} and N_{CH_2}, where the intercept includes contributions from the terminal methyl plus the head-group. Since $\Delta G^{\circ}_{CH_3}$ is independent of the chain length of the surfactant, its contribution is constant in a homologous series. Therefore, the differences between the intercepts of the three surfactant series essentially reflect effects of the transfer of the head-groups from bulk solution to the micelle [1–3]. Equations similar to Eq. 9, and a similar line of reasoning apply to ΔH°_{mic}, and ΔS°_{mic}. The results (thermodynamic property/CH_2 and/or CH_3 plus head-group; and correlation coefficient) are listed in Table 2.

Table 2 shows the following:

(i) For the three homologue series, the contributions of the CH_2 groups of the alkyl chain to ΔG°_{mic} are similar, -3.5 ± 0.1 kJ/mol. This is expected because the transfer of these groups from water to the micellar core is practically independent of the structure of the head-group [1–3]. Other compounds show similar values: $\Delta G^{\circ}_{CH_2}$ for the transfer of alkanes from water to bulk hydrocarbon is $-3.6\,\text{kJ mol}^{-1}$ [61]; $\Delta G^{\circ}_{CH_2}$ are -3.3 and $-3.1\,\text{kJ mol}^{-1}$ for the aggregation in water of *n*-alkylmethylsulfoxides and *n*-alkyldimethylphosphine oxides, respectively [62, 63];

(ii) On the other hand, $\Delta G^{\circ}_{CH_3+\text{head-group}}$ for $RAPrBzMe_2Cl$ and $RAEtBzMe_2Cl$ are smaller, i.e., more favorable than the corresponding one of $RBzMe_2Cl$, as a consequence of smaller (i.e., less unfavorable) $\Delta H_{CH_3+\text{head-group}}$ and larger $\Delta S_{CH_3+\text{head-group}}$. As

Table 2 Contribution of the surfactant discrete segments, CH_2 and CH_3 + head-group to the thermodynamic parameters of micellization, at 25 °C

	ΔG°_{mic} (kJ mol^{-1})			ΔH°_{mic} (kJ mol^{-1})			$T\Delta S^{\circ}_{mic}$ (kJ mol^{-1})		
	CH_3 + head-group	CH_2	r [a]	CH_3 + head-group	CH_2	r [a]	CH_3 + head-group	CH_2	r [a]
$RAPrBzMe_2Cl$	−6.7 (±0.8)	−3.4 (±0.1)	0.9996	11.1 (±0.9)	−1.3 (±0.1)	0.9967	18 (±2)	2.1 (±0.1)	0.9953
$RAEtBzMe_2Cl$	−6.1 (±0.9)	−3.4 (±0.1)	0.9994	13.4 (±0.7)	−1.60 (±0.6)	0.9986	19.5 (±1)	1.8 (±0.1)	0.9947
$RBzMe_2Cl$	1.7 (±0.9)	−3.6 (±0.1)	0.9996	18 (±1)	−1.5 (±0.1)	0.9928	16 (±2)	2.1 (±0.2)	0.9914

[a] Correlation coefficient of the regression analysis

discussed above, the head-groups of $RAPrBzMe_2Cl$ and/or $RAEtBzMe_2Cl$ dehydrate on micelle formation because of inter-molecular hydrogen-bonding of the amide groups. This de-solvation is expected to be endothermic, because the enthalpy of transfer of quaternary ammonium ions from water to aqueous organic solvents (a model for interfacial water) is positive [64]. This (endothermic) process is compensated by an exothermic one (hydrogen-bonding between the amide groups), leading to energy compensation and the observed smaller contribution of $\Delta H_{CH_3+\text{head-group}}$. A couple of factors increase the degrees of freedom in micellar solutions of the amide group-carrying surfactants: release of water of hydration from the head-group due to amide group hydrogen-bonding; the higher flexibility of the tethers to which the benzyl groups of $RAPrBzMe_2Cl$ and/or $RAEtBzMe_2Cl$ are attached, relative to the relatively constrained benzyl group of $RBzMe_2Cl$;

(iii) Finally, a couple of important points emerge from examination of Gibbs free energies of the surfactant moieties: $|\Delta G^\circ_{CH_3+\text{head-group}}|$ of $RAPrBzMe_2Cl$ is slightly larger than that of $RAEtBzMe_2Cl$, due to the presence of an additional CH_2 group in the tether. The difference (0.6 kJ/mol) is small, however, because this group is still appreciably hydrated in the micelle, vide supra. Additionally, $(\Delta G^\circ_{CH_3+\text{head-group}})_{RAPrBzMe_2Cl} - (\Delta G_{CH_3+\text{head-group}})^\circ_{RAPrMe_3Cl}$ [65] measure the difference (at a constant spacer length, *n*-propyl) between the free energies of transfer of the benzyl group, relative to that of the methyl group, from bulk solution to the micellar pseudo-phase. This $\Delta\Delta G^\circ$ is relatively large, -4.9 kJ/mol, ca. $1.4 \times \Delta G^\circ_{CH_2}$, showing that the benzyl group in the micelle is present in a relatively hydrophobic environment, as depicted by structure 5 of Fig. 2.

Conclusions

A homologous series of benzyl (3-acylaminopropyl) dimethylammonium chloride surfactants has been synthesized and their aggregation in aqueous solution studied by ^1H NMR, FTIR (in D_2O), conductivity and calorimetry (in H_2O). The results indicate that the micelle/water interface lies close to the amide group, and that the benzyl moiety "folds back" toward the micellar interior. Thermodynamic parameters of micelle formation have been calculated and separated into contributions from the transfer of the discrete surfactant segments from bulk water to the micellar pseudo-phase. Micellization of surfactants that carry an amide head-group is more favorable than that of $RBzMe_2Cl$, due to direct or water-mediated hydrogen-bonding between these groups.

Acknowledgement We thank the State of São Paulo Research Foundation (FAPESP) for financial support and the Brazilian National Research Council (CNPq) for a research productivity fellowship to O.A. El Seoud, Prof. Watson Loh, UNICAMP for making the calorimeter available to us, and Dr. S. Shimizu for running the spectra of dodecylpyridinium chloride, Fig. 6.

References

1. Attwood D, Florence AT (1984) Surfactant Systems: Their Chemistry, Pharmacy, and Biology. Chapman and Hall, London
2. Rosen MJ (1989) Surfactants And Interfacial Phenomena. Wiley, New York
3. Hiemenz PC, Rajagopalan R (1997) Principles of Colloid and Surface Chemistry, 3rd ed. Marcel Dekker, New York
4. Bunton CA, Quina FH, Romsted LS (1991) Acc Chem Res 24:357
5. Bunton CA, Savelli G (1986) Adv Phys Org Chem 22:213
6. Bunton CA (1997) J Mol Liq 72:231
7. Birdi KS (1997) Handbook of Surface and Colloid Chemistry. CRC Press, Boca Raton, FL
8. Zana R (1997) Colloids Surfaces A 27:123
9. Okano LT, El Seoud OA, Halstead T (1997) Colloid Polym Sci 138:275
10. El Seoud OA, Blásko A, Bunton CA (1995) Ber Bunsenges Phys Chem 99:1214
11. Okano LT, Quina F, El Seoud OA (2000) Langmuir 16:3119
12. Blackmore ES, Tiddy GTJ (1988) J Chem Soc Faraday Trans 2 84:1115
13. Malliaris A, Paleos CM (1984) J Colloid Interface Sci 101:364
14. Burczyk B, Wilk KA (1990) Prog Colloid Polym Sci 82:249
15. Nowak JR, Pomianowski A, Szczena EN (1990) J Surface Sci Tecnol 6:287
16. Bazito RC, El Seoud OA, Barlow GK, Halstead TK (1997) Ber Bunsenges Phys Chem 101:1933
17. Kollman P (1993) Chem Rev 93:2395
18. Ludwig R, Reis O, Winter R, Weinhold F, Farrar TC (1998) J Phys Chem B 102:9312
19. Huelsekopf M, Ludwig R (2001) Mag Res Chem 39:127
20. Tsubone K, Rosen MJ (2001) J Colloid Interface Sci 244:394
21. Shimizu S, El Seoud OA (2003) Colloid Polym Sci 282:21
22. Shimizu S, El Seoud OA (2003) Langmuir 19:238
23. Shimizu S, Pires PAR, El Seoud OA (2003) Langmuir 19:9645
24. Shimizu S, Pires PAR, Fish H, Halstead TK, El Seoud OA (2003) Phys Chem Chem Phys 5:3489
25. Shimizu S, Pires PAR, Loh W, El Seoud OA (2004) Colloid Polym Sci 282:1026
26. Shimizu S, Pires PAR, El Seoud OA (2004) Langmuir 20:9551
27. Armarego WLF, Chai CLL (2003) Purification of Laboratory Chemicals. 5 ed. Elsevier, New York
28. Lide DR (ed) (1992) CRC Handbook of Chemistry and Physics. 73 ed. CRC Press, Boca Raton, FL

29. Carpena A, Aguiar J, Bernaola-Galván P, Ruiz CC (2002) Langmuir 18:6054
30. Frahm J, Diekmann S, Haase A (1980) Ber Bunsenges Phys Chem 84:566
31. Evans HC (1956) J Chem Soc 579
32. Király Z, Dékany I (2001) J Colloid Interface Sci 242:214
33. Solans C, Infante R, Azemar N, Wärnheim T (1989) Prog Colloid Polym Sci 79:70
34. Kunieda H, Nakamura K, Infante R, Solans C (1992) Adv Mat 4:291
35. Miyazawa T, Shimanouchi T, Mizushima S (1958) J Chem Phys 29:611
36. Chen CYS, Swenson CA (1969) J Phys Chem 73:2999
37. Eaton G, Symons MCR, Rastogi PP (1989) J Chem Soc Faraday Trans 1 85:3257
38. Symons MCR (1993) J Mol Structure 297:133
39. Schweitzer-Stenner R, Sieler G, Mirkin NG, Krimm S (1998) J Phys Chem A 102:118
40. Tada EB, Novaki LP, El Seoud OA (2001) Langmuir 17:652
41. Soldi V, Keiper J, Romsted LS, Cuccovia I, Chaimovich H (2000) Langmuir 16:59
42. Uemura J, Mantsch HH, Cameron DG (1981) J Colloid Interface Sci 83:558
43. Possidonio S, Siviero F, El Seoud AO (1999) J Phys Org Chem 12:325
44. Rózycka-Roszak B, Cierpicki T (1999) J Colloid Interface Sci 218:529
45. Nusselder JJH, Engberts JBFN (1992) J Colloid Interface Sci 148:353
46. Bijma K, Engberts JBFN, Blandamer MJ, Cullis PM, Last PM, Irlam KD, Soldi LG (1997) J Chem Soc Faraday Trans 93:1579
47. Blandamer MJ, Cullis PM, Engberts JBFN (1998) J Chem Soc Faraday Trans 94:2261
48. Mukerjee P, Kapauan P, Meyer HG (1966) J Phys Chem 70:783
49. Chou SI, Shah DO (1981) J Colloid Interface Sci 80:49
50. Candau S, Hirsch E, Zana R (1982) J Colloid Interface Sci 88:428
51. Elvingson C (1987) J Phys Chem 91:1455
52. Umemura J, Mantsch HH, Cameron DG (1981) J Colloid Interface Sci 83:558
53. Yang PW, Mantsch HH (1986) J Colloid Interface Sci 113:218
54. Etori F, Yamada H, Taga Y, Okabayashi K, Ohshima HK, O'Connor C (1997) J Vibrational Spect 14:133
55. Lafrance D, Marion D, Pézolet M (1990) Biochem 29:4592
56. Nilsson A, Holmgren A, Lindblom G (1994) Chem Phys Lipids 69:219
57. Domingo JC, Mora M, de Madariaga MA (1994) Chem Phys Lipids 69:229
58. Domingo JC, de Madariaga MA (1996) Chem Phys Lipids 84:147
59. Zana R (2002) J Colloid Interface Sci 246:182
60. Bijma K, Blandamer MJ, Engberts JBFN (1988) Langmuir 14:79
61. Nelson HD, de Ligny CL (1968) Rec Trav Chim 87:528
62. Clint JH, Walker T (1974) J Chem Soc Faraday Trans I 71:946
63. Lah J Pohar C, Vesnaver G (2000) J Phys Chem B 104:2522
64. Hefter G, Marcus Y, Waghorne WE (2002) Chem Rev 102:2773
65. $\Delta G^{\circ}_{\mathrm{CH_3+head\text{-}group}}$ for the series 3-(acylaminopropyl) trimethylammonium chloride was found to be -1.8 kJ/mol, Pires PAR Ph D, thesis, the University of São Paulo, 2002
66. Mukerjee P, Mysels KJ (1971) Critical Micelle Concentrations of Aqueous Surfactant Systems, NSRDS: Washington

Progr Colloid Polym Sci (2006) 133: 142–146
DOI 10.1007/2882_068

Beate Ullrich
Ewa Ilska
Norbert Höhn
Doris Vollmer

Long Range Particle Transport in Liquid Crystal-alkane Mixtures

Beate Ullrich · Ewa Ilska · Norbert Höhn · Doris Vollmer (✉)
Max-Planck-Institut für Polymerforschung,
Ackermannweg 10, 55128 Mainz,
Germany
e-mail: vollmerd@mpip-mainz.mpg.de

Abstract Microscopic tracking of silica tracer particles suspended in mixtures of a nematogen (5CB) and small amounts of alkane reveals that during an isotropic-nematic phase transition induced by slow cooling particle transport is dominated by long-range interaction with the isotropic-nematic interface for the most part of phase transition. According to the phase diagram of liquid crystal-alkane mixtures, this long-range interaction was attributed to hydrodynamic (advection) or thermodynamic (local concentration gradients) effects of alkane redistribution from the nematic into the isotropic domains during phase transformation.

Keywords Liquid Crystals · Colloids · Phase Transition · Long-range Interaction

Introduction

Many natural and industrial processes involve complex mixtures of solvents with macromolecular or colloidal ingredients. In mixtures of colloids and liquid crystal, the movement of the colloids is complicated by phase transitions of the solvent from the isotropic to an anisotropic (in most cases nematic) state [1–6]. Because in pure nematogens the phase transition is almost instantaneous, most studies focused on an investigation of the direct interaction of the colloids with the anisotropic solvent [7–12]. The movement of colloids *during* the phase transition has only recently been addressed: West et al. [1] demonstrated that colloids are dragged along by a moving isotropic-anisotropic interface generated by a slowly moving temperature gradient. In the anisotropic phase the drag force on colloids is dominated by the interaction of the colloid surface with the director field (anchoring energy) and, thus, strongly depends on the surface properties and the size of the particles or particle clusters [10]. The results of Andrienko et al. [1, 5, 6] imply that interaction of colloids with the orientational field of the nematic phase dominate events within the range of one particle diameter from the interface. In contrast, in other experiments suspensions of PMMA particles in the nematogen 5CB were uniformly cooled below phase transition temperature [2–4]. In this situation, migration of particles during the phase transition of the medium resulted in foam-like colloidal networks that completely changed the rheological properties of the mixture. Moreover, the elastic modulus did not dependent on particle size for a broad range of particle sizes [4]. In addition, the mechanical properties of the networks depended on the equilibration periods of the colloidal suspensions prior to the experiment [4], and networks have so far only been seen using sterically stabilized PMMA particles as colloids. The dependence on the equilibration period prompted us to suspect that a third, low molecular component influences particle movement. Possible low molecular weight components re-distributing during particle homogenisation could be alkane or monomer remnants from particle synthesis or trace impurities in the liquid crystal. This led us to investigate whether diffusion of small amounts of added low molecular weight components has a direct effect on or can even dominate the movement of particles during the isotropic to nematic transition.

In mixtures of liquid crystal and an additional low molecular isotropic component (alkane), the alkane concentration is directly correlated to a shift of the calorimetric onset of phase transition to lower temperatures during cooling [4, 15, 16]. The temperature gap between the beginning and the end of phase transition also increases with alkane concentration. This implies that within this interval of phase transformation, isotropic and nematic domains coexist. Microscopically, they can be visualized as slowly growing nematic and shrinking isotropic domains with sharp boundaries. In this study, we attempted to describe the interrelationship between phase transition kinetics and particle transport by correlating our conclusions from differential scanning calorimetry (DSC) with data from microscopic tracking of phase boundaries and individual silica tracer particles. Surprisingly, we found a long-range interaction with colloids at a distance of several particle diameters from the interface. This interaction dominated particle movement for the most part of phase transformation and its time and length scales were consistent with it being caused by alkane flow.

Methods

Differential Scanning Calorimetry (DSC)

Phase diagrams of mixtures of 4-pentyl-cyanobiphenyl (5CB, Merck, Germany) with different weight fractions of hexane were determined by DSC in a VP-DSC calorimeter (Microcal Inc.). Isooctane was used as a reference because it does not show any temperature-induced transitions within the temperature interval of interest and has a similar heat capacity as 5CB. We refer to the specific heat values as $C_p^{rel}(T)$ because only changes relative to this reference solution were determined. Mixtures were cooled from 40 °C to 20 °C at a cooling rate of −4 K/h.

Microscopy

Silica spheres ($R = 1500$ nm) were equilibrated with 5CB for at least 1 week at a concentration of 0.1% (w/w). From this stock, samples were further diluted to 0.01% with fresh 5CB. Immediately before use, alkane (hexane or octane) was added at concentrations of 0.1–10% (v/v) and mixed thoroughly. 2.5 μl of the mixture were pipetted onto a pre-heated glass cover slip and covered with a cover slip 12 mm in diameter. The sample was sealed immediately with UV-cured Norland 88 glue.

A Linkam heating stage was preheated above 36 °C ($T_{IN} = 35.2$ °C in pure 5CB), heated to 50 °C for 10 min to dissolve any particle clusters formed during loading, and cooled at 5 K/min to 36 °C. By keeping the system at this temperature for 10 min any solvent flow induced by this fast temperature ramp was allowed to subside. The sample was then cooled further at 0.05 K/min. Images were taken every 2 seconds on an Olympus BX-51 microscope using an Evolution MP camera and Image Pro Plus software. The positions of particles and isotropic/nematic interfaces were semi-automatically recorded on each frame using homemade algorithms. For later determination of the interface position, we used the outer rim of the contrast-enhanced interface band.

Results

Phase Transition Kinetics

We determined the phase transition temperature isotropic-nematic by microcalorimetry for different hexane concentrations. Figure 1A shows typical thermograms as a function of the dimensionless temperature ($(T - T_{IN})/T_{IN}$), taking the onset of the sharp increase of the specific heat as the onset of the phase transition T_{IN}. This permits an easy comparison of the effects of increasing hexane concentration on the width of the phase transition interval. Likewise, the normalized integral of the heat curve reflecting the fraction of nematic material is given in terms of the dimensionless temperature (Fig. 1B). The inset of Fig. 1A shows that the onset temperature of the phase transformation was lowered in a concentration-dependent manner as long as the hexane concentration did not exceed a few percent. In line with expectations [15, 16], the linear decrease of T_{IN} (solid squares), was given by

$$T_{IN} = [308.4 - (4.0 \pm 0.3)\phi_{hex}]K , \qquad (1)$$

where ϕ_{hex} denotes the weight fraction of hexane [4].

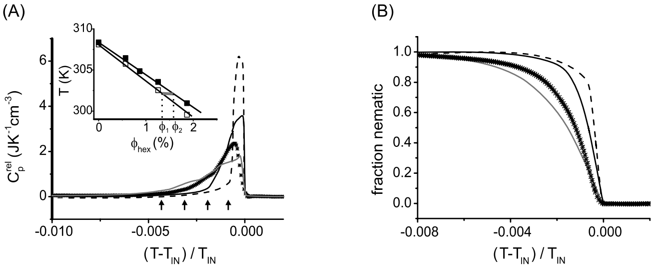

Fig. 1 Dependence of the specific heat (**A**) and fraction of nematic material (**B**) on the dimensionless temperature for mixtures of 5CB and hexane. **A** Specific heat C_V^{rel} as a function of temperature, where T_{IN} denotes the beginning of the phase transition. The *arrows* give the end of phase transformation. Because the integrated heat should be almost constant, the maxima of the heat curves decrease when the transition interval broadens. *Dashed line*: pure 5CB; *solid line*: $\phi_{hex} = 0.6$ wt %; *crosses*: $\phi_{hex} = 1.3$ wt %; *grey line*: $\phi_{hex} = 1.9$ wt %. Cooling rate: 4 K/h. *Inset*: Section of the phase diagram of 5CB-hexane mixture. The *solid squares* show the beginning and the open ones the end of the phase transformation. At a given temperature, within the transition region domains with different hexane concentrations (ϕ_1 and ϕ_2) coexist as indicated by the *vertical dashed lines*. **B** Increase of the volume fraction of nematic material during the phase transformation at different alkane concentrations. *Lines* as in (**A**)

The same was true for the end of phase transformation, although this point was generally hard to determine as the left branch of the heat curve was smeared out.

In Fig. 1, we marked the end of phase transformation by arrows. The corresponding temperatures are given by the open squares in the inset of Fig. 1A. The width of the temperature interval increases linearly with the volume fraction of hexane. This implies that at a given temperature the hexane concentration in the isotropic domains is higher than that in the coexisting nematic domains. Therefore, during the phase transformation hexane is redistributed between the coexisting phases.

Microscopy

To gain further insight into the phase transition kinetics we have recorded the phase transformation microscopically, see Fig. 2. The appearance of nematic droplets in the microscopic observation field was considered the onset, the disappearance of isotropic areas the end of the phase transformation. In general, the observed phase transition temperatures were higher than in DSC because the sample is observed through a glass-covered hole in the centre of the heating stage, while temperature is measured inside the heating block in the periphery of the sample.

In Fig. 2A an image of the sample is given where most of the sample is still isotropic. A small nematic droplet is visible on the left margin. During continuous slow cooling, this droplet grows and a second nematic droplet protrudes into the observation field, Fig. 2B. Cooling for another few seconds causes both nematic domains to coalesce, Fig. 2C. Tracking the isotropic-nematic front coordinates and calculating the corresponding interface velocities yielded that at an early stage, the interface velocities were fairly constant at 0.1 to 1 µm/s and the velocities of different fronts in the same sample were almost identical (Fig. 2A,B). At a later stage, coalescence of droplets gave rise to high local interface velocities (up to 10 µm/s) over short periods of time, as shown in Fig. 2C.

Above the phase transition temperature the particles (seen as small dark dots in Fig. 2) were homogeneously distributed and all particles essentially showed Brownian motion. Surprisingly, while cooling through the phase transition the particles moved ahead of the approaching interface. Figure 3A shows the correlation of particle and front coordinates by illustrating the time evolution of the distance between selected silica particles (marked with circles, rectangles, and triangles) and the isotropic-nematic interface. At early stages, particle velocities were somewhat lower than that of the interface. This is reflected by a shrinking particle-interface distance; however, most particles were not reached by the interface. Well within the phase transformation interval, particle and interface velocities were almost identical and, accordingly, particle-interface distance was nearly constant (Fig. 3A, 90–150 s). As phase transformation proceeded, particles were increasingly influenced by more than one interface. Coalescence of droplets was typically accompanied by high local interface velocities that sometimes caused sudden changes of the particle-interface distance. Even before coalescence, the approaching of a second droplet changed the direction of particle movement, although the particle-interface velocity remained almost constant until particles were confined between droplets (Fig. 3C, > 150 s). At these later

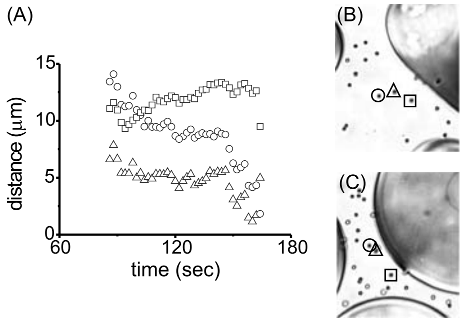

Fig. 3 **A** Time evolution of the distance of three different particle from the isotropic-nematic front. The particles are marked by the symbols shown in images (**B**) and (**C**). Whereas **B** shows the image corresponding to the first data points in (**A**), image **B** shows the position of the particles and the nematic domains 80 s later. Cooling rate: 3 K/h

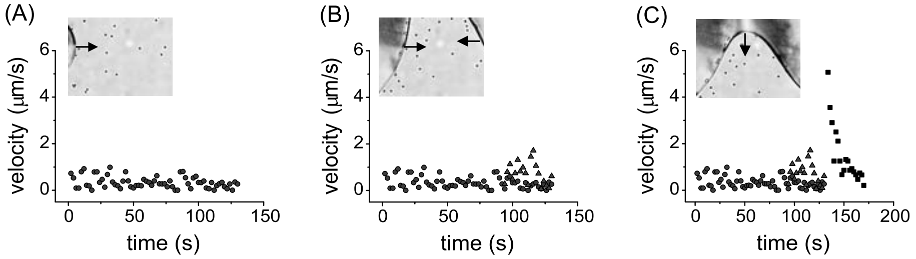

Fig. 2 Velocity of the isotropic-nematic interface for mixtures of 5CB and 0.6 wt % hexane. The velocity was calculated from the difference of the front coordinates in successive images and the time lapsed between the respective frames. By keeping either the y-coordinate (**A** and **B**) or the x-coordinate (**C**) fixed, the progression of the interface was measured in x- or y-direction as indicated by *arrows*. The *small dark dots* on the images represent silica particles added as tracer particles. Cooling rate: 3 K/h

stages the distance began to shrink increasingly slowly until the entire sample was nematic.

Discussion

The aim of the present study was to gain insight into the relevant mechanisms of interaction between the isotropic-anisotropic interfaces in mixtures of a mesogenic solvent with non-mesogenic components undergoing phase transition with colloidal particles in suspension. The interaction between colloids and a nematic solvent has been studied previously. The length scales of the observed interactions [West 02, Andrienko] resulting from the elastic constant of the nematogen, the surface tension, and the anchoring strength were in the range of one particle diameter from the isotropic-nematic interface. In these investigations, either a stationary interface [Andrienko] or an interface moving according to a temperature gradient (which implies that at the interface, temperature was constant) was treated. In our experimental setup, phase transition was induced by slow cooling of the entire sample, which implies that we are considering systems far from equilibrium where neither temperature nor interface position are constant.

Using silica particles as tracers in 5CB-alkane mixtures, we have detected a long-range repulsive interaction between the moving isotropic-nematic interface and the particles. Long-range effects became evident at distances of more than five, often ten particle diameters, with particles moving ahead of the interface (Fig. 2B). This interaction cannot be due to liquid crystalline order, since the distance between the particles and the interface exceeds several particle diameters. The time course of long-range particle transport also shows that long-range repulsion increases during early stages of phase transition and is maintained as long as there is significant growth of nematic domains.

Although local alkane concentrations cannot be measured directly, we conjecture that alkane diffusion is responsible for this long-range interaction. To verify the plausibility of this conjecture, we estimated the length scales of alkane diffusion. Since the diffusion constant of low molecular solvents in isotropic media is about $D \cong 10^{-9}\,\mathrm{m}^2/\mathrm{s}$, the time ($t$) alkane takes to diffuse a distance (x), of $x = 10\,\mu\mathrm{m}$ is about $t = x^2/D \cong 0.1$ s, i.e. alkane diffuses with an average velocity in the order of $100\,\mu\mathrm{m/s}$. Thus, at cooling rates of a few K/h, alkane diffusion is faster than the velocity of the isotropic-nematic interface even during coalescence of nematic droplets (Fig. 2A). Therefore, it can be assumed that alkane concentration within the nematic domains remains close to equilibrium. The equilibrium concentration of alkanes at a given temperature is lower in the nematic than in the isotropic phase, as illustrated by the phase diagram (Fig. 1A, inset). Thus, alkane redistribution leads to accumulation of alkane at the isotropic-nematic interface. Because solubility of alkanes is higher in the isotropic phase, alkane diffuses further into alkane-poorer isotropic regions. According to Fick‘s law, this concentration gradient gives rise to an alkane flow that tends to reduce the concentration gradient. The alkane concentration gradient between the interfacial region and the bulk isotropic material, however, is maintained by expulsion of more alkane from the growing nematic domains under constant cooling. Therefore, the source term of alkane flow is given by the growth of the nematic domains.

Our results demonstrate that in 5CB-alkane mixtures, the forces acting on particles due to short-range interaction [5, 6] (which we also observed for some particles) can be vastly outmatched by those due to long-range interaction induced by alkane flow.

Alkane flow can couple to particle motion in two ways: (i) Advection: Because alkane redistribution takes place in a closed container, it should give rise to convection. The flow force should strongly depend on the growth rates of nematic domains and of the interface area through which alkane diffuses. However, at the observed length scales and cooling rates we so far have not identified any convection-like patterns. (ii) Migration due to interaction of the particle surface with alkane: A radial alkane concentration gradient between the boundary of a nematic droplet (high alkane) and distant isotropic areas (low alkane) could cause hydrophilic silica particles to migrate to lower alkane concentrations. In this case particle velocity should not exceed the estimated velocity of alkane flow and particle transport should depend on the alkane affinity of the particle surface.

We conclude that the movement of silica particles suspended in a mixture of nematogens with low molecular isotropic solvents (in this case, alkanes) during phase transition induced by slow temperature ramps proved to be dominated by long-range effects for long periods of time. It remains to be elucidated if this long-range interaction is mediated by hydrodynamic (alkane flow) or thermodynamic effects (concentration gradients and alkane affinity of the particle surface).

Acknowledgement The authors thank Mike Cates, Harald Pleiner, Burkhard Dünweg, and Jürgen Vollmer for stimulating discussions. D.V. acknowledges funding by LEA, and SFB-TR6. B.U. is supported by the German Science Foundation (DFG Vo 639).

References

1. West JL, Glushchenko A, Liao G, Reznikov Y, Andrienko D, Allen MP (2002) Phys Rev E 66:012702
2. Meeker SP, Poon WCK, Crain J, Terentjev EM (2000) Phys Rev E 61:R60836
3. Vollmer D, Hinze G, Poon WCK, Cleaver J, Cates ME (2005) J Phys Cond Matter 16:L227
4. Vollmer D, Hinze G, Ullrich B, Poon WCK, Cates ME, Schofield AB (2005) Langmuir 21:4921
5. Andrienko D, Tasinkevych M, Patricio P, Allen MP, da Gama MMT (2003) Phys Rev E 68:051702
6. Andrienko D, Tasinkevych M, Patricio P, da Gama MMT (2004) Phys Rev E 69:021706
7. Terentjev EM (1995) Phys Rev E 51:1330
8. Kuksenok OV, Ruhwandl RW, Shiyanovskii SV, Terentjev EM (1996) Phys Rev E 54:5198
9. Poulin P, Stark H, Lubensky TC, Weitz DA (1997) Science 275:1770
10. Poulin P, Weitz DA (1998) Phys Rev E 57:626
11. Loudet JC, Barois P, Poulin P (2000) Nature 407:611
12. Stark H (2001) Phys Rep 351:387
13. Kovevar K, Blinc R, Musevic I (2000) Phys Rev E 62:R3055
14. Gu Y, Abbott N (2000) Phys Rev Lett 85:4719
15. Oweimreen GA, Martire DE (1980) J Chem Phys 72:2500
16. Orendi H, Ballauff M (1992) Ber Bunsenges Phys Chem 96:96

Progr Colloid Polym Sci (2006) 133: 147–151
DOI 10.1007/2882_054

P. Wilhelm
C. Zetzsch
D. Stephan

Titania Coated Silica Nano-spheres as Catalyst in the Photodegradation of Hydrocarbons

P. Wilhelm · D. Stephan (✉)
Technische Universität München,
Lehrbereich Anorganische Chemie,
Lichtenbergstr. 4, 85747 Garching,
Germany
e-mail:
dietmar.stephan@bauchemie-tum.de

C. Zetzsch
Universität Bayreuth,
Forschungsstelle Atmosphärische Chemie,
Dr. Hans-Frisch-Str. 1–3, Bayreuth,
Germany

Abstract Nano-scaled spherical silica particles were directly coated with titania nanoparticles by means of heterocoagulation. Silica was prepared by the Stöber method, titania by a hydrolysis-condensation reaction of tetrapropyl-orthotitanate under acidic conditions. The photocatalytic activity of the coated spheres was investigated by a smog chamber technique, designed for the simulation of tropospheric photodegradation of hydrocarbons adsorbed on aerosol surfaces. In the chamber different solar spectra and irradiation intensities can be simulated and therefore the degradation can be monitored under different conditions. The degradation itself is dominated by OH radicals. Besides the monitoring, the reaction kinetics of particular hydrocarbon degradations was determined in the smog chamber. The steady-state concentration of OH radicals is higher in the presence of titania, and furthermore a heterogeneous photodegradation on the titania surface occurs.

Keywords Core-shell · Nano-spheres · Photodegradation · Smog chamber · Stöber Method

Introduction

Besides the usage of titania as compound in sun lotions, ceramics or pigments, the usage as photocatalyst under UV radiation is well known [1, 2] and utilized in important applications like treatment of waste water and drinking water [3–5], degradation of air pollutants [6–8] or development of self-cleaning surfaces [9].

The photocatalytic activity of titania is based on its semiconducting properties in the presence of moisture and oxygen. If photons of sufficient energy are absorbed (above the titania band gap), electrons are excited to the conduction band, which results in a hole in the valence band. These electron-hole pairs can react with adsorbed electron-acceptors (e.g. oxygen) or -donors (e.g. hydroxyl ions) on the surface of titania or recombine inside or on the surface of titania. The resulting hydroxyl radicals $OH\cdot$ and superoxide ions $O_2{}^-$ are known to be oxidants capable of oxidising organic compounds [1, 7].

Since the described effects mainly concern the surface of the particle, a nanoscaled core-shell system with titania as shell and an inert particle (e.g. silica) as core is highly applicable, because the photocatalytic traits of titania can be used without using pure titania particles, which leads to a cost reduction in the preparation of the photocatalyst. Core-shell systems already have various fields of application (catalysis, electronics, coatings, etc.) and their properties can be varied with the size, composition and thickness of both core and shell [10–12]. In this paper we present a simple synthesis for the well-known system $SiO_2@TiO_2$ [13, 14] and investigations regarding its photocatalytic activity – the degradation of hydrocarbons – by a smog chamber technique, to simulate its behaviour as aerosol in the atmosphere. One possible application of $SiO_2@TiO_2$ as photocatalyst in the atmosphere is the usage as fuel additive for aircrafts to introduce it directly to the troposphere, where it can degrade existing air pollutants.

Experimental

Preparation of Silica, Titania and $SiO_2@TiO_2$

The starting materials for the coating via heterocoagulation were prepared by well known one-step synthesis. The silica spheres in different sizes were prepared by the Stöber method [15] through variation of the reagent ratios. The obtained particles in alcoholic solution were centrifuged (10 000 g, 10 min) and the supernatant liquid discarded. The particles were redispersed in ultra-pure deionised water using an ultrasonic bath. In order to completely remove the ethanol, the process was repeated 3 times [16]. The resulting silica dispersion had a concentration of 3.6 wt % SiO_2 in water.

The titania sol was prepared by hydrolysis-condensation reaction under acidic conditions [17, 18]. The reagents were added to the titania precursor in ethanol under continuous stirring. After the peptisation of the intermediate gel by the acid, the solvent was removed completely under reduced pressure. The residue was vacuum dried and dissolved in deionised water in order to obtain the slightly blue and translucent titania sol with 5.8 wt % titania in water [16].

To coat the silica spheres with titania by means of a heterocoagulation, the titania sol (5.8 wt %) was gradually added to the silica dispersion (3.6 wt %). Before the addition, the pH had to be adjusted to 7.5 for the silica dispersion and 2.0 for titania nanosol. After the experiment, excess titania was removed by centrifugation (10 000 g, 10 min) and discarding the supernatant liquid. The coated particles were then redispersed in ultra-pure deionised water using an ultrasonic bath [16].

Characterization of Silica, Titania and $SiO_2@TiO_2$

The size of titania, silica and coated silica was measured using acoustic attenuation spectroscopy. The zeta potential of the particles was calculated from the colloidal vibration current (CVI) determined by electroacoustic measurements [19]. Both methods were performed by using a DT 1200 from Dispersion Technology. Additionally, the particle and crystallite size of titania were measured by dynamic light scattering (DLS) (Horiba LB-550) and X-ray diffraction (XRD) (Bruker AXS D8 Advance) respectively. The phase composition of titania nanosol was determined using Rietveld refining techniques with the fundamental parameter approach (Bruker AXS, Topas 2.1). The morphologies of silica and $SiO_2@TiO_2$ were determined by zeta potential measurements and scanning electron microscopy studies (SEM) (Philips XL 30 ESEM FEG).

Smog Chamber Experiments

The test chamber, designed for the simulation of the photodegradation of hydrocarbons in the troposphere in presence of aerosols, has been described elsewhere in detail [20, 21]. Different solar spectra and irradiation and exposure atmospheres can be applied for the experiments. As explained above, the degradation process is dominated by radicals, mainly hydroxyl radicals (OH·). The degradation process refers to two different effects, the homogeneous degradation in the gas phase through free radicals and the heterogeneous degradation of absorbed hydrocarbons on the surface of the air-borne particles [20, 21]. In the present study, the degradation rate of hydrocarbons (propane, *n*-butane, 2,2,3,3-tetramethylbutane and 2,2-dimethylbutane) and the total concentration of OH· were determined in a qualitative manner. To distinguish clearly between homogeneous and heterogeneous processes (i.e. gaseous and particle bound OH radicals) would require a larger set of hydrocarbons with a wider range of vapour pressures [20, 21].

The $SiO_2@TiO_2$ catalysed photodegradation of hydrocarbons was investigated in a modified chamber, consisting of a teflon bag (FEP 200A, Dupont) with a volume of 200 litre and 16 solarium lamps (Osram-Eversun, 80 W each). The particles were injected via an ultrasonic nebuliser from an aqueous suspension with a resulting relative humidity in the chamber of about 2%. Titania coated silica particles with a mean diameter of 470 nm were injected and the resulting mass concentration of the aerosol in the beginning of the experiment was between 2–4 mg/m^3 which corresponds to number densities of $10^5\ cm^{-3}$. The applied solar irradiation is slightly less than that of a typical European summer day, and the spectral distribution corresponds reasonably well to the sunlight spectrum at the earth surface [22]. The hydrocarbons were injected with a concentration of about 30 ppb. Perfluorohexane was used as internal standard since it is not decomposed through photocatalysis. The decay of the hydrocarbons was monitored every 20 min using gas chromatography/flame ionization detection (GC/FID, Sichromat, Siemens). The OH radical concentration in the gas phase was calculated from the decay rates of *n*-alkanes using known rate constants [20, 21]. The average temperature in the smog chamber during the experiments was 300 ± 3 K.

Results and Discussion

Characteristics of Silica, Titania and $SiO_2@TiO_2$

The particle diameter in the titania sol was 20 nm according to DLS and 10 nm to acoustic attenuation spectroscopy. The isoelectric point (IEP) determined by zeta potential measurements (Fig. 1) was at pH 6.7. This is in good agreement with the data found in literature (4.5–7.0 depending on the synthesis) [23]. Besides that, XRD studies were made to determine the crystallite size and the phase composition of the synthesized sol, dried at ambient temperature. These studies showed that, according to Rietveld refinement data, the crystallite size is about 5 nm, the major phase is anatase and the minor rutile. Exact

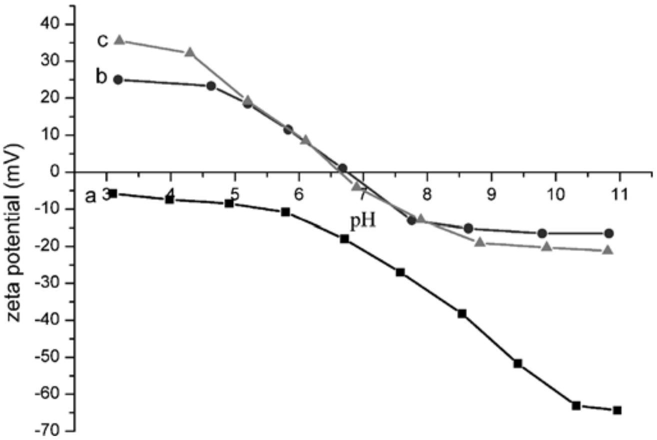

Fig. 1 Change in zeta potential of 220 nm silica (a), 10 nm titania (b), and 470 nm $SiO_2@TiO_2$ (c) with pH

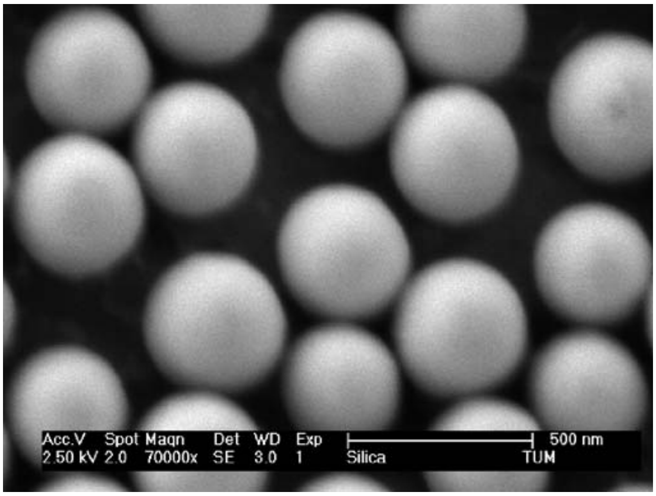

Fig. 2 The SEM image shows silica particles with an uniform particle size distribution

quantification was not possible due the lack of sharp reflection signals in the diffraction pattern, which is a consequence of the nanocrystallinity of the material. The phase composition of the dried sol makes sense, as the temperature of the synthesis and drying was not high enough for the sole formation of rutile crystallites, which form at temperatures higher than 850 °C [23]. Regarding the photocatalytic activity of the synthesized titania sol, the phase composition is advantageous, as recent reports show, that mixtures of rutile and anatase have a higher photocatalytic activity than pure anatase [24].

Silica spheres with a size of 150, 220, 470 and 590 nm were synthesized. The SEM studies showed that the particles are monodisperse, spherical and have a smooth surface (Fig. 2). In Fig. 1 the zeta potential measurements for 220 nm sized silica are shown. In the pH range employed (3.0–11.0) the zeta potential is negative, which also means that the surface is negatively charged. The IEP is between pH 1–2, depending on the particle size. This is close to the one reported by Iler (2.0) [25].

The coating was performed by gradual addition of titania sol to the silica dispersion, which leads to a heterocoagulation [26]. In terms of this experiment, the smaller titania particles are bound to the surface of the larger silica particles. Important for the success of this experiment is the pH, because the particles need to have a different surface charge, otherwise no coating will take place. A pH of 7.5 for silica and 2.0 for titania was used. This appeared to be a good compromise in colloid stability and difference in surface charge (Fig. 1). Titania is not very stable in the neutral pH range because of its low surface charge (Fig. 1). According to Iler [25], silica has its lowest stability between pH 5–6 with rapid gelling in the absence of salts, whereas in the presence of sodium salts it is around pH 7.0.

The progress of the coating was monitored by zeta potential measurements. In the course of the experiment, the pH drops from 7.5 to 2.5–3.0 after the last addition of titania sol, and the zeta potential becomes more and more positive, which is a consequence of the decreasing pH and the coating with titania, until a plateau is reached. At this plateau, where the zeta potential does not change anymore (except for small changes related to fluctuations in pH), the coating process is complete and the silica spheres are fully covered by titania [16].

In order to confirm the successful coating, the zeta potential of the coated particles was measured in dependency of the pH. As can be seen in Fig. 1, the coated particles show a pH dependency which is similar to the one of pure titania. For further characterization, SEM studies of the coated particles were made. Figure 3 illustrates that the

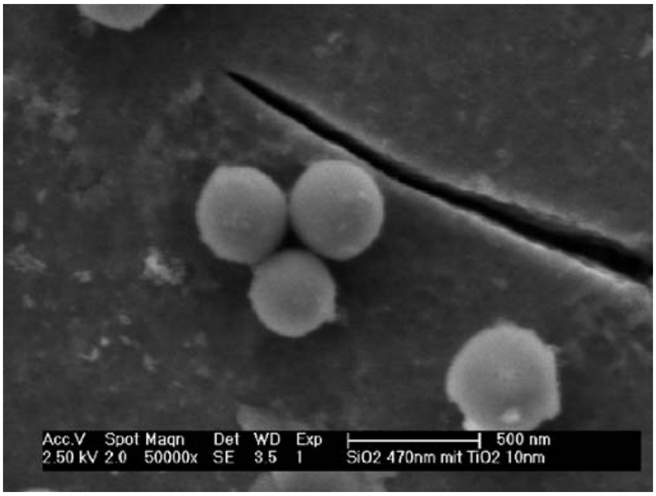

Fig. 3 The SEM image shows titania coated 470 nm silica particles

coated particles have a surface more rough than the uncoated spheres, which is related to the coating with titania.

$SiO_2@TiO_2$ Catalyzed Photodegradation

The $SiO_2@TiO_2$ catalyzed photodegradation of hydrocarbons was investigated by a smog chamber technique. The degradation process is dominated by radicals, and the mechanism of the degradation can be drawn from the semiconducting properties of titania [1]. Figure 4 shows the reaction on the surface of $SiO_2@TiO_2$ particles in the presence of water (humidity). After the absorption of a photon with energy higher than the gap between valence (VB) and conduction band (CB), electrons are excited from the VB to the CB, resulting in an electron excess in the CB and an electron hole in the VB. These electron-hole pairs can recombine in the interior, on the surface of titania or react with electron acceptors or donors. The excess electrons react with molecular oxygen and the electron holes with hydroxyl ions, resulting in the formation of superoxide ions and hydroxyl radicals. Superoxide ions can either react with water under the formation of hydroxyl ions [7] or, as can be seen in Fig. 4, with protons under formation of $HO_2\cdot$ radicals.

The desorption of OH· from the aerosol surface leads to an enrichment of free radicals and a homogenous degradation of the hydrocarbons in the gas phase, which is a bimolecular reaction. Besides this homogeneous part, the heterogeneous degradation on the aerosol surface occurs. Heterogeneous degradation means that the hydrocarbons are degraded while adsorbed on the aerosol surface through OH radicals on the aerosol surface. Studies made before showed that the heterogeneous degradation is accelerated when the relative humidity in the chamber is low. This is due the fact, that the water layer adsorbed on the aerosol at high humidity prevents the hydrocarbons to adsorb on the aerosol surface. If there is less humidity, less water is adsorbed on the aerosol and the surface is accessible more easily for the hydrocarbons and the heterogeneous reaction is accelerated [20].

In the experimental set-up used, it is not possible to clearly differentiate between homogeneous and heterogeneous degradation. The time profiles for the hydrocarbons are shown in Fig. 5. The slope of the lines refer to the rate constants (1. order) of the individual hydrocarbons. The increase in reaction rate from propane to *n*-butane indicates that the degradation is dominated by heterogeneous degradation, since alkanes with longer chain length have a longer adsorption time on the aerosol surface. The low relative humidity in the experiment also leads to the assumption that the degradation is dominated by the heterogeneous part of the reaction. The faster degradation of methylated alkanes is unexpected and might indicate that analytical problems perturbed the experiment or that these compounds are more strongly affected by the heterogeneous loss mechanism.

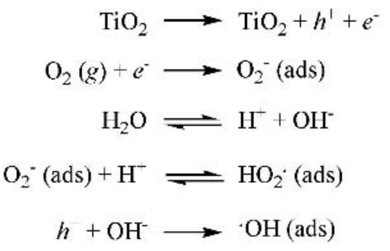

$$TiO_2 \longrightarrow TiO_2 + h^+ + e^-$$
$$O_2\,(g) + e^- \longrightarrow O_2^-\,(ads)$$
$$H_2O \rightleftharpoons H^+ + OH^-$$
$$O_2^-\,(ads) + H^+ \rightleftharpoons HO_2^\cdot\,(ads)$$
$$h^+ + OH^- \longrightarrow {}^\cdot OH\,(ads)$$

Fig. 4 Reactions occurring on the $SiO_2@TiO_2$ surface in the presence of water (humidity)

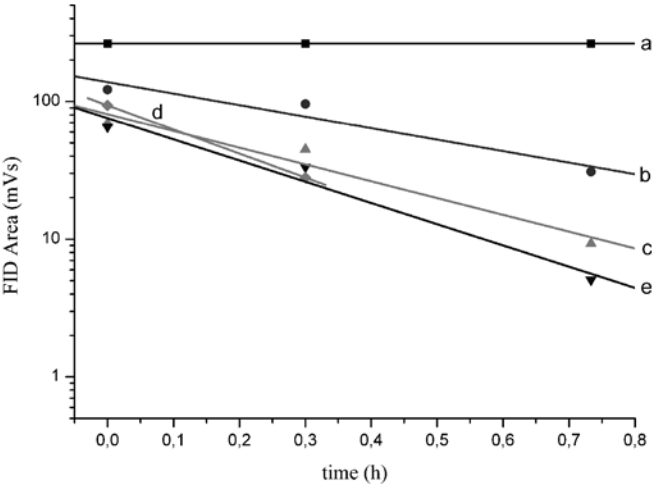

Fig. 5 The graphic shows the time profiles of the flame ionisation detector signals for perfluorohexane (a), propane (b), *n*-butane (c), 2,2,3,3-tetramethylbutane (d) and 2,2-dimethylbutane (e) in a semi-logarithmic diagram

Figure 6 shows the time integral of OH radicals in the smog chamber calculated as sum of the OH· concen-

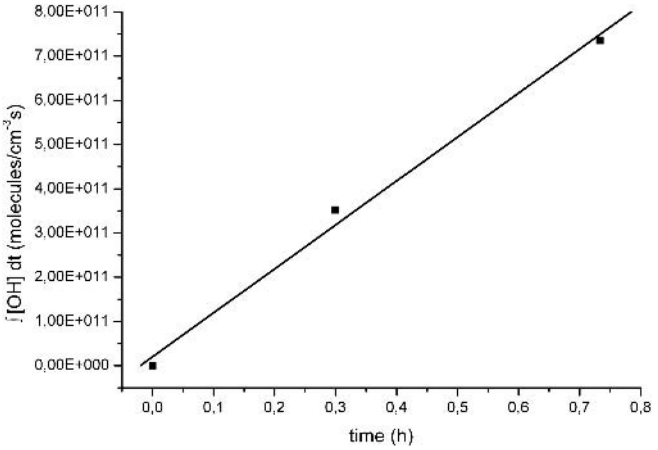

Fig. 6 Time integral of OH radicals in the smog chamber as a function of time. The slope delivers the mean concentration of OH, about 3×10^8 molecules cm^{-3}

trations derived from the individual rate constants of the hydrocarbons in dependency of the time. The slope yields a mean concentration around $3 \times 10^8\,\mathrm{cm}^{-3}$ (error 20%), which is about 100 times the concentration of OH· compared to the typical OH· concentration outdoors during daytime.

Summary

The preparation of $SiO_2@TiO_2$ from silica spheres and titania nanosol, which are easily accessible through a well known one-step synthesis, via heterocoagulation proved to be an appropriate method for synthesis, where the progress of the coating process can be monitored by zeta potential measurements. First investigations by a smog chamber technique showed that the material has a fairly high photocatalytic activity regarding the photodegradation of hydrocarbons. For the future, optimization of the synthesis is planned in order to increase the photocatalytic activity of the material. Further smog chamber studies will show whether the degradation is dominated by heterogeneous or homogeneous processes and how the reactivity of the photocatalyst depends on the diameter of the core particles.

Acknowledgement We would like to thank Dr. P. Chatziagorastou for the SEM images, Heinz-Ulrich Krüger for performing the smog chamber experiments and Prof. J. Plank for continuous support of the work and helpful discussions.

References

1. Carp O, Huisman CL, Reller A (2004) Prog Solid State Chem 32:33
2. Anpo M, Dohshi S, Kitano M, Hu Y, Takeuchi M, Matsuoko M (2005) Annu Rev Mater Res 35:1
3. Berns B, Jentoft FC, Schlögl R (1999) Appl Catal B 20:155
4. Hermann JM, Guillard C, Disdier J, Lehaut C, Malato S, Blanco J (2002) Appl Catal B 35:281
5. Araña J, Herrera Melián JA, Doña Rodriguez JM, González Diaz O, Viera A, Pérez Peña J, Marrero Sosa PM, Espino Jiménez V (2002) Catal Today 76:279
6. Dalton JS, Janes PA, Jones NG, Nicholson JA, Hallam KR, Allen GC (2002) Environ Pollut 120:415
7. Tennakone K, Wijayantha KGU (2005) Appl Catal B 57:9
8. Strini A, Cassese S, Schiavi L (2005) Appl Catal B 61:94
9. Zhang XT, Sato O, Taguchi M, Einaga Y, Murakami T, Fujishima A (2005) Chem Mater 17:696
10. Caruso F (2004) Colloids and Colloid Assemblies. Wiley, Weinheim
11. Schmid G (2004) Nanoparticles. Wiley, Weinheim
12. Caruso F (2001) Adv Mater 13:11
13. Hsu WP, Yu R, Matijevic E (1994) J Colloid Interface Sci 156:56
14. Holgado M, Cintas A, Ibisate M, Serna CJ, Lopez C, Meseguer F (2000) J Colloid Interface Sci 229:6
15. Stöber W, Fink A, Bohn E (1968) J Colloid Interface Sci 26:62
16. Wilhelm P, Stephan D (2006) J Colloid Interface Sci 293:88
17. Bartlett JR, Woolfrey JL (1995) J Aust Ceram Soc 31:35
18. Bartlett JR, Woolfrey JL (1997) Ceram Trans 81:3
19. Dukhin AS, Goetz PJ (2002) Ultrasound for Characterizing Colloids. Elsevier, Amsterdam
20. Behnke W, Nolting F, Zetzsch C (1987) J Aerosol Sci 18:65
21. Behnke W, Holländer W, Koch W, Nolting F, Zetzsch C (1988) Atmos Environ 22:1113
22. Möller F (1973) Einführung in die Meteorologie Band 2. Wissenschaftsverlag, Mannheim
23. Winkler J (2003) Titandioxid. Vincentz Network, Hannover
24. Sun J, Gao L, Zhang Q (2003) J Am Ceram Soc 86:1677
25. Iler RK (1979) The Chemistry of Silica. Wiley, New York
26. Chen GC, Kuo CY, Lu SY (2005) J Am Ceram Soc 88:277

Progr Colloid Polym Sci (2006) 133: 152–158
DOI 10.1007/2882_057

Q. Tong
S. Kosmella
J. Koetz

Formation of Rod-like CdS Nanoparticles in SDS/Decanol Based Multilamellar Vesicles

Q. Tong · S. Kosmella · J. Koetz (✉)
Institut für Chemie, Universität Potsdam,
Karl-Liebknecht-Str. 24–25, Haus 25,
14476 Golm, Germany
e-mail: koetz@rz.uni-potsdam.de

Abstract In polycation-modified SDS/decanol systems, dense multilamellar structures, i.e. multilamellar vesicles are formed by self-organization, which were used as an organic template for CdS nanoparticle preparation. Specific amounts of precursors, $CdCl_2$ and Na_2S, were incorporated into the multilamellar vesicles without losing the multilamellar structure. Structural changes of the lamellar liquid crystalline template induced by the incorporation of the polycation and the inorganic precursors were investigated by differential scanning calorimetry in combination with small angle X-ray scattering. By mixing both precursors within the multilamellar vesicles CdS nanoparticles are formed. After decomposition of the vesicle template, quite different shaped and sized CdS-nanoparticles were observed by transmission electron microscopy. At lower polymer concentration spherical CdS nanoparticles of about 10 nm can be obtained. At higher polymer concentration predominantly rod-like CdS aggregates were produced with an average length of 120 nm and width of 30 nm.

Keywords Interlayer spacing · Multilamellar vesicles · Nanoparticles · Phase transition

Introduction

Nanosized semiconductor particles (“Quantum dots”), such as CdS and CdSe, have attracted much attention in recent years because of their characteristic size-dependent optical, electronic, magnetic, and chemical properties [1–3]. Since nanosized particles are liable to aggregate or grow in order to reduce their surface energy, well-controlled synthetic methods are required for their preparation.

Numerous synthesis methods that employ polymers [4–6], glasses [7], zeolites [8], inverse micelles [9–11], capping molecules [12] and coordinating solvents [13] have been used to control particle nucleation and growth and the final particle size. Nature has solved this problem by producing inorganic crystalline materials of predetermined size, shape and structure in vesicles consisting of surfactant bilayers (e.g. liposomes). Mimicking such natural functions has led to the use of synthetic bilayer membranes as a template phase since these multilayer systems provide unique interlayer spaces which can be used as molecular templates [14–16].

Recently we have shown that the cationic polyelectrolyte poly(diallyldimethylammonium chloride) (PDADMAC) can be incorporated into anionic surfactant based lamellar liquid crystalline systems (SDS/decanol/H_2O) without a macroscopic phase separation, and this polymer-modified phase (LC-phase) has significantly changed properties [17–20]. Due to the polymer bilayer interactions, i.e. the adsorption of the PDADMAC onto the SDS head groups of the individual lamellae, the bending rigidity of the amphiphilic film has been changed and the formation of onion-like spheres in the order of 1–50 μm is induced. Small angle scattering experiments have shown that the interlayer spacing can be tuned by increasing the polycation concentration. Micro-DSC measurements indicate a temperature dependent swelling and deswelling behaviour of the polymer modified LC-phase. However, the phase transition peak can be shifted to higher temperatures by adding PDADMAC [17].

Concerning the highly regular multilamellar structure and its structure dependence on temperature and added polymer we initiated studies on the application of this multilamellar vesicle system as a template for the nanoparticle preparation. This opens a way to control the size of the particles formed in the LC phase by tuning the reaction temperature and the polymer concentration.

In the present study we investigated first of all the influence of the inorganic components $CdCl_2$ and Na_2S on structure formation in the lamellar phase of SDS/decanol/H_2O system by varying the concentration of PDADMAC. In the next step we investigated the process of CdS nanoparticle formation in the template phase. Finally the CdS nanoparticles were separated from the LC-phase and redispersed in ethanol/water mixtures.

Experimental

Materials

The main components of multilamellar vesicles are anionic surfactant sodium dodecyl sulphate (SDS) (99%, Fluka) and decanol (95%, Fluka), which are used without further purification. The polycation poly(diallyldimethylammonium chloride) (PDADMAC) was synthesized according to [21]. After ultrafiltration the molecular weight was determined by size exclusion chromatography ($M_n = 21.000$ g/mol). The precursors for CdS nanoparticle formation are $CdCl_2$ (99%, Fluka) and Na_2S hydrate (32–38%, Fluka) and were used as obtained.

Vesicle Preparation

Each sample was prepared by mixing equal amounts of H_2O with SDS/decanol (1 : 1 by weight) for each polymer concentration. The amount of PDADMAC varied between 1% and 8% with respect to the mass of water. 1.0 wt % of $CdCl_2$ (0.055 M in H_2O) and 0.52 wt % of $Na_2S \cdot H_2O$ (0.055 M in H_2O) were dissolved in the aqueous polymer solutions. The mixtures were sheared manually in glass tubes and centrifuged repeatedly until the samples appeared to be homogenous. The composition of the different samples is given in Table 1.

Table 1 Sample composition

Sample	composition	molar ratio anionic : cationic group
I	50 wt % aqueous phase (0% PDADMAC, 0.055 M precursor) – 50 wt % decanol/SDS(1 : 1)	—
II	50 wt % aqueous phase (1% PDADMAC, 0.055 M precursor) – 50 wt % decanol/SDS(1 : 1)	28 : 1
III	50 wt % aqueous phase (2% PDADMAC, 0.055 M precursor) – 50 wt % decanol/SDS(1 : 1)	14 : 1
IV	50 wt % aqueous phase (3% PDADMAC, 0.055 M precursor) – 50 wt % decanol/SDS(1 : 1)	9 : 1
V	50 wt % aqueous phase (5% PDADMAC, 0.055 M precursor) – 50 wt % decanol/SDS(1 : 1)	6 : 1
VI	50 wt % aqueous phase (8% PDADMAC, 0.055 M precursor) – 50 wt % decanol/SDS(1 : 1)	3.5 : 1

CdS Nanoparticle Formation

Two different methods were used to form CdS particles.

Approach A. Two adequate concentrated multilamellar vesicle phases with each precursor, i.e. $CdCl_2$ and Na_2S, were mixed together in glass tubes by manually shearing and centrifuging repeatedly until the samples appeared to be homogenous. The mixing process was carried out at room temperature and 8 °C respectively, i.e. above and below phase transition temperature determined by micro-DSC measurements.

Approach B. Two multilamellar vesicle phases containing each precursor were separately dispersed in H_2O and stirred gently for 2 h at room temperature. The resulting two vesicle dispersions with a vesicle concentration of 200 g/l were mixed than dropwise at room temperature by gently stirring.

Vesicle Characterization

Optical Microscopy and Transmission Electron Microscopy (TEM). The optical patterns of the vesicles before and after dissolution in water were examined with a polarized light microscope.

In addition the structures were investigated by freeze fracture transmission electron microscopy. The samples were mounted on gold grids and quickly frozen by dipping into liquid propane. Freeze-fracturing, etching, and coating were carried out at −100 °C using a Blazers BAF 400 freeze-etching unit (Blazers, Liechtenstein). The platinum/carbon-coated replicas were collected on uncoated copper grids. The cleaned replicas were examined in a transmission electron microscope.

Nanoparticle characterization. To isolate the nanoparticles, the multilamellar vesicles were destroyed by dissolving in an excess of EtOH/H_2O mixture (1 : 1 vol. ratio). A drop of solution was deposited onto a carbon film supported by a copper grid. After solvent evaporation the CdS particles can be detected by TEM. The mean diameter, d, and the standard deviation, σ are obtained from an average of approximately 100 particles. The polydispersity is defined as σ/d.

Differential Scanning Calorimetry (DSC). DSC is widely used to study phase transitions of surfactant based multicomponent systems. Ultra high resolution DSC-measurements were carried out with a Micro DSC-III (Setaram, France) in the temperature region from +25 °C to +5 °C with a cooling rate 0.3 K/min. The enthalpy was calculated in relation to the total amount of water.

Small Angle X-Ray Scattering (SAXS). The interlayer spacing of the concentrated lamellar liquid crystalline phase can be calculated from the peak maximum of the first order Bragg peak. A small amount of sample was mounted on a transparent film placed on a sample holder and measured with a 40 KV 100 mA pinhole setup. Ni-filtrated Cu K_α X-ray radiation ($\lambda = 1.54$ Å) by a rotating anode from Bruker-Nonius was used, and the signals were detected with imaging plates at a distance 74 cm from the sample.

Bragg peaks of a lamellar phase are related to the interlayer spacing by the following equation:

$$d = \frac{2\pi}{q} \cdot n\,,$$

where the q-value [nm^{-1}] is associated with the peak-maximum in the scattering curve, and n is the order of Bragg peak. All SAXS measurements were performed at room temperature.

Results and Discussion

Optical Microscopy

All concentrated samples produced by **Approach A** show optical patterns of "Maltese crosses" and oily streaks which are typical for lamellar liquid crystals under polarized light. There was no phase separation independent of the added amount of precursor $CdCl_2$ or Na_2S. After mixing the two precursor LC-phases, a homogeneous lamellar phase still exists.

When the PDADMAC-modified lamellar phases were dissolved in water (**Approach B**), the multilamellar vesicles were surprisingly still stable resulting in a vesicle-dispersion (Fig. 1). It has to be mentioned here that the multilamellar vesicles in absence of PDADMAC are not stable in water and disappear.

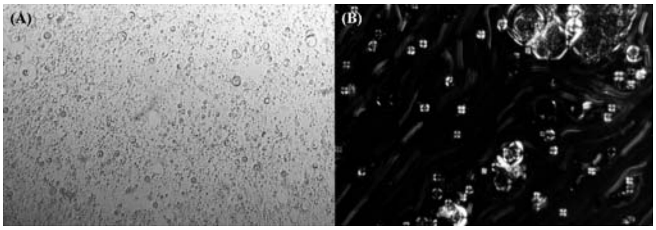

Fig. 1 Light microscopy image of sample V (5 wt % PDADMAC) after dissolution in water. **A** without crossed polarizers; **B** with crossed polarizers

Differential Scanning Calorimetry (DSC)

Our previous studies of SDS/decanol/H_2O based lamellar liquid crystalline systems suggest that the exothermic peak in the cooling curve of micro-DSC measurements can be correlated to the phase transition from a more swollen LC-phase to a more compact LC-phase. In addition, the phase transition peak can be shifted to higher temperatures by increasing the amount of added PDADMAC [17]. Figure 2 shows the dependence of the phase transition peak top temperature on the polymer concentration for all samples listed in Table 2. All exothermic peaks associated with transition enthalpies in the order of 30 J/g occur in the temperature range from +14 °C to +20 °C as summarized in Table 2. It has to be mentioned here, that at a PDADMAC concentration of 2–3 wt % the phase transition region is at about room temperature, as already outlined in more detail in [17].

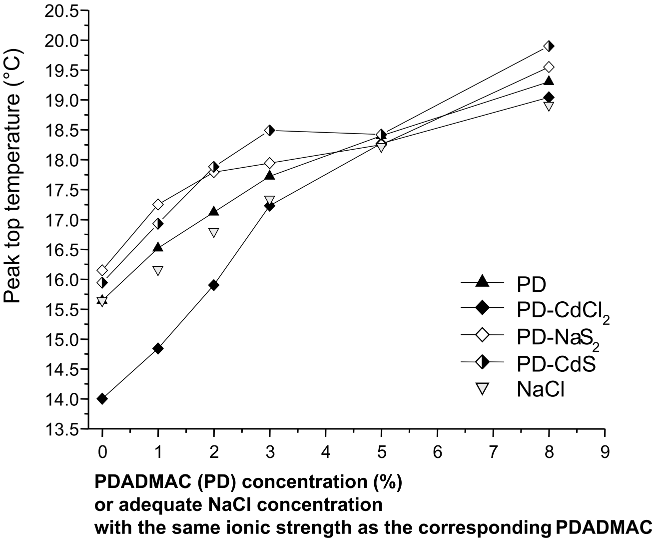

Fig. 2 Dependence of the phase transition peak top temperature on the added polymer concentration in presence of inorganic precursor components, or adequate amounts of NaCl with the same ionic strength as the corresponding PDADMAC

Table 2 Interlayer spacing (in nm) calculated from the first order peak top of the small angle X-ray scattering curves in Fig. 3

Sample IV	interlayer spacing *d* (nm) 1st order peak a	 b1	 b2	 2nd order peak corresponding to peak
3% PD	5.4	4.4	3.9	a
3% PD-CdCl$_2$	5.3	4.2	3.9	a;b
3% PD-Na$_2$S	5.1	4.1	—	b
3% PD-CdS	—	4.2	—	b

When CdCl$_2$ and Na$_2$S are added to the system, a similar shift of the phase transition peak to higher temperatures in comparison to the PDADMAC-modified one can be induced as to be shown in Fig. 2. However, in comparison to the samples without precursors, the peak tops of the CdCl$_2$-containing systems are shifted to lower, and in presence of Na$_2$S to higher temperatures. It has to be mentioned here, that the effect is much more enhanced in the case of CdCl$_2$ in comparison to the Na$_2$S modified system. These results suggest that both the ionic strength and the counterion interactions can influence the phase transition temperature. To verify the influence of the ionic strength, adequate amounts of NaCl, containing the same ionic strength as corresponding the PDADMAC solutions, were added. When PDADMAC was substituted by NaCl (Fig. 2), the shift of the peak top to higher temperatures with increasing ionic strength was observed as well, but in comparison to the PDADMAC system, the temperature shift is less pronounced. In general, the increase of the ionic strength in the system is correlated to a screening effect of the SDS head groups, which leads to a decrease of the electrostatic repulsion of the bilayers, and in consequence more compact structures with a smaller interlayer spacing are formed.

Based on this knowledge the peak shifts in CdCl$_2$ and Na$_2$S modified systems can be explained by stronger interactions between Cd^{2+} ions and SO$_4{}^{2-}$ head groups of the SDS surfactant, and less pronounced interactions between S^{2-} and ammonium units of the polycation, which are competitive with the interactions between PDADMAC and SDS.

After CdS nanoparticle formation, a similar shift of the phase transition peak top temperature by increasing polymer concentration was observed. However, the peak top temperatures at a polymer concentration $\geq 2\%$ are higher than those of the other samples. This may imply that the formation of nanoparticles can induce more densely packed lamellar structures as well. This is consistent with the results of SAXS measurements presented later.

It has to be stated here that at a polymer concentration of 5 wt % PDADMAC, the differences in the phase transition peak top become much smaller, but increase again at a polymer concentration of 8 wt %.

Small Angle X-Ray Scattering (SAXS)

The influence of the type of added precursor on the Bragg peak in the small angle scattering curve at a given PDADMAC concentration of 3 wt % (sample IV) is shown in Fig. 3. The 2nd order peaks (c, d) were observed in all four samples, indicating the existence of a lamellar structure. The interlayer spacing was calculated from the maximum of the first order Bragg peak. The results are summarized in Table 2.

Concerning the 1st order peaks, consistent with our former studies [17], the SDS/decanol/H$_2$O system with 3% PDADMAC shows two Bragg peaks (a, b) corresponding to two different lamellar structures, a swollen and a non-swollen one, with an interlayer spacing of 5.4 nm and about 4 nm, respectively. Taking into account that the measurements are realized at room temperature the coexistence of the two lamellar structures can be well understood in combination to our DSC measurements. That means, due to the fact that the measurements were performed in the actual transition temperature range from the swollen to the non-swollen range both lamellar structures can detect simultaneously at room temperature.

Surprisingly, an additional peak splitting of the peak *b* into b_1 (4.4 nm) and b_2 (3.9 nm) has to be mentioned here, which may imply the coexistence of two different non-swollen structures. However, the incorporation of each precursor shows different effects. In the case of CdCl$_2$, a similar peak splitting was observed, but the area of peak b_1 is significantly larger than that of b_2. In the case of Na$_2$S only one peak in the order of 4 nm can be observed, and peak *a* is reduced to a shoulder. Taking into account the different types of precursors, one can conclude that

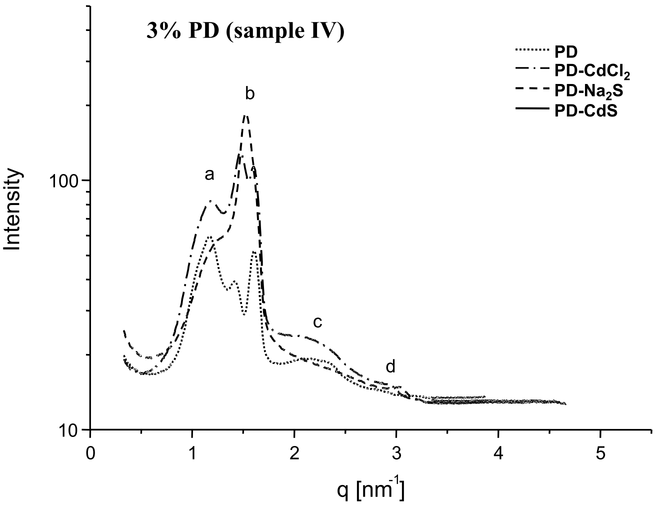

Fig. 3 Small angle X-ray scattering curves (performed at room temperature) of sample IV (3 wt % PDADMAC) after incorporation of precursors and CdS particle formation (a,b – first order Bragg peaks; c,d – second order Bragg peaks)

the Coulombic interactions are much more important in presence of Na_2S. Without any precursor the interactions between PDADMAC and SDS induce a deswelling of the lamellar bilayer and multilamellar vesicular structures are observed [18]. After incorporation of $CdCl_2$, Cd^{2+} competes with the positively charged groups of the polycation in the interactions with the $SO_4{}^{2-}$ head groups of the surfactant, which leads to structural changes on the supramolecular level. By incorporating S^{2-} more compact multilamellar vesicular structures can be observed.

After the formation of CdS nanoparticles in the LC-phase, only one peak in the order of 4 nm was detected, which suggests that the nanoparticle formation may have a deswelling effect on the lamellar structure as well.

However, at a polymer concentration of 8 wt %, the incorporation of $CdCl_2$ or Na_2S as well as the CdS nanoparticle formation process does not change the interlayer spacing at all. This means in all cases a compact interlayer spacing of 3.9 nm was observed, as to be seen in Fig. 4.

Transmission Electron Microscopy (TEM)

Measurements presented before, suggest a correlation between the phase transition peak and structural changes in the LC-phase. Freeze-fracture electron micrographs in combination with DSC measurements give evidence that the supramolecular structure of the polycation modified SDS/decanol/H_2O system can be tuned by the temperature, too.

Figure 5 shows TEM micrographs of sample III (2 wt % PDADMAC) after CdS particle-formation at different temperatures as indicated on the DSC curve. One can see more compact spherical multilamellar vesicles below the phase transition peak (Fig. 5A), and a more swollen planar lamellar bilayer structure above the phase transition peak (Fig. 5B).

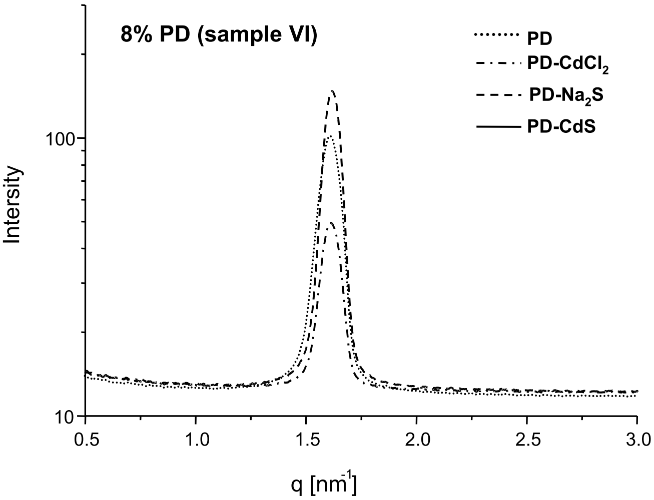

Fig. 4 Small angle X-ray scattering curves (performed at room temperature) of sample VI (8 wt % PDADMAC) after incorporation of precursors and CdS particle formation

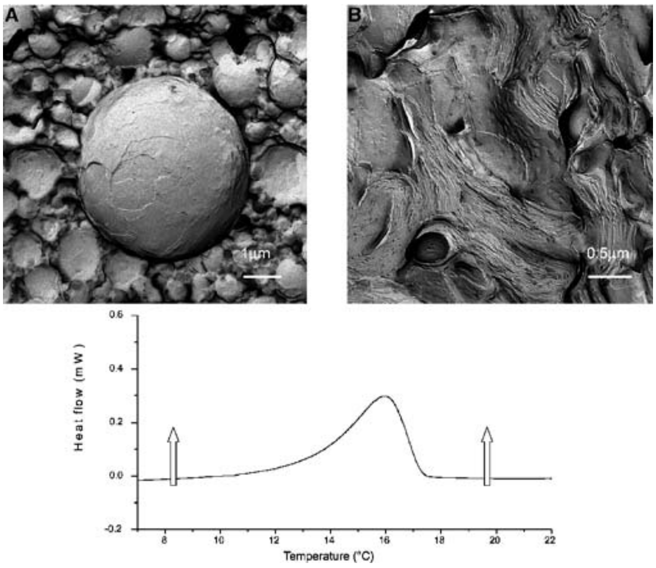

Fig. 5 Freeze fracture micrographs of sample III (2 wt % PDADMAC) after formation of CdS particles at different temperatures as indicated in the DSC curve

SANS measurements have shown that with increasing temperature, the first order Bragg peak was shifted to smaller q-values i.e. a larger interlayer spacing between the lamellae [17]. Based on this knowledge, we assume that the size of particles produced in the lamellar phase can be influenced by the temperature of the mixing process, too.

After decomposition of the multilamellar vesicles in an ethanol/water (1 : 1 vol.) mixture, single CdS nanoparticles can be observed in TEM micrographs. The mean particle diameter d and standard deviation σ calculated from the size histogram of CdS nanoparticles produced at room temperature (**Approach A**) within the sample containing 3 wt % PDADMAC is 17.6 nm and 5.1, respectively, with a polydispersity of 0.29. Making the same experiments below the phase transition temperature, we obtained smaller particles with mean diameter of 11.5 nm and standard deviation σ 2.8, with a polydispersity of 0.24 as to be seen in Figs. 6 and 7. But in both cases the particles exhibit a nearly spherical shape (Fig. 6). In addition, the particles produced at room temperature by **Approach B** also exhibit a spherical shape but with larger dimension of mean diameter 26.2 nm, standard deviation σ 8.2, and polydispersity 0.31. In general, it can be concluded that smaller aggregates can be realized by using Approach A.

Furthermore, the particle formation depends on the polycation concentration. At a polymer concentration $\geq 5\%$, multilamellar vesicles are predominantly formed already at room temperature (Fig. 8). When the polymer concentration was increased to 8 wt %, we observe anisotropic aggregates of CdS particles, which exhibit

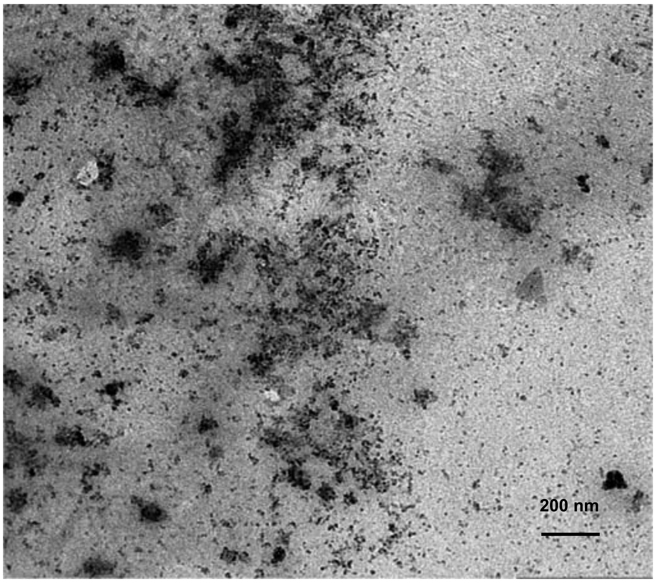

Fig. 6 TEM micrograph of CdS nanoparticles produced in sample IV (3 wt % PDADMAC)

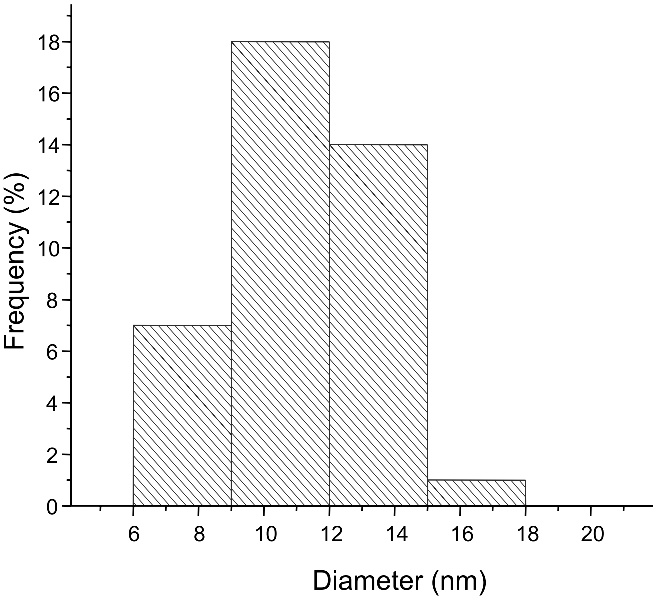

Fig. 7 Size histogram of CdS nanoparticles produced in sample IV (3 wt % PDADMAC)

a defined cylindric shape with an average length of 120 nm and a width of 30 nm as shown in Fig. 9.

Conclusion

The dissolution experiments of multilamellar vesicles in water have shown that the presence of PDADMAC is essential for the stability of vesicular structures in aqueous solution, which suggests that the polycation induces a bridging in the aqueous bilayers and therefore stabilizes the spherical multilamellar structures. However, this opens a new way to separate the compact polymer-modified multilamellar vesicles.

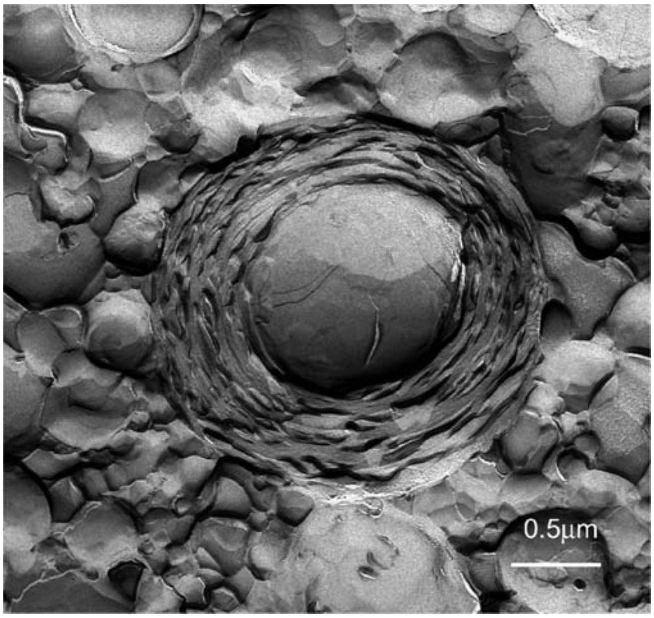

Fig. 8 Freeze fracture micrographs of sample V (5 wt % PDADMAC) after formation of CdS particles at room temperature

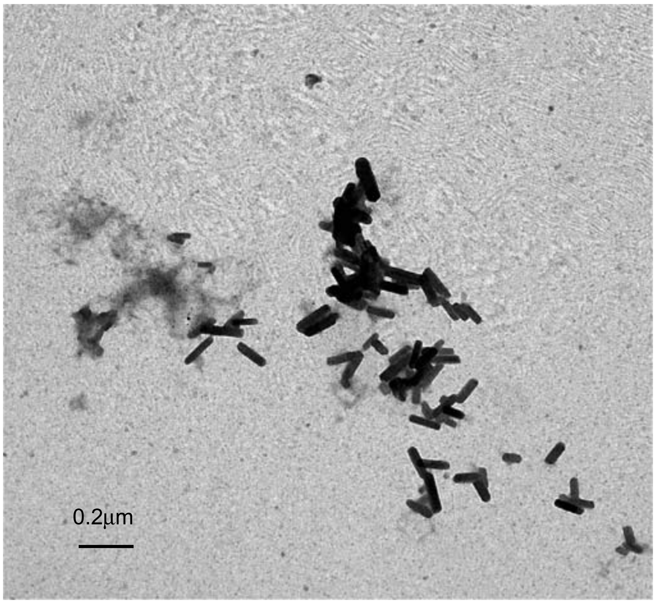

Fig. 9 TEM micrograph of CdS nanoparticles produced in sample VI (8 wt % PDADMAC)

SAXS measurements carried out at a 3 wt % PDADMAC concentration show that the incorporation of inorganic salt ions can influence the coexistence of a swelling and a non-swelling lamellar structure. This means the incorporation of Na_2S leads to a more compact bilayer with

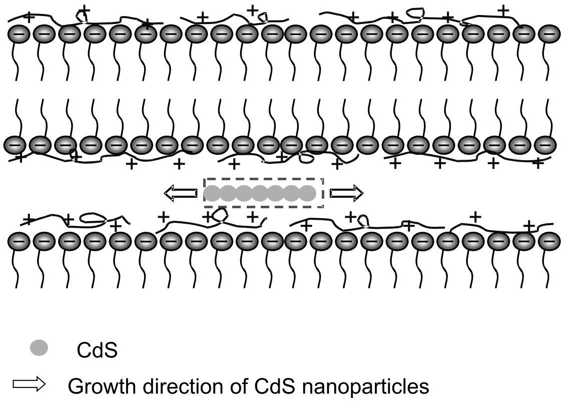

Scheme 1 Formation of cylindric CdS aggregates

an interlayer spacing of 4.1 nm combined by a shift of the phase transition peak in the DSC curve to higher temperatures. In contrast to these results the addition of $CdCl_2$ leads only to a small effect on the interlayer spacing combined by a decrease of the phase transition temperature. From these results one can conclude that the S^{2-} ions are predominantly incorporated into the compact bilayer structure and Cd^{2+} ions into the more swollen bilayer structure. However, after mixing both LC-phases the final CdS containing system exhibits only the compact bilayer structure, demonstrating that the nanoparticle formation process leads to the formation of a more compact multilamellar structure.

When the polymer concentration is increased to 8 wt % (sample VI) compact multilamellar vesicles are formed, and the interlayer spacing keeps constant at 3.9 nm independent of the formation of the CdS nanoparticles. Taking into account that the charge distance of a fully charged PDADMAC in a zigzag chain is about 0.4 nm and the size of SDS head group is 0.15 nm, a nearby complete flat adsorption of the polycation onto the SDS-head groups can be assumed for sample VI at a molar ratio of anionic to cationic groups of 3.5 : 1.

By using the PDADMAC-modified SDS/decanol/H_2O systems as templates, at a polycation concentration of 3 wt % spherical CdS nanoparticles in the order of 20 nm were obtained after redispersion in an ethanol-water mixture. Under these conditions, the anionic surfactant bilayers are only partially compensated by the adsorbed oppositely charged polymer chain, therefore the incorporated precursors salt ions are distributed randomly in the aqueous phase and spherical CdS particles tend to form. The size of particles produced here is bigger than the diameter predicted according to the interlayer spacing of the multilamellar vesicles. This can be explained by an aggregation of originally formed nanosized particles after decomposition of the template. However, the smallest particle dimensions of about 10 nm can be realized by using Approach A at temperatures below the phase transition, that means in the template phase consisting of compact multilamellar vesicles.

When the amount of polycation was increased up to 8 wt %, the initially formed spherical CdS nanoparticles aggregate predominantly along the bilayer, because of a transversal hindrance due to the polymer-modified lamellae, which results in rod-like structures (compare Scheme 1). After decomposition of the template, these polymer stabilized cylindric structures can be visualized by TEM. These results give evidence that the incorporated polycation in SDS/decanol based multilamellar vesicles has a significant influence on the nanoparticle formation and final particle aggregation. However, further investigations should be focused on the mechanism of particle formation in the lamellar phase in dependence on the polymer concentration, the temperature, and the redispersion conditions. Therefore, kinetic studies of the nanoparticle formation process seems to be of special interest, too.

Acknowledgement The financial support from the Polymer Science Program is gratefully acknowledged. The authors thank Dr. Paris from the Max Planck Institute of Colloids and Interfaces for the SAXS measurements.

References

1. Fendler JH (1987) Chem Rev 87:877
2. Henglein A (1989) Chem Rev 89:1861
3. Pileni MP (2001) J Phys Chem B 105:3358
4. Persans PD, Tu A, Wu WJ, Lewis M (1989) J Opt Soc Am B 6:818
5. Yu SH, Coelfen H, Mastai Y (2004) J Nanosci Nanotechnol 4:291
6. Qi L, Coelfen H, Antonietti (2004) Nano Letters 1:61
7. Nirmal M, Murray CB, Bawendi MG (1994) Physic Rev B 50:2293
8. Stucky GD, Mac Dougall JE (1990) Science 247:669
9. Lisiecki I, Pileni MP (1993) J Am Chem Soc 115:3887
10. Bagwe RP, Khilar KC (2000) Langmuir 16:905
11. Capek I (2004) Advances in Colloid Interface Sci 110:49
12. Vossmeyer T, Katsikas L, Giersig M (1994) J Phy Chem 98:7665
13. Katari J, Colvin VL, Alivisatos AP (1994) J Phy Chem 98:4019
14. Gauffre F, Roux D (1999) Langmuir 15:3738
15. Vassiltsova OV, Chunilin AL (1999) J Photochem Photobio A 125:127
16. Faure C, Derré A, Neri W (2003) J Phys Chem B 107:4738
17. Hellweg T, Brulet A, Lapp A, Robertson D, Koetz J (2002) Phys Chem Chem Phys 4:2612
18. Koetz J, Tiersch B, Bogen I (2000) Colloid Polymer Sci 278:164
19. Koetz J, Kosmella S (1997) Colloids Surface A 123-124:265
20. Robertson D, Hellweg T, Tiersch B, Koetz J (2004) J Colloid Interface Sci 270:187
21. Jaeger W, Hahn M, Wandery C (1984) J Macromol Sci Chem A 21:593

Progr Colloid Polym Sci (2006) 133: 159–168
DOI 10.1007/2882_059

Arno Nennemann
Matthias Voetz
Gabriele Hey
Lothar Puppe
Stephan Kirchmeyer

Colloidchemical Interactions of Silica Particles in the Cu-CMP-Process

Abstract Polishing slurries for the copper chemical mechanical planarization (CMP) process consist of a complex composition of highly stable nanoparticle suspensions in the presence of chemical additives for etching and protecting the surface. The target of such dispersions is to achieve perfectly smooth surfaces of low topography. Key factors are the surface roughness, local geometry and total flatness of the whole wafer. Surface defects like scratches, dishing, etching and erosion e.g. due to strong particle adsorption, aggregates or chemical impact have to be avoided. Particle wafer interactions between silica particles of a silica CMP-dispersion and a copper wafer surface were analyzed by electron cpectroscopy for chemical analysis (ESCA), scanning electon microscopy (SEM) and zetapotential-measurements. The colloidal stability of the silica dispersion over a broad pH-range of 2.3 to 9.8 was analyzed in the presence of Na^+-, Mg^{2+}-, Cu^{2+}-, and Al^{3+}-ions in terms of the critical coagulation concentration (CCC), change in particle size and pH. Silica particles strongly and irreversibly adsorbed to the predominantly oxidic copper wafer surface at pH 2.3 but not at pH > 4. Over the whole pH-range a high colloidal stability was observed with a maximum at pH 2.3. CCC-values of 100–300 mmol/L versus Cu^{2+} were obtained. Even at high pH of 9.8, the behaviour could not be explained by the Derjaguin-Landauer-Verley-Overbeek (DLVO) theory. In the presence of Cu^{2+}-ions a higher colloidal stability compared to divalent Mg^{2+}-ions was observed at high initial slurry-pH of 9.8. Due to the acidic reaction of Cu^{2+} in the aqueous environment, the pH was reduced to 2–3, where colloidal silica showed the highest stability. Even at high removal rates in the polishing process of 1000 nm/min, the released Cu^{2+}-concentration (40 mmol/L) was lower than the critical coagulation concentration (100 mmol/L).

Keywords
Copper chemical mechanical planarization (CMP) · Colloidal stability · Critical coagulation concentration · Derjaguin-Landauer-Verley-Overbeek (DLVO) theory · Electron spectroscopy for chemical analysis (ESCA) · Nanoparticle · Particle adhesion · Removal rate · Scanning electron microscopy (SEM) · Silica dispersion

Arno Nennemann (✉) · Matthias Voetz
Bayer Material Science AG, Building Q1,
51368 Leverkusen, Germany
e-mail:
arno.nennemann@bayermaterialscience.com

Gabriele Hey · Lothar Puppe ·
Stephan Kirchmeyer
H.C. Starck GmbH, Building B202,
51368 Leverkusen, Germany

Introduction

Technology driver in the semiconductor industry is the permanent shrinkage of structures in integrated circuits (IC). This development requires a perfectly smooth surface of low topography of bare silicon wafers as well as for the different layers in the course of IC manufacturing. Key factors are the surface roughness, local geometry and total flatness of the whole wafer [1–3]. Therefore the controll of colloidal stability is one of several important aspects during the development of CMP-slurries. The heterogeneity of CMP-slurries makes their development very ambicious. The combination with complexing agents, corrosion inhibitors, oxidizing agents and a varying pH leads to high demands in product development [1, 4]. The choice of pH and oxidizing agents for example determine the formation of a protective copper oxide layer versus soluble copper ions. While complexing agents enhance the solublitiy, local corrosion (etching) as a side effect has to be kept under controll by addition of a corrosion inhibitor [5–8]. The nanoscaled silica particles combined with the pad properties are responsible for the mechanical polishing parameter [1]. Chemical and mechanical parameters have to be controlled while maintaining a high colloidal performance to avoid scratching [1, 4, 9].

Already in absence of multiple additives necessary for the performance of CMP-slurries, colloidal silica dispersions have a complex coagulation behaviour. Depending on the pH, different DLVO and non-DLVO stabilizing and destabilizing mechanisms occur. These special characteristics of silica dispersions concerning their colloidal stability were analyzed by several authors and gave rise to different theories of explanation [10–16]. Repulsive interactions were discussed by several authors as mainly being of steric, electrosteric or hydration layer origin, but also electrostatic effects have to be considered. The stabilizing mechanism strongly depends on the pH. Allen & Matijevic explained the high salt stability at low pH by a steric barrier or hydration forces [10]. Colic et al. stated adsorbed cations together with a hydration layer as reason for the high colloidal stability [15, 16]. Kobayashi & Juillerat [12] concluded, that whereas the charging behaviour of silica particles is consistent with the basic Stern model, aggregation behaviour is Non-DLVO. The authors interpreted, that an adsorbed polysilicic acid layer increases stability at lower pH. This effect is decreasing at increasing particle size. Healy [13] studied the influence of alkaliions on the stability of silica dispersions. At pH 11 electrostatic effects were predominant, leading to a DLVO sol behaviour in absence of polymeric or oligomeric silica species. At pH 6–8 electrosteric stabilization due to adsorbed oligomeric silicic acid was predominant. Coagulation occured in a secondary minimum. At pH 2 Healy found steric stabilization due to adsorbed oligomeric silicic acid. The Silanol groups were protonated, therefore low electrostatic influence can be expected. The depth of the secondary minimum was reported to be less deep than at pH 6. Due to ion-specific effects, strongly hydrated cations like Na^+ and Li^+ enhanced the electrosteric stabilization whereas Cs^+ and K^+ decreased the colloidal stability.

Attractive interactions can principially be of Van der Waals type, but the contribution is seen to be of minor importance by Depasse and Watillon [14], because the refractive index of amorphous silica and aqueous solutions is very close, especially at high electrolyte concentration. The authors suggest acid-base interparticle bridges between Silanol and Silanolate ($Si-O-...HO-Si$) as decisive attractive interactions. Alternative, hydroxo bridges between the particles in the presence of acidic surface hydrogens can occur [11]. The acidic hydrogens can be supplied by the silanol groups at low pH or alternatively by the hydration shells of Lithium or sodium cations at high pH.

Besides discussing and reviewing several existing hypothesis on the colloidal behaviour of silica sols, Depasse [11] analyzed the peculiar coagulation behaviour at high pH concerning different alkali cations. He found silica sols becoming turbid in a pH-range of 7.3 to 11.1, in presence of a constant KCl-concentration of 3 mol/liter. The pH was shifted from the starting point at pH 2 by addition of KOH. At pH 12, the dispersion could repeatedly be shifted between turbid at addition of 3 mol/L NaCl and clear at addition of KCl. The hypothesis delivered to explain the anomalous behaviour, was that bonding ions like Na^+ and Li^+ adsorb to OH^-, whereas nonbonding ions like K^+, Rb^+, Cs^+ do not. Therefore Na^+ bound to OH^- allows to bridge particles together, when adsorbed at the surface.

Basim and Moudgil [17] analyzed Surface roughness and surface damages of wafer material in the presence of differently agglomerated silica dispersions. Polymer flocculated, polymer dispersed, salt coagulated (Na^+) silica dispersions as well as dried agglomerates were analyzed. Strongest influence was seen with dried agglomerates and salt coagulated dispersions, but also “soft agglomerates” influenced the surface properties. Basim et al. [18] analyzed dispersions stabilized by surfactants in the presence of Na^+. Removal rate and surface roughness depended on particle or agglomerate size. Kuntzsch et al. [19] reported an increasing number of scratches on a wafer surface in the presence of dried agglomerates. Filtration could reduce scratches both for previously dried or fresh CMP-sols. Mazaheri and Ahmadi [20] developed a model for the colloidal forces during CMP and evaluated the influence of silica and alumina abrasives in a tantalum-CMP process. Park and Busnaina [21] analyzed the adhesion of silica particles on Cu-, Silk™-, TEOS-, and TaN-surfaces. Particle adhesion on copper wafer surface occured primarily at low pH based on electrostatic interactions.

In the copper CMP process, it is essential to avoid both particle agglomeration in the dispersion as well as strong particle adhesion to the wafer surface to avoid surface defects like scratches or particle residues on the surface.

Focus of this work was to analyze the influence of monovalent, divalent and trivalent cations on the agglomeration behaviour of silica dispersions developed for the copper CMP process. Especially the effect of copper-ions that are removed during the copper damascene process was of interest. The copper amounts released during polishing were related to the coagulation behaviour. Additionally, interactions between silica particles and the copper wafer surface were analyzed.

Experimental

Material

Silica dispersions of the type Levasil® (H.C. Starck GmbH) were used in this study. The Levasil® 50CK/30%-V1 was supplied at pH 2.3, Levasil® 50CK/30% at pH 9.8. Both primary dispersions had solid contents of 30% w/w and an average particle size of 80 nm (determined by TEM). Copper and copper oxide powders were supplied by Aldrich (CuO, 98% purity, $< 5\,\mu$m particle size), Acros (Cu_2O, 97% purity) and Merck (Cu, 99.7% purity, $< 63\,\mu$m particle size). As coagulants NaCl, $MgCl_2$, $AlCl_3$ and $CuCl_2$ were used (Merck/Aldrich, p.a.). HCl (KMF Comp., 0.1 mol/L, p.a.) and NaOH (KMF Comp., 0.1 mol/L, p.a.) were used to adapt the pH. Blanket copper wafers consisted of a 1 μm electroplated Cu layer on top of a sputtered 150 nm copper seed layer (Source: IMEC, Belgium).

Particle Adhesion and Surface Properties of the Copper Wafer

Silica particle adhesion was analyzed by dipping copper wafer pieces in diluted Levasil® dispersions (< 1% w/w) at pH 2.3, pH 4 and pH 9.4 for 15 min. The wafer pieces were then rinsed with deionized water and Scanning Electron Microscope images were taken (Philipps XL30 SEM). In an additional experiment the reversibility of particle adhesion by pH-shift was analyzed. A copper wafer piece was equilibrated with Levasil® at pH 2.3 for 5 min, rinsed with water and Levasil® at pH 9.4 added for additional 5 min with consecutive rinsing. SEM images were then recorded. Additionally to SEM analysis, the wafer surface chemistry was analyzed by ESCA measurements (ESCA 220IXL, Thermo VG Scientific Comp.) to determine the type of copper or copper oxide species on the surface after treatment with Levasil® Serum in the presence of a typically applied oxidizing agent, H_2O_2.

Determination of the Isoelectric Point (IEP)

Aqueous copper and copper oxide suspensions were prepared by treating the powders for 15 min with ultrasound, adjusting the pH and then shaking overnight. The electrophoretic mobilities in the aqueous copper and copper oxide suspensions were determined in a Lazer Zee Meter 501 (PenKem Inc.) after sample dilution in a range between pH 1 and pH 10. The electrophoretic mobilities of the silica dispersions were measured in a Malvern Zeta-Sizer 3000HS after dilution in the dispersion serum. The serum was obtained by centrifugation at 48 500 g for 1 h. One drop of silica dispersion was added to approx. 2 ml of the serum. The electrophoretic mobility measurements were repeated four times. The zetapotentials were calculated from the electrophoretic mobilities according to the Helmholtz-Smoluchowski-equation [27].

Determination of the Critical Coagulation Concentration

The Levasil® dispersions were diluted to 0.5% w/w and the pH adapted to pH 2.3, 4.9 and 9.8 to simulate polishing slurries at these pH-values. The chosen pH values represent characteristic points in the stability behaviour of silica dispersions. According to Iler [22], at pH 2.3 silica dispersions are close to the IEP but nevertheless the gelation and coagulation tendency is extremely low due to electrosteric effects or a hydration layer. In the range of pH 4 to pH 6 the gelation and coagulation tendency is strongest as small amounts of OH^--ions catalyze the condensation reaction between silanol groups. At increasing pH > 7 the stability versus gelation and coagulation increases due to increasing electrostatic repulsion. In the presence of salt the electrostatic repulsion is overcome and gelation and aggregation can occur [22].

After pH adjustment, 1 ml salt solution (NaCl, $MgCl_2$, $CuCl_2$, $AlCl_3$) in deionized water was added to 1 ml 0.5% w/w Levasil® dispersion. At this weight concentration gelation was avoided whereas aggregation can occur (this is even realistic for the application, as weight concentrations of silica dispersions applied for copper CMP are low). Samples at increasing salt concentration were prepared and after 24 h equilibration particle size, Extinction and resulting pH were determined. The pH was not adapted after salt addition to simulate the resulting conditions in the CMP process: CMP slurries are supplied at a certain pH, but the resulting pH during polishing can change strongly due to the release of copper ions. Particle size measurements (hydrodynamic diameter) were performed by Dynamic Light Scattering (ZetaPals, Brookhaven), Extinction was determined photometrically at 650 nm (Photometer LP1W – Dr. Lange) after shaking the samples. The experimentally determined critical coagulation concentration (CCC_{exp}/mmol/L) was derived by extrapolating at the first steep increase in the particle size or Extinction curves.

The experimentally determined critical coagulation concentrations were compared to theoretical expectations derived from the DLVO theory [23, 24]:

$$CCC_{\text{calc}} = \left(\frac{49.6(4\pi\varepsilon\varepsilon_0)^3 (RT)^5}{F^6} \right) \frac{\gamma^4}{A^2 z^6} , \tag{1}$$

where γ is the dimensionless potential

$$\gamma = \frac{e^{x/2} - 1}{e^{x/2} + 1} \quad \text{with} \quad x = \frac{zF\Psi_\delta}{RT} , \tag{2}$$

with the calculated critical coagualtion concentration CCC_{calc} (mmol/L), the gas constant R ($JK^{-1}mol^{-1}$), the temperature T (K), the electrical field constant ε_0 ($CV^{-1}m^{-1}$), the dielectricity constant ε of water, the counter ion valency z, the Faraday constant F ($Cmol^{-1}$), the Sternpotential ψ_δ (V) and the Hamakerkonstant A (J). The CCC-values were considered at RT (298 K). The Sternpotential ψ_δ was approximated with the experimentally determined Zetapotential as derived from Fig. 2. The Hamaker-constant A for aqueous silica dispersions is $A \cong 6.5 \times 10^{-20}$ J [25].

Released Copper Concentration During Polishing

The concentration of copper-ions released during a CMP-process was calculated for two industrial polishing mashines and a self-constructed mini-polishing mashine according to Eq. 3:

$$C_{\text{Cu}} = \frac{RRA_{\text{wafer}}\rho_{\text{Cu}}}{M_{\text{Cu}} V_{\text{disperion}}} \quad [\text{mol/L}] , \tag{3}$$

where $RRA_{\text{wafer}}\rho_{\text{Cu}}$ determined the mass of copper released per minute with the removal rate RR (cm/min), the polished wafer surface A_{wafer} (cm^2) and the density ρ_{Cu} of copper (8.92 g/cm^3). The molar concentration C_{Cu} per volume flow $V_{\text{dispersion}}$ (L/min) of the CMP-slurry was derived by dividing the released copper mass by the atomic mass of copper M_{Cu} (63.5 g/mol). For the industrial polishing mashines (LamTeres and Mecapol 460, Steag) calculations were performed for a wafer with 20 cm diameter ($A_{\text{wafer}} = 314\ cm^2$), for the minipolisher for a wafer with 3 cm diameter ($A_{\text{wafer}} = 7.1\ cm^2$). Polishing experiments on the minipolisher were performed with a slurry volume $V_{\text{dispersion}}$ of 0.0025 liter in a batch experiment. The industrial mashines worked under continuous flow $V_{\text{dispersion}}$ of 0.2 liter/min [4, 9]. The calculated C_{Cu}-values are shown in Table 3.

Results and Discussion

Particle-wafer Interactions

For the evaluation of particle wafer interactions, both the knowledge of the surface chemistry as well as the charging behaviour of the copper wafer are essential. When a copper wafer surface is in contact with water, different copper species can be present, depending on pH and potential. Pourbaix diagramms describe the various reactions and reaction products in an aqueous electrochemical system in equilibrium, thereby allowing a certain prediction of the various phases [1, p. 90]. At pH < 7 and noble potential copper dissolves as Cu^{2+}, at lower potential the metallic species will be more abundant. When increasing the pH to pH 7–13 Cu_2O will form at median potential, CuO at high potential. At pH > 13 $CuO_2{}^{2-}$ species can be formed. During copper CMP, the aim is to achieve soluble copper species by chemical means additional to the pure mechanical polishing component. Additional to the polishing particles, a strong oxidizer like H_2O_2 is applied to transfer metal copper into copper ions. A protective oxide layer has to be overcome. The dissolution of copper can be achieved by adjusting a low pH or additionally adding complexing agents e.g. on amine or ammonium basis [26].

ESCA measurements revealed, that the untreated copper wafer surface showed both the presence of metallic copper Cu^0 as well as a passivating CuO-layer (Fig. 1a). The sharp peak at a binding energy of 932.3 eV can be designated to metallic Cu ($2p3/2$ electrons). A small shoulder CuO-peak is observed at 933.4 eV. The peak at 950–955 eV belongs to Cu^0 ($2p1/2$ electrons) – with a small shoulder for CuO. After treatment with an acidic serum of Levasil® 50CK30-V1 at pH 2.3, the CuO-peak dissappeared, indicating, that soluble Cu^{2+}-ions were generated from the oxide species and removed during rinsing at this low pH (Fig. 1b) uncovering a bare Cu^0-surface. When additionally adding a high concentration of H_2O_2 to the Levasil® dispersion, a strong passivation with CuO occured. Metallic Cu^0-peaks dissappeared and additional typical CuO-satellite peaks at binding energies of 940–945 eV and 960–965 eV appeared (Fig. 1c). Additional experiments were performed with the finally developed polishing slurry consisting of Levasil® 50CK30-V1, H_2O_2 as oxidizing agent, Benzotriazole as corrosion inhibitor and Glycine as complexing agent. Cu^0- and CuO-species were found on the surface, irrespective of the additional agents Benzotriazole and Glycine. Cu_2O-species were not observed under existing conditions.

Measurements of surface charge or surface potential on metallic surfaces is rather tricky due to the conductivity of the material. In this study, we tried to approach a probable surface potential by measuring Zetapotentials of Cu-, CuO- and Cu_2O-powder suspensions. The powders were seen as modells for the probable copper species found on the copper wafer surface as proven by ESCA-measurements.

The Zetapotential in the copper powder suspension increased from approx. −75 mV at pH 10 at decreasing pH (Fig. 2). The IEP was found at pH 2.2, charge reversal was not measured. Both CuO and Cu_2O-suspension showed lower Zetapotentials of approx. −30 mV at pH 10. The IEP of Cu_2O was approx. pH 6.5 with following charge re-

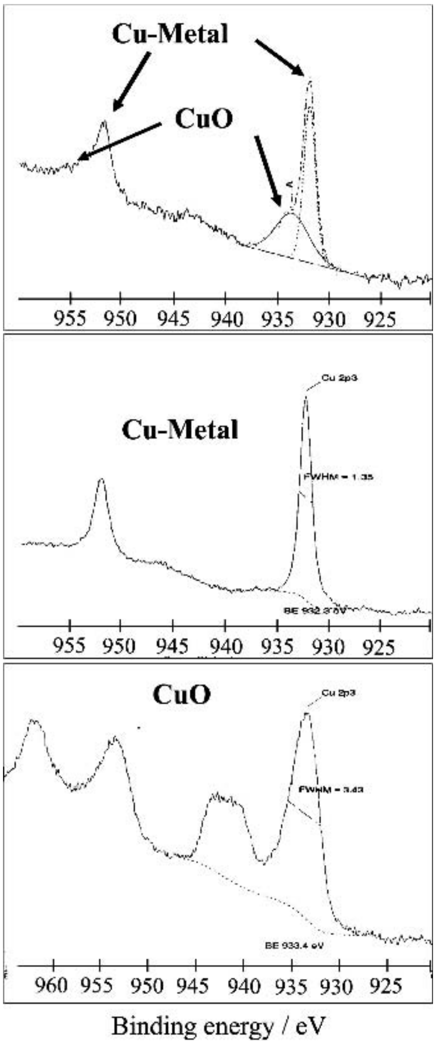

Fig. 1 ESCA analysis of a copper wafer surface **a** untreated, **b** after treatment with Levasil 50CK/30%-V1 serum, **c** after treatment with Levasil 50CK/30%-V1 serum in the presence of 5% w/w H_2O_2

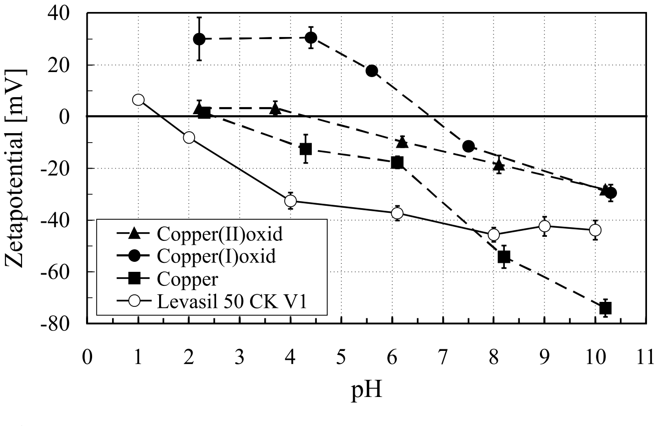

Fig. 2 Zetapotential-pH diagramms for aqueous Cu-, CuO-, Cu_2O-suspensions and a silica dispersion (Levasil 50CK/30%-V1, diluted in serum)

versal at lower pH-values. A Zetapotential of +30 mV was achieved at pH 2.2. The IEP of CuO was approx. pH 4 with only a slight tendency to a positive Zetapotential (+5 mV) at lower pH. The negative Zetapotentials at higher pH can be assigned to the dissociation of Cu – OH-groups, that are also present in case of the metal powder due to partial oxidation. In the latter case, the absolute Zetapotential value has to be seen critical due to the surface conductivity of copper metal. At pH < 6.5, Cu – OH-groups of Cu_2O can be protonated, exhibiting a positive surface potential. The effect can be seen for CuO-groups but only at pH < 4 and to a lower extend.

The IEP of both the acidic Levasil® 50CK30-V1- and the basic Levasil® 50CK30-dispersions was at pH 1–1.5 (Fig. 2, only shown for Levasil® 50CK30-V1 as both curves are similar). At pH 10, a Zetapotential of approx. −42 mV was found. The coagulation studies with the model CMP-Levasil-dispersions were performed at pH values of 2.3, 4.9 and 9.8. The relevant Zetapotentials are −15 mV, −38 mV and −42 mV, respectively (Table 1).

At pH 2.4 stronger particle adhesion on the copper wafer surface was observed compared to the higher pH values 4.9 or 9.4 (Fig. 3). A consecutive treatment with silica dispersions at pH 2.4 in a first step and pH 9.4 in a second step increased the amount of adsorbed silica particles. Probably the primarily adsorbed particles functioned as coagulation seeds. Interactions between silica particles added at high pH then can be of additional specific type. Condensation between silica is known to be catalyzed by OH-ions. In the presence of salts (e.g. due to acid or base addition) repulsive electrostatic interactions are reduced. Particles can aggregate, thereby allowing condensation reactions between neighbouring silanol groups.

The reason for the tendency of silica particles to adsorb on the copper wafer surface at low pH can clearly be derived from Fig. 2 and Table 1. At low pH the copper surface is partially positively charged due to protonation of oxidic copper species. At pH 2.3 silica particles were negatively charged whereas both CuO- and Cu_2O-species showed positive zetapotentials and the metallic Cu species showed no charging. As was proven by the ESCA-measurements, mainly CuO-species existed at the wafer surface at the prevailing conditions (Fig. 1). At this pH

Table 1 Zetapotentials at selective pH-values of a Silicadispersion (Levasil 50CK30-V1) and Cu-, Cu_2O- and CuO-suspensions as derived from Fig. 2

	Zetapotential [mV]			
	SiO_2	Cu	Cu_2O	CuO
pH 2.3	−15	0	+30	+5
pH 4.9	−38	−15	+25	−5
pH 9.8	−42	−75	−30	−30

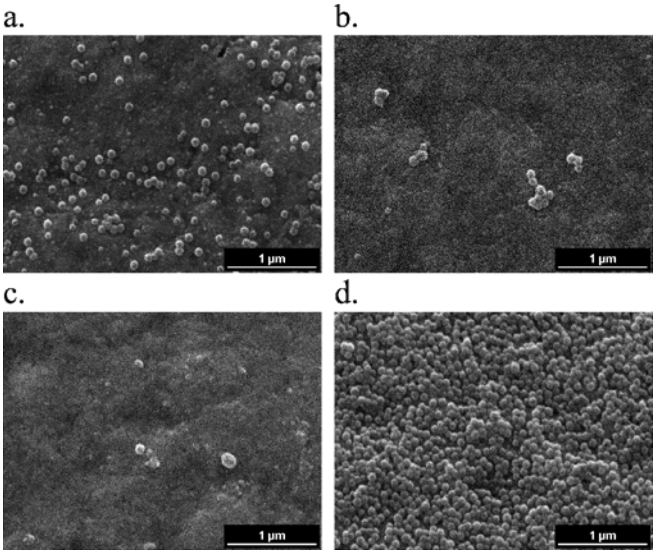

Fig. 3 SEM images of copper wafer surfaces treated with a diluted silica dispersion (Levasil® 50CK/30%-V1, solid content ≪ 1% w/w derived from the serum) **a** at pH 2.4, **b** at pH 4, **c** at pH 9.4, **d** consequtive treatment at pH 2.4 and pH 9.4. Each treatment was performed for 15 min and the wafer piece was rinsed with deionized water inbetween every step

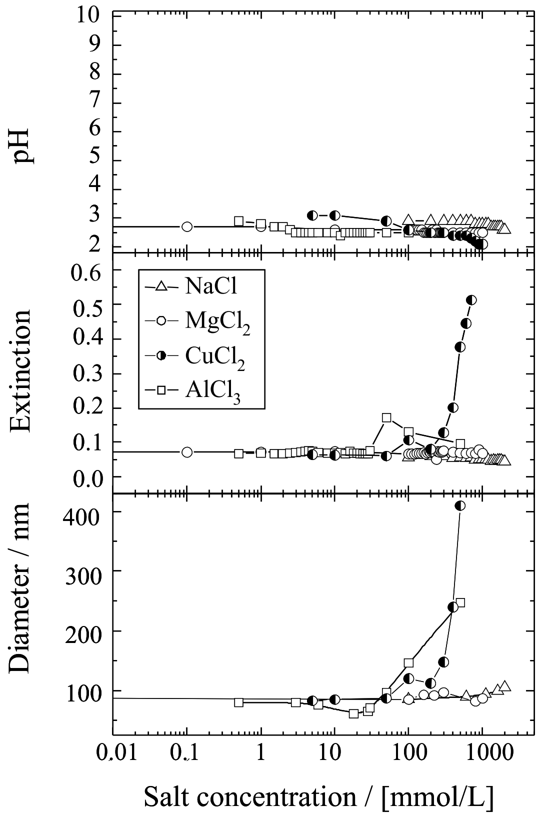

Fig. 4 Particle size (hydrodynamic diameter), Extinction (at 650 nm) and pH of silica dispersions at increasing salt concentrations of monovalent NaCl, divalent $MgCl_2$, $CuCl_2$ and trivalent $AlCl_3$. The silica dispersion (Levasil 50CK/30%-V1 at 0.25% w/w) was applied at an initial pH of 2.3

attractive Coulomb forces prevail. At pH 4.9 silica particles and CuO-groups were negatively charged whereas only Cu_2O-groups showed positive surface charges. The metallic Cu suspension showed a negative zetapotential at this pH, indicating a preferred divalent CuO-species at the surface under selected conditions. At higher pH, all surface groups in the system were negatively charged. At these conditions repulsive electrostatic forces defined the particle-wafer-interactions.

Particle adhesion occured primarily at low pH. The particles could not be removed by rinsing or pH-shift. At pH > 3.5 repulsive interactions will prevail. In terms of CMP properties, strong particle adhesion has to be overcome to avoid wafer surface defects like scratches and particle residues on the surface are not accepted in the process.

Colloidal stability

At a low initial pH 2.3 of the silica dispersion neither Na^+- nor Mg^{2+}-ions could coagulate the silica dispersion up to very high salt concentrations. Up to 1500 mmol/L Mg^{2+} and up to 2000 mmol/L Na^+ could be added without a change in particle size or extinction (Fig. 4, Table 2). After addition of Cu^{2+}-ions, extinction and particle size started to increase at a salt concentration ≥ 300 mmol/L. Al^{3+}-ions coagulated the silica dispersion at salt concentrations of ≥ 30 mmol/L, resulting in increasing extinction and particle size. The resulting pH after addition of NaCl- or $MgCl_2$ solution stayed nearly constant at approx. pH 2.8 or pH 2.5–2.7 respectively at increasing salt concentration. A slight decrease in pH from pH 3–2.2 and from pH 2.9–2.5 was observed at addition of increasing amounts of $CuCl_2$ or $AlCl_3$ respectively. The general increase of the initial silica dispersion pH from 2.3 to pH 2.7–3 after salt addition can be explained by the higher pH inherent in the salt solutions. The *CCC*-values calculated from Equation 1 strongly differed from the experimental results for all salts (Table 2). The theoretical CCC_{calc} were calculated as 0.7 mmol/L for Na^+, 0.1–0.3 mmol/L for the divalent salts Mg^{2+} and Cu^{2+} and 0.07 mmol/L for Al^{3+}.

At an initial pH 4.9 of the silica disperson the coagulation behaviour was more pronounced for all applied salts (Fig. 5, Table 2). Extinction and particle size increased at salt concentrations of ≥ 500 mmol/L Na^+, ≥ 200 mmol/L Mg^{2+}, ≥ 200 mmol/L Cu^{2+}, and ≥ 50 mmol/L Al^{3+}. The pH values in the presence of Na^+ and Mg^{2+} stayed nearly constant at pH 5.9. At addition of Al^{3+} the pH slightly increased from pH 6 to pH 6.9, at addition of Cu^{2+} it decreased from pH 7 to pH 2.3 at increasing salt concentrations. The *CCC*-values calculated from Eq. 2 strongly differed from the experimental results

Table 2 Calculated and experimental Critical Coagulation Concentration CCC_{calc} and CCC_{exp} respectively of Levasil® 50CK/30%-V1 dispersions in dependance of pH-value and salt type. The $\text{pH}_{\text{silica}}$-values were determined in the initial silica dispersions before salt addition. The pH determined after salt addition "pH_{exp}" was shifting at increasing salt concentrations of Cu^{2+} or Al^{3+} (*start* and *end*). This was taken into account for the calculation of the theoretical *CCC*-values as derived from Eq. 1. The Zetapotential was taken from Fig. 2, according to the experimentally determined pH. The experimental *CCC*-values were derived from Figs. 4, 5 and 6

Counter-ion	$\text{pH}_{\text{silica}}$	pH_{exp}		Zetapotential [mV]		CCC_{calc} [mmol/l]		CCC_{exp} [mmol/l]
		start	end	start	end	start	end	
Na^+	9.8	9		−42		20.5		500
	4.9	5.9		−38		14.3		500
	2.3	2.8		−17		0.7		2000
Mg^+	9.8	8		−42		2.9		50
	4.9	5.9		−38		2.2		200
	2.3	2.6		−17		0.1		1500
Cu^{2+}	9.8	7	2.3	−42	−12	2.9	0.04	100
	4.9	7	2.3	−42	−12	2.9	0.04	200
	2.3	3	2.2	−20	−12	0.3	0.04	300
Al^{3+}	9.8	8	3.5	−42	−30	0.6	0.30	0.5
	4.9	6	6.9	−38	−42	0.5	0.60	50
	2.3	2.9	2.5	−18	−15	0.07	0.04	30

for all salts (Table 2). The theoretical CCC_{calc} were calculated as 14.5 mmol/L for Na^+, 2–3 mmol/L for the divalent salts Mg^{2+} and Cu^{2+} and 0.6 mmol/L for Al^{3+}.

At an initial pH 9.8 of the silica disperson coagulation occured at far lower salt concentrations compared to the above stated initial pH values (Fig. 6, Table 2). Extinction and particle size increased at salt concentrations of ≥ 500 mmol/L Na^+, ≥ 50 mmol/L Mg^{2+}, ≥ 100 mmol/L Cu^{2+}, and 0.5 mmol/L Al^{3+}. In case of Al^{3+} both particle size and extinction again decreased at further increasing the salt concentration until the original values were reached at salt concentrations of ≥ 5 mmol/L. The pH values in the presence of Na^+ and Mg^{2+} stayed nearly constant at pH 9 or 8 respectively. At addition of Al^{3+} the pH decreased from pH 8 to pH 3.5 at salt concentrations > 0.5 mmol/L. At addition of Cu^{2+} the pH decreased from pH 7 to pH 2.3 at increasing salt concentrations. The *CCC*-values calculated from Eq. 1 differed from the experimental results for Na^+, Mg^{2+} and Cu^{2+} (Table 2). In contrast to the lower silica pH ranges, the theoretical values fit quite well with Al^{3+}. The theoretical CCC_{calc} (Eq. 1) were calculated as 20.5 mmol/L for Na^+, 3 mmol/L for the divalent salts Mg^{2+} and Cu^{2+} and 0.6 mmol/L for Al^{3+}.

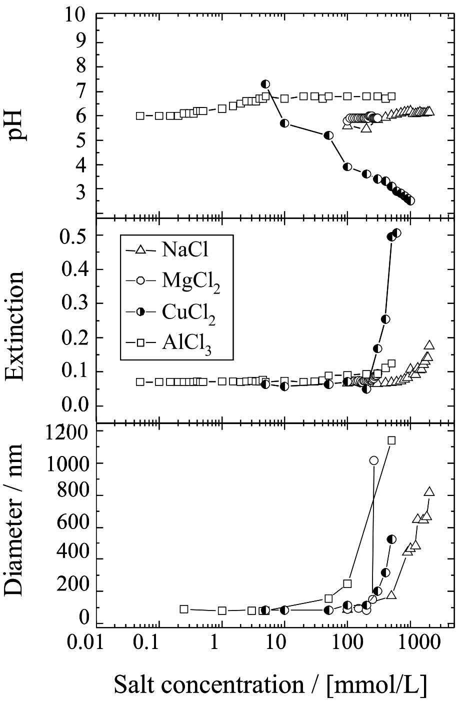

Fig. 5 Particle size (hydrodynamic diameter), Extinction (at 650 nm) and pH of silica dispersions at increasing salt concentrations of monovalent NaCl, divalent $MgCl_2$, $CuCl_2$ and trivalent $AlCl_3$. The silica dispersion (Levasil 50CK/30%-V1 at 0.25% w/w) was applied at an initial pH of 4.9

A contrast existed between the experimentally determined and the calculated critical coagulation concentrations CCC_{exp} and CCC_{calc} (Fig. 7, Table 2). In most cases, the silica dispersions were far more stable then theoretically expected. The strongest contrast between experimental and theoretical results was observed at low pH. The values for the critical coagulation concentrations differed for more than three decades at pH ~ 2.3–3, and for one to two decades at pH > 4 for Na^+, Mg^{2+} and Cu^{2+}. At high initial pH of 9.8 of the silica dispersion, only Al^{3+} coagulated the dispersion as proposed by the DLVO-theory ($CCC_{\text{exp}} = 0.5$ mmol/L; $CCC_{\text{calc}} = 0.6$ mmol/L). This coagulation behaviour versus Cu^{2+} and Al^{3+} at initial pH of 9.8 was especially interesting, as a pH-shift from pH 7 to pH 2.3 and pH 8 to pH 3.5 respectively at increasing salt concentration was observed (Fig. 6). The silica dispersion was restabilized at increasing Al^{3+}-concentration. Due to the pH shift, cationic oligomeric alumina species adsorbed at the silica surface, thereby stabilizing the silica particles (charge reversal was qualitatively proven by measuring the electrophoretic mobility; explanation see below).

Another important aspect was the difference in coagulation behaviour between the divalent cations Mg^{2+} and Cu^{2+}. Whereas at an initial pH 4.9 of the silica dispersion the colloidal stability (CCC_{exp}) was similar for Mg^{2+} and Cu^{2+} (Fig. 5), at low pH 2.3 it was lower in presence of the

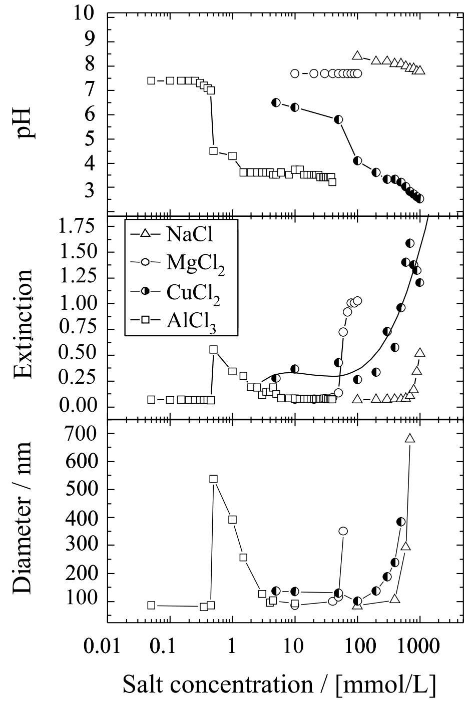

Fig. 6 Particle size (hydrodynamic diameter), Extinction (at 650 nm) and pH of silica dispersions at increasing salt concentrations of monovalent NaCl, divalent $MgCl_2$, $CuCl_2$ and trivalent $AlCl_3$. The silica dispersion (Levasil 50CK/30%-V1 at 0.25% w/w) was applied at an initial pH of 9.8

divalent Cu^{2+}-ions (Fig. 4). This difference was not analyzed in detail due to the different focus of this work, but it can be presumed, that specific ion-binding occurs. Again at high pH, the silica dispersion was more stable in the presence of Cu^{2+} than for Mg^{2+} due to the pH-shift to 2.3 (Fig. 6).

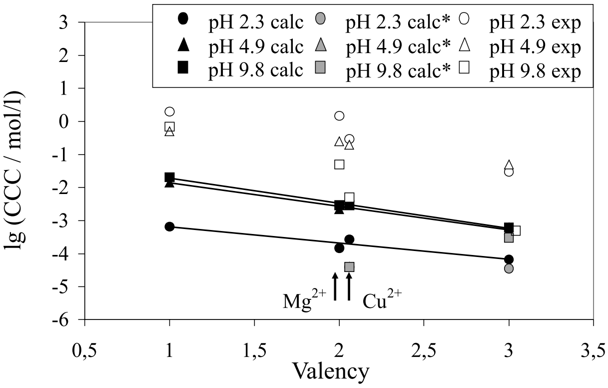

Fig. 7 Critical coagulation concentrations of Levasil silica dispersions in dependance of the counterion type and valency. The experimentally determined CCC_{exp} were derived from Fig. 4, Fig. 5, Fig. 6. The calculated CCC_{calc} was derived according to Eq. 1, Table 2. The values marked with * were calculated from the "end"-values according to Table 2

Some aspects of the specific beviour of copper- and aluminum-ions can be explained by their amphoteric behaviour in aqueous solution and the formation of polyhydroxo-species. Lagaly et al. [27] give a review of the complex coagulation behaviour of oxidic colloids in the presence of cations that form polyhydroxo-species (see also [28, 29]). As $Cu(OH)_2$ is a weak base, Cu(II)-salts react acidic in aqueous environment [30, p. 1335]: $[Cu(H_2O)_6]^{2+} \leftrightarrow [Cu(OH)(H_2O)_5]^+ + H^+$. At pH > 7, $Cu(OH)_2$ can precipitate. This effect could complicate the polishing process, as precipitated particles could create scratches and polute polishing pads. Dissolved aluminum-ions even show a more complex coordinative properties [30, p. 1079]. At low concentrations of approx. 10^{-5} mol/L, $[Al(H_2O)_6]^{3+}$-species can be present at pH < 6. $[Al(H_2O)_6]^{3+}$ is a weak acid with a pK_s-value of 4.97. Dissociation can occur according $[Al(H_2O)_6]^{3+} \leftrightarrow [Al(OH)(H_2O)_5]^+ + H^+$. In the range of pH 5–9 even alumina $Al(OH)_3$ can precipitate. At higher concentrations of approx. 0.1 mol/L the $[Al(H_2O)_6]^{3+}$-species only exists at pH < 3. At higher pH of e.g. 4–8 at this concentration of alumina salt oligomeric alumina species of the type $[Al_{13}O_4(OH)_{12}(H_2O)_{24}]^{7+}$ will prevail. No alumina precipitation is found at this salt concentration. The coagulation behaviour in the presence of aluminum salts was analyzed in detail in the literature [10, 28, 29, 31]. The released Hydronium-ions explain the pH-shift observed at increasing salt concentration for Al^{3+} and Cu^{2+}. The repeptization in the presence of aluminum salt (Fig. 6) can be explained by adsorption of oligomeric cationic alumina species.

The extremely high coagulation stability at low pH can not be explained by the DLVO theory. Close to the IEP, the repulsive electrostatic forces are too low to stabilize the dispersion due to the low dissociation of the silanol groups. In the literature several authors have studied this phenomenon. It was proposed, that a hydration layer of adsorbed cations or electrosteric repulsive forces due to adorbed polysilicium species cause the high colloidal stability – as well as the strong stability versus gelation [10, 12, 13, 15, 16]. Only at high pH > 11 pure electrostatic interactions according to the DLVO-theory can be of importance due to the absence of polymeric or oligomeric silica species [13]. At pH 6–8, Healy proposed electrosteric stabilization due to adsorbed oligomeric silicic acid as predominant mechanism.

Copper Ion Release during Polishing

At a removal rate of 10 nm/min, the concentration of copper-ions released into the polishing cell was < 1 mmol/L, at 100 nm/min approx. 2–4 mmol/L and at 1000 nm/min approx. 20–40 mmol/L (Table 3, Fig. 8). A 1st-step copper CMP-slurry with a good performance

Table 3 Copperion-concentration released during polishing in dependance of the Removal Rate determined in a mini polishing mashine (own construction) and two industrial polishing mashines (Mecapol 406 and LamTeres) (Eq. 3). The mini polishing mashine was constructed for batch experiments with a total liquid volume of 2.5 ml and polishing areas of 7.1 cm^2 (pieces of 3 cm diameter). Polishing on the commercial mashines was performed under constant flow, which was optimized to flow rates of 200 ml/min on 20 cm wafer material respectively

Removal rate [nm/min]	Released Cu^{2+}-concentration [mmol/L]	
	Mini-polisher	Mecapol/Lam Teres
1	0.04	0.02
10	0.40	0.25
100	3.97	2.45
1000	39.72	24.52

has to show on the one hand high selectivity towards copper as well as high removal rates for copper. In Nennemann et al. [4] copper removal rates for a silica-based high selective copper-slurry of 700 nm/min are reported. Such a silica-polishing-slurry would not even coagulate at initial pH of 9.8 ($CCC_{\text{exp}} \geq 100$ mmol/L, Table 2) in the polishing process. At medium pH 4.9 and low pH 2.3 the slurry was stable up to copperion-concentrations of 200–300 mmol/L. Even high removal rates will not destabilize the dispersion. The calculated values CCC_{calc} were between 0.04 and 2.9 mmol/L and let expect a strong coagulation even at low removal rates < 100 nm/min.

The released amounts of copperions in a CMP-polishing process are difficult to estimate. Industrial polishing mashines (Mecapol or LamTeres polishing mashines) work under continuous flow. Released copper ions are supposed to be removed constantly. Nevertheless, on a microscopic scale the porous, polymeric polishing pad has contact to the wafer surface. In the pores, polishing slurry is captured. The local concentration of released copper-ions therefore can be much higher than the macroscopic solution would expect. Our calculations are only a rough estimation of the complex CMP-process, but the strong difference between tolerable copperion-concentration and estimated released copper amounts shows the strong potential stability of the silica-slurries during the CMP-process.

Conclusion

The copper wafer surface exhibited a CuO-layer under oxidative conditions (Fig. 1). This oxide layer could be removed by acid addition. Particle adhesion to the copper wafer surface occured primarily at low pH 2.3, when the silica particle surface was negatively and the copper wafer surface positively charged due to the formation of a CuO-layer (Figs. 2 and 3). The particles could not be removed by rinsing or pH-shift. At pH > 3.5 repulsive interactions prevailed and only very few particles adsorbed to the wafer surface. In terms of CMP properties, scratching due to particle adsorption can be overcome at pH > 3.5.

In the Levasil®-silica dispersions strong repulsive interactions prevailed over a broad pH range from pH 2.3 to pH 9.8, that could not be explained by the electrostatic DLVO-model (Fig. 7, Table 2). Steric stabilization and hydration forces were seen as reason for such a high colloidal stability. The highest colloidal stability was observed at initial pH 2.3, close to the IEP. The silica dispersion could not be coagulated by Na^+ or Mg^{2+} up to 1500 or 2000 mmol/L. At initial pH 2.3 $\geq$ 300 mmol/L, at initial pH 4.9 $\geq$ 200 mmol/L and at initial pH 9.8 $\geq$ 100 mmol/L Cu^{2+}-concentration were necessary to coagulate the dispersion. The high *CCC* in the presence of Cu^{2+} even at high pH was not observed for the divalent cation Mg^{2+}. Copper salts react acidic in aqueous environment. Due to released Hydronium-ions, the pH was shifted below pH 3, were silica sols are highly stable (Fig. 6). During a copper CMP-process, only up to 40 mmol/L Cu^{2+} were released even at high removal rates of 1000 nm/min (Fig. 8). Though this is an estimation that does not take into account the confined geometry due to pad-wafer interactions and probable high local Cu^{2+}-concentrations at the wafer surface, it can be expected, that Levasil®-silica dispersions are highly stable during the CMP-process. Defects due to Agglomeration could be avoided. Hey et al. and Nennemann et al. [4, 9] could prove, that such dispersions showed a very good long-term-stability, high polishing efficiency and low defect density during application. As optimal pH-range pH 4–5 was obtained. At this pH, no particle adhesion to the wafer surface occured, a high coagulation stability was obtained and no $Cu(OH)_2$-precipitation is expected.

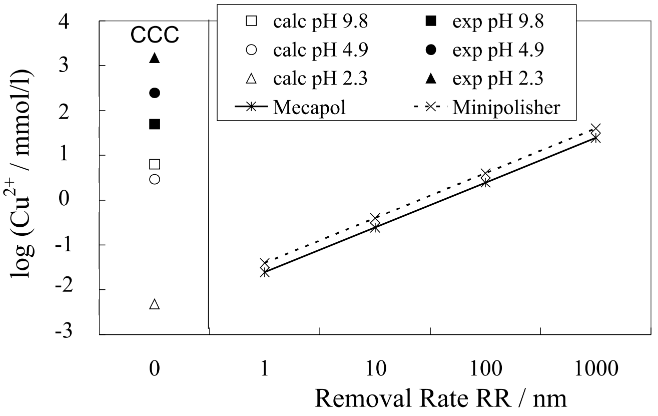

Fig. 8 Copperion-concentration released during polishing in dependance of the Removal Rate according to Table 3 and critical coagulation concentration CCC_{calc} and CCC_{exp} according to Table 2

Acknowledgement We acknowledge Valentina Terzieva (IMEC, Belgium) for supply of the wafer material and polishing experiments on the industrial machines and Lars Krueger (Bayer Technology Services GmbH) for experimental support.

References

1. Steigerwald JM, Murarka SP, Gutmann RJ (1997) Chemical mechanical planarization of microelectronic materials. Wiley, Inc
2. Semiconductor processing overview [1.1]. (1995) Texas Engineering. Ref Type: Computer Program
3. 2te Dresdner Sommerschule Mikroelektronik (2001) AMD Saxony Manufacturing GmbH, Infineon Technologies Dresden GmbH & Co. OHG, Infineon Technologies SC 300 GmbH & Co. KG, Technische Universität Dresden and Wacker Siltronic AG. Ref Type: Conference Proceeding
4. Nennemann A, Krueger L, Puppe L, Passing G, Hey G, Kirchmeyer S (2005) Chem Ing Tech 77(1-2):137
5. Tsai TH, Yen SC (2003) Appl Surf Sci 210(3-4):190–205
6. Steigerwald JM, Murarka SP, Gutmann RJ, Duquette DJ (1995) Mater Chem Phys 41:217–28
7. Aksu S, Doyle F M (2001) J Electrochem Soc 148(1):B51–B57
8. Aksu S, Doyle FM (2001) J Electrochem Soc 149(6):G352
9. Hey G, Kirchmeyer S, Passing G, Puppe L, Nennemann A (2004) Nanoscaled silicon dioxide particles as polishing agents in IC manufacturing. In: Conference Proceeding. Partec2004, Nuremberg
10. Allen LH, Matijevic E (1970) J Colloid Interf Sci 33:420
11. Depasse J (1999) J Colloid Interf Sci 220(1):174–6
12. Kobayashi M, Juillerat F, Galletto P, Bowen P, Borkovec M (2005) Langmuir 21(13):5761
13. Healy TW (1994) Adv Chem Ser 234:147
14. Depasse J, Watillon A (1970) J Colloid Interf Sci 33:430
15. Colic M, Fischer LF (1998) Chem Phys Lett 291:24
16. Colic M, Fischer LF, Franks GV (1998) Langmuir 14:6107
17. Basim GB, Moudgil BM (2002) J Colloid Interf Sci 256(1):137–42
18. Basim GB, Vakarelski IU, Moudgil BM (2003) J Colloid Interf Sci 263(2):506–15
19. Kuntzsch T, Stintz M, Ripperger S, Witnik U (2003) VDI-Berichte 1803:103–108
20. Mazaheri AR, Ahmadi G (2003) J Electrochem Soc 150(4):G233
21. Park JG, Busnaina AA (2003) Proceedings of the Annual Meeting of the Adhesion Society 26:538–540
22. Iler RK (1973) Surf Colloid Sci 6:1–100
23. Lagaly G, Schulz O, Zimehl R (1997) Die Stabilität elektrostatisch stabilisierte Dispersionen. In: Dispersionen und Emulsionen. Steinkopff Verlag, Darmstadt, p 75
24. Verwey EJW, Overbeek JTG (1948) Theory of the stability of lyophobic colloids, Amsterdam, p 117
25. Lagaly G, Schulz O, Zimehl R (1997) Elektrostatisch stabilisierte Dispersionen (DLVO-Theorien). In: Dispersionen und Emulsionen. Steinkopff Verlag, Darmstadt, p 15
26. Steigerwald JM, Duquette DJ, Murarka SP, Gutmann RJ (1995) J Electrochem Soc 142–7:2379
27. Lagaly G, Schulz O, Zimehl R (1997) Oberflächenpotential und elektrokinetisches Potential. In: Dispersionen und Emulsionen. Steinkopff Verlag, Darmstadt, p 347
28. Hahn HH, Stumm W (1968) J Colloid Interf Sci 28:134
29. Allen LH, Matijevic E (1971) J Colloid Interf Sci 35:66
30. Hollemann AF, Wiberg E (1995) Lehrbuch der Anorganischen Chemie. Auflage 101. Walter de Gruyter, Berlin, New York, pp 1079, 1335
31. Duan J, Gregory J (1996) Colloid Surface A 107:309

Progr Colloid Polym Sci (2006) 133: 169–172
DOI 10.1007/2882_073

T. Sobisch
D. Lerche
S. Fischer
C. Fanter

Characterization of Porous Bead Celluloses by Analytical Centrifugation

Abstract Porous bead celluloses have wide ranging applications as separation media and carrier systems. Physicochemical characterization of these materials and related suspensions is essential for quality control and technical applications. This includes their surface properties, porosities and mechanical properties.

The paper describes the application of multisample analytical centrifugation for porous bead celluloses.

Bead celluloses of different sizes and differing in the preparation process were chosen and analysed in respect to porosity and particle interactions.

The consolidation, packing behaviour and elasticity of the bead celluloses was analysed in an alternating centrifugal field.

Differences in packing density obtained under controlled conditions were used to calculate the porosities of the samples. Multisample analytical centrifugation provides a powerful alternative for determination of the cumulative porosity, which was elaborated in this study. This approach is generally applicable for other particulate material if strong flocculation between particles can be avoided.

Further, different preparation processes lead to an alteration of the surface properties of the bead celluloses. Bead celluloses revealed a markedly different behaviour than cellulose powder manufactured from native cellulose.

Keywords
Analytical centrifugation · Cellulose beads · Packing behaviour · Particle interaction · Porosity

T. Sobisch (✉) · D. Lerche
L.U.M. GmbH, Rudower Chaussee 29
(OWZ), 12489 Berlin, Germany
e-mail: info@lum-gmbh.de

S. Fischer · C. Fanter
Fraunhofer IAP, Geiselbergstr. 69,
14476 Potsdam-Golm, Germany

Introduction

Bead cellulose is a regenerated spherical porous cellulose which is manufactured by special dispersing methods. Characteristic properties of bead cellulose are spherical morphology with defined particle size and distribution, highly porous structure, high specific surface area, hydrophilic properties, chemical reactivity and high mechanical strength. It maintains the typical cellulose properties. It has a virtually uncharged surface in water and is highly insoluble in common solvents. Bead cellulose found many applications mainly in methods and processes utilizing solid phase techniques, liquid chromatography, immobilization of enzymes or ion exchange [1, 2].

By variation of cellulose raw material and solvents a range of bead celluloses with different properties can be obtained. The general preparation procedure can be described by the following steps: emulsification of a solution of cellulose, gelation of the emulsified droplets, washing and fractionation, chemical modification.

Examples of cellulose material for preparation of bead cellulose are viscose or cellulose acetate leading to beads with particle size ranges from 30–300 μm and 5–20 μm, respectively.

Development and application of cellulose bead products requires efficient means for characterization of particle interactions, swelling properties and packing behaviour. To this end the potential of multisample analytical centrifugation was evaluated, which already proved capable for characterization of particle interactions in suspensions [3].

Characterization of porosity of swollen cellulose beads by reverse chromatography or water vapour adsorption is especially laborious. Multisample analytical centrifugation provides a powerful alternative for determination of the cumulative porosity, which was elaborated in this study. This approach is generally applicable for other particulate material if strong flocculation between particles can be avoided.

Experimental

Materials

The samples used for the experiments are two commercial underivatized bead celluloses Perloza ST 30–50 µm and Perloza ST 150–300 µm (IONTOSORB, Czech Republic) and one sample prepared from cellulose acetate [4] with a particle size of 1 to 12 µm.

As shown in Fig. 1 the cellulose beads prepared from cellulose acetate are of spherical shape and highly porous. This product has a narrow particle size distribution around 3 µm (Fig. 2, particle size distribution determined by raster electron microscopy).

In the following the cellulose beads will be denoted as 3 µm (beads prepared from cellulose acetate), 30–50 µm and 150–300 µm (beads prepared from viscose), respectively.

The porous structure of the beads in the dry state was characterized with mercury porosimeter systems Pascal 140 and Pascal 440 (Fisons CE Instruments, Italy) (Fig. 3). The highest cumulative volume was traced for cellulose beads with 3 µm in diameter. However, the volume determined includes the space between the beads because mercury porosimetry cannot distinct between inner pores and space between the beads.

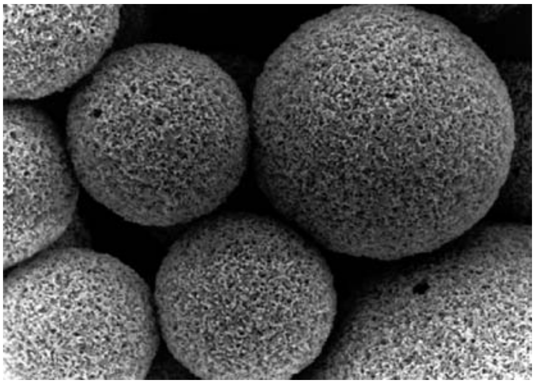

Fig. 1 Raster electron microscope image of cellulose beads 3 µm

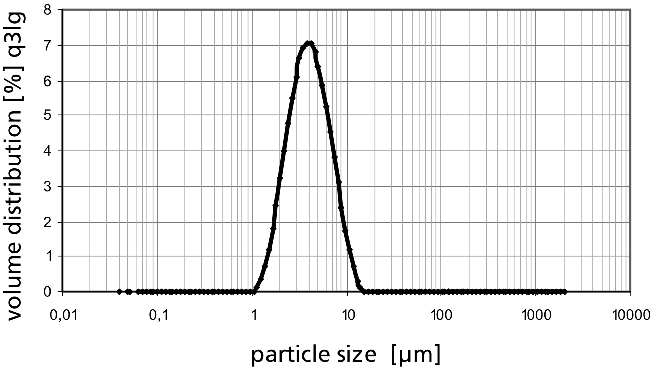

Fig. 2 Particle size distribution of cellulose beads 3 µm determined by raster electron microscopy

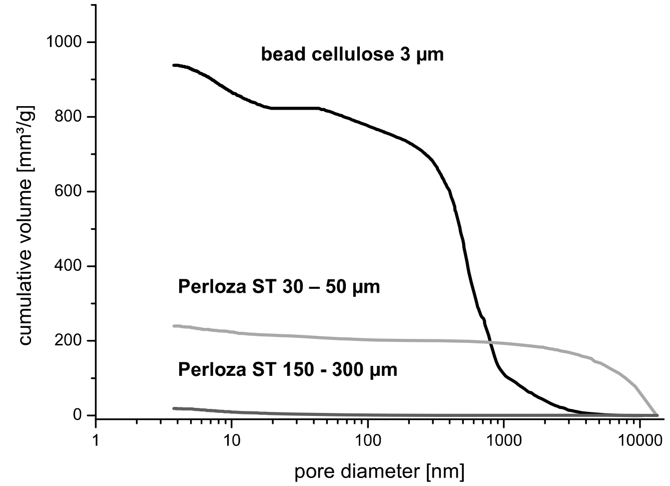

Fig. 3 Pore size distribution of dry cellulose beads determined by mercury porosimetry

Cellulose has a net density of 1.5 g/cm^3 (density without pores).

Analytical Centrifuge – Principle of Measurement

The multisample analytical centrifuge (LUMiFuge – L.U.M. GmbH, Germany) used in this study employs the STEP™-Technology (Space and Time resolved Extinction Profiles), which allows to measure the intensity of the transmitted light as function of time and position over the entire sample length simultaneously (Measurement scheme see Fig. 4).

The data are displayed as function of the radial position, as distance from the centre of the rotation (Fig. 4). The progression of the transmission profiles contains the information on the kinetics of the separation process and allows particle characterization [3, 5, 6]. Up to 12 different samples can be analysed simultaneously at constant or variable centrifugal speed up to 2300 g. The sequence of

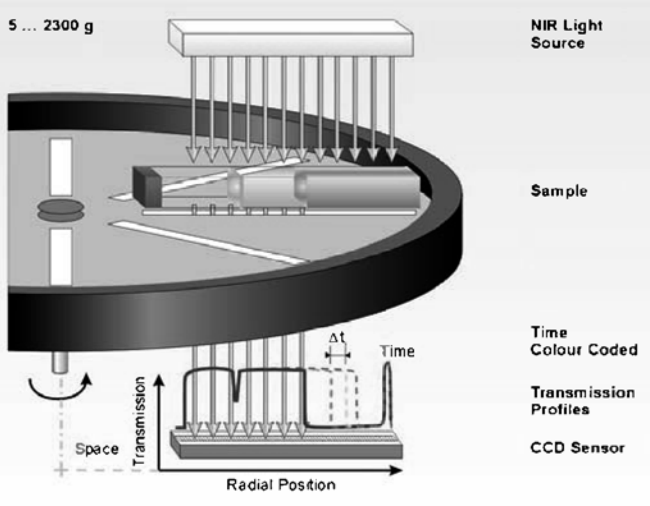

Fig. 4 Measurement scheme of the multisample analytical photocentrifuge. Parallel NIR-light is passed through the sample cells and the distribution of local transmission is recorded at preset time intervals over the entire sample length

centrifugal speed can be varied as step function, therefore alternating compression–dilatation cycles can also be conducted.

The separation behaviour of the individual samples can be compared and analysed in detail by tracing the variation in transmission at any part of the sample or by tracing the movement of any phase boundary. As for a given type of sample cells the position of a phase boundary corresponds to a defined sample volume the relationship position–volume can be established by calibration. Thus the alteration of packing density can be directly measured.

Characterization of Packing and Elasticity Behaviour in an Alternating Centrifugal Field

Stock suspensions were prepared dispersing cellulose beads in deionised water (mass ratio 1/2) and then further diluted in plastic (polycarbonate) rectangular sample cells (optical path length of 2 mm) to result in dispersions with a cellulose mass fraction of 0.2. After consolidation at normal gravity the samples were subjected to 5 consecutive compression/dilatation cycles (every cycle consists of 3 centrifugation steps at 130 g, 1100 g and 11 g, each step for 21 minutes). This corresponds to an excess pressure of 2500, 22 000 and 200 N/m^2, respectively (calculation of excess pressure see below).

Results and Discussion

The results obtained during the first compression/dilatation cycle are depicted in Fig. 5 as variation of the position of the interface between sediment and supernatant upon sequential compression at 130 and 1100 g followed by dilation at 11 g. The position of the interface is added as distance from the centre of rotation (the sediment height is the difference between the position of the bottom of the cell at 113.8 mm and the position of the interface).

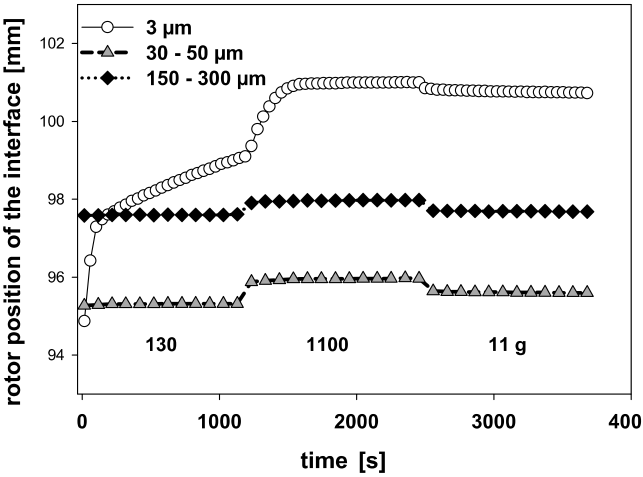

Fig. 5 Compression/dilatation behaviour during centrifugation with stepwise variation of centrifugal acceleration (130, 1100, 11 g)

Beads have a random disordered local distribution initially, which is transferred during consolidation at gravity and centrifugal compression into a more ordered arrangement. In the range of excess pressures applied measurable resistance against compaction is due to attractive particle interactions, i.e. particle aggregates prevent ideal packing. Repulsive particle interactions are necessary to approach ideal packing. Only weak links between particles can be broken during compression. Strong links hinder a regular particle arrangement. Multiple compression/dilatation cycles lead to a gradual approach to optimal packing.

Clear differences between the packing/compression behaviour of beads prepared from viscose (30–50 µm, 150–300 µm) and cellulose acetate (3 µm) are obvious. The former reach the steady states almost instantaneously and exhibit elastic behaviour after dilatation, the latter exhibits a higher resistance to compaction, i.e. a close packing of beads is only slowly approached.

In the following the average packing density (volume fraction) of the sediment Φ is examined as function of the excess pressure applied at the position of the cell bottom P_L. The values of Φ and P_L can be computed as follows [7–9].

$$\Phi = m/(\rho V) \tag{1}$$

$$P_L = (\rho - \rho_0) L \omega^2 m/(\rho A) , \tag{2}$$

where L is the distance of the bottom of the cell from the axis of rotation, ρ and ρ_0 are the densities of the unswollen solid and the liquid, respectively, m the mass of the net solid in the sediment, A the cross sectional area of the rect-

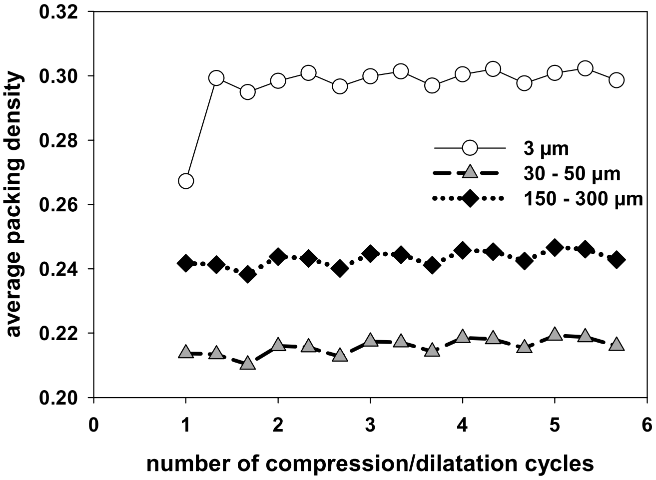

Fig. 6 Dynamic compaction in an alternating centrifugal field, effect of number of compression/dilatation steps

angular cell, ω the angular velocity and V the volume of the sediment.

Equilibrium values for the volume fractions at different compaction pressures are derived from the repeated compression dilatation cycles (Fig. 6).

Figure 6 depicts the average packing densities obtained after sequential compression/dilatation at 130, 1100 and 11 g, that is 3 points for each of the 5 compression/dilatation cycles. The behaviour of the 3 µm beads differs from the others only during the first step of compression. Only a minor increase of packing density with the number of compression/dilatation cycles is detected for all beads. The sediments exhibit nearly ideal elastic behaviour upon release of pressure, i.e. there is no irreversible breakdown of flocculated structure.

The behaviour of cellulose beads is opposite to that of dispersed cellulose powder made from cotton linters [3, 10], which can be considered as a strongly flocculated sample. For the dispersed cellulose powder an increase in packing density of approx. 0.07 during the first compression and an additional increase of 0.01 was experienced during the following cycles resulting in a packing density of 0.32 only.

Based on the approach to equilibrium packing density [3, 10] the interaction between cellulose beads with 3 µm can be classified as weakly attractive, that of beads 30–50 and 150–300 µm as repulsive. Weak attractive forces between the 3 µm cellulose beads may be the result of a small fraction of residual acetyl groups. In contrast to strong attractive interparticle forces an equilibrium packing density close to random close packing has to be expected [10] in both cases. Therefore the difference to the volume fraction for close packing can only be due to the inner porosity of the beads. Assuming a volume fraction of 0.6 for close packing of nonporous particles the maximum packing density obtained for the porous beads of 0.3, 0.24 and 0.215 relates to porosities of 0.5, 0.6 and 0.64 for 3, 150–300 and 30–50 µm beads, respectively. Thus multisample analytical centrifugation provides a powerful alternative for the approximate determination of the cumulative porosity in the swollen state, which is otherwise very laborious. Furthermore, the influence of preparation conditions and solvent effects can easily be traced.

References

1. Wolf B, Horsch W (1991) Pharmazie 46:392
2. Fanter C (2004) Das Papier 4:68
3. Sobisch T, Lerche D (2003) Interaction between tailored particle interfaces characterized by analytical centrifugation. Chemistry Preprint Archive, Volume 2003, Issue 7, p 198–218, http://www.sciencedirect.com/preprintarchive
4. EP AZ 96109778.9 (1999)
5. Lerche D (2002) Dispersion stability and particle characterization by sedimentation kinetics in a centrifugal field. J Dispersion Sci Techn 23:699
6. Sobisch T, Lerche D, Detloff T, Beiser M, Erk A (2005) Tracing the centrifugal separation of fine-particle slurries. Effect of centrifugal acceleration, particle interaction and concentration. Filtration, in press
7. Gilány T, Horváth-Szabó G, Wolfram E (1984) J Coll Interface Sci 98:72
8. Tombácz E, Deér I, Dékány I (1993) Colloids Surfaces A 71:269
9. Tombácz E, Horváth B, Ábráhám I (1993) Colloids Surfaces A 71:277
10. Sobisch T, Lerche D (2004) Characterization of colloidal dispersions by analytical centrifugation. In: Ulrich Teipel (ed) Produktgestaltung in der Partikeltechnologie, Band 2. Fraunhofer IRB Verlag, Stuttgart, p 433–448

Progr Colloid Polym Sci (2006) 133: 173–180
DOI 10.1007/2882_065

J. Köser
F. Kuhnen
D. Saracsan
W. Schröer

Light-scattering in Turbid Fluids: Scattering Intensity and Amplitude of the Auto-correlation Function

J. Köser · F. Kuhnen · D. Saracsan ·
W. Schröer (✉)
Institut für Anorganische und
Physikalische Chemie, Universität Bremen,
28359 Bremen, Germany
e-mail: schroer@uni-bremen.de

Abstract The paper reports a methodological light-scattering study, which compares experimental observations with theoretical concepts and simulation results. The intensity and the amplitude of the auto-correlation function of transparent and turbid suspensions of polystyrene-latex (diameter $\sigma = 112$ nm) with transmissions in the range of $T = 0.9$–99% are investigated. The theory that is applied, corrects for the dead-time effects of the multiplier, the non-ideality of the mono-mode fibre detection optics, and the influence of uncorrelated scattering contributions, which are caused by orthogonal fields and fluctuations that are too fast to be processed by the correlator. The intensities and the amplitudes of the correlation functions of the polarized and the totally scattered light determined experimentally are compared with the results of Monte-Carlo simulations of the polarized and depolarized components of single and multiple scattering.

Keywords Correlation functions · Fibre optics · Light-scattering methodology · Multiple scattering · Simulation

Introduction

Scattered light provides information about size, shape, dynamics and correlations of particles of mesoscopic size [1]. Conventionally, the sources of information are the scattering intensity and the time dependence of the auto-correlation function. Using mono-mode fibres, the amplitudes, also termed intersect, of the correlation functions may become an additional source of information.

While in the traditional setup 0.7 is regarded as a rather good figure for the amplitude of the auto-correlation function, applying mono-mode fibres the amplitude of correlation functions is near to its ideal value of unity [2], provided the scattered light is polarized, and the time scale of the intensity fluctuations is in the range, which can be processed by the correlator. Therefore, mono-mode fibres with integrated gradient index lens (GRIN) replace the aperture system of pin holes and lenses selecting the light for a particular scattering angle in the traditional setup. The fibre technique simplifies the setup and the alignment procedure considerably. The selectivity for the scattering angle is improved substantially, thus the quality of the correlation functions. Deviations of the amplitude from unity provide additional information about the system investigated.

New techniques were developed because of the availability of mono-mode fibres. Of particular interest are the cross-correlation techniques that enable to separate the single scattering from multiple scattering contributions. In the cross-correlation experiments the scattered light of two different experiments with identical scattering vector and identical scattering volume is cross-correlated. Only the singly scattered light contributes to the cross-correlation function [4–13]. Although the pioneering work of Schätzel et al. [4], which analyzes the cross-correlation of the scattered light of two different frequencies, was carried out without using mono-mode fibres, it can be said that other rather delicate cross-correlation experiments as the 3d-cross-correlation technique [5–11] and the one-speckle technique [12, 13] rely on mono-mode fibres. The cross-correlation techniques are useful as long as single scattering is sufficiently strong to allow evaluation. If the transmission is below 1% other methods are more apt e.g. the investigation of backscattering [14] or light-diffusion [15]. These methods also take advantage of fibre optics.

The amplitude of the cross-correlation functions depends in a rather complicated way on the optical details of the setup [16]. Beside that it is determined by the ratio of the single-scattering intensity to the total scattering intensity. Therefore, multiplying this ratio by the total scattering intensity yields the single-scattering intensity [4–13]. Vice versa the intensity of the multiply scattered light and the sum of the multiple-scattering correlation functions [8, 17, 18] can be determined by subtracting the single-scattering correlation function from the auto-correlation function. This straight forward procedure, applied in former work [8, 17], implies linearity of the multiplier and unity of the amplitude of the auto-correlation function. Those presumptions are correct only approximately: The multiplier is not linear and the amplitudes of the autocorrelation functions deviate from unity even when using mono-mode fibres. Hence appropriate corrections should be applied.

It is the purpose of this paper to provide and test tools that enable accurate estimates of the scattering intensities and of the contributions to the correlation functions of the single- and multiple-scattering. This requires corrections for deficits of the multiplier as dead-time effects and dark current, for the non-ideality of the mono-mode fibres and for uncorrelated scattering contributions. In this work we analyze the count rate and the amplitude of the experimental auto-correlation function of the total scattering intensity and of the polarized component. We investigate transparent and highly turbid suspensions of polystyrene latex spheres. The theory applied is based on the work of Flammer and Rička [20, 21], which is quite general but focuses on the multiplier dead-time effect. The influence of the dead-time effect was investigated experimentally in [21] and taken into account in [18]. Extending the work of [20] we consider in theory and experiment non-ideal fibres using the theory of Schätzel, which was developed for the conventional aperture optic, and include the contributions of the dark current and other non-correlated scattering contributions. In particular we discuss the influence of the depolarized scattering, which in the system investigated is caused by multiple-scattering. Finally, we compare the amplitudes of the auto-correlation function obtained from the experiment with that estimated from simulation results of the scattering processes in the sample.

Theory

In light-scattering experiments the count rate r, which is the number of photons counted by a multiplier in a certain time interval, is measured and the correlation between count rates at different times is determined by means of a correlator. For an ideal detector, the photons are counted once and only once. With the photon energy $h\nu$ the intensity is $I = r \cdot h\nu$. The electro-dynamic theory, given in the textbooks, concerns the average intensity $\langle I(\boldsymbol{q})\rangle$ and the auto-correlation function of the intensity of the scattered light [1]. The scattering vector $\boldsymbol{q}$ is the difference between the wave vectors of the incident and of the scattered light. The intensity-correlation function is given by the average intensity and the normalized field correlation function $g^{(1)}(\boldsymbol{q}, t)$

$$\begin{aligned}&\langle I(\boldsymbol{q}, 0) \cdot I(\boldsymbol{q}, t)\rangle \\ &= \langle I(\boldsymbol{q})\rangle^2 \left(1 + \beta^2 g^{(1)}(\boldsymbol{q}, t) \cdot g^{(1)}(\boldsymbol{q}, t)^*\right), \end{aligned} \tag{1}$$

$$g^{(1)}(\boldsymbol{q}, t) = \frac{\left\langle \boldsymbol{E}(\boldsymbol{q}, 0) \cdot \boldsymbol{E}(\boldsymbol{q}, t)^*\right\rangle}{\left\langle \boldsymbol{E}(\boldsymbol{q}, 0) \cdot \boldsymbol{E}(\boldsymbol{q}, 0)^*\right\rangle} \tag{2}$$

for stationary systems, if Gaussian statistics applies to the fluctuations of the electric field $\boldsymbol{E}$ at the detector. Note, that $I = \frac{c}{8\pi}\boldsymbol{E} \cdot \boldsymbol{E}$, where c is the velocity of light. The field $\boldsymbol{E}(\boldsymbol{q}, t)$ of the scattered light is determined by the spatial Fourier transform of the dielectric permittivity at time t, so that the experiment yields the correlation function of the Fourier transform of the fluctuations of the dielectric permittivity. In the ideal experiment the amplitude factor β equals unity. In the traditional setup β deviates, because the wave vector selectivity is rather poor, so that light of different $\boldsymbol{q}$-vectors, which is uncorrelated, is received by the detector. To large extend this shortcoming is remedied by the fibre optics [2]. However, deficiencies of the fibre optics and the characteristic of photon multiplier as well as background scattering cause β to deviate from its ideal value and remain to be accounted for.

The interrelation between Eq. 1 and the photon count rate is trivial for an ideal detector. More generally, except for a factor (Eq. 1) applies for linear detectors, where the experimental count rate is linearly related by the quantum efficiency to the light-intensity. In general the relation between the photon count rate r and the intensity I of photons is nonlinear [19], which should be taken into account, when estimating the time average $\langle I(\boldsymbol{q})\rangle$, which is also a nonlinear function of the average count rate $\langle r\rangle$. While it is simple matter to determine the nonlinearity of the detector beforehand, the intensity correlation function given in Eq. 1 is in a nontrivial way related to the correlation function of the photon count rates r obtained from the experiment. As shown by Flammer and Rička the amplitude of the correlation function may be used to determine the multiplier characteristic [20, 21].

Schätzel [19] has discussed two models for non-linear detectors, the paralyzable and the non-paralyzable detector, characterized by the response functions

$$r = I \cdot \exp(-\theta \cdot I) \tag{3}$$

and

$$r = I / \left(1 + \theta \cdot I\right) \ , \tag{4}$$

respectively. Here θ is the dead time of the multiplier. The quantum efficiency of the multiplier would enter the equations as a linear factor and is therefore put to unity for simplicity of notation. With the paralyzable detector the count rate vanishes at high intensities, while the non-paralyzable detector reaches a constant limit. Schätzel investigated also a superposition of the two cases. According to Flammer and Rička an expansion up to third order in I is sufficient for the light-scattering purposes [20].

$$r = I(1 - \theta I + \theta^2 \phi I^2) \tag{5}$$

The coefficient ϕ accounts for the superposition of the two cases. For the non-paralyzable detector it holds $\phi = 1$, while $\phi = 1/2$ for the paralyzable detector.

The photon statistics is expected to satisfy a Γ-distribution [19]

$$p\left(I\right) = \left(\frac{\gamma I}{\langle I \rangle}\right)^{\gamma - 1} \frac{\gamma \exp\left(-\gamma I / \langle I \rangle\right)}{\langle I \rangle \, \Gamma\left(\gamma\right)} \ . \tag{6}$$

Here γ denotes the number of coherence areas accepted by the aperture. For mono-mode fibres it holds $\gamma = 1$ and the distribution reduces to the exponential distribution. The momentum generating function or characteristic function $M_1\left(s\right)$ [19, 22]

$$M_1\left(s\right) = \langle \mathrm{e}^{-sI} \rangle = \left(1 + \frac{s \langle I \rangle}{\gamma}\right)^{-\gamma} \tag{7}$$

is obtained by averaging the exponential e^{-sI} with the distribution $p\left(I\right)$.

The required moments $\langle I^n \rangle$ can be derived either by integration using the distribution $p\left(I\right)$ or else by differentiating the characteristic function in respect of the parameter s at $s = 0$. The Γ-distribution implies

$$\langle I^2 \rangle = \langle I \rangle^2 \left(1 + \frac{1}{\gamma}\right) \ , \tag{8}$$

which describes the reduction of the amplitude of the correlation function by the number of coherence areas passing the aperture.

Averaging the count rate given in Eq. 5 yields

$$\langle r \rangle = \langle I \rangle \left(1 - \theta \langle I \rangle \frac{1 + \gamma}{\gamma} + \phi \cdot \theta^2 \langle I \rangle^2 \frac{\left(1 + \gamma\right)\left(2 + \gamma\right)}{\gamma^2}\right) \ . \tag{9}$$

Mathematica 5.1 is used for carrying out lengthy algebra. If the characteristic parameters θ, ϕ, and γ of the detection optics are known, the true intensity can be calculated by inversion of Eq. 9 from the experimental count rate. Solving the cubic Eq. 9 and expanding in $\langle r \rangle$, θ and ϕ yields

$$\begin{aligned} \langle I \rangle = \ & \langle r \rangle \left(1 + \theta \langle r \rangle \frac{\gamma + 1}{\gamma} \right. \\ & \left. + \theta^2 \langle r \rangle^2 \frac{\gamma + 1}{\gamma} \cdot \frac{2(1 + \gamma) - \phi \cdot (\gamma + 2)}{\gamma}\right) \ . \end{aligned} \tag{10}$$

Flammer and Rička [20] proposed an elegant way to determine parameters θ and ϕ from the amplitude of the auto-correlation function. For this purpose the correlation function $\langle r_1 \cdot r_2 \rangle$ of two photon currents r_1 and r_2 as given in Eq. 5 is calculated. The indices here refer to different times. This calculation is straight forward, when employing the characteristic function of the two-point Γ-distribution for correlated events, given by Schätzel [19].

$$\begin{aligned} M_2\left(s_1, s_2\right) &= \langle \mathrm{e}^{-s_1 I_1 - s_2 I_2} \rangle \\ &= \left(1 + \frac{1}{\gamma} \langle I_1 \rangle s_1 + \frac{1}{\gamma} \langle I_2 \rangle s_2 \right. \\ & \qquad \left. + \left(\frac{1}{\gamma}\right)^2 \langle I_1 \rangle \langle I_2 \rangle s_1 s_2 \left(1 - g^2\right)\right)^{-\gamma} \end{aligned} \tag{11}$$

For $\gamma = 1$ the Γ-distribution reduces to the exponential distribution [17].

For simplicity of notation we use a shorthand notation $g \equiv g^{(1)}\left(\boldsymbol{q}, t\right)$. The various moments $\left\langle I_1^m I_2^n \right\rangle$, required for evaluating the count-rate correlation function $\langle r_1 \cdot r_2 \rangle$, are calculated as the derivatives of the characteristic function in respect to s_1 and s_2 at $s_1 = 0$ and $s_2 = 0$. The result is

$$\begin{aligned} \langle r_1 r_2 \rangle &\equiv \langle r \rangle^2 \left(1 + g_{\mathrm{exp}}^2\right) \\ &= \langle I \rangle^2 \left(1 + \frac{1}{\gamma} g^2\right) - 2\theta \langle I \rangle^3 \frac{1 + \gamma}{\gamma^2} \left(2g^2 + \gamma\right) \\ & \quad + \theta^2 \langle I \rangle^4 \frac{1 + \gamma}{\gamma^2} \left(2g^4 + \gamma\left(1 + \gamma + 2\left(2 + \gamma\right)\phi\right) \right. \\ & \quad \left. + 2g^2\left(2 + 6\phi + \gamma(2 + 3\phi)\right)\right) \ . \end{aligned} \tag{12}$$

By g_{exp} we have denoted the correlation function of the experimental count rate, commonly identified with g, which is not quite correct. It remains to express $\langle I \rangle$ by the measurable quantity $\langle r \rangle$, which leads to a quadratic equation relating g^2 to g_{exp}^2.

$$\begin{aligned} g_{\mathrm{exp}}^2 = \frac{1}{\gamma} g^2 & \left(1 - 2 \langle r \rangle \frac{1 + \gamma}{\gamma} \theta \right. \\ & \left. + \langle r \rangle^2 \frac{1 + \gamma}{\gamma^2} \left(2g^2 - 3\left(1 + \gamma\right) + 4\left(2 + \gamma\right)\phi\right)\right) \end{aligned} \tag{13}$$

By solving the quadratic equation for g^2 an expression of g^2 as function of g_{exp}^2 is obtained. For zero time, when $g\left(0\right) = 1$ Eq. 13 describes the amplitude of the count rate correlation function $g_{\mathrm{exp}}(0)$ as function of $\langle r\rangle$ with the fit parameters γ, θ and ϕ.

Methods

Experiment

The apparatus is the 3d-cross-correlation setup, which was used in former work and described in detail there [8, 17, 18]. Here we have analyzed the light of one scattering plane. The beam of a 10 mW He – Ne laser (Uniphase) is split into two parallel beams (intensity ratio 82.8%) and focused into the sample. The intensities of the incoming and transmitted light are measured with the help of photodiodes calibrated with a power meter (field master, Coherent Radiation). On the detection side the scattered light is collected by two mono-mode fibres with an integrated GRIN optics (BFI Optilas), detected by the double photon multiplier (ALV/SO-SIPD) and processed by a digital correlator (ALV-5000/E). In order to allow measurements at different scattering angles the detection arm carrying the fibre optics is rotated by a computer controlled turntable (Newport 496).

Cylindrical (inner diameter 0.80 cm) sample cells (Hellma) were filled by weight, flame sealed and positioned in a glass cylinder (outer diameter 9.93 cm) (Hellma) filled with water and thermostated to 295.150 ± 0.002 K using a computer controlled two stage heating. The polarization of the scattered light was fixed by a polarization foil with an extinction ratio 3/1000 fitted around the thermostating glass cylinder. Suspensions of spherical latex particles (DOW, EM-specified diameter $\sigma = 112 \pm 1.5$ nm, refractive index $n_{\mathrm{L}} = 1.59$) in a solution 0.4 g/l Sodium dodecyl sulfat in deionized water cleaned further by a Millipore filter were investigated. Intensity and correlation functions of the total scattering intensity and of the polarized contribution were measured. Measurements of the depolarized scattering were not carried out because the separation of the depolarized component from the polarized part by the polarization foil appeared to be insufficient. The transmissions of the samples (weight fraction 2.61×10^{-3}, 1.57×10^{-3}, 8.73×10^{-4}, 4.04×10^{-4}, 9.72×10^{-5}, 2.8×10^{-5}, 1.0×10^{-5}, 3.4×10^{-6}) were determined to be 0.9%, 5.3%, 19%, 40%, 71%, 90%, 97% and 99%.

Monte Carlo Simulations

We compare our experimental results with Monte Carlo simulations performed on the basis of the method of Bailey and Cannell [23]. The program used was written by Kleemeier [24] and modified for this work. The program was originally developed to account for multiple-scattering effects in opalescent fluids near the critical point. Therefore the angle dependence of the scattering cross-section was described by a Lorentz-function. For simulating colloidal systems we have included other forms of scattering cross-sections namely the form factor predicted by the Rayleigh–Gans theory [25] and the Gaussian approximation $\exp[-q^2\sigma^2/20]$, which is used in this work.

The simulation method models the incident laser beam as a large number of photons (10^8–10^9), which are launched into the sample. The probability distribution for the distance a photon travels in the sample and between two scattering events is determined by the turbidity of the scattering medium, which is the reciprocal length of the free path of the photons. The probability for a certain scattering direction is given by the angle dependence of the scattering cross section of the particles. After scattering the photon travels again a randomly chosen free path length and is scattered anew. If the last scattering event of the photon before leaving the sample is within a predefined volume given by the geometry of the sample the scattering event is recorded. In that way the numbers of singly, doubly and multiply scattered photons for various scattering angles are available. We select the contributions of polarized and depolarized scattering within the plane perpendicular to the field of the incident beam to be compared with the experiment.

The Monte Carlo calculations were performed by assuming a Gaussian intensity distribution with a $1/\mathrm{e}^2$ diameter of 0.254 mm and a Gaussian aperture function with a $1/\mathrm{e}^2$ diameter of 1.24 mm.

Results

Analysis of Polarized Scattered Light

For linear detectors the amplitude of the experimental correlation function g_{exp} is $1/\sqrt{\gamma}$, where γ is the number of coherence areas. Nonlinearity of the multiplier causes a variation of the amplitude with the detected photon current, which is in general a nonlinear function of the intensity.

The Fig. 1a shows the amplitude of the auto-correlation functions $g^{(1)}_{\mathrm{exp}}$ of the *polarized* component of the scattered light. With the exception of the data at very small count rates, the experiment yields a linear dependence of $g^{(1)}_{\mathrm{exp}}$ from the count rate $\langle r\rangle$. Independent of the transmission of the samples and of the scattering angles all data are located at a master plot, which is linear in $\langle r\rangle$ with an intercept near unity. The deviation of γ from unity is small, so that we write $\gamma = 1 + \Delta\gamma$ and use an expansion of Eq. 13, which is linear in $\Delta\gamma$ and $\langle r\rangle$.

$$g_{\mathrm{exp}} = \left(1 - \frac{\Delta\gamma}{2} - 2\,\langle r\rangle\,\theta\,(1-\Delta\gamma)\right)\cdot g\,. \tag{14}$$

The fit yields $\Delta\gamma = 0.007 \pm 0.002$ and $\theta = (1.41 \pm 0.2)\cdot 10^{-8}$ s.

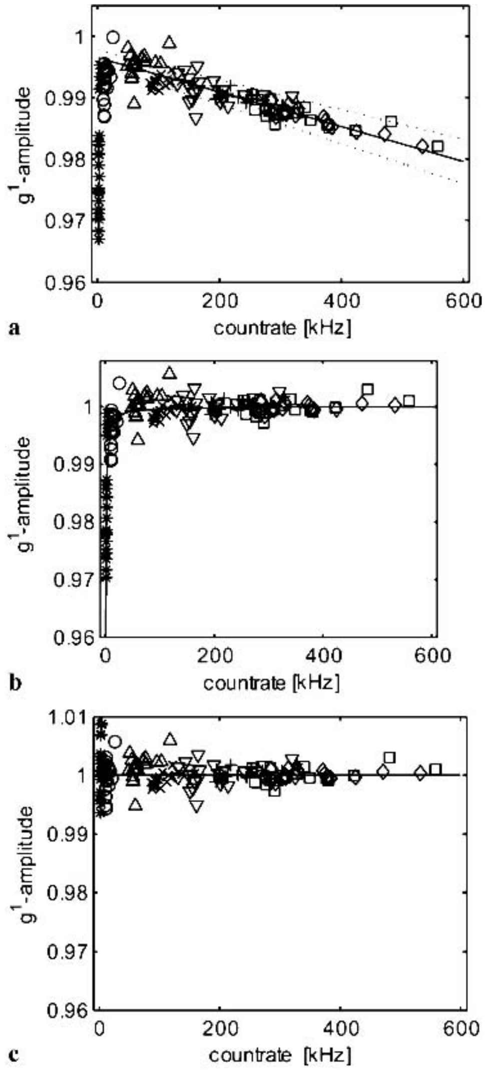

Fig. 1 Amplitude of the field correlation function $g^{(1)}$ as function of the count rate. **a** as determined from the count rate correlation function of the polarized light; the *line* is the fit with Eq. 14 the *dashed lines* give the confidence interval, **b** after correcting for the dead time of the multiplier and the deviation of the single mode detection; the *line* is the fit with Eq. 18, **c** after correcting also for fast processes; the *line* is calculated from the inversion of Eq. 18. The data concern different scattering angles. The symbols refer to samples of different transmission T, which are 99% (*), 97% (○), 90% (△), 71% (▽), 40% (□) 19% (◇), 5.3% (+), and 0.9% (×)

The inversion of Eq. 14, shown in Fig. 1b shows no variation of the amplitude with the count rate with the exception of the drop at count rates below 26 kHz, which is not described by Eq. 14. This effect is based on the fact that different processes may contribute to the correlation function. In general, the scattering intensity I is a sum of a contribution of the desired scattering intensity I_s, and two background intensities I_b and I_f that are either too slow or too fast to be processed by the photon-correlator [20]. Analogously the corresponding field is

$$\boldsymbol{E} = \boldsymbol{E}_\text{f} + \boldsymbol{E}_\text{s} + \boldsymbol{E}_\text{b}\,. \tag{15}$$

The intensity correlation function is then obtained by averaging

$$\begin{aligned}\langle I(0)\cdot I(t)\rangle &= \left(\frac{c}{8\pi}\right)^2 \left\langle \boldsymbol{E}(0)\cdot\boldsymbol{E}(0)^*\cdot\boldsymbol{E}(t)\cdot\boldsymbol{E}(t)^*\right\rangle\\ &= \langle I\rangle^2 + \left(\frac{c}{8\pi}\right)^2 \left\langle \boldsymbol{E}(0)\cdot\boldsymbol{E}(t)^*\right\rangle\\ &\quad\times\left\langle \boldsymbol{E}(0)^*\cdot\boldsymbol{E}(t)\right\rangle\,.\end{aligned} \tag{16}$$

When working out the field correlation functions, all terms involving $\boldsymbol{E}_\text{f}$ and all mixed terms as $\left\langle \boldsymbol{E}_\text{b}(0)\cdot\boldsymbol{E}_\text{s}(t)^*\right\rangle$ vanish, while $\frac{c}{8\pi}\left\langle \boldsymbol{E}_\text{b}(0)\cdot\boldsymbol{E}_\text{b}(t)^*\right\rangle = I_\text{b}$ and $\frac{c}{8\pi}\left\langle \boldsymbol{E}_\text{s}(0)\cdot\boldsymbol{E}_\text{s}(t)^*\right\rangle = I_\text{s}g_\text{s}$.

Applying those rules one gets

$$g^2 = j_\text{b}^2 + 4j_\text{b}j_\text{s}g_\text{s} + j_\text{s}^2g_\text{s}^2\,, \tag{17}$$

where $j_\text{b} = \langle I_\text{b}\rangle/\langle I\rangle$ and $j_\text{s} = \langle I_\text{s}\rangle/\langle I\rangle$. By g_s we denote the normalized field correlation function of $\boldsymbol{E}_\text{s}$. The term linear in g_s is the heterodyne contribution. In our experiment a static background j_b is not present. If heterodyne contributions (e.g., due to scratches at the windows) were present, the correlation function g would not vanish at large times and the amplitude would exceed unity at $t = 0$. The background caused by processes too fast to be accepted by the correlator may be due to the dark current of the multiplier (0.025 kHz) and fast motions of smaller particles. With Eq. 17, putting $j_\text{s} = 1 - j_\text{f}$ and $j_\text{f} = \langle I_\text{f}\rangle/\langle I\rangle$ Eq. 14 becomes

$$g_\text{exp} = \left(1 - \frac{\langle r_\text{f}\rangle}{\langle r\rangle}\right)\left(1 - \frac{\Delta\gamma}{2} - 2\langle r\rangle\,\theta\,(1-\Delta\gamma)\right)\cdot g_\text{s}\,. \tag{18}$$

The intensity ratio j_f is approximated by the ratio of the count rates as this correction becomes important only at low count rates. The count rates measured at 90° on a sample without latex is 0.058 kHz. The best fit yields 0.043 ± 0.008 kHz for $\langle r_\text{f}\rangle$, which is larger than the dark current and indicates the presence of some faster processes in the sample that cannot specified any further here. Putting $g_\text{s}(\boldsymbol{q}, 0) = 1$, the amplitudes shown in Fig. 1b are well described by Eq. 18. The inversion of Eq. 18 yields $g_\text{s}(\boldsymbol{q}, 0) \approx 1$ from $g_\text{exp}(\boldsymbol{q}, 0)$. This is shown in Fig. 1c.

By definition a time correlation function should start with unity at $t = 0$. However, the experimental correlation functions of the photon current do not. It is therefore quite remarkable that the inversion of Eq. 18 suffices to transform the real data into such of an ideal experiment, which may be compared with simulations. In order to compare simulation results with experiments it is necessary to correct the experiments for the deficiencies of the setup beforehand. In Fig. 2a we show the count rates measured for the samples of different turbidity. The data have been corrected using a simplified form of Eq. 10 that takes into

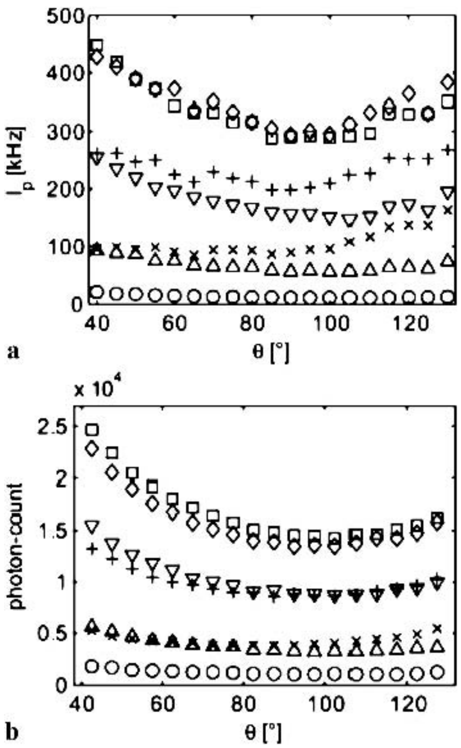

Fig. 2 Measured (**a**) and simulated (**b**) photon count rate of the polarized scattering intensity of samples of different transmission as function of the scattering angle. The experimental data are corrected for the dead time, the dark current of the multiplier and the deviation of the fibre from the mono-mode specification. The samples and the corresponding symbols are the same as in Fig. 1

account only terms linear in θ and $\Delta\gamma$. The difference to the original data would not be visible in the figure as it is only 2%. Figure 2b shows the corresponding results of the simulation, which agree rather well with the experimental data, shown in Fig. 2a. The deviations between experiments and simulation at large scattering angles in samples with high turbidity need further investigations.

The intensity becomes large for scattering angles near 0° and 180°, where the scattering volume reaches maximal values. In order to get the scattering cross-section, the data have to be corrected for the angular dependence of the scattering volume, the loss due turbidity, and for the number density of the sample.

The method applied for correcting the experimental correlation functions for the deficiencies of the apparatus does not depend on specific properties of the sample as the scattering cross section of the particles, the scattering volume, the turbidity or multiple scattering contributions. Although in the samples of low transmission multiple scattering contributes to the scattering intensity and to the correlation function, the sum of the correlation functions of single scattering and of the various multiple scattering contributions is normalized so that $g_s(\boldsymbol{q}, 0) \approx 1$. The normalization is ensured, because the polarization of the detected fields is the same. When fields differing in the direction of polarization contribute, one finds $g_s(\boldsymbol{q}, 0) < 1$, which is the case, when investigating the total scattering intensity.

Analysis of the Total Scattering

Figure 3a shows the amplitudes of the correlation functions, when the *total* scattered intensity is analyzed.

The data have been corrected for apparatus deficiencies, determined in Analysis of Polarized Scattered Light using Eq. 18. Nevertheless, we see a rather complicated variation of the amplitudes with the scattering intensity. For small concentrations of the colloid the amplitude is reduced linearly with increasing scattering intensity. At a transmission between 40% and 19% the amplitude becomes smaller although the total scattering intensity is reduced because of the loss due turbidity. For a given sample the amplitudes are rather unsymmetrical to the minimum at 90°. The lower branch represents the amplitude for scattering angles above 90°.

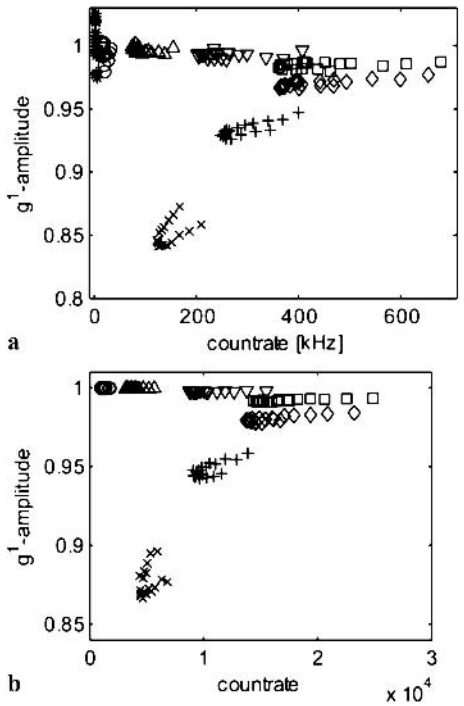

Fig. 3 Measured (**a**) and calculated (**b**) amplitude of the field correlation function of the total intensity of the scattered light as function of the count rate. The experimental data (**a**) are corrected for the dead time of the multiplier, fast processes, and the deviation of the single mode detection in order to allow for comparison with the simulations. At transmissions below $T \approx 30\%$ the amplitude is reduced in spite the fact that the count rate is also reduced. The amplitude varies as described by Eq. 21 because the measured polarized and depolarized scattering contributions are not correlated. Samples and the corresponding symbols are the same as in Fig. 1

In order to analyse this effect, the intensity correlation function, given in Eq. 16, is worked out. The total scattered intensity $\langle I_\mathrm{s} \rangle$ is a sum of $\langle I_\mathrm{p} \rangle$, the part with the electric field vector perpendicular to the scattering plane termed polarized, and $\langle I_\mathrm{d} \rangle$, the depolarized contribution where the field is parallel to the scattering plane. As the fields $\boldsymbol{E}_\mathrm{p}$ and $\boldsymbol{E}_\mathrm{d}$ are orthogonal, the scalar products $\boldsymbol{E}_\mathrm{p} \cdot \boldsymbol{E}_\mathrm{d}$ do not contribute to the fluctuating intensity. We apply this rule when evaluating Eq. 16 and get

$$\langle I_\mathrm{s} \rangle^2 \left(1 + g_\mathrm{s}^2\right) = \left(\langle I_\mathrm{p} \rangle + \langle I_\mathrm{d} \rangle\right)^2 + \langle I_\mathrm{p} \rangle^2 g_\mathrm{p}^2 + \langle I_\mathrm{d} \rangle^2 g_\mathrm{d}^2 \,. \quad (19)$$

$$g_\mathrm{s}^2 = \frac{\langle I_\mathrm{p} \rangle^2}{\langle I_\mathrm{s} \rangle^2} g_\mathrm{p}^2 + \frac{\langle I_\mathrm{d} \rangle^2}{\langle I_\mathrm{s} \rangle^2} g_\mathrm{d}^2 \,. \quad (20)$$

Therefore, the amplitude is

$$g_\mathrm{s}\left(\boldsymbol{q}, 0\right)^2 = \frac{\langle I_\mathrm{p} \rangle^2 + \langle I_\mathrm{d} \rangle^2}{\left(\langle I_\mathrm{p} \rangle + \langle I_\mathrm{d} \rangle\right)^2} \,. \quad (21)$$

Figure 3b shows the results of the simulations of Eq. 21. The results of the simulation agree nicely with the experimental findings shown in Fig. 3a.

In order to gain insight, we have a closer look on the simulation results of the scattering intensities. The data presented in Fig. 4 show that for a transmission of 0.9% the majority of the scattered light is scattered more than once.

The contributions of depolarized scattering are about one order of magnitude smaller than that of the polarized scattering. The contribution of single scattering has no depolarized component $\langle I_\mathrm{d} \rangle$. The depolarized contribution of the double scattering is also expected to be small since the two scattering processes occur within the scattering plane. Even, the triple scattering contributes only 10% to the depolarized scattered light, which arises from higher order multiple scattering.

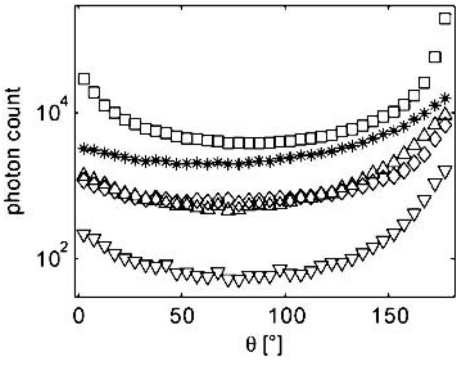

Fig. 4 Contributions of the scattering intensity as calculated for a highly turbid sample ($T = 0.9\%$) as function of the scattering angle. The figure shows the calculation results for polarized scattering (□), depolarized scattering (◇), triple scattering (△), multiple scattering beyond double scattering (*), and the depolarized contribution to the triple scattering (∇)

Measuring the amplitude of the auto-correlation function Eq. 21 enables determining the ratio the depolarized component $\langle I_\mathrm{d} \rangle$ of the scattered light to the total scattering intensity $\langle I_\mathrm{s} \rangle$.

This is shown in Fig. 5, where we compare the figures of $j_\mathrm{d} = \langle I_\mathrm{d} \rangle / \langle I_\mathrm{s} \rangle$ derived from the amplitudes of the auto-correlation functions with that obtained from the simulations. The agreement is reasonable, but the experimental values are systematically larger than that obtained from the simulations. It is outside the scope of this work to clarify this discrepancy.

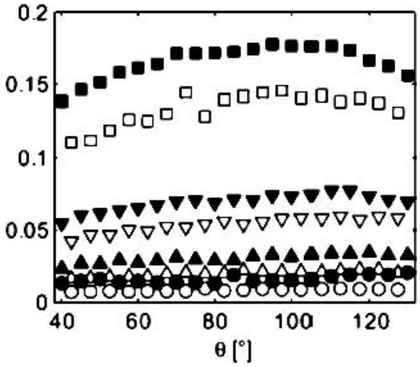

Fig. 5 Ratio of the depolarized to the total scattering intensity $j_\mathrm{d} = \langle I_\mathrm{d} \rangle / \langle I_\mathrm{s} \rangle$. The data represented by *full symbols* are derived from the experimental amplitudes of the auto-correlation function, while the data represented by *open symbols* are the simulation results. The symbols refer to samples of different transmission T, which are 0.9% (□, ■), 5.3% (▽, ▼), 19% (△, ▲), and 40% (○, ●)

Conclusions

In this work we have reviewed, modified and tested the theories of Schätzel [19] and Flammer and Rička [20, 21]. In general the measured count rates and their correlation functions are in a non-trivial way related to the desired scattering intensity and to the intensity correlation function. Applying the theory, the investigation of the amplitude of the auto-correlation function of the polarized scattered light enables to determine the dead time of the multiplier, and the number of modes accepted by the fibre optics. For transparent samples, the amplitude is determined by the dark current and uncorrelated background scattering due to processes faster than processed by the correlator. With the parameters determined in this way the experimental count rate and correlation function obtained from the correlator can be transformed into the scattering intensity and the corresponding correlation function of the scattering processes. Considering the total scattering intensity the theory needs a further modification, which takes into account that the polarized and depolarized components are not correlated.

The theory assesses the deficiencies of the setup and the influence of fast and depolarized scattering contributions on the correlation function. It is independent of the microscopic properties of the sample, thus applies generally. The interpretation of the fast processes and/or the depolarized contributions influencing the amplitudes of the correlation functions is a different matter. For getting more detailed information additional work is required e.g., measurements of the concentration dependence, investigations by other scattering techniques as Rayleigh-Brillouin or Raman-spectroscopy and simulations.

For the latex suspensions, considered here, simulations of the polarized and depolarized components of the scattering intensities allow the modelling of the amplitudes of the auto-correlation functions in reasonable agreement with the experiment. The depolarized scattering intensity results from triple and higher order scattering. The simulations carried out assume uncorrelated, spherical particles, which give no depolarized contribution to the single-scattering intensity. A Gaussian scattering function was chosen as an approximate of the Mie scattering function. Noticeable, the Gauss function is exact, when considering polymers described by a Gaussian coil. Other scattering functions for particles with spherical symmetry can easily be adopted, while the consideration of non-spherical particles with depolarized single-scattering contributions and correlated particles would require a different approach.

Concluding we emphasize that deviations of the amplitudes from unity, that remain after correcting for the deficiencies of the setup, indicate contributions of orthogonal fields and/or such of scattering processes that are too fast to be processed by the correlator. Neglecting such contributions can lead to erroneous interpretations of the measured scattering intensity e.g. to wrong critical exponents [26]. Therefore, the analysis of the amplitudes of the correlation functions can provide additional useful information missed in the conventional light scattering experiment.

Acknowledgement Dr. M. Kleemeier is thanked for discussions and the simulation program, modified in this work. Support by the Zentrale Forschungskommission of the Universität Bremen is appreciated.

References

1. Berne BJ, Pecora R (1976) Dynamic Light Scattering. Wiley, New York
2. Rička J (1993) Applied Optics 32:2860
3. Schätzel K (1991) J Mod Optics 38:1849
4. Schätzel K, Drewel M, Ahrens J (1990) J Phys Condens Matter 2SA:393
5. Overbeck E, Sinn EC, Palberg T (1997) Prog Colloid Polym Sci 104:117
6. Overbeck E, Sinn C (1999) J Mod Opt 46:303
7. Aberle LB, Wiegand S, Schröer W, Staude W (1997) Prog Colloid Polym Sci 104:121
8. Aberle LB, Hülstede P, Wiegand S, Schröer W, Staude W (1998) Appl Opt 37:6511
9. Urban C, Schurtenberger P (1997) Prog Colloid Polym Sci 110:61
10. Urban C, Schurtenberger P (1998) J Colloid Interface Sci 207:150
11. Pusey PN (1999) Curr Opin in Coll and Interf Sci 4:177
12. Meyer WV, Cannell DS, Smart AE, Taylor TW, Tin P (1997) Appl Opt 36:7551
13. Schröder JM, Wiegand S (2000) Phys Chem Chem Phys 2:1493
14. Wiese H, Horn D (1991) J Chem Phys 94:6429
15. Maret G, Wolf PE (1987) Z Phys B Condens Matter 65:409
16. Schröer W (2002) J Mol Liquids 98/99:225
17. Aberle LB, Kleemeier M, Hülstede P, Wiegand S, Schröer W, Staude W (1999) J Physics D Appl Physics 32:22
18. Sevenard E, Schröer W (2002) Phys Chem Chem Phys 4:1900
19. Schätzel K, Kahlström R, Stampa B, Ahrens J (1998) J Opt Soc A B6:937
20. Flammer I, Rička J (1997) Appl Opt 36:7508
21. Overbeck E, Sinn C, Flammer I, Rička J (1998) Rev Sci Instr 69:3515
22. Saleth B (1978) Photoelectron Statistics. Springer, Berlin
23. Bailey A, Cannell DS (1994) Phys Rev E 50:4853
24. Wiegand S, Briggs ME, Levelt Sengers JMH, Kleemeier M, Schröer W (1998) J Chem Phys 109:9038
25. Bohren CF, Huffmann DR (1983) Absorption and Scattering of Light by Small Particles. Wiley, New York
26. Wagner M (2004) PhD Thesis, Bremen

Progr Colloid Polym Sci (2006) 133: 181–182

AUTHOR/TITLE INDEX

Progr Colloid Polym Sci (2006) 133: 183–184

KEY WORD INDEX